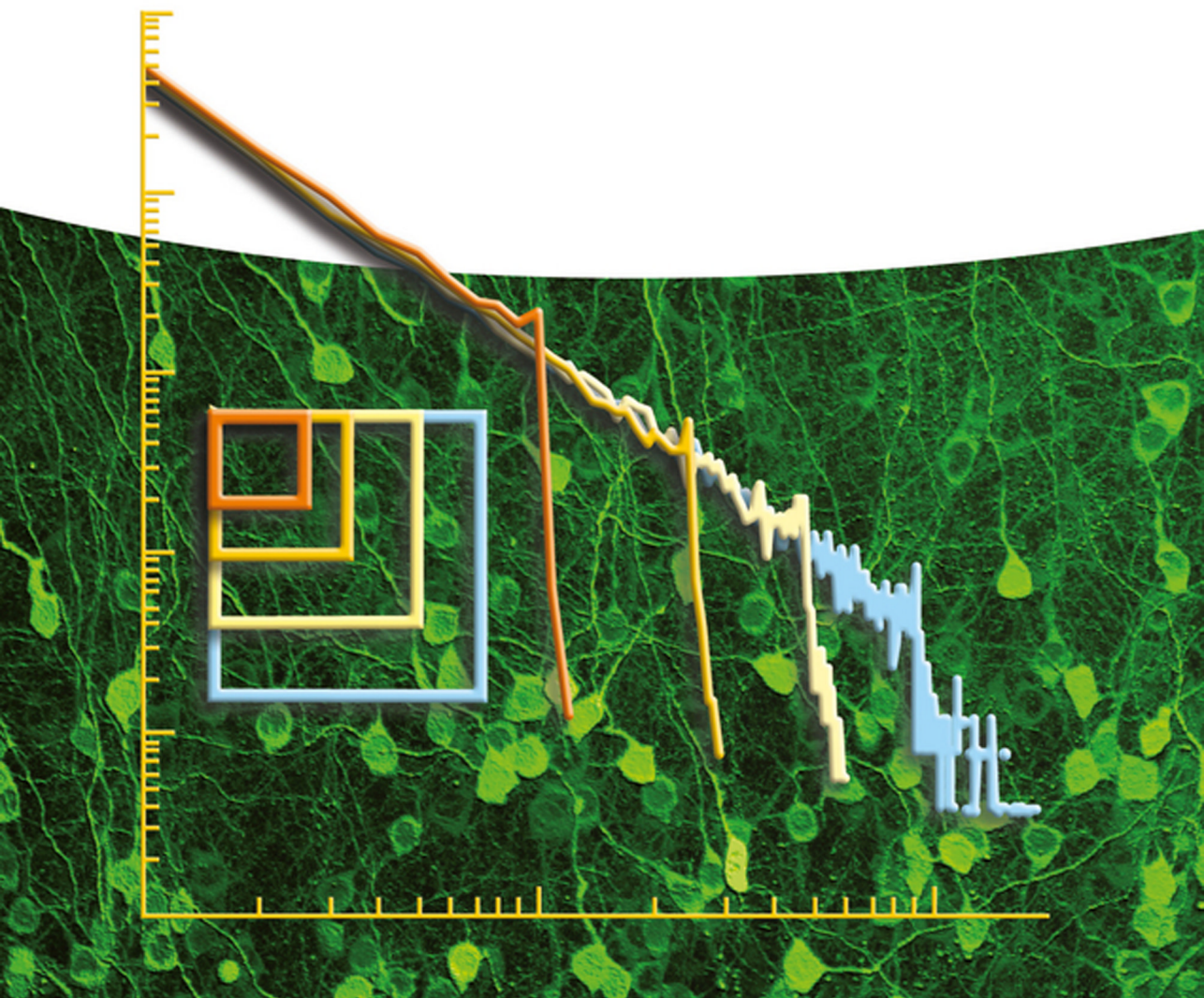


Edited by

Dietmar Plenz and Ernst Niebur

Criticality in Neural Systems



Reviews of Nonlinear Dynamics and Complexity

Edited by

Dietmar Plenz and Ernst Niebur

Criticality in Neural Systems

Reviews of Nonlinear Dynamics and Complexity

Schuster, H. G. (ed.)

Reviews of Nonlinear Dynamics and Complexity

Volume 1

2008

ISBN: 978-3-527-40729-3

Schuster, H. G. (ed.)

Reviews of Nonlinear Dynamics and Complexity

Volume 2

2009

ISBN: 978-3-527-40850-4

Schuster, H. G. (ed.)

Reviews of Nonlinear Dynamics and Complexity

Volume 3

2010

ISBN: 978-3-527-40945-7

Grigoriev, R. and Schuster, H.G. (eds.)

Transport and Mixing in

Laminar Flows

From Microfluidics to Oceanic Currents

2011

ISBN: 978-3-527-41011-8

Lüdge, K. (ed.)

Nonlinear Laser Dynamics

From Quantum Dots to Cryptography

2011

ISBN: 978-3-527-41100-9

Klages, R., Just, W., Jarzynski (eds.)

Nonequilibrium Statistical Physics of Small Systems

Fluctuation Relations and Beyond

2013

ISBN: 978-3-527-41094-1

Plenz, D., Niebur, E., Schuster, H.G. (eds.)

Criticality in Neural Systems

2014

ISBN: 978-3-527-41104-7

Pesenson, M. M. (ed.)

Multiscale Analysis and Nonlinear Dynamics

From Genes to the Brain

2013

ISBN: 978-3-527-41198-6

Edited by Dietmar Plenz and Ernst Niebur

Criticality in Neural Systems

WILEY-VCH
Verlag GmbH & Co. KGaA

The Editors

Sr. Invest. Dr. Dietmar Plenz
Nat. Inst. of Mental Health
Systems Neuroscience
Sect. Critical Brain Dynamics
Bethesda, USA

Prof. Dr. Ernst Niebur
The Zanvyl Krieger Mind/ Brain
Inst./John Hopkins University
Baltimore, USA

A book of the series 'Reviews of Nonlinear
Dynamics and Complexity'

The Series Editor

Prof. Dr. Heinz Georg Schuster
Saarbrücken, Germany

Cover Picture

Neuronal avalanches in the awake brain follow a power law in sizes that grows with the area of cortex observed, a hallmark of criticality (see chapter 02 for details).

Background: Cultured pyramidal neurons from the mammalian brain expressing a genetically encoded calcium indicator to study neuronal avalanches.

From Plenz, NIMH.

All books published by Wiley-VCH are carefully produced. Nevertheless, authors, editors, and publisher do not warrant the information contained in these books, including this book, to be free of errors. Readers are advised to keep in mind that statements, data, illustrations, procedural details or other items may inadvertently be inaccurate.

Library of Congress Card No.: applied for

British Library Cataloguing-in-Publication Data

A catalogue record for this book is available from the British Library.

Bibliographic information published by the Deutsche Nationalbibliothek

The Deutsche Nationalbibliothek lists this publication in the Deutsche Nationalbibliografie; detailed bibliographic data are available on the Internet at <<http://dnb.d-nb.de>>.

© 2014 Wiley-VCH Verlag GmbH & Co. KGaA, Boschstr. 12, 69469 Weinheim, Germany

All rights reserved (including those of translation into other languages). No part of this book may be reproduced in any form – by photostriping, microfilm, or any other means – nor transmitted or translated into a machine language without written permission from the publishers. Registered names, trademarks, etc. used in this book, even when not specifically marked as such, are not to be considered unprotected by law.

Print ISBN: 978-3-527-41104-7

ePDF ISBN: 978-3-527-65103-0

ePub ISBN: 978-3-527-65102-3

mobi ISBN: 978-3-527-65101-6

oBook ISBN: 978-3-527-65100-9

Cover Design Grafik-Design Schulz,
Fußgönheim, Germany

Typesetting Laserwords Private Limited,
Chennai, India

Printing and Binding Strauss GmbH,
Mörlnbach

Printed on acid-free paper

Contents

List of Contributors XVII

1	Introduction	1
	<i>Dietmar Plenz and Ernst Niebur</i>	
1.1	Criticality in Neural Systems	1
2	Criticality in Cortex: Neuronal Avalanches and Coherence Potentials	5
	<i>Dietmar Plenz</i>	
2.1	The Late Arrival of Critical Dynamics to the Study of Cortex Function	5
2.1.1	Studying Critical Dynamics through Local Perturbations	7
2.1.2	Principles in Cortex Design that Support Critical Neuronal Cascades	8
2.2	Cortical Resting Activity Organizes as Neuronal Avalanches	11
2.2.1	Unbiased Concatenation of Neuronal Activity into Spatiotemporal Patterns	11
2.2.2	The Power Law in Avalanche Sizes with Slope of $-3/2$	15
2.2.3	Neuronal Avalanches are Specific to Superficial Layers of Cortex	17
2.2.4	The Linking of Avalanche Size to Critical Branching	17
2.3	Neuronal Avalanches: Cascades of Cascades	20
2.4	The Statistics of Neuronal Avalanches and Earthquakes	23
2.5	Neuronal Avalanches and Cortical Oscillations	23
2.6	Neuronal Avalanches Optimize Numerous Network Functions	28
2.7	The Coherence Potential: Threshold-Dependent Spread of Synchrony with High Fidelity	30
2.8	The Functional Architecture of Neuronal Avalanches and Coherence Potentials	33
	Acknowledgement	36
	References	36

3	Critical Brain Dynamics at Large Scale	43
	<i>Dante R. Chialvo</i>	
3.1	Introduction	43
3.1.1	If Criticality is the Solution, What is the Problem?	43
3.2	What is Criticality Good for?	45
3.2.1	Emergence	46
3.2.2	Spontaneous Brain Activity is Complex	46
3.2.3	Emergent Complexity is Always Critical	47
3.3	Statistical Signatures of Critical Dynamics	47
3.3.1	Hunting for Power Laws in Densities Functions	48
3.3.2	Beyond Fitting: Variance and Correlation Scaling of BrainNoise	50
3.3.2.1	Anomalous Scaling	51
3.3.2.2	Correlation Length	52
3.4	Beyond Averages: Spatiotemporal Brain Dynamics at Criticality	55
3.4.1	fMRI as a Point Process	56
3.4.2	A Phase Transition	57
3.4.3	Variability and Criticality	59
3.5	Consequences	60
3.5.1	Connectivity versus Functional Collectivity	60
3.5.2	Networks, Yet Another Circuit?	62
3.5.3	River Beds, Floods, and Fuzzy Paths	62
3.6	Summary and Outlook	63
	References	64
4	The Dynamic Brain in Action: Coordinative Structures, Criticality, and Coordination Dynamics	67
	<i>J. A. Scott Kelso</i>	
4.1	Introduction	67
4.2	The Organization of Matter	68
4.3	Setting the Context: A Window into Biological Coordination	72
4.4	Beyond Analogy	74
4.5	An Elementary Coordinative Structure: Bimanual Coordination	75
4.6	Theoretical Modeling: Symmetry and Phase Transitions	76
4.7	Predicted Signatures of Critical Phenomena in Biological Coordination	80
4.7.1	Critical Slowing Down	80
4.7.2	Enhancement of Fluctuations	81
4.7.3	Critical Fluctuations	81
4.8	Some Comments on Criticality, Timescales, and Related Aspects	82
4.9	Symmetry Breaking and Metastability	84
4.10	Nonequilibrium Phase Transitions in the Human Brain: MEG, EEG, and fMRI	87
4.11	Neural Field Modeling of Multiple States and Phase Transitions in the Brain	88

4.12	Transitions, Transients, Chimera, and Spatiotemporal Metastability	89
4.13	The Middle Way: Mesoscopic Protectorates	92
4.14	Concluding Remarks	94
	Acknowledgments	95
	References	96
5	The Correlation of the Neuronal Long-Range Temporal Correlations, Avalanche Dynamics with the Behavioral Scaling Laws and Interindividual Variability	105
	<i>Jaakko Matias Palva and Satu Palva</i>	
5.1	Introduction	105
5.2	Criticality in the Nervous System: Behavioral and Physiological Evidence	106
5.2.1	Human Task Performance Fluctuations Suggest Critical Dynamics	106
5.2.2	Two Lines of Empirical Evidence for Critical-State Dynamics in Neuronal Systems	108
5.3	Magneto- and Electroencephalography (M/EEG) as a Tool for Noninvasive Reconstruction of Human Cortical Dynamics	109
5.4	Slow Neuronal Fluctuations: The Physiological Substrates of LRTC	111
5.4.1	Infra-Slow Potential Fluctuations Reflect Endogenous Dynamics of Cortical Excitability	111
5.4.2	Slow Fluctuations in Oscillation Amplitudes and Scalp Potentials are Correlated with Behavioral Dynamics	113
5.4.3	Slow BOLD Signal Fluctuations in Resting-State Networks	114
5.5	Neuronal Scaling Laws are Correlated with Interindividual Variability in Behavioral Dynamics	115
5.6	Neuronal Avalanches, LRTC, and Oscillations: Enigmatic Coexistence?	117
5.6.1	The Mechanistic Insights from Interindividual Variability in Scaling Laws	118
5.7	Conclusions	119
	Acknowledgment	120
	References	120
6	The Turbulent Human Brain: An MHD Approach to the MEG	127
	<i>Arnold J. Mandell, Stephen E. Robinson, Karen A. Selz, Constance Schrader, Tom Holroyd, and Richard Coppola</i>	
6.1	Introduction	127
6.2	Autonomous, Intermittent, Hierarchical Motions, from Brain Proteins Fluctuations to Emergent Magnetic Fields	129
6.3	Magnetic Field Induction and Turbulence; Its Maintenance, Decay, and Modulation	130

6.4	Localizing a Time-Varying Entropy Measure of Turbulence, <i>Rank Vector Entropy (RVE)</i> [35, 107], Using a <i>Linearly Constrained Minimum Variance (LCMV) Beamformer</i> Such as <i>Synthetic Aperture Magnetometry (SAM)</i> [25, 34], Yields State and Function-Related Localized Increases and Decreases in the <i>RVE Estimate</i> 139
6.5	Potential Implications of the MHD Approach to MEG Magnetic Fields for Understanding the Mechanisms of Action and Clinical Applications of the Family of TMS (Transcranial Magnetic Stimulation) Human Brain Therapies 142
6.6	Brief Summary of Findings 145
	References 145
7	Thermodynamic Model of Criticality in the Cortex Based on EEG/ECoG Data 153
	<i>Robert Kozma, Marko Puljic, and Walter J. Freeman</i>
7.1	Introduction 153
7.2	Principles of Hierarchical Brain Models 154
7.2.1	Freeman K-Models: Structure and Functions 154
7.2.2	Basic Building Blocks of Neurodynamics 155
7.2.3	Motivation of Neuropercolation Approach to Neurodynamics 157
7.3	Mathematical Formulation of Neuropercolation 158
7.3.1	Random Cellular Automata on a Lattice 158
7.3.2	Update Rules 159
7.3.3	Two-Dimensional Lattice with Rewiring 160
7.3.4	Double-Layered Lattice 161
7.3.5	Coupling Two Double-Layered Lattices 162
7.3.6	Statistical Characterization of Critical Dynamics of Cellular Automata 163
7.4	Critical Regimes of Coupled Hierarchical Lattices 164
7.4.1	Dynamical Behavior of 2D Lattices with Rewiring 164
7.4.2	Narrow Band Oscillations in Coupled Excitatory–Inhibitory Lattices 165
7.5	BroadBand Chaotic Oscillations 167
7.5.1	Dynamics of Two Double Arrays 167
7.5.2	Intermittent Synchronization of Oscillations in Three Coupled Double Arrays 170
7.5.3	Hebbian Learning Effects 170
7.6	Conclusions 173
	References 174
8	Neuronal Avalanches in the Human Brain 177
	<i>Oren Shriki and Dietmar Plenz</i>
8.1	Introduction 177
8.2	Data and Cascade-Size Analysis 178
8.3	Cascade-Size Distributions are Power Laws 181

8.4	The Data are Captured by a Critical Branching Process	181
8.5	Discussion	186
8.6	Summary	188
	Acknowledgements	188
	References	188
9	Critical Slowing and Perception	191
	<i>Karl Friston, Michael Breakspear, and Gustavo Deco</i>	
9.1	Introduction	191
9.1.1	Perception and Neuronal Dynamics	191
9.1.2	Overview	192
9.2	Itinerant Dynamics	193
9.2.1	Chaotic Itinerancy	193
9.2.2	Heteroclinic Cycling	194
9.2.3	Multistability and Switching	194
9.2.4	Itinerancy, Stability, and Critical Slowing	195
9.3	The Free Energy Principle	196
9.3.1	Action and Perception	197
9.3.2	The Maximum Entropy Principle and the Laplace Assumption	198
9.3.3	Summary	199
9.4	Neurobiological Implementation of Active Inference	199
9.4.1	Perception and Predictive Coding	202
9.4.2	Action	204
9.4.3	Summary	204
9.5	Self-Organized Instability	205
9.5.1	Conditional Lyapunov Exponents and Generalized Synchrony	205
9.5.2	Critical Slowing and Conditional Lyapunov Exponents	207
9.5.3	Summary	210
9.6	Birdsong, Attractors, and Critical Slowing	211
9.6.1	A Synthetic Avian Brain	212
9.6.2	Stimulus Generation and the Generative Model	213
9.6.3	Perceptual Categorization	214
9.6.4	Perceptual Instability and Switching	216
9.6.5	Perception and Critical Slowing	219
9.6.6	Summary	221
9.7	Conclusion	223
	References	224
10	Self-Organized Criticality in Neural Network Models	227
	<i>Matthias Rybarsch and Stefan Bornholdt</i>	
10.1	Introduction	227
10.2	Avalanche Dynamics in Neuronal Systems	228
10.2.1	Experimental Results	228
10.2.2	Existing Models	229

10.3	Simple Models for Self-Organized Critical Adaptive Neural Networks	231
10.3.1	A First Approach: Node Activity Locally Regulates Connectivity	231
10.3.2	Correlation as a Criterion for Rewiring: Self-Organization on a Spin Lattice Neural Network Model	235
10.3.3	Simplicity versus Biological Plausibility – and Possible Improvements	238
10.3.3.1	Transition from Spins to Boolean Node States	238
10.3.3.2	Model Definitions	239
10.3.3.3	Exploration of Critical Properties – Activity-Dependent Criticality	240
10.3.3.4	Extension of the Model: Thermal Noise	242
10.3.4	Self-Organization on the Boolean State Model	243
10.3.4.1	Model Definitions	244
10.3.4.2	Rewiring Algorithm	245
10.3.4.3	Observations	247
10.3.5	Response to External Perturbations	249
10.4	Conclusion	252
	Acknowledgments	252
	References	252
11	Single Neuron Response Fluctuations: A Self-Organized Criticality Point of View	<i>Asaf Gal and Shimon Marom</i>
11.1	Neuronal Excitability	255
11.2	Experimental Observations on Excitability Dynamics	257
11.3	Self-Organized Criticality Interpretation	261
11.4	Adaptive Rates and Contact Processes	263
11.5	Concluding Remarks	265
	References	269
12	Activity Dependent Model for Neuronal Avalanches	<i>Lucilla de Arcangelis and Hans J. Herrmann</i>
12.1	The Model	274
12.1.1	Plastic Adaptation	276
12.2	Neuronal Avalanches in Spontaneous Activity	277
12.2.1	Power Spectra	278
12.3	Learning	280
12.4	Temporal Organization of Neuronal Avalanches	283
12.5	Conclusions	288
	References	289

13	The Neuronal Network Oscillation as a Critical Phenomenon	293
	<i>Richard Hardstone, Huibert D. Mansvelder, and Klaus Linkenkaer-Hansen</i>	
13.1	Introduction	293
13.2	Properties of Scale-Free Time Series	294
13.2.1	Self-Affinity	294
13.2.2	Stationary and Nonstationary Processes	298
13.2.3	Scaling of an Uncorrelated Stationary Process	298
13.2.4	Scaling of Correlated and Anticorrelated Signals	300
13.3	The Detrended Fluctuation Analysis (DFA)	302
13.4	DFA Applied to Neuronal Oscillations	304
13.4.1	Preprocessing of Signals	304
13.4.2	Filter Design	305
13.4.3	Extract the Amplitude Envelope and Perform DFA	305
13.4.4	Determining the Temporal Integration Effect of the Filter	305
13.5	Insights from the Application of DFA to Neuronal Oscillations	305
13.5.1	DFA as a Biomarker of Neurophysiological Disorder	309
13.6	Scaling Behavior of Oscillations: a Sign of Criticality?	310
13.6.1	CRITICAL OScillations Model (CROS)	310
13.6.2	CROS Produces Neuronal Avalanches with Balanced Ex/In Connectivity	311
13.6.3	CROS Produces Oscillations with LRTC When there are Neuronal Avalanches	313
13.6.4	Multilevel Criticality: A New Class of Dynamical Systems?	315
	Acknowledgment	316
	References	316
14	Critical Exponents, Universality Class, and Thermodynamic “Temperature” of the Brain	319
	<i>Shan Yu, Hongdian Yang, Oren Shriki, and Dietmar Plenz</i>	
14.1	Introduction	319
14.2	Thermodynamic Quantities at the Critical Point and Their Neuronal Interpretations	320
14.3	Finite-Size Scaling	324
14.4	Studying the Thermodynamics Properties of Neuronal Avalanches at Different Scales	325
14.5	What Could be the “Temperature” for the Brain?	330
	Acknowledgment	331
	References	331
15	Peak Variability and Optimal Performance in Cortical Networks at Criticality	335
	<i>Hongdian Yang, Woodrow L. Shew, Rajarshy Roy, and Dietmar Plenz</i>	
15.1	Introduction	335
15.2	Fluctuations Are Highest Near Criticality	336

15.3	Variability of Spatial Activity Patterns	338
15.4	Variability of Phase Synchrony	339
15.5	High Variability, but Not Random	342
15.6	Functional Implications of High Entropy of Ongoing Cortex Dynamics	343
	References	344
16	Criticality at Work: How Do Critical Networks Respond to Stimuli?	347
	<i>Mauro Copelli</i>	
16.1	Introduction	347
16.1.1	Phase Transition in a Simple Model	347
16.1.2	What is the Connection with Neuronal Avalanches?	350
16.1.3	What if Separation of Time Scales is Absent?	351
16.2	Responding to Stimuli	351
16.2.1	What Theory Predicts	352
16.2.1.1	Self-Regulated Amplification via Excitable Waves	352
16.2.1.2	Enhancement of Dynamic Range	354
16.2.1.3	Nonlinear Collective Response and Maximal Dynamic Range at Criticality	355
16.2.2	What Data Reveals	356
16.2.2.1	Nonlinear Response Functions in Sensory Systems	356
16.2.2.2	Enhanced Dynamic Range	356
16.2.2.3	Scaling In Brain Dynamics	357
16.3	Concluding Remarks	359
	Acknowledgements	361
	References	361
17	Critical Dynamics in Complex Networks	365
	<i>Daniel B. Larremore, Woodrow L. Shew, and Juan G. Restrepo</i>	
17.1	Introduction: Critical Branching Processes	365
17.2	Description and Properties of Networks	367
17.2.1	Network Representation by an Adjacency Matrix	368
17.2.2	Node Degrees	368
17.2.3	Degree Distribution	369
17.2.4	Degree Correlations	370
17.2.5	Largest Eigenvalue and the Corresponding Eigenvector	372
17.3	Branching Processes in Complex Networks	373
17.3.1	Subcritical Regime	378
17.3.2	Supercritical Regime	381
17.3.3	Critical Regime	383
17.4	Discussion	387
	References	390

18	Mechanisms of Self-Organized Criticality in Adaptive Networks	393
	<i>Thilo Gross, Anne-Ly Do, Felix Drost, and Christian Meisel</i>	
18.1	Introduction	393
18.2	Basic Considerations	393
18.3	A Toy Model	395
18.4	Mechanisms of Self-Organization	397
18.5	Implications for Information Processing	399
18.6	Discussion	400
	References	401
19	Cortical Networks with Lognormal Synaptic Connectivity and Their Implications in Neuronal Avalanches	403
	<i>Tomoki Fukai, Vladimir Klinshov, and Jun-nosuke Teramae</i>	
19.1	Introduction	403
19.2	Critical Dynamics in Neuronal Wiring Development	404
19.3	Stochastic Resonance by Highly Inhomogeneous Synaptic Weights on Spike Neurons	405
19.4	SSWD Recurrent Networks Generate Optimal Intrinsic Noise	409
19.5	Incorporation of Local Clustering Structure	410
19.6	Emergence of Bistable States in the Clustered Network	412
19.7	Possible Implications of SSWD Networks for Neuronal Avalanches	413
19.8	Summary	414
	Acknowledgment	414
	References	415
20	Theoretical Neuroscience of Self-Organized Criticality: From Formal Approaches to Realistic Models	417
	<i>Anna Levina, J. Michael Herrmann, and Theo Geisel</i>	
20.1	Introduction	417
20.2	The Eurich Model of Criticality in Neural Networks	417
20.2.1	Model Description	418
20.2.2	Simulations and Analysis	419
20.3	LHG Model: Dynamic Synapses Control Criticality	420
20.3.1	Model Description	420
20.3.2	Mean-Field Approximation	423
20.3.3	Toward a Realistic Model: Network Structure, Leakage, and Inhibition	424
20.3.4	Synaptic Facilitation	427
20.4	Criticality by Homeostatic Plasticity	429
20.4.1	Branching Processes	429
20.4.2	Self-Organization by Long-Term Plasticity	430
20.4.3	Effects of Spike-Time-Dependent Plasticity and Network Structure	431
20.5	Conclusion	433

	Acknowledgment	434
	References	434
21	Nonconservative Neuronal Networks During Up-States Self-Organize Near Critical Points	<i>437</i>
	<i>Stefan Mihalas, Daniel Millman, Ramakrishnan Iyer, Alfredo Kirkwood, and Ernst Niebur</i>	
21.1	Introduction	437
21.2	Model	439
21.2.1	Analytical Solution	440
21.2.2	Numerical Evolution of the Fokker–Planck Equation	441
21.2.3	Fixed-Point Analysis	442
21.3	Simulations	444
21.3.1	Up- and Down-States	444
21.3.1.1	Up-/Down-State Transitions	446
21.3.2	Up-States are Critical; Down-States are Subcritical	448
21.3.3	More Biologically Realistic Networks	449
21.3.3.1	Small-World Connectivity	449
21.3.3.2	NMDA and Inhibition	450
21.3.4	Robustness of Results	452
21.4	Heterogeneous Synapses	454
21.4.1	Influence of Synaptic Weight Distributions	454
21.4.2	Voltage Distributions for Heterogeneous Synaptic Input	455
21.4.3	Results for Realistic Synaptic Distributions in the Absence of Recurrence and STSD	456
21.4.4	Heterogeneous Synaptic Distributions in the Presence of Synaptic Depression	458
21.5	Conclusion	460
	Acknowledgment	460
	References	460
22	Self-Organized Criticality and Near-Criticality in Neural Networks	<i>465</i>
	<i>Jack D. Cowan, Jeremy Neuman, and Wim van Drongelen</i>	
22.1	Introduction	465
22.1.1	Neural Network Dynamics	466
22.1.2	Stochastic Effects Near a Critical Point	468
22.2	A Neural Network Exhibiting Self-Organized Criticality	468
22.2.1	A Simulation of the Combined Mean-Field Equations	470
22.2.2	A Simulation of the Combined Markov Processes	471
22.3	Excitatory and Inhibitory Neural Network Dynamics	472
22.3.1	Equilibria of the Mean-Field Wilson–Cowan Equations	473
22.4	An E–I Neural Network Exhibiting Self-Organized Near-Criticality	475
22.4.1	Modifiable Synapses	475
22.4.2	A Simulation of the Combined Mean-Field <i>E/I</i> equations	477

22.4.3	Balanced Amplification in <i>E/I</i> Patches	477
22.4.4	Analysis and Simulation of the Combined <i>E/I</i> Markov Processes	479
22.5	Discussion	481
	Acknowledgements	482
	References	482
23	Neural Dynamics: Criticality, Cooperation, Avalanches, and Entrainment between Complex Networks	485
	<i>Paolo Grigolini, Marzieh Zare, Adam Svenkeson, and Bruce J. West</i>	
23.1	Introduction	485
23.2	Decision-Making Model (DMM) at Criticality	487
23.2.1	Intermittency	489
23.2.2	Response to Perturbation	492
23.3	Neural Dynamics	493
23.3.1	Mittag-Leffler Function Model Cooperation	494
23.3.2	Cooperation Effort in a Fire-and-Integrate Neural Model	496
23.4	Avalanches and Entrainment	501
23.5	Concluding Remarks	504
	References	505
24	Complex Networks: From Social Crises to Neuronal Avalanches	509
	<i>Bruce J. West, Małgorzata Turalska, and Paolo Grigolini</i>	
24.1	Introduction	509
24.2	The Decision-Making Model (DMM)	510
24.3	Topological Complexity	514
24.4	Temporal Complexity	517
24.5	Inflexible Minorities	518
24.6	Conclusions	521
	References	522
25	The Dynamics of Neuromodulation	525
	<i>Gerhard Werner[†] and Bernhard J. Mitterauer</i>	
25.1	Introduction	525
25.2	Background	525
25.2.1	Gap Junctions and Neuroglia	525
25.2.2	Brain Cell Microenvironment (Extracellular Fluid)	527
25.2.3	Neuromodulatory Processes	528
25.3	Discussion and Conclusions	529
25.4	A Final Thought	532
25.5	Summary	532
	References	532
	Color Plates	539
	Index	559



Participants of the 'Criticality in Neural Systems' conference held April 30 - May, 1st, 2012, at the National Institutes of Health, Bethesda, MD, USA. The conference was organized to increase the coherence of the volume at hand.

List of Contributors

Lucilla de Arcangelis

Second University of Naples
Department of Industrial and
Information Engineering &
CNISM
81031 Aversa, CE
Italy

and

Consejo Nacional de
Investigaciones Científicas y
Técnicas (CONICET)
Rivadavia 1917
1033 Buenos Aires
Argentina

Stefan Bornholdt

Universität Bremen
Institut für Theoretische Physik
Hochschulring 18
28359 Bremen
Germany

Mauro Copelli

Federal University of
Pernambuco (UFPE)
Physics Department
50670-901 Recife-PE
Brazil

Michael Breakspear

Queensland Institute of Medical
Research, Royal Brisbane
Hospital
Brisbane, QLD 4029
Australia

Richard Coppola

National Institute of Mental
Health
MEG Core Facility
10 Center Drive
Bethesda, MD 20892
USA

Dante R. Chialvo

David Geffen School of Medicine
UCLA
Department of Physiology
1500 Wilshire Boulevard
Bldg, 115
Los Angeles, CA 90017
USA

Jack D. Cowan

University of Chicago
Dept. of Mathematics
5734 S. University Ave.
Chicago, IL 60637
USA

Gustavo Deco

Universitat Pompeu Fabra
 Theoretical and Computational
 Neuroscience Center for Brain
 and Cognition
 Roc Boronat 138
 08018 Barcelona
 Spain

Anne-Ly Do

Max-Planck Institute for the
 Physics of Complex Systems
 Nöthnitzer Str. 38
 01187 Dresden
 Germany

Wim van Drongelen

University of Chicago
 Departments of Pediatrics and
 Neurology
 KCBD 4124
 900 E. 57th St.
 Chicago, IL 60637
 USA

Felix Droste

Bernstein Center for
 Computational Neuroscience
 Haus 2
 Philippstrasse 13
 10115 Berlin
 Germany

Walter J. Freeman

University of California at
 Berkeley
 Department of Molecular & Cell
 Biology
 Division of Neurobiology
 Berkeley, CA 94720-3206
 USA

Karl Friston

University College London
 Institute of Neurology
 The Wellcome Trust Centre for
 Neuroimaging
 12 Queen Square
 London WC1N 3BG
 United Kingdom

Tomoki Fukai

RIKEN Brain Science Institute
 2-1 Hirosawa
 Wako
 Saitama 351-0198
 Japan

and

CREST
 JST
 4-1-8 Honcho
 Kawaguchi-shi
 Saitama 332-0012
 Japan

Asaf Gal

Technion – Israel Institute of
 Technology
 Network Biology Research
 Laboratories and the Faculty of
 Electrical Engineering
 Haifa 32000
 Israel

Theo Geisel

Max Planck Institute for
 Dynamics and Self-Organization
 Bernstein Center for
 Computational Neuroscience
 Am Fassberg 12
 37077 Göttingen
 Germany

Paolo Grigolini

University of North Texas
 Department of Physics
 Center of Nonlinear Science
 1155 Union Circle 311427
 Denton, Texas 76203
 USA

Thilo Gross

University of Bristol
 Department of Engineering
 Mathematics
 Merchant Venturers Building
 Bristol BS8 1UB
 UK

Richard Hardstone

VU University Amsterdam
 Department of Integrative
 Neurophysiology
 Center for Neurogenomics and
 Cognitive Research (CNCR)
 Neuroscience Campus
 Amsterdam (NCA)
 De Boelelaan 1085, 1081 HV
 Amsterdam
 The Netherlands

Hans J. Herrmann

ETH Zürich
 Institute for Building Materials
 Computational Physics for
 Engineering Materials
 Schafmattstrasse 6, HIF
 8093 Zürich
 Switzerland

and

Universidade Federal do Ceará
 Departamento de Física
 Campus do Pici
 60455-760 Fortaleza
 Ceará
 Brazil

J. Michael Herrmann

Max Planck Institute for
 Dynamics and Self-Organization
 Bernstein Center for
 Computational Neuroscience
 Am Fassberg 12
 37077 Göttingen
 Germany

and

University of Edinburgh
 Institute of Perception, Action
 and Behaviour School of
 Informatics
 The Informatics Forum
 10 Crichton Street
 Edinburgh EH8 9AB
 United Kingdom

Tom Holroyd

National Institute of Mental
 Health
 MEG Core Facility
 10 Center Drive
 Bethesda, MD 20892
 USA

Ramakrishnan Iyer

Allen Institute for Brain Science
 Seattle, WA 98103
 USA

J. A. Scott Kelso

Florida Atlantic University
 Center for Complex Systems and
 Brain Sciences
 777 Glades Road
 Boca Raton, FL 33431
 USA

and

University of Ulster (Magee Campus)
Intelligent Systems Research Centre
Londonderry, Derry City BT48 7JL
Northern Ireland
United Kingdom

Alfredo Kirkwood

Johns Hopkins University
Department of Neuroscience
Zanvyl Krieger Mind/Brain Institute
Baltimore, MD 21218
USA

Vladimir Klinshov

RIKEN Brain Science Institute
2-1 Hirosawa
Wako
Saitama 351-0198
Japan

and

Institute of Applied Physics of the Russian Academy of Sciences
46 Ul'yanov Street
Nizhny Novgorod 603950
Russia

Robert Kozma

University of California at Berkeley
Department of Molecular & Cell Biology
Division of Neurobiology
Berkeley, CA 94720-3206
USA

Daniel B. Larremore

Harvard School of Public Health
Department of Epidemiology
Center for Communicable Disease Dynamics
Boston, MA 02115
USA

Anna Levina

Max Planck Institute for Dynamics and Self-Organization
Bernstein Center for Computational Neuroscience
Am Fassberg 12
37077 Göttingen
Germany

and

University of Edinburgh
Institute of Perception, Action and Behaviour School of Informatics
The Informatics Forum
10 Crichton Street
Edinburgh EH8 9AB
United Kingdom

Klaus Linkenkaer-Hansen

VU University Amsterdam
Department of Integrative Neurophysiology
Center for Neurogenomics and Cognitive Research (CNCR)
Neuroscience Campus
Amsterdam (NCA)
De Boelelaan 1085
1081 HV Amsterdam
The Netherlands

Arnold J. Mandell

University of California San Diego
Department of Psychiatry
9500 Gilman Drive
La Jolla, CA 92037-0603
USA

and

National Institute of Mental Health
MEG Core Facility
10 Center Drive
Bethesda, MD 20892
USA

and

Fetzer Franklin Trust
1240 West VW Ave.
Schoolcraft, MI 49087
USA

and

Cielo Institute Inc.
486 Sunset Drive
Asheville, NC 28804-3727
USA

Huibert D. Mansvelder

VU University Amsterdam
Department of Integrative
Neurophysiology
Center for Neurogenomics and
Cognitive Research (CNCR)
Neuroscience Campus
Amsterdam (NCA)
De Boelelaan 1085
1081 HV Amsterdam
The Netherlands

Shimon Marom

Technion – Israel Institute of
Technology
Network Biology Research
Laboratories and the Faculty of
Medicine
Haifa 32000
Israel

Christian Meisel

Universitätsklinikum Carl Gustav
Carus
Fetscherstraße 74
01307 Dresden
Germany

Stefan Mihalas

Allen Institute for Brain Science
511 North 34th Street
Seattle, WA 98103
USA

Daniel Millman

Harvard University
Graduate Program in
Neuroscience
Cambridge, MA 02138
USA

Bernhard J. Mitterauer

University of Salzburg
Forensic Psychiatry and Guenther
Archives
Autobahnweg 7
Wals A-5071
Austria

Ernst Niebur

John Hopkins University
The Zanvil Krieger Mind/Brain
Institute
Department of Neuroscience
3400 N. Charles St.
Baltimore, MD 21218
USA

Jeremy Neuman

University of Chicago
Department of Physics
5720 South Ellis Avenue
Chicago, IL 60637
USA

Jaakko Matias Palva

University of Helsinki
Neuroscience Center
P.O Box 56, Viikinkaari 4
FIN-00014 Helsinki
Finland

Satu Palva

University of Helsinki
Neuroscience Center
P.O Box 56, Viikinkaari 4
FIN-00014 Helsinki
Finland

Dietmar Plenz

National Institute of Mental
Health
Section on Critical Brain
Dynamics
Bethesda, MD 20892-3726
USA

Marko Puljic

University of California at
Berkeley
Department of Molecular & Cell
Biology
Division of Neurobiology
Berkeley, CA 94720-3206
USA

Juan G. Restrepo

University of Colorado
Department of Applied
Mathematics
526 Engineering Center
Boulder, CO 80309-0526
USA

Stephen E. Robinson

National Institute of Mental
Health
MEG Core Facility
10 Center Drive
Bethesda, MD 20892
USA

and

Fetzer Franklin Trust
1240 West VW Ave.
Schoolcraft, MI 49087
USA

Rajarshi Roy

University of Maryland
Institute for Physical Science and
Technology (IPST)
College Park, MD 20742-2431
USA

Matthias Rybarsch

Universität Bremen
Institut für Theoretische Physik
Hochschulring 18
28359 Bremen
Germany

Constance Schrader

University of North Carolina
Department of Health and
Wellness
Asheville, NC 28804
USA

Karen A. Selz

Fetzer Franklin Trust
1240 West VW Ave.
Schoolcraft, MI 49087
USA

and

Cielo Institute Inc.
486 Sunset Drive
Asheville, NC 28804-3727
USA

Woodrow L. Shew

National Institute of Mental
Health
Section on Critical Brain
Dynamics
Bethesda, MD 20892-3726
USA

and

University of Arkansas
Department of Physics
Fayetteville, AR 72701
USA

and

Harvard School of Public Health
Department of Epidemiology
Center for Communicable
Disease Dynamics
Boston, MA 02115
USA

Oren Shriki

National Institute of Mental
Health
Section on Critical Brain
Dynamics
Bethesda, MD 20892-3726
USA

and

Ben-Gurion University of the
Negev
Department of Brain and
Cognitive Sciences
Beer-Sheva 84105
Israel

Adam Svenkeson

BioCircuit Institute
University of California San
Diego
Mathematical and Information
Science Directorate
Army Research Office
Research Triangle Park
NC 27709-2211
USA

Malgorzata Turalska

University of North Texas
Department of Physics
Center for Nonlinear Science
1155 Union Circle 311427
Denton, TX 76203
USA

Jun-nosuke Teramae

RIKEN Brain Science Institute
2-1 Hirosawa
Wako
Saitama 351-0198
Japan

and

Osaka University
Graduate school of Information
Science and Technology
1-5 Yamadaoka
Suita, Osaka 565-0871
Japan

Gerhard Werner[†]

University of Texas
Department of Biomedical
Engineering
Austin, TX 78712
USA

Bruce J. West

US Army Research Office
ResearchTriangle Park (Research)
Mathematical and Information
Sciences Directorate
Research Triangle Park
NC 27709
USA

Hongdian Yang

National Institute of Mental
Health
Section on Critical Brain
Dynamics
Bethesda, MD 20892-3726
USA

Shan Yu

National Institute of Mental
Health
Section on Critical Brain
Dynamics
Bethesda, MD 20892-3726
USA

Marzieh Zare

BioCircuit Institute
University of California San
Diego
Mathematical and Information
Science Directorate
Army Research Office
Research Triangle Park
NC 27709-2211
USA

1

Introduction

Dietmar Plenz and Ernst Niebur

1.1

Criticality in Neural Systems

Neuroscience is currently experiencing a revolution in the area of monitoring brain activity at ever higher spatial and temporal resolutions. The simultaneous recording of the activity of hundreds or thousands of nerve cells and the observation of averaged activity of large fractions of the whole human brain with ever-increasing precision is leading to a new generation of Big Data. The complexity of the myriads of observed neuronal interactions promises deep insights into how real brains work – how brains assure the survival of the species in highly complex and dynamically changing environments. At the same time, this complexity poses an enormous challenge to our analytical skills and our willingness to break traditional approaches to explore and explain brain function. The nearly century-old and still highly successful approach to neuroscience that maps single neuron responses to select sensory, motor, or associative processes is challenged by the view that it is activity from wide-spread organized neuronal populations that underlies the computational operations of the brain. The view that brain circuits are analogous to both precisely and permanently wired electronic circuits is making way to a picture in which circuit elements continuously change affiliations leading to the emergence of complex spatio-temporal patterns. Yet, will these metaphors provide us with the precision and manipulative potential that is ultimately required to understand brain functions? Are we forced to leave the realm of precise biophysical laws at the single neuron level to enter a level of description in which insights can be expressed only in terms of probabilistic patterns that loosely correlate with brain operations?

In fact, there is a theoretical framework that allows for more than just that, a framework in which precise rules and laws govern the interactions of many elements in distributed, complex systems. It is the theory of criticality that has transformed the study of complex systems in physics and other areas, but has been neglected for a long time in the study of the most complex system in biology – the brain. This volume provides the first comprehensive account of the recent cross-fertilization between neuroscience and the interdisciplinary science of criticality.

The firework of insights that this interaction has sparked ranges from studies of isolated neuronal networks to a deep understanding of results of the most advanced imaging of the human brain.

The origins of this book lie in a series of experimental findings predicted by criticality theory, of which the discovery of ‘neuronal avalanches’ at the National Institute of Mental Health in 2001 was particularly influential. Avalanches are cascades of events that emerge in systems at a critical point, where order and disorder are perfectly balanced. At criticality, the sizes of avalanches in the brain are distributed according to a power law, which establishes a direct link to the theory of critical branching processes and the theory of self-organized criticality introduced by Per Bak and his co-workers in the early nineties. These experiments also tied together earlier work by Arnold Mandell, Scott Kelso, Walter Freeman, Dante Chialvo and others on neuronal phenomena such as critical slowing down in motor program switching, intermittency/variability in neuronal populations, and learning by mistakes at the network level. Over the past decade, the field has experienced rapid expansion with a flurry of new results, both experimental and theoretical. These results, coming from a correspondingly increasing number of researchers, have been published in a variety of journals, as might be expected for a topic at the intersection of two very different fields (the theory of critical phenomena on one side, and neuroscience on the other), both of which are interdisciplinary by themselves. There was, however, not a single place where these various results are shown in context and related to each other.

It was in these circumstances that the editors decided that a compendium summarizing the current state of criticality in nervous systems would be helpful. This is the perfect time to *faire le point* of the field: An impressive body of work has been compiled but it can just fit in one book. When contemplating potential chapter authors, we realized that something similar is true for the primary workers in the field: they could just fit in one (largish) room. As many of them knew of each other only through their publications, we felt that an in-person meeting and ensuing discussions would contribute considerably to the coherence of the book as well as to the field as a whole. We therefore decided to organize a workshop in 2012 on the NIH campus where nearly all contributors to the book would meet for two days of talks and intense discussions. This workshop was made possible by funding from the National Institute of Mental Health and from the Office of Naval Research. In particular we would like to acknowledge support of this project by Dr. Thomas McKenna from ONR. Because of unavoidable conflicts we could not include some important contributors to the field, but we feel that those left out are a small minority and that we have the field covered nearly completely. That first meeting also spawned a series of annual follow-up conferences, one taking place in Capri, Italy, in 2013, and the next planned for 2014 at the HRL laboratories in Malibu, California.

The book’s target audience consists of graduate students and advanced scholars seeking to understand the impact of the paradigm-shifting application of criticality theory on the understanding of neural systems. The first half of the book summarizes current experimental evidence on criticality in the brain, ranging from the

discovery of neuronal avalanches, to spatial correlation functions and long-term temporal relationships covering small networks, all the way to observations of critical phenomena in the human brain. A rich mixture of experimental and modeling approaches that include graph theory and neuronal modeling at various levels of detail, from realistic network simulations to more formal and abstract network analysis, introduces the reader to a multitude of modeling approaches regarding criticality and neuroscience. Chapters toward the end of the book expand the theory of criticality formally and conceptually to levels beyond neuronal networks and the brain.

This book fills an important need in the rapidly rising interdisciplinary field of criticality in systems neuroscience. It establishes a solid compendium of current research in this field and we are confident that it will serve as an important entry point for students and future scholars.

2

Criticality in Cortex: Neuronal Avalanches and Coherence Potentials

Dietmar Plenz

2.1

The Late Arrival of Critical Dynamics to the Study of Cortex Function

Complex systems are composed of a large number of weakly interacting elements. Their dynamics and collective behavior are not dominated by a few components, but instead emerge from the multitude of interactions among many components. For complex systems to operate, they have to avoid falling into either one of two extremes: a disordered, noisy state (when interactions are too weak) or a simple, globally ordered state in which all elements are locked (when interactions are too strong). Neither state supports the dualism essential to all complex systems: they must maintain some order to ensure coherent functioning (i.e., produce a given behavior in response to a certain stimulus) while allowing for a certain degree of disorder to enable flexibility (i.e., generate adaptive changes to varying external conditions). Many degrees of order/disorder are of course possible, but the long-range spatial and temporal correlations that emerge when system dynamics become *critical* stand out, as they allow systems to function coherently and to retain a history of previous activity (for excellent books on this topic, see [1–3]. On the basis of these general arguments, in the 1990s, the hypothesis was put forward that the brain, in the face of an ever-changing environment, might show self-organized criticality (SOC) [1].

The provocative suggestion that the brain might operate at or near criticality was strongly driven by theoretical concepts. In fact, numerous early simulations pointed to the potential equivalence between neuronal networks and many-element systems [4] that exhibit a phase transition such as cellular automata (CA) (e.g., [5]) and spin-glasses (e.g., [6–9]). At the phase transition, these systems and models exhibit critical dynamics that typically separate a chaotic from a frozen dynamical regime. However, given the required precise internal tuning to remain at such a border and the suspicious lack of experimental evidence at the time of these early suggestions, the fact that the brain might operate exactly at such a border was generally considered unrealistic. Not surprisingly, attention was given to regimes distant from the phase transition, for example, for information storage [10]. This situation has not changed much despite the introduction of the concept of SOC;

[1], which provided insights into how a plastic neural network might position itself and the benefits from residing at such a border [11].

The explosive growth in the ability to study and examine the intricate working of single nerve cells and their synaptic connections within the field of neuroscience in the 1980s and 1990s did nothing to help this matter. This was driven by powerful new techniques such as patch-clamp recording [12] complemented by enhanced software tools that allowed for detailed compartmental modeling of single neurons and small networks [13, 14] within a well-established theoretical framework of electrical circuits [15]. Given that critical systems establish universal behavior that does not rely on the physical details of the system at hand [1–3, 16], the idea of a “critical brain” seemed to have arrived at a time when neuroscience was looking in the opposite direction – understanding the functioning of the brain by mapping its circuits to the greatest detail possible.

Criticality, as a theory of brain function, faced at least two more obstacles that needed to be overcome before seriously entering system neuroscience at all levels. Technically, it has been and still is extremely challenging to record from many neurons simultaneously, a prerequisite to study the brain as a many-element dynamical system. This limitation is now slowly being overcome, with advances in numerous techniques allowing researchers to record from many neurons simultaneously at different scales using microelectrode arrays, genetically encoded calcium indicators, the electroencephalogram (EEG), functional magnetic resonance imaging (fMRI), and magnetoencephalography (MEG) (see, e.g., Chapters 3–8 and 13–16 in this book). Besides technical limitations, though, there were also strong competing theories on how to deal with the complexity that arises in large, distributed systems such as the brain. A conference at the National Institute of Mental Health (NIMH) in 1987 on dynamical systems exemplifies this challenge quite well [17]. The conference’s progressive vision was that dysfunctions seen in patients suffering from psychiatric illnesses might have their roots in complex nonlinear dynamics of normal and abnormal brain activities. Or to quote the then NIMH director Sherrill H. Frazier in his introductory remarks “... we in psychiatry have been trying to understand the global dynamics of biomedical systems from our beginnings. We have been deeply involved, for example, in general systems theory, and all its ramifications for illness, health, and the human condition. When after checking all the parts of sick patients and failing to find anything that is ‘wrong’, other specialists usually refer those patients to us. We have been aware for at least two centuries that everything can be wrong when nothing is wrong; ...” [17]. Thus, while the idea of emergent properties that cannot be explained by the sum of all parts of a system was alive and well recognized, most contributions at that conference elaborated on complex phenomena that could be studied well in low-dimensional systems. Chaos theory was the dominating framework that demonstrated how “strange attractors” of striking complexity emerge in systems with just a few dynamical variables. On the other hand, the theory of criticality had already been very successfully applied to explain transitions, critical fluctuations, and slowing down in global system variables that capture human motor behavior [18–23]. This early body of work suggested that the underlying many-element

neural circuits that control human movements might themselves embody critical dynamics. However, only now with the arrival of advanced technologies has the stage been set to ultimately put the idea of a critical brain to the experimental testing ground.

2.1.1

Studying Critical Dynamics through Local Perturbations

A particular successful approach to criticality, that is, that allows one to dig into the “mechanics” of a critical system, has focused on a system’s response to small perturbations or inputs [24–28]. It is intuitively clear that any complex system needs to be able to receive inputs, to transmit the consequences of an input within the system, and to produce a more or less unique system response (that hopefully contributes to the survival, i.e., robustness of the system). Accordingly, one specific aspect of a system at criticality is that the response to local perturbations, on average, is neither damped nor amplified. This is just one specific solution to avoid being locked into one of the two extremes pointed out at the beginning of this chapter: if a local perturbation was to be amplified as it percolates through the system, the potential explosive dynamics might result in a simple, noninformative global state of activity. Conversely, if the consequences of a local perturbation prematurely terminate as they unfold within the system, dynamically integrating numerous local inputs into a selective, coherent system response is simply not possible.

At first glance, the required precision for such balanced propagation seems to be beyond the realm of most biological systems, because out-of-balance conditions will accumulate during propagation. It was therefore particularly encouraging that such critically balanced propagation was discovered experimentally in the form of neuronal avalanches [26]. Balanced propagation is also at the core of the work by Kauffman and coworkers in gene regulation using Boolean networks, which has recently found strong experimental support [25, 29, 30]. This approach has also been used to identify interesting computational regimes in CA [31, 32] that give rise to soliton-like objects. In the brain, these soliton-like objects form a subset of neuronal avalanches that have been termed *coherence potentials* [33, 34] (see also this chapter).

Through the window of balanced propagation and the resulting properties of the emerging cascades, this chapter introduces and elaborates on how criticality relates to some of the most profound aspects of brain organization and function that have been discovered over the past two decades. It is written for the experimentalist with a strong neuroscience background, and the curious modeler. It will provide a number of tools and phenomena to look out for when studying critical neuronal networks in various laboratory settings *in vitro* in neuronal cultures and acute brain slices, or *in vivo* in rodents, nonhuman primates, and ultimately humans. Appropriate references are given to point the reader to additional aspects of criticality that otherwise would distract too much from the main flow of arguments presented here.

2.1.2

Principles in Cortex Design that Support Critical Neuronal Cascades

The mammalian cortex is the most complex system to emerge from ~100 Mio years of evolution. Understanding its design and function remains one of science's greatest challenges. Its complexity is unsurpassed and, at whatever level of examination, an extraordinarily complicated picture of intertwined dependencies between cortical elements and a seemingly unending plethora of rules emerge. This holds for the subcellular molecular machinery that controls the thousands of connections every cortical neuron makes to the global macroscopic dynamics of billions of neurons and their trillions of connections. These interactions at and between levels incorporate all functionally specialized cortical areas and serve as the hierarchical mold of higher brain functions that allow mammals to adapt and survive in a complex world. Why would anybody ever assume that the principle of criticality could serve as a robust guide to unravel the mysteries of the brain? After all, there are other competing approaches that have been extremely successful in studying the brain, such as viewing the nervous system as a complicated electrical circuit similar to a computer based on microprocessors with von Neumann architecture (e.g., [35]). Why does criticality stand out and what makes this principle so seemingly well suited for brain dynamics? The answer has its root in the ability to link criticality to core insights into brain organization and to test whether criticality provides a robust and general framework for brain function.

That any theory about the cortex has to be anchored in the statistics of cortex structure has been superbly exemplified by the groups of Braatenberg and Schüz [36] and Abeles [37, 38]. Using the Golgi stain method, electron microscopy, and axonal tracers, Braatenberg established that, most of the time, a single pyramidal neuron makes just a few connections with any other neuron in the cortex. Given that a cortical neuron receives input from thousands of other neurons and distributes its output to a similar number of neurons, this connection scheme spans an enormous combinatorial space of inputs. Connection probabilities between a neuron and its neighbors are largely predicted by axonal and dendritic densities and by the chance of dendrites and axons occupying the same neuronal volume (i.e., Peter's rule [39]). There have been exceptions from this general approach (e.g., selective innervation of subclasses of cortical neurons (e.g., [40])), yet the basic idea that most connectivity in the cortex is captured by statistical densities of neuronal processes and soma locations has survived (e.g., [41]). Importantly, for most neurons, any one connection is too weak to solely elicit action potentials in another cortical neuron. This electrophysiological principle combined with the statistics of cortex anatomy naturally leads to the requirement for neuronal synchronization, that is, neurons have to fire together within a reasonable period of time so that their inputs can have a combined effect in the receiving neuron to make it fire in turn. This demand is completely in line with early writings by Hebb [42] on cell assembly formation as a principle of cortex function. But what kind of synchronization dominates cortical dynamics? The predominant view of synchronized activity in the cortex is that of oscillations [43–45] and it is

assumed that phase-locked neuronal oscillations are the underlying mechanism of neuronal cooperation. In fact, the groups of Singer [46] and Eckhorn [47] provided solid experimental evidence that phase-locking of γ -oscillations correlates with elementary operations of binding low-level information into a “gestalt.” In humans, transient phase locking during γ -oscillations has been found when subjects report perceiving such “gestalts” in otherwise ambiguous figures [48]. However, oscillations, while relatively easy to measure, seem to be a rather rigid framework to capture transient and sequential aspects of brain function such as decision making and temporal sequencing of internal programs. Oscillations are mostly studied in the context of stationary, constant, and potential nonzero phase locking between cortical sites that are correlated with a particular outcome in computation. In contrast, propagating waves [49–51] or wave packets [52] seem more natural for encoding temporal sequences with spatially distant cortical representations, which is required in more complex sensorimotor tasks. It was Abeles [38] finally, in his monograph “Corticonics,” who distilled the tremendous convergence and divergence encountered in the many connections of a cortical neuron into a particular type of neuronal synchronization, that is, the sequential activation of neuronal groups, which he termed *synfire chains*. Note that a synfire chain is identical to a wave without any particular spatial ordering of its activated neurons. By dropping the requirement of spatial ordering, the idea of activity propagation in cortical networks as the essential dynamical property supported by the statistics of cortical anatomy was born in its basic outline. Unfortunately, electrophysiological and computational evidence supporting neuronal cascades at the level of neuronal spiking, that is, “synfire chains,” remained scarce for over a decade [53, 54]; for a review, see [34]).

To really appreciate why cascading neuronal activity might be at the core of cortical functions, though, another principle of cortical dynamics needs to be pointed out. The essential function of the cortex is to learn and adapt in order to support the survival of an animal in a fairly unpredictable environment. It was well established that neuronal synchronization lies at the root of activity-dependent changes in synaptic connections between neurons, such as demonstrated by long-term potentiation [55] and succinctly summarized as the general principle that “neurons that fire together, wire together” [56]. That is, when a presynaptic neuron has formed a synaptic connection with another, postsynaptic neuron, the strength of the connection increases when both neurons are active together. The discovery of spike-timing-dependent plasticity (STDP; [57–59]) established two further requirements for the strengthening of a synaptic connection: (i) a temporal order of activation such that the presynaptic neuron had to fire *before* the postsynaptic neuron was active and (ii) the postsynaptic neuron had to fire an action potential, which, through dendritic spike backpropagation, selectively links previously active synapses to subsequent action potential success of the postsynaptic neuron. Thus, STDP introduces sequential activation and causality as two principles of synaptic plasticity – refined aspects of neuronal synchronization that are naturally realized in neuronal cascades. STDP also established that a

delay of ~ 5 ms is the most efficient time scale to strengthen synaptic activity, thus supporting the formation of cascades by locally neighboring cortical groups.

These principles of cortical statistics combined with a causal and temporally asymmetrical learning rule suggest that cortical networks naturally should support activity cascades. However, they are insufficient to explain why cascade formation should happen at criticality, that is, when cascades are perfectly balanced. Numerous computational studies have shown that neuronal activity cascades are difficult to stabilize in neuronal networks [60]. The conundrum is familiar: if a neuronal group recruits a smaller neuronal group as the cascade unfolds, activity is more likely to terminate within a few steps of synaptic transmission – the dynamics are “subcritical.” Alternatively, if groups grow during cascade formation, neuronal activity might quickly engage the global network in a nonselective manner – cascade dynamics turn “supercritical” and prevent any meaningful mapping between network input and network response. This sharp divide between premature termination and explosive growth has been recognized from the very beginning when cascades were suggested as potential candidate dynamics [38] and since then has been demonstrated in many modeling studies on cascade propagation [60–63]. A potential solution to circumvent this problem would be to operate far away from explosive growth, that is, in the “subcritical” regime. There are several arguments, though, that this solution, while stable, might be inefficient. First, for cascading dynamics to underlie cortical function, cascades have to be able to link distant sites in cortex in a selective manner. That cortical design principles take into account the need for areas to remain interconnected is clearly reflected in scaling relationships found across species as the mammalian cortex expanded in evolution. The cortical white matter volume, that is, the space taken up by axonal connections between cortical areas, expanded much faster during evolution than the cortical gray matter volume, the space taken up by cell bodies, dendrites, and local axon collaterals [64]. This is in line with the gross anatomical design of the cortex as a layered, two-dimensional sheet. As cortical areas expand and new areas are added, the number of fibers connecting areas with each other has to grow supralinearly, that is, according to a power law, to keep up with the expanding demand of interconnectivity. Second, during ontogeny, the cortex expands too, with increasing demand to link distant cortical areas. This demand is most likely met by increasing cascade lengths. Axonal delays that grow with distance and the corresponding dispersion of neuronal propagation make it rather difficult for synchronized groups to form and initiate or sustain cascading activity. In fact, attempts to incorporate such dispersions into a theory of neuronal cascade formation, that is, by focusing on the coincidental arrival of synaptic inputs in a postsynaptic neurons only, poses severe limits to group formation leading to relatively short cascades [65]. In contrast, neuronal groups that participate in a cascade carried by local connectivity benefit from less dispersion through axonal delays and relatively high axonal and dendritic densities, which should increase the likelihood of sufficient convergence to sustain cascades [38]. Although it is possible to enforce long-distance cascading activity by embedding very strong synapses in a network (e.g., [63]), this approach maps dynamics back into a rather rigid connection anatomy. Such a solution to embed cascades in a larger

network, while robust, seems counterintuitive to the original promise that synfire chains could provide a way for rapid associative memory formation [36, 38]. In conclusion, the formation of local neuronal groups that trigger cascades in spatially or functionally nearby cortical regions seems to be a likely realization in cortical dynamics. In addition, if group sizes are accurately balanced, thus minimizing premature termination or explosive growth, this scheme should provide both flexibility in the participation of individual neurons and dynamical stability. A further requirement is that such cascades need to be able to exist in neuronal networks with highly heterogeneous synaptic weights [66, 67].

2.2

Cortical Resting Activity Organizes as Neuronal Avalanches

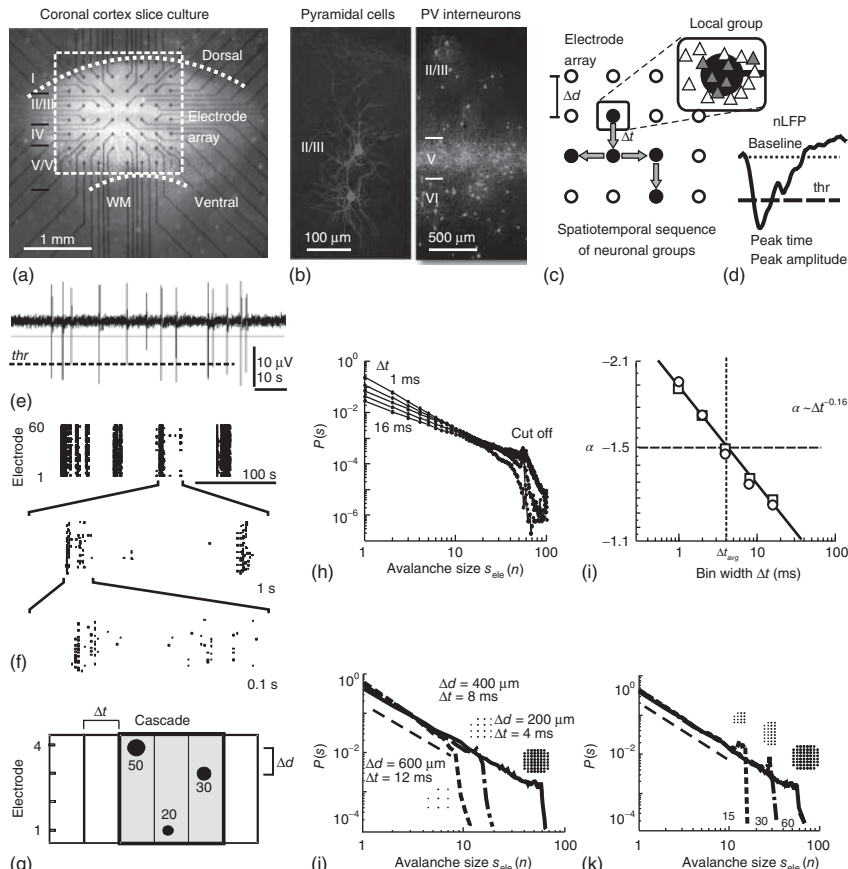
On the basis of the arguments in the preceding sections, in order to demonstrate that critical cascades are at the core of cortex dynamics, one has to demonstrate that (i) there is indeed a significant amount of cascading activity in cortical networks and (ii) that those cascades are perfectly balanced, that is, reflect critical dynamics. This section shows that neuronal avalanches fulfill these requirements. Avalanches were first discovered *in vitro* in organotypic cortex cultures [26], which allow for stable recordings of cortical population activity (Figure 2.1). Organotypic cultures are prepared by growing slabs, or thin, usually coronal, slices of cortex on a glass surface. In contrast to dissociated cultures, they retain the general cortical cytoarchitecture of layers and corresponding cell types [68–71] (Figure 2.1a,b). These latter aspects are of particular importance, as it is now fairly well established that neuronal avalanches are most easily identified in superficial layers [72–74] (see subsequent text). Importantly, neuronal activity spontaneously emerges in organotypic cultures in the form of intracellular up- and down-states [71, 75–78] that are visible as synchronized activity in the local field potential (LFP; see Figure 2.1c–f). Up-states are driven by reverberating pyramidal neuron activity and represent the spontaneous organization of intrinsic cortical activity in the absence of subcortical modulation or external stimulus. The demonstration that neuronal avalanches spontaneously emerge during up-states in organotypic cultures thus demonstrated avalanches to be critical dynamics intrinsic to the cortex. It is now well established that avalanches are particularly prominent during resting activity *in vivo* [74, 79] and ongoing or spontaneous activity *in vitro* [26, 72, 73]. Finally, organotypic cultures can be grown on glass surfaces, which allowed this preparation to be combined with planar microelectrode arrays (MEAs) for long-term, stable recordings of cortical population activity (Figure 2.1a; [80]).

2.2.1

Unbiased Concatenation of Neuronal Activity into Spatiotemporal Patterns

Once these basic aspects of cortical anatomy and activity are captured in an experimental system, testing for the presence of cascades of synchronized activity

is quite straightforward, yet requires a fairly unbiased approach. First, local, synchronized population activity is assessed by the LFP (Figure 2.1c,d). Commonly filtered between 1 and 100 Hz, the LFP reflects synchronized neuronal activity near a microelectrode. Simply by choosing a minimal threshold value thr for the LFP to cross, one identifies fast transients that report the formation of local, synchronous neuronal activity. Accordingly, in organotypic cortex cultures [81, 82], acute slices [72], and awake monkey recordings [74, 83], it is usually the negative local field potential (nLFP) deflection that is more directly related to neuronal firing. Spontaneous activity in the cortex is typically characterized by a complex spatiotemporal organization of nLFP clusters (Figure 2.1e,f). In a second step, therefore, one has to estimate whether this organization in nLFP clusters suggests that local, synchronized activity has an impact on the formation of local synchrony at distant sites, that is, postsynaptic neurons that receive converging input from the group of currently active neurons. This is done by concatenating nLFPs that occur within one time bin of duration Δt or in successive time bins on the microelectrode array into a spatiotemporal pattern (Figure 2.1g). The concatenation approach



identifies potential patterns that give rise to neuronal cascades in its broadest sense. Thus, it identifies patterns where all events occur within Δt , which would commonly be classified as “instantaneous,” that is, within temporal resolution Δt , synchronous group activity. It also captures patterns with single events in successive bins of Δt , the purest form of cascading activity, and captures any intermediate organization between these two extremes. The approach is also not biased toward elongation or termination of cascades. In fact, any ongoing activity, that is, spontaneous propagation of activity with temporal delays larger than Δt , is being fractured into distinct patterns. It does not preselect events within a cascade based on a particular size, but simply requires a local event to be of minimal significant amplitude. This aspect will be of particular importance when identifying avalanches as balanced (see subsequent text). And finally, cascading activity can emerge from single or several local groups that give rise to future groups in the next time step. Given these remarks upfront, the importance of introducing the temporal bin width Δt as a parameter should not be understated,

periods of high activity separated by periods of relative quiescence (top), an organization that repeats at higher temporal resolutions (middle and bottom). (g) Sketch of five electrodes for the definition of neuronal cascades. A neuronal cascade arises from the concatenation of successive time bins of width Δt that contain at least one nLFP. The size of a cascade can be expressed in various forms. For example, here the cascade has a size of $n=5$ electrodes, analog to “area,” and $100\mu V$, based on the summation of nLFP peak amplitudes (numbers). (h) Power law in cascade sizes and power law cutoff identifies the spontaneous activity as neuronal avalanches. When Δd is constant, the slope alpha (α) of the power law is a function of Δt . (i) Change in α with Δt for data shown in (h) (circles) and for size distributions calculated on the basis of summed nLFP peak amplitudes (squares), for the average inter nLFP interval on the array Δt_{avg} and given Δd the slope function crosses $\alpha=-3/2$. (j) If the ratio of $\Delta d/\Delta t$ is held constant, approximating the velocity of neuronal propagation, the slope of the power law is independent of Δd and Δt (for further details, see [26]). (k) Cutoff of the power law changes with array size used for analysis, and thus reflects the limitation of the observation window. Broken line: slope of power law $-3/2$ as guide to the eye.

and therefore the question arises why such temporal discretization is required in the first place. In fact, if one knew all synaptic connections within a network, one could reconstruct neuronal avalanches based on that information alone without discretization, as successfully shown in simulations (e.g., [84]). In the case of real cortical networks and given current technology, though, population activity, such as captured in the LFP, can only be sampled in spatially discrete locations. Insights from current-source density analysis [85, 86] dictate that, for the cerebral cortex, these locations should be separated by about $100\text{--}200\,\mu\text{m}$ to strike an optimum between proper spatial tiling and minimizing sampling overlap between neighboring electrodes [87, 88]. Thus, it is the experimentally imposed *spatial* discretization of the LFP that requires a corresponding *temporal* discretization in concatenation to properly map the unfolding of spatiotemporal activity in a system. Naturally, if Δt is too small, every local group will be its own pattern, whereas if Δt is too long, every local group will be combined into one single pattern with other local groups. The correct Δt depends on the propagation velocity of neuronal activity in the system and the spatial sampling distance, or interelectrode distance Δd , of the microelectrode array (Figure 2.1c,g). More precisely, when viewed in the context of finite propagation velocity, if Δt is chosen to be very short, for example, $<1\,\text{ms}$ for $\Delta d = \sim 100\text{--}200\,\mu\text{m}$, the propagation of activity from one site to another will be missed and cascades will be considered to have terminated prematurely. Conversely, if Δt is set too long, cascades that have already ended will be concatenated with future cascades. Note that for neuronal avalanche dynamics, it is only the slope of the cascade size distribution that changes systematically with Δt , if Δd is kept constant (Figure 2.1h,i). The basic form of the cascade size distribution, that is, the power law, is maintained. A good first estimate of Δt is the average or median Δt of successively activated nLFPs on the whole array (for details, see [26, 72, 73]). The relationship between Δt and the more hidden parameter Δd is sometimes mistakenly interpreted as essential characteristics of neuronal avalanche dynamics, for example, the exponent $-3/2$ of the avalanche size distribution, to depend on these parameters. However, this is not correct. If the ratio of Δd and Δt is held constant, that is, proper sampling is maintained, the exponent of the power law for avalanche sizes will not change (Figure 2.1j). If the average Δd is not known, for example, when mapping a regular sensor grid onto the convoluted cortex surface, nevertheless, it can still be shown that proper and absolute avalanche parameters are established for one particular value of Δt (e.g., [26, 79]). The cutoff of the power law is imposed by the limited array size, which is readily revealed when analyzing cascade sizes for different array sizes (Figure 2.1k). The third and remaining parameter in the concatenation algorithm is the threshold thr used to identify significant events in the data set. It reveals equally interesting insights into neuronal avalanche dynamics. This parameter also does not affect the principal signature of neuronal avalanches, that is, the power law in avalanche sizes, if it is set beyond the noise threshold. As will be shown (Figure 2.3), when the threshold thr is increased, the remaining larger nLFPs also organize as avalanches, and thus avalanches of smaller nLFP peaks are integrated into avalanches of larger nLFP peaks [34, 74]. This important property in the

organization of nLFP amplitudes is the basic signature that will eventually lead to the identification of avalanches as recursive cascades within cascades of activity governed by a number of basic power laws.

2.2.2

The Power Law in Avalanche Sizes with Slope of $-3/2$

The concatenation algorithm outlined in the previous section will extract spatiotemporal patterns of great variability from almost any data set. Because patterns can simply form by chance, for example, when two independently formed groups appear in the same or successive time bin, one requires criteria to demonstrate that pattern organizations emerge indeed from neuronal interactions. This is readily achieved by studying the distribution of pattern sizes, that is, the number of recording sites or microelectrodes that show activity in a cluster. For example, if nLFPs emerge independently and there is no interaction formed between local groups at different sites, the size distribution of simultaneously and successively occurring nLFPs that constitute a pattern follows an exponential-like distribution (cf. Figure 2.2c). Conversely, if the distribution deviates from an exponential function, spatial correlations are likely to exist in the network. In the original finding on neuronal avalanches (Figure 2.1h–k), we reported that the distribution of pattern size s obeys a power law with slope α

$$P(s) \sim s^\alpha; \quad \alpha = -\frac{3}{2} \quad (2.1)$$

This distribution significantly deviates from an exponential distribution [89]. Thus, the spatiotemporal organization in the emergence of local neuronal groups as captured in Eq. (2.1) suggests that one synchronized group at one site interacts with local groups that form at distant sites. In fact, neuronal avalanches are defined by spatiotemporal patterns that distribute in size according to Eq. (2.1). If the distribution deviates from Eq. (2.1), and if the deviation cannot be traced to measurement limits such as under sampling, one still might deal with cascading activity, but not avalanche dynamics [90, 91]. Eq. (2.1) provides two important insights about spontaneous avalanches in cortical tissue. First, the relative probability of avalanches occurring with size $s_1 = n \cdot s$ is independent of s ,

$$\frac{P(s_1)}{P(s)} = \frac{s_1^\alpha}{s^\alpha} = \left(\frac{n \cdot s}{s} \right)^\alpha = n^\alpha \quad (2.2)$$

For example, avalanches that are 10 times as big as the currently observed avalanche will occur $10^\alpha = 10^{-1.5} = 0.031$ less often than the current avalanche. Second, because $\alpha = -3/2$ is less than -2 , the unbounded integral of the average size of an avalanche does not converge,

$$\langle s \rangle \sim \int s \cdot P(s) ds = \int s^{\alpha+1} ds = \int s^{-0.5} ds \rightarrow \infty \quad (2.3)$$

In other words, the average avalanche size is only restricted by the physical size of the system and not by the dynamics. This important aspect of the distribution

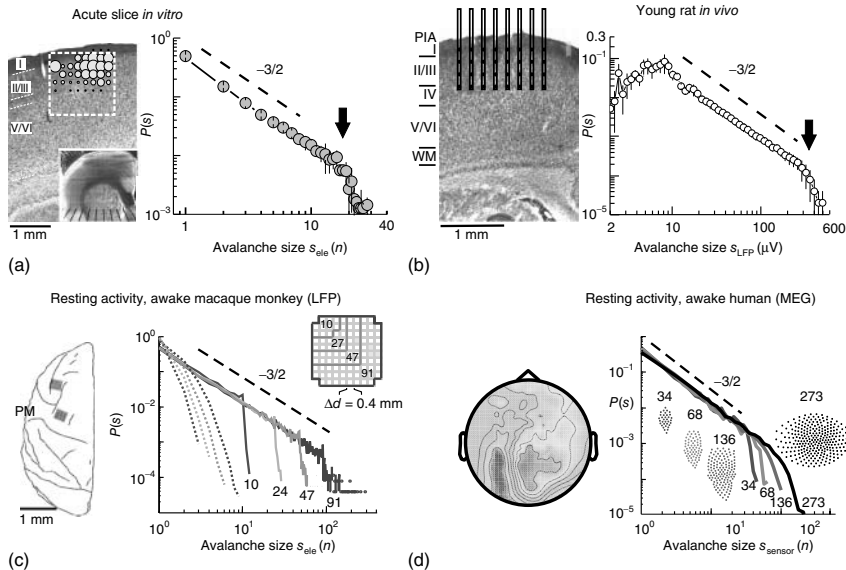


Figure 2.2 Power law in avalanche sizes in four different preparations of ongoing spontaneous activity. (a) Induction of neuronal avalanches by bath application of dopamine and NMDA at moderate concentrations. Left: Nissl-stain of somatosensory cortex region with superimposed nLFP density observed primarily in superficial layers II/III. Absence of activity in deep layers V/VI. Box: Microelectrode array (MEA) outline. Inset: Overview of coronal slice position on MEA. Right: Corresponding power law in neuronal avalanche sizes. Note slope of $-3/2$ (broken line) at optimal dopamine D_1 -receptor stimulation and cutoff (arrow; for details, see [72]). (b) Spontaneous neuronal avalanches in early differentiated superficial layers in the rat *in vivo*. Left: Nissl reconstruction of the position of the 32-MEA positioned in superficial layers (postnatal

day 13). Right: Corresponding power law in neuronal avalanche sizes (for details, see [81]). (c) Neuronal avalanches in the awake macaque monkey. Cutoff changes with area of the array used for analysis. Four distributions from the same original data set (solid lines) are overplotted using different areas (n). The power law reflects interactions between neuronal groups at different sites on the array and is not found for shuffled data (broken lines) (for details, see [83]). (d) Neuronal avalanches in the resting MEG of the human brain. Cascade size distributions are subsamples of the sensor array. Line gray scale and numbers indicate the number of sensors N in the analysis. Inset: Diagrams of the sensor array with corresponding subsamples. Broken lines: slope of $-3/2$ as guide to the eye.

also invalidates recent attempts to compare neuronal avalanches with processes that produce power laws steeper than -2 and have a well-defined average size [92]. Thus, $\alpha = -3/2$ implies that neuronal avalanches can provide spatial correlations in cortical networks of any size. Accordingly, we showed that neuronal avalanches describe the activity in small patches of cortex *in vitro* ($\sim 4 \text{ mm}^2$) [26, 72] and *in vivo* [81], and large cortex areas *in vivo* in nonhuman primates ($\sim 100 \text{ mm}^2$; Figure 2.2a–c). In fact, the scale invariance of neuronal avalanches extends to the whole human cortex (Figure 2.2d). Noninvasive measures of resting activity

in humans based on the millisecond precise MEG signal [79, 93] or the spatially more precise fMRI BOLD (blood-oxygenation-level-dependent) signal [94] revealed neuronal cluster sizes that obey this Eq. (2.1), and thus carry the signature of neuronal avalanches.

2.2.3

Neuronal Avalanches are Specific to Superficial Layers of Cortex

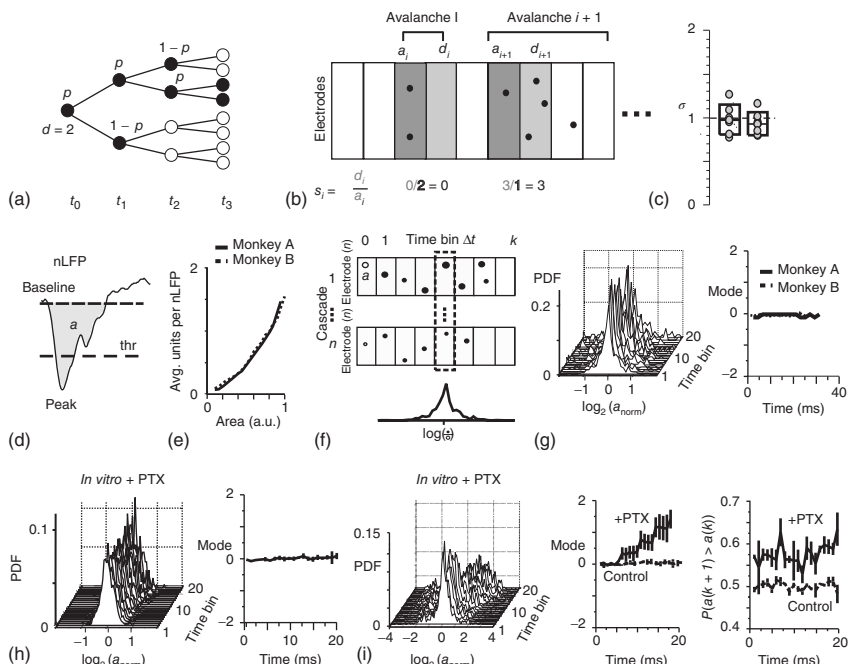
It is now soundly established that neuronal avalanches, when based on the LFP, are specific to the superficial layers of cortex [72–74, 81]. In acute slices and slice cultures, where the microelectrode arrays covered all cortical layers, nLFPs comprising avalanches were only found at electrodes overlying the superficial layers (Figure 2.2a; [72, 73, 81]). In the urethane-anesthetized rat and *in vitro*, a comparative, developmental study revealed that, indeed, neuronal avalanches emerge during development when superficial layers form; that is, when the cortical plate differentiates into a primordial network (Figure 2.2b; [81]) shortly before the arrival of layer 4 inputs [95]. In awake macaque monkeys, staggered arrays that allow for simultaneous recording in shallow and deep cortical layers show avalanches only in shallow, but not deep, cortical layers (Figure S4 in [74]). The localization of avalanche dynamics to superficial layers provides guidance for experimentalists and suggests simple explanations for negative findings on neuronal avalanches [92]. For example, recordings in the suprasylvian gyrus of cats using long-shank electrodes ($\sim 0.8\text{--}1\text{ mm}$) [96] will sample neuronal activity most likely from deep layers, given that this cortical area has a thickness of $1.5\text{--}2\text{ mm}$ [97].

2.2.4

The Linking of Avalanche Size to Critical Branching

The connection between a power law in size distribution with a slope of $-3/2$ and critical dynamics arises from the analysis of simple branching processes that model cascade formation, for example, the Galton–Watson branching process [98–100]. To be precise, if an ancestor at generation t_n leads to k new descendants in the next generation t_{n+1} and the probability of having descendants is p , then the average number of descendants from generation to generation will be $\sigma = kxp$, which is also called the *branching parameter* (Figure 2.3a). This branching model is rather simple because all ancestors/descendants behave the same. There is no overlap in descendants/ancestors between generations, and the parameters k and p are stationary. Yet, it captures cascade formation in the brain surprisingly well. In a recursion to the topic on criticality outlined in the introduction, if $\sigma = 1$, the population of events from generation to generation, on average, does not grow nor does it shrink. While many cascades will be short (there is after all a significant probability to not have descendants), some cascades will be long and some even longer. Theory dictates that, if $\sigma = 1$, cascade size distributes according to a power law with exponent alpha, α , equal to $-3/2$, that is, Eq. (2.1) [98, 99]. Thus, if neuronal avalanches fulfill $(\alpha, \sigma) = (-3/2, 1)$, then avalanches represent

critical dynamics. To demonstrate this relationship, one has to define ancestors for successive time steps of cascades and estimate the ratio of descendants to ancestors. For $\sigma = 1$, this ratio should be 1. Branching parameters are inherently difficult to measure as they require the calculation of ratios from noisy data at relatively high temporal resolution. The first analysis was carried out in binary form *in vitro*, that is, each nLFP in an avalanche was counted as a singular event, allowing the ratio of descendants/ancestor to be simply estimated by counting nLFPs in successive time bins [26]. It was found that, on average, one nLFP, that is, local, synchronized group of neurons (ancestor), is followed by exactly one new group (descendant) somewhere else in the network (Figure 2.3b,c). This result was recently confirmed for neuronal avalanches in the human brain based on the MEG [79] (see also Chapter 8). On the other hand, one could argue that whether or not an nLFP crosses a threshold is a very crude attempt to estimate neuronal group sizes. In fact, the nLFP amplitude and nLFP area monotonically grow with the number of isolated spikes at the same electrode, demonstrating that these nLFP parameters encode the size of the locally firing neuronal group, as shown for neuronal avalanches in organotypic cultures [82] and in awake nonhuman primates [74] (Figure 2.3d,e). Branching parameter analysis should take those dimensionalities between significant nLFPs into account. We therefore normalized each nLFP within an avalanche by the first nLFP of that avalanche (Figure 2.3f), and sorted normalized nLFP amplitudes from all avalanches into their respective time from the start of the avalanche. Critical branching predicts that neuronal group size at the beginning of an avalanche is maintained throughout the avalanche, and consequently normalized nLFPs should



distribute around the value of 1 for any time starting from the beginning of the avalanche. This was indeed the case for avalanches in organotypic cultures, in nonhuman primates (Figure 2.3g,h) [34] and in humans (Shriki and Plenz; see Chapter 8). The relationship is destroyed when changing the balance of excitation and inhibition. That is, under slightly disinhibited conditions, for example, using the GABA_A-receptor (GABA, gamma-aminobutyric acid) antagonist picrotoxin at modest concentration, nLFPs will grow during a cascade in accordance with the idea of supercritical branching (Figure 2.3i). The demonstration of a critical branching parameter quantifies the intuition introduced at the beginning of this chapter of how systems can achieve coherent, stable activity: if one local group triggers more than one group on average, propagated activity simply explodes. Conversely, if the ratio is less than 1, activity propagation terminates prematurely. The identification of neuronal avalanches shows that these intuitions can be quantified, and that this balance sets important constraints for the unfolding of

Figure 2.3 Balanced propagation according to a critical branching process characterizes avalanche dynamics *in vivo* and *in vitro*. (a) Sketch of a branching process with nonoverlapping generations. At each generation t , an ancestor can branch with likelihood p (filled circles) and average number of descendants d , here $d=2$. Shown is one realization of the stochastic process. (b) Interpretation of avalanches as a branching process. At each bin Δt , initiating events are interpreted as ancestors that lead to descendants in the next time bin. The average descendant-to-ancestor ratio provides approximates of the branching parameter sigma, σ , with $\sigma=p \times d$. (c) For neuronal avalanches in cultures, σ has been found to be close to 1 (for details, see [26]). (d) Definition of nLFP area a (gray; from baseline to baseline excursion). (e) The area a provides a quantitative measure about the output, that is, action potential firing, of the local neuronal group near the micro-electrode. Correlation between LFP area a and the number of action potentials, that is, “units,” fired during the nLFP (ongoing activity in awake macaque monkeys, left motor cortex in monkey A, averages over four arrays in premotor and motor cortex of monkey B; for details on monkey recordings, see [74]). (f) Sketch of estimating the change in a during cascades. For each time bin k , the log-values of $a(k)$ normalized to

initial nLFP area, $a(0)$, (open circle) are calculated for all cascades (box with broken lines) and collected into a histogram. Dot diameter indicates nLFP area. (g) Within avalanches, the initial nLFP area is maintained on average for all nLFPs throughout avalanche lifetime. *Left:* Stacked plot of probability density functions (PDFs) for successive time bin k during avalanches (monkey A). *Right:* Corresponding mode plot for all k and both monkeys. Monkey B averages over all four arrays. Note that mode = 0 indicates a ratio of $a(k)/a(0)=1$ equivalent to a critical branching parameter $\sigma=1$. (h) Corresponding analysis for spontaneous avalanche activity in organotypic slice cultures *in vitro*. (i) *Left:* Partial reduction in inhibition using 3–5 μM of picrotoxin (PTX) results in a systematic increase of nLFP area during cascade lifetime deviating from avalanche dynamics. *Middle:* Corresponding modes in cultures before (*control*) and during picrotoxin (PTX). *Right:* For avalanche dynamics, the probability of the next nLFP to be larger than the preceding nLFP, $P(a(k+1) > a(k))$, is equal to 0.5 throughout an avalanche’s life time. Thus, nLFPs are equally likely to be larger or smaller in the next time step. In contrast, this probability is larger by about 0.56, but constant when inhibition is reduced (for details, see [74, 34]).

activity in cortex – the size of the group that initiates an avalanche is maintained until the avalanche ends.

2.3

Neuronal Avalanches: Cascades of Cascades

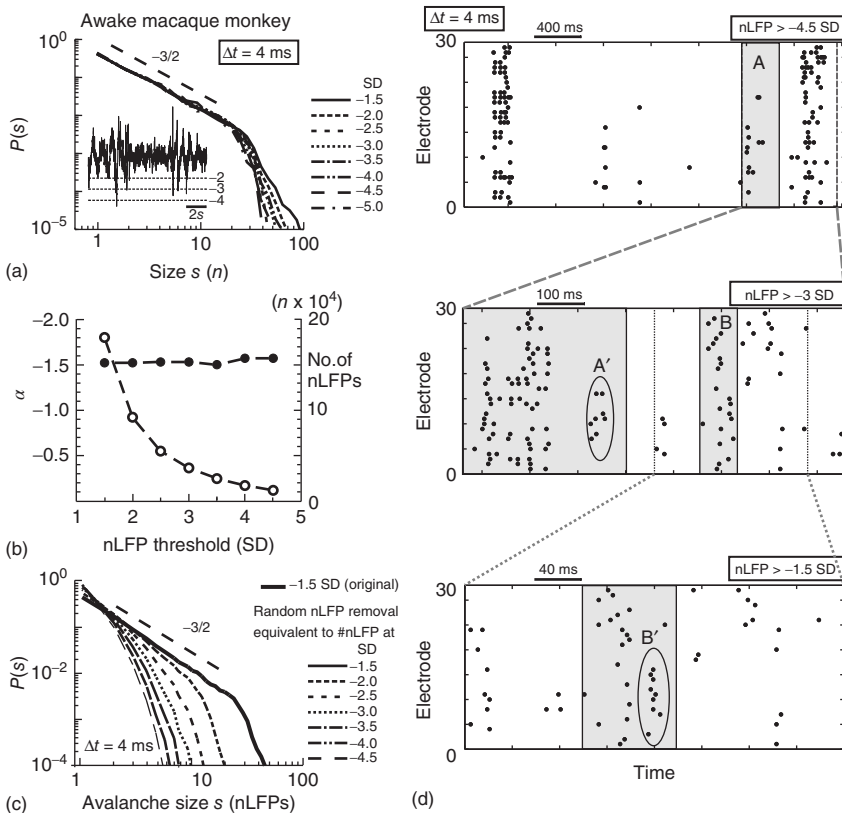
If neuronal avalanches are indeed the signature of a critical state of the cortex, one expects many aspects of avalanches should be scale invariant and obey power law statistics [2, 16]. In fact, our initial report that avalanches are robust to the threshold used to detect local significant events [26] led to further insight into the temporal organization of avalanches and their respective amplitudes. The sensitivity of avalanche organization to the detection of significant nLFPs was first systematically explored in neuronal avalanches from ongoing activity in the premotor (PM) and primary motor (M1) cortex in awake macaque monkeys (Figure 2.4) [74]. Simply ignoring nLFPs below a given threshold amplitude, that is, by increasing the threshold from -1.5 to -4.5 SD, removes hundreds of thousands of nLFPs from the analysis. Despite this amplitude-dependent loss of local events and no change in temporal resolution, we found the same size distribution for avalanches regardless of what proportion of smaller nLFPs were removed (Figure 2.4a,b). Conversely, if nLFPs are removed randomly and the number of nLFPs removed is matched to the loss of nLFPs encountered when one changes the threshold, the power law is readily destroyed (Figure 2.4c). This finding reveals a very specific relationship between the temporal organization of neuronal avalanches and their local group sizes – avalanches made up of large local

Figure 2.4 The power law in avalanche sizes is threshold invariant, which reveals embedding of avalanches within avalanches. (a) The power law in avalanche sizes does not change with minimal local neuronal group activity, that is, nLFP amplitude. Overplot of PDFs in avalanche sizes for different minimal nLFP threshold (in multiples of SD; $\Delta t = 4$ ms). Ongoing activity in primary motor area ($M1_{left}$) of a macaque monkey. Note cutoffs at respective array size of $n = 32$ electrodes. *Inset:* LFP time course at single electrode and superimposed thresholds thr of -2 , -3 , -4 SD for comparison. (b) The power law slope α (left axis) is constant despite a two orders of magnitude drop in the number of nLFPs participating in the clustering process (right axis). (c) Random removal of nLFPs differs from threshold-dependent nLFP removal and does not maintain scale invariance of

clusters. *Solid line:* Cluster size distribution at $thr = -1.5$ SD (original data). *Broken lines:* nLFPs were randomly removed from the original -1.5 SD raster to match number of nLFPs found for rasters at $thr = -2$, -2.5 , \dots , -4.5 SD respectively (see (a)). Corresponding cluster size distributions rapidly deviate from a power law. (d) Avalanches are found to “spawn” new avalanches when lowering threshold thr ($\Delta t = \text{constant}$). *Top:* nLFP raster period at $thr = -4.5$ SD (nLFP clusters appear “columnar”). *Middle:* Raster of expanded time period from *top* (gray box) at $thr = -3$ SD. Note segment A now contains more nLFPs at the lower threshold, which form new clusters, for example, A' (ellipsoid). *Bottom:* Raster of expanded time period from *middle* (gray box B) for $thr = -1.5$ SD. Filling in of new clusters in *middle* box B indicated by B' (ellipsoid).

events spawn new avalanches of smaller local event size in the near future, which in turn spawn avalanches with even smaller local events, and so on (Figure 2.4d). In other words, sequences of avalanches organize themselves as avalanches with a decrease in event amplitudes (Figure 2.5). This finding completes the essential picture of a scale-invariant organization of avalanches for all three dimensions: space, time, and nLFP amplitude, that is, size or degree of local synchrony.

This scale invariance to nLFP threshold led to the identification of a new temporal organization for neuronal avalanches, which describes the decay rate of after-avalanches following a main avalanche (Figure 2.5A). Historically, the Omori–Utsu aftershock law, or Omori law [101, 102], was found to describe the decay rate, R , of aftershocks that follow a major earthquake. R decays as a power law, $R \sim T^{-\beta}$, where T is the time since the last main shock, and the exponent β is close to -1 . A similar relationship describes the probability of avalanche occurrence after an avalanche of minimal size s_0 [34]. This power law demonstrates scale invariance in time for up to 1 s (Figure 2.5B). For example, the relative decay in after-avalanche rate between 10 and 50 ms is similar to that between 100 and 500 ms. As found for the avalanche size distribution, the Omori law is also



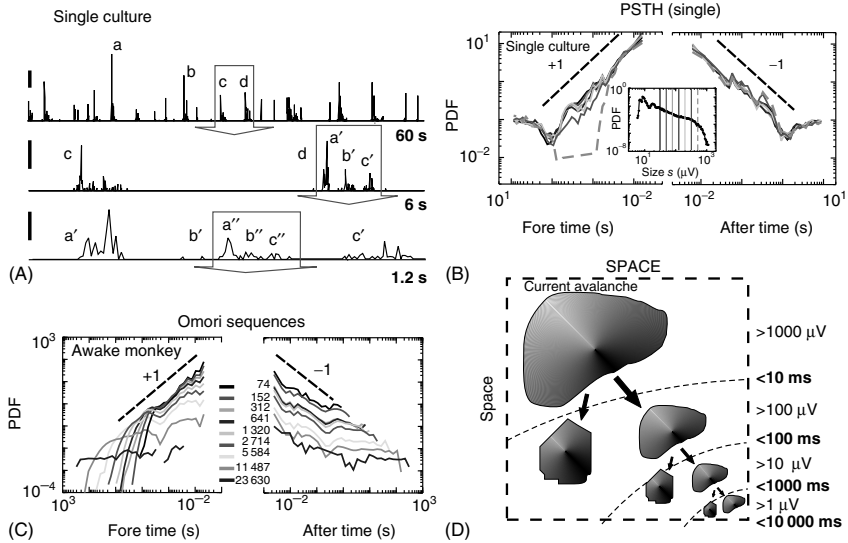


Figure 2.5 The Omori law and aftershock organization of neuronal avalanches. (A) Neuronal avalanche dynamics show a hierarchical organization of nLFPs in time for time scales <200 s. Integrated nLFP activity on the array ($\Delta t = 6$ ms; $n = 60$ electrodes) forms temporal clusters, where many large events are successively followed by smaller events ($a \rightarrow b \rightarrow c \rightarrow d \rightarrow \dots$). Large events are composed of self-similar hierarchical events at higher temporal resolution (e.g., left: $d \rightarrow a'$, b' , c' ; $b' \rightarrow a''$, b'' , c''). Three different time scales (top, middle, and bottom) are plotted. Arrows indicate subsequently enlarged time periods. (B) The frequency of avalanches occurring before (foreshock) or after a main avalanche (aftershock) follows power laws with a unity exponent similar to Omori's law for earthquake aftershocks. The equivalent to the Omori law is independent of main avalanche size, as shown by the superimposed plots of the shock probability leading to (fore time) or following (after time) main avalanches of different size s . Size bands $<32 \mu\text{V}$, 32 to $<50 \mu\text{V}$, and so on are indicated by the gray-scale-coded vertical line in the PDF size distribution (inset; single organotypic culture).

Note that foreshock and aftershock PDFs are symmetrical until the trigger size falls outside the power law regime of avalanche sizes ('broken line'; *inset*). For that size, the foreshock, but not aftershock probability is drastically reduced (*broken line*). (C) Omori and inverse Omori sequences for neuronal avalanches in the ongoing activity of an awake macaque monkey (monkey A from [74]). In contrast to the peristimulus time histogram, which considers all shocks within a fixed period after a main shock of size s_0 , Omori sequences are calculated by considering aftershocks up to the next main shock of size s_0 or foreshocks since the last main shock of size s_0 . (D) The organization of avalanches within avalanches. Sketch of current avalanche (compact spatial, gray region) that spawns future avalanches (arrows), some of which similarly spawn new avalanches, and so on. Relative changes between successive avalanches in spatial extent, temporal succession, and neuronal group size are constant, resulting in a scale-invariant organization quantified by power laws as predicted for critical state dynamics. For simplicity, power laws are assumed to have unitary slopes.

invariant to the minimal size of the main avalanche, which is in line with previous reports on the Omori law for earthquakes (cf. Figure 2.6). On the other hand, one can show that small avalanches on average spawn fewer avalanches than large avalanches. This can be shown by calculating the so-called Omori sequences, in which the avalanche density for avalanches smaller than the trigger avalanche is estimated (Figure 2.5C). This is summarized in the law of productivity that relates an avalanche with subsequent avalanches. For earthquakes, given the Omori law, it is natural to calculate the average number of aftershocks that follow a main quake of size s until the rate of aftershocks has reached seismic background levels. The number of aftershocks is known to increase by $N_A \sim s^\delta$, with size of the main shock s and exponent $\delta = 0.8$. We found that a similar law predicts the number of after-avalanches the cortex will generate given a main avalanche of minimal size s_0 . Indeed, the number of after-avalanches N_A increases with minimal size s_0 as $N_A \sim s_0^\delta$ and $\delta = 0.8 \pm 0.05$ ($n = 13$ cortex cultures) [34]. The sketch in Figure 2.5D summarizes the essential power law relationships between successive avalanches with respect to inter-avalanche time, avalanche size, and nLFP intensity.

2.4

The Statistics of Neuronal Avalanches and Earthquakes

For comparison, the three relationships in the organization of neuronal avalanches and their corresponding laws for earthquakes have been plotted in Figure 2.6. These laws have also been found for solar flares [106], and thus they point to universal dynamics in certain complex systems believed to be critical. The discovery of equivalent relationships for neuronal avalanche dynamics has a series of important implications for cortex dynamics. First, the Omori law is a law pertaining to the temporal aspects of avalanche dynamics – it describes the likelihood of future avalanches. In contrast to our intuition, the change in decay rate does not depend on the size of the trigger avalanche. Thus, it demonstrates invariance in the temporal domain of avalanche organization. In fact, the productivity law truly introduces size as an important factor in brain dynamics. Large avalanches are followed by more after-avalanches than small avalanches. This is the first result on avalanche dynamics that demonstrates size matters.

2.5

Neuronal Avalanches and Cortical Oscillations

Synchronized activity in the cortex has been studied predominantly in the context of oscillations [43–45] and strong experimental evidence correlates phase locking of γ -oscillations with elementary cortical operations such as binding low-level information into high-level concepts, that is, a “gestalt” [46–48, 107]. If critical dynamics are true alternatives to “bind” elementary features in cortical information

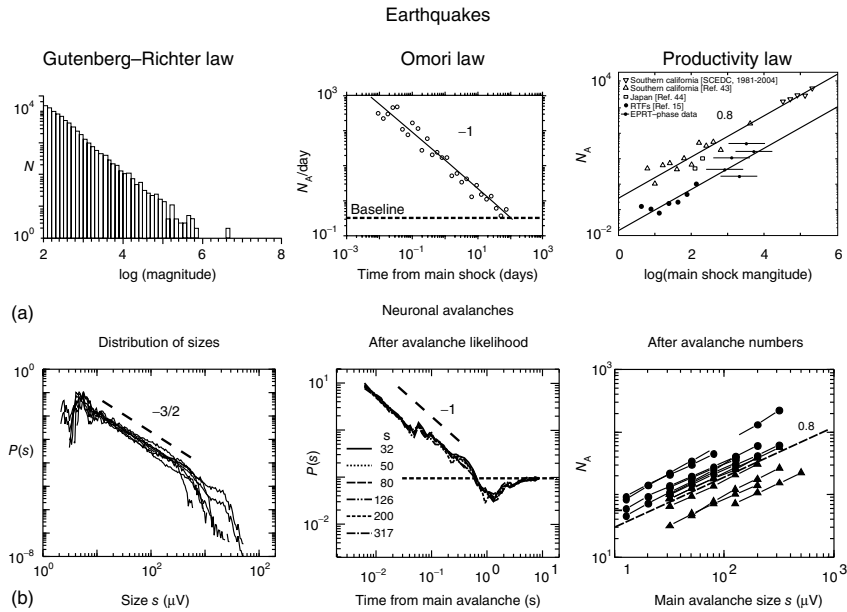


Figure 2.6 Three power laws describe the statistical organization of earthquakes that are also found for neuronal avalanches. (a) *Left:* The Gutenberg–Richter law links the probability of an earthquake with magnitude M to a power law that decays with an exponent close to -1.6 , here shown for Southern California earthquakes [103]. *Middle:* The Omori law describes the decay in aftershocks as a power law of T^{-1} (recent earthquake in Vrancea, Bulgaria [104]). *Right:* The law of productivity links the number of aftershocks N_A to the size of the main shock s by a power law $N_A \sim s^{0.8}$ [105]. (b) Corresponding relationships describe the

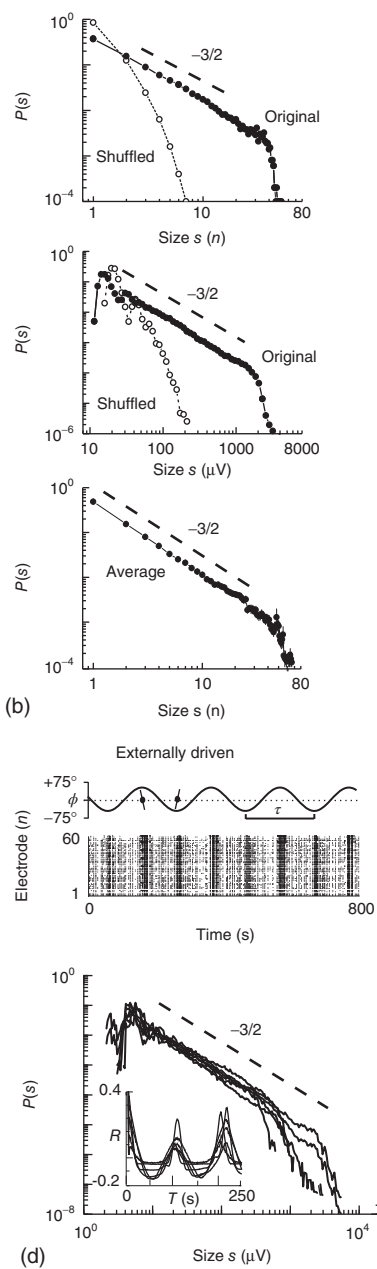
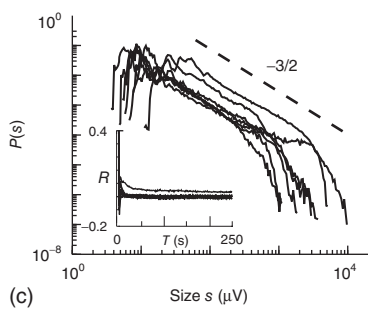
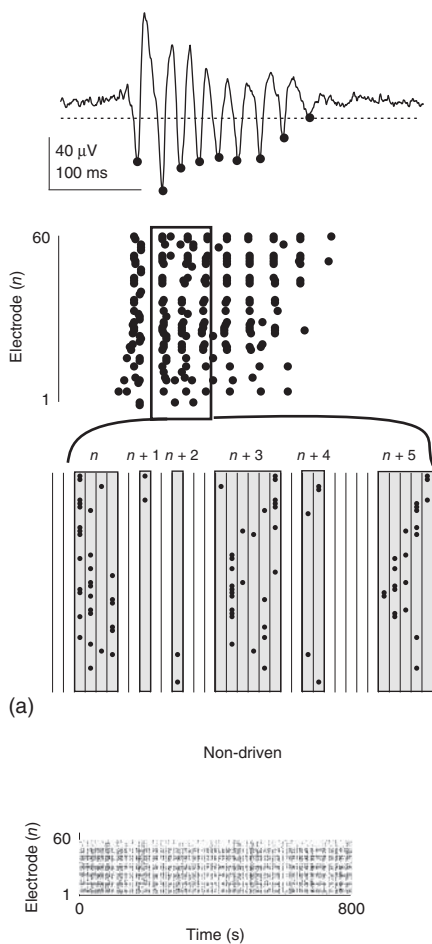
organization of neuronal avalanches. *Left:* The probability of an avalanche of size s follows a power law with slope -1.5 ($n=6$ slowly rocked cortex cultures). *Middle:* Decay in avalanche probability following a main avalanche. The power law with slope of -1 does not depend on the trigger avalanche size s (single cortex culture). *Right:* Productivity law for avalanches with an average exponent of $\delta=0.8 \pm 0.05$ (filled circles; $n=12$ organotypic cortex cultures; see also Figure 2.7d; triangles: awake macaque monkeys; broken line: slope of -1). For further details, see [34].

processing through cascading activity, the dynamical concepts of oscillations and neuronal avalanches need to be reconciled. At a minimum, they have to be shown to coexist or, at best, to complement each other to improve cortical information processing. A key aspect in our present understanding of the connection between cortical oscillations and avalanches is that oscillations in the cortex do not represent simple, stationary recurrent activity limited to narrow frequency bands. On the contrary, all major physiological frequency bands – theta (θ)/alpha (α), beta (β), and gamma (γ) – correlate with diverse cortical functions [108]. These frequency bands often emerge together, thereby forming complex spatiotemporal dynamics of nested oscillations that wax and wane in amplitude and phase locking. For

example, while initial reports emphasized zero phase lag between cortical sites that exhibit gamma oscillations [109], recent analysis provides a rich picture of varied nonzero phase locking at γ -frequency that is amendable to stimulus presentation [110, 111]. In fact, we demonstrated experimentally that the diversity in broadband phase locking is maximized at criticality [112] (see also Chapter 15). We further showed in a comparative *in vivo* and *in vitro* study [81] that neuronal avalanches emerge together with short-lasting β - and γ -oscillations nested into θ -oscillations at the time of superficial layer differentiation. When superficial layers form, the coherence in each frequency band is high and decays only slowly over distance, demonstrating synchrony in the form of phase-locked oscillations between distant cortical sites. On the other hand, participation of individual cortical sites during these nested oscillations appeared irregularly and with varied phase lag (Figure 2.7a). When extracting nLFPs from these oscillations, the resulting spatiotemporal nLFP patterns distributed on the basis of size with a power law of -1.5 , the hallmark of neuronal avalanches (Figure 2.7b). The precise match between nested oscillations and avalanches was highly regulated and shown to be sensitive to dopamine (DA) D_1 -, glutamate, and GABA_A-receptor antagonists. These findings demonstrate that (i) nested cortical oscillations coexist with neuronal avalanches and (ii) the variability in the oscillations of amplitude and phase locking observed in nested oscillations is highly organized in the form of neuronal avalanches.

This rather challenging picture of cortical dynamics opens a wide corridor between criticality and oscillatory activity in the brain that needs to be explored further. One of the first concerns is an understanding of how an avalanche can fit into a continuous oscillation, for example, γ -oscillation. If multiple cycles contribute to an avalanche, avalanche patterns would reflect recurrent activation of single cortical sites. This is typically not the case as recurrent activations of sites are, in fact, rare, which allows the spatiotemporal pattern of avalanches to be collapsed into spatial objects for analysis [83]. This constraint in the temporal organization of avalanches is implicit, given the relationship between avalanche size and avalanche duration or life time. The life time of neuronal avalanches follows a power law with slope of -2 [26, 34] in line with expectations for a critical branching process (e.g., [113]). Notwithstanding that spatially more extended (i.e., larger) avalanches also last longer on average [74], avalanche lifetime still drops much faster than avalanche size owing to the differences in their respective power law exponents (-2 for lifetime vs $-3/2$ for size). Even if the power law is not observed, the lifetime distribution drops closer to a lognormal or exponential distribution (e.g., [74]). In fact, within an area of $2\text{ mm} \times 2\text{ mm}$, a typical correlation length for γ -oscillations for even large avalanches lasts no longer than $10\text{--}12\text{ ms}$ [26, 34] and multiple avalanches fit neatly into one γ -cycle.

Another concern is related to the obvious ability of avalanches to form despite the presence of an imposed, slow dynamic, such as oscillations. This, in fact, is an important property of Selforganized Criticality (SOC) and is generally known as *separation of time scales* (e.g., [1]). It is fundamental to systems that exhibit SOC as they are slowly driven far from equilibrium. If the forced driving occurs



at a time scale slower than the relaxation process intrinsic to avalanche formation, avalanching is not affected. In fact, simulations of SOC usually track avalanching until it stops before adding new driving, carefully separating intrinsic dynamics from external forcing. A sand pile at SOC can serve as a simple analogy for this phenomenon. The addition of grains is required to trigger new avalanches and thus the rate of avalanches will change in proportion to the slowly varying rate of grain addition. Using a custom-designed incubator [114], we experimentally demonstrated such separation of time scales for neuronal avalanche dynamics by slowly rocking organotypic cultures grown on multi-electrode arrays while recording their neuronal activity [34]. The slow rocking periodically increased the rate of spontaneous nLFPs up to 500% from baseline activity, as evidenced in the oscillatory autocorrelation function at driving frequency (Figure 2.7c,d). Despite the externally imposed change in activity level, neuronal avalanche dynamics, that is, a power law in cascade size distribution with slope of -1.5 as well as the respective lifetime distributions, were maintained. Incidentally, these experiments also imply that homeostatic regulation of neuronal avalanches is not tied to a particular average rate of nLFP activity, which is in line with our recent study on avalanche formation during cortex development *in vitro* [73].



Figure 2.7 The diversity of nested oscillations is captured by the power law of neuronal avalanches. (a) *Top*: Single-electrode LFP of a spontaneous nested γ -oscillation in a cortex culture *in vitro* (for further details and *in vivo* example, see [81]). Broken line indicates threshold for nLFP extraction (black dots). *Middle*: Corresponding period of nLFPs on the array reveals heterogeneous electrode participation and temporal delays during repeated oscillation cycles. *Bottom*: Zoomed view of $n=6$ consecutive avalanches that form during three consecutive γ -cycles. *Vertical lines*: temporal resolution Δt . *Gray areas*: neuronal avalanches. Note diversity of avalanche patterns between cycles. (b) nLFPs during spontaneous nested oscillations organize as neuronal avalanches. nLFP pattern sizes distribute according to a power law with slope of -1.5 for single cultures when based on nLFP numbers (*top*) or on summed nLFP amplitude (*middle*) as well as for the average (*bottom*, $n=15$ cultures). (c,d) Separation of time scales supports the view that avalanche dynamics indicate self-organized criticality (SOC). (c) Power law in avalanche sizes in the absence of externally modulated

activity rates. *Top*: Spontaneous nLFPs recorded in cortex slice cultures grown on 60-channel microelectrodes (for details on cultures and recording conditions, see [73]). *Bottom*: Avalanche size distributions with exponent of $-3/2$ (broken line) for all $n=7$ cultures. Sizes are calculated in summed, absolute nLFP peak amplitudes. PDFs calculated using log-binning. *Inset*: Corresponding autocorrelation function for nLFPs averaged over all electrodes for each culture. Note low correlations for time $T > 10-25$ s. (d) Separation of time scale in externally modulated cultures with avalanche dynamics. *Top*: Slow rocking ($\tau=200$ s cycle time; Top) inside an incubator induces rhythmic changes in nLFP rate at extreme angles (symbols) with period $\tau/2$. Raster display of cortical nLFPs (dots) for 60 electrodes (single experiment; cortex-ventral tegmental area (VTA) co-culture; for details on cultures, see [73]). *Bottom*: The power law in size s with exponent $\alpha=-3/2$ (broken line) is preserved during slow rocking ($n=7$ cultures). *Inset*: Corresponding average autocorrelation for nLFPs demonstrates strong temporal correlations induced by external slow modulation in nLFP rate (for details, see [34]).

The picture that emerges from these experiments is that the diverse, transient phase locking observed in cortical oscillations reflects the underlying organization of neuronal avalanches. If this is correct, then cortical oscillations alone are an inaccurate assessment of cortical dynamics. In fact, theories on cortical oscillations lack insight into the rather demanding constraints of avalanche dynamics, such as the temporal and spatial organization of cascades quantified by power law exponents for sizes, life times, aftershocks, productivity, and a critical branching parameter. From a more practical point of view, cortical oscillations add a frame of temporal reference to intrinsically scale-invariant dynamics, which might facilitate temporally precise interactions of the brain with environmental cues.

Recent neuronal simulations have succeeded in capturing a relationship between alpha oscillations and neuronal avalanches [115]. The avalanche organization was found within each oscillation cycle, proving similar to our earlier reports *in vitro* and *in vivo* [81]. Importantly, the simulations demonstrated that long-range critical scaling in oscillation amplitude emerged when the model exhibited avalanches. They thus link a large body of work on criticality in humans based on long-range scaling laws for oscillatory activity to neuronal avalanche dynamics (e.g., [93, 116]; see also Chapters 5 and 13). Recent modeling work also demonstrated long-range temporal correlations in the organization between successive up-states that trigger avalanche formation [117].

2.6

Neuronal Avalanches Optimize Numerous Network Functions

One of the central questions about neuronal avalanches has been their potential benefit for cortex function. Recent work has shown that their intricate organization in time, space, and neuronal group sizes optimizes several properties of cortical networks. It is well accepted that cortical networks have to be balanced in order to be responsive; otherwise, they are either overly inhibited or epileptic, both compromising their ability to adequately respond to inputs. This rather qualitative picture was put on more solid theoretical and experimental ground in a series of recent publications. On the basis of computer simulations, Kinouchi and Copelli [27] predicted that networks with neuronal avalanches have maximized dynamic range; that is, they are able to produce a distinct network response to weaken as well as strengthen stimuli (see also [118, 119]). This was confirmed experimentally [120] using cortical slice cultures grown on microelectrode arrays (Figure 2.8a). In that study, neuronal avalanche activity was monitored in individual cultures over the course of weeks. Bath application of small concentrations of ionotropic glutamate and GABA_A-receptor antagonists were used to change the ratio of fast excitation to fast inhibition (E/I) in the cultures and to move spontaneous activity away from avalanche dynamics. Dynamic range was measured by recording evoked responses to single-shock stimuli delivered through the electrode array as a function of how far the network was from avalanche dynamics. Remarkably, not only did the dynamic range peak when networks showed neuronal avalanches but the absolute change

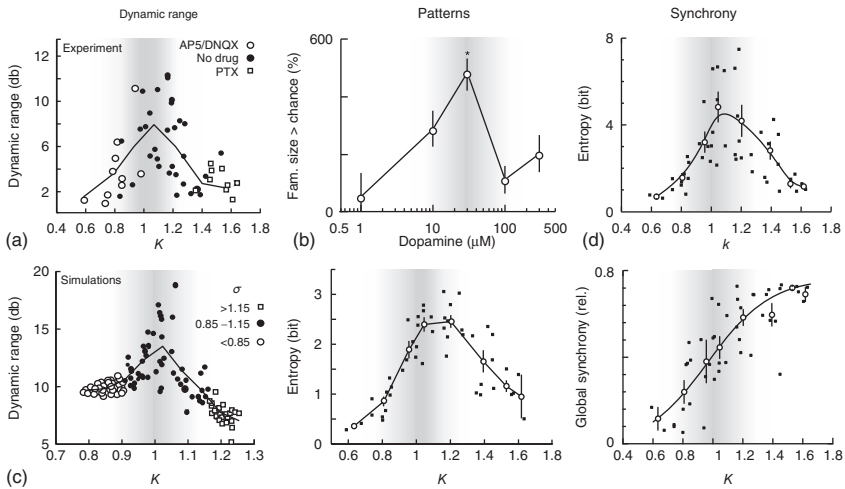


Figure 2.8 Neuronal avalanche dynamics optimize numerous aspects of information processing in cortical networks. (a) Dynamic range is maximized in cortical networks with neuronal avalanche dynamics. *Top:* The balance of excitation and inhibition (E/I) was changed pharmacologically to deviate the activity in organotypic cultures from avalanche dynamics quantified by κ , that is, the similarity of the measured cluster size distribution, to the expected power law with slope of $-3/2$ distribution. For $\kappa \sim 1$, activity represents neuronal avalanches, $\kappa < 1$ indicates hypo-excitability (E/I low), $\kappa > 1$ indicates disinhibited dynamics (E/I high). *Bottom:* Neuronal network simulation showing maximal dynamic range for $\kappa = 1$ (for

details, see [82]. (b) Pattern variability and recurrence peaks for cortical networks at moderate dopamine concentration when spontaneous activity organizes as avalanches (acute slice; see [72] for details). (c) The entropy, that is, information capacity, of binary nLFP patterns peaks for avalanche dynamics (single dots: individual experiments; open circles: average; for details, see [120]). (d) The ability to synchronize and desynchronize for neuronal groups is maximized for neuronal avalanche dynamics. *Top:* Entropy of synchronized nLFP patterns as a function of κ . *Bottom:* Maximal entropy is found when global synchronization is intermediate (see [112] for details).

in dynamic range, as networks moved away from the avalanche dynamics, was also in line with predictions from a system in a critical state [27, 82].

Cortical networks with neuronal avalanche dynamics also exhibit the largest diversity in spontaneously recurring spatiotemporal patterns [72]. The ability of cortical networks to produce a large diversity of recurrent patterns is considered to be important for memory storage (in the form of a specific pattern) and memory recall (the likelihood of pattern recurrence). Indeed, spontaneous pattern recurrence has been demonstrated during sleep in hippocampus–cortex interplay [121] and the involvement of spontaneous patterns in memory formation is suggested by findings that sensory evoked patterns are more likely to recur during subsequent spontaneous activity [122, 123]. In acute slices of medial prefrontal cortex (mPFC) from adult rats (>9 weeks old), bath application of DA and *N*-methyl-d-aspartate (NMDA) together induces avalanches in superficial cortex layers. Avalanche induction as well as diversity in recurrent patterns was maximal at moderate DA concentrations,

and reduced at low or high DA concentration, revealing an inverted-U profile (Figure 2.8b). The effect was specific for the DA D₁-receptor and required NMDA glutamate-receptor stimulation, as well as an intact GABA_A-system [72]. This rather complex pharmacological profile is well known from studies on working memory, where performance peaks at moderate DA D₁-receptor stimulation [124, 125] and decreases when the NMDA receptor is blocked [126, 127]. This important role of DA in regulating neuronal avalanches was confirmed *in vivo* at the earliest time of superficial layer formation. In young, urethane-anesthetized rats, reduction of the DA D₁-receptor tone destroys neuronal avalanche dynamics in these layers early during development [81]. Other optimizations at criticality that were demonstrated experimentally are the maximization of information capacity (Figure 2.8c) [82] and the ability to synchronize and desynchronize at moderate global synchronization level (Figure 2.8d; [112]; for further reading, see [128] and Chapter 15).

2.7

The Coherence Potential: Threshold-Dependent Spread of Synchrony with High Fidelity

Research described in the previous section focused on various aspects of information processing that are improved when a network is in a critical state. Yet, quite a different aspect of information processing in many-body systems, at or near a border that resembles a second-order phase transition, has played out in the context of Cellular Automata (CA) under the key phrase “edge of chaos” [32]. CA are models in which the status of a cell in the next generation depends on the current status of a cell and its neighbors [129, 130]. Popularized by John H. Conway’s “Game of Life” [131], CA became particularly interesting when it was found that some CA exhibit computational universality; that is, suitable initial conditions imply arbitrary algorithm procedures [31]. Langton [32] divided the enormous rule space that exists even for simple CA into rules that support versus rules that do not support survival to the next generation. He showed that when death rules dominate, patterns die out quickly, whereas if survival rules dominate, dynamics become chaotic. Long-lasting and spatially complex but ordered patterns evolve when the number of survival rules matches the number of nonsurvival rules, that is, the probability of survival versus death is balanced. The fact that interesting computation can only be found in the balanced regime is not correct [132], but “the edge of chaos” nevertheless became an interesting transition regime, which was demonstrated to support the formation of long-range temporal correlations and to improve input spike train classification [118, 119, 133–135] if average connectivity is low in neuronal networks [136]. Strikingly, at that border, CA can spawn so-called propagating structures [32] similar to those one-dimensional class IV CA attributed by Wolfram [31] to have computational universality. These propagating structures emerge at the network level from an initial configuration of active cells (e.g., a “glider” in the “Game of Life”) and propagate while periodically revisiting their

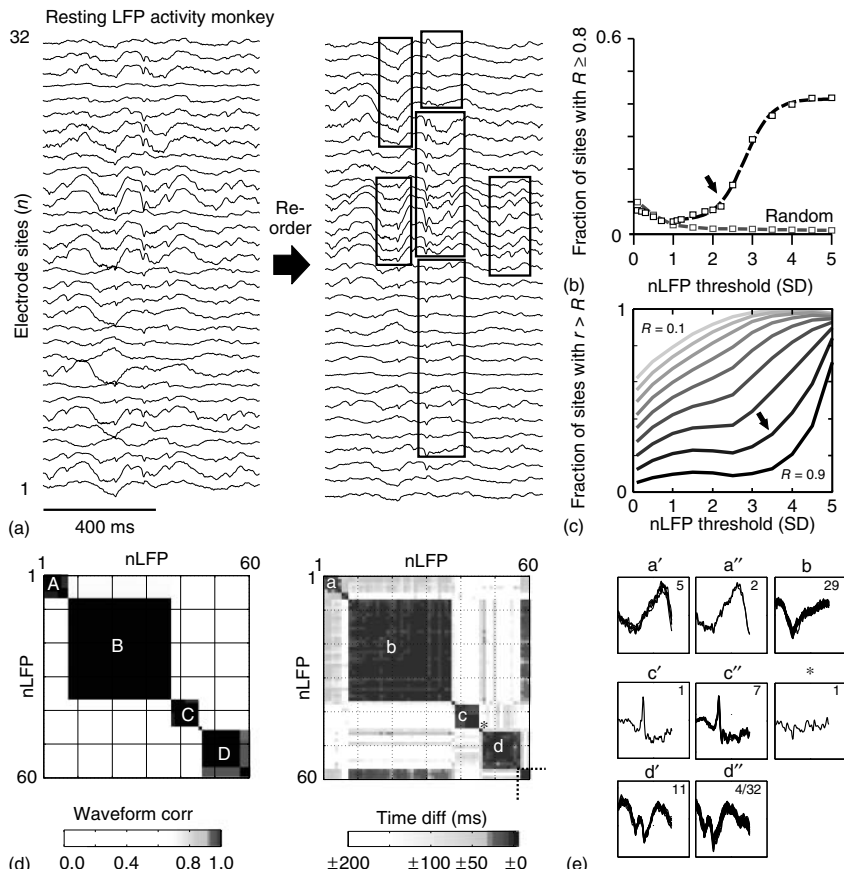
initial configuration. This allows information to be transferred with great precision within the system [137].

In cortical networks, in which the excitation (“survival”) and inhibition (“death”) are appropriately balanced to establish neuronal avalanche dynamics, we found a new dynamical subclass that was separated by a threshold function for synchrony at the network level [33]. Avalanches within this subclass shared many features of propagating structures described for CA. In the preceding sections, it was shown how within one avalanche, the initial nLFP size, whether measured as area or amplitude, is preserved, which is in line with the expectation for a critical branching process. When analyzing for the preservation of the nLFP waveform, it was found that if the nLFP amplitude reached beyond a threshold, then its amplitude *and* waveform was exactly replicated by all other nLFPs within an avalanche (Figure 2.9a–c). We termed these avalanches with amplitude and waveform identical nLFPs – *coherence potentials* [33]. They reflect broadband synchrony that engages multiple sites in cortex for hundreds of milliseconds, and were found in ongoing neuronal avalanche activity in awake, nonhuman primates, and in organotypic cultures. Because the nLFP amplitude correlates with the local firing rate and the number of synchronized neurons, we concluded that once a synchronized group of sufficient size has formed locally, it becomes engaged in producing an exact replica of its activity profile at multiple distant sites. We, therefore, equated the coherence potential at the population level to the action potential at the single-cell level. The coherence potential has also recently been found to correlate with the initiation of specific motor movements in humans [138].

It is well established at the single-cell level that the nervous system uses two fundamentally different mechanisms for the transfer of information. Subthreshold processing of inputs is governed by cable equations [15], physical laws found in many other physical systems. It allows neurons to gradually integrate inputs, a preparatory step for the nonlinear process to fire an action potential and to pass this decision on to other nerve cells. Once the action potential has formed, it is spatially distributed with great fidelity. This essentially binary process is often associated with a sigmoidal, threshold function. For example, at the single neuron level, the probability of an action potential is a sigmoidal function of the membrane potential value. The probability is high and saturates if the membrane potential is high. Conversely, the probability is low and quickly drops to negligible values if the membrane potential is low. We found that a similar nonlinearity, that is, threshold, exists at the network level for coherence potentials (Figure 2.9b,c). Most avalanches reflect “sub”-threshold activity, whereas coherence potentials reflect a binary decision process analogous to an action potential generation at the single-cell level.

Coherence potentials have numerous important properties. (i) In a coherence potential, LFPs from different sites are shifted in time, with the total delay between the first and last LFP of up to 50 ms given a cortical area of $\sim 8 \text{ mm} \times 8 \text{ mm}$. Such delays are expected for synaptic propagation of neuronal activity and are inconsistent with the idea of volume conduction as a potential mechanism. (ii) Most coherence potentials are spatially noncontiguous, that is, coherent LFPs are not necessarily near each other. This, again, excludes volume conduction

as a potential explanation of this activity. (iii) The coherence potential is in line with balanced propagation found for neuronal avalanches. The local LFP at different sites that belong to the same coherence potential LFPs, because of their replication in waveform *and* amplitude, maintain the same LFP area. The fact that there is no growth (explosion) or decay (dissipation) in the space within a coherence potential is in line with expectations from critical state dynamics. (iv) The nonlinear threshold function that describes the spatial coverage of the coherence potential (Figure 2.9b,c) [83] is destroyed when the balance of E/I is shifted pharmacologically. Thus, coherence potentials arise when the network has balanced E/I and spontaneous activity organizes as neuronal avalanches. (v) LFP waveforms of successive coherence potentials are *not* similar (Figure 2.9d,e). The *a priori* similarity of successive coherence potential does not differ from random similarity. In that respect, coherence potentials differ from action potentials in their stereotypical waveform. However, similar to the action potential, the waveforms of nLFPs for a given coherence potential are identical at all participating sites, except for a shift in time. This allows the waveform of a coherence potential to



be proposed as a high-dimensional coding space. (vi) The specific waveform of a coherence potential correlates with a specific local spike sequence [33]. Thus, successive coherence potentials reflect fast transitions between temporally stable forms of synchrony, the hallmark of “metastability” [139, 140].

Multiple coherence potentials can exist simultaneously within a given cortical region [33]. Thus, coherence potentials allow us to lift Ashby’s original question about neurons connected with each other to the network level itself: “the general question then becomes: if large numbers of dynamically active parts are joined at random and allowed to act and interact freely on one another, what will happen?” [141]. Currently, our understanding of the interactions between coherence potentials in the form of cortical syntax or compositionality is still in its infancy, and simulations of cascade interactions reveal a complex picture. Excitatory wave packets in a homogeneous network architecture, such as a synfire chain, the closest analog to coherence potentials, carry a nonspecific “shadow” inhibition (Aviel [62]) that makes cascades or wave fronts merely “bounce” off each other [142]. On the other hand, more heterogeneous interconnectivity between different synfire chains can allow chains to merge or spontaneously synchronize [143].

2.8

The Functional Architecture of Neuronal Avalanches and Coherence Potentials

The functional relationships that describe neuronal avalanches and coherence potentials so far provide little insight into the specific spatiotemporal unfolding of avalanches. Avalanche size, life time, the Omori law, and productivity law all address the spatial or temporal “envelope” of avalanches. But these measures are

Figure 2.9 Coherence potentials reveal a sigmoid function for the probability of multiple sites exhibiting exactly the same neuronal activity. (a) Ongoing activity in an awake macaque monkey (MI; 32 electrodes) with avalanche dynamics (for details, see [74]). The 800 ms time traces reveal unique deflections (left) that seem to be repeated at other sites and are particularly obvious after reordering (right). Some waveform repeats are grouped for visual display (rectangles). (b) Coherence potential function has a nonlinear, threshold-like shape. For the monkey in A, the fraction of sites at which nLFPs with $R \geq 0.8$ correlated waveforms are found increases rapidly for nLFP amplitudes >-2 to -3 SD (arrow). *Random:* Expected fraction for comparison between randomly chosen initiation times. (c) Change in threshold function with

increase in similarity demand. The nonlinear rise is clearly visible ($R > 0.8$) for high similarities. (d) 60 successive nLFPs with amplitude exceeding -3 SD threshold in the monkey from A. nLFPs cluster in waveform correlation (left) and temporal delay (right) into 4–5 clusters, that is, coherence potentials. (e) nLFP waveforms for each coherence potential are peak aligned and over plotted. Note the exact replication of complex waveforms for each coherence potential and dissimilarity of successive coherence potentials. Waveforms separated by the cluster algorithm because of large temporal delays nevertheless show high similarities and are labeled (‘) and (‘‘), respectively. Last waveform continues into the next coherence potential (44 nLFPs), of which only the first 15 have been analyzed in (d).

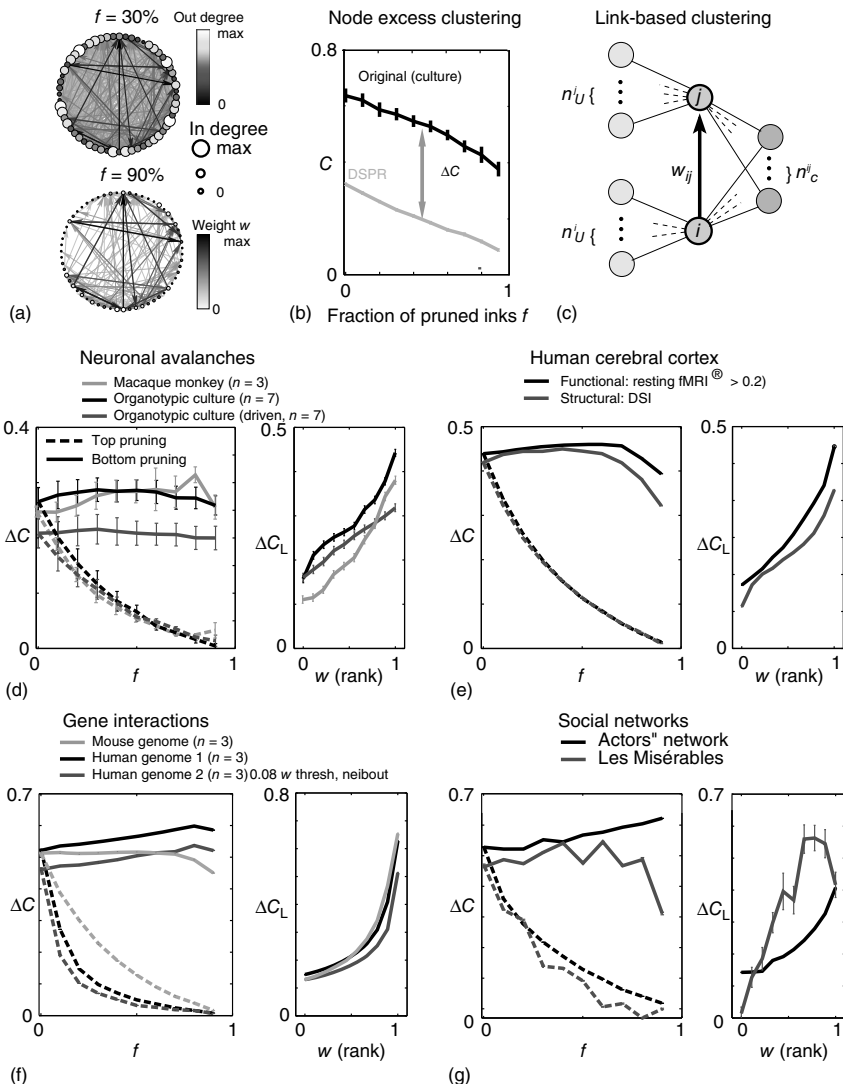
ambiguous with respect to the actual pattern, and an avalanche of a given size can be realized by many spatial configurations of participating sites. Surely, if cascading activity in the form of avalanches “bind” diverse cortical neuronal groups and cortical sites into a higher order concept, that is, “gestalt,” the specific spatial and temporal organization of an avalanche should carry information and one might expect at least some avalanche patterns to recur more often than what would be expected by chance. This, indeed, was shown in early studies using greedy clustering algorithms to extract significant avalanche patterns in organotypic cultures [144] and acute cortex slices [72]. Clustering algorithms, however, established significance only for a small group of avalanches, which seems in contradiction to the power law in avalanche sizes stating that all avalanches are related to each other. In fact, more elaborate studies of significant patterns established a power law for pattern recurrence of avalanches that was independent of the threshold used to cluster avalanche patterns [72]. Recently, we also showed that when taking individual avalanche patterns into account, specific scaling laws are fulfilled, identifying a unique set of universal exponents [145].

To identify more specifically the rules that might govern avalanche patterns, we developed a Bayesian inference method that incorporates critical or near-critical branching process dynamics to map directed avalanche propagation in the network into a weighted, directed graph (Figure 2.10a; [146]). We showed analytically and through network simulations that this approach reliably maps propagation within

Figure 2.10 Small-world topology with weight-based, excess node clustering and link clustering characterizes neuronal avalanche, brain, gene, and social networks. (a) Weighted, directed functional network identifying the flow of spontaneous neuronal avalanche activity between 60 sites in a single neuronal cortex culture. Visualization of 30% and 90% of the weakest links removed (“bottom pruning”) and corresponding in- and out-degree changes for each site. Max: Maximal values of the original network. (b) Bottom-pruning analysis of the clustering coefficient C for $n=7$ cultures from A. *DSPR*, degree-sequence-preserved randomization; ΔC , excess node clustering. (c) Link-clustering coefficient C_L of a single directed link is defined as the relative overlap between the neighborhoods of the end nodes. Dark gray, common nodes; gray, uncommon nodes. (d) In functional cortex networks, ΔC is robust to removal of the weakest links and activity preferential travels between sites with overlapping neighborhoods. Left: ΔC plotted against the fraction

of links pruned, f . Functional connectivity derived from ongoing neuronal avalanche activity of nondriven cultures (black; $n=7$; [26], externally driven cultures (red; $n=7$; [34]), and left premotor cortex of awake macaque monkey (green; $n=3$ [74]). ΔC is virtually constant for most of the weakest links removed (bottom pruning; solid lines), but decays rapidly when the strongest links are pruned (top pruning; broken lines). Right: Strong links are formed preferentially between nodes with overlapping neighborhoods. Average link clustering ΔC_L plotted versus the weight rank. Neighborhoods based on outgoing links. (e) Analysis of the human cortex. The functional architecture was based on resting state activity in the fMRI (black; regions of interest (nodes) and $\sim 15\,000$ links; $n=5$ subjects). The corresponding structural cortex core was based on fiber-bundle densities (weights) between nodes (red; [150]). (f) Analysis of the gene expression networks derived from human and mouse gene expression data. (g) Analysis of social networks. For details, see [149].

avalanches into a corresponding directed, weighted graph. Instead of comparing the full avalanche pattern with shuffled patterns for significance, we constructed the likelihood of a particular pattern to arise in the next time step, given the currently active sites. In this approach, local sites in the network recorded with high-density microelectrode array represent the nodes of the network. Correspondingly, link weights w_{ij} reflect the likelihood of active node j to be followed by node i within time period Δt , the temporal resolution of avalanche propagation. This analysis showed that avalanche patterns establish strong links preferentially within a small-world topology with high clustering coefficient and small network diameter, which has been suggested to be beneficial for many complex systems (Figure 2.10b) [147, 148].



In this graph theoretical approach, a strong link between two nodes quantifies the high probability of activity to propagate between the two sites, which translates into more recurrent avalanche patterns. We found that link strength in functional networks based on avalanches follows the principle of relative neighborhood overlap (Figure 2.10c) [149]. That is, two nodes in a network that have a high number of common neighbors (i.e., they send activity directly to or receive activity directly from common sites) also establish a strong link between each other. This principle is well known from social networks in which communication between two friends is high if they have a large number of common friends. We showed that this principle captures the spatially heterogeneous organization of activity propagation in cortical networks with avalanche dynamics when normalized by the total number of common neighbors (Figure 2.10d). The organization supports cooperative dynamics by providing strong links within highly clustered neighborhoods. In contrast, weak connections show a more random organization between cortical sites. These principles establish a highly ordered, nontrivial relationship in the weight organization and topology of functional avalanche networks that are significantly different from random, and not necessarily scale invariant. They were also shown to hold for a large number of other biological networks, such as functional brain networks from human fMRI resting activity, the structural white matter network of the human brain, gene interaction networks, and social networks (Figure 2.10e–g) [149].

Acknowledgement

I thank the members of my lab and the many experts on criticality that contributed over the years to this work. This research was supported by the Intramural Research Program of the National Institute of Mental Health, NIH, USA.

References

1. Bak, P. (1997) *How Nature Works*, Oxford University Press, Oxford.
2. Jensen, H.J. (1998) *Self-Organized Criticality*, Cambridge University Press.
3. Sornette, D. (2000) *Critical Phenomena in Natural Sciences*, Springer-Verlag, Berlin.
4. Hopfield, J.J. (1982) Neural networks and physical systems with emergent collective computational abilities. *Proc. Natl. Acad. Sci. U.S.A.*, **79** (8), 2554–2558.
5. Chen, D.M., Wu, S. et al. (1995) Self-organized criticality in a cellular automaton model of pulse-coupled integrate-and-fire neurons. *J. Phys. A: Math. Gen.*, **28**, 5177–5182.
6. Anninos, P. (1972) Cyclic modes in artificial neural nets. *Kybernetik*, **11** (1), 5–14.
7. Choi, M.Y. and Huberman, B.A. (1983) Dynamic behavior of nonlinear networks. *Phys. Rev. A*, **28** (2), 1204–1206.
8. Derrida, B. (1987) Dynamical phase transition in non-symmetric spin glasses. *J. Phys. A.: Math. Gen.*, **20**, L751–L725.
9. Kürten, K.E. (1988) Critical phenomena in model neural networks. *Phys. Lett. A*, **129** (3), 157–160.
10. Amit, D.J., Gutfreund, H. et al. (1985) Spin-glass models of neural networks. *Phys. Rev. A*, **32** (2), 1007–1018.

11. Chialvo, D.R. and Bak, P. (1999) Learning from mistakes. *Neuroscience*, **90** (4), 1137–1148.
12. Neher, E., Sakmann, B. *et al.* (1978) The extracellular patch clamp: a method for resolving currents through individual open channels in biological membranes. *Pflugers Arch.*, **375**, 219–228.
13. Hines, M.L. and Carnevale, N.T. (1997) The NEURON simulation environment. *Neural Comput.*, **9**, 1179–1209.
14. Bower, J.M., Beeman, D. *et al.* (1998) *The Book of GENESIS: Exploring Realistic Neural Models with the General Neural SImulation System*, Telos, New York.
15. Rall, W. (1962) Electrophysiology of a dendritic neuron model. *Biophys. J. (New York)*, **2**, 145–167.
16. Stanley, H.E. (1971) *Introduction to Phase Transitions and Critical Phenomena*, Oxford University Press, New York.
17. Koslow, S.H., Mandell, A.J. *et al.* (1987) *Perspectives in Biological Dynamics and Theoretical Medicine*, The New York Academy of Sciences, New York.
18. Kelso, J.A. (1984) Phase transitions and critical behavior in human bimanual coordination. *Am. J. Physiol.*, **246** (6, Pt 2), R1000–1004.
19. Haken, H., Kelso, J.A. *et al.* (1985) A theoretical model of phase transitions in human hand movements. *Biol. Cybern.*, **51** (5), 347–356.
20. Schöner, G., Haken, H. *et al.* (1986) A stochastic theory of phase transitions in human hand movement. *Biol. Cybern.*, **53** (4), 247–257.
21. Schöner, G. and Kelso, J.A. (1988) Dynamic pattern generation in behavioral and neural systems. *Science*, **239** (4847), 1513–1520.
22. Kelso, J.A., Buchanan, J.J. *et al.* (1991) Order parameters for the neural organization of single, multijoint limb movement patterns. *Exp. Brain Res.*, **85** (2), 432–444.
23. Kelso, J.A., Dumas, G. *et al.* (2013) Outline of a general theory of behavior and brain coordination. *Neural Netw.*, **37**, 120–131.
24. Bak, P., Tang, C. *et al.* (1988) Self-organized criticality. *Phys. Rev. A*, **38** (1), 364–374.
25. Kauffman, S.A. (1993) *The Origins of Order: Self Organization and Selection in Evolution*, Oxford University Press, New York.
26. Beggs, J.M. and Plenz, D. (2003) Neuronal avalanches in neocortical circuits. *J. Neurosci.*, **23** (35), 11167–11177.
27. Kinouchi, O. and Copelli, M. (2006) Optimal dynamical range of excitable networks at criticality. *Nat. Phys.*, **2**, 348–351.
28. Rämö, P., Kesseli, J. *et al.* (2006) Perturbation avalanches and criticality in gene regulatory networks. *J. Theor. Biol.*, **242** (1), 164–170.
29. Kauffman, S.A. (1969) Metabolic stability and epigenesis in randomly constructed genetic nets. *J. Theor. Biol.*, **22** (3), 437–467.
30. Nykter, M., Price, N.D. *et al.* (2008) Gene expression dynamics in the macrophage exhibit criticality. *Proc. Natl. Acad. Sci. U.S.A.*, **105** (6), 1897–1900.
31. Wolfram, S. (1984) Universality and complexity in cellular automata. *Physica D*, **10**, 1–35.
32. Langton, C.G. (1990) Computation at the edge of chaos: phase transitions and emergent computation. *Physica D: Nonlinear Phenom.*, **42** (1), 12–37.
33. Thiagarajan, T.C., Lebedev, M.A. *et al.* (2010) Coherence potentials: lossless, all-or-none network events in the cortex. *PLoS Biol.*, **8** (1), e1000278.
34. Plenz, D. (2012) Neuronal avalanches and coherence potentials. *Eur. Phys. J. Spec. Top.*, **205** (1), 259–301.
35. Rall, W. (1970) Cable properties of dendrites and effects of synaptic location. In *Excitatory Synaptic Mechanisms*, vol. 1 (eds P. Andersen and J.K.S. Janzen), Oslo Universitaetsverlag, Oslo, pp. 175–187.
36. Braintenberg, V. and Schüz, A. (1992) *Anatomy of the Cortex: Statistics and Geometry*, Springer-Verlag, Berlin, Heidelberg, New York.
37. Abeles, M. (1982) *Local Cortical Circuits*, Springer-Verlag, Berlin, Heidelberg, New York.

38. Abeles, M. (1991) *Corticonics: Neural Circuits of the Cerebral Cortex*, Cambridge University Press, New York, Melbourne, Sydney.
39. Peters, A., Palay, S.L. et al. (1991) *The Fine Structure of the Nervous System: Neurons and their Supporting Cells*, Oxford University Press, New York.
40. Kiritani, T., Wickersham, I.R. et al. (2012) Hierarchical connectivity and connection-specific dynamics in the corticospinal–corticostriatal microcircuit in mouse motor cortex. *J. Neurosci.*, **32** (14), 4992–5001.
41. Oberlaender, M., de Kock, C.P. et al. (2012) Cell type-specific three-dimensional structure of thalamocortical circuits in a column of rat vibrissal cortex. *Cereb. Cortex*, **22** (10), 2375–2391.
42. Hebb, D. (1949) *The Organization of Behavior. A Neuropsychological Theory*, John Wiley & Sons, Inc., New York.
43. Freeman, W.J. (1975) *Mass Action in the Nervous System*, Academic Press, New York.
44. Basar, E. (1998) *Brain Oscillations: Principles and Approaches. Brain Function and Oscillations*, Springer-Verlag, Heidelberg.
45. Buzsaki, G. (2009) *Rhythms of the Brain*, Oxford University Press.
46. Gray, C.M., Konig, P. et al. (1989) Oscillatory responses in cat visual cortex exhibit inter-columnar synchronization which reflects global stimulus properties. *Nature*, **338** (6213), 334–337.
47. Eckhorn, R., Bauer, R. et al. (1988) Coherent oscillations: a mechanism of feature linking in the visual cortex? *Biol. Cybern. (Berlin)*, **60**, 121–130.
48. Varela, F.J., Lachaux, J.P. et al. (2001) The brainweb: phase synchronization and large-scale integration. *Nat. Rev. Neurosci.*, **2** (4), 229–239.
49. Prechtel, J.C., Cohen, L.B. et al. (1997) Visual stimuli induce waves of electrical activity in turtle cortex. *Proc. Natl. Acad. Sci. U.S.A.*, **94** (14), 7621–7626.
50. Rubino, D., Robbins, K.A. et al. (2006) Propagating waves mediate information transfer in the motor cortex. *Nat. Neurosci.*, **9** (12), 1549–1557.
51. Takahashi, K., Saleh, M. et al. (2011) Propagating waves in human motor cortex. *Front. Hum. Neurosci.*, **5**, 40.
52. Freeman, W.J. (2003) The wave packet: an action potential for the 21st century. *J. Integr. Neurosci.*, **2** (1), 3–30.
53. Ikegaya, Y., Aaron, G. et al. (2004) Synfire chains and cortical songs: temporal modules of cortical activity. *Science*, **304** (5670), 559–564.
54. Mokeichev, A., Okun, M. et al. (2007) Stochastic emergence of repeating cortical motifs in spontaneous membrane potential fluctuations in vivo. *Neuron*, **53** (3), 413–425.
55. Gustafsson, B., Wigström, H. et al. (1987) Long-term potentiation in the hippocampus using depolarizing current pulses as the conditioning stimulus to single volley synaptic potentials. *J. Neurosci.*, **7**, 774–780.
56. Shatz, C.J. (1996) Emergence of order in visual system development. *J. Physiol. Paris*, **90**, 141–150.
57. Markram, H., Lübke, J. et al. (1997) Regulation of synaptic efficacy by coincidence of postsynaptic APs and EPSPs. *Science*, **275**, 213–215.
58. Bi, G.Q. and Poo, M.M. (1998) Synaptic modifications in cultured hippocampal neurons: dependence on spike timing, synaptic strength, and postsynaptic cell type. *J. Neurosci.*, **18** (24), 10464–10472.
59. Dan, Y. and Poo, M.M. (2006) Spike timing-dependent plasticity: from synapse to perception. *Physiol. Rev.*, **86** (3), 1033–1048.
60. Kumar, A., Rotter, S. et al. (2008) Conditions for propagating synchronous spiking and asynchronous firing rates in a cortical network model. *J. Neurosci.*, **28** (20), 5268–5280.
61. Aviel, Y., Mehring, C. et al. (2003) On embedding synfire chains in a balanced network. *Neural Comput.*, **15** (6), 1321–1340.
62. Mehring, C., Hehl, U. et al. (2003) Activity dynamics and propagation of synchronous spiking in locally connected random networks. *Biol. Cybern. (Berlin)*, **88** (5), 395–408.
63. Vogels, T.P. and Abbott, L.F. (2005) Signal propagation and logic gating in

- networks of integrate-and-fire neurons. *J. Neurosci.*, **25** (46), 10786–10795.
64. Zhang, K. and Sejnowski, T.J. (2000) A universal scaling law between gray matter and white matter of cerebral cortex. *Proc. Natl. Acad. Sci. U.S.A.*, **97** (10), 5621–5626.
 65. Izhikevich, E.M., Gally, J.A. *et al.* (2004) Spike-timing dynamics of neuronal groups. *Cereb. Cortex*, **14** (8), 933–944.
 66. Song, S., Sjostrom, P.J. *et al.* (2005) Highly nonrandom features of synaptic connectivity in local cortical circuits. *PLoS Biol.*, **3** (3), e68.
 67. Ikegaya, Y., Sasaki, T. *et al.* (2013) Interpyramidal spike transmission stabilizes the sparseness of recurrent network activity. *Cereb. Cortex*, **23** (2), 293–304.
 68. Cäser, M., Bonhoeffer, T. *et al.* (1989) Cellular organization and development of slice cultures from rat visual cortex. *Exp. Brain Res.*, **477**, 234–244.
 69. Götz, M. and Bolz, J. (1992) Formation and Preservation of cortical layers in slice cultures. *J. Neurobiol.*, **23**, 783–802.
 70. Plenz, D. and Aertsen, A. (1996) Neural dynamics in cortex-striatum co-cultures. I. Anatomy and electrophysiology of neuronal cell types. *Neuroscience*, **70**, 861–891.
 71. Plenz, D. and Kitai, S.T. (1996) Generation of high-frequency oscillations in local circuits of rat somatosensory cortex cultures. *J. Neurophysiol.*, **76** (6), 4180–4184.
 72. Stewart, C.V. and Plenz, D. (2006) Inverted-U profile of dopamine-NMDA-mediated spontaneous avalanche recurrence in superficial layers of rat prefrontal cortex. *J. Neurosci.*, **26** (31), 8148–8159.
 73. Stewart, C.V. and Plenz, D. (2007) Homeostasis of neuronal avalanches during postnatal cortex development *in vitro*. *J. Neurosci. Methods*, **169**, 405–416.
 74. Petermann, T., Thiagarajan, T. *et al.* (2009) Spontaneous cortical activity in awake monkeys composed of neuronal avalanches. *Proc. Natl. Acad. Sci. U.S.A.*, **106** (37), 15921–15926.
 75. Plenz, D. and Aertsen, A. (1996) Neuronal dynamics in cortex-striatum co-cultures. II. Spatio-temporal characteristics of neuronal activity. *Neuroscience*, **70**, 893–924.
 76. Sanchez-Vives, M.V. and McCormick, D.A. (2000) Cellular and network mechanisms of rhythmic recurrent activity in neocortex. *Nat. Neurosci.*, **3**, 1027–1034.
 77. Cossart, R., Aronov, D. *et al.* (2003) Attractor dynamics of network UP states in the neocortex. *Nature*, **423**, 283–288.
 78. McCormick, D.A., Shu, Y. *et al.* (2003) Persistent cortical activity: mechanisms of generation and effects on neuronal excitability. *Cereb. Cortex*, **13** (11), 1219–1231.
 79. Shriki, O., Alstott, J. *et al.* (2013) Neuronal avalanches in the resting MEG of the human brain. *J. Neurosci.*, **33** (16), 7079–7090.
 80. Plenz, D., Stewart, C.V. *et al.* (2011) Multi-electrode array recordings of neuronal avalanches in organotypic cultures. *J. Vis. Exp.*, **54**, e2949.
 81. Gireesh, E.D. and Plenz, D. (2008) Neuronal avalanches organize as nested theta- and beta/gamma-oscillations during development of cortical layer 2/3. *Proc. Natl. Acad. Sci. U.S.A.*, **105**, 7576–7581.
 82. Shew, W.L., Yang, H. *et al.* (2009) Neuronal avalanches imply maximum dynamic range in cortical networks at criticality. *J. Neurosci.*, **29** (49), 15595–15600.
 83. Yu, S., Yang, H. *et al.* (2011) Higher-order interactions characterized in cortical activity. *J. Neurosci.*, **31** (48), 17514–17526.
 84. Millman, D., Mihalas, S. *et al.* (2010) Self-organized criticality occurs in non-conservative neuronal networks during ‘up’ states. *Nat. Phys.*, **6**, 801–805.
 85. Freeman, J.A. and Nicholson, C. (1975) Experimental optimization of current source-density technique for anuran cerebellum. *J. Neurophysiol.*, **38** (2), 369–382.
 86. Nicholson, C. and Freeman, J.A. (1975) Theory of current source density analysis and determination of conductivity

- tensor for anuran cerebellum. *J. Neurophysiol.*, **38**, 356–368.
87. Mitzdorf, U. (1985) Current source density method and application in cat cerebral cortex: investigation of evoked potentials and EEG phenomena. *Physiol. Rev.*, **65**, 37–100.
88. Plenz, D. and Aertsen, A. (1993) Current source density profiles of optical recording maps: a new approach to the analysis of spatio-temporal neural activity patterns. *Eur. J. Neurosci.*, **5**, 437–448.
89. Klaus, A., Yu, S. *et al.* (2011) Statistical analyses support power law distributions found in neuronal avalanches. *PLoS ONE*, **6** (5), e19779.
90. Priesemann, V., Munk, M.H. *et al.* (2009) Subsampling effects in neuronal avalanche distributions recorded in vivo. *BMC Neurosci.*, **10** (1), 40.
91. Ribeiro, T.L., Copelli, M. *et al.* (2010) Spike avalanches exhibit universal dynamics across the sleep-wake cycle. *PLoS ONE*, **5** (11), e14129.
92. Touboul, J. and Destexhe, A. (2010) Can power-law scaling and neuronal avalanches arise from stochastic dynamics? *PLoS ONE*, **5** (2), e8982.
93. Palva, J.M., Zhigalov, A. *et al.* (2013) Neuronal long-range temporal correlations and avalanche dynamics are correlated with behavioral scaling laws. *Proc. Natl. Acad. Sci. U.S.A.*, **110** (9), 3585–3590.
94. Fraiman, D. and Chialvo, D.R. (2012) What kind of noise is brain noise: anomalous scaling behavior of the resting brain activity fluctuations. *Front. Physiol.*, **3**: 307. doi: 10.3389/fphys.2012.00307.
95. Stern, E.A., Maravall, M. *et al.* (2001) Rapid development and plasticity of layer 2/3 maps in rat barrel cortex in vivo. *Neuron*, **31** (2), 305–315.
96. Destexhe, A., Contreras, D. *et al.* (1999) Spatiotemporal analysis of local field potentials and unit discharges in cat cerebral cortex during natural wake and sleep states. *J. Neurosci.*, **19** (11), 4595–4608.
97. Ferrer, I., Hernandez-Marti, M. *et al.* (1988) Formation and growth of the cerebral convolutions. I. Postnatal development of the median-suprasylvian gyrus and adjoining sulci in the cat. *J. Anat. (London)*, **160**, 89–100.
98. Otter, R.A.M.S. (1949) The multiplicative process. *Ann. Math. Statist.*, **20**, 206–224.
99. Harris, T.E. (1989) *The Theory of Branching Processes*, Dover, New York.
100. Zapperi, S., Baekgaard, L.K. *et al.* (1995) Self-organized branching processes: Mean-field theory for avalanches. *Phys. Rev. Lett.*, **75** (22), 4071–4074.
101. Omori, F. (1895) On the aftershocks of earthquakes. *J. Coll. Sci. Imper. Univ. Tokyo*, **7**, 111–200.
102. Utsu, T., Ogata, Y. *et al.* (1995) The centenary of the Omori formula for a decay law of aftershock activity. *J. Phys. Earth*, **43**, 1–33.
103. Shearer, P., Hauksson, E. *et al.* (2005) Southern California hypocenter relocation with waveform cross-correlation, part 2: results using source-specific station terms and cluster analysis. *Bull. Seismol. Soc. Am.*, **95** (3), 904–915.
104. Enescu, B., Struzik, Z. *et al.* (2008) On the recurrence time of earthquakes: insight from Vrancea (Romania) intermediate-depth events. *Geophys. J. Int.*, **172**, 395–404.
105. McGuire, J.J., Boettcher, M.S. *et al.* (2005) Foreshock sequences and short-term earthquake predictability on East Pacific Rise transform faults. *Nature*, **434**, 457–461.
106. de Arcangelis, L., Godano, C. *et al.* (2006) Universality in solar flare and earthquake occurrence. *Phys. Rev. Lett.*, **96** (5), 051102.
107. Fries, P., Nikolic, D. *et al.* (2007) The gamma cycle. *Trends Neurosci.*, **30** (7), 309–316.
108. Başar, E., Başar-Eroglu, C. *et al.* (2001) Gamma, alpha, delta, and theta oscillations govern cognitive processes. *Int. J. Psychophysiol.*, **39** (2), 241–248.
109. Roelfsema, P.R., Engel, A.K. *et al.* (1997) Visuomotor integration is associated with zero time-lag synchronization among cortical areas. *Nature*, **385**, 157–161.

110. Wang, P., Havenith, M.N. *et al.* (2010) Time delays in the beta/gamma cycle operate on the level of individual neurons. *Neuroreport*, **21** (11), 746–750.
111. Havenith, M.N., Yu, S. *et al.* (2011) Synchrony makes neurons fire in sequence, and stimulus properties determine who is ahead. *J. Neurosci.*, **31** (23), 8570–8584.
112. Yang, H., Shew, W.L. *et al.* (2012) Maximal variability of phase synchrony in cortical networks with neuronal avalanches. *J. Neurosci.*, **32** (3), 1061–1072.
113. Eurich, C.W., Herrmann, J.M. *et al.* (2002) Finite-size effects of avalanche dynamics. *Phys. Rev. E Stat. Nonlin. Soft Matter Phys.*, **66** (6, Pt. 2), 066137.
114. Pfeffer, L., Ide, D. *et al.* (2004) *A Life Support Systems for Stimulation of and Recording from Rodent Neuron Networks Grown on Multi-Electrode Arrays*, IEEE Computer Society, Washington, DC, ISBN: 0-7695-2104-5.
115. Poil, S.S., Hardstone, R. *et al.* (2012) Critical-state dynamics of avalanches and oscillations jointly emerge from balanced excitation/inhibition in neuronal networks. *J. Neurosci.*, **32** (29), 9817–9823.
116. Linkenkaer-Hansen, K., Nikouline, V.V. *et al.* (2001) Long-range temporal correlations and scaling behavior in human brain oscillations. *J. Neurosci.*, **21** (4), 1370–1377.
117. Lombardi, F., Herrmann, H.J. *et al.* (2012) Balance between excitation and inhibition controls the temporal organization of neuronal avalanches. *Phys. Rev. Lett.*, **108** (22), 228703.
118. Bertschinger, N. and Natschläger, T. (2004) Real-time computation at the edge of chaos in recurrent neural networks. *Neural Comput.*, **16** (7), 1413–1436.
119. Legenstein, R. and Maass, W. (2007) Edge of chaos and prediction of computational performance for neural circuit models. *Neural Netw.*, **20** (3), 323–334.
120. Shew, W.L., Yang, H. *et al.* (2011) Information capacity is maximized in balanced cortical networks with neuronal avalanches. *J. Neurosci.*, **5**, 55–63.
121. Skaggs, W.E., McNaughton, B.L. *et al.* (1996) Theta phase precession in hippocampal neuronal populations and the compression of temporal sequences. *Hippocampus*, **6** (2), 149–172.
122. Ohl, F.W., Scheich, H. *et al.* (2001) Change in pattern of ongoing cortical activity with auditory category learning. *Nature*, **412**, 733–736.
123. Han, F., Caporale, N. *et al.* (2008) Reverberation of recent visual experience in spontaneous cortical waves. *Neuron*, **60** (2), 321–327.
124. Arnsten, A.F., Cai, J.X. *et al.* (1994) Dopamine D1 receptor mechanisms in the cognitive performance of young adult and aged monkeys. *Psychopharmacology (Berl.)*, **116** (2), 143–151.
125. Mattay, V.S., Goldberg, T.E. *et al.* (2003) Catechol O-methyltransferase val158-met genotype and individual variation in the brain response to amphetamine. *Proc. Natl. Acad. Sci. U.S.A.*, **100** (10), 6186–6191.
126. Abi-Saab, W.M., D’Souza, D.C. *et al.* (1998) The NMDA antagonist model for schizophrenia: promise and pitfalls. *Pharmacopsychiatry*, **31** (Suppl 2), 104–109.
127. Krystal, J.H., D’Souza, D.C. *et al.* (2003) NMDA receptor antagonist effects, cortical glutamatergic function, and schizophrenia: toward a paradigm shift in medication development. *Psychopharmacology (Berl.)*, **169** (3–4), 215–233.
128. Shew, W.L. and Plenz, D. (2013) The functional benefits of criticality in the cortex. *Neuroscientist*, **19** (1), 88–100.
129. Farmer, D., Toffoli, T. *et al.* (1984) *Cellular Automata: Proceedings of an Interdisciplinary Workshop*, North Holland, Amsterdam.
130. Gutwitz, H.A. (1991) *Cellular Automata: Theory and Experiment*, Elsevier Science Publisher, B.V., Amsterdam.
131. Gardner, M. (1970) The fantastic combinations of John Conway’s new solitaire game “life”. *Sci. Am.*, **223**, 120–123.

132. Mitchel, M., Hraber, P. *et al.* (1993) Revisiting the edge of chaos: evolving cellular automata to perform computations. *Complex Syst.*, **7**, 89–130.
133. Natschlaeger, T., Bertschinger, N. *et al.* (2005) At the edge of chaos: real-time computations and self-organized criticality in recurrent neural networks, in *Advances in Neural Information Processing Systems*, MIT Press, Cambridge, MA.
134. Schrauwen, B., Buesing, L. *et al.* (2009) On computational power and the order-chaos phase transition in reservoir computing, in *Proceeding of NIPS, Advances in Neural Information Processing Systems*, MIT Press.
135. Toyoizumi, T. and Abbott, L.F. (2011) Beyond the edge of chaos: amplification and temporal integration by recurrent networks in the chaotic regime. *Phys. Rev. E*, **84** (5), 051908.
136. Wallace, E., Maei, H.R. *et al.* (2013) Randomly connected networks have short temporal memory. *Neural Comput.*, **25** (6), 1408–1439.
137. Lizier, J.T., Prokopenko, M. *et al.* (2008) Local information transfer as a spatiotemporal filter for complex systems. *Phys. Rev. E*, **77** (2), 026110.
138. Parameshwaran, D., Crone, N.E. *et al.* (2012) Coherence potentials encode simple human sensorimotor behavior. *PLoS ONE*, **7** (2), e30514.
139. Kelso, J.A.S. (1995) *Dynamic Patterns: the Self-Organization of Brain and Behavior*, MIT Press, Cambridge, MA.
140. Friston, K.J. (1997) Transients, metastability, and neuronal dynamics. *Neuroimage*, **5** (2), 164–171.
141. Ashby, W.R. (1950) The stability of a randomly assembled nerve-network. *Electroencephalogr. Clin. Neurophysiol.*, **2** (1), 471–482.
142. Gong, P. and van Leeuwen, C. (2009) Distributed dynamical computation in neural circuits with propagating coherent activity patterns. *PLoS Comput. Biol.*, **5** (12), e1000611.
143. Abeles, M., Hayon, G. *et al.* (2004) Modeling compositionality by dynamic binding of synfire chains. *J. Comput. Neurosci.*, **17** (2), 179–201.
144. Beggs, J. and Plenz, D. (2004) Neuronal avalanches are diverse and precise activity patterns that are stable for many hours in cortical slice cultures. *J. Neurosci.*, **24** (22), 5216–5229.
145. Yu, S., Yang, H. *et al.* (2013) Universal organization of resting brain activity at the thermodynamic critical point. *Front. Syst. Neurosci.*, 22 August 2013, doi: 10.3389/fnsys.2013.00042.
146. Pajevic, S. and Plenz, D. (2008) Efficient network reconstruction from dynamical cascades identifies small-world topology from neuronal avalanches. *PLoS Comp. Biol.*, **5** (1), e1000271.
147. Watts, D.J. and Strogatz, S.H. (1998) Collective dynamics of ‘small-world’ networks. *Nature*, **393**, 440–442.
148. Strogatz, S.H. (2001) Exploring complex networks. *Nature*, **410**, 268–276.
149. Pajevic, S. and Plenz, D. (2012) The organization of strong links in complex networks. *Nat. Phys.*, **8** (5), 429–436.
150. Hagmann, P., Cammoun, L. *et al.* (2008) Mapping the structural core of human cerebral cortex. *PLoS Biol.*, **6** (7), e159.

3

Critical Brain Dynamics at Large Scale

Dante R. Chialvo

Prologue

“Essentially, all modeling of brain function from studying models of neural networks has ignored the self-organized aspects of the process, but has concentrated on designing a working brain by engineering all the connections of inputs and outputs.”

Bak [1]

3.1

Introduction

In these notes, we discuss the idea put forward two decades ago by Bak [1] that the working brain stays at an intermediate (critical) regime characterized by power-law correlations. Highly correlated brain dynamics produces synchronized states with no behavioral value, while weakly correlated dynamics prevent information flow. In between these states, the unique dynamical features of the critical state endow the brain with properties that are fundamental for adaptive behavior. This simple proposal is now supported by a wide body of empirical evidence at different scales, demonstrating that the spatiotemporal brain dynamics exhibit key signatures of critical dynamics, previously recognized in other complex systems.

3.1.1

If Criticality is the Solution, What is the Problem?

Criticality, in simple terms, refers to a distinctive set of properties found only at the boundary separating regimes with different dynamics, for instance, between an ordered and a disordered phase. The dynamics of critical phenomena are a peculiar mix of order and disorder, whose detailed understanding constitute one of the major achievements of statistical physics in the past century [2].

What is the problem for which critical phenomena can be relevant in the context of the brain? The first problem is to understand how the *very large* conglomerate

of interconnected neurons produce a *wide repertoire* of behaviors in a *flexible* and self-organized way. This issue is not resolved at any rate, demonstrable by the fact that detailed models constructed to account for such dynamics fail at some of the three *emphasized* aspects: either (i) the model is an unrealistic low-dimensional version of the neural structure of interest or (ii) it produces a single behavior (i.e., a hardwired circuit), and consequently (iii) it cannot flexibly perform more than one simple thing. A careful analysis of the literature will reveal that only by arbitrarily changing the neuronal connections can current mathematical models play a reasonable wide repertoire of behaviors. Of course, this rewiring implies a kind of supplementary brain governing which connections need to be rewired in each case. Consequently, generating behavioral variability out of the same neural structure is a fundamental question which is screaming to be answered, but seldom is even being asked.

A second related problem is how stability is achieved in such a large system with an astronomical number of neurons, each one continuously receiving thousands of inputs from other neurons. We still lack a precise knowledge of how the cortex prevents an explosive propagation of activity while still managing to share information across areas. It is obvious that if the average number of neurons activated by one neuron is too high (i.e., supercritical), a massive activation of the entire network will ensue, while if it is too low (i.e., subcritical), propagation will die out. About 50 years ago [3], Turing was the first to speculate that the brain, in order to work properly, needs to be at a critical regime, that is, one in which these opposing forces are balanced.

Criticality as a potential solution to these issues was first explored by Bak [1] and colleagues [4–8] while attempting to apply ideas of self-organized criticality [9, 10] to the study of living systems. Throughout the last decade of his short but productive life, in uncountable lively lectures, Bak enthusiastically broadcasted the idea that if the world at large is studied as any other complex system, it will reveal a variety of instances in which critical dynamics will be recognized as the relevant phenomena at play. Basically, the emphasis was in considering criticality as another attractor. The claim was that “*dynamical systems with extended spatial degrees of freedom naturally evolve into self-organized critical structures of states which are barely stable. The combination of dynamical minimal stability and spatial scaling leads to a power law for temporal fluctuations*” [9].

These ideas were only a portion of Bak’s much broader and deeper insight about how nature works in general, often communicated in his unforgiving way, as, for instance, when challenging colleagues by asking: “*Is biology too difficult for biologists? And what can physics, dealing with the simple and lawful, contribute to biology, which deals with the complex and diverse. These complex many-body problems might have similarities to problems studied in particle and solid-state physics.*” [11]. Thus, Bak was convinced that the critical state was a novel dynamical attractor to which large distributed systems will eventually converge, given some relatively simple conditions. From this viewpoint, the understanding of the brain belongs to the same problem of understanding complexity in nature.

These comments should inspire us to think again about the much larger question underlying the study of brain dynamics using ideas from critical phenomena. Bak's (and colleagues') legacy will be incomplete if we restrict ourselves (for instance) to find power laws in the brain and compare it in health and disease. By its theoretical foundations, critical phenomena offer the opportunity to understand how the brain works, in the same magnitude that it impacted in some other areas, as, for instance, in the mathematical modeling of Sepkoski fossil record of species extinction events, which opened a completely novel strategy to study how macroevolution works [12].

The rest of this chapter is dedicated to review recent work on large-scale brain dynamics inspired by Bak's ideas. The material is organized as follows: Section 3.2 dwells on what is essentially novel about critical dynamics; Sections 3.3 and 3.4 are dedicated to a discussion on how to recognize criticality. Section 3.5 discusses the main implications of the results presented and Section 3.6 closes with a summary.

3.2

What is Criticality Good for?

According to this program, the methods used in physics to study the properties of matter must be useful to characterize brain function [13]. How reasonable is that? A simple but strong assumption needs to be made: that the mind is nothing more than the emergent global dynamics of neuronal interactions, in the same sense than ferromagnetism is an emergent property of the interaction between neighboring spins and an external field. To appreciate the validity of this point, a key result from statistical physics is relevant here: universality. In brief, this notion says that a huge family of systems will follow the same laws and exhibit the same dynamics providing that some set of minimum conditions are met. These conditions involve only the presence of some nonlinearity, under some boundary conditions and some types of interactions. Any other details of the system will not be relevant, meaning that the process will arise in the same quantitative and qualitative manner in very diverse systems, where order, disorder, or the observation of one type of dynamics over another will be dictated by the strength and type of the interactions. This is seen throughout nature, from cell function (warranted by the interaction of multiple metabolic reactions) to global macroeconomics (modulated by trade), and so on.

Perhaps, considering the unthinkable one could appreciate better what universality means, in general, and later translate it to complex systems. The world would be a completely different place without universality, imagine if each phenomena would be explained by a different “relation” (as it would not be possible to talk in terms of general laws) between intervening particles and forces. Gravity would be different for each metal or different materials, Galileo's experiments would not repeat themselves unless for the same material he used, and so on. It can be said that without universality, each phenomenon we are familiar with would be foreign and strange.

3.2.1

Emergence

Throughout nature, it is common to observe similar collective properties emerging independently of the details of each system. But what is emergence and why is it relevant to discuss it in this context? Emergence refers to the unexpected collective spatiotemporal patterns exhibited by *large* complex systems. In this context, “unexpected” refers to our inability (mathematical and otherwise) to derive such emergent patterns from the equations describing the dynamics of the individual parts of the system. As discussed at length elsewhere [1, 14], complex systems are usually *large* conglomerates of *interacting* elements, each one exhibiting some sort of *nonlinear* dynamics. Without entering into details, it is known that the interaction can also be indirect, for instance, through some mean field. Usually, energy enters into the system, and therefore some sort of driving is present. The three *emphasized* features (i.e., large number of interacting nonlinear elements) are necessary, although not sufficient, conditions for a system to exhibit emergent complex behavior at some point.

As long as the dynamics of each individual element is nonlinear, other details of the origin and nature of the nonlinearities are not important [1, 15]. For instance, the elements can be humans, driven by food and other energy resources, from which some collective political or social structure eventually arises. It is well known that whatever the type of structure that emerges, it is unlikely to appear if one of the three above-emphasized properties is absent. Conversely, the interaction of a *small number of linear* elements will not produce any of this “unexpected” complex behavior (indeed, this is the case in which everything can be mathematically anticipated).

3.2.2

Spontaneous Brain Activity is Complex

It is evident, from the very early electrical recordings a century ago, that the brain is spontaneously active, even in absence of external inputs. However obvious this observation could appear, it was only recently that the dynamical features of the spontaneous brain state began to be studied in any significant way.

Work on brain rhythms at small and large brain scales shows that spontaneous healthy brain dynamics is not composed of completely random activity patterns nor by periodic oscillations [16]. Careful analysis of the statistical properties of neural dynamics under no explicit input has identified complex patterns of activity previously neglected as background noise dynamics. The fact is that brain activity is always essentially arrhythmic regardless of how it is monitored, whether as electrical activity in the scalp (EEG, electroencephalography), by techniques of functional magnetic resonance imaging (fMRI), in the synchronization of oscillatory activity [17, 18], or in the statistical features of local field potential peaks [19].

It has been pointed out repeatedly [20–24] that, under healthy conditions, no brain temporal scale takes primacy over average, resulting in power spectral densities

decaying of “ $1/f$ noise.” Behavior, the ultimate interface between brain dynamics and the environment, also exhibits scale-invariant features as shown in human cognition [25–27], human motion [28], as well as in animal motion [29]. The origin of the brain scale-free dynamics was not adequately investigated until recently, probably (and paradoxically) due to the ubiquity of scale invariance in nature [9]. The potential significance of a renewed interpretation of the brain’s spontaneous patterns in terms of scale invariance is at least double. On one side, it provides important clues about brain organization, in the sense that our previous ideas cannot easily accommodate these new findings. Also, the class of complex dynamics observed seems to provide the brain with previously unrecognized robust properties.

3.2.3

Emergent Complexity is Always Critical

The commonality of scale-free dynamics in the brain naturally leads one to ask what physics knows about very general mechanisms that are able to produce such dynamics. Attempts to explain and generate nature’s nonuniformity included several mathematical models and recipes, but few succeeded in creating complexity without embedding the equations with complexity. The important point is that including the complexity in the model will only result in a simulation of the real system, without entailing any understanding of complexity. The most significant efforts were those aimed at discovering the conditions in which something complex emerges from the interaction of the constituting noncomplex elements [1, 9]. Initial inspiration was drawn from work in the field of phase transitions and critical phenomena. Precisely, one of the novelties of critical phenomena is the fact that out of the short-range interaction of simple elements, eventually long-range spatiotemporal correlated patterns emerge. As such, critical dynamics have been documented in species evolution [1], ants’ collective foraging [30, 31] and swarm models [32], bacterial populations [33], traffic flow on highways [1] and on the Internet [34], macroeconomic dynamics [35], forest fires [36], rainfall dynamics [37–39], and flock formation [40]. The same rationale leads to the conjecture [1, 6, 7] that the complexity of brain dynamics is just another signature of an underlying critical process. Because the largest number of metastable states exists at the point near the transition, the brain can access the largest repertoire of behaviors in a flexible way. That view claimed that the most fundamental properties of the brain are possible only by staying close to that critical instability, independently of how such a state is reached or maintained. In the following sections, recent empirical evidence supporting this hypothesis is discussed.

3.3

Statistical Signatures of Critical Dynamics

The presence of scaling and correlations spanning the size of the system are usually hints of critical phenomena. While, in principle, it is relatively simple to identify

these signatures, in the case of finite data and the absence of a formal theory, as is the case of the brain, any initial indication of criticality needs to be checked against many known artifacts. In the next paragraphs, we discuss the most relevant efforts to identify these signatures in large-scale brain data.

3.3.1

Hunting for Power Laws in Densities Functions

As we will discuss later in more detail, the dynamical skeleton of a complex system can be derived from the correlation network, that is, the subsets of the nodes linked by some minimum correlation value (computed from the system activity). As early as 2003, Eguiluz and colleagues [41] used fMRI data to extract the

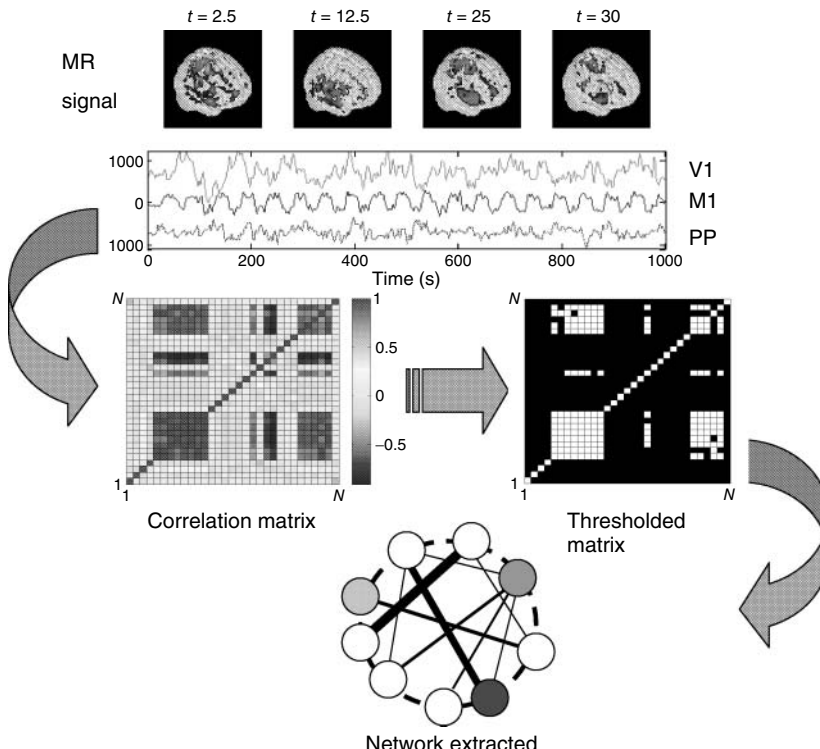


Figure 3.1 Methodology used to extract functional networks from the brain fMRI BOLD signals. The correlation matrix is calculated from all pairs of BOLD time series. The strongest correlations are selected to define the networks nodes. The top four images represent examples of snapshots

of activity at one moment and the three traces correspond to time series of activity at selected voxels from visual (V1), motor (M1), and posterioparietal (PP) cortices. (Figure redrawn from [41].) (Please find a color version of this figure on the color plates.)

very first *functional networks* connecting correlated human brain sites. Networks were constructed (see Figure 3.1) by connecting the brain sites with the strongest correlations between their blood-oxygenated-level-dependent (BOLD) signal. The analysis of the resulting networks in different tasks showed that (i) the distribution of functional connections and the probability of finding a link versus distance were both scale-free, (ii) the characteristic path length was small and comparable with those of equivalent random networks, and (iii) the clustering coefficient was orders of magnitude larger than those of equivalent random networks. It was suggested that these properties, typical of scale-free small-world networks, should reflect important functional information about brain states and provide mechanistic clues.

This was investigated in subsequent work by Fraiman *et al.* [42] who studied the dynamics of the spontaneous (i.e., at “rest”) fluctuations of brain activity with fMRI. Brain “rest” is defined – more or less unsuccessfully – as the state in which there is no explicit brain input or output. Now it is widely accepted that the structure and location of large-scale brain networks can be derived from the interaction of cortical regions during rest, which closely match the same regions responding to a wide variety of different activation conditions [43, 44]. These so-called resting-state networks (RSNs) can be reliably computed from the fluctuations of the BOLD signals of the resting brain, with great consistency across subjects [45–47] even during sleep [48] or anesthesia [49]. Fraiman *et al.* [42] focused on the question of whether such states can be comparable to any known *dynamical* state. For that purpose, correlation networks from human brain fMRI were contrasted with correlation networks extracted from numerical simulations of the Ising model in 2D, at different temperatures. For the critical temperature T_c , striking similarities (as shown in Figure 3.2) appear in the most relevant statistical properties, making the two networks indistinguishable from each other. These results were interpreted as lending additional support to the conjecture that the dynamics of the functioning brain is near a critical point.

Kitzbichler *et al.* [50] analyzed fMRI and magnetoencephalography (MEG) data recorded from normal volunteers at resting state using phase synchronization between diverse spatial locations. They reported a scale-invariant distribution for the length of time that two brain locations on the average remained locked. This distribution was also found in the Ising and the Kuramoto model [51] at the critical state, suggesting that the data exhibited criticality. This work was revisited recently by Botcharova *et al.* [52] who investigated whether the display of power-law statistics of the two measures of synchronization – phase-locking intervals and global lability of synchronization – can be analogous to similar scaling at the critical threshold in classical models of synchronization. Results confirmed only partially the previous findings, emphasizing the need to proceed with caution in making direct analogies between the brain dynamics and systems at criticality. Specifically, they showed that “the pooling of pairwise phase-locking intervals from a non-critically interacting system can produce a distribution that is similarly assessed as being power law. In contrast, the global lability of synchronization measure is shown to better discriminate critical from non critical interaction” [52].

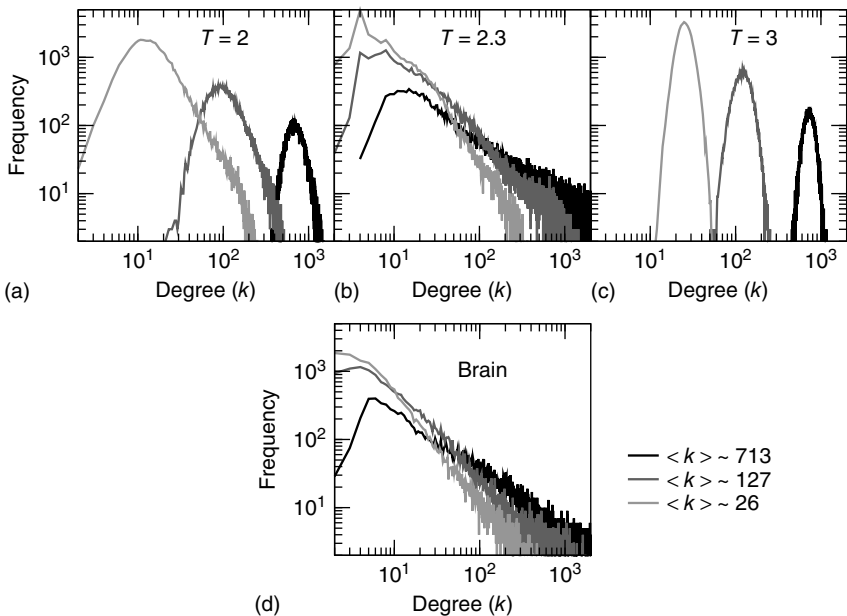


Figure 3.2 At criticality, brain and Ising networks are indistinguishable from each other. The graphs show a comparison of the link density distributions computed from correlation networks extracted from brain data (d) and from numerical simulations of the Ising model (a–c) at three temperatures: critical ($T = 2.3$), subcritical ($T = 2$), and supercritical ($T = 3$). (a–c) The degree

distribution for the Ising networks at $T = 2$, $T = 2.3$, and $T = 3$ for three representative values of $\langle k \rangle \approx 26, 127$, and 713 . (d) Degree distribution for correlated brain network for the same three values of $\langle k \rangle$. (Figure redrawn from Fraiman *et al.* [42].) (Please find a color version of this figure on the color plates.)

The works commented up until now rely on determining if probability density functions (i.e., node degree, or synchronization lengths) obey power laws. The approach from Expert *et al.* [53] looked at a well-known property of the dynamics at criticality: self-similarity. They investigated whether the two-point correlation function can be renormalized. This is a very well-understood technique used in critical phenomena in which the data sets are coarse grained at successive scales while computing some statistic. They were able to show that the two-point correlation function of the BOLD signal is invariant under changes in the spatial scale as shown in Figure 3.3, which together with the temporal $1/f$ scaling exhibited by BOLD time series, suggests critical dynamics.

3.3.2

Beyond Fitting: Variance and Correlation Scaling of BrainNoise

An unexpected new angle in the problem of criticality was offered by the surging interest in the source of the BOLD signal variability and its information content.

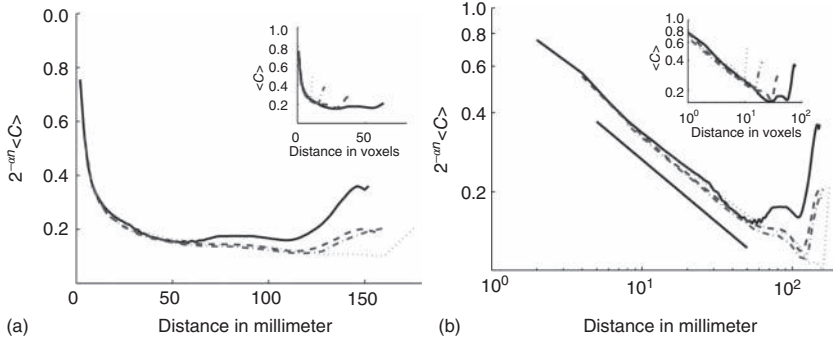


Figure 3.3 Self-similarity of the brain fMRI two-correlation function. The plot shows the renormalized average correlation function versus distance for the four levels of description: solid line: $128 \times 128 \times 31$ ($n = 0$); dashed line: $64 \times 64 \times 16$ ($n = 1$);

dashed-dotted, $32 \times 32 \times 8$ ($n = 2$); and dotted line: $16 \times 16 \times 4$ ($n = 3$). (a) Linear–linear and (b) log–log axis. The exponent $\beta = 0.47 +/- 0.2$ describes well the data. (Figure redrawn from Expert *et al.* [53].)

For instance, it was shown recently [54] in a group of subjects of different ages, that the BOLD signal standard deviation can be a better predictor of the subject age than the average. Furthermore, additional work focused on the relation between the fMRI signal variability and a task performance, concluded that faster and more consistent performers exhibit significantly higher brain variability across tasks than the poorer performing subjects [55]. Overall, these results suggested that the understanding of the resting brain dynamics can benefit from a detailed study of the BOLD variability *per se*.

Precisely, at this aim was directed the work in [56], which studied the statistical properties of the spontaneous BOLD fluctuations and its possible dynamical mechanisms. In these studies, an ensemble of brain regions of different sizes were defined and the statistics of the fluctuations and correlations were computed as a function of the region’s size. The report identifies anomalous scaling of the variance as a function of the number of elements and a distinctive divergence of the correlations with the size of the cluster considered. We now proceed to describe these findings in detail.

3.3.2.1 Anomalous Scaling

The objects of interest are the fluctuations of the BOLD signal around its mean, which for the 35 RSN clusters used by Fraiman and Chialvo [56], are defined as

$$B_h(\vec{x}_i, t) = B(\vec{x}_i, t) - \frac{1}{N_H} \sum_{i=1}^{N_H} B(\vec{x}_i, t) \quad (3.1)$$

where \vec{x}_i represents the position of the voxel i that belongs to the cluster H of size N_H . These signals are used to study the correlation properties of the activity in each cluster.

The mean activity of each h cluster is defined as

$$\bar{B}(t) = \frac{1}{N_H} \sum_{i=1}^{N_H} B(\vec{x}_i, t) \quad (3.2)$$

and its variance is defined as

$$\sigma_{\bar{B}(t)}^2 = \frac{1}{T} \sum_{t=1}^T (\bar{B}(t) - \bar{\bar{B}})^2 \quad (3.3)$$

where $\bar{\bar{B}} = \frac{1}{T} \sum_{t=1}^T \bar{B}(t)$ and T is the number of temporal points. Note that the average subtracted in Eq. (3.1) is the mean at time t (computed over N voxels) of the BOLD signals, not to be confused with the BOLD signal averaged over T temporal points.

As the BOLD signal fluctuates widely and the number N of voxels in the clusters can be very large, one might expect that the aggregate of Eq. (3.1) obeys the law of the large numbers. If this was true, the variance of the mean field $\sigma_{\bar{B}(t)}^2$ in Eq. (3.3) would decrease with N as N^{-1} . In other words, one would expect a smaller amplitude fluctuation for the average BOLD signal recorded in clusters (i.e., $\bar{B}(t)$) comprised by a large number of voxels compared with smaller clusters. However, the data in Figure 3.4a shows otherwise, the variance of the average activity remains approximately constant over a change of four orders of magnitude in cluster sizes. The strong departure from the N^{-1} decay is enough to disregard further statistical testing, which is confirmed by recomputing the variance for artificially constructed clusters having a similar number of voxels but composed of the randomly reordered $B_k(t)$ BOLD raw time series (as the four examples in the top left panels of Figure 3.4a). As expected, in this case, the variance (plotted using square symbols in the bottom panel of Figure 3.4a) obeys the N^{-1} law).

3.3.2.2 Correlation Length

A straightforward approach to understanding the correlation behavior commonly used in large collective systems [40] is to determine the correlation length at various systems' sizes. The correlation length is the average distance at which the correlations of the fluctuations around the mean crosses zero. It describes how far one has to move to observe any two points in a system behaving independently of each other. Notice that, by definition, the computation of the correlation length is done over the fluctuations around the mean, and not over the raw BOLD signals; otherwise, global correlations may produce a single spurious correlation length value commensurate with the brain size.

Thus, we start by computing for each voxel BOLD time series their fluctuations around the mean of the cluster to which they belong. Recall the expression in Eq. (3.1), where B is the BOLD time series at a given voxel and \vec{x}_i represents the position of the voxel i that belongs to the cluster H of size N_H . By definition, the mean of the BOLD fluctuations of each cluster vanishes,

$$\sum_{i=1}^{N_h} \bar{B}_h(\vec{x}_i, t) = 0 \quad \forall t \quad (3.4)$$

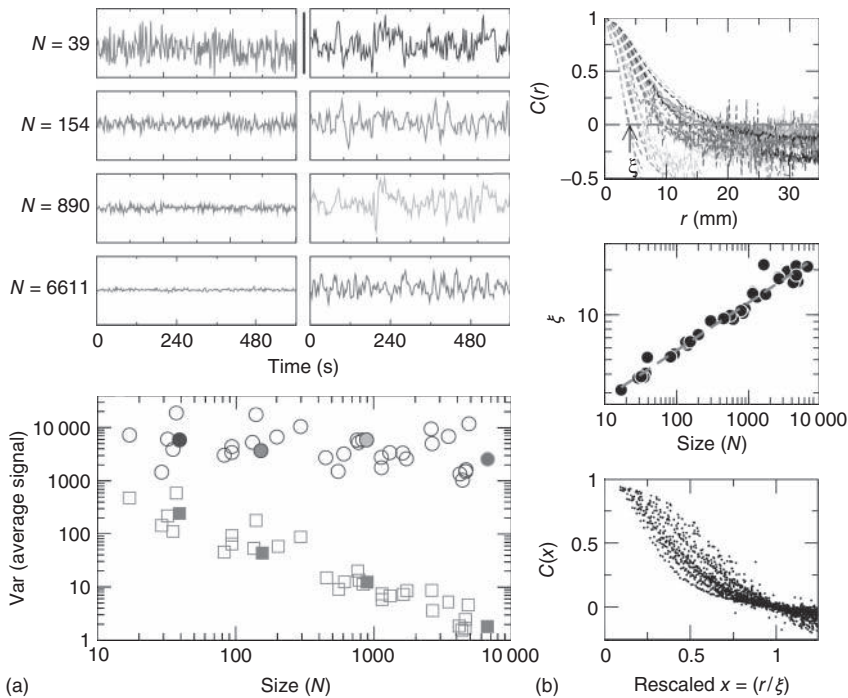


Figure 3.4 Spontaneous fluctuations of fMRI data show anomalous behavior of the variance (a) and divergence of the correlation length (b). Top figures in panel a show four examples of average BOLD time series (i.e., $\bar{B}(t)$ in Eq. (3.2)) computed from clusters of different sizes N . Note that while the amplitude of the raw BOLD signals (right panels) remains approximately constant, in the case of the shuffled data sets (left panels) the amplitude decreases drastically for increasing cluster sizes. The bottom graph in panel a shows the calculations for the 35 clusters (circles) plotted as a function of the cluster size, demonstrating that variance is independent of the RSN's cluster size. The square symbols show similar computations for a surrogate time series constructed by randomly reordering the original BOLD time series, which exhibit the expected $1/N$ scaling (dashed line). Filled symbols in the bottom panel are used to denote the values for the time series used as examples in the

top panel. In panel b, there are three graphs: the top one shows the correlation function $C(r)$ as a function of distance for clusters of different sizes. Contrary to naive expectations, large clusters are as correlated as relatively smaller ones: the correlation length increases with cluster size, a well-known signature of criticality. Each line in the top panel shows the mean cross-correlation $C(r)$ of BOLD activity fluctuations as a function of distance r averaged over all time series of each of the 35 clusters. The correlation length ξ , denoted by the zero crossing of $C(r)$ is not a constant. As shown in the middle graph scale, ξ grows linearly with the average cluster diameter d for all the 35 clusters (filled circles), $\xi \sim N^{1/3}$. The bottom graph shows the collapse of $C(r)$ by rescaling the distance with ξ . (Figure redrawn from Fraiman and Chialvo [56].) (Please find a color version of this figure on the color plates.)

Next we compute the average correlation function of the BOLD fluctuations between all pairs of voxels in the cluster considered, which are separated by a distance r :

$$\langle C_H(r) \rangle = \frac{\langle B_H(\vec{x}, t) - \langle B_H(\vec{x}, t) \rangle_t \rangle_t \langle B_H(\vec{x} + r\vec{u}, t) - \langle B_H(\vec{x} + r\vec{u}, t) \rangle_t \rangle_t}{\langle \langle B_H(\vec{x}, t)^2 \rangle_t - \langle B_H(\vec{x}, t) \rangle_t^2 \rangle_t^{\frac{1}{2}} \langle \langle B_H(\vec{x} + r\vec{u}, t)^2 \rangle_t - \langle B_H(\vec{x} + r\vec{u}, t) \rangle_t^2 \rangle_t^{\frac{1}{2}}} >_{t, \vec{x}, \vec{u}} \quad (3.5)$$

where \vec{u} is a unitary vector and $\langle \cdot \rangle_w$ represents averages over w .

The typical form we observe for $C(r)$ is shown in the top panel of Figure 3.4b. The first striking feature to note is the absence of a unique $C(r)$ for all clusters. Nevertheless, they are qualitatively similar, being at short distances close to unity, to decay as r increases, and then becoming negative for longer voxel-to-voxel distances. Such behavior indicates that within each and any cluster, on an average, the fluctuations around the mean are strongly positive at short distances and strongly anticorrelated at larger distances, whereas there is no range of distance for which the correlation vanishes.

It is necessary to clarify whether the ξ divergence is trivially determined by the structural connectivity. In that case, C must be constant throughout the entire recordings. Conversely, if the dynamics are critical, their average value will not be constant, as it is the product of a combination of some instances of high spatial coordination intermixed with moments of discoordination. In order to answer this question, we study the mean correlation ($\langle C \rangle$) as a function of time for regions of interest of various sizes, for nonoverlapping periods of 10 temporal points.

Figure 3.5 shows the behavior of $\langle C \rangle$ over time for four different cluster sizes. Notice that, in all cases, there are instances of large correlation followed by moments of weak coordination, as those indicated by the arrows in the uppermost panel. We have verified that this behavior is not sensitive to the choice of the length of the window in which $\langle C \rangle$ is computed. These bursts keep the variance of the correlations almost constant (i.e., in this example, there is a minor decrease in variance (by a factor of 0.4) for a huge increase in size (by a factor of 170). This is observed for any of the cluster sizes as shown in the bottom panel of Figure 3.4, where the variance of $\langle C \rangle$ is approximately constant, despite the four order of magnitude increase in sizes. The results of these calculations imply that independent of the size of the cluster considered, there is always an instance in which a large percentage of voxels are highly coherent and another instance in which each voxel activity is relatively independent.

Thus, to summarize Fraiman and Chialvo, their work [56] revealed three key statistical properties of the brain BOLD signal variability.

- The variance of the average BOLD fluctuations computed from ensembles of widely different sizes remains constant (i.e., anomalous scaling).
- The analysis of short-term correlations reveals bursts of high coherence between arbitrarily far apart voxels, indicating that the variance anomalous scaling has a dynamical (and not structural) origin.
- The correlation length measured at different regions increases with the region's size, as well as its mutual information.

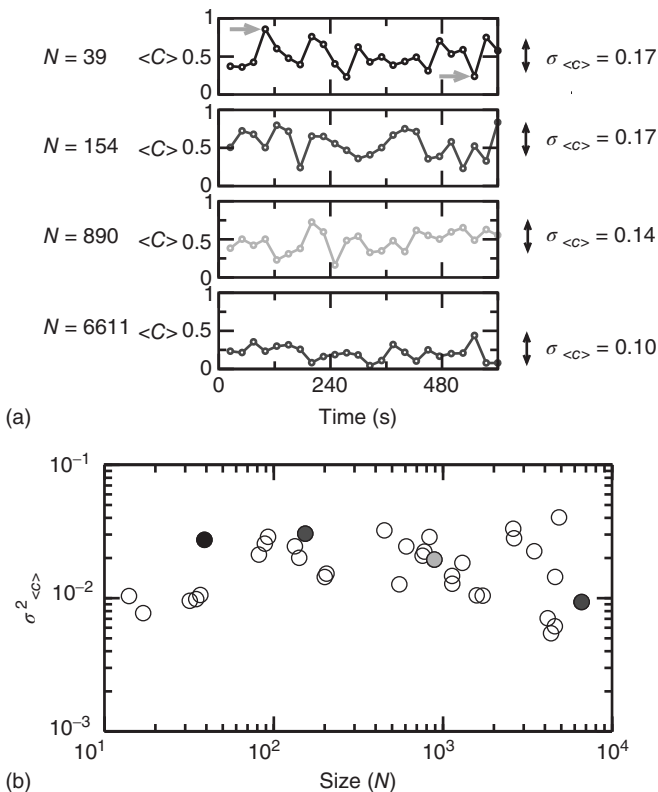


Figure 3.5 Bursts of high correlations are observed at all cluster sizes, resulting in approximately the same variance, despite the four orders of magnitude change in the cluster size. (a) Representative examples of short-term mean correlation $\langle C \rangle$ of the BOLD signals as a function of time for four sizes spanning four orders of magnitude.

The arrows show examples of two instances of highly correlated and weakly correlated activity, respectively. (b) The variance of $\langle C \rangle$ as a function of cluster sizes. The four examples on (a) are denoted with filled circles in (b). (Figure redrawn from Fraiman and Chialvo [56].)

3.4

Beyond Averages: Spatiotemporal Brain Dynamics at Criticality

Without exception, all the reports considering large-scale brain critical dynamics resorted to the computation of averages over certain time and/or space scales. However, as time and space are essential for brain function, it would be desirable to make statements of *where* and *when* the dynamics is at the brink of instability, that is, the hallmark of criticality. In this section, we summarize novel ideas that attempt to meet this challenge by developing techniques that consider large-scale dynamics in space and time in the same way that climate patterns are dealt with, tempting us to call these efforts “brain meteorology.”

Tagliazucchi *et al.* departed from the current brain imaging techniques based on the analysis of *gradual and continuous* changes in the brain BOLD signal. By doing that, they were able to show that the relatively large amplitude BOLD signal peaks [57] contain substantial information. These findings suggested the possibility that relevant dynamical information can be condensed in *discrete* events. If that were true, then the possibility of capturing space and time was possible, an objective ultimately achieved in a subsequent report by Tagliazucchi and colleagues [58], which demonstrated how brain dynamics at the resting state can be captured just by the timing and location of such events, that is, in terms of a spatiotemporal point process.

3.4.1

fMRI as a Point Process

The application of this novel method allowed, for the first time, to define a theoretical framework in terms of an order and control parameter derived from fMRI data, where the dynamical regime can be interpreted as one corresponding to a system close to the critical point of a second-order phase transition. The analysis demonstrated that the resting brain spends most of the time near the critical point of such transition and exhibits avalanches of activity ruled by the same dynamical and statistical properties described previously for neuronal events at smaller scales.

The data in Figure 3.6 shows an example of a point process extracted from a BOLD time series. A qualitative comparison with the established method of deconvolving the BOLD signal with the hemodynamics response function suggests that at first order, the point process is equivalent to the peaks of the deconvolution.

As shown in [58], the point process can efficiently compress the information needed to reproduce the underlying brain activity in a way comparable with conventional methods such as seed correlation and independent component analysis demonstrated by, for instance, its ability to replicate the right location of each of the RSN. While the former methods represent averages over the entire data sets, the point process, by construction, compresses and *preserves* the temporal information. This potential advantage, unique to the current approach, may provide additional clues on brain dynamics.

This is explored here by compiling the statistics and dynamics of clusters of points both in space and time. Clusters are groups of contiguous voxels with signals above the threshold at a given time, identified by a scanning algorithm in each fMRI volume. Figure 3.7a shows examples of clusters (in this case nonconsecutive in time) depicted with different colors. Typically (Figure 3.7b, top), the number of clusters at any given time varies only an order of magnitude around the mean (~ 50). In contrast, the size of the largest active cluster fluctuates widely, spanning more than four orders of magnitude.

The analysis reveals four novel dynamical aspects of the cluster variability, which could have hardly been uncovered with the previous methods.

- At any given time, the number of clusters and the total activity (i.e., the number of active voxels) follows a nonlinear relation resembling that of percolation [59].

At a critical level of global activity (~ 2500 voxels, dashed horizontal line in Figure 3.7b, vertical in Figure 3.7c), the number of clusters reaches a maximum (~ 100 – 150), together with its variability.

- The correlation between the number of active sites (an index of total activity) and the number of clusters reverses above a critical level of activity, a feature already described in other complex systems in which some increasing density competes with limited capacity [1, 59].
- The rate at which the very large clusters (i.e., those above the dashed line in 3.7b) occurs (\sim one every 30–50 s) corresponds to the low frequency range at which RSNs are typically detected using probabilistic independent component analysis (PICA) [45].
- The distribution of cluster sizes (Figure 3.7d) reveals a scale-free distribution (whose cutoff depends on the activity level; see panel f).

3.4.2

A Phase Transition

The four features just described are commonly observed in complex systems undergoing an order–disorder phase transition [1, 10, 13]. This scenario was explored in [58] by defining control and order parameter from the data. To

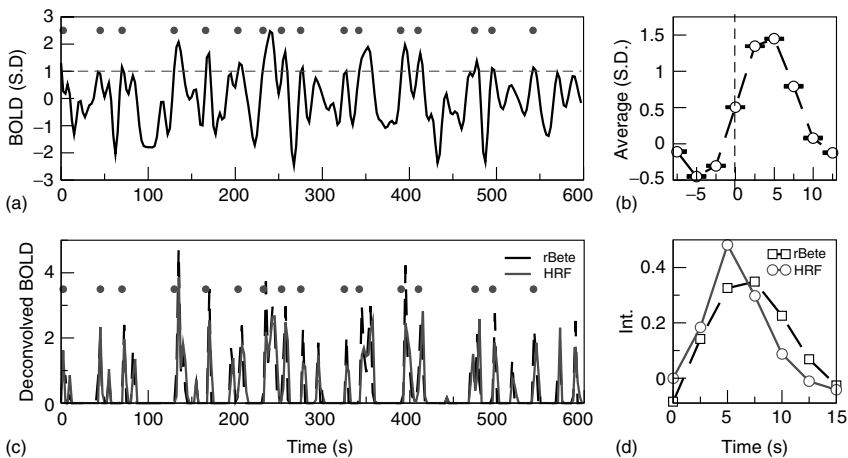
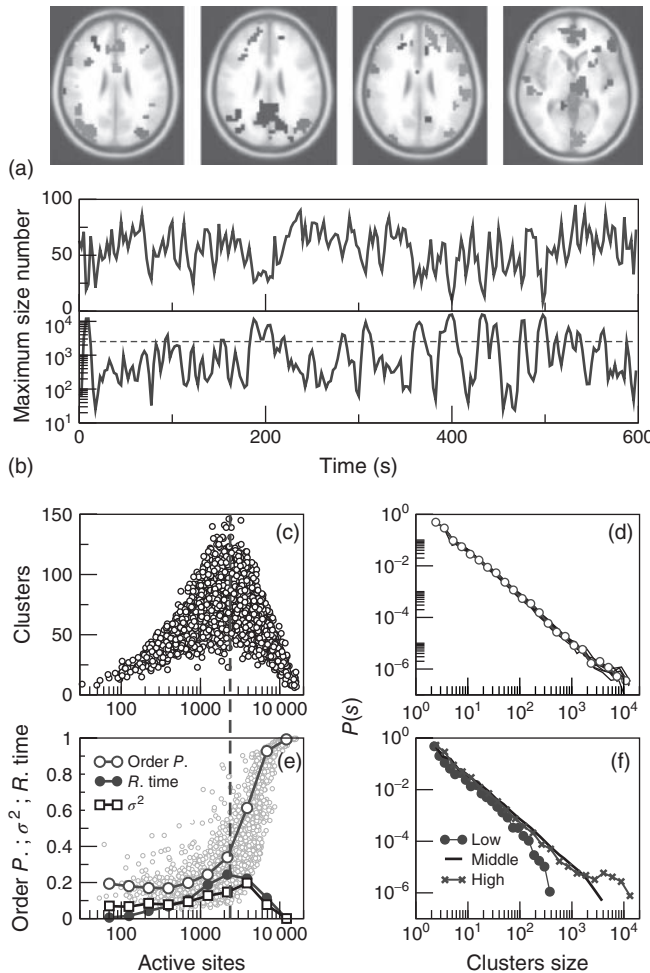


Figure 3.6 (a) Example of a point process (filled circles) extracted from the normalized BOLD signal. Each point corresponds to a threshold (dashed line at 1 SD) crossing from below. (b) Average BOLD signal (from all voxels of one subject) triggered at each threshold crossing. (c) The peaks of

the deconvolved BOLD signal, using either the hemodynamic response function (HRF) or the rBeta function [57] depicted in panel d, coincide on a great majority with the timing of the points shown in panel a. (Figure redrawn from Tagliazucchi *et al.* [58].)



represent the degree of order (i.e., the *order* parameter), the size of the largest cluster (normalized by the number of active sites) in the entire brain was computed and plotted as a function of the number of active points (i.e., the control parameter). This was done for all time steps and plotted in Figure 3.7e (small circles). As a control parameter, the global level of activity was used as in other well-studied models of order-disorder transitions (the clearest example being percolation [59]).

Several features in the data reported in [58] suggest a phase transition: first, there is sharp increase in the average order parameter (empty circles in Figure 3.7e), accompanied by an increase of its variability (empty squares). Second, the transition coincides with the peak in the function plotted in Figure 3.7c, which accounts for the number of clusters. Finally, the calculation of the relative frequency of the number of active sites (i.e., the residence time distribution) shows

Figure 3.7 The level of brain activity continuously fluctuates above and below a phase transition. (a) Examples of coactivated clusters of neighbor voxels (clusters are 3D structures; thus, seemingly disconnected clusters may have the same color in a 2D slice). (b) Example of the temporal evolution of the number of clusters and its maximum size (in units of voxels) in one individual. (c) Instantaneous relation between the number of clusters versus the number of active sites (i.e., voxels above the threshold) showing a positive/negative correlation depending on whether activity is below/above a critical value (~ 2500 voxels, indicated by the dashed line here and in panel b). (d) The cluster size distribution follows a power law spanning four orders of magnitude. Individual statistics for each of the 10 subjects are plotted with lines and the average with symbols. (e) The order parameter, defined here as the (normalized)

size of the largest cluster, is plotted as a function of the number of active sites (isolated data points denoted by dots, averages plotted with circles joined by lines). The calculation of the residence time density distribution ("R. time", filled circles) indicates that the brain spends relatively more time near the transition point. Note that the peak of the R. time in this panel coincides with the peak of the number of clusters in panel c, as well as the variance of the order parameter (squares). (f) The computation of the cluster size distribution calculated for three ranges of activity (low: 0–800; middle: 800–5000; and high >5000) reveals the same scale invariance plotted in panel d for relatively small clusters, but shows changes in the cutoff for large clusters. (Figure redrawn from [58].) (Please find a color version of this figure on the color plates.)

that the brain spends, on an average, more time near the transition than in the two extremes, the highly ordered and the highly disordered states. This supports the earlier conjecture that the brain works near criticality [1, 13, 53]. It would be interesting to investigate whether and how this transition diagram changes with arousal states, unhealthy conditions, and anesthesia, as well as to develop ways to parametrize such changes to be used as objective markers of mind state.

3.4.3 Variability and Criticality

It is important to note that the description in terms of a point process allows the observation of activity fluctuations in space and time. In particular, note that the results in Figure 3.7c,e show that the resting brain dynamics achieves maximum variability at a particular level of activation which coincides with criticality. As it is known that the peak of variability in critical phenomena is found at criticality, it is tempting to speculate that the origin of the spontaneous brain fluctuations can be traced back to a phase transition. This possibility is further strengthened by the fact that the data shows the brain spends most of the time around such transitions.

Thus, overall the results point to a different class of models that needs to emphasize nonequilibrium self-generated variability. The data is orthogonal to most of the current models in which, without the external noise, the dynamics are stuck in a stable equilibrium state. On the other hand, nonequilibrium systems near criticality do not need the introduction of noise: variability is self-generated by the collective dynamics, which spontaneously fluctuate near the critical point.

3.5

Consequences

As discussed in previous sections, critical dynamics implies coherence of activity beyond what is dictated by nearest neighbor connections and correlations longer than that of the neural structure and nontrivial scaling of the fluctuations. These anomalies suggest the need to turn the page on a series of concepts derived from the idea that the brain works as a circuit. While it is not suggested here that such circuits do not exist, fundamentally different conclusions should be extracted from their study. As a starting point, the following paragraphs discuss which of the associated notions of connectivity and networks should be revised under the viewpoint of criticality. At the end of the section, an analogy with river beds is offered to summarize the point.

3.5.1

Connectivity versus Functional Collectivity

The present results suggest that the current interpretation of functional connectivity, an extensive chapter of the brain neuroimaging literature, should be revised. The three basic concepts in this area are brain functional connectivity, effective connectivity, and structural connectivity [60–62]. The first one “is defined as the correlations between spatially remote neurophysiological events” [60]. *Per se*, the definition is a statistical one, and it “is simply a statement about the observed correlations; it does not comment on how these correlations are mediated” [60]. The second concept, effective connectivity, is closer to the notion of causation between neuronal connections and “is defined as the influence one neuronal system exerts over another.” Finally, the concept of structural or anatomical connectivity refers to the identifiable physical or structural (synaptic) connections linking neuronal elements.

The problem with the use of these three concepts is that, intentionally or not, they emphasize “the connections” between brain regions. This is so, despite cautionary comments emphasizing that “depending on sensory input, global brain state, or learning, the same structural network can support a wide range of dynamic and cognitive states” [61].

An initial demonstration of the ambiguity in the functional connectivity definition was shown by the results of Fraiman in the Ising model, which, almost as an exercise, showed [42] the emergence of nontrivial collective states over an otherwise trivial regular lattice (i.e., the Ising’s structural connectivity). As it is well known that the brain structural connectivity is not a lattice, the replication in the Ising model of many relevant brain network properties suggested the need to revise our assumptions at the time of interpreting functional connectivity studies.

The second blow to the connectivity framework was given by recent results from Haimovici *et al.* [63]. They compared the RSN from human fMRI with numerical results obtained from their network model, which is based on the structural connectivity determined earlier by Hagmann *et al.* [64], plus a simple excitable dynamics endowed to each network node. Different dynamics were obtained by changing the

excitability of the nodes, but only the results gathered at criticality compared well with the human fMRI. These striking results indicate that the spatiotemporal brain activity in human RSN represents a collective emergent phenomena exhibited by the underlying structure *only at criticality*. By indicating under which specific dynamical conditions the brain structure will produce the empirically observed functional connectivity, Haimovici's results not only reemphasized that "the same structural network can support a wide range of dynamic and cognitive states" but it also showed, for the first time, how it can be done. Of course, these modeling results only scratched the surface of the problem, and a theory to deal with dramatic changes in functionality as a function of global parameters is awaiting.

The third concept in the circuit trio is effective connectivity, which, as mentioned, implies the notion of influence of one neuronal group over another. Implicit to this idea is the notion of causation, which needs to be properly defined to prevent confusion. In this context, the causation for a given variable boils down to identify which one of all the other covariables (i.e., degrees of freedom sharing some correlations) predicts best its own dynamics. This is done by observing the past states of all the interactions to a given site and estimating which one contributes more to determine the present state of such a site. While the idea is always the same, the question of causation can be framed in different ways, by specific modeling, by calculating partial correlations, different variants of Granger causality, transfer entropies, and so on. Independent of the implementation, in systems at criticality, the notion of effective connectivity suffers from a severe limitation as emergent phenomena cannot be dissected in the interaction pairs. To illustrate such a limitation, it suffices to mention the inability to predict the next avalanche in the sandpile model [9] by computing causation between the nearest neighbor sites.

An important step forward is the work reported recently by Battaglia and colleagues [65], who in the same spirit as in the earlier discussion begin by stating:

"The circuits of the brain must perform a daunting amount of functions. But how can "brain states" be flexibly controlled, given that anatomic inter-area connections can be considered as fixed, on timescales relevant for behavior?"

The authors conjectured, on the basis of dynamical first principles, that even relatively simple circuits (of brain areas) could produce many "effective circuits" associated with alternative brain states. In their language, "effective circuits" are different effective connectivities arising from circuits with identical structural connectivity. In a proof of principle model, the authors demonstrated convincingly how a small perturbation can change at will from implementing one effective circuit to another. The effect of the perturbation is, in dynamical terms, a switch to different phase-locking patterns between the local neuronal oscillations. We shall add that for this switch to be possible, the basins of attraction between patterns need to be close to each other or, in other words, the system parameters need to be tuned to a region near instability. Furthermore, they found that "information follows causality," which implies that under this condition brief dynamics perturbations can produce completely different modalities of information routing between brain areas of a fixed structural network. It is clear that this is the type of theoretical

framework needed to tackle the bigger problem of how, at a large scale, integration and segregation of information is permanently performed by the brain.

3.5.2

Networks, Yet Another Circuit?

The recent advent of the so-called network approach has produced, without any doubt, a tremendous impact across several disciplines. In all cases, accessing the network graph represents the possibility of seeing the skeleton of the system over which the dynamics evolves, with the consequent simplification of the problem at hand. In this way, the analysis focuses on defining the interaction paths linking the systems' degrees of freedoms (i.e., the nodes). The success of this approach in complex systems probably is linked to the universality exhibited by the dynamics of this class of systems. Universality tells us that, in the same class, in many cases, the only relevant information is the interactions; thus, in that case a network represents everything needed to understand how they work.

Thus, in the case at hand, the use of network techniques could bring the false hope that knowing where the connections between neuronal groups are, then the brain problem will be solved. This illusion will affect even those who are fully aware that this is not possible, because the fascination with the complexity of networks will at least produce an important distraction and delay. The point is that we could be fooling ourselves in choosing for our particular problem a description of the brain determined by graphs, constructed by nodes, connected by paths, and so on.

The reflection we suggest is that, despite changing variables and adopting different names, this new network approach preserves the same idea that we consider is (dangerously) rigid for understanding the brain: the concept of a circuit. This notion, introduced as the most accepted neural paradigm for the past century, was adopted by neuroscience from the last engineering revolution (i.e., electronics). Thus, while it is true that action potentials traverse, undoubtedly, and circulate through paths, the system is not a circuit in the same sense of electronic systems, where nothing unexpected emerges out of the collective interaction of resistors, capacitors, and semiconductors. Thus, if these new ideas will move the field ahead, it will depend heavily on resisting this fascination and preventing the repetition of old paradigms with new names.

3.5.3

River Beds, Floods, and Fuzzy Paths

The question often appears on how the flow of activity during any given behavior could be visualized if the brain operates as a system near criticality.¹⁾

1) When asked, it is difficult to resist the temptation to reply by posing another question: considering that, in accordance with current ideas, behavior is produced by the activity (action potentials) flowing through a given circuit, how is visualized the mechanism responsible for switching between one to the other circuit?

The answer, in the absence of datum, necessarily involves the use of caricatures and analogies. In such a hypothetical framework, we imagine a landscape where the activity flows, and to be graphical let us think of a river. If the system is near criticality, first and most importantly, such a landscape must exclude the presence of deep paths (i.e., no “Grand Canyon”), only relatively shallow river beds, some of them with water and others dry. On the other hand, if the system is ordered, the stream will always flow following deep canyons. In this context, let us imagine that “information” is transmitted by the water, and in that sense it is its flow that “connects” regions (whenever at a given time two or more regions are wet simultaneously). Under relatively constant conditions erosion, owing to water flow, it will be expected to deepen the river beds. Conversely, changes in the topology of this hypothetical network can occur anytime that a sudden increase makes a stream overflow its banks. After that, it will be possible to observe that the water changed course, a condition that will be stable only until the next flooding.

Thus, in this loose analogy, the river network structural connectivity (i.e., the relatively deeper river beds) is the less relevant part of the story for predicting where information will be shared. The effective connectivity is created through the history of the system, and its paths can not be conceived as being fix. The moral behind this loose analogy is to direct attention to the fact that the path’s flexibility, which is absolutely essential for brain function, depends on having a landscape composed by shallow river beds.

3.6 Summary and Outlook

The program reviewed here considers the brain as a dynamical object. As in other complex systems, the accessible data to be explained are spatiotemporal patterns at various scales. The question is whether it is possible to explain all these results from a single fundamental principle. And, in case the answer is affirmative, what does this unified explanation of brain activity imply about goal-oriented behavior? We submit that, to a large extent, the problem of the dynamical regime at which the brain operates is already solved in the context of critical phenomena and phase transitions. Indeed, several fundamental aspects of brain phenomenology have an intriguing counterpart, with dynamics seen in other systems when posed at the edge of a second-order phase transition.

We have limited our review here to the large-scale dynamics of the brain; nevertheless, as discussed elsewhere [13], similar principles can be demonstrated at other scales. To be complete, the analysis must incorporate behavioral and cognitive data, which will show similar signatures indicative of scale invariance. Finally, and hopefully, overall, these results should give us a handle for a rational classification of healthy and unhealthy mind states.

References

1. Bak, P. (1996) *How Nature Works: The Science of Self-Organized Criticality*, Springer, New York.
2. Stanley, H. (1987) *Introduction to Phase Transitions and Critical Phenomena*, Oxford University Press.
3. Turing, A. (1950) Computing machinery and intelligence. *Mind*, **59** (236), 433–460.
4. Stassinopoulos, D. and Bak, P. (1995) Democratic reinforcement: a principle for brain function. *Phys. Rev. E*, **51** (5), 5033–5039.
5. Ceccato, A., Navone, H., and Waelbroeck, H. (1996) Stable criticality in a feedforward neural network. *Rev. Mex. Fis.*, **42**, 810–825.
6. Chialvo, D. and Bak, P. (1999) Learning from mistakes. *Neuroscience*, **90** (4), 1137–1148.
7. Bak, P. and Chialvo, D. (2001) Adaptive learning by extremal dynamics and negative feedback. *Phys. Rev. E*, **63** (3), 031912.
8. Wakeling, J. and Bak, P. (2001) Intelligent systems in the context of surrounding environment. *Phys. Rev. E*, **64** (5), 051920.
9. Bak, P., Tang, C., and Wiesenfeld, K. (1987) Self-organized criticality: an explanation of 1/f noise. *Phys. Rev. Lett.*, **59** (4), 381–384.
10. Jensen, H.J. (1998) *Self-Organized Criticality: Emergent Complex Behavior in Physical and Biological Systems*, Cambridge University Press, New York.
11. Bak, P. (1998) Life laws. *Nature*, **391** (6668), 652–653.
12. Bak, P. and Sneppen, K. (1993) Punctuated equilibrium and criticality in a simple model of evolution. *Phys. Rev. Lett.*, **71** (24), 4083–4086.
13. Chialvo, D. (2010) Emergent complex neural dynamics. *Nat. Phys.*, **6** (10), 744–750.
14. Bak, P. and Paczuski, M. (1995) Complexity, contingency, and criticality. *Proc. Natl. Acad. Sci. U.S.A.*, **92** (15), 6689–6696.
15. Anderson, P. (1972) More is different. *Science*, **177** (4047), 393–396.
16. Buzsaki, G. (2009) *Rhythms of the Brain*, Oxford University Press, New York.
17. Linkenkaer-Hansen, K., Nikouline, V., Palva, J., and Ilmoniemi, R. (2001) Long-range temporal correlations and scaling behavior in human brain oscillations. *J. Neurosci.*, **21** (4), 1370–1377.
18. Stam, C. and de Bruin, E. (2004) Scale-free dynamics of global functional connectivity in the human brain. *Hum. Brain Mapp.*, **22** (2), 97–109.
19. Plenz, D. and Thiagarajan, T.C. (2007) The organizing principles of neuronal avalanches: cell assemblies in the cortex? *Trends Neurosci.*, **30** (3), 101–110.
20. Bullock, T., McClune, M., and Enright, J. (2003) Are the electroencephalograms mainly rhythmic? Assessment of periodicity in wide-band time series. *Neuroscience*, **121** (1), 233–252.
21. Logothetis, N. (2002) The neural basis of the blood-oxygen-level-dependent functional magnetic resonance imaging signal. *Philos. Trans. R. Soc. London, Ser. B*, **357** (1424), 1003–1037.
22. Eckhorn, R., van Pelt, J., Corner, M.A., Uylings, H.B.M., and Lopes da Silva, F.H. (1994) Oscillatory and non-oscillatory synchronizations in the visual cortex and their possible roles in associations of visual features, in *Progress in Brain Research*, Vol. **102**, Chapter 28, Elsevier Science, pp. 405–425.
23. Miller, K., Sorensen, L., Ojemann, J., and Den Nijs, M. (2009) Power-law scaling in the brain surface electric potential. *PLoS Comput. Biol.*, **5** (12), e1000609.
24. Manning, J., Jacobs, J., Fried, I., and Kahana, M. (2009) Broadband shifts in local field potential power spectra are correlated with single-neuron spiking in humans. *J. Neurosci.*, **29** (43), 13613–13620.
25. Gilden, D. (2001) Cognitive emissions of 1/f noise. *Psychol. Rev.*, **108** (1), 33–56.
26. Maylor, E., Chater, N., and Brown, G. (2001) Scale invariance in the retrieval of retrospective and prospective memories. *Psychon. Bull. Rev.*, **8** (1), 162–167.
27. Ward, L. (2001) *Dynamical Cognitive Science*, MIT Press.

28. Nakamura, T., Kiyono, K., Yoshiuchi, K., Nakahara, R., Struzik, Z., and Yamamoto, Y. (2007) Universal scaling law in human behavioral organization. *Phys. Rev. Lett.*, **99** (13), 138103.
29. Anteneodo, C. and Chialvo, D. (2009) Unraveling the fluctuations of animal motor activity. *Chaos*, **19** (3), 033123.
30. Beckers, R., Deneubourg, J., Goss, S., and Pasteels, J. (1990) Collective decision making through food recruitment. *Insects Soc.*, **37** (3), 258–267.
31. Beekman, M., Sumpter, D., and Ratnieks, F. (2001) Phase transition between disordered and ordered foraging in pharaoh's ants. *Proc. Natl. Acad. Sci. U.S.A.*, **98** (17), 9703–9706.
32. Rauch, E., Millonas, M., and Chialvo, D. (1995) Pattern formation and functionality in swarm models. *Phys. Lett. A*, **207** (3), 185–193.
33. Nicolis, G. and Prigogine, I. (1977) *Self-Organization in Nonequilibrium Systems: From Dissipative Structures to Order Through Fluctuations*, Wiley-Interscience, New York.
34. Takayasu, M., Takayasu, H., and Fukuda, K. (2000) Dynamic phase transition observed in the internet traffic flow. *Physica A*, **277** (1), 248–255.
35. Lux, T. and Marchesi, M. (1999) Scaling and criticality in a stochastic multi-agent model of a financial market. *Nature*, **397** (6719), 498–500.
36. Malamud, B.D., Morein, G., and Turcotte, D.L. (1998) Forest fires: an example of self-organized critical behavior. *Science*, **281** (5384), 1840–1842.
37. Peters, O. and Neelin, J. (2006) Critical phenomena in atmospheric precipitation. *Nat. Phys.*, **2** (6), 393–396.
38. Peters, O., Hertlein, C., and Christensen, K. (2002) A complexity view of rainfall. *Phys. Rev. Lett.*, **88**, 018701.
39. Peters, O. and Christensen, K. (2002) Rain: relaxations in the sky. *Phys. Rev. E*, **66**, 036120.
40. Cavagna, A., Cimarelli, A., Giardina, I., Parisi, G., Santagati, R., Stefanini, F., and Viale, M. (2010) Scale-free correlations in starling flocks. *Proc. Natl. Acad. Sci. U.S.A.*, **107** (26), 11865–11870.
41. Eguiluz, V., Chialvo, D., Cecchi, G., Baliki, M., and Apkarian, A. (2005) Scale-free brain functional networks. *Phys. Rev. Lett.*, **94**, 018102.
42. Fraiman, D., Balenzuela, P., Foss, J., and Chialvo, D. (2009) Ising-like dynamics in large-scale functional brain networks. *Phys. Rev. E*, **79** (6), 061922.
43. Fox, M. and Raichle, M. (2007) Spontaneous fluctuations in brain activity observed with functional magnetic resonance imaging. *Nat. Rev. Neurosci.*, **8** (9), 700–711.
44. Smith, S., Fox, P., Miller, K., Glahn, D., Fox, P., Mackay, C., Filippini, N., Watkins, K., Toro, R., Laird, A., and Beckmann, C. (2009) Correspondence of the brain's functional architecture during activation and rest. *Proc. Natl. Acad. Sci. U.S.A.*, **106** (31), 13040–13045.
45. Beckmann, C., DeLuca, M., Devlin, J., and Smith, S. (2005) Investigations into resting-state connectivity using independent component analysis. *Philos. Trans. R. Soc. London, Ser. B*, **360** (1457), 1001–1013.
46. Xiong, J., Parsons, L., Gao, J., and Fox, P. (1999) Interregional connectivity to primary motor cortex revealed using mri resting state images. *Hum. Brain Mapp.*, **8** (2-3), 151–156.
47. Cordes, D., Haughton, V., Arfanakis, K., Wendt, G., Turski, P., Moritz, C., Quigley, M., and Meyerand, M. (2000) Mapping functionally related regions of brain with functional connectivity MR imaging. *Am. J. Neuroradiol.*, **21** (9), 1636–1644.
48. Fukunaga, M., Horovitz, S., van Gelderen, P., de Zwart, J., Jansma, J., Ikonomidou, V., Chu, R., Deckers, R., Leopold, D., and Duyn, J. (2006) Large-amplitude, spatially correlated fluctuations in bold fmri signals during extended rest and early sleep stages. *Magn. Reson. Imaging*, **24** (8), 979–992.
49. Vincent, J., Patel, G., Fox, M., Snyder, A., Baker, J., Van Essen, D., Zempel, J., Snyder, L., Corbetta, M., and Raichle, M. (2007) Intrinsic functional architecture in the anaesthetized monkey brain. *Nature*, **447** (7140), 83–86.
50. Kitzbichler, M., Smith, M., Christensen, S., and Bullmore, E. (2009) Broadband

- criticality of human brain network synchronization. *PLoS Comput. Biol.*, **5** (3), e1000314.
- 51.** Kuramoto, Y. (1984) *Chemical Oscillators, Waves and Turbulence*, Springer Verlag, Berlin.
- 52.** Botcharova, M., Farmer, S., and Berthouze, L. (2012) A power-law distribution of phase-locking intervals does not imply critical interaction. *Phys. Rev. E*, **86**, 051920.
- 53.** Expert, P., Lambiotte, R., Chialvo, D., Christensen, K., Jensen, H., Sharp, D., and Turkheimer, F. (2011) Self-similar correlation function in brain resting-state functional magnetic resonance imaging. *J. R. Soc. Interface*, **8** (57), 472–479.
- 54.** Garrett, D., Kovacevic, N., McIntosh, A., and Grady, C. (2010) Blood oxygen level-dependent signal variability is more than just noise. *J. Neurosci.*, **30** (14), 4914–4921.
- 55.** Garrett, D., Kovacevic, N., McIntosh, A., and Grady, C. (2011) The importance of being variable. *J. Neurosci.*, **31** (12), 4496–4503.
- 56.** Fraiman, D. and Chialvo, D. (2012) What kind of noise is brain noise: anomalous scaling behavior of the resting brain activity fluctuations. *Front. Physiol.*, **3**: 307. doi: 10.3389/fphys.2012.00307.
- 57.** Tagliazucchi, E., Balenzuela, P., Fraiman, D., Montoya, P., and Chialvo, D. (2011) Spontaneous bold event triggered averages for estimating functional connectivity at resting state. *Neurosci. Lett.*, **488** (2), 158–163.
- 58.** Tagliazucchi, E., Balenzuela, P., Fraiman, D., and Chialvo, D. (2012) Criticality in large-scale brain fMRI dynamics unveiled by a novel point process analysis. *Front. Physiol.*, **3**: 15. doi: 10.3389/fphys.2012.00015.
- 59.** Stauffer, D. and Aharony, A. (1994) *Introduction to Percolation Theory*, CRC Press.
- 60.** Friston, K. (2004) Functional and effective connectivity in neuroimaging: a synthesis. *Hum. Brain Mapp.*, **2** (1-2), 56–78.
- 61.** Sporns, O., Tononi, G., and Kötter, R. (2007) The human connectome: a structural description of the human brain. *PLoS Comput. Biol.*, **1** (4), e42.
- 62.** Horwitz, B. (2003) The elusive concept of brain connectivity. *Neuroimage*, **19** (2), 466–470.
- 63.** Haimovici A., Tagliazucchi, E., Balenzuela, P., and Chialvo, D.R. (2013) Brain organization into resting state networks emerges at criticality on a model of the human connectome. *Phys. Rev. Lett.*, **110**, 178101.
- 64.** Hagmann, P., Cammoun, L., Gigandet, X., Meuli, R., Honey, C., Wedeen, V., and Sporns, O. (2008) Mapping the structural core of human cerebral cortex. *PLoS Biol.*, **6** (7), e159.
- 65.** Battaglia, D., Witt, A., Wolf, F., and Geisel, T. (2012) Dynamic effective connectivity of inter-areal brain circuits. *PLoS Comput. Biol.*, **8** (3), e1002438.

4

The Dynamic Brain in Action: Coordinative Structures, Criticality, and Coordination Dynamics

J. A. Scott Kelso

4.1

Introduction

The pairing of meaning and matter is the most profound feature of the world and the clue to understanding not only ourselves but all existence. Science takes the meaning out of matter through the principle of objectivization [1]. Yet, as evolved living things, we all know that meaning lurks behind everything we do. Should science exorcise meaning or try to come to grips with it? And if so, how? The key to understanding meaningful matter as it is manifested in behavior and the brain lies in understanding coordination. Coordination refers not just to matter in motion, nor to complex adaptive matter: it refers to the *functional* – informationally meaningful – coupling among interacting processes in space and time. Such functional spatiotemporal ordering comes in many guises in living things, from genes to cells to neural ensembles and circuitry to behavior (both individual and group) and cognition. It is a truism nowadays that biological processes, at all scales of observation, are highly degenerate [2, 3] and obey the principle of functional equivalence [4, 5]. Since the late 1970s, an approach grounded in the concepts, methods, and tools of self-organization in physical and chemical systems (synergetics, dissipative structures) yet tailored specifically to the behavioral and neural activities of animate, living things (moving, perceiving, feeling, deciding, thinking, learning, remembering, etc.) has emerged – a theoretical and empirical framework that aims to understand how the parts and processes of living things come together and break apart in space and time. It is called *coordination dynamics* (e.g., [6–14]). Coordination Dynamics (CD for short) is a line of scientific inquiry that aims to understand how functionally significant patterns of coordinated behavior emerge, persist, adapt, and change in living things in general and human beings in particular. “Laws of coordination” and their numerous mechanistic realizations are sought in a variety of different systems at multiple levels of description. CD addresses coordination within a part or process of a system, between different parts and processes and between different kinds of system (For a trilogy of encyclopedia articles on CD, and the many references contained therein, the reader is referred to Fuchs and Kelso [15], Oullier and Kelso [16], and Kelso [17]; see also

Huys and Jirsa [9] for an excellent treatment). CD contains two complementary aspects (“cornerstones,” cf. [11]), that are necessary to understand biological coordination: a spontaneous self-organizing aspect, as we shall see intimately connected to the concepts and empirical facts surrounding phase transitions and critical phenomena in nature’s nonequilibrium, highly heterogeneous systems; and information, viewed not as a mere communication channel but as functionally meaningful and specific to the coordination dynamics.

Self-organizing processes and meaningful information in animate, living things are deeply entwined and inseparable aspects of CD. Self-organizing processes create meaningful information in coupled dynamical systems, which in turn are capable of sculpting or guiding the self-organizing dynamics to suit the needs of an organism [18]. In CD, the organism *qua* agent and the environment are not two separate things, each with their own properties, but rather one single coevolving system (see also [19]). As far as CD is concerned, to refer to a system *in* its environment or to analyze a system *plus* an environment, although common in practice, are questionable assumptions. As Poincaré said, many years ago, it is not the things themselves that matter, “but the relations among things; outside these relations there is no reality knowable” (cited in [11], p. 97). “Atoms by themselves, John Slater (1951) remarked, have only a few interesting parameters. It is when they come into combination with each other that problems of real physical and chemical interest arise” (cited in [20], p. 19). For the coordination of the brain and indeed for coordination at all levels, we will have to identify our own informationally relevant structures, our own “atomisms of function.” They will be partly but not totally autonomous, and never context independent. They will be relational and dynamic, evolving on many spatiotemporal scales. Although they will be bounded by levels above and below, on any given level of description they will have their own emergent descriptions [11, 21]. Coordination in living things will have its own geometry, dynamics, and logic that will have to be identified. We explore the ramifications of this in what follows.

4.2

The Organization of Matter

The study of matter has undergone a profound revolution in the past 40 odd years with the discovery of emergent phenomena and self-organization in complex, nonequilibrium systems. One can trace these developments to the work of scientists such as Wilson, Kadanoff, and others in their fundamental research on phase transitions; to crucial extensions of phase transition theory to nonequilibrium systems by “the father of laser theory” Hermann Haken and his generalizations thereof in a field he named *Synergetics*; to Ilya Prigogine and colleagues for their work on the thermodynamics of chemical reactions and irreversible processes, the “Brusselator” and generalizations thereof to “Dissipative Structures”; to Manfred Eigen and Peter Schuster’s autocatalytic cycles and “hypercycles” as necessary underpinnings of prebiotic life. Lesser known, but no less important figures include Arthur Iberall

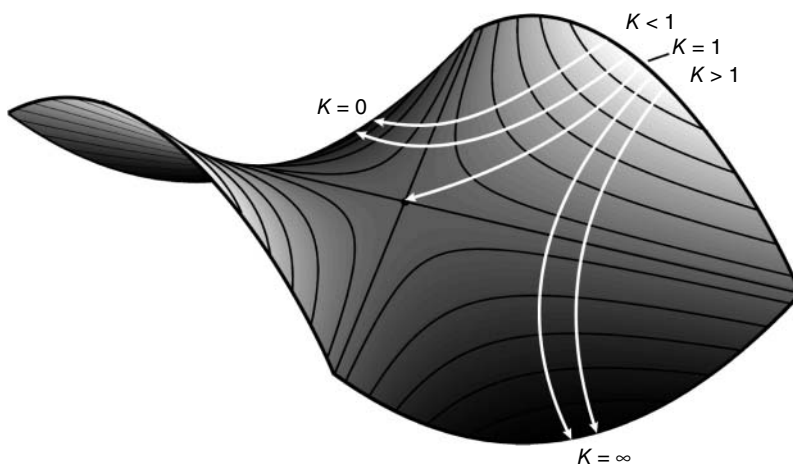


Figure 4.1 The renormalization group transformation can be described as the motion of a point on a surface constructed in a multidimensional parameter space. The form of the surface is defined by all the couplings between block spins, but only

nearest-neighbor coupling, K , is shown here. The surface has two peaks and two sinkholes, which are connected to a saddle point. The saddle defines the system's critical point. (Adapted from Wilson [24].) See text for details.

and the field he named *Homeokinetics* – a kind of social physics in the broadest sense where atomisms at one level create continua at another – an up-down as well as a side to side physics of living things [22, 23]. All the aforementioned – and many others, of course – have, I think, something essential in common: they exemplify a search for the connections between the ways different kinds of processes behave, at many different levels of description and scales of energy, length, and time.¹⁾ They follow, in a sense, whether consciously or not, the goal of identifying principles of organization that transcend different kinds of things. They are reductionists, not (or not only) to elementary entities such as cells, molecules, and atoms, but to finding a minimum set of organizing principles for how patterns in nature form and change.

For a concrete yet conceptually rich example, take the work of the late Kenneth Wilson (1936–2013) who won the Nobel Prize in Physics in 1982 for a quantitative understanding of phase transitions – how matter changes from one form to another. Through his renormalization group and block spin methods, Wilson was able to show that many different systems behave identically at critical points: whether a ferromagnet changing its magnetization at a critical temperature (the reciprocal of the coupling strength between its elements) or a fluid hovering between its liquid and vaporous state. Wilson envisaged the transformation of the system from one state to another as the motion of a marble rolling on a surface constructed in an imaginary multidimensional space: the system's parameter space

1) The word “process” is chosen carefully. What we call a structure in biology (say a bone, or a piece of a creature’s neuroanatomy) or an institution in sociology is a slowly evolving process. Such processes range across many scales of magnitude and functioning timescales.

(Figure 4.1). Each frame of motion reveals the effect of his mathematical method (the so-called block spin transformation). This transformation allows the marble to move but the speed and direction of the marble are dictated by the slope of the surface. Knowing the slope of the surface as the system approaches the critical point, one can calculate how the properties of the system vary as the coupling strength between the block spins changes – precisely the information one needs to understand critical phenomena.

The test, of course, of any good theory is how it matches (and even predicts) experimental data; in the case of phase transitions, the data base is very rich indeed. Imagine what the early humans must have felt when they heated up water and it turned into vapor or during the winter when the ponds outside their caves turned into ice. Measurable macroscopic properties of a ferromagnet, such as its spontaneous magnetization or in the case of a fluid the density difference between the liquid and vapor phases, are called *order parameters*. A magnet's susceptibility (meaning how the magnetization changes for a small change in an applied magnetic field) or the compressibility of the fluid (how density changes with changes in pressure) all exhibit the same critical behavior. In the case of the ferromagnet, the order parameter, its susceptibility, and its correlation length (a measure of fluctuations) are all functions of how much the temperature deviates from the critical temperature. On an ordinary temperature scale, different systems have different critical temperatures. However, by simply expressing the actual temperature T (which we may call a *control parameter*) and the critical temperature T_c as a ratio, $t = (T - T_c)/T_c$, all critical points are the same. That is, the macroscopic properties of different systems are proportional to the absolute value of t raised to some power. This means that to properly characterize critical phenomena in thermodynamic systems, one needs to determine what that power is, that is, the value of the critical exponents. Wilson showed that fluids and ferromagnets lie on the same surface in parameter space (Figure 4.1) and, although they start with different initial positions, both converge on the same saddle point and hence have the same critical exponents. This similarity in the critical behavior of fluids and ferromagnets attests to the more general principle of *universality*: fluids, long chain polymers, alloys, superfluids like helium 4, even mixtures of liquids such as oil and water all belong to the same universality class.

My purpose in saying something about Wilson's work is certainly *not* to “physicalize” neural and behavioral systems. Analogy is often useful in science and sometimes leads to important insights. In this case, analogy leads us to inquire if the theoretical concepts and methods used to understand collective or cooperative behavior in nature may enable us to better understand the brain and its relation to what people do. With its billions of neurons, astrocytes, and vast connectivity, does the brain exhibit collective behavior and phase transitions? Important though it may be to study the many varieties of neurons and their molecular and atomic constituents as individual entities, is the emergence of collective or coordinative behavior a fundamental aspect of brain and behavioral function? Once one grasps the analogy, the answer might seem as obvious as an apple falling from a tree, but we cannot assume it to be so. One message from studies of

cooperative phenomena in physics is that we have come to appreciate what the relevant macroscopic variables such as pressure, volume, temperature, and density are and how they relate lawfully. We also know that many parameters in physical systems are irrelevant and have no effect whatsoever on how the system behaves. The numerous different crystalline structures in ferromagnets, for example, exhibit the same critical behavior. In complex nervous systems, with very many variables and high-dimensional parameter spaces, it is difficult to tell the wheat from the chaff. In complex nervous systems, neither the order parameters nor the control parameters are known in advance, never mind their lawful relationship.

Although some of the same concepts of phase transitions in physical systems at thermodynamic equilibrium are useful, entirely new methods and tools are needed to handle phenomena associated with *nonequilibrium* phase transitions [25]. The latter occur in open systems whose internal and external components form a mutually coupled dynamical system. In his influential little book, “What is Life?” written in Dublin in 1943, Schrödinger noted that the enormously interesting disorder–order transitions studied by physicists (as in the case of ferromagnetism where matter changes its structure as temperature is lowered) are irrelevant to the emergence of life processes and the functioning of living things. Without a metabolism, for example, a living system cannot function. Without exchanges of energy, matter, or information with their surroundings, living things can maintain neither structure nor function. We will go into these ramifications a little further later. In actual fact, viewed through a certain lens, the entire range of transition behavior (order to order, order to disorder, disorder to order), resulting phases, and the many mixtures thereof can be observed in biological coordination in different systems.

Whether patterns of coordination emerge as collective effects in nervous systems composed of a large number and variety of heterogeneous microscopic components and connections is an open question.²⁾ Are phase transitions and criticality even relevant in neurobehavioral complex systems? Is there any reason to think that the brain, body, and environment are fundamentally self-organized? If such a complex system is governed by laws of coordination dynamics, how would we even go about establishing that? What are these putative laws and what are their consequences for the ways we investigate complex systems such as the brain? Further, what are the implications for understanding, in the words of President Obama when he unveiled the BRAIN initiative to the National Academy of Sciences in April 2013, “who we are”: the profound challenge of understanding “the dynamic brain in action” and what it does – how we move and think and perceive and decide and learn and remember?

2) One might argue that the recent notion of so-called resting state networks – spontaneous coherent brain activity in the absence of any task (see [26] for review) – qualifies as an example of self-organizing coordinative structures. Theoretical research has indeed hypothesized that the brain’s resting state dynamics operates close to criticality (see, e.g., [27] for a review, and papers by Plenz, Chialvo,

Breakspear, and others in this book). Empirical evidence suggests that resting-state networks number between 6 and 10 and appear to be related to vision, audition, attention, and so forth. Similar to resting-state networks, coordinative structures are low-dimensional representations of typically very high-dimensional systems, but they are not a tidy set of fixed patterns nor are they restricted in number.

The rest of this chapter elaborates on these issues and tries to provide some initial answers. As just one hint of the mindset that criticality involves, we note that some years ago a book entitled “23 Problems in Systems Neuroscience” [28] appeared containing a chapter entitled “Where are the switches on this thing?” A nice book review was published in the journal *Nature* with the same title [29]. Here is what is potentially at stake: if brains and behavior are shown to exhibit critical phenomena; if they display quantitative signatures of nonequilibrium phase transitions predicted by specific theoretical models, then they will certainly exhibit switching, but – at least in the first instance – there will be no need to posit switches.

4.3

Setting the Context: A Window into Biological Coordination

We begin with some general but vague principle, then find an important case where we can give that notion a concrete precise meaning. And from that case we gradually rise again in generality ... and if we are lucky we end up with an idea no less universal than the one from which we began. Gone may be much of its emotional appeal, but it has the same or even greater unifying power in the realm of thought and is exact instead of vague

[30], p. 6

So where to begin? Definitely close to Weyl’s approach in his beautiful book on symmetry quoted here, but not quite. The Editors of this volume have invited me to describe our experimental research on critical fluctuations and critical slowing down in the brain and behavior. In particular, they invite some historical perspective on the Haken–Kelso–Bunz (HKB) model. Judged in light of recent research in fields such as ecosystems, climate, and population change, there is much current interest in anticipatory indicators of tipping points ([31, 32]; see [33] commentary). Tipping points, similar to catastrophe theory, are just another catchy word for criticality. Anticipating them is what critical slowing down, enhancement of fluctuations, critical fluctuations, switching time distributions, and so on – that is, quantifiable measures of nonequilibrium phase transitions – are all about.

To put things in a specific context, let us make the familiar strange. Consider an ordinary movement. The human body itself consists of over 790 muscles and 100 joints that have coevolved in a complex environment with a nervous system that contains $\sim 10^{12}$ neurons and neuronal connections, never mind astrocytes [34]. On the sensory side, billions of receptor elements embedded in skin, joints, tendons, and muscles inform the mover about her movement. And this occurs in a world of light and sound and smell. Clearly, any ordinary human activity would seem to require the coordination among very many structurally diverse elements – at many scales of observation. As Maxine Sheets-Johnstone [35] says in her wonderful book, the primacy of movement for living things has gone unrecognized and unexamined. We come into the world moving. We are never still.

It must be said that physics as the science of inanimate matter and motion has left animate motion virtually untouched.³⁾ It has yet to take the next step of understanding living movement. (Just to be clear, we are not talking about the many useful *applications* of physics to biological systems, i.e., biophysics, biomechanics, etc.). Rather, what is at issue here is the problem of meaningful movement: the “self-motion,” which the great Newton remarked, “is beyond our understanding” ([36]; see also [37]). Newtonian mechanics defines limits on what is possible at the terrestrial scale of living things, but says nothing about how biological systems are coordinated to produce functionally relevant behavior. If “the purpose of brain function is to reduce the physical interactions, which are enormous in number, to simple behavior” [38], how is this compression to be understood? Instead of (or along with) inquiring how complexity can arise from simple rules [39], we may also ask how an extremely high-dimensional space is compressed into something lower dimensional and controllable that meets the demands of the environment and the needs of the organism. What principles underlie how enormous compositional complexity produces behavioral simplicity? This is a fundamental problem of living movement, and perhaps of life itself.

In science, we often make progress by taking big problems and breaking them into smaller pieces. This strategy works fine for physics and engineering. But what are the significant informational units of neural and behavioral function? In the late 1970s and early 1980s, my students and I produced empirical evidence for a candidate called a *coordinative structure* [42, 43]. Coordinative structures are functional linkages among structural elements that are temporarily constrained to act as a single coherent unit. They are not (or at least, not only as we now know) hardwired and fixed in the way we tend to think of neural circuits; they are context dependent.⁴⁾ Coordinative structures are softly assembled: all the parts are weakly interacting and interdependent. Perturbing them in one place produces remote compensatory effects somewhere else without disrupting, indeed preserving, functional integrity (for the history and evidence behind this proposal, see [11, 17, 44, 45]). Although beyond the scope of this chapter, a strong case can be made that coordinative structures – structural or functional effects produced by combining different elements – are units of selection in evolution [46, 47] and intentional change [48, 49]. Coordinative structures are the embodiment of the principle of functional equivalence: they handle the tremendous degeneracy of living things, using different parameter settings, combinations of elements, and recruiting new pathways “on the fly” to produce the same outcome [4].

- 3) Just as neuroscience, until quite recently, has not in general looked to contemporary physical theories of cooperative phenomena to help provide “a picture of the dynamic brain” never mind the principles for how the brain works (but see [40] and for a modern example, [41]).
- 4) Coordinative structures are synonymous with the term *synergy* – which has a long and checkered history in many fields of inquiry. Coordinative structures are preferred here because they are an expression of both structure (the context-dependent elements and their interaction) and function (e.g., when an organism moves purposely to accomplish a goal). One imagines that coordinative structures are used to accomplish many behavioral, cognitive, and affective functions.

Just as new states of matter form when atoms and molecules form collective behavior, is it possible that new states of biological function emerge when large ensembles of different elements form a coordinative structure? In other words, is the problem of coordination in living things continuous with cooperative and critical phenomena in open, nonequilibrium systems? The hexagonal forms produced in Bénard convection, the transition from incoherent to coherent light in lasers, the oscillating waves seen in chemical reactions, the hypercycles characteristic of catalytic processes, and so on are all beautiful examples of pattern generation in nature [50]. Such systems organize themselves: the key to their understanding lies in identifying the necessary and sufficient conditions for such *self-organization* to occur. Strictly speaking, there is no “program” inside the system that represents or prescribes the pattern before it appears or changes. This is not to say that very special boundary conditions do not exist in neurobehavioral coordination, intention among them [11, 51].

4.4

Beyond Analogy

As Weyl did, we start out with a vague idea. The vague idea or intuition is that biological coordination is fundamentally a self-organizing dynamical process. As nonequilibrium phase transitions lie at the heart of self-organization in many of nature’s pattern-forming systems, this means it should be possible to demonstrate that they exist in biological coordination. To prove they exist, however, all the hallmark features of nonequilibrium phase transitions should be observable and quantifiable in biological coordination at behavioral and neural levels. But as Weyl says, for this approach to work, we need a specific case. That means specific experiments and specific theoretical modeling.

Ideally, one would like to have a simple model system that affords the analysis of pattern formation and pattern change, both in terms of experimental data and theoretical tools. Rhythmic finger movements are a potentially good model system because they can be studied in detail at both behavioral and brain levels. An experimental advantage is that rhythmic movements, although variable and capable of adjusting to circumstances, are highly reproducible. If I ask you to voluntarily move your finger back and forth as if you were going to do it all day, the variability in periodicity would be about 2–4% of the period you choose. Moreover, an extensive and informative literature on rhythmical behavior exists in neurobiological systems in vertebrates and invertebrates [52–60], the brain [61–64], and biological clocks in general [65]. Rhythmic behavior in living things is produced by a diversity of mechanisms. The goal here – by analogy to the theory of phase transitions – is to understand how all these different mechanisms might follow the same basic rules. To go beyond metaphor and analogy, we need an experimental *window* into biological coordination that might allow us to transcend different systems and reveal the operation of higher order principles. Could it be that bimanual rhythmic finger (or hand) movements in humans might be akin to the dynamically stable

gaits of creatures and that “gait switching” might be similar to a nonequilibrium phase transition indicative of self-organizing processes? But, of course, an aim of science is to move from analogy to reality, from “this is like that” to “what is.”

4.5

An Elementary Coordinative Structure: Bimanual Coordination

Much of the early central pattern generator (CPG) literature was based on creatures doing one thing, such as flying, swimming, feeding, or walking (e.g., [66, 53]). Yet, in addition to being degenerate, different anatomical combinations capable of accomplishing the same outcome, coordinative structures are also multifunctional: they often use the same anatomical components to accomplish different functions. What was needed was to invent an experimental model system that affords looking at how people do more than one thing under the same conditions. One of the early ways we used to identify coordinative structures in perceptuomotor behavior was to seek invariants under transformation. More simply, to see if despite many variations, for example, in the activity of neurons, muscles, and joints, some quantities are preserved, while other variables, such as the forces that have to be generated to accomplish a given task, are altered. We used this strategy to uncover a coordinative structure in studies of discrete interlimb coordination: we found, in these experiments on voluntary movement, that the brain does not coordinate the limbs independently but rather preserves their relative timing by means of functional linkages – neurons, joints, and muscles are constrained to act as a single unit [42]. The same seems to hold in speech [67]. Even earlier work, by ourselves and others [68–70] was suggestive that discrete movements are equilibrium seeking; they exhibit equifinality regardless of initial conditions very much as a (nonlinear) mass spring system oscillates or not depending on parameters [71].⁵⁾ Ironically enough, given the apparent significance of rhythms and synchronization in the brain [61, 72, 73], the nonlinear oscillator was viewed as the most elementary form of a coordinative structure [71, 74, 75].

In the original experiments, subjects were tasked to rhythmically move their index fingers back and forth in one of two patterns (in-phase or antiphase). In the former pattern, homologous muscles contract simultaneously; in the latter, the muscles contract in an alternating manner. In various experiments, subjects either just increased frequency voluntarily or a pacing metronome was used, the frequency of which was systematically changed from 1.25 to 3.50 Hz in 0.25 Hz steps [79, 80]. What was discovered was that when subjects began in the antiphase pattern, at a certain frequency or movement rate they spontaneously shifted into the in-phase pattern. On the other hand, if the subject started at a high or low rate with an in-phase movement and the rate was slowed down or sped up, no such transition occurred. Of further note was that although the transitions occurred at

5) The equilibrium point hypothesis continues to be actively explored in the field of motor control (e.g., [76–78]) but will not concern us further here.

different rates of finger or hand motion for different subjects, and were lowered when subjects did the same experiment under resistive loading conditions, when the critical transition frequency was scaled to the subject's preferred frequency and expressed as a ratio (by analogy to the reduced temperature in the phase transitions described earlier), the resulting dimensionless number was constant. Moreover, invariably, the relative phase fluctuated before the transition and – despite the fact that subjects were moving faster – these fluctuations decreased after the switch. Many experimental studies of bimanual rhythmic movements demonstrate that humans – without prior learning [81, 82] – are able to stably produce two patterns of coordination at low frequency values, but only one – the symmetrical, in-phase mode – as frequency is scaled beyond a critical value. This is a remarkable result given the complexity of the nervous system, the body, and their interaction with the world.⁶⁾

4.6

Theoretical Modeling: Symmetry and Phase Transitions

In order to understand the patterns of coordination observed and the changes they undergo in terms of dynamics, we need to address the following questions: first, what are the essential variables (*order parameters*) and how is their dynamics to be characterized? Second, what are the *control parameters* that move the system through its collective states? Third, what are the subsystems and the nature of the interactions that give rise to such collective effects? Fourth, can we formulate a theoretical model, and if so what new experimental observations does the theoretical model predict?

In a first step, the relative phase, ϕ may be considered a suitable collective variable that can serve as an order parameter. The reasons are as follows: (i) ϕ characterizes the patterns of spatiotemporal order observed, in-phase and antiphase; (ii) ϕ changes far more slowly than the variables that describe the individual coordinating components (e.g., position, velocity, acceleration, electromyographic activity of contracting muscles, neuronal ensemble activity in particular brain regions, etc.); (iii) ϕ changes abruptly at the transition and is only weakly dependent on parameters outside the transition; and (iv) ϕ has simple dynamics in which the ordered phase relations may be characterized as attractors. As the prescribed frequency of oscillation, manipulated during the experiment, is followed very closely, frequency does not appear to be system dependent and therefore qualifies as a control parameter.

6) It might seem to some that just as an apple falling on one's head or a ball rolling down an inclined plane are very limited examples of inanimate motion, bimanual finger movements constitute a very limited example of human behavior. That's hardly the point. Nevertheless, recent work in Daniel Wolpert's

group [83], shows that the same effects occur in a wide variety of natural everyday tasks recorded over 30 h, namely, symmetric and antisymmetric movements are predominant at low frequencies, whereas only symmetric movements are predominant at high frequencies.

Determining the coordination dynamics means mapping observed, reproducible patterns of behavior onto attractors of the dynamics. Symmetry may be used to classify patterns and restrict the functional form of the coordination dynamics. Symmetry means “no change as a result of change”: pattern symmetry means a given pattern is symmetric under a group of transformations. A transformation is an operation that maps one pattern onto another, for example, left-right transformation exchanges homologous limbs within a bimanual pattern. If all relative phases are equivalent after the transformation, then the pattern is considered invariant under this operation. Symmetry serves two purposes. First, it is a pattern classification tool allowing for the identification of basic coordination patterns that can be captured theoretically. Given a symmetry group, one can determine all invariant patterns. Second, imposing symmetry restrictions on the dynamics itself limits possible solutions and allows one to arrive at a dynamics that contains the patterns as *different* coordinated states of the *same* nonlinear dynamical system (see also [84]). In other words, basic coordination patterns correspond to attractors of the relative phase for certain control parameter values. Left-right symmetry of homologous limbs leads to invariance under the transformation $\phi \rightarrow -\phi$, so that the simplest dynamical system that accommodates the experimental observations is:

$$\dot{\phi} = f(\phi) = -a \sin(\phi) - 2b \sin(2\phi) \quad (4.1)$$

where ϕ is the relative phase between the movements of the two hands, $\dot{\phi}$ is the derivative of ϕ with respect to time, and the ratio b/a is a control parameter corresponding to the movement rate in the experiment. An equivalent formulation of Eq. (4.2) is:

$$\begin{aligned} \dot{\phi} &= \frac{-dV(\phi)}{d\phi} \\ \text{with } V(\phi) &= -a \cos \phi - b \cos 2\phi \end{aligned} \quad (4.2)$$

Using a scaling procedure commonly employed in the theory of nonlinear differential equations, Eqs. (4.1) and (4.2) can be written with only a single control parameter $k = b/a$ in the form

$$\begin{aligned} \dot{\phi} &= -\sin \phi - 2k \sin \phi \\ &= -\frac{dV(\phi)}{d\phi} \quad \text{with } V(\phi) = -a \cos \phi - k \cos 2\phi \end{aligned} \quad (4.3)$$

In the literature, Eqs. (4.1–4.3) are known as the *HKB model* after Haken, Kelso, and Bunz, first published in 1985 [85]. An attractive feature of HKB is that when visualized as a phase portrait or a potential function⁷⁾ (Figure 4.2), it allows one to develop an intuitive understanding of what is going on in the experiments. It also

7) A detailed mathematical analysis by Liese and Cohen [86], which earned them the Ford Prize of the American Mathematical Society, derives the potential function starting from a theoretical model system of nonlinearly coupled nonlinear oscillators (as opposed to the other way round in HKB where the simplest nonlinear coupling was chosen – eventually found to be biophysically relevant [87] – and the functional form of the nonlinear oscillators was based on empirical knowledge).

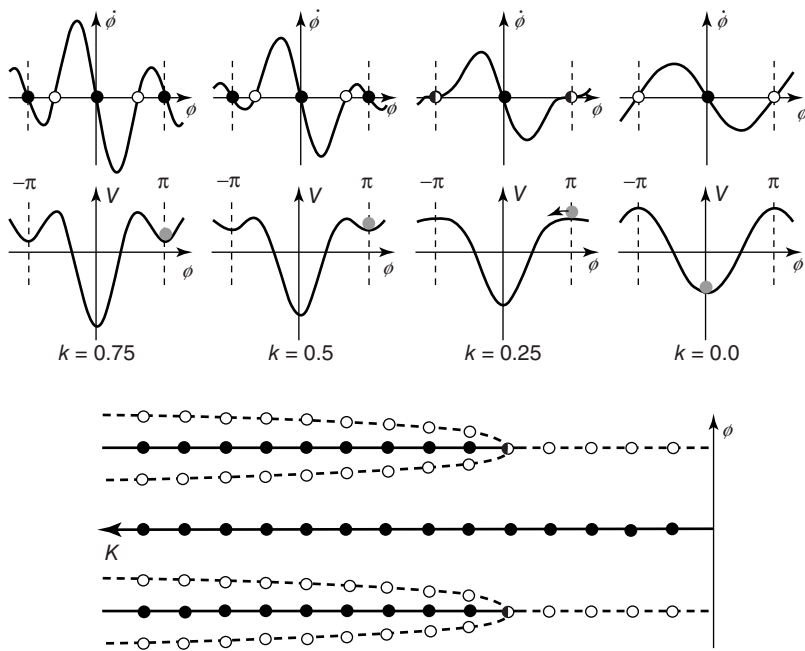


Figure 4.2 Dynamics of the basic HKB model as a function of the control parameter $k = b/a$. Top row: Phase flows of $\dot{\phi}$ (the derivative of ϕ with respect to time) as a function of ϕ . Stable and unstable fixed points are filled and open circles respectively (Eq. (4.3)). Middle: Landscapes of the potential function $V(\phi)$. Note the movement of

the gray ball as the landscape deforms due to control parameter changes. Bottom: Bifurcation diagram, where solid lines with filled circles correspond to attractors and dashed lines with open circles denote repellors. Note that k decreases from left ($k = 0.75$, bistable) to right ($k = 0$, monostable).

facilitates the connection (which should not be assumed) between the key concepts of stability and criticality and the observed experimental facts. Just as the coupling among spins, K in Wilson's model of ferromagnetism varies with temperature, so the coupling among the fingers $k = b/a$ in the HKB formulation varies with movement frequency/rate in the Kelso [79, 80] experiments. In Figure 4.2 a large value of k corresponds to a slow rate, whereas k close to zero indicates that the movement rate is high.

In the phase space plots (Figure 4.2 top row) for $k = 0.75$ and 0.5 , there exist two stable fixed points at $\phi = 0$ and π (rad) where the function crosses the horizontal axis (derivative of ϕ with respect to time goes to zero with a negative slope), marked by solid circles (the fixed point at $-\pi$ is the same as the fixed point at π as the function is 2π -periodic). These attractors are separated by repellors, zero crossings with a positive slope, and marked by open circles. For movement rates corresponding to these two values of k , HKB shows that both antiphase and in-phase are stable. When the rate is increased, corresponding to a decrease in the coupling or control parameter k to the critical point at $k_c = 0.25$, the former stable fixed point at $\phi = \pi$

collides with the unstable fixed point and becomes neutrally stable as indicated by a half-filled circle. Beyond k_c , that is, for faster rates and smaller values of k , the antiphase pattern is unstable and the only remaining stable coordination pattern is in-phase.

The potential functions, shown in the second row in Figure 4.2, contain the same information as the phase portraits: they are just a different representation of the coordination dynamics. However, the strong hysteresis (a primitive form of memory) is more intuitive in the potential landscape than in phase space, and is best seen by mapping experimental data in which slow movements start out in an antiphase mode (the gray ball in the minimum of the potential at $\phi = \pi$) and rate is increased. After passing the critical value of $k_c = 0.25$, the slightest perturbation puts the ball on the downhill slope and initiates a switch to in-phase. If the movement is now slowed down again, going from right to left in the plots, even though the minimum at $\phi = \pi$ reappears, the ball cannot jump up and populate it again but stays in the deep minimum at $\phi = 0$.

Finally, a bifurcation diagram is shown at the bottom of Figure 4.2. The locations of stable fixed points for the relative phase ϕ are plotted as solid lines with solid circles and unstable fixed points as dashed lines with open circles. Around $k_c = 0.25$, the system undergoes a subcritical pitchfork bifurcation. Note that the control parameter k in this plot increases from right to left. Evidently, the HKB coordination dynamics represented by Eqs. (4.1–4.3), is capable of reproducing all the basic experimental findings listed earlier. From the viewpoint of theory, this is a necessary criterion for a model that has to be fulfilled but it is not sufficient. More important is whether the theoretical model predicts novel effects that can be tested experimentally. This is where we see the full power of the theory of nonequilibrium phase transitions, predicted hallmarks of critical phenomena, and self-organization in biological coordination. (The reader may rightfully ask about the subsystems, the individual components, and how they are coupled. This is a major feature of HKB [85] and has been addressed in detail both experimentally and theoretically but we will not consider it further here, see, e.g., [15, 86, 89], for recent reviews.)

A chief strategy of HKB is to map the reproducibly observed patterns onto attractors of a dynamical system. (In practical terms, we use transitions to define what the coordination states actually are, i.e., to separate the relevant from the irrelevant variables.) Thus, *stability* is a central concept, not only as a characterization of the two attractor states but also because (if biological coordination is really self-organized) it is *loss of stability* that plays a critical role in effecting the transition. Stability can be measured in several ways: (i) if a small perturbation drives the system away from its stationary state, the time it takes to return to a stationary state is independent of the size of the perturbation (as long as the latter is small). The “local relaxation time,” τ_{rel} , (i.e., local with respect to the attractor) is therefore an observable system property that measures the stability of the attractor state. The smaller τ_{rel} is, the more stable is the attractor. The case $\tau_{\text{rel}} \rightarrow \infty$ corresponds to a loss of stability. (ii) A second measure of stability is related to noise sources. Any real system is composed of and coupled to, many subsystems. (Think of the number of neurons necessary to activate a purposeful movement of a single

finger, never mind playing the piano.) Random fluctuations exist in all systems that dissipate energy. In fact, there exists a famous theorem that goes back to Einstein, known as the *fluctuation–dissipation theorem*, which states that the amount of random fluctuations is proportional to the dissipation of energy in a system. The importance of this theorem for a wide class of nonequilibrium states and irreversible processes in general has been recognized for a long time. It is an explicit statement of the general relationship between the response of a given system to an external disturbance and the internal fluctuations of the system in the absence of the disturbance (see, e.g., [90]).

In our case, fluctuations may be seen to act to a certain degree as *stochastic forces* on the order parameter, relative phase. The presence of stochastic forces and hence of fluctuations of the macroscopic variables, is not merely a technical issue, but of both fundamental and functional importance. In the present context, stochastic forces act as continuously applied perturbations and therefore produce deviations from the attractor state. The size of these fluctuations as measured, for example, by the variance or standard deviation (SD) of ϕ around the attractor state, is a metric of its stability. Stability and biological variability are two sides of the same coin. The more stable the attractor, the smaller the mean deviation from the attractor state for a given strength of fluctuations.

4.7

Predicted Signatures of Critical Phenomena in Biological Coordination

4.7.1

Critical Slowing Down

Critical slowing down corresponds to the time it takes the system to recover from a small perturbation Δ . In Figure 4.3 (bottom), as long as the coupling k corresponding to the experimental movement rate is larger than k_c , the effect of a small perturbation will decay in time. However, as the system approaches the critical point, this decay will take longer and longer. At the critical parameter value, the system will not return to the formerly stable state: it will even move away from it. Direct evidence of critical slowing down was obtained originally from perturbation experiments that involved perturbing one of the index fingers with a brief torque pulse (50 ms duration) as subjects performed in the two natural coordinative modes. Again, frequency was used as a control parameter, increasing in nine steps of 0.2 Hz every 10 s beginning at 1.0 Hz. Again, when subjects began in the antiphase mode, a transition invariably occurred to the in-phase mode, but not vice versa. Relaxation time was defined as the time from the offset of the perturbation until the continuous relative phase returned to its previous steady state. As the critical frequency was approached, the relaxation time was found to increase monotonically – and to drop, of course, when the subject switched into the in-phase mode [91]. Using another measure of relaxation time, the inverse of

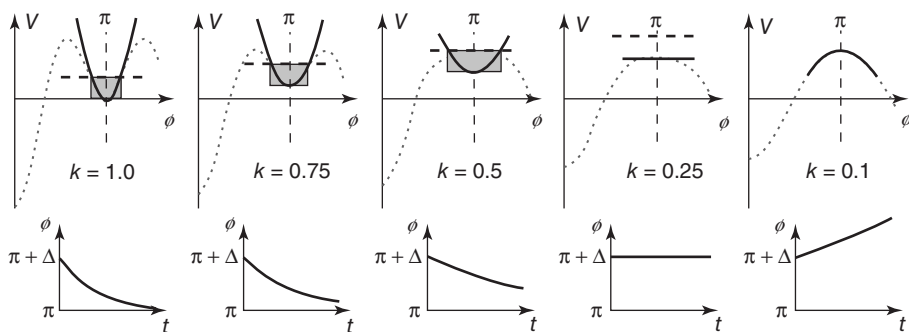


Figure 4.3 Hallmarks of a nonequilibrium (HKB) system, approaching criticality under the influence of a control parameter, k corresponding to the coupling between the fingers and directly related to the frequency of movement in experiments. Enhancement of fluctuations is indicated by the

widening shaded area; critical slowing down is shown by the time it takes for the system to recover from a perturbation (bottom); critical fluctuations occur where the top of the shaded area is higher than the closest maximum in the potential, initiating a switch even though the system may still be stable.

the line width of the power spectrum of relative phase [92], strong enhancement of relaxation time, was clearly observed.

4.7.2

Enhancement of Fluctuations

Fluctuations are sources of variability that exist in all dissipative systems. They kick the system away from the minimum and (on average) to a certain elevation in the potential landscape, indicated by the shaded areas in Figure 4.3. For large values of k , the horizontal extent of this area is small but becomes larger and larger when the transition point is approached. The SD of the relative phase is a direct measure of such fluctuation enhancement and is predicted to increase when the control parameter approaches a critical point. Even cursory examination of typical experimental trajectories in the original experiments revealed the presence of fluctuations (e.g., [80]). As the control parameter frequency was increased in the antiphase mode, relative phase plots became increasingly variable near the transition and were slower to return from deviations. Follow-up experiments designed to test the specific prediction of nonequilibrium phase transitions clearly demonstrated the existence of fluctuation enhancement before the transition ([93]; see also [94]).

4.7.3

Critical Fluctuations

Even before it reaches the critical point, fluctuations may kick the system into a new mode of behavior. In Figure 4.3, if fluctuations reach a height higher than the closest maximum – the hump that has to be crossed – a transition will occur,

even though the fixed point is still classified as stable. Again, this often happens in experiments (e.g., [95]).

All these hallmarks of critical phenomena can be (and have been) treated in a quantitative manner by adding a stochastic term Q to Eq. (4.3) and treating the coordination dynamics as a Langevin equation with both a deterministic and a stochastic aspect

$$\dot{\phi} = \frac{dV(\phi)}{d\phi} + \sqrt{Q}\xi_t \quad (4.4)$$

with

$$\langle \xi_t \rangle = 0; \langle \xi_t \xi_{t'} \rangle = \delta(t - t')$$

In this case, the system is no longer described by a single time series but by a probability distribution that evolves in time. Such time-dependent processes are given by the corresponding Fokker–Planck equation. Using experimental information on the local relaxation times and the SD in the noncritical régime of the bimanual system, all model parameters a, b in Eq. (4.2) and the stochastic term Q were determined ([96, 97], Chapter 11 for details; see also [98]). In the critical régime, the full Fokker–Planck equation was solved numerically: without any parameter adjustment, the stochastic version of HKB accounted for all the transient behavior seen experimentally. That is, quantitative measures of enhancement of fluctuations, critical fluctuations, and critical slowing down in a biological system were accounted for both qualitatively and quantitatively by a straightforward extension of the HKB model. Moreover, attesting further to the interplay between theory and experiment, new aspects were predicted such as the duration of the transient from the antiphase to the in-phase state – which we called the *switching time*. The basic idea is that during the transition, the probability density of relative phase – initially concentrated around $\phi = \pi$ flows to $\phi = 0$ and accumulates there. In this case, it is easy to calculate the time between the relative phase immediately before the transition and the value assumed immediately after the transition. The match between theoretically predicted and empirically observed switching time distributions was impressive, to say the least [92, 94]. This aspect is particularly interesting, because it shows that the switching process itself is closely captured by a specific model of stochastic nonlinear HKB dynamics.

4.8

Some Comments on Criticality, Timescales, and Related Aspects

In the HKB system (Eq. (4.4)), as the transition is approached (i.e., the antiphase mode loses its stability), the local relaxation time (with respect to the antiphase mode) increases, while the global relaxation time decreases (because the potential hill between 0° and 180° vanishes). At the critical point, both are of the same order as the observed time and one can see the transition. Thus, at the transition point, the time scales relation breaks down, and an additional timescale assumes

importance, namely, the *time scale of parameter change*, τ_p . This reflects the fact (as occurs often in biological systems and nearly all experiments) that the control parameter that brings about the instability is itself changed in time. The relation of the time scale of parameter change to other system times (local relaxation times, global equilibration time, etc.) plays a decisive role in predicting the nature of the phase transition. If the system changes only as the old state becomes unstable, transition behavior is referred to as a *second-order phase transition* (because of an analogy with equilibrium phase transitions, see, e.g., [99]). In that case, features of critical phenomena (such as critical fluctuations and critical slowing down) are predicted. If, on the other hand, the system, with overwhelming probability, always seeks out the lowest potential minimum, it may switch before the old state becomes unstable. Jumps and hysteresis (among other features) are generally predicted. This behavior is called a *first-order phase transition*. Notice that the origin of critical phenomena in the present case is different from equilibrium phase transitions. In particular, in the original HKB model symmetry breaking does not occur, but rather a breakdown of timescales relations.⁸⁾ In real experiments, timescale relations have to be considered.

The main conclusion to be drawn from this empirical and theoretical work is that it demonstrates – in both experimental data and theoretical modeling – predicted features of nonequilibrium phase transitions in human behavior. Nonequilibrium phase transitions are the most fundamental form of self-organization that Nature uses to create spatial, temporal (and now functional) patterns in open systems. *Fluctuations and variability play a crucial role*, testing whether a given pattern is stable, allowing the system to adapt and discover new patterns that fit current circumstances. The notion – dominant in those days – that movements are controlled and coordinated by a “motor program” is brought into question. Critical fluctuations, for instance, although typical of nonequilibrium phase transitions, are problematic for stored programs in a computer-like brain.

Currently, it is quite common for investigators to take a time series from some task such as tapping or drawing a circle or reacting to stimuli or balancing a pole for a long period of time and to describe its variability using, for example, detrended fluctuation analysis to assess long-range correlations. Basically, long-range correlations refer to the presence of positive autocorrelations that remain substantially high over large time lags, so that the autocorrelation function of the series exhibits a slow asymptotic decay, never quite reaching zero. Basic physiological functions such as walking and heart beats and neural activity have also been examined. Such analyses are useful, even important, for example, for heartbeat monitoring and other dynamic diseases or for distinguishing human performance in different task conditions over the long term (e.g., [100–103]) – or even individual differences between people in performing such tasks. One should be conscious, however, of the ancient saying attributed to Heraclitus; “no man ever steps in the same river twice, for it's not the same river and he's not the same

8) At an early presentation of this work [92], the late Rolf Landauer (1927–1999) suggested that we call it a limiting case of a first-order transition. This is a technical point.

man.” There are reasons to be cautious about taking a single time series, calculating its statistical properties such as long-range correlations and concluding that the latter arise as a universal statistical property of complex systems with multiple interdependent components ranging from the microscopic to the macroscopic that are, as it were, allowed to fluctuate on their own (see also [104] for measured, yet positive criticism). This looks too much like science for free, rather like the way calculations of correlation dimension from time series were pursued in the 1980s and 1990s. With respect to individual differences, for example, it would seem more important to identify preferences, dispositions, and biases in a given context so that one may know what can be modified and the factors that determine the nature of change [81].

Criticality and phase transitions can be used in a constructive manner, as a way to separate the relevant variables and parameters from the irrelevant ones – and as a means of identifying dynamical mechanisms of pattern formation and change in biological coordination. As mentioned previously, in neuroscience, as well as the cognitive, behavioral, and social sciences, neither the key coordination quantities nor the coordination dynamics are known *a priori*. Criticality and instability can be used to identify them. Brain structure–function appears to be both hierarchically (top to down and bottom to up) as well as heterarchically (side to side) organized (e.g., [105]); the component elements and their interactions are heterogeneous (e.g., [106]); and the relevant coordination variables characterizing ongoing neural and cognitive processes are invariably dependent on context, task or function [11, 107].

4.9

Symmetry Breaking and Metastability

Notice that the HKB Eqs. (4.1–4.4) are *symmetric*: the elementary coordination dynamics is 2π periodic and is identical under left–right reflection (ϕ is the same as $-\phi$). This assumes that the individual components are identical, which is seldom, if ever the case. Nature thrives on broken symmetry. To accommodate this fact, Kelso *et al.* [108] incorporated a symmetry-breaking term $\delta\omega$ into the dynamics

$$\begin{aligned}\dot{\phi} &= \delta\omega - a \sin \phi - 2b \sin 2\phi, \quad \text{and} \\ V(\phi) &= -\delta\omega\phi - a \cos \phi - b \cos 2\phi\end{aligned}\tag{4.5}$$

for the equation of motion and the potential, respectively. The resulting coordination dynamics is now a function of the interplay between the coupling $k = b/a$ and symmetry breaking. Small values of $\delta\omega$ shift the attractive fixed points (Figure 4.4 middle) in an adaptive manner. For larger values of $\delta\omega$ the attractors disappear entirely (e.g., moving left to right on the two bottom rows of Figure 4.4). Note, however, that the dynamics still retain some curvature: even though there are no attractors there is still attraction to where the attractors used to be (“ghosts” or “remnants”). The reason is that the difference ($\delta\omega$) between the individual components is sufficiently large and the coupling (k) sufficiently weak that the

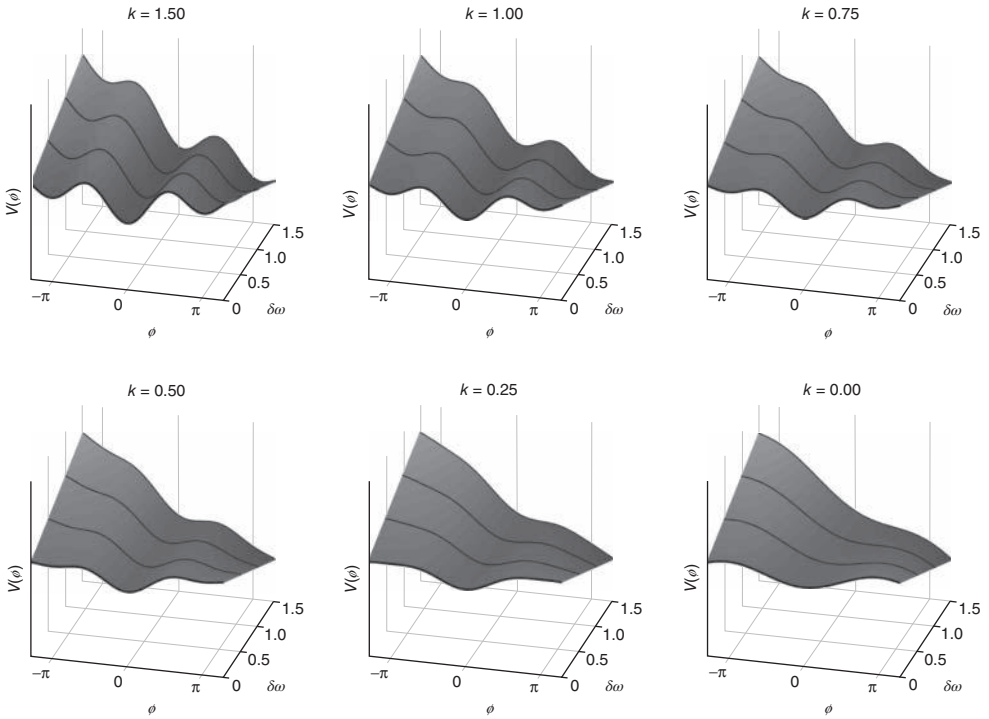


Figure 4.4 Potential landscapes of Eq. (4.5) as a function of symmetry breaking between the interacting components, $\delta\omega$ and coupling, $k = b/a$ (Eq. (4.5)). The bottom curve in each picture is the standard HKB model, that is, $\delta\omega = 0$. Remaining rows show how HKB is deformed because of the combination of coupling and symmetry-breaking parameters; as a consequence, entirely new phenomena are observed.

The dynamical mechanism is a tangent or saddle-node bifurcation. Attractors shift, drift,

and disappear with weaker coupling and larger differences (heterogeneity) between components. Note, however, that there is still attraction to where the attractors once were, “ghosts” or “remnants” indicated by slight curvature in the potential landscapes after minima disappear. This is the metastable régime of the elementary coordination dynamics, where coordination takes the form of coexisting tendencies for interaction and independence among the components.

components tend to do their own thing, while still retaining a tendency to cooperate. This is the metastable régime of the CD.

The interplay of two simultaneously acting forces underlies metastability: an integrative tendency for the coordinating elements to couple together and a segregative tendency for the elements to express their individual autonomy ([11, 109]; see also [4, 23, 110] for most recent discussion of metastability’s significance for brain and behavior).

A number of neuroscientists have embraced metastability as playing a key role in various cognitive functions, including consciousness (e.g., [111–119]; see [110] for review). Especially impressive is the work of Rabinovitch and colleagues, which

ties metastable dynamics (robust transients among saddle nodes referred to as *heteroclinic channels*) to neurophysiological experiments on smell (e.g., [120]). The significance of metastability lies not in the word itself but in what it means for understanding coordination in the brain and its complementary relation to the mind [4, 23]. In CD, metastability is not a concept or an idea, but a product of the broken symmetry of a system of (nonlinearly) coupled (nonlinear) oscillations. The latter design is motivated by empirical evidence that the coordinative structures of the brain that support sensory, motor, affective, and cognitive processes express themselves as oscillations with well-defined spectral properties. At least 12 different rhythms from the infraslow (less than 1 Hz) to the ultra-fast (more than 100 Hz) have been identified, all connected to various behavioral and cognitive functions (e.g., [121–123]). Indeed, brain oscillations are considered to be one of the most important phenotypes for studying the genetics of complex (non-Mendelian) disorders [124]. The mechanisms that give rise to rhythms and synchrony exist on different levels of organization: single neurons oscillate because of voltage-gated ion channels depolarizing and hyperpolarizing the membrane; network oscillations, for example, in the hippocampus and neocortex strongly depend on the activity of inhibitory GABAergic interneurons in the central nervous system (so-called inhibition-based rhythms, see, e.g., [125]); neuronal groups or assemblies form as transient coalitions of discharging neurons with mutual interaction. Neuronal communication occurs by means of synapses and glia (e.g., [126]). Synaptic connections between areas may be weak but research shows that synchrony among different inputs strengthens them, thereby enhancing communication between neurons (for one of the many recent examples, see [127]). Phase coupling, for example, allows groups of neurons in distant and disparate regions of the brain to synchronize together (e.g., [128, 129] for review). According to CD, nonlinear coupling among oscillatory processes and components that possess different intrinsic dynamics (broken symmetry) is necessary to generate the broad range of behaviors observed, including pattern formation, multistability, instability, metastability, phase transitions, switching (sans “switches”), hysteresis, and so forth. Although the mechanisms of coupling multiple oscillations within and between levels of organization are manifold, the principle is clear enough: dynamic patterns of brain behavior *qua* coordinative structures arise as an emergent consequence of self-organized interactions among neurons and neuronal populations. The said self-organization is a fundamental source of behavioral, cognitive, affective, and social function [11, 61, 72, 73, 130–133]. Transition behaviors are facilitated by dynamical mechanisms of criticality and metastability: the former reflects neural systems that tune themselves to be poised delicately between order and disorder [99, 134, 135]; the latter where there are no attractors in the nervous system but only the coexistence of segregative and integrative tendencies that give rise to robust metastable behavior – transient functional groupings and sequences [110, 136–138].

4.10

Nonequilibrium Phase Transitions in the Human Brain: MEG, EEG, and fMRI

In a long series of studies beginning in the late 1980s, my students, colleagues, and I used the *nonlinear paradigm* (varying a control parameter to identify transition-revealing collective variables or order parameters) as a means to find signature features of self-organizing nonequilibrium phase transitions in human brain activity recorded using large SQuID (e.g., [139–146]), and multielectrode arrays [88, 147–149] along with a variety of statistical measures of spatiotemporal (re)organization in the brain.

We and others followed this work up using functional magnetic resonance imaging (fMRI) to identify the neural circuitry involved in behavioral stability and instability (e.g., [150, 151]). We can mention just a couple of key findings here. First, a study by Meyer-Lindenberg *et al.* [152] demonstrated that a transition between bistable coordination patterns can be elicited in the human brain by transient transcranial magnetic stimulation (TMS). As predicted by the HKB model of coordination dynamics (Eq. (4.3)), TMS perturbations of relevant brain regions such as premotor and supplementary motor cortices caused a behavioral transition from the less stable antiphase state to the more stable in-phase state, but not vice versa. In other words, in the right context, that is, near criticality, tickling task-relevant parts of the brain at the right time caused behavior to switch.

CD theory predicts that cortical circuitry should be extremely sensitive to the dynamic stability and instability of behavioral patterns. If we did not know how behavioral patterns form and change in the first place, such predictions would be moot. Jantzen *et al.* [153] demonstrated a clear separation between the neural circuitry that is activated when a control parameter (rate) changes and those connected to a pattern's stability (see also [154]). As one might expect, activity in sensory and motor cortices increased linearly with rate, independent of coordination pattern. The key result, however, was that the activation of cortical regions supporting coordination (e.g., left and right ventral premotor cortex, insula, pre-SMA (supplementary motor area), and cerebellum) scaled directly with the *stability* of the coordination pattern. As the antiphase pattern became increasingly less stable and more variable, so too did the level of activation of these areas. Importantly, for identical control parameter values, the same brain regions did not change their activation at all for the more stable (less variable) in-phase pattern. Thus it is that these parts of the brain – which form a functional circuit – have to work significantly harder to hold coordination together. And thus it is that the difficulty of a task, often described in terms of “information processing load,” is captured by a dynamic measure of stability that is directly and lawfully related to the amount of energy used by the brain, measured by BOLD activity.

The Jantzen *et al.* [153] paper shows that different patterns of behavior are realized by the same cortical circuitry (multifunctionality). Earlier, it was shown that the same overt patterns of behavior [155] and cognitive performance [156] can be produced by different cortical circuitry (degeneracy). Together with the Meyer-Lindenberg *et al.* study, the Jantzen *et al.* [153] work demonstrates that dynamic

stability and instability are major determinants of the recruitment and dissolution of brain networks, providing flexibility in response to control parameter changes (see also [157]). Multifunctionality *qua* multistability confers a tremendous selective advantage to the brain and to nervous systems in general: it means that the brain has multiple patterns at its disposal in its “restless state” and can switch among them to meet environmental or internal demands. Shifting among coexisting functional states whether through noise or exposure to changing conditions is potentially more efficient than having to create states *de novo* [4].

4.11

Neural Field Modeling of Multiple States and Phase Transitions in the Brain

Theoretical modeling work at the neural level [87, 158] has complemented experiments and theory at the behavioral level (see [21]). Neurobiologically grounded accounts based on known cellular and neural ensemble properties of the cerebral cortex (motivated by the original works of Wilson, Cowan, Ermentrout, Nunez, and others; see Chapter 22, this volume) have been proffered for both unimanual [141, 159–162] and bimanual coordination ([163]; see also [164–168]). In particular, the behavioral HKB equations were successfully derived from neural field equations, allowing for an interpretation of the phenomenological coupling terms [163]. An important step was to extend neural field theory to include the heterogeneous connectivity between neural ensembles in the cortex ([106, 169]; see also [170]). Once general laws at the behavioral and brain levels have been identified, it has proved possible to express them in terms of the excitatory and inhibitory dynamics of neural ensembles and their long- and short-range connectivities, thereby relating different levels of description ([171, 172]; see [21] and references therein for updates). In showing that stability and change of coordination at both behavioral and neural levels is due to quantifiable nonlinear interactions among interacting components – whether fingers or the neural populations that drive them – some of the mysticism behind the contemporary terms *emergence* and *self-organization* is removed. More important, this body of empirical and theoretical work reveals the human dynamic brain in action: phase transitions are described by the destabilization of a macroscopic activity pattern when neural populations are forced to reorganize their spatiotemporal behavior. Destabilization is typically controlled via unspecific scalar control parameters. In contrast, traditional neuroscience describes reorganization of neural activity as changes of spatial and timing relations among neural populations. Both views are tied together by our most recent formulation of neural field theory: here, the spatiotemporal evolution of neural activity is described by a nonlinear retarded integral equation, which has a *heterogeneous* integral kernel. The latter describes the connectivity of the neocortical sheet and incorporates both continuous properties of the neural network as well as discrete long-distance projections between neural populations. Mathematical analysis (e.g., [106]) of such heterogeneously connected systems shows that local changes in connectivity alter the timing relationships between neuronal populations. These changes enter the

equations as a control parameter and can destabilize neural activity patterns globally, giving rise to macroscopic phase transitions. Heterogeneous connectivity also addresses the so-called stability–plasticity dilemma: stable transmission of directed activity flow may be achieved by projecting directly from area A to area B and from there to area C (stability). However, if necessary, area A may *recruit* neighboring populations of neurons (plasticity), as appears to be the case in bimanual coordination [88].

Reorganization of spatiotemporal neural activity may be controlled via local changes in the sigmoidal response curves of neural ensembles, the so-called conversion operations (see also [173] for an account based on synaptic depression). Conversion operations have been investigated in quantitative detail as a function of attention (e.g., [174]). The main result is that the slope and the height of the sigmoid vary by a factor of 2.5 between minimal and maximal attention. The sigmoidal variation of the ensemble response is realized biochemically by different concentrations of neuromodulators such as dopamine and norepinephrine. Mathematically, the neural dynamics described by the spatiotemporal integral equations can be coupled to a one-dimensional concentration field in which elevated values designate increased values of slope and height of the sigmoidal response curve of neural ensembles. An increased slope and height of the sigmoid typically causes increased amplitude and excitability of the neural sheet. It is known that novel (or more difficult) tasks require more attention/arousal than an automated behavioral pattern [175, 176]. Increased attention demand is realized in the cortical sheet via a larger concentration of the neurotransmitter, resulting in a steeper slope and elevation of the sigmoid response function. As a consequence, excitability and amplitude of neural activity are increased in task conditions, requiring more attention. During learning, changes in connectivity occur. After learning, the task condition is no longer novel, but rather more “automated,” reflected in decreased concentrations of neurotransmitters and thus decreased excitability and amplitude of ongoing neural activity (see also [175]). Notably, in all our experiments, spanning the range from magnetoencephalography (MEG) to fMRI BOLD measurements, neural activity in stability-dependent neural circuitry increases before and drops across the antiphase to in-phase transition, even though the system is moving faster – attesting further to the significance of dynamic stability and instability for functionally organized neural circuitry (coordinative structures) in the brain and behavior.

4.12

Transitions, Transients, Chimera, and Spatiotemporal Metastability

Here, we mention only a few further points that are relevant to critical behavior in humans and human brains. The first illustrates the power of Eq. (4.6) and the message of complex, nonlinear dynamical systems: where a system lives in parameter space dictates how it behaves. Figure 4.5 displays an array of transients and transitions found in simple experiments on social coordination in which pairs

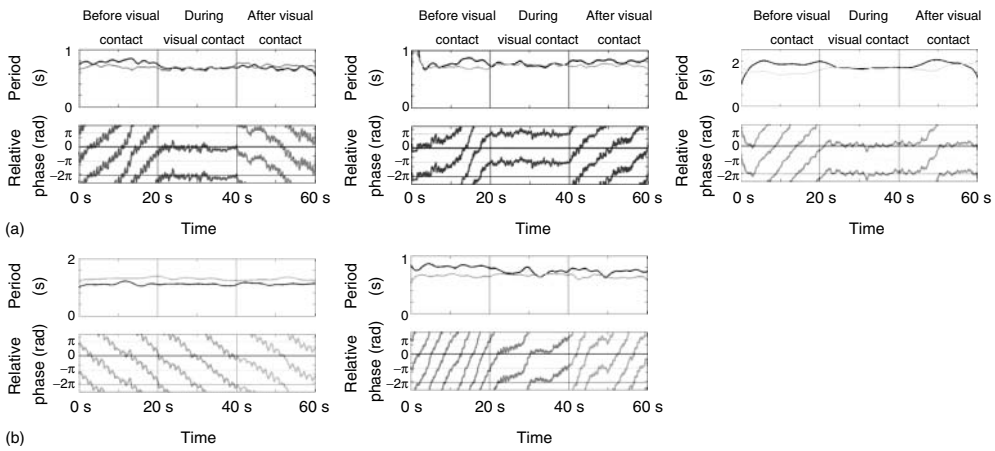


Figure 4.5 Spontaneous patterns of social coordination. Each pair of rectangular boxes shows the instantaneous period (above) and relative phase (below) of voluntary finger movements of each member of a social dyad over the course of a 60-s trial. In the first and last 20 s of each trial, subjects are prevented from seeing each other's movements. Vision is available only in the middle 20 s of the trial (see text and [123] for details). (a) Different kinds of disorder-to-order and order-to-disorder transitions before

and after vision of the other's movements are shown. (b) (Left) Shown here is a kind of “social neglect”: subjects do not spontaneously coordinate when they see each other's movements. They continue to move at their self-chosen frequency and the relative phase wraps continuously throughout the trial. (Right) Transient but robust metastable behavior is revealed during visual coupling. Disorder (phase-wrapping) transitions shift toward in-phase and drifting behavior during visual information exchange.

of subjects move their fingers at their own preferred frequency with and without the vision of the other's movements ([123, 132]; see also [133, 177]). Although a main goal, for example, of the Tognoli *et al.* [123] research was to identify neural signatures (“neuromarkers”) of effective, real-time coordination between people and its breakdown or absence, this is not the main point we wish to convey or of Figure 4.5. Each rectangular box in the figure shows the instantaneous period (in seconds) of each person's flexion–extension finger movements and the relative phase (in radians) between them in a single trial lasting 60 s.

Throughout each trial, subjects were simply asked to adopt a frequency or rate of movement that they felt most comfortable “as if you can do it all day.” The vertical lines in each box correspond to the three manipulations or phases in every trial of the experiment; each phase lasts 20 s. In the first 20 s, subjects were prevented from seeing each other's finger movements by means of an opaque liquid crystal (LC) screen. Then, in the next 20 s, the LC screen became transparent so that subjects could see each other's movements. In the last 20 s, the LC screen became opaque, again preventing vision of the other. The top row of boxes (a) illustrate disorder (measured as phase wrapping) to order (in-phase, left and right; antiphase, middle) transitions and vice-versa. Notice the effect of current conditions on whether disorder to order transitions are toward in-phase or antiphase coordination; the

relative phase just before the LC screen becomes transparent (i.e., neither member of the pair has vision of the other's movements) dictates the nature of the transition process. If the relative phase is wrapping near in-phase (Figure 4.5a, left and right) or antiphase when subjects suddenly see each other's movements, transitions occur to the nearest dynamically stable state. Notice also that in the top right part of the figure, the relative phase lingers at in-phase even though subjects are no longer visually coupled – a kind of “social memory” or remnant of the interaction is observed before subjects' movement periods diverge. Many interesting questions may be raised about this paradigm: who leads, who follows, who cooperates, who competes, who controls, and why. For now, the point is that all these states of coordination, disorder, transients, and transitions fall out of a path (itself likely idiosyncratic and time dependent) through the parameter space of the extended, symmetry-breaking HKB landscapes shown in Figure 4.4 (see also Figure 4e in [4]). Interestingly, many of the same patterns have been observed when a human interacts with a surrogate or avatar driven by a computationally implemented model of the HKB equations, a scaled-up, fully parameterizable human dynamic clamp akin to the dynamic clamp of cellular neuroscience [178, 179].

Even more exotic kinds of criticality and coexistence states can be observed in simple forms of biological coordination – although they have taken their time to see the light of day. Consider the Kelso [80] experiments in which subjects are instructed to coordinate both left and right finger movements with the onset of a flash of light emitted periodically by a diode placed in front of them or by an auditory metronome. Sensory input from visual or auditory pacing stimuli are used as a control parameter to drive the system beyond criticality to discover new coordination states (see also [180]). Harkening back to Bohr's [181] use of the word *phenomenon*, that is, “to refer exclusively to observations obtained under specified circumstances, including an account of the whole experiment,” one can see that a closer look at this experimental arrangement affords a unique possibility to study the interplay of the coupling between the two hands and the coupling between each hand and environmental stimuli. This makes for three kinds of interactions. “The whole experiment” contains a combination of symmetry (left and right hands), symmetry breaking (fingers with visual pacing stimulus), and different forms of coupling (proprioceptive-motor and visuomotor). Figure 4.6 shows an example of behavioral data from a more recent study that used the Kelso paradigm for a different purpose, namely, to examine how spatiotemporal brain activity was reorganized at transitions [88].

The data shown in Figure 4.6 suggest that the coupling between the left and right hands is stronger than the coupling between hands and rhythmic visual stimuli. At high frequency, that is, after the usual transition from antiphase to in-phase coordination has occurred, a mixed CD composed of phase coupling and metastability is observed. That is, left and right finger movements are in-phase, and at the same time, the relative phase between the fingers and visual stimuli exhibits bistable attracting tendencies, alternating near in-phase and near antiphase. This is the empirical footprint of the emergence of a so-called chimera dynamics – named after the mythological creature composed of a lion's head, a goat's body, and a

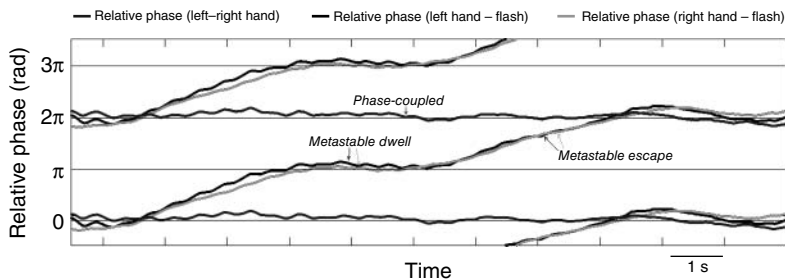


Figure 4.6 Evidence for a “chimera” in visuomotor coordination: the coexistence of phase coupling (between the left and right index fingers) and metastability (dwell and escape) between each finger and visual pacing stimuli.

serpent’s tail [182–184]. The key point is that two seemingly incompatible kinds of behavior (phase locking and metastability) coexist in the same system and appear to arise due to *nonlocal* coupling.⁹⁾ Although so-called chimera are a relatively new area of empirical and theoretical research, the data presented in Figure 4.6 clearly show that both stable and metastable dynamics are part and parcel of the basic repertoire of human sensorimotor behavior. The paradigm allows for the study of integrative and segregative tendencies at the same time – an important methodological and conceptual advantage when it comes to understanding the spatiotemporal (re)organization of brain activity [185, 186].

4.13

The Middle Way: Mesoscopic Protectorates

In the past 30 years or so, principles of self-organizing dynamical systems have been elaborated and shown to govern patterns of coordination (i) within a moving limb and between moving limbs; (ii) between the articulators during speech production; (iii) between limb movements and tactile, visual, and auditory stimuli; (iv) between people interacting with each other spontaneously or intentionally; (v) between humans and avatars; (vi) between humans and other species, as in riding a horse; and (vii) within and between the neural substrates and circuitry that underlie the dynamic brain in action, as measured using MEG, electroencephalography (EEG), and fMRI ([8, 16, 17, 21] for reviews). There are strong hints that laws of coordination in neurobehavioral dynamical systems such as HKB and its extensions are universal and deal with collective properties that emerge from microscopic dynamics. Phase transitions are the core of self-organization. Since their original discovery in

9) Coexistent states are well known in fluid dynamics, where the classical example is the onset of turbulence in fluid flow through a pipe. Linear stability analysis is unusual because it predicts that the laminar flow is always stable for any Reynolds number Re . However, as a function of Re , the lowest

eigenvalue approaches zero asymptotically. In reality, imperfections in the pipe and in the energy injection cause bursts of turbulence (plugs) to be observed also at finite Re , such that the flows shows laminar section with intermittent plugs of turbulence (I. Procaccia, personal communication, 24 August 2012).

experiments and consequent theoretical modeling, phase transitions and related dynamical phenomena have been observed in many different systems at different levels of description ranging from bimanual and sensorimotor coordination and their neural correlates, to interpersonal and interbrain coordination (for reviews, see [15–17, 173, 187–189]). The *bidirectional* nature of the coupling proves to be a crucial aspect of dynamic coordination, regardless of whether hands, people, and brains are interacting for social functions [21] or astrocytes and neurons are interacting through calcium waves for normal synaptic transmission [34].

Although in some cases, akin to HKB and more recent extensions such as the Jirsa–Kelso Excitator model of discrete and continuous behavior [89, 190–192], it has proved possible to derive the order parameter dynamics at one level from the nonlinear components and their nonlinear interaction (e.g., in HKB using the well-known rotating wave and slowly varying amplitude approximations of nonlinear oscillator theory), in general it is not possible to deduce higher level descriptions from lower level ones. Laughlin and Pines [193] present a broad range of emergent phenomena in physics that are regulated by higher organizing principles and are entirely insensitive to microscopic details. The crystalline state, they remark, is the simplest known example of what they call a quantum “protectorate,” a stable state of matter whose low-energy properties are determined by a higher organizing principle and nothing else. More is different, to use Anderson’s [194] apt phrase. Self-organization is not inherently quantum mechanical, but has more to do with hierarchies and separation of time scales (mathematically, the center manifold and/or the inertial manifold where slow time scale processes tend to dominate faster ones, cf. [50, 195]). In recognizing emergent rules, physics has given up reductionism for the most part, although biology still clings to it. In the spirit of the complementary nature [11, 196, 197], both are important, perhaps for different reasons.

So-called laws of coordination (e.g., [9, 45, 198, 199]) – CD – some of the basic ones of which are described briefly here, correspond to emergent rules of pattern formation and change that cut across different systems, levels, and processes. They contain universal features such as symmetry, symmetry breaking, multistability, bifurcations, criticality, phase transitions, metastability, and chimera. They are likely candidates for Laughlin and Pines’s “protectorates”: generic, emergent behaviors that are reliably the same from one system to another regardless of details and repeatable within a system on multiple levels and scales [45]. If laws of coordination are truly emergent and *sui generis* as they seem to be, it may not be possible – even in principle – to deduce, say, psychological-level descriptions from (more microscopic) neural- or molecular-level descriptions. This does not mean that we should not try to understand the relationships between different levels. Rather, the task of CD is to come up with lawful descriptions that allow us to understand emergent behavior at all levels and to respect the (near) autonomy of each. Evidence suggests that one of CD’s most elementary forms – the extended HKB model with its subtle blend of broken symmetry and informationally based coupling – constitutes an intermediate level, a middle ground, or “mesoscopic protectorate” that emerges from nonlinear interaction among context-dependent components from below and boundary conditions from above [11].

4.14

Concluding Remarks

We have reviewed empirical and theoretical evidence showing that criticality is a prominent aspect of the brain and what brains do. All the predictions of nonequilibrium phase transitions have been observed and modeled, indicating that dynamic patterns of human behavioral and brain activity emerge fundamentally as cooperative phenomena in complex, nonlinear dynamical systems. After 70-odd years of “circuit breaking” in invertebrates and vertebrates, plus many conceptual and empirical developments, it appears that the notion of circuit – forced by data – is an unlikely metaphor for the way the cerebral cortex works. Once you “free the creature up” and take into account behavior, multifunctionality, indeterminacy, and degeneracy are the organism’s *modus operandi*. Many years of brilliant research on central pattern generators (note the noun form) has led to the need for a more flexible and dynamical construct to account for behavior. Neural circuits of structurally connected context-independent parts responsible for particular functions are more likely the exception than the rule. Multifunctional, context-dependent neural circuitry with recruitment capabilities and a context-dependent “parts list” seems closer to reality. In this respect, the work of Prinz *et al.* [84] is illuminating. Following the common assumption that neural circuits must be regulated in a highly specific manner to function properly, Prinz *et al.* simulated the pyloric network of the crustacean stomatogastric ganglion using different combinations of synaptic strengths and neuron properties. In over 20 million versions of a three-cell model, they showed that virtually indistinguishable network activity can arise from widely disparate sets of underlying mechanisms. Many different combinations of synaptic strengths and intrinsic membrane properties were found to be capable of producing the same outcome. Likewise, as shown here as a natural aspect of CD, for example, in the symmetry-breaking version of HKB, many different combinations of coupling (k) and intrinsic parameters ($\delta\omega$) produce the same outcome: degeneracy and functional equivalence in spades. In addition, at critical values of parameters abrupt change happens – a different outcome emerges.

As CD has shown, nonlinearity is essential for biological functions such as switching, decision making, pattern selection, and stabilization. Here, we proposed a flexible yet stable concept of behavioral and neural function that accommodates the degeneracy and multifunctionality of biological things or processes. Unlike fixed circuitry, coordinative structures in the nervous system are softly assembled; all the parts are context dependent and weakly interacting. Perturbing one part may produce a remote effect somewhere else without disrupting (indeed preserving) integrity of function. Coordinative structures have been shown to form and change by means of nonequilibrium phase transitions, a basic self-organizing mechanism for spontaneous pattern formation and change in natural systems. The dynamics of coordinative structures is plastic yet stable; change may be sudden or gradual, and persist or not. The (essentially nonlinear) dynamics determines not only which new patterns are formed but also their sustainability, that is, which patterns

persist following smooth or abrupt change. Analysis shows that the spatiotemporal dynamics of neural ensembles and fields and the behavior they give rise to is extremely rich: they exhibit the full range of phase transitions along with interesting transient régimes that are neither fully ordered nor disordered in space and time.

Returning to where we started, this means that dynamic patterns and their pattern-generating dynamics are about the organization of matter, not (or not only) matter itself. With respect to the human brain, CD is about processes such as sniffing and smelling, listening and seeing, anticipating, moving and touching, feeling and deciding, choosing, learning, remembering and forgetting. It is about the restless mind at work in space and time, not only its contents. Thinking and thoughts go together.

Natural selection has created an enormous diversity of forms and patterns. It is not possible – nor does it make sense – to describe all of these at a molecular or atomic level, no more than to describe the huge and beautiful variety of crystalline forms. Nonequilibrium phase transitions and criticality are mechanisms that nature uses to create dynamic patterns of coordination in complex, heterogeneous systems, brains included. They provide ways to compress information and dimensionality in systems with uncountably large numbers of degrees of freedom and huge parameter spaces. The empirical and theoretical framework of CD offers a means to understand biological coordination in different creatures for diverse functions on multiple space and time scales. For CD, the reduction is to nature's strategic principles for functional pattern formation and change. It seems that only under quite peculiar circumstances – “making the familiar strange” as Sheets-Johnstone [35] would say – do basic laws for a qualitative and quantitative description of coordination emerge. One of these days, perhaps, the strange coordination dynamics of behavior and the brain, “simple” forms of which we have described here, may become familiar. Perhaps, the day will come when the interplay between criticality, multistability, and metastability, which allows neuronal assemblies *qua* coordinative structures to form, break, unite, dissolve, and harmonize in space and in time – “the dynamic brain in action” – will be realized. Without coordination, one suspects we would not be alive.

Acknowledgments

The research described herein is currently supported by grants from the National Institute of Mental Health (MH080838), the National Science Foundation (BCS0826897), the US Office of Naval Research (N000140910527), the Chaire d'Excellence Pierre de Fermat, and Florida Atlantic University. Much of the work described herein has depended on long-term support from these agencies and institutions, which are composed of people, friends, students, and colleagues, to whom the author is extremely grateful.

References

1. Schrödinger, E. (1958) *Mind and Matter*, Cambridge University Press, Cambridge.
2. Edelman, G.E. and Gally, J. (2001) Degeneracy and complexity in biological systems. *Proc. Natl. Acad. Sci. U.S.A.*, **98**, 13763–13768.
3. Greenspan, R.J. (2012) Biological indeterminacy. *Sci. Eng. Ethics*, **18**, 447–452. doi: 10.1007/s11948-012-9379-2
4. Kelso, J.A.S. (2012) Multistability and metastability: understanding dynamic coordination in the brain. *Philos. Trans. R. Soc., B*, **367**, 906–918.
5. Kelso, J.A.S. and Tuller, B. (1984) in *Handbook of Cognitive Neuroscience* (ed. M.S. Gazzaniga), Plenum Press, New York, pp. 321–356.
6. Beek, P.J., Peper, C.E., and Stegman, D.F. (1995) Dynamical models of movement coordination. *Hum. Mov. Sci.*, **14**, 573–608.
7. Coey, C.A., Varlet, M., and Richardson, M.J. (2012) Coordination dynamics in a socially situated nervous system. *Front. Hum. Neurosci.*, **6**, 164. doi: 10.3389/fnhum.2012.00164
8. Fuchs, A. and Jirsa, V.K. (eds) (2008) *Coordination: Neural, Behavioral and Social Dynamics*, Springer, Berlin.
9. Huys, R. and Jirsa, V.K. (eds) (2010) *Nonlinear Dynamics of Human Behavior*, Springer-Verlag, Berlin, Heidelberg.
10. Kelso, J.A.S. (1992) Coordination dynamics of human brain and behavior. *Springer Proc. Phys.*, **69**, 223234.
11. Kelso, J.A.S. (1995) *Dynamic Patterns: The Self Organization of Brain and Behavior*, The MIT Press, Cambridge, MA, Paperback ed. 1997.
12. Jirsa, V.K. and Kelso, J.A.S. (eds) (2004) *Coordination Dynamics: Issues and Trends, Understanding Complex Systems*, Springer Series in, Springer, Berlin, Heidelberg.
13. Tschacher, W. and Dauwalder, J.P. (eds) (2003) *The Dynamical Systems Approach to Cognition: Concepts and Empirical Paradigms Based on Self-Organization, Embodiment and Coordination Dynamics*, World Scientific, Singapore.
14. von der Malsburg, C., Phillips, W.A., and Singer, W. (eds) (2010) *Dynamic Coordination in the Brain: From Neurons to Mind*, Strüngmann Forum Report, vol. 5, MIT Press, Cambridge, MA.
15. Fuchs, A. and Kelso, J.A.S. (2009) Movement coordination, in *Encyclopedia of Complexity and System Science* (ed. R.A. Meyers), Springer, Heidelberg.
16. Oullier, O. and Kelso, J.A.S. (2009) Social coordination from the perspective of coordination dynamics, in *Encyclopedia of Complexity and Systems Science* (ed. R.A. Meyers), Springer, Heidelberg, pp. 8198–8212.
17. Kelso, J.A.S. (2009) in *Encyclopedia of Complexity and System Science* (ed. R.A. Meyers), Springer, Heidelberg, pp. 1537–1564.
18. Kelso, J.A.S. (2002) The complementary nature of coordination dynamics: self-organization and the origins of agency. *J. Nonlinear Phenom. Complex Syst.*, **5**, 364–371.
19. Turvey, M.T. (2004) in *Coordination Dynamics: Issues and Trends* (eds V.K. Jirsa and J.A.S. Kelso), Springer, Berlin, Heidelberg, pp. 2–20.
20. Scott, A. (1995) *Stairway to the Mind*, Springer-Verlag, New York.
21. Kelso, J.A.S., Dumas, G., and Tognoli, E. (2013) Outline of a general theory of behavior and brain coordination. *Neural Netw.*, **37**, 120–131 (25th Commemorative Issue).
22. Yates, F.E. (2008) Homeokinetics/homeodynamics: a physical heuristic for life and complexity. *Ecol. Psychol.*, **20**, 148–179.
23. Kelso, J.A.S. (2008) An essay on understanding the mind. *Ecol. Psychol.*, **20**, 180–208.
24. Wilson, K.G. (1979) Problems in physics with many scales of length. *Scientific American*, **241**, 158–179.
25. Kelso, J.A.S. and Haken, H. (1995) in *What is Life? The Next 50 Years* (eds M. Murphy and L. O'Neill), Cambridge University Press, pp. 137–160.

26. Raichle, M.E. (2010) Two views of brain function. *Trends Cognit. Sci.*, **14**, 180–190.
27. Deco, G., Jirsa, V.K., and Mc Intosh, A.R. (2011) Emerging concepts for the dynamical organization of resting state activity in the brain. *Nat. Rev. Neurosci.*, **12**, 43–56.
28. van Hemmen, J.L. and Sejnowski, T.J. (eds) (2006) *23 Problems in Systems Neuroscience*, Oxford University, Oxford.
29. Martin, K.A.C. (2006) Where are the switches on this thing? Asking the big questions in neuroscience. *Nature*, **440**, 1113–1114.
30. Weyl, H. (1952) *Symmetry*, Princeton University Press, Princeton, NJ.
31. Dai, L., Vorselen, D., Korolev, K.S., and Gore, J. (2012) Generic indicators for loss of resilience before a tipping point leading to population collapse. *Science*, **336**, 1175–1177.
32. Scheffer, M., Carpenter, S.R., Lenton, T., Bascompte, J. et al. (2012) Anticipating critical transitions. *Science*, **338**, 344–348.
33. Kelso, J.A.S. (2010) Instabilities and phase transitions in human brain and behavior. *Front. Hum. Neurosci.*, **4**, 23. doi: 10.3389/fnhum.2010.00023
34. Wade, J.J., McDaid, L.J., Harkin, J., Crunelli, V., and Kelso, J.A.S. (eds) (2013) Biophysically-based computational models of astrocyte-neuron coupling and their functional significance. *Front. Comput. Neurosci.* (e-book).
35. Sheets-Johnstone, M. (2011) *The Primacy of Movement*, Expanded 2nd edn, John Benjamins, Amsterdam.
36. Gleick, J. (2003) *Isaac Newton*, Pantheon, New York.
37. Crease, R.P. (2012) Critical Point: Primate Physics. *Physics World* (Nov.), p. 18.
38. Pattee, H.H. (1979) in *A Question of Physics* (eds P. Buckley and F.D. Peat), University of Toronto Press, Toronto & Buffalo, p. 85.
39. May, R.M. (1976) Simple mathematical models with very complicated dynamics. *Nature*, **261**, 459–467.
40. Katchalsky, A.K., Rowland, V., and Blumenthal, R. (1974) Dynamic patterns of brain cell assemblies. *Neurosci. Res. Program Bull.*, **12** (1), 1–187.
41. Rabinovich, M.I., Friston, K.J., and Varona, P. (2012) *Principles of Brain Dynamics*, The MIT Press, Cambridge, MA.
42. Kelso, J.A.S., Southard, D., and Goodman, D. (1979) On the nature of human interlimb coordination. *Science*, **203**, 1029–1031.
43. Kelso, J.A.S., Tuller, B., Bateson, E.V., and Fowler, C.A. (1984) Functionally specific articulatory cooperation following jaw perturbations during speech: evidence for coordinative structures. *J. Exp. Psych: Hum. Percept. Perform.*, **10**, 812–832.
44. Turvey, M.T. (2007) Action and perception at the level of synergies. *Hum. Mov. Sci.*, **26**, 657–697.
45. Turvey, M.T. and Carello, C. (2012) On intelligence from first principles: guidelines for inquiry into the hypothesis of physical intelligence (PI). *Ecol. Psychol.*, **24**, 3–32.
46. Maynard-Smith, J. and Szathmary, E. (1995) *The Major Transitions in Evolution*, Freeman Press, Oxford.
47. Corning, P.A. (2005) *Holistic Darwinism*, University of Chicago Press, Chicago and London.
48. Wilson, D.S., Hayes, S.C., Biglan, A., and Embry, D.D. (2014) Evolving the future: toward a science of intentional change. *Behav. Brain Sci.* (in press).
49. Kostrubiec, V. and Kelso, J.A.S. (2014) Incorporating coordination dynamics into an evolutionarily-grounded science of intentional change. *Behav. Brain Sci.* (in press).
50. Haken, H. (1977/83) *Synergetics, an Introduction: Non-Equilibrium Phase Transitions and Self-Organization in Physics, Chemistry and Biology*, Springer, Berlin.
51. DeLuca, C., Jantzen, K.J., Comani, S., Bertollo, M., and Kelso, J.A.S. (2010) Striatal activity during intentional switching depends on pattern stability. *J. Neurosci.*, **30** (9), 3167–3174.

52. Briggman, K.L. and Kristan, W.B. (2008) Multifunctional pattern-generating circuits. *Ann. Rev. Neurosci.*, **31**, 271–294.
53. Grillner, S. (1975) Locomotion in vertebrates: central mechanisms and reflex interaction. *Physiol. Rev.*, **55** (2), 247–304.
54. Grillner, S. (1985) Neurobiological bases of rhythmic motor acts in vertebrates. *Science*, **228**, 143–149.
55. Grillner, S. (2011) Human locomotor circuits conform. *Science*, **334**, 912–913.
56. Marder, E. (2001) Moving rhythms. *Nature*, **410**, 755.
57. Marder, E. and Bucher, D. (2001) Central pattern generators and the control of rhythmic movements. *Curr. Biol.*, **11**, R986–R996.
58. Marder, E. and Bucher, D. (2007) Understanding circuit dynamics using the stomatogastric ganglion of lobsters and crabs. *Ann. Rev. Physiol.*, **69**, 291–316.
59. Selverston, A.I. (1980) Are central pattern generators understandable? *Behav. Brain Sci.*, **3**, 535–571. doi: 10.1017/S0140525X00006580
60. Selverston, A.I. (1987) Invertebrate central pattern generators as computational data bases, in *Dynamic Patterns in Complex Systems* (eds J.A.S. Kelso, A.J. Mandell, and M.F. Shlesinger), World Scientific, Singapore.
61. Buzsáki, G. (2006) *Rhythms of the Brain*, Oxford University Press, Oxford.
62. Buzsáki, G. and Draguhn, A. (2004) Neuronal oscillations in cortical networks. *Science*, **304**, 1926–1929.
63. Buzsáki, G. and Watson, B.O. (2012) Brain rhythms and neural syntax: implications for efficient coding of cognitive content and neuropsychiatric disease. *Dialogues Clin. Neurosci.*, **14**, 345–367.
64. Yuste, R., MacLean, J.N., Smith, J., and Lansner, A. (2005) The cortex as a central pattern generator. *Nat. Rev. Neurosci.*, **6**, 477–483.
65. Winfree, A.T. (1987) *The Timing of Biological Clocks*, W.H. Freeman, New York.
66. Delcomyn, F. (1980) Neural basis of rhythmic behavior in animals. *Science*, **210**, 492–498.
67. Tuller, B., Harris, K.S., and Kelso, J.A.S. (1982) Stress and rate: differential transformations of articulation. *J. Acoust. Soc. Am.*, **71**, 1534–1543.
68. Feldman, A.G. (1966) Functional tuning of the nervous system with control of movement or maintenance of a steady posture. II. Controllable parameters of the muscle. *Biophysics*, **11**, 565–578.
69. Kelso, J.A.S. (1977) Motor control mechanisms underlying human movement reproduction. *J. Exp. Psychol. Hum. Percept. Perform.*, **3**, 529543.
70. Polit, A. and Bizzi, E. (1978) Processes controlling arm movements in monkeys. *Science*, **201**, 1235–1237.
71. Kelso, J.A.S., Holt, K.G., Kugler, P.N., and Turvey, M.T. (1980) in *Tutorials in Motor Behavior* (eds G.E. Stelmach and J. Requin), North Holland, Amsterdam, pp. 49–70.
72. Başar, E. (2004) *Memory and Brain Dynamics: Oscillations Integrating Attention, Perception, Learning, and Memory*, CRC Press, Boca Raton, FL.
73. Singer, W. (2005) The brain—an orchestra without a conductor. *Max Planck Res.*, **3**, 15–18.
74. Kelso, J.A.S., Holt, K.G., Rubin, P., and Kugler, P.N. (1981) Patterns of human interlimb coordination emerge from the properties of nonlinear oscillatory processes: theory and data. *J. Motor Behav.*, **13**, 226–261.
75. Kugler, P.N., Kelso, J.A.S., and Turvey, M.T. (1980) in *Tutorials in Motor Behavior* (eds G.E. Stelmach and J. Requin), North Holland, Amsterdam, pp. 1–40.
76. Feldman, A.G. (2009) in *Progress in Motor Control V. A Multidisciplinary Perspective* (ed. D. Sternad), Springer, New York, pp. 637–644.
77. Feldman, A.G. and Levin, M.F. (1995) The origin and use of positional frames of reference in motor control. *Behav. Brain Sci.*, **18**, 723–744.
78. Latash, M.L. (2012) *Fundamentals of Motor Control*, Academic Press, New York.

79. Kelso, J.A.S. (1981) On the oscillatory basis of movement. *Bull. Psychonomic Soc.*, **18**, 63.
80. Kelso, J.A.S. (1984) Phase transitions and critical behavior in human bimanual coordination. *Am. J. Physiol.: Regul. Integr. Comp.*, **15**, R1000–R1004.
81. Kostrubiec, V., Zanone, P.-G., Fuchs, A., and Kelso, J.A.S. (2012) Beyond the blank slate: routes to learning new coordination patterns depend on the intrinsic dynamics of the learner – experimental evidence and theoretical model. *Front. Hum. Neurosci.*, **6**, 212. doi: 10.3389/fnhum.2012.00222
82. Zanone, P.G. and Kelso, J.A.S. (1992) The evolution of behavioral attractors with learning: Nonequilibrium phase transitions. *J. Exp. Psychol.: Hum. Percept. Perform.*, **18** (2), 403421.
83. Howard, I.S., Ingram, J.N., Körding, K.P., and Wolpert, D.M. (2009) Statistics of natural movements are reflected in motor errors. *J. Neurophysiol.*, **102**, 1902–1910.
84. Prinz, A.A., Bucher, D., and Marder, E. (2004) Similar network activity from disparate circuit parameters. *Nat. Neurosci.*, **7**, 1345–1352.
85. Haken, H., Kelso, J.A.S., and Bunz, H. (1985) A theoretical model of phase transitions in human hand movements. *Biol. Cybern.*, **51**, 347–356.
86. Liese, T. and Cohen, A. (2005) Non-linear oscillators at our fingertips. *Am. Math. Mon.*, **114**, 14–28.
87. Jirsa, V.K., Friedrich, R., Haken, H., and Kelso, J.A.S. (1994) A theoretical model of phase transitions in the human brain. *Biol. Cybern.*, **71**, 2735.
88. Banerjee, A., Tognoli, E., Kelso, J.A.S. and Jirsa, V.K. (2012) Spatiotemporal reorganization of large-scale neural assemblies mediates bimanual coordination. *Neuroimage*, **62**, 1582–1592. doi: org/10.1016/j.neuroimage.2012.05.046
89. Calvin, S. and Jirsa, V.K. (2010) Perspectives on the dynamic nature of coupling in human coordination, in *Nonlinear Dynamics of Human Behavior* (eds R. Huys and V.K. Jirsa), Springer-Verlag, Berlin, Heidelberg.
90. Kubo, R. (1966) The fluctuation-dissipation theorem. *Rep. Prog. Phys.*, **29**, 255–283.
91. Scholz, J.P., Kelso, J.A.S., and Schöner, G. (1987) Nonequilibrium phase transitions in coordinated biological motion: critical slowing down and switching time. *Phys. Lett. A*, **8**, 390–394.
92. Kelso, J.A.S., Schöner, G., Scholz, J.P., and Haken, H. (1987) Phase-locked modes, phase transitions and component oscillators in coordinated biological motion. *Phys. Scripta*, **35**, 79–87.
93. Kelso, J.A.S., Scholz, J.P., and Schöner, G. (1986) Nonequilibrium phase transitions in coordinated biological motion: critical fluctuations. *Phys. Lett. A*, **118**, 279–284.
94. Schöner, G. and Kelso, J.A.S. (1988) Dynamic pattern generation in behavioral and neural systems. *Science*, **239**, 1513–1520.
95. Buchanan, J.J. and Kelso, J.A.S. (1993) Posturally induced transitions in rhythmic multijoint limb movements. *Exp. Brain Res.*, **94**, 131–143.
96. Schöner, G., Haken, H., and Kelso, J.A.S. (1986) A stochastic theory of phase transitions in human hand movement. *Biol. Cybern.*, **53**, 247–257.
97. Haken, H. (1988) *Information and Self-Organization*, Springer, Berlin.
98. Daffertshofer, A. (2010) Benefits and pitfalls in analyzing noise in dynamical systems – On stochastic differential equations and system identification, in *Nonlinear Dynamics of Human Behavior* (eds R. Huys and V.K. Jirsa), Springer-Verlag, Berlin, Heidelberg.
99. Chialvo, D. (2010) Emergent complex neural dynamics. *Nat. Phys.*, **6**, 744–750.
100. Chen, Y., Ding, M., and Kelso, J.A.S. (1997) Long term memory processes ($1/f^\alpha$ type) in human coordination. *Phys. Rev. Lett.*, **79**, 4501–4504.
101. Chen, Y., Ding, M., and Kelso, J.A.S. (2003) in *Processes with Long-Range Correlations* (eds G. Rangarajan and M. Ding), Springer, Berlin, pp. 309–323.
102. Ding, M., Chen, Y., and Kelso, J.A.S. (2002) Statistical analysis of timing errors. *Brain Cognit.*, **48**, 98–106.

103. Treffner, P.J. and Kelso, J.A.S. (1999) Dynamic encounters: long memory during functional stabilization. *Ecol. Psychol.*, **11**, 103–137.
104. Beggs, J.M. and Timme, N. (2012) Being critical of criticality in the brain. *Front. Physiol.*, **3**, 163.
105. Kelso, J.A.S. and Tuller, B. (1981) Toward a theory of apractic syndromes. *Brain Lang.*, **12**, 224–245.
106. Jirsa, V.K. and Kelso, J.A.S. (2000) Spatiotemporal pattern formation in neural systems with heterogeneous connection topologies. *Phys. Rev. E*, **62**, 8462–8465.
107. Bressler, S.L. and Kelso, J.A.S. (2001) Cortical coordination dynamics and cognition. *Trends Cognit. Sci.*, **5**, 26–36.
108. Kelso, J.A.S., DelColle, J., and Schöner, G. (1990) Action-perception as a pattern formation process, in *Attention and Performance XIII* (ed. M. Jeannerod), Erlbaum, Hillsdale, NJ, pp. 139–169.
109. Kelso, J.A.S. (1991) Behavioral and neural pattern generation: the concept of Neurobehavioral Dynamical System (NBDS), in *Cardiorespiratory and Motor Coordination* (eds H.P. Koepchen and T. Huopaniemi), Springer-Verlag, Berlin.
110. Kelso, J.A.S. and Tognoli, E. (2007) Toward a complementary neuroscience: metastable coordination dynamics of the brain, in *Neurodynamics of Higher-level Cognition and Consciousness* (eds R. Kozma and L. Perlovsky), Springer, Heidelberg.
111. Edelman, G.M. (2004) Naturalizing consciousness: a theoretical framework. *Proc. Natl. Acad. Sci. U.S.A.*, **100**, 520–524.
112. Edelman, G. and Tononi, G. (2000) *A Universe of Consciousness*, Basic Books, New York.
113. Fingelkurts, A.A. and Fingelkurts, A.A. (2004) Making complexity simpler: multivariability and metastability in the brain. *Int. J. Neurosci.*, **114**, 843–862.
114. Freeman, W.J. and Holmes, M.D. (2005) Metastability, instability, and state transition in neocortex. *Neural Netw.*, **18**, 497–504.
115. Friston, K.J. (1997) Transients, metastability, and neuronal dynamics. *Neuroimage*, **5**, 164–171.
116. Koch, C. (2005) *The Quest for Consciousness*, Roberts and Co., Englewood, CO.
117. Sporns, O. (2004) in *Coordination Dynamics: Issues and Trends* (eds V.K. Jirsa and J.A.S. Kelso), Springer-Verlag, Berlin, pp. 197–215.
118. Sporns, O. (2010) *Networks of the Brain*, MIT Press, Cambridge.
119. Varela, F.J., Lachaux, J.-P., Rodriguez, E., and Martinerie, J. (2001) The brainweb: phase synchronization and large-scale integration. *Nat. Rev. Neurosci.*, **2**, 229–239.
120. Rabinovich, M.I., Huerta, R., and Laurent, G. (2008) Transient dynamics for neural processing. *Science*, **321**, 48–50.
121. Chen, Y., Ding, M., and Kelso, J.A.S. (2003) Task-related power and coherence changes in neuromagnetic activity during visuomotor coordination. *Exp. Brain Res.*, **148**, 105–116.
122. Dumas, G., Chavez, M., Nadel, J., and Martinerie, J. (2012) Anatomical connectivity influences both intra- and inter-brain synchronizations. *PLoS ONE* **7** (5), e36414. doi: 10.1371/journal.pone.0036414.
123. Tognoli, E., Lagarde, J., DeGuzman, G.C., and Kelso, J.A.S. (2007) The phi complex as a neuromarker of human social coordination. *Proc. Natl. Acad. Sci.*, **104**, 8190–8195 (from the cover; see also *Scientific American Mind*, August, 2007).
124. Begleiter, H. and Porjesz, B. (2006) Genetics of human brain oscillations. *Int. J. Psychophysiol.*, **60**, 162–171.
125. Whittington, M.A., Traub, R.D., Kopell, N., Ermentrout, B., and Buhl, E.H. (2000) Inhibition-based rhythms: experimental and mathematical observations on network dynamics. *Int. J. Psychophysiol.*, **38**, 315–336.
126. Wade, J.J., McDaid, L.J., Harkin, J.G., Crunelli, V., and Kelso, J.A.S. (2011) Bidirectional coupling between astrocytes and neurons mediates learning and dynamic coordination in the brain: a multiple modeling approach. *PLoS One*, **6**, e29445.

127. Womelsdorf, T., Schöffelen, J.-M., Oostenveld, R., Singer, W., Desimone, R., Engel, A.K., and Fries, P. (2007) Modulation of neuronal interactions through neuronal synchronization. *Science*, **316**, 1609–1612.
128. Canolty, R.T., Edwards, E., Dalal, S.S., Soltani, M., Nagarajan, S.S., Kirsch, H.E., Berger, M.S., Barbaro, N.M., and Knight, R.T. (2006) High gamma power is phase-locked to theta oscillations in human neocortex. *Science*, **313**, 1626–1628.
129. Fries, P. (2009) Neuronal gamma-band synchronization as a fundamental process in cortical computation. *Ann. Rev. Neurosci.*, **32**, 209–224.
130. Haken, H. (1996) *Principles of Brain Functioning*, Springer, Berlin.
131. Van Orden, G.C., Holden, J.G., and Turvey, M.T. (2005) Human cognition and 1/f scaling. *J. Exp. Psychol. Gen.*, **134**, 117–123.
132. Oullier, O., DeGuzman, G.C., Jantzen, K.J., Lagarde, J., and Kelso, J.A.S. (2008) Social coordination dynamics: measuring human bonding. *Social Neurosci.*, **3**, 178–192. doi: 10.1080/17470910701563392
133. Schmidt, R.C. and Richardson, M.J. (2008) Dynamics of interpersonal coordination, in *Coordination: Neural, Behavioral and Social Dynamics* (eds A. Fuchs and V.K. Jirsa), Springer, Berlin.
134. Plenz, D. and Thiagaran, T. (2007) The organizing principles of neuronal avalanche activity: cell assemblies and cortex. *Trends Neurosci.*, **30**, 101–110.
135. Plenz, D. (2013) The critical brain. *Physics*, **6**, 47.
136. Kelso, J.A.S. (2001) Metastable coordination dynamics of brain and behavior. *Brain Neural Networks (Jpn.)*, **8**, 125–130.
137. Kelso, J.A.S. (2001) How the brain changes its mind. in: *The Emergence of the Mind*, Fondazione Carlo Erba, Milano, pp. 93–101.
138. Rabinovich, M.I. and Varona, P. (2012) Transient brain dynamics, in *Principles of Brain Dynamics* (eds M.I. Rabinovich, K.J. Friston, and P. Varona), The MIT Press, Cambridge, MA.
139. Fuchs, A., Kelso, J.A.S., and Haken, H. (1992) Phase transitions in the human brain: Spatial mode dynamics. *Int. J. Bifurcation Chaos*, **2**, 917939.
140. Fuchs, A., Deecke, L., and Kelso, J.A.S. (2000) Phase transitions in human brain revealed by large SQUID arrays: response to Daffertshofer, Peper and Beek. *Phys. Lett. A*, **266**, 303–308.
141. Fuchs, A., Jirsa, V.K., and Kelso, J.A.S. (2000) Theory of the relation between human brain activity (MEG) and hand movements. *Neuroimage*, **11**, 359–369.
142. Fuchs, A., Mayville, J.M., Cheyne, D., Weinberg, H., Deecke, L., and Kelso, J.A.S. (2000) Spatiotemporal analysis of neuromagnetic events underlying the emergence of coordinative instabilities. *Neuroimage*, **12**, 71–84.
143. Kelso, J.A.S., Bressler, S.L., Buchanan, S., DeGuzman, G.C., Ding, M., Fuchs, A., and Holroyd, T. (1991) Cooperative and critical phenomena in the human brain revealed by multiple SQUIDS, in *Measuring Chaos in the Human Brain* (eds D. Duke and W. Pritchard), World Scientific, New Jersey, pp. 97–112.
144. Kelso, J.A.S., Bressler, S.L., Buchanan, S., DeGuzman, G.C., Ding, M., Fuchs, A., and Holroyd, T. (1992) A phase transition in human brain and behavior. *Phys. Lett. A*, **169**, 134–144.
145. Kelso, J.A.S. and Fuchs, A. (1995) Self-organizing dynamics of the human brain: critical instabilities and Sil'nikov chaos. *Chaos*, **5** (1), 64–69.
146. Mayville, J.M., Fuchs, A., Ding, M., Cheyne, D., Deecke, L., and Kelso, J.A.S. (2001) Event-related changes in neuromagnetic activity associated with syncopation and synchronization tasks. *Hum. Brain Mapp.*, **14**, 65–80.
147. Banerjee, A., Tognoli, E., Jirsa, V.K., Assisi, C., and Kelso, J.A.S. (2008) Mode Level Cognitive Subtraction (MLCS) quantifies spatiotemporal reorganization in large-scale brain topographies. *Neuroimage*, **15**, 663–674.
148. Mayville, J.M., Bressler, S.L., Fuchs, A., and Kelso, J.A.S. (1999) Spatiotemporal reorganization of electrical activity in the human brain associated with a

- phase transition in rhythmic auditory-motor coordination. *Exp. Brain Res.*, **127**, 371–381.
149. Wallenstein, G.V., Kelso, J.A.S., and Bressler, S.L. (1995) Phase transitions in spatiotemporal patterns of brain activity and behavior. *Physica D*, **84**, 626–634.
150. Mayville, J.M., Jantzen, K.J., Fuchs, A., Steinberg, F.L., and Kelso, J.A.S. (2002) Cortical and subcortical networks underlying syncopated and synchronized coordination tasks revealed using functional MRI. *Hum. Brain Mapp.*, **17**, 214–229.
151. Oullier, O., Jantzen, K.J., Steinberg, F.L., and Kelso, J.A.S. (2005) Neural substrates of real and imagined sensorimotor coordination. *Cereb. Cortex*, **15** (7), 975–985.
152. Meyer-Lindenberg, A., Zieman, U., Hajak, G., Cohen, L., and Berman, K. (2002) Transition between dynamical states of differing stability in the human brain. *Proc. Natl. Acad. Sci. U.S.A.*, **99**, 10948–10953.
153. Jantzen, K.J., Steinberg, F.L., and Kelso, J.A.S. (2009) Coordination dynamics of large-scale neural circuitry underlying sensorimotor behavior. *J. Cognit. Neurosci.*, **21**, 2420–2433. doi: 10.1162/jocn.2008.21182
154. Oullier, O., Lagarde, J., Jantzen, K.J., and Kelso, J.A.S. (2006) Dynamiques comportementale et cérébrale des coordinations sensorimotrices: (in)stabilité et métastabilité rythmiques. *J. Soc. Biol.*, **200** (2), 145–167. (Medline Version: Coordination Dynamics: (in)stability and metastability in behavioural and neural systems. *J. Soc. Biol.*, **200**(2), 145-167).
155. Jantzen, K.J., Steinberg, F.L., and Kelso, J.A.S. (2004) Brain networks underlying timing behavior are influenced by prior context. *Proc. Natl. Acad. Sci. U.S.A.*, **101**, 6815–6820.
156. Jantzen, K.J., Anderson, B., Steinberg, F.L., and Kelso, J.A.S. (2004) A prospective functional magnetic resonance imaging study of Mild Traumatic Brain Injury (MTBI) in college football players. *Am. J. Neuroradiol.*, **25**, 738–745.
157. Houweling, S., Beek, P.J., and Daffertshofer, A. (2010) Spectral changes of interhemispheric cross talk during movement instabilities. *Cereb. Cortex*, **20**, 2605–2613.
158. Uhl, C., Friedrich, R., and Haken, H. (1995) Analysis of spatiotemporal signals of complex systems. *Phys. Rev. E: Stat. Phys. Plasmas Fluids Relat. Interdisciplin. Top.*, **51** (5), 3890–3900.
159. Jirsa, V.K. and Haken, H. (1996) Field theory of electromagnetic brain activity. *Phys. Rev. Lett.*, **77**, 960–963.
160. Jirsa, V. and Haken, H. (1997) A derivation of a macroscopic field theory of the brain from the quasi-microscopic neural dynamics. *Physica D (Nonlinear Phenom.)*, **99**, 503–526.
161. Frank, T.D., Daffertshofer, A., Peper, C.E., Beek, P.J., and Haken, H. (2000) Towards a comprehensive theory of brain activity: coupled oscillator systems under external forces. *Physica D*, **144**, 62–86.
162. Kelso, J.A.S., Fuchs, A., Holroyd, T., Lancaster, R., Cheyne, D., and Weinberg, H. (1998) Dynamic cortical activity in the human brain reveals motor equivalence. *Nature*, **392**, 814–818.
163. Jirsa, V.K., Fuchs, A., and Kelso, J.A.S. (1998) Connecting cortical and behavioral dynamics: bimanual coordination. *Neural Comput.*, **10**, 2019–2045.
164. Beek, P.J., Peper, C.E., and Daffertshofer, A. (2002) Modeling rhythmic interlimb coordination: beyond the Haken–Kelso–Bunz Model. *Brain Cognition*, **48** (1), 149–165. doi: 10.1006/brcg.2001.1310
165. Carson, R.G. (2005) Neural pathways mediating bilateral interactions between the upper limbs. *Brain Res.*, **49**, 641–622.
166. Daffertshofer, A., Peper, C.E., Frank, T.D. and Beek, P.J. (2000) Spatio-temporal patterns of encephalographic signals during polyrhythmic tapping. *Human Movement Sci.*, **19**, 475–498.
167. Daffertshofer, A., Peper, C.E., and Beek, P.J. (2005) Stabilization of bimanual coordination due to active inhibition: a dynamical account. *Biol. Cybern.*, **92**, 101–109.

168. Swinnen, S.P. (2002) Intermanual crosstalk: from behavioural models to neural-network interactions. *Nat. Neurosci.*, **3**, 350–361.
169. Assisi, C.G., Jirsa, V.K., and Kelso, J.A.S. (2005) Synchrony and clustering in heterogeneous networks with global coupling and parameter dispersion. *Phys. Rev. Lett.*, **94**, 018106.
170. Deco, G., Jirsa, V.K., and Friston, K.J. (2012) The dynamical and structural basis of brain activity, in *Principles of Brain Dynamics* (eds M.I. Rabinovich, K.J. Friston, and P. Varona), The MIT Press, Cambridge, MA.
171. Kelso, J.A.S., Fuchs, A., and Jirsa, V.K. (1999) Traversing scales of brain and behavioral organization, in *Analysis of Neurophysiological Brain Functioning* (ed. C. Ühl), Springer-Verlag, Berlin, pp. 73–125.
172. Kelso, J.A.S., Jirsa, V.K., and Fuchs, A. (1999) From level to level in brain and behavior, in *Statistical Physics on the Eve of the 21st Century* (eds M.T. Bachelor and L.T. Wille), World Scientific, Singapore, pp. 113–130.
173. Daffertshofer, A. and van Wijk, C.M. (2012) Transient motor behavior and synchronization in the cortex, in *Principles of Brain Dynamics* (eds M.I. Rabinovich, K.J. Friston, and P. Varona), The MIT Press, Cambridge, MA.
174. Freeman, W.J. (1975) *Mass Action in the Nervous System*, Academic Press, New York.
175. Jantzen, K.J., Fuchs, A., Mayville, J.M., and Kelso, J.A.S. (2001) Neuromagnetic activity in alpha and beta bands reflects learning-induced increases in coordinative stability. *Clin. Neurophysiol.*, **112**, 1685–1697.
176. Temprado, J.J., Zanone, P.G., Monno, A., and Laurent, M. (1999) Attentional load associated with performing and stabilizing preferred bimanual patterns. *J. Exp. Psych: Hum. Percept. Perform.*, **25**, 1595–1608.
177. Riley, M.A., Richardson, M.C., Shockley, K., and Ramenzoni, V.C. (2011) Interpersonal synergies. *Front. Psychol.*, **2**, 38. doi: 10.3389/fpsyg.2011.00038
178. Kelso, J.A.S., DeGuzman, G.C., Reveley, C., and Tognoli, E. (2009) Virtual Partner Interaction (VPI): exploring novel behaviors via coordination dynamics. *PLoS One*, **4** (6), e5749.
179. Prinz, A.A., Abbott, L.F., and Marder, E. (2004) The dynamic clamp comes of age. *Trends Neurosci.*, **27**, 218–224.
180. Lagarde, J. and Kelso, J.A.S. (2006) Binding of movement, sound and touch: multimodal coordination dynamics. *Exp. Brain Res.*, **173**, 673–688.
181. Bohr, N. (1948) On the notions of causality and complementarity. *Dialectica*, **2**, 312 . Cited In Pais, A., *Niels Bohr's Times*, Oxford University Press, Oxford, p. 433.
182. Abrams, D.M. and Strogatz, S.H. (2006) Chimera states in a ring of nonlocally coupled oscillators. *Int. J. Bifurc. Chaos*, **16**, 21–37.
183. Kuramoto, Y. and Battogtokh, D. (2002) Coexistence of coherence and incoherence in nonlocally coupled phase oscillators: a soluble case. *J. Nonlin. Phenom. Complex Syst.*, **5** (4), 380–385.
184. Shanahan, M. (2010) Metastable chimera states in community structured oscillator networks. *Chaos*, **20** (1), 013108.
185. Kelso, J.A.S. and Tognoli, E. (2010) Spatiotemporal metastability: design for a brain. *Soc. Neurosci., San Diego*, **343**, 16.
186. Tognoli, E. and Kelso, J.A.S. (2014) The metastable brain. *Neuron*, **81**, 35–48.
187. Dumas, G., Nadel, J., Soussignan, R., Martinerie, J., and Garnero, L. (2010) Inter-brain synchronization during social interaction. *PLoS One*, **5** (8), e12166. doi: 10.1371/journal.pone.0012166
188. Kelso, J.A.S. (2009) Synergies: atoms of brain and behavior. *Adv. Exp. Med. Biol.*, **629**, 83–91. (Also Sternad, D. (ed.) *A Multidisciplinary Approach to Motor Control*, Springer, Heidelberg).
189. Tognoli, E. (2008) EEG coordination dynamics: neuromarkers of social coordination, in *Coordination: Neural, Behavioral and Social Dynamics* (eds A. Fuchs and V.K. Jirsa), Springer, Berlin.

190. Huys, R., Studenka, B.E., Rheame, N., Zelaznik, H.N., and Jirsa, V.K. (2008) Distinct timing mechanisms produce discrete and continuous movements. *PLoS Comput. Biol.*, 4, e1000061.
191. Huys, R., Perdikis, D., and Jirsa, V.K. (2014) Functional architectures and structured flows on manifolds: a dynamical framework for perceptual-motor behavior. *Psych. Rev.* (in press).
192. Jirsa, V.K. and Kelso, J.A.S. (2005) The excitor as a minimal model for the coordination dynamics of discrete and rhythmic movements. *J. Motor Behav.*, 37, 35–51.
193. Laughlin, R.B. and Pines, D. (2000) The theory of everything. *Proc. Natl. Acad. Sci. U.S.A.*, 97, 28–31.
194. Anderson, P.W. (1972) More is different. *Science*, 177, 393–396.
195. Perdikis, D., Huys, R., and Jirsa, V.K. (2011) Time scale hierarchies in the functional organization of complex behaviors. *PLoS Comput. Biol.*, 7 (9), e1002198. doi: 10.1371/journal.pcbi.1002198
196. Kelso, J.A.S. (2005) The complementary nature of coordination dynamics: toward a science of the in-between, in *Uncertainty and Surprise*, vol. 3 (eds R. Mc Daniel and D. Driebe), Springer Series in *Understanding Complex Systems*, Springer-Verlag, Berlin, Heidelberg.
197. Kelso, J.A.S. and Engström, D.A. (2006) *The Complementary Nature*, MIT Press, Cambridge, MA. (Paperback Edition March 2008).
198. Newell, K.M., Liu, Y.-T., and Mayer-Kress, G.M. (2008) Landscapes beyond the HKB model, in *Coordination: Neural, Behavioral and Social Dynamics* (eds A. Fuchs and V.K. Jirsa), Springer, Berlin, Heidelberg.
199. Park, H. and Turvey, M.T. (2008) Imperfect symmetry and the elementary coordination law, in *Coordination: Neural, Behavioral and Social Dynamics* (eds A. Fuchs and V.K. Jirsa), Springer, Berlin, Heidelberg.

5

The Correlation of the Neuronal Long-Range Temporal Correlations, Avalanche Dynamics with the Behavioral Scaling Laws and Interindividual Variability

Jaakko Matias Palva and Satu Palva

5.1

Introduction

Numerous complex systems from sand piles [1] to earthquakes [2], stock markets [3], and genetic regulatory networks [4] exhibit behavior typical of systems in a self-organized critical state. In recent years, accumulating empirical evidence for criticality in neuronal systems has led to widespread interest in using this framework for understanding the character and functional implications of variability in brain activity [5–7]. In the sand-pile example of criticality, the dropping of new sand grains causes avalanches, that is, propagating waves of activity with size and lifetime distributions that are characterized by power laws. Spatial and temporal correlations with power-law decay are another salient property of systems in critical state. Such long-range correlations as well as avalanche dynamics have been found to characterize spontaneous brain activity.

The metastability of critical systems maximizes their dynamic range [8], storage capacity [9], and computational power [10], which in neuronal systems could conceivably support adaptive behavior and yield an evolutionary advantage. However, the presence of similar dynamics in a variety of systems raises the question of whether fractal neuronal dynamics are an epiphenomenon [11] without functional relevance or, in this case, without significant impact at the behavioral or cognitive level. Until recently, there has been little evidence to support an essential functional role for criticality in human cognition or behavior. In this chapter, we explore the interactions among the ménage à trois of behavioral performance fluctuations, slow and fast neuronal fluctuations, and evidence for shared critical dynamics therein.

5.2

Criticality in the Nervous System: Behavioral and Physiological Evidence

5.2.1

Human Task Performance Fluctuations Suggest Critical Dynamics

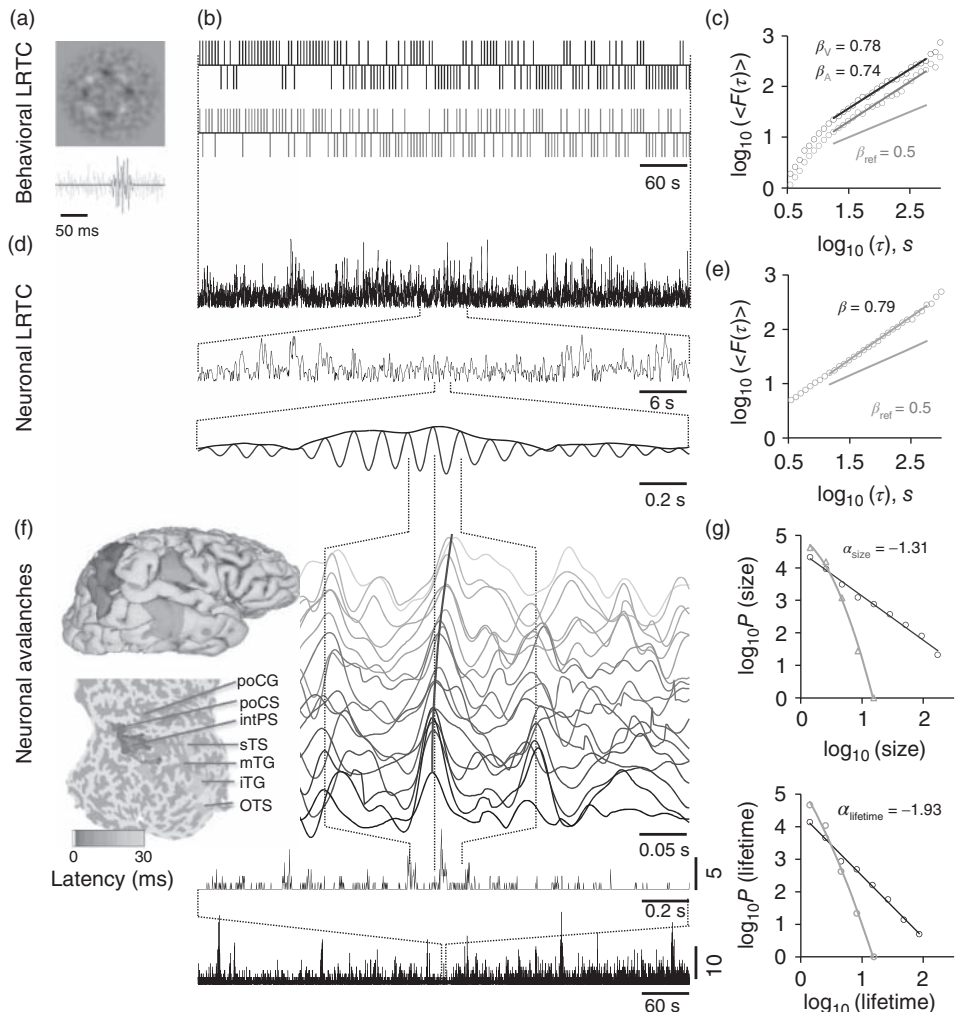
Even under unchanging experimental conditions, human performance in sensorimotor and cognitive tasks is highly variable at all observable time scales and exhibits pronounced slow fluctuations. These fluctuations are particularly salient in continuous performance tasks (CPTs) [12], wherein the subjects perform a task for several minutes without interruptions or feedback. Psychophysical time series under such conditions have been known since the early 1950s to be nonrandomly clustered [13–15], that is, instead of being independent, consecutive trials in psychophysical experiments are autocorrelated so that similar behavioral outcomes are much more likely to appear in clusters or “streaks” than expected by chance [15–17].

Classical examples of CPTs revealing slow behavioral fluctuations are threshold-stimulus-detection tasks (TSDTs) and motor timing tasks. In TSDTs, subjects detect stimuli with an intensity adjusted before the experiment to yield ~50% detection rate and then maintained constant. In timing tasks, the subjects are presented a rhythm that they then sustain endogenously and report, for example, by finger tapping. For example, in auditory, visual, and somatosensory TSDT, successful perception of the target stimulus is associated with an enhanced probability for detecting the subsequent stimulus as well [14, 18] (Figure 5.1a,b). In time series analyses, this clustering is reflected in performance fluctuations spanning slow (0.1–1 Hz) and infra-slow (0.1–0.01 Hz) frequency bands. TSDTs are a powerful

Figure 5.1 The individual scaling laws of individual behavioral LRTC, neuronal LRTC, and neuronal avalanches can be quantified with threshold-stimulus detection tasks (TSDT) and source-reconstructed M/EEG recordings. (a) Examples of noise-embedded visual and auditory stimuli whose signal-to-noise ratios are tuned before the experiment to yield a ~50% hit rate and then maintained constant. (b) Behavioral performance time series of detected (upward ticks) and undetected (downward ticks) display-rich dynamics in a bimodal audiovisual TSDT (visual, red; auditory, blue; time series are for the first 10 min of a 30 min session of a representative subject). (c) Visual and auditory detection time series exhibit long-range temporal correlations (LRTC) that can be characterized for each individual subject by DFA exponents, β_V and β_A . (d) Amplitude fluctuations of neuronal oscillations in local cortical patches (here, 10 Hz in inferior parietal

gyrus) are fractally self-similar and (e) show robust LRTC. (f) Avalanche dynamics are salient in source-reconstructed broadband data. The time series of cortical patches in the example avalanche are color coded by the peak latency. These colors correspond to those displayed on pial and flattened cortical surfaces and show the progression of this activity cascade from posterior parietal-to-temporal and post-central loci. The avalanche time series (bottom, black lines) show the number of cortical patches where a peak was found with zeros, indicating interavalanche periods. (g) The sizes and lifetimes of cortical avalanches are approximately power-law distributed with exponents, α , close to those of a critical branching process (-1.5 and -2 , respectively). All data in this figure are from the same 30 min session of a subject that is representative in having β closest to population mean. (Adapted from [18].) (Please find a color version of this figure on the color plates.)

experimental approach for elucidating the role of spontaneous brain activity in stimulus processing because in there the very weak stimuli minimally disrupt ongoing brain dynamics [12]. Conversely, weak stimuli evoke only minimal bottom-up synaptic drive and thus facilitate the identification of top-down influences or brain states that facilitate or suppress task performance. As has been observed in somatosensory [14], auditory, and visual [18] modalities, psychophysical TSST data is characterized by alternating streaks, or “runs,” of detected (hits) and undetected (misses) stimuli. The power-law tail of the run-size distribution shows that long runs are much more frequent in the recorded than in randomized data [14]. These time series are also autocorrelated across lags of more than 100 s [14]. Crucially, in all three sensory modalities, TSST time series exhibit scale-free, fractal-like long-range temporal correlations (LRTCs).



Overall, similar observations have been made with a diverse body of TSDT, motor timing, and other CPT experiments, which show that the hit-rate (TSDT), timing-error, or reaction-time fluctuations in healthy human subjects are autocorrelated for tens to hundreds of seconds and exhibit salient, scale-free LRTCs [13, 14, 18–24] (Figure 5.1c).

Such fractal self-similarity, power-law scaling behavior, and “ $1/f$ noise” at the phenomenological level are typical of systems exhibiting “avalanche dynamics” and operating in a critical [25, 26] or self-organized critical state [1]. The CPT data hence suggest that human behavioral performance fluctuations are a reflection of underlying critical-state brain dynamics, which implies that criticality in the human nervous system may have profound functional consequences for human cognition and behavior.

5.2.2

Two Lines of Empirical Evidence for Critical-State Dynamics in Neuronal Systems

Two principal lines of evidence suggest that similarly to those in behavioral performance, the fluctuations of collective neuronal activity at many levels of the nervous system are scale free and governed by power-law scaling laws.

On “long” time scales from seconds to hundreds of seconds, scale-free fluctuations and LRTC are salient in the amplitude envelopes of spontaneous neuronal oscillations in data recorded with magnetoencephalography and electroencephalography (MEG/EEG) [5] (Figure 5.1d,e). These LRTC have been repeatedly observed with power spectral, autocorrelation, and detrended fluctuation analyses (DFAs) of theta- (4–8 Hz), alpha- (8–14 Hz), beta- (14–30 Hz), and gamma- (30–80 Hz) band oscillation amplitudes. Power spectra, DFA, and correlation analyses show that fluctuations of blood-oxygenation-level-dependent (BOLD) signals in functional magnetic resonance imaging (fMRI) data also exhibit scale-free temporal [27–29] and spatiotemporal correlations [30–32]. Hence, slow neuronal fluctuations with long-range and power-law-governed temporal and spatial correlations are a unifying feature of spontaneous large-scale brain activity *in vivo* [7, 12, 33].

Pioneering work by Plenz and colleagues [6, 34, 35] has revealed that on “short” subsecond time scales, negative deflections in local field potentials form spatiotemporal cascades of activity, “neuronal avalanches” with power-law size and lifetime distributions (Figure 5.1f,g). Neuronal avalanches characterize spontaneous neuronal network activity in a wide range of species and scales ranging from organotypic cultures [6], rat brain slices *in vitro* [36], to the monkey [35]. A study using invasive electrocorticography (ECoG) to record human cortical potentials [37] reported power-law size distributions for neuronal avalanches, but did not observe consistent scaling across subjects or find the exponents to be in the range of previous studies. Using MEG and M/EEG, two recent studies [18, 38] did, however, find neuronal avalanches with scaling properties matching closely those found earlier. *In vitro*, as expected theoretically from a critical branching process [34], the scaling exponent of the avalanche size distribution is close to $-3/2$ when the branching parameter obtains a value of 1 [6]. The branching parameter is the

descendents-per-ancestors ratio and a value of 1 indicates balanced propagation of activity; a hallmark of critical dynamics. A converging body of data thus indicates that spontaneous cascades of activity in neuronal networks are statistically structured, similar to those in a critical branching process. Together, the power-law scaling of neuronal LRTC and avalanches provide converging evidence at both long and short time scales, respectively, for the fact that the brain operates near a critical state [5–7, 26, 34].

5.3

Magneto- and Electroencephalography (M/EEG) as a Tool for Noninvasive Reconstruction of Human Cortical Dynamics

In humans, neuronal activity can be noninvasively recorded with MEG and EEG (or together M/EEG) that yield millisecond-range recordings of electrical neuronal activity. MEG and EEG are the primary tools for studying the neuronal substrates of human cognitive operations by enabling the assessment of cortical dynamics concurrently with task performance. MEG and EEG have been extensively used to investigate LRTCs [39] and, more recently, also neuronal avalanches [18].

Per se, MEG and EEG are anatomically largely uninformative because the magnetic fields and electric potentials of cortical sources become linearly mixed at the sensor level [40, 41]. Nevertheless, a variety of source reconstruction techniques can be used to obtain anatomically localized M/EEG source time series for scaling-law analyses – with appropriate source model parcellations and inverse methods, the spatiotemporal correlations in spontaneous brain activity can be estimated with a good and quantifiable accuracy from most regions of the cerebral cortex. Cortically constrained minimum-norm estimate (MNE) is one straightforwardly applicable, computationally efficient, and linear approach for reconstructing the source time series with given M/EEG signals and a cortical source model.

M/EEG signals, $Y(t)$, are related to the source activity by relation $Y(t) = \Gamma X(t) + N(t)$, where Γ is the lead field matrix (forward operator) that relates the source dipole strengths to the sensor level data, $X(t)$ is the source dipole data, and $N(t)$ noise. $X(t)$ can be obtained from the measured $Y(t)$, by utilizing an MNE so that $X(t) = MY(t) = R\Gamma^T(\Gamma R\Gamma^T + \lambda^2\chi)^{-1}Y(t)$, where M is the inverse operator, R the source covariance matrix, λ^2 a regularization parameter, and χ the noise covariance matrix [42, 43]. We illustrate the inverse modeling in Figure 5.2, where first a neuronal avalanche has been identified from spontaneous inverse modeled M/EEG data (Figure 5.2a). Taking these spontaneous patch time series as original cortical source time series and finding the forward solution $Y(t) = \Gamma X(t)$, we effectively perform a virtual M/EEG recording (Figure 5.2b). The temporal structure of the avalanche is largely preserved but the signal-space topography sheds little light on the actual cortical propagation pattern. MNE source reconstruction $X(t) = MY(t)$ of these time series largely restores the original spatiotemporal source topography (Figure 5.2c).

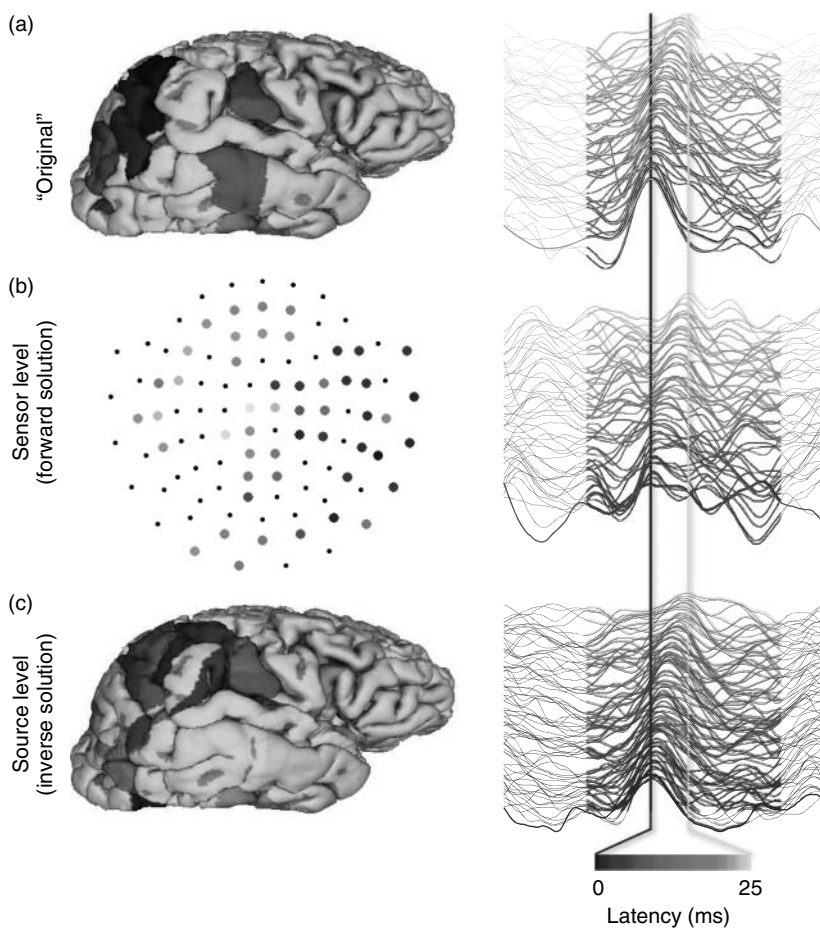


Figure 5.2 Source modeling of spontaneous M/EEG data can be used to reconstructs cortical current time series for analyses of LRTC and neuronal avalanches: a schematic illustration of the sensor- and source-level of a cortical activity cascade. (a) A neuronal avalanche was identified from source-reconstructed, real-valued, and broad-band (1–25 Hz) M/EEG data of a representative subject. In this illustration, we use these source time series as “original” waveforms of cortical currents. The left panel shows cortical patches where the peak amplitude exceeded a threshold of three standard deviations. The right panel shows the time series

of these patches. The patches and time series are color coded by the latency of the peak from the first peak in this cascade. (b) All patch time series in (a), including those not participating in the avalanche, were forward transformed to perform virtual M/EEG data acquisition and visualize the sensor level data in MEG planar gradiometers. (c) Cortically constrained minimum-norm-estimate source modeling of the sensor data (b) reconstructs the relatively well spatiotemporal characteristics of the original cascade. (Please find a color version of this figure on the color plates.)

M/EEG- and source-reconstruction-based approaches thus pave the way for investigating brain-subsystem-specific dynamics in normal and pathological conditions as well as for understanding the links between behavioral scaling laws and those of task-relevant cortical circuitry.

5.4

Slow Neuronal Fluctuations: The Physiological Substrates of LRTC

Similar to behavioral performance, several facets of neuronal activity have also been observed to fluctuate in slow (0.1–1 Hz) and infra-slow (0.01–0.1 Hz) frequency bands. In narrow-band oscillation amplitudes and BOLD signals, the slow fluctuations are characterized by scale-free LRTC as discussed already, but these fluctuations have also been found in neuronal firing rates and even in cortical and scalp potentials. Slow fluctuations in large-scale neuronal activity could thus be seen as the primary physiological underpinning for neuronal LRTC. In this section, we examine the spectrum of slow neuronal phenomena and their interconnectedness.

MEG, EEG [5, 18, 44], and ECoG [45, 46] have revealed that the amplitude fluctuations of human cortical oscillations in theta-, alpha-, beta-, and gamma-frequency bands are power-law autocorrelated in time scales from tens to hundreds of seconds and exhibit salient scale-free, fractal-like dynamics (Figure 5.1d,e). Also, in monkey EEG, infra-slow amplitude fluctuations characterize theta-, alpha-, and beta-band oscillations [47]. Moreover, in direct cortical recordings from both monkeys [48] and humans [45], the amplitudes as well as the inter-areal coherence of oscillations from delta- (1–4 Hz) to high-gamma- (100–150 Hz) frequency bands exhibit robust slow and infra-slow fluctuations (ISFs) and spectral power-law scaling throughout this frequency range. Finally, in rats [49], rabbits [50], and freely moving cats [51] theta/alpha-range oscillations exhibit spontaneous infra-slow amplitude fluctuations. While LRTC have not been quantified in all of these studies, they show unequivocally that the amplitudes of fast (>1 Hz) neuronal oscillations in general exhibit ISFs across a range of species and anatomical scales.

5.4.1

Infra-Slow Potential Fluctuations Reflect Endogenous Dynamics of Cortical Excitability

In addition to oscillation amplitude dynamics, direct cortical recordings with direct-current (DC)-coupled EEG have revealed spontaneous infra-slow potential fluctuations in rabbit [50] and cat cortices [52] *in vivo*. Later studies have observed spontaneous infra-slow cortical potential fluctuations in rats, for example, in the hippocampus [53], in primary auditory and visual cortices, as well as in several thalamic and brain stem nuclei [54–56] in both awake and anesthetized animals. In humans, spontaneous infra-slow potential fluctuations are observable

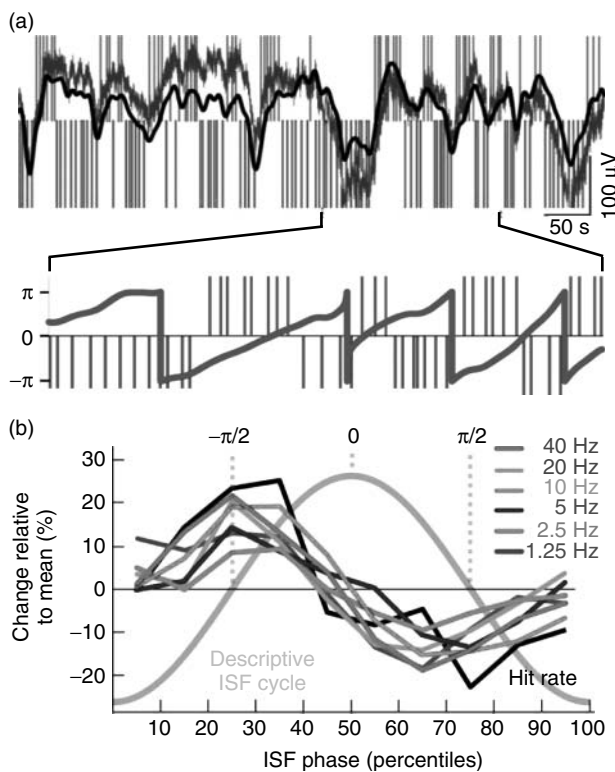


Figure 5.3 EEG ISFs are salient in an awake human EEG and correlated with behavioral ISFs. (a) Large-amplitude ISFs are readily observable in raw full-band EEG data (gray line: unfiltered, black line: band-pass filtering from 0.01 to 0.1 Hz) and reveal a correlation of the ISF phase (green line) with

psychophysical performance (blue and red ticks as in Figure 5.2). (b) Amplitudes of 1–40 Hz oscillations are correlated with the ISF phase similarly to behavior. (Adapted from [14].) (Please find a color version of this figure on the color plates.)

in human scalp EEG recordings [57, 58]. A recent series of studies has showed that spontaneous ISFs are a salient characteristic of the DC-EEG, or “full-band electroencephalography” (fbEEG) of preterm neonates [59, 60], sleeping adult subjects [61–63], and, importantly, in awake adults during TSDT task performance [14] (Figure 5.3a,b). Taken together, ISFs of neuronal activity are a fundamental characteristic observed in many species and brain structures of the nervous system.

Intriguingly, the phase of infra-slow electric potential fluctuations has been found to be correlated with the amplitudes of fast oscillations in several studies. In the lateral geniculate nucleus (LGN) of freely moving cats as well as in the cat LGN *in vitro*, spontaneous alpha-oscillation amplitude fluctuations co-vary with concurrent slow potentials [51, 64, 65]. Similarly, in the human brain, the *phase* of both neonatal

[60] and adult-sleep [63] slow potentials is strongly correlated with the amplitudes of fast neuronal oscillations. During non-rapid eye movement (REM) sleep, the slow phase is also correlated with the occurrence of transient EEG phenomena such as the K complexes and inter-ictal epileptic events [61–63]. Finally, in task-performing subjects, the phase of slow potentials is strongly correlated with the amplitudes of 1–40 Hz oscillations [14].

These data together suggest that spontaneous ISFs in cortical potential reflect variability in gross cortical excitability [66] similar to the 0.5–1 Hz sleep oscillations and the alternating cortical up- and down-states therein [67]. Hence, although LRTC can emerge even in very limited systems, such as in models of narrow-band neuronal oscillations [68], LRTC of neuronal amplitude envelopes *in vivo* are likely to reflect coupled spatiotemporal dynamics of a wide range of fast neuronal oscillations and underlying slow fluctuations in cortical excitability.

5.4.2

Slow Fluctuations in Oscillation Amplitudes and Scalp Potentials are Correlated with Behavioral Dynamics

Despite the long history of studies on slow neuronal fluctuations, their relevance at the behavior level remained unclear for decades. Two recent studies shed light on this. Monto and colleagues [14] used a somatosensory TSDT with fbEEG recordings to assess the relationship of performance fluctuations and spontaneous scalp potential fluctuations. These data revealed a relationship between stimulus detection performance and infra-slow potential fluctuations, which was conspicuous even in spontaneous unaveraged data. Quantification of this phenomenon showed that the phase but not the amplitude of the slow potential fluctuations was strongly correlated with behavioral performance so that the clusters of hits were in the same phase of the ISF cycle, whereas the misses were in the other. In addition, the amplitudes of 1–40 Hz oscillations peaked in the same phase of the ISF cycle as the successful behavioral performance, showing that these three kinds of slow fluctuations are intimately intertwined [14]. Extending these observations to reaction times, a similar correlation of spontaneous 0.06–0.2 Hz EEG fluctuations and CPT reaction time fluctuations was reported by Helps and colleagues [21]. In these data, the correlation was weaker than in the somatosensory TSDT [14], possibly because of a suppression of infra-slow variability by periodic suprathreshold stimuli (cf. [69]) and the associated strong feed-forward synaptic drive.

Taken together, these data indicate a strong covariance of the slow fluctuations in oscillation amplitudes, scalp potentials, and behavioral performance, which suggests that slow neuronal fluctuations are functionally significant at behavioral level. Although there are no data establishing a causal relationship, these studies suggest that the slow fluctuations in neuronal activity levels emerging from self-organized spontaneous brain activity might be the *raison d'être* for the clustering and slow fluctuations in behavioral performance.

5.4.3

Slow BOLD Signal Fluctuations in Resting-State Networks

Intriguingly, it appears that slow amplitude fluctuations of fast oscillations reflect the underlying dynamic architecture of spontaneous brain activity that was discovered with fMRI and defined by correlated slow fluctuations in BOLD signals among well-delineated functional brain systems [70–74]. Investigations of spontaneous brain activity in fMRI recordings have revealed a slow waxing and waning of the BOLD signal [70–75]. The amplitudes of fast neuronal oscillations are both directly correlated with these BOLD fluctuations [48, 75–79] and exhibit inter-areal correlations that closely match the patterns of BOLD signal correlations among distributed cortical regions [48, 80–83]. For instance, both the oscillation amplitudes [82, 83] and BOLD signal fluctuations [70] are positively correlated between bilateral homologous regions as well as among specific stable constellations of brain regions known as *resting-state network (RSN)* or *intrinsic connectivity network (ICN)*.

The default mode network (DMN) was among the first RSNs to be recognized. The regions belonging to DMN exhibit BOLD signal decreases during task execution [84, 85], when the BOLD signal is concurrently enhanced in task-related cortical networks. Importantly, ongoing fluctuations of neuronal activity appear to be anticorrelated between task control (“task-positive”) networks such as the frontoparietal (FP), cingulo-opercular (CO), and dorsal attention (DA) networks, and the “task-negative” DMN [86–88], although this out-of-phase connectivity is complex, directed [89], and dynamic [90].

The intermittent states of enhanced neuronal activity in the task-positive and task-negative networks could conceivably underlie the clustering of behavioral performance in CPTs. A number of fMRI studies does indeed report that pre-stimulus BOLD signals in these specific networks predict behavioral detection in somatosensory [91] and auditory [92] TSDTs. However, in tasks where behavioral performance is dependent on perceptual or executive processing, pre-stimulus BOLD signals in the specific sensory [93, 94] or frontal [95], respectively, cortical structures predict behavioral performance [96]. Already, these few studies suggest that antagonistic task-positive and task-negative network fluctuations are not a generic physiological substrate for behavioral variability in CPTs but rather the behavioral fluctuations are likely to be caused by neuronal activity fluctuations in a very task-specific brain circuitry. Nevertheless, as discussed later, this will have profound implications for understanding both the origins of criticality in behavioral time series and the concept of criticality in the brains.

Taken together, slow fluctuations in neuronal firing rates, amplitudes of fast oscillations, cortical potentials, and BOLD signals appear to be reflections of a shared underlying phenomenological entity [97]; endogenous brain dynamics with intricate spatiotemporal correlation structures that are scale-free and yet have a specific quasistable architecture. While these fluctuations are correlated with those observed in CPT performance, more studies will be needed to test the hypothesis that slow fluctuations in neuronal activity levels are the neurophysiological basis for intertrial variability in human cognitive performance.

5.5

Neuronal Scaling Laws are Correlated with Interindividual Variability in Behavioral Dynamics

The correlations between slow fluctuations in neuronal activity and behavioral performance, as well as the similar values of their mean LRTC scaling exponents, inspire the hypothesis that the behavioral LRTC scaling laws could be correlated with or even causally predicted by those of neuronal LRTCs. Whether this is the case cannot be inferred from the correlations between neuronal and behavioral fluctuations, because it is possible to have a correlation between scaling exponents without a correlation in the time-series, and vice versa, it is also possible for correlated time series to have uncorrelated scaling laws.

To test this hypothesis, we used an audiovisual TSDT with auditory, visual, and audiovisual conditions to record sensory-modality specific and uni-/bi-sensory behavioral LRTC scaling exponents, while neuronal LRTC and avalanche scaling laws were estimated with source-reconstructed M/EEG data. The behavioral scaling exponents were significantly dependent on the stimulus modality and task, but much more of the total variance was attributable to interindividual variability. Both during task performance and in a separate resting-state session, 5–30 Hz oscillation and 1–45 Hz broadband amplitude fluctuations exhibited LRTCs that were highly significant in each individual and yet showed large interindividual variability in scaling exponents. A correlation analysis of the behavioral and neuronal exponents showed that, indeed, the interindividual variability in the behavioral exponents was largely explained by the variability in neuronal LRTC scaling exponents during task performance as well as during rest (Figure 5.4a,b) and the performance of another task [18]. Moreover, the correlation of behavioral exponents with neuronal exponents in resting state and during the performance of a different task indicates that this relationship is not specific to the concurrent task but rather to traitlike individual characteristics of endogenous slow fluctuations that persist during task performance.

As source-reconstructed M/EEG data yield insight into the neuroanatomical origins of the observed signals, we also examined the topography of the brain–behavior correlations in LRTC exponents. Fascinatingly, the correlations between these scaling exponents were also localized both to the task-relevant and to task-negative, default-mode regions (Figure 5.4c). This is in line with earlier studies, suggesting that the behavioral dynamics in TSDTs could be governed by anticorrelated fluctuations among the resting-state and task-specific networks. During rest, the correlations between neuronal and behavioral LRTCs were observed to be similar, albeit slightly more widespread in cortical regions than during task execution. This provides anatomical support for the notion that correlations between the scaling exponents of neuronal and behavioral LRTC during task performance reflect persisting, fully endogenous, and individual neuronal dynamics that during task performance are confined more precisely to the task-relevant cortical regions (Figure 5.5).

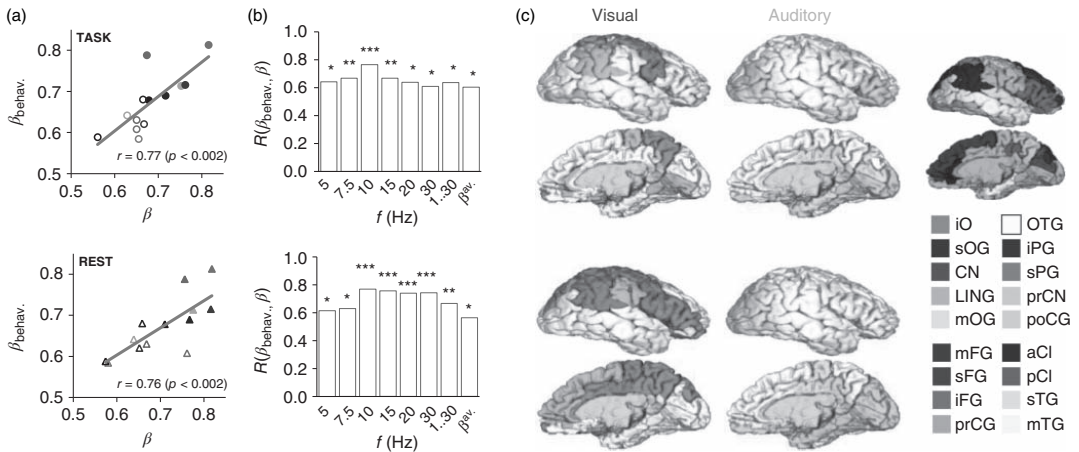


Figure 5.4 Scale-free neuronal dynamics are correlated with interindividual variability in behavioral scaling laws. (a) Mean local LRTC in the 10 Hz band (β) both during the TSDT task performance and in a separate resting-state session are correlated with the mean behavioral scaling exponents ($\beta_{\text{behav.}}$). (b) This correlation was significant in frequency bands from 5 to 30 Hz, in broadband data, and for the avalanche DFA (* $p < 0.05$, ** $p < 0.01$; *** $p < 0.005$). (c) Neuroanatomical source regions for the correlation between neuronal and behavioral LRTC scaling exponents. Pearson correlation coefficients were computed between $\beta_{\text{behav.}}$ and β in the beta and gamma (15, 20, and 30 Hz) bands for each cortical patch and significant ($p < 0.05$, FDR (false discovery rate) corrected) correlations were displayed on cortical surfaces. For each cortical patch of the Destrieux parcellation, the color intensity indicates the fraction of significant correlations across the three bands (pale 1/3, medium 2/3, full 3/3). Red: Correlation of visual behavioral scaling exponents, β_V , with the β of neuronal LRTC during visual task performance (*upper panel*) and in separate resting-state data (*lower panel*). Blue: Correlation of auditory behavioral scaling exponents, β_A , with the β of neuronal LRTC during auditory task performance and in separate resting-state data. Abbreviations: a, anterior; i, inferior; m, middle; p, posterior; pr, pre-; s, superior; C, central; Cl, cingulate; CN, cuneus; F, frontal; G, gyrus; LIN, lingual; O, occipital; P, parietal; T, temporal. Red colors, occipital; green, parietal; blue, frontal; yellow, temporal; purple, cingulate. IPG shows the angular part. (Adapted from [18].) (Please find a color version of this figure on the color plates.)

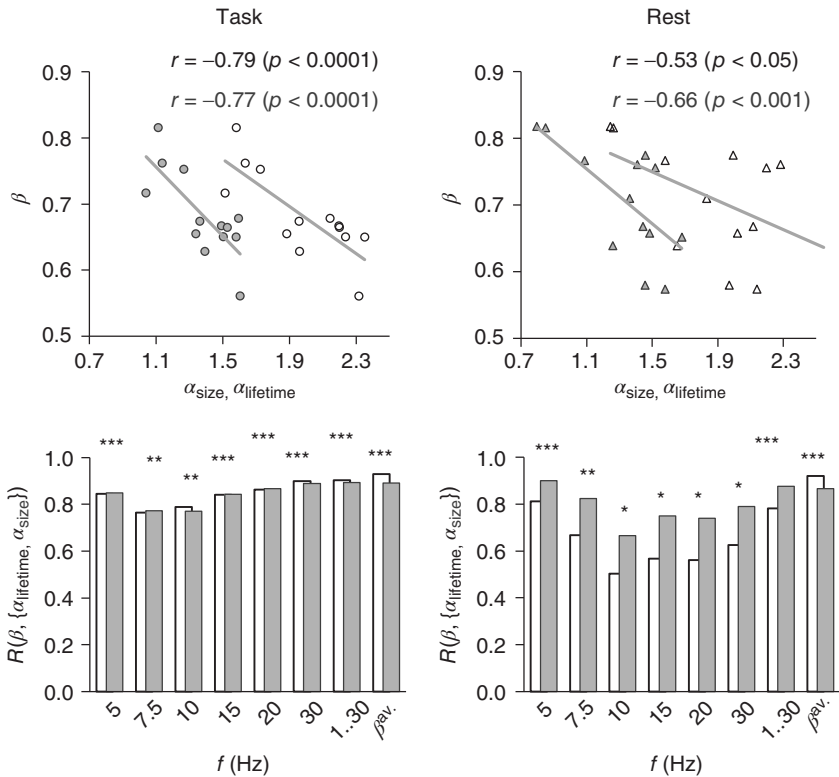


Figure 5.5 LRTC scaling exponents of neuronal amplitude fluctuations in the 10 Hz and all other studied frequency bands are strongly correlated with the scaling exponents of neuronal avalanches. (Adapted from [18].)

Taken together, these data indicate that neuronal LRTC are functionally significant at the behavioral level. The phase of ISFs appears to be a central determinant for intertrial variability, whereas the scaling laws of these fluctuations are predictively correlated with interindividual variability.

5.6

Neuronal Avalanches, LRTC, and Oscillations: Enigmatic Coexistence?

In the monkey cortex, neuronal avalanches are delimited by cycles of ongoing neuronal oscillations [35]. Also, in the human brain, neuronal avalanches may be observed noninvasively with MEG or M/EEG during periods of salient oscillatory activity [18, 38]. As in the monkey cortex, avalanches in the human cortex appear to largely have subcycle lifetimes, although this has not so far been quantified properly. In any case, it is clear that in addition to LRTC [5], neuronal avalanches also coexist with neuronal oscillations. More importantly, these data suggest that

neuronal oscillations are a conceptual, and probably also a mechanistic, watershed for temporal “macro-” and “micro”scales associated with LRTC and avalanches, respectively. LRTC are a property of the oscillation amplitude fluctuations and hence span the time scale of many cycles, whereas the avalanches are bound to subcycle time scales. Thus, for neuronal communication, the scaling laws of LRTC and avalanches relate directly to the “slow” amplitude–amplitude and “fast” phase–phase interactions, respectively [12, 41]. One could, in fact, posit that individual avalanches *per se* are propagating waves of oscillatory neuronal communication and hence conceptually indissociable from time-delayed phase–phase coupling of neuronal oscillations that is thought to underlie the coordination of neuronal communication. So far, however, this claim is confounded by the fact that analytical definitions of neuronal avalanches and phase interactions are not independent. Future studies are needed to assess the interplay between avalanche propagation statistics and patterns of oscillatory phase–phase coupling, and their possible joint role in neuronal communication.

A recent computational model of neuronal oscillations shows that at an optimal excitation–inhibition (E/I) balance, critical-state dynamics with scale-free subcycle avalanches, and multicycle LRTCs emerge [68]. Other computational modeling studies suggest that LRTC and avalanches coemerge from neuronal interactions in a critical regime [18]. These data therefore confirm the theoretical predictions [68] that the power-law exponents of avalanche size and lifetime distributions of avalanches and LRTCs are strongly correlated.

Overall, the brain appears to be unique in being a system that exhibits both scale-specific (oscillatory) phenomena as well as scale-free dynamics. *In vivo*, numerous scale-specific cellular-level mechanisms produce network oscillations in a wide frequency range from at least 1 to \sim 100 Hz [98] and there are examples of cellular oscillators even in the infra-slow frequency band (0.01–0.1 Hz) [64, 65]. Especially when considering the intricate architecture of structural connectivity [99], this multiscale nature of neuronal oscillations and their complex within- and cross-frequency interactions [14, 100] suggest that the emergence of criticality *in vivo* may be modular in a nontrivial manner. Indeed, there are already some data indicating distinct scaling exponents in different frequency bands [5, 18, 46], brain subsystems [29], and individuals [101]. This suggests that dynamically or structurally demarcated brain modules operate not “at the critical point” but in different zones of the pericritical regime.

5.6.1

The Mechanistic Insights from Interindividual Variability in Scaling Laws

Strong correlations among the scaling exponents of neuronal avalanches and of behavioral and neuronal LRTC across individuals suggest that these exponents *per se* are individual, traitlike characteristics. This is in line with the findings that LRTC in oscillation amplitude fluctuations are highly heritable [101] and correlated with individual properties such as reaction time [28]. Importantly, abnormal LRTC scaling exponents are also biomarkers for several brain diseases such as major

depression [44], epilepsy [46], Alzheimer's disease [102], schizophrenia [103], and autism [104]. Individual consistency in the behavioral LRTC scaling exponents both in sensory detection [18] and in motor timing [24] also speaks for traitlike properties.

It is thus likely that interindividual variability in neuronal scaling laws underlies the variability in behavioral dynamics, but it is unclear what mechanisms underlie and mediate these correlations. We suggest that this relationship arises mechanistically from the emergent dynamics of neuronal activity in the individual brain architecture of structural connectivity [105, 106] together with individual variability in the expression of cellular level mechanisms [107–109] that regulate, for instance, the E/I balance [68]. Cortical E/I balance is an individual trait that in part depends on expression of genes underlying especially GABAergic and serotonergic transmission and has been shown by computational modeling studies to be the critical control parameter for neuronal scaling laws [68]. Direct empirical evidence for this notion has been obtained by showing that neuronal avalanches can be shifted into a super- or subcritical regime by pharmacological suppression or enhancement, respectively, of inhibitory neurotransmission *in vitro* [110, 111]. These data together provide initial support for the hypothesis that the interindividual variability in behavioral/neuronal scaling laws is causally related to individual cortical E/I balance. While rodent optogenetic data linking E/I balance, neuronal oscillations, and social behavior on rodents indirectly supports this possibility [112], further studies are required to address this issue specifically.

5.7 Conclusions

Repeated observations of power-law long-range correlations in the behavioral and neuronal data as well as power-law-distributed neuronal avalanches suggest together that the human brain operates in a critical regime [5–7, 34]. The functional significance and causal implications of criticality in human cognitive and behavioral processes have, however, remained unclear. Recent observations demonstrate that well-delineated and task-specific cortical substrates underlie the correlation between neuronal and behavioral scaling laws and indicate that neuronal scaling laws only in specific brain systems are significant for human behavior in these tasks and hence, overall, unlikely to be epiphenomenal. Moreover, anatomical differences and task effects on scaling exponents [18, 29] show that, in addition to being a stable and heritable properties of individual nervous systems, the scaling exponents are also task-dependently malleable, dynamic, and dependent on brain states in time scales at least from minutes or tens of minutes. In other words, if the scaling exponents are taken as indicators of the brain operating near a critical state, then this operating point even in the healthy brain may flexibly fluctuate in the pericritical regime. In conclusion, we posit that the most plausible physiological explanation for behavioral scaling laws is that they arise from individual traitlike endogenous neuronal dynamics in task-specific brain circuitry [18].

Acknowledgment

We thank Klaus Linkenkaer-Hansen for many helpful discussions.

References

1. Bak, P., Tang, C., and Wiesenfeld, K. (1987) Self-organized criticality: an explanation of the 1/f noise. *Phys. Rev. Lett.*, **59**, 381–384.
2. Bak, P., Christensen, K., Danon, L., and Scanlon, T. (2002) Unified scaling law for earthquakes. *Phys. Rev. Lett.*, **88**, 178501.
3. Stanley, H.E., Amaral, L.A., Buldyrev, S.V., Gopikrishnan, P., Plerou, V., and Salinger, M.A. (2002) Self-organized complexity in economics and finance. *Proc. Natl. Acad. Sci. U.S.A.*, **99** (Suppl 1), 2561–2565.
4. Balleza, E., Alvarez-Buylla, E.R., Chaos, A., Kauffman, S., Shmulevich, I., and Aldana, M. (2008) Critical dynamics in genetic regulatory networks: examples from four kingdoms. *PLoS ONE*, **3**, e2456.
5. Linkenkaer-Hansen, K., Nikouline, V.V., Palva, J.M., and Ilmoniemi, R.J. (2001) Long-range temporal correlations and scaling behavior in human brain oscillations. *J. Neurosci.*, **21**, 1370–1377.
6. Beggs, J.M. and Plenz, D. (2003) Neuronal avalanches in neocortical circuits. *J. Neurosci.*, **23**, 11167–11177.
7. Chialvo, D.R. (2010) Emergent complex neural dynamics. *Nat. Phys.*, **6**, 744–750.
8. Kinouchi, O. and Copelli, M. (2006) Optimal dynamical range of excitable networks at criticality. *Nat. Phys.*, **2**, 348–351.
9. Shew, W.L., Yang, H., Petermann, T., Roy, R., and Plenz, D. (2009) Neuronal avalanches imply maximum dynamic range in cortical networks at criticality. *J. Neurosci.*, **29**, 15595–15600.
10. Shew, W.L. and Plenz, D. (2012) The functional benefits of criticality in the cortex. *Neuroscientist*, **19**, 88–100.
11. Stumpf, M.P. and Porter, M.A. (2012) Critical truths about power laws. *Science*, **335**, 665–666.
12. Palva, J.M. and Palva, S. (2011) Roles of multiscale brain activity fluctuations in shaping the variability and dynamics of psychophysical performance. *Prog. Brain Res.*, **193**, 335–350.
13. Gilden, D.L. and Wilson, S.G. (1995) On the nature of streaks in signal detection. *Cognit. Psychol.*, **28**, 17–64.
14. Monto, S., Palva, S., Voipio, J., and Palva, J.M. (2008) Very slow EEG fluctuations predict the dynamics of stimulus detection and oscillation amplitudes in humans. *J. Neurosci.*, **28**, 8268–8272.
15. Verplanck, W.S., Collier, G.H., and Cotton, J.W. (1952) Nonindependence of successive responses in measurements of the visual threshold. *J. Exp. Psychol.*, **44**, 273–282.
16. Verplanck, W.S., Cotton, J.W., and Collier, G.H. (1953) Previous training as a determinant of response dependency at the threshold. *J. Exp. Psychol.*, **46**, 10–14.
17. Wertheimer, M. (1953) An investigation of the randomness of threshold measurements. *J. Exp. Psychol.*, **45**, 294–303.
18. Palva, J.M., Zhigalov, A., Hirvonen, J., Korhonen, O., Linkenkaer-Hansen, K., and Palva, S. (2013) Neuronal long-range temporal correlations and avalanche dynamics are correlated with behavioral scaling laws. *Proc. Natl. Acad. Sci. U.S.A.*, **110**, 3585–3590.
19. Gilden, D.L., Thornton, T., and Mallon, M.W. (1995) 1/f noise in human cognition. *Science*, **267**, 1837–1839.
20. Gilden, D.L. (2001) Cognitive emissions of 1/f noise. *Psychol. Rev.*, **108**, 33–56.
21. Helps, S.K., Broyd, S.J., James, C.J., Karl, A., and Sonuga-Barke, E.J.S.

- (2010) The attenuation of very low frequency brain oscillations in transitions from a rest state to active attention. *J. Psychophysiol.*, **23**, 191–198.
22. Ihlen, E.A. and Vereijken, B. (2010) Interaction-dominant dynamics in human cognition: Beyond 1/f(alpha) fluctuation. *J. Exp. Psychol. Gen.*, **139**, 436–463.
23. Thornton, T.L. and Gilden, D.L. (2005) Provenance of correlations in psychological data. *Psychon. Bull. Rev.*, **12**, 409–441.
24. Torre, K., Balasubramaniam, R., Rheaume, N., Lemoine, L., and Zelaznik, H.N. (2011) Long-range correlation properties in motor timing are individual and task specific. *Psychon. Bull. Rev.*, **18**, 339–346.
25. Werner, G. (2009) Viewing brain processes as critical state transitions across levels of organization: neural events in cognition and consciousness, and general principles. *BioSystems*, **96**, 114–119.
26. Werner, G. (2010) Fractals in the nervous system: conceptual implications for theoretical neuroscience. *Front. Physiol.*, **1**, 1–28.
27. Suckling, J., Wink, A.M., Bernard, F.A., Barnes, A., and Bullmore, E. (2008) Endogenous multifractal brain dynamics are modulated by age, cholinergic blockade and cognitive performance. *J. Neurosci. Methods*, **174**, 292–300.
28. Wink, A.M., Bullmore, E., Barnes, A., Bernard, F., and Suckling, J. (2008) Monofractal and multifractal dynamics of low frequency endogenous brain oscillations in functional MRI. *Hum. Brain Mapp.*, **29**, 791–801.
29. He, B.J. (2011) Scale-free properties of the functional magnetic resonance imaging signal during rest and task. *J. Neurosci.*, **31**, 13786–13795.
30. Eguiluz, V.M., Chialvo, D.R., Cecchi, G.A., Baliki, M., and Apkarian, A.V. (2005) Scale-free brain functional networks. *Phys. Rev. Lett.*, **94**, 018102.
31. Expert, P., Lambiotte, R., Chialvo, D.R., Christensen, K., Jensen, H.J., Sharp, D.J., and Turkheimer, F. (2010) Self-similar correlation function in brain resting-state functional magnetic resonance imaging. *J. R. Soc. Interface*, **8**, 472–479.
32. Tagliazucchi, E., Balenzuela, P., Fraiman, D., and Chialvo, D.R. (2012) Criticality in large-scale brain fMRI dynamics unveiled by a novel point process analysis. *Front. Physiol.*, **3**, 15.
33. He, B.J., Zempel, J.M., Snyder, A.Z., and Raichle, M.E. (2010) The temporal structures and functional significance of scale-free brain activity. *Neuron*, **66**, 353–369.
34. Plenz, D. and Thiagarajan, T.C. (2007) The organizing principles of neuronal avalanches: cell assemblies in the cortex? *Trends Neurosci.*, **30**, 101–110.
35. Petermann, T., Thiagarajan, T.C., Lebedev, M.A., Nicolelis, M.A., Chialvo, D.R., and Plenz, D. (2009) Spontaneous cortical activity in awake monkeys composed of neuronal avalanches. *Proc. Natl. Acad. Sci. U.S.A.*, **106**, 15921–15926.
36. Stewart, C.V. and Plenz, D. (2006) Inverted-U profile of dopamine-NMDA-mediated spontaneous avalanche recurrence in superficial layers of rat prefrontal cortex. *J. Neurosci.*, **26**, 8148–8159.
37. Solovey, G., Miller, K.J., Ojemann, J.G., Magnasco, M.O., and Cecchi, G.A. (2012) Self-regulated dynamical criticality in human ECoG. *Front. Integr. Neurosci.*, **6**, 44.
38. Shriki, O., Alstott, J., Carver, F., Holroyd, T., Henson, R.N., Smith, M.L., Coppola, R., Bullmore, E. and Plenz, D. (2013) Neuronal avalanches in the resting MEG of the human brain. *J. Neurosci.*, **33** (16), 7079–7090.
39. Hardstone, R., Poil, S.S., Schiavone, G., Jansen, R., Nikulin, V.V., Mansvelder, H.D., and Linkenkaer-Hansen, K. (2012) Detrended fluctuation analysis: a scale-free view on neuronal oscillations. *Front. Physiol.*, **3**, 450.
40. Hamalainen, M., Hari, R., Ilmoniemi, R.J., Knuutila, J., and Lounasmaa, O.V. (1993) Magnetoencephalography theory, instrumentation, and applications to noninvasive studies of the working

- human brain. *Rev. Mod. Phys.*, **65**, 413–497.
41. Palva, S. and Palva, J.M. (2012) Discovering oscillatory interaction networks with M/EEG: challenges and breakthroughs. *Trends Cogn. Sci.*, **16**, 219–230.
 42. Hamalainen, M.S. and Ilmoniemi, R.J. (1994) Interpreting magnetic fields of the brain: minimum norm estimates. *Med. Biol. Eng. Comput.*, **32**, 35–42.
 43. Lin, F.H., Belliveau, J.W., Dale, A.M., and Hamalainen, M.S. (2006) Distributed current estimates using cortical orientation constraints. *Hum. Brain Mapp.*, **27**, 1–13.
 44. Linkenkaer-Hansen, K., Monto, S., Ryttsala, H., Suominen, K., Isometsa, E., and Kahkonen, S. (2005) Breakdown of long-range temporal correlations in theta oscillations in patients with major depressive disorder. *J. Neurosci.*, **25**, 10131–10137.
 45. Ko, A.L., Darvas, F., Poliakov, A., Ojemann, J., and Sorensen, L.B. (2011) Quasi-periodic fluctuations in default mode network electrophysiology. *J. Neurosci.*, **31**, 11728–11732.
 46. Monto, S., Vanhatalo, S., Holmes, M.D., and Palva, J.M. (2007) Epileptogenic neocortical networks are revealed by abnormal temporal dynamics in seizure-free subdural EEG. *Cereb. Cortex*, **17**, 1386–1393.
 47. Ehlers, C.L. and Foote, S.L. (1984) Ultradian periodicities in EEG and behavior in the squirrel monkey (saimiri sciureus). *Am. J. Primatol.*, **7**, 381–389.
 48. Leopold, D.A., Murayama, Y., and Logothetis, N.K. (2003) Very slow activity fluctuations in monkey visual cortex: implications for functional brain imaging. *Cereb. Cortex*, **13**, 422–433.
 49. Allers, K.A., Ruskin, D.N., Bergstrom, D.A., Freeman, L.E., Ghazi, L.J., Tierney, P.L., and Walters, J.R. (2002) Multisecond periodicities in basal ganglia firing rates correlate with theta bursts in transcortical and hippocampal EEG. *J. Neurophysiol.*, **87**, 1118–1122.
 50. Aladjalova, N.A. (1957) Infra-slow rhythmic oscillations of the steady potential of the cerebral cortex. *Nature*, **179**, 957–959.
 51. Hughes, S.W., Lorincz, M., Cope, D.W., Blethyn, K.L., Kekesi, K.A., Parri, H.R., Juhasz, G., and Crunelli, V. (2004) Synchronized oscillations at alpha and theta frequencies in the lateral geniculate nucleus. *Neuron*, **42**, 253–268.
 52. Norton, S. and Jewett, R.E. (1965) Frequencies of slow potential oscillations in the cortex of cats. *Electroencephalogr. Clin. Neurophysiol.*, **19**, 377–386.
 53. Penttonen, M., Nurminen, N., Miettinen, R., Sirvio, J., Henze, D.A., Csicsvari, J., and Buzsaki, G. (1999) Ultra-slow oscillation (0.025 hz) triggers hippocampal after discharges in wistar rats. *Neuroscience*, **94**, 735–743.
 54. Filippov, I.V. and Frolov, V.A. (2004) Very slow potentials in the lateral geniculate complex and primary visual cortex during different illumination changes in freely moving rats. *Neurosci. Lett.*, **373**, 51–56.
 55. Filippov, I.V., Williams, W.C., Krebs, A.A., and Pugachev, K.S. (2007) Sound-induced changes of infraslow brain potential fluctuations in the medial geniculate nucleus and primary auditory cortex in anaesthetized rats. *Brain Res.*, **1133**, 78–86.
 56. Filippov, I.V., Williams, W.C., Krebs, A.A., and Pugachev, K.S. (2008) Dynamics of infraslow potentials in the primary auditory cortex: component analysis and contribution of specific thalamic-cortical and non-specific brainstem-cortical influences. *Brain Res.*, **1219**, 66–77.
 57. Aladjalova, N.A. (1964) in *Progress in Brain Research*, Slow Electrical Processes in the Brain, vol. 7 (ed. N.A. Aladjalova), Elsevier Publishing Company, pp. 39–58.
 58. Trimmel, M., Mikowitzsch, A., Groll-Knapp, E., and Haider, M. (1990) Occurrence of infraslow potential oscillations in relation to task, ability to concentrate and intelligence. *Int. J. Psychophysiol.*, **9**, 167–170.
 59. Vanhatalo, S., Tallgren, P., Andersson, S., Sainio, K., Voipio, J., and Kaila, K. (2002) DC-EEG discloses prominent,

- very slow activity patterns during sleep in preterm infants. *Clin. Neurophysiol.*, **113**, 1822–1825.
60. Vanhatalo, S., Palva, J.M., Andersson, S., Rivera, C., Voipio, J., and Kaila, K. (2005) Slow endogenous activity transients and developmental expression of K+-cl- cotransporter 2 in the immature human cortex. *Eur. J. Neurosci.*, **22**, 2799–2804.
 61. Marshall, L., Molle, M., Fehm, H.L., and Born, J. (1998) Scalp recorded direct current brain potentials during human sleep. *Eur. J. Neurosci.*, **10**, 1167–1178.
 62. Marshall, L., Molle, M., Fehm, H.L., and Born, J. (2000) Changes in direct current (DC) potentials and infra-slow EEG oscillations at the onset of the luteinizing hormone (LH) pulse. *Eur. J. Neurosci.*, **12**, 3935–3943.
 63. Vanhatalo, S., Palva, J.M., Holmes, M.D., Miller, J.W., Voipio, J., and Kaila, K. (2004) Infraslow oscillations modulate excitability and interictal epileptic activity in the human cortex during sleep. *Proc. Natl. Acad. Sci. U.S.A.*, **101**, 5053–5057.
 64. Lorincz, M.L., Geall, F., Bao, Y., Crunelli, V., and Hughes, S.W. (2009) ATP-dependent infra-slow (<0.1 hz) oscillations in thalamic networks. *PLoS ONE*, **4**, e4447.
 65. Hughes, S.W., Lorincz, M.L., Parri, H.R., and Crunelli, V. (2011) Infraslow (<0.1 hz) oscillations in thalamic relay nuclei basic mechanisms and significance to health and disease states. *Prog. Brain Res.*, **193**, 145–162.
 66. Aladjalova, N.A. (1964) in *Progress in Brain Research*, Slow Electrical Processes in the Brain, vol. 7 (ed. N.A. Aladjalova), Elsevier Publishing Company, pp. 60–88.
 67. Destexhe, A., Hughes, S.W., Rudolph, M., and Crunelli, V. (2007) Are corticothalamic 'up' states fragments of wakefulness. *Trends Neurosci.*, **30**, 334–342.
 68. Poil, S.S., Hardstone, R., Mansvelder, H.D., and Linkenkaer-Hansen, K. (2012) Critical-state dynamics of avalanches and oscillations jointly emerge from balanced excitation/inhibition in neuronal networks. *J. Neurosci.*, **32**, 9817–9823.
 69. Linkenkaer-Hansen, K., Nikulin, V.V., Palva, J.M., Kaila, K., and Ilmoniemi, R.J. (2004) Stimulus-induced change in long-range temporal correlations and scaling behavior of sensorimotor oscillations. *Eur. J. Neurosci.*, **19**, 203–211.
 70. Biswal, B., Yetkin, F.Z., Haughton, V.M., and Hyde, J.S. (1995) Functional connectivity in the motor cortex of resting human brain using echo-planar MRI. *Magn. Reson. Med.*, **34**, 537–541.
 71. Cooper, R., Crow, H.J., Walter, W.G., and Winter, A.L. (1966) Regional control of cerebral vascular reactivity and oxygen supply in man. *Brain Res.*, **3**, 174–191.
 72. Damoiseaux, J.S., Rombouts, S.A., Barkhof, F., Scheltens, P., Stam, C.J., Smith, S.M., and Beckmann, C.F. (2006) Consistent resting-state networks across healthy subjects. *Proc. Natl. Acad. Sci. U.S.A.*, **103**, 13848–13853.
 73. De Luca, M., Beckmann, C.F., De Stefano, N., Matthews, P.M., and Smith, S.M. (2006) fMRI resting state networks define distinct modes of long-distance interactions in the human brain. *Neuroimage*, **29**, 1359–1367.
 74. Lowe, M.J., Mock, B.J., and Sorenson, J.A. (1998) Functional connectivity in single and multislice echoplanar imaging using resting-state fluctuations. *Neuroimage*, **7**, 119–132.
 75. Mantini, D., Perrucci, M.G., Del Gratta, C., Romani, G.L., and Corbetta, M. (2007) Electrophysiological signatures of resting state networks in the human brain. *Proc. Natl. Acad. Sci. U.S.A.*, **104**, 13170–13175.
 76. Goldman, R.I., Stern, J.M., Engel, J. Jr., and Cohen, M.S. (2002) Simultaneous EEG and fMRI of the alpha rhythm. *Neuroreport*, **13**, 2487–2492.
 77. Laufs, H., Krakow, K., Sterzer, P., Eger, E., Beyerle, A., Salek-Haddadi, A., and Kleinschmidt, A. (2003) Electroencephalographic signatures of attentional

- and cognitive default modes in spontaneous brain activity fluctuations at rest. *Proc. Natl. Acad. Sci. U.S.A.*, **100**, 11053–11058.
78. Sadaghiani, S., Scheeringa, R., Lehongre, K., Morillon, B., Giraud, A.L., and Kleinschmidt, A. (2010) Intrinsic connectivity networks, alpha oscillations, and tonic alertness: a simultaneous electroencephalography/functional magnetic resonance imaging study. *J. Neurosci.*, **30**, 10243–10250.
79. Scholvinck, M.L., Maier, A., Ye, F.Q., Duyu, J.H., and Leopold, D.A. (2010) Neural basis of global resting-state fMRI activity. *Proc. Natl. Acad. Sci. U.S.A.*, **107**, 10238–10243.
80. Brookes, M.J., Woolrich, M., Luckhoo, H., Price, D., Hale, J.R., Stephenson, M.C., Barnes, G.R., Smith, S.M., and Morris, P.G. (2011) Investigating the electrophysiological basis of resting state networks using magnetoencephalography. *Proc. Natl. Acad. Sci. U.S.A.*, **108**, 16783–16788.
81. de Pasquale, F., Della Penna, S., Snyder, A.Z., Lewis, C., Mantini, D., Marzetti, L., Belardinelli, P., Ciancetta, L., Pizzella, V., Romani, G.L., and Corbetta, M. (2010) Temporal dynamics of spontaneous MEG activity in brain networks. *Proc. Natl. Acad. Sci. U.S.A.*, **107**, 6040–6045.
82. Nikouline, V.V., Linkenkaer-Hansen, K., Huttunen, J., and Ilmoniemi, R.J. (2001) Interhemispheric phase synchrony and amplitude correlation of spontaneous beta oscillations in human subjects: a magnetoencephalographic study. *Neuroreport*, **12**, 2487–2491.
83. Hipp, J.F., Hawellek, D.J., Corbetta, M., Siegel, M., and Engel, A.K. (2012) Large-scale cortical correlation structure of spontaneous oscillatory activity. *Nat. Neurosci.*, **15**, 884–890.
84. Raichle, M.E., MacLeod, A.M., Snyder, A.Z., Powers, W.J., Gusnard, D.A., and Shulman, G.L. (2001) A default mode of brain function. *Proc. Natl. Acad. Sci. U.S.A.*, **98**, 676–682.
85. Gusnard, D.A. and Raichle, M.E. (2001) Searching for a baseline: functional imaging and the resting human brain. *Nat. Rev. Neurosci.*, **2**, 685–694.
86. Clare Kelly, A.M., Uddin, L.Q., Biswal, B.B., Castellanos, F.X., and Milham, M.P. (2008) Competition between functional brain networks mediates behavioral variability. *Neuroimage*, **39**, 527–537.
87. Fox, M.D., Snyder, A.Z., Vincent, J.L., Corbetta, M., Van Essen, D.C., and Raichle, M.E. (2005) The human brain is intrinsically organized into dynamic, anticorrelated functional networks. *Proc. Natl. Acad. Sci. U.S.A.*, **102**, 9673–9678.
88. Fox, M.D., Zhang, D., Snyder, A.Z., and Raichle, M.E. (2009) The global signal and observed anticorrelated resting state brain networks. *J. Neurophysiol.*, **101**, 3270–3283.
89. Uddin, L.Q., Kelly, A.M., Biswal, B.B., Xavier Castellanos, F., and Milham, M.P. (2009) Functional connectivity of default mode network components: correlation, anticorrelation, and causality. *Hum. Brain Mapp.*, **30**, 625–637.
90. Chang, C. and Glover, G.H. (2010) Time-frequency dynamics of resting-state brain connectivity measured with fMRI. *Neuroimage*, **50**, 81–98.
91. Boly, M., Balteau, E., Schnakers, C., Degueldre, C., Moonen, G., Luxen, A., Phillips, C., Peigneux, P., Maquet, P., and Laureys, S. (2007) Baseline brain activity fluctuations predict somatosensory perception in humans. *Proc. Natl. Acad. Sci. U.S.A.*, **104**, 12187–12192.
92. Sadaghiani, S., Hesselmann, G., and Kleinschmidt, A. (2009) Distributed and antagonistic contributions of ongoing activity fluctuations to auditory stimulus detection. *J. Neurosci.*, **29**, 13410–13417.
93. Hesselmann, G., Kell, C.A., and Kleinschmidt, A. (2008) Ongoing activity fluctuations in hMT+ bias the perception of coherent visual motion. *J. Neurosci.*, **28**, 14481–14485.
94. Hesselmann, G., Kell, C.A., Eger, E., and Kleinschmidt, A. (2008) Spontaneous local variations in ongoing

- neural activity bias perceptual decisions. *Proc. Natl. Acad. Sci. U.S.A.*, **105**, 10984–10989.
95. Coste, C.P., Sadaghiani, S., Friston, K.J., and Kleinschmidt, A. (2011) Ongoing brain activity fluctuations directly account for intertrial and indirectly for intersubject variability in stroop task performance. *Cereb. Cortex*, **21**, 2612–2619.
96. Sadaghiani, S., Hesselmann, G., Friston, K.J., and Kleinschmidt, A. (2010) The relation of ongoing brain activity, evoked neural responses, and cognition. *Front Syst. Neurosci.*, **4**, 20.
97. Palva, J.M. and Palva, S. (2012) Infra-slow fluctuations in electrophysiological recordings, blood-oxygenation-level-dependent signals, and psychophysical time series. *Neuroimage*, **62**, 2201–2211.
98. Buzsaki, G. and Draguhn, A. (2004) Neuronal oscillations in cortical networks. *Science*, **304**, 1926–1929.
99. Cammoun, L., Gigandet, X., Meskaldji, D., Thiran, J.P., Sporns, O., Do, K.Q., Maeder, P., Meuli, R., and Hagmann, P. (2012) Mapping the human connectome at multiple scales with diffusion spectrum MRI. *J. Neurosci. Methods*, **203**, 386–397.
100. Palva, J.M., Palva, S., and Kaila, K. (2005) Phase synchrony among neuronal oscillations in the human cortex. *J. Neurosci.*, **25**, 3962–3972.
101. Linkenkaer-Hansen, K., Smit, D.J., Barkil, A., van Beijsterveldt, T.E., Brussaard, A.B., Boomsma, D.I., van Ooyen, A., and de Geus, E.J. (2007) Genetic contributions to long-range temporal correlations in ongoing oscillations. *J. Neurosci.*, **27**, 13882–13889.
102. Montez, T., Poil, S.S., Jones, B.F., Manshanden, I., Verbunt, J.P., van Dijk, B.W., Brussaard, A.B., van Ooyen, A., Stam, C.J., Scheltens, P., and Linkenkaer-Hansen, K. (2009) Altered temporal correlations in parietal alpha and prefrontal theta oscillations in early-stage alzheimer disease. *Proc. Natl. Acad. Sci. U.S.A.*, **106**, 1614–1619.
103. Nikulin, V.V., Jonsson, E.G., and Brismar, T. (2012) Attenuation of long-range temporal correlations in the amplitude dynamics of alpha and beta neuronal oscillations in patients with schizophrenia. *Neuroimage*, **61**, 162–169.
104. Lai, M.C., Lombardo, M.V., Chakrabarti, B., Sadek, S.A., Pasco, G., Wheelwright, S.J., Bullmore, E.T., Baron-Cohen, S., MRC AIMS Consortium, and Suckling, J. (2010) A shift to randomness of brain oscillations in people with autism. *Biol. Psychiatry*, **68**, 1092–1099.
105. Honey, C.J., Sporns, O., Cammoun, L., Gigandet, X., Thiran, J.P., Meuli, R., and Hagmann, P. (2009) Predicting human resting-state functional connectivity from structural connectivity. *Proc. Natl. Acad. Sci. U.S.A.*, **106**, 2035–2040.
106. Deco, G., Jirsa, V.K., and McIntosh, A.R. (2011) Emerging concepts for the dynamical organization of resting-state activity in the brain. *Nat. Rev. Neurosci.*, **12**, 43–56.
107. Eagleson, K.L., Campbell, D.B., Thompson, B.L., Bergman, M.Y., and Levitt, P. (2011) The autism risk genes MET and PLAUR differentially impact cortical development. *Autism Res.*, **4**, 68–83.
108. Bruening, S., Oh, E., Hetzenauer, A., Escobar-Alvarez, S., Westphalen, R.I., Hemmings, H.C. Jr., Singewald, N., Shippenberg, T., and Toth, M. (2006) The anxiety-like phenotype of 5-HT receptor null mice is associated with genetic background-specific perturbations in the prefrontal cortex GABA-glutamate system. *J. Neurochem.*, **99**, 892–899.
109. Won, H., Mah, W., Kim, E., Kim, J.W., Hahn, E.K., Kim, M.H., Cho, S., Kim, J., Jang, H., Cho, S.C., Kim, B.N., Shin, M.S., Seo, J., Jeong, J., Choi, S.Y., Kim, D., Kang, C., and Kim, E. (2011) GIT1 is associated with ADHD in humans and ADHD-like behaviors in mice. *Nat. Med.*, **17**, 566–572.
110. Shew, W.L., Yang, H., Petermann, T., Roy, R., and Plenz, D. (2009) Neuronal avalanches imply maximum dynamic

- range in cortical networks at criticality. *J. Neurosci.*, **29**, 15595–15600.
111. Shew, W.L., Yang, H., Yu, S., Roy, R., and Plenz, D. (2011) Information capacity and transmission are maximized in balanced cortical networks with neuronal avalanches. *J. Neurosci.*, **31**, 55–63.
112. Cardin, J.A., Carlen, M., Meletis, K., Knoblauch, U., Zhang, F., Deisseroth, K., Tsai, L.H., and Moore, C.I. (2009) Driving fast-spiking cells induces gamma rhythm and controls sensory responses. *Nature*, **459**, 663–667.

6

The Turbulent Human Brain: An MHD Approach to the MEG

Arnold J. Mandell, Stephen E. Robinson, Karen A. Selz, Constance Schrader, Tom Holroyd, and Richard Coppola

6.1

Introduction

Among the currently available time-dependent functional imaging technologies for the human brain [1], the noninvasive magnetoencephalograph (MEG) is unique in providing excellent temporal resolution and good spatial resolution of cortical activity. The MEG signals are relatively insensitive to the boundaries of conductivity in the head, allowing for simple electromagnetic modeling of sources. MEG has been found useful in diverse function-related neuroanatomical source localizations. Some examples include brain tumors [2], epilepsy [3, 4], neurogenic pain [5], and affective priming [6]. MEG has also contributed to the characterization of brain states in response to psychopharmacological agents [7–9] and global brain disorders such as Down's syndrome [10], Alzheimer's disease [11], the Parkinson syndrome [12], and schizophrenia [13, 14]. MEG source imaging techniques, analogous to those reflecting brain activity involving oxygen and glucose brain energy utilization such as positron emission tomography (PET) and blood-oxygenation-level-dependent (BOLD) imaging, quantifies localized changes of source amplitude and power [15, 16].

Linear MEG signal analyses include methods making use of linear analyses, including the correlation functions and band-limited time–power–frequency spectra (e.g., the Stockwell transform) [17–19]. Nonlinear analyses of the MEG using measure theoretic approaches to dynamical systems have included a variety of entropies and characteristic dimension [20–23]. Most, if not all, MEG studies that have focused on localizing sources or characterizing fields have treated the MEG record as an implicitly epiphenomenal reflection of underlying electrophysiological events [24]. Source space analysis of the MEG signals use localization techniques such as the *linearly constrained minimum variance* (LCMV) beamformer (SAM, *synthetic aperture magnetometry*) to estimate the relevant electrical sources from the magnetic signal [25–27].

In these studies, we regard the MEG recording of magnetic signals as themselves, $B = \mu H$; where B is the magnetic flux density, μ is the magnetic permeability (of the material in a vacuum), and H is the magnetic field strength. Although the MEG is generally modeled using quasi-static electromagnetic equations, the signals are time varying and therefore are more accurately described by the Maxwell equations. It has been assumed that this correction is small enough, below frequencies of about 1 kHz, to be ignored. We minimize the emphasis on the inferred E field and its associated electrical currents, J_i , except when required by the *magnetohydrodynamic*, MHD approach's development. Deemphasizing E and J_i is almost similar to the treatment of generic B and E fields in space plasmas, in which the electrical field E (the curl of which is the magnetic field), conducts fast enough to outrun the slower, potentially information-bearing B field [28–30].

It is more typical in MHD magnetic induction and conservation equations to consider, relative to the E currents, the B field as “frozen in,” whereas our premises are different with respect to the temporal disparity. The MHD assumption is that the magnetic field may travel unchanged, $\nabla \cdot B = 0$. Our fluctuating brain MEG data suggests something different. In this change in the usual MHD emphasis, the faster conducting E field has disappeared out of the frame and the B field is fluctuating as a time-dependent dynamical system.

We characterize the magnetic flows of the brain's B fields as dynamical systems in the context of MHD; the study of magnetic field dynamics in an electrically conducting fluid setting [31], which may involve aqueous solutions of electrolytes such as those found in the brain's interstitial and cerebrospinal fluids [32].

This orientation has led us to a set of new ideas concerning the potential information processing roles of both global and local brain magnetic field dynamics resembling those of MHD turbulence. Studies of 171 subjects' global resting MEG records have yielded evidence, through the use of multiple measures, for turbulent magnetic field dynamics. This includes possibilities for a pathophysiology and therapy involving dynamical entropy deficits [33]. A new combination of MEG source localization techniques [25, 34] and a new measure of topological/metric entropy, *rank vector entropy (RVE)* [35], has resulted in a localization technique using the *RVE* measure of complexity that appears more sensitive to neocortical dynamics than is simple power. The known informational richness of turbulent (chaotic) dynamics [36, 37] and the evidence for the existence of this state(s) in the human brain's local and global magnetic fields [38, 39] combine to suggest a new MHD field dynamic approach to MEG studies of human brain mechanisms and behavior. For example, might it be possible through frequency and nonlinear parameter optimization to configure a *very weak external dynamical magnetic field in the pT range* that would interact with the brain's intrinsic magnetic field directly (too weak for the induction of local electrical events), yielding increases or decreases in the brain's *magnetic field dynamical entropy* of potential therapeutic benefit.

6.2

Autonomous, Intermittent, Hierarchical Motions, from Brain Proteins Fluctuations to Emergent Magnetic Fields

Intuitively, outlining the spatial-temporal, anatomical-dynamical hierarchies [40] of the taskless, resting human neocortex in action, we imagine the neuronal intracellular structural and functional aqueous entropy-driven proteins in autonomous motion with a documented range of characteristic times from 10^4 to 10^{-12} s [41–43]; scaling (fractal) subthreshold ion channel membrane-conductance fluctuations [44]; a variety of intermittent single-neuron spike discharge patterns [45]; local and global neuronal network dynamics [46] including intermittent bursting and avalanches [47]; surrounding the network are the local E field potentials [48, 49]; and finally, the subject of this work, the dynamical patterns found in the brain's emergent magnetic fields [32]. Studies of the influence of weak fields on neuronal thresholds and activity [12–14] suggest a physiological role for “feedback fields” [50] in emergent E and B fields.

Analogous to the shift in focus from the particle to the field in quantum field theory, we move our attention from neuronal and neural network electrical sources to the dynamics found in attendant brain magnetic fields. Although dipolar and multipolar magnetic polarity have played a prominent role in linear static models of the MEG record [51–53], from the nonlinear graphical and measure point of view, magnetic field diffusivity leading to sharing and crossing of magnetic field lines and their apparently intrinsic stretch and fold dynamics (in R^2) result in complicated fields. In these MEG studies of the task-free, “resting” human brain, we consider the behavior of the brain's magnetic field, B qua B , and not as an inferential, epiphenomenal reflection of the activity of its electrophysiological source [10]. A (necessarily) three-dimensional magnetic field in an electrical conducting fluid, such as the ionic interstitial fluid of the brain, behaves akin to an ensemble of differential material line elements that are being stretched and folded into turbulent flows [29]. It is usually represented graphically in R^3 with the stretch in the x direction, fold in the y direction, and E field (via charge velocity v)– B field shear in the z direction [54]. Dynamically, this stretch–fold–shear, SFS, mechanism operates in thin magnetic diffusive layers at the boundaries of repeating arrays of magnetic helical vortices (solenoidal flows) [55].

As noted earlier, a natural theoretical context for the examination of the behavior of human brain magnetic fields is MHD, particularly in light of our discovery that human brain magnetic fields are measure-theoretically turbulent [56]. Heisenberg's heuristic formulation of statistically isotropic and homogeneous hydrodynamic turbulence, his use of the physical mixing length of eddy viscosity, and energy (power) spectral functions [57] inspired Chandrasekhar to launch a dozen year (1949–1961) investigation of turbulent electrically conducting fluids in the presence of magnetic fields [58]. His initial finding was that Heisenberg's integral equations could be reduced to a linear first-order differential equation by a change in variables using wave number spectral representation, $F(k)$, as the dependent variable and vorticity, $\omega = \nabla \times v$, curl of the flow velocity, as the independent variable. This

led to his studies of convective dynamic instabilities in electrical conducting fields and MHD turbulence using techniques such as double and triple correlation tensors involving the interactions of charge velocity and the scalar intensity of magnetic fields. He used equations with eddy viscosity and electrical conductivity to elucidate dissipative energy exchanges between velocity and magnetic fields. His formulations of MHD turbulence included the recovery of the Kolmogorov inertial zone spectral scaling exponent of 5/3. Chandrasekhar can be said to have played a large part in creating the mathematical discipline of MHD.

6.3

Magnetic Field Induction and Turbulence; Its Maintenance, Decay, and Modulation

Using general vectorial field equations and their graphical representations, Figure 6.1 summarizes an MHD context for the dynamical analyses of the time dependent changes in human brain magnetic flux density, B . Figure 6.1a portrays the vectorial flow of the magnetic field generated by the flow of the impressed ionic current (and return current, not shown) via the dendritic tree of Cahal's classical pyramidal neuron, which lies orthonormal to the surface of the neocortex. We assume a charge velocity, v , estimated to be 150 ms^{-1} [59], field strength of $2\text{--}4\text{ mV mm}^{-1}$ [50], and designate arbitrarily a current $I \approx 10^{-7}\text{ A}$, a free space permeability (ease of magnetization of the material) of $\mu_0 = 4\pi \times 10^{-7}$ and making measurement at distance r^3 (m). This leads to an estimate of the B field Faraday induction (Figure 6.1b,c) within the range

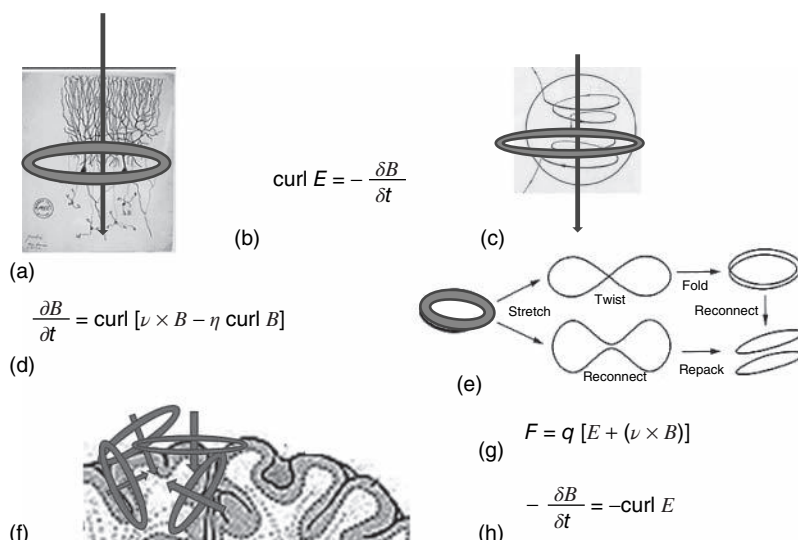


Figure 6.1 (a–h) Graphical and symbolic representations of the putative MHD of the neocortical magnetic fields.

of the human brain B fields we have observed experimentally using the MEG: $B = \mu_0 I / 2\pi r \approx 2 \times 10^{-13 \text{ to } -15} T \approx (500\text{--}4000) \text{ fT}$, Figure 6.1b,c [11, 13].

As noted, the generic dynamical motions of turbulent field lines are the *nonuniform stretch and fold mechanism* [54, 60, 61]. It is responsible for increased “multifractal” magnetic flux density [62] and results from the *nonaxisymmetric, nonuniform mutual shear of electrical charge flow velocity, v , and magnetic fields fluxes, B* [30]. Magnetic field turbulent *mixing* arises from shear-induced, nonuniform stretching and folding of magnetic field lines, magnetic loop diffusivity engendered connections and their reconnections. This accompanies volume preserving folding and packing, thereby increasing the local magnetic flux density in regional B fields (Figure 6.1d,e), while not violating the conservation equations of MHD [58]. The vectorial direction of the traveling charges of pyramidal cell dendritic trees is orthogonal to the sulci and gyri of the neocortical surface. The transverse magnetic field B loops are generally parallel to the neocortical surface but they also become involved in its gyri and sulci corrugation-induced multidirectionality of E and B fields as shown (Figure 6.1f). It is of interest in this regard that recent studies of spatial order in neocortical pyramidal layers (layer V in mouse) have revealed that the repeating patterns of pyramidal cell “clusters” are arranged tangentially, a parallel orientation with the neocortical magnetic field [63]. Shear engendered eddy viscosity is minimal when the two fields are mutually transverse. Shear viscosity is maximal (and B is better maintained against dissipative loss) when E and B fields are aligned. In astrophysical contexts, magnetic-field-aligned currents are called *Birkeland currents* [64]. Evolutionarily (say from chicken to man), the increasing corrugation of the neocortical surface increases sheer when E and B fields are parallel (Figure 6.1f). This contributes further to magnetic field line diffusivity, crossings, and turbulence in the MEG signal.

Another contribution to the turbulent mixing of the B field is the Lorentz force, F , on a point charge, q , with instantaneous velocity, v . Along with its electric E , and magnetic B fields, F is given by equation, Figure 6.1g. It is similar to a modulating “feedback” term in the electromagnetic system. Of particular interest here is what some call the Lorentz or *magnetic force* $= qv \times B$ [65]. In Figure 6.1h, the Lorentz force field reversal of the induction equation, Figure 6.1b, is the (“left-hand rule”) Lenz electromagnetic version of the Newtonian conservation of energy law. Currents arising from a magnetic flux engender a magnetic flux with its curl counter in field direction to the original current [65]. There cannot be an infinite regress of increasing magnetic energy. On the other hand, a possible net B field yield is possible in turbulent MHD in which the presence of turbulence is equivalent to the presence of a magnetic dynamo. This is clearest in the context of the *kinetic dynamo problem*, transient dynamos have been found to be theoretically and experimentally possible in nonaxisymmetric, three-dimensional MHD turbulent systems with a relatively large charge v [28]. The graphics and equations of Figure 6.1 serve as frameworks for the following ergodic measure theoretic, statistical studies of human brain MHD turbulence. In this context, we study magnetic field “resting” human MEG data [14, 66] and their statistical characterizations using quantities

from ergodic measure theory [37, 67–69] to test the hypothesis that the *taskless human brain magnetic fields are intrinsically turbulent*.

In the interest of examining time-dependent, spatially extended human brain magnetic field activity, we study time series of the spatial derivatives of B field, $\partial B / \partial l$ where l is the distance between symmetrically placed MEG sensors constituting a symmetric sensor differences series, $ssds$. The values ranged between 10^{-15} and 10^{-13} T , $\approx 50\text{--}4000 \text{ fT}$ as recorded from pairs of centrally located MEG sensors; in these studies, the difference $[C16(L) - C16(R)]$ constitutes the $ssds$. The use of $ssds$ exploits the approximate hemispheric symmetry of the human brain [70] by quantifying the *asymmetry*, the nonaxiosymmetry, required to avoid magnetic field cancellations and allowing the observations of turbulence-related (“dynamo-like”) dynamics [28, 71]. The *ssds transformation* serves several purposes: (i) it includes a turbulent spatial-derivative parameter over time; (ii) imposes a local gauge, $[(0-ssds \text{ max}) \text{ fT} / \sqrt{\text{Hz}}]$; (iii) serves as a time traveling, local regularized comparison; (iv) reduces the penetrance of electromagnetic field correlates of blink, cough, and movement as well as the cardiac and respiratory signals that both symmetric sensors generally share; (v) tends to cancel the symmetrically shared MEG (and electroencephalography (EEG)) $\Delta, \theta, \alpha, \beta, \gamma$ modes. In their place, we find the dynamics in the *scaling, similarity regime* [72]; (vi) is similar to the difference over space of the paired velocity probes used in experimental hydrodynamic turbulence studies; and (vii) minimizes central values and emphasizes higher moments and outliers, an effect facilitating the quantitative description of the dynamical and statistical properties of turbulent intermittency [73, 74].

Figure 6.2 represents the spatial sensitivity profile of a single central pair difference recording, the single $ssds = [C23(L) - C23(R)]$ in which the difference is considered a single differential sensor, that is, the planar gradient, ∇B , of the normal field. Note that the lighter colored portion of the graphs include a significant portion of the three-dimensional region including neocortical layers II and III in central, parietal, frontal, and some temporal areas. The techniques similar to that used here, of the paired sensor difference series, $ssds(i)$, have been used to reduce or remove the mean and *double or more the higher moments* in analyses of nonstationary neural membrane conductance noise [73–75].

Figure 6.2 illustrates (on the same subject’s magnetic resonance imaging (MRI) the MEG-correlated voxels from a single C16, $ssds$ pair difference recording seen in

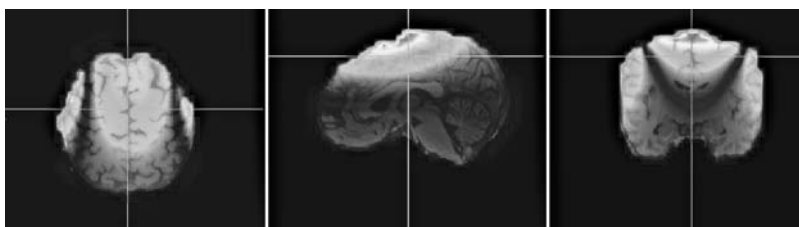


Figure 6.2 In lighter color, the neocortical magnetic field $r > 0.70$ correlated with the activity of the single sensor pair difference, $[C23(L) - C23(R)] = ssds$.

the axial, sagittal, and coronal planes. Lighter areas indicate the voxel neocortical volume to which the red C23 sensor pair's ssds is ($r > 0.70$) correlated. The single (one pair difference) ssds sensor (in red) appears to capture much of the magnetic neocortical surface we study in the central brain's global B field dynamics.

The B field pair difference is a field property ($\partial B / \partial l$) with a centimeter length scale) being naturally equipped with a tangential gradient, in our studies (with the exception of Figure 6.2) $\nabla[C16(L) - C16(R)] = ssds$. This spatial derivative is the primary time-dependent data in our studies of the properties of the MEG magnetic field time series. In constructing and using measures on ssds, we recall Ornstein's theorem, using isomorphism in measure as criteria, says there was only 1 equiv measure on expanding, mixing dynamical systems, its *entropy* [76, 77]. If one were to inquire further as to how the entropy should be computed, the answer (as of now) would be that there is no single method. In its place, there are many measure-theoretic equivalent ones [78]. Our effort to make this estimation has been to use multiple (each acknowledged as incomplete) measures, simultaneously noting the patterns among their values relative to those of other measures and patterns of relative changes among them [79–82]. With respect to changing relationships between measures, a robust example is the variably inverse relationship between topological entropy, h_T , and the scaling exponent α , the slope of the middle third of the log–log plot of the frequency (power) spectral transformation [32].

Measures are computed on the time-dependent behavior of orbits embedded in n -dimensional phase space. This corresponds to tracking the smooth ssds orbital visits to available “states” or “configurations.” Phase space orbits are typically graphed in dimension R^n , with values corresponding to those at time t , time $t - 1 \dots t - n$, as in Figure 6.3, in which $n = 3$. Most of the mathematical foundations of ergodic invariant measures to be used in an examination of these phase portraits has been established in the settings of well-defined, uniformly hyperbolic (expanding, contracting, mixing) statistically stationary states such as Axiom A diffeomorphisms [76, 83] that have Gaussian statistics. Real human brain magnetic field data, similar to hydrodynamic turbulence itself, is nonstationary, nonuniform, and prominent as the dynamic that has made for the most difficulty in mathematical hydrodynamic theory, intermittency [84–86]. Its statistics tend to have nonfinite variance. It is also the case that intermittency is a dominant dynamical pattern at many levels of observation in time series of brain function, from bursting in membrane conductance and neuronal spike trains [87], neuronal avalanches [47], local field potentials (LFPs), and regional and more global magnetic fields [32, 88, 89]. Intermittency in paired velocity-probe-difference time series is characteristic of hydrodynamic and MHD turbulence [36, 84, 90].

The recurrence plot [91], Figure 6.4, is an $[i, j]$ array of dots in an n -square space in which a dot is placed at $[i, j]$ whenever $x(j)$ is sufficiently close to $x(i)$ (close to be empirically defined). Recurrence plots of orbits composed of uniformly random, transitive point sets look pale and smooth, whereas orbits with intermittent “runs” of close-by values, that is, intermittency, demonstrate variously sized, denser aggregates of points. The recurrence plot of intermittent dynamics appears to “bunch up” in the recurrence plots [92]. This affords an immediate qualitative

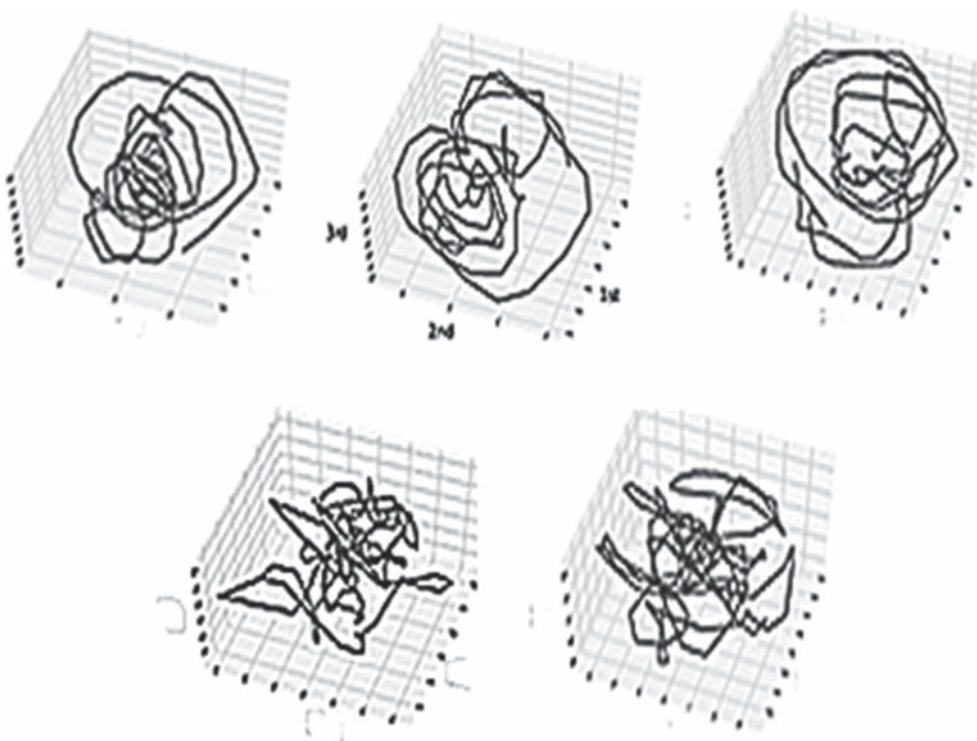


Figure 6.3 Phase-delay portraits of MEG from a central, C16, region of *ssds* orbits embedded in R^3 .

picture of the *extent of the intermittency*, which then can be quantified in a variety of ways including the *reciprocal of the leading Lyapounov exponent*, Λ , or in the form of a related computable entropy, the logarithm of the leading Lyapounov exponent, $\ln \Lambda$ [93, 94]. For example, given that the average $\Lambda > 0$, the longer the average relative time of laminar flow, $\Lambda = 0$, $\log \Lambda = 1$, between the aperiodic bursts, the lower the value of $\Lambda > 0$.

Figure 6.5 displays the Morlet wavelet transformations of the leading autocovariance matrix eigenfunction. These results are obtained from determining the leading eigenvector of a correlation-decay-determined, lagged autocovariance matrix computed on 16.6 s of MEG (recorded at 600 Hz with 150 Hz cut-off). This leading eigenvector is then convolved with the original *ssds* series, leading to a new series named for their originators, Broomhead–King autocovariance eigenfunctions [95, 96]. The resulting process is analogous to what might be viewed as a leading autocovariance matrix eigenvector-weighted, nearest neighbor averaged series [97]. Morlet wavelet transformation of this autocovariance eigenfunction (Figure 6.5) demonstrates obvious intermittency in greater than three orders of magnitude of wavelengths (from 10 ms to 10 s). This results in wavelet time-frequency modes we call *strudels* (German for *whirlpools*). In dimension R^3 , the geometry would resemble

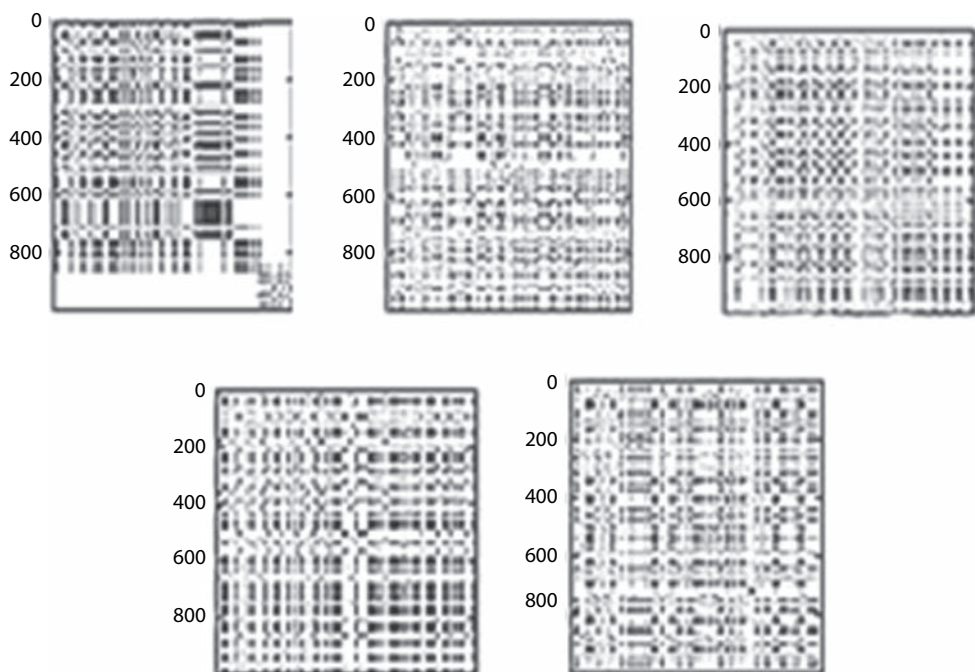


Figure 6.4 Recurrence plots corresponding to the phase space dynamics seen in Figure 6.3.

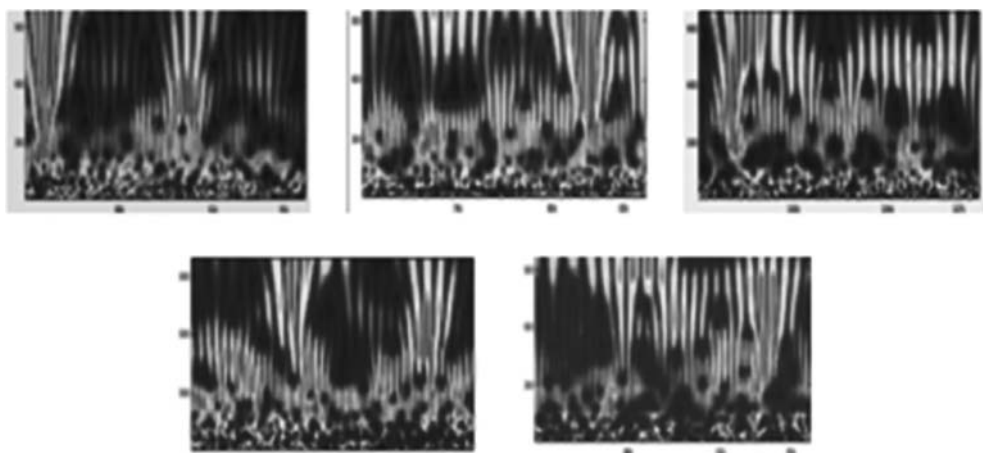


Figure 6.5 Morlet wavelet transformations of the leading autocovariance eigenfunctions of the ssds corresponding to the phase-delay portraits and recurrence plots of Figures 6.3 and 6.4.

vortices. In the context of MHD turbulence, these almost simultaneous, multiscale wavelet modes might be called *turbulent eddies*. They are defined generally as color-coded amplitudes originating below the bottom third of the wavelet graph and dilating past wavelet graph's upper boundary. We have speculated that these strudels, occurring in the taskless “resting” condition and occurring irregularly every 3–8 s, mirror the subjective experience of episodes of “daydreaming” [38] manifesting similar time scales [98, 99].

In Figure 6.5, notice that the intermittent and sometimes close to regular, smallest scale magnetic field activity (at the bottom of the graph) appears to seed the expansion of the *strudels* into larger scale, longer, mother wavelet wave lengths into the upper part and beyond of the wavelet graphs. As noted earlier, these electromagnetic dynamics are similar to those observed in studies of the “kinetic magnetic dynamo problem” in the low-resistivity domain [61, 62]. This problem as stated is “... given a flow in a conducting fluid, will a small magnetic seed amplify exponentially with time ...” [29, 30, 61]. Among the possible interpretations of the strudels of Figure 6.5 are possible propagating “coherence potentials” as aggregations of critical avalanches in neocortical neural networks [47, 100] or in the context of neural network percolation theory [101]. As a smooth dynamical MHD system, these strudels are intermittent turbulent eddies [28–30, 32].

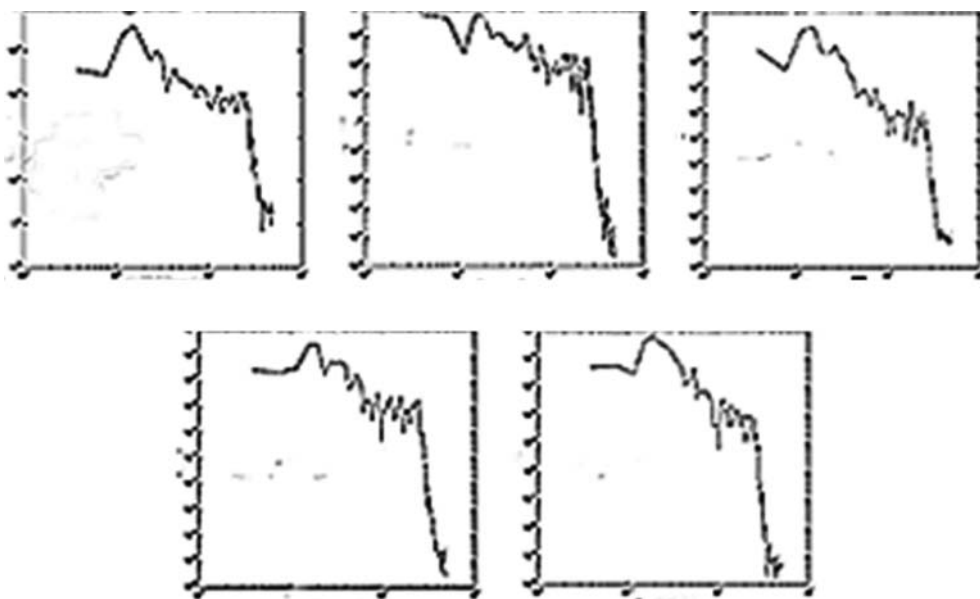


Figure 6.6 The power law scaling $ssds$, characteristically ranges from $3/2$ to $5/3$ as seen in these log-log graphs of power (frequency) spectra. The range of exponents are consistent with both critical behavior [47, 100] and

as in Figure 6.3, Figure 6.4, and Figure 6.5, turbulent intermittency. In Figure 6.6, the x axis is the log frequency and the y axis is the log power.

Figure 6.6 illustrates power spectra of the central, C16 *ssds* with *similarity dimension* [90] or scaling parameter, α . We minimize the mean square deviation in the middle third of the plot to estimate the log–log spectral slope yielding an $f^{-\alpha}$ fractional power law, $\alpha = 1.54 \pm 0.27$ ($n = 171$). Generally, this finding is consistent with “self-similar” dynamics, manifesting a hierarchy of time scales. The observable 150 Hz acquisition cutoff serves as the upper bound on the frequency range available to examine for “scale freeness” such that the power spectral scaling approximates three orders of magnitude in range. Fractional power law, “self-similar” behavior in human MEG signals, has been reported by others as evidence of intermittent turbulent flow [90] as well as critical behavior of neuronal avalanches [47, 101]. These findings are not definitively diagnostic of either as the brain qualifies more generally as a practically infinite variable cooperative system with strong interactions and many degrees of freedom that almost always demonstrate fractional power laws [40, 72, 89]. It should also be noted that the time scale(s) of the observations, the sample length(s) being studied, and choices of relevant limit laws interact with the intrinsic dynamics such that a discriminating diagnosis using the power law scaling exponent alone is not reasonably possible.

The theoretical frame of reference for the results in Figure 6.7 derive from the confluence of the Poincare–Thom’s geometric-topological thinking about differential equations and Boltzmanns–Gibbs thoughts about populations, distributions

Invariant Measure	Phase Shase	Computational Methods	Mean/SD $n = 171$
Lyapounov, Λ	Divergence of neighboring trajectories	Exponential rate of separation of nearby initial conditions, $\Lambda = 1 \rightarrow$ doubling in time between sample points	0.4865 ± 0.11
Topological entropy, $h(T)$	Emergence of new orbits	Growth rate of the trace of exponentiated transition-incidence matrix	0.8042 ± 0.10
Capacity dimension, D_C	Complexity of manifold of support	Slope log of fraction of hypercubes occupied/ log linear size of hypercubes	2.254 ± 0.192
Spectral scaling Exponent, α ($f^{-\alpha}$)	Relative power of frequency modes	Slope of least squares fit of log frequency-log power plot of frequency(power) spectra	1.50 ± 0.34

Figure 6.7 Summary of MEG *ssds* studies of $n = 171$ subjects’ dynamical measures. Each value is the result of 1197 individual computations derived from the mean values of the measures obtained from seven consecutive

10 s samples from each subject recorded at 600 Hz with a 150 Hz corner frequency. In the absence of turbulence, the values would approximate, $\Lambda \leq 0$, $h_T \leq 0$, $D_C = 3.0$, and as unstructured white noise, $\alpha = 1$ (log 0).

of solutions to differential equations as in statistical mechanics. Behind both those points of view are last century's advances in topology, point set topology and differential topology. These gave us systematic "rules of form" such as stable and unstable fixed points, limit cycles, quasi-periodic n-tori, and chaotic attractors. It is these kinds of intuitions that underlie the current revolution in understanding of even quite subtle dynamical patterns in the data.

It is this conceptual background that has evolved into the modern "applied" ergodic theory of dynamical systems [37, 102–104]. In this context, real-valued time series can be reconstructed as phase space objects whose orbits fill up their shape (on) smooth manifolds for geometric, topological, and statistical characterization [67, 68, 105]. The Bowen shadow lemma taught us that early data points are filling up the same manifold in phase space as the later points, and the lemma states that the early points will (in an approximate way) outline the manifold(s).

Entropies (and their quasi-equivalent measures) arise as statistical invariants of those phase space objects. What is meant these days by "ergodic" is the maintenance of n , $n \leq 1$, measures, $\mu_{i \dots n}$ in spite of (i) differing initial conditions and, often, (ii) parametric distortions of the attractor's manifold geometry short of violating its topological constraints. We study "ergodic" measures [78] on many single-orbit dynamics on these manifolds [106]. The symmetric MEG sensor difference sequences, a field property in its spatial differential form, $\nabla B(t)$ or in the form of our data, $ssds_i$, are treated as the output of dynamical systems on differentiable manifolds, here, treating the field as a manifold. Computationally, the system's dynamics can be seen as a smooth map on an n -dimensional manifold. In passing, we note that a change in topological properties such as nearness, continuity, or dimension often, if not always, is associated with the universal dynamics of phase transitions.

Figure 6.7 is a summary of the results of an $n = 171$ subjects study of ergodic, invariant measures [78] computed on the $ssds$ derived from the C16 difference pairs in the MEG records of 4 min, taskless resting condition. Seven consecutive 10 s samples from each of the 171 subjects were each analyzed for the measures indicated in Figure 6.6 and then averaged to obtain that subject's values. Each individual's average was then averaged over the 171 subjects to obtain the population average for that measure. Thus, each value in Figure 6.7 is the result of 1197 individual computations of 10 s each of $ssds$ from recordings from C16 difference pairs recorded at 600 Hz with 150 Hz cutoff. The leading Lyapounov exponent has a strongly positive average consistent with the stretch and fold dynamics of MHD turbulence; the value would be ≤ 0 for the nonturbulent state. Figure 6.7 shows that the *lim sup* of entropies, the topological entropy, h_T , is also strongly positive, consistent with the value of the positive leading Lyapounov exponent and consistent with MHD turbulence.

Figure 6.7 indicates the box counting capacity dimension $D_C = 2.254$ (fractionally less than the phase embedding space dimension of 3.0), which, in a lower dimensional, nonphysical model [30] has been attributed to the nonuniformity of the stretch and fold dynamics of MHD turbulence. The power spectral scaling exponent of approximately 3/2 (ranging up to 5/3) is consistent with the scaling exponents

found in classical MHD turbulent intermittency as well as the critical behavior of neocortical neuronal network avalanches [47]. As noted, these comparisons are subject to the influence of the timescales of observations, sample lengths, and choice of limit.

From Figures 6.3, 6.4, 6.5, and 6.6 and the measure table (Figure 6.7) one concludes that *ssds*-MEG resting record yields both qualitative graphical and quantitative measure-statistical evidence consistent with the presence of intermittent MHD turbulence in the global neocortical MEG fields. We now pursue the possibility that in addition to being representative of the human brain's *global* magnetic fields, measure-theoretic indications of turbulence can also be found to be discriminatively *local* source activity.

6.4

Localizing a Time-Varying Entropy Measure of Turbulence, Rank Vector Entropy (RVE) [35, 107], Using a *Linearly Constrained Minimum Variance* (LCMV) Beamformer Such as *Synthetic Aperture Magnetometry* (SAM) [25, 34], Yields State and Function-Related Localized Increases and Decreases in the RVE Estimate

Localization of regions of neocortical pyramidal cell networks as putative MEG sources has, until recently, been the major focus of MEG development and applications [108, 109]. The operational assumption of brain magnetic field linearity [110] supports the central role of *independent static magnetic dipoles* as commonly used in localization algorithms [27, 111]. Magnetic fields associated with the imposed intracellular ionic and extracellular return currents are postulated to be independent and thus directly superimposable in the determination of power. The characteristic deficiencies in matrix rank, the one to many observation-to-source, inverse MEG mapping makes more direct inverse techniques poorly approximate at best [4]. In addition, we recall that these point equivalent magnetic dipoles [51, 112, 113] are embedded in temporally and spatially fluctuating, power law distributions of turbulent magnetic fields [32, 56, 114].

A significant advance in source localization, particularly well suited for time-dependent, nonaveraged MEG signals is the volumetric mapping of estimated source activity using what has been called the *synthetic aperture magnetometer* (SAM) [25, 34, 115]. It is a member of the class of minimum variance spatially filtering techniques called *beamformers* [116]. Generally, both the multiple dipole, LCMV beamformer [111] and the sequentially singular, four-dimensional SAM approach to localizing the time-dependent source contribution of a specific voxel involves spatial and temporal correlations or equivalent covariances [27] among the sensor array. Beamformers can be considered spatially selective filters that minimize variance (power) because of all coherent signals except for particular cerebral locations. Thus, SAM may be regarded as "spatially selective noise reduction," where the remaining signal after minimization of all signals subject to a gain one constraint for the location being examined is an estimate of the activity at that location.

The (idealized) standard setting consists of multiple fixed, uncorrelated magnetic (linear) dipoles in a spherical, homogeneous, conducting medium with tangential sources. SAM scans in this three-dimensional, R^3 space and at each position estimates the dominant dipole vector such that sources are estimated for three locations and one directional dimension in R^4 . By including dipolar direction in addition to location, SAM serves as a higher resolution localization technique than vector LCMV beamformers [27, 111]. Because location and volumetric complexity, rather than directionality, was the focus of this work, we have elected to use a scalar LCMV beamformer in these studies.

The assumptions of independence of the magnetic fluxes, decomposability, the finite variance of the MEG field distributions, and the associated superimpositions of linear systems all serve to support the use of the sequence of linear transformations to construct source estimates [25, 34]. However, following this localization, there is, here, a change in computational context to that of *symbolic dynamics* and *ergodic measure theory* of the nonlinear dynamics (of turbulence) [36, 84, 102, 117, 118]. Unlike most of the older techniques, the *RVE* does not require the difficult choices of embedding dimension and partitions of the phase space forming adjacency or transition matrices. The object of the analyses is the one-dimensional time series of the magnetic field densities as the observables [35]. The symbolic dynamic-related technique of *RVE* combines the topological property of order as rank [77] and the metric property of normalized probability measures over the space of available rank-ordered states [119].

The one-dimensional series of discretely sampled, MEG-recorded, magnetic flux densities, $B_{i \dots t}$, define a time series with t samples. Where f_s defines the sample frequency and f_c is the cutoff or corner frequency, lag $\xi = f_s/2f_c$ is the integer intervals composing the window of W lagged samples beginning with the k th sample. $W_k = [B_{k, k+\xi, k+2\xi, \dots, k+W\xi}]$. These measurements are then converted to their integer *ranks*, $R_k = [R_{k, k+\xi, k+2\xi, \dots, k+W\xi}]$ such that the number of possible rank-ordered states = $W!$ unique symbols. The partition of states is defined by the number of discrete steps in the chosen window size; for example, a windowed ordering of $W = 5$ has five factorial, $5! = 120$ possible integer-ordered states. As an example, the rank ordering of an MEG time series in a $W = 5$ window of observations: ... [3.2, 4.5, 2.3, 1.1, 5.1] ... would be ordered as [3, 4, 2, 1, 5] with added weight 1 to its symbol place as one of the possible orderings in the 120 place histogram, which, when normalized, becomes the probability distribution. The histogram contains the cumulative number of each rank vector state. To continue to register the local time dependence, the frequency count of the occurrence of symbols is allowed to exponentially decay with time, that is, the symbols counts are derived from a “leaky integrator.” From the histogram-derived probability distribution, the rank vector metric entropy is computed as the Shannon/Kolmogorov entropy, $h_{rve} = -\sum_n p_n \log_2 p_n$ [120, 121]. *RVE* remained in the turbulent regime with the median $RVE \approx 0.92$ around which it decreased (coded blue) or increased (coded red) in response to perturbations by exogenous stimuli or tasks and spontaneously in the task-free, “resting” condition. Note that this value for *RVE* is within our standard error of the mean topological entropy, $h_T = 0.8042 \pm 0.10$, reported in the results of the 171 subject study

summarized in Figure 6.7 using the entirely different algorithmic method. This serves as a quantitative validation for the new RVE entropy estimate [35].

The averaged MEG signal shows the prominent N100 (lower right). The averaged RVE (lower left) demonstrates a faster decrease corresponding to the N100 and a slower increase in RVE. In this study, $W = 5$ with 120 possible configurations of rank. The band width examined ranged from 4 to 150 Hz.

Time-locked, event-related electromagnetic responses to external, sensory, and internal, cognitive, events have often been viewed as perturbations of ongoing oscillatory (fluctuating) brain processes [122, 123]. Called *EROs*, *event-related oscillations*, they have been speculated to result from a stimulus-evoked ordering of oscillatory phase [124, 125] which can be apparent in several band widths simultaneously [126]. As in Figure 6.8, observation of the RVE decrement was found in band width of 4–150 Hz and was also observed when the generic MEG and EEG frequency bands were examined individually [35]. On the other hand, band width specificity of phase synchronization processes has also been reported to differ among brain regions and brain states [127, 128].

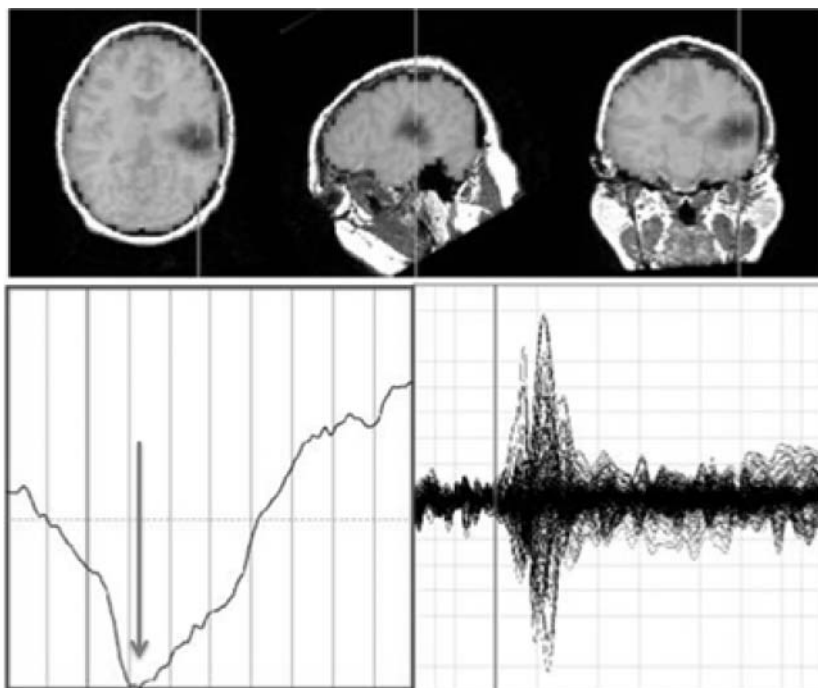


Figure 6.8 In this P300 envelope, -0.2 to $+0.8$ s with 100 ms intervals, the transient decrease in MEG RVE (darker grey brain areas) corresponding to the N100 localizes to the primary auditory cortex as seen in axial, sagittal, and coronal views. It

accompanies an auditory evoked response to rarer tone bursts in an “odd ball” task [131], marked in time by the arrow. No characteristic changes in RVE that marked the associated P200 or P300 were observed.

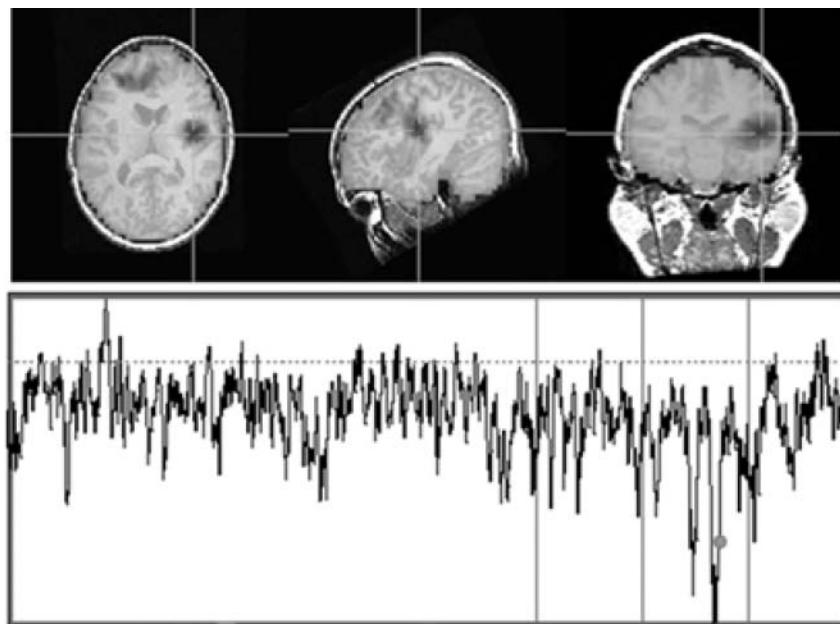


Figure 6.9 In the taskless, “resting” condition, time series of *RVE* (bottom) and their neuroanatomical localization (top), reveal spontaneous, multiple, intermittent, localized regions of decreased *RVE* (from

the horizontal dotted line median ≈ 0.92). These can be seen in the axial, sagittal, and coronal views of the frontal, temporal, and parietal areas.

It is not difficult to imagine that increased coherence of phase in ongoing magnetic field turbulent oscillations could account for the apparent reduced complexity reflected in the decrement of *RVE* (shown as darker gray scale) as seen in Figure 6.8. Pharmacological studies have demonstrated such relationships between electromagnetic phase coherence and measures of complexity used to characterize nonlinear dynamical systems [129, 130] (Figure 6.9 and Figure 6.10).

6.5

Potential Implications of the MHD Approach to MEG Magnetic Fields for Understanding the Mechanisms of Action and Clinical Applications of the Family of TMS (Transcranial Magnetic Stimulation) Human Brain Therapies

Experiments directed toward elucidating endogenous or exogenous field effects on brain-related dynamics until recently have been relatively rare. An early exception was the systematic studies of field effects on the behavior of large, *Mauthner cells* in some fish and amphibian brains [48, 132]. It was found that their associated, interleaved, parallel interneurons generated a positive extracellular current that led to a threshold increasing “down state.” The positive current field was observed to hyperpolarize the M-cell axon hillock and initial axonal segment, reducing

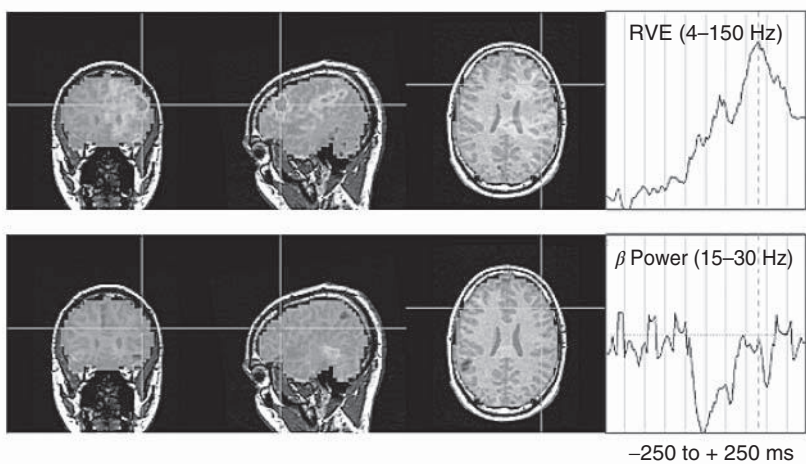


Figure 6.10 Tracking both RVE and MEG power simultaneously during 500 ms of the resting condition reveals an apparent dissociation between the time-dependent average virtual sensor's RVE and average virtual sensor's *beta power* (right panels) and their corresponding neocortical locations (left panels). This opens up the possibility that

minimal additional energy beyond maintenance of “resting” may be required for magnetic field, neocortical entropic-informational processing. This suggests the possibility that an electromagnetic nondissipative Hamiltonian equations related to the Lorenz force may be representative of neocortical magnetic field dynamics, Section 6.3, Figure 6.1.

the probability of the occurrence of action potentials. The spatial ordering of the interneurons facilitated the extracellular spread of the positive field, which inhibited or retarded M-cell depolarization. Because this effect occurred without known electrotonic gap junctions, the investigator concluded that the coupling of positive and negative fields was occurring in extracellular ionic fluid space. Similar phenomena involving the parallel arrangement of basket and pyramidal cells in the hippocampus have been reported [133, 134]. As we have noted earlier (Section 6.3 and Figure 6.1f) that from an MHD point of view, nonaxisymmetric, near-parallel magnetic and current fields are turbulent and can exist (equivalently, identically [28]) as *magnetic dynamos* [28–30].

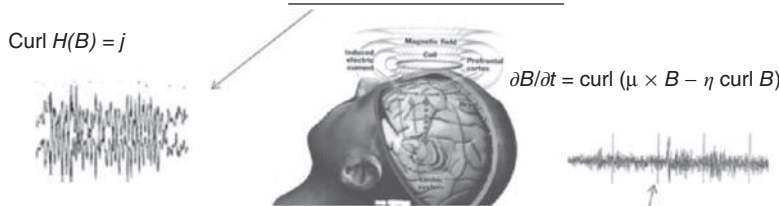
In a series of principally Russian neurophysiological studies, exogenous, weak, static, and alternating magnetic fields (sometimes DC and AC simultaneously) were shown to have intensity-dependent influences on rat behavior [135], ion flux through cellular membranes [136, 137], and ionic calcium release in brain tissue [138]. The latter has been known as the *Hall effect* for magnetic field influences in membranes with ion channels restrained directionally in calcium-ion-channel-containing membranes. Another, more controversial explanation of the transduction of weak magnetic field influences into biological changes involves calcium-specific 7.0 Hz *electron–cyclotron resonances*. This process involving the calcium ion magnetic field target for resonance was protected from aqueous dampening by its putative location in a protein hydrophobic pocket [139]. The

B -field-induced changes in the electronic properties of calcium become reflected in changes in brain protein conformation via the ion's actions as an induced-fit allosteric ligand [140]. At a cellular level, exposure of pituitary corticotrope cells to calcium resonant, 7.0 Hz, 9.2 μT , weak magnetic fields have been shown to initiate neurite formation [141]. It is of particular interest that studies have emphasized the importance of the magnetic relative to the electric field in the radiation-induced efflux of calcium ions from brain tissue [142].

We postulate that the driving of endogenous brain magnetic flux fields further into the turbulent regime would be associated with increases in the brain's global field dynamical entropies (Figure 6.7). If confirmed, this effect has both pathophysiological and therapeutic significance. Over the past three decades, studies of a variety of self-excitatory biological systems [33, 40, 81, 143] have suggested that deficits in dynamical entropy and their repletion outline a scenario for a pathophysiology and treatment in dynamical disorders [144]. Augmenting the turbulence in brain magnetic field dynamics with its attendant increment in measure-theoretic entropies may be major mechanisms of action of the transcranial magnetic stimulation (TMS) therapies [145, 146]. Figure 6.11 summarizes the current and proposed theories of the action of the transcranial magnetictherapies.

Implications of two contrasting theories of TMS

- (1) Current rTMS theory and practice assumes that relatively strong B field induction of electric current stimulates neocortical network activity graded in strength in the MRI range 0.5 – 2.0 T and standardized with a stimulus-induced thumb jerk. Moving magnetic fields induce an electric current resulting in effect a regional mini-shock treatment.



- (2) In the turbulent MHD context, treating a B flux field as itself and its rTMS periodic driving term in a non-autonomous second order nonlinear differential equation in the very weak magnetic field turbulent regime, we hypothesize that empirical exploration of frequency and nonlinear parameter spaces will result in effective treatment in the few μT regim or below, chatic resonace induced increases in dynamical entropies.



Figure 6.11 Summary of two points of view concerning the actions of the variety of *transcranial magnetic stimulation* therapies. (1) The strong magnetic field induction of local electrical events and (2) the weak magnetic field as a TMS-frequency-forced nonlinear dynamical system exemplifying the putative

TMS entropy generation through increasing MHD turbulence. The bottom panel portrays generic quasiperiodic and chaotic attractors of the periodically driven, nonlinear van der Pol equation, which could be empirically tuned for optimal magnetic field frequency driving effect [147].

6.6

Brief Summary of Findings

- 1) The results of the use of a set of graphical and ergodic measures on time series of central (C16) spatial derivatives of the near global neocortical magnetic field, $\nabla B(t) = ssds$, are consistent with the presence of MHD turbulence in the intermittency regime.
- 2) Ergodic measures on the symbolic dynamics of these magnetic flux fields are consistent with them having the capacity for quantifiable information transport.
- 3) Beamformer localization combined with Robinson's new topological-metric entropy measure, *RVE*, demonstrates localized brain regions of increases and/or decreases in *RVE* entropy in response to auditory stimuli, cognitive tasks, and spontaneously in the "resting" condition. These localizations of entropic activity tend not to be accompanied by broad band or beta band power. This suggests that a nondissipative electromagnetic Hamiltonian treatment may be justified.
- 4) The presence of brain magnetic-field-entropy-generating weak magnetic field turbulence, the past two decades of findings of entropy deficits in clinical brain pathophysiological dynamics, and the deficit "repair" accompanying standard therapies suggest the possibility that transcranial turbulent-entropy generation with a nonlinear dynamical system may be effective at very low field levels, *pTs*, in place of the large current from very much stronger magnetic field induction of local titanic activity and refractoriness.

References

1. Raichle, M. (2009) A paradigm shift in functional brain imaging. *J. Neurosci.*, **29** (41), 12729–12734.
2. Taniguchi, M. et al. (2004) Cerebral motor control in patients with gliomas around the central sulcus studied with spatially filtered magnetoencephalography. *J. Neurol. Neurosurg. Psychiatry*, **75** (3), 466–471.
3. Anninos, P.A., Jacobson, J., Tsagas, N., and Adamopoulos, A. (1997) Spatiotemporal stationarity of epileptic focal activity evaluated by analyzing magnetoencephalographic (MEG) data and the theoretical implications. *Panminerva Med.*, **39** (3), 189–201.
4. Brockhaus, A. et al. (1997) Possibilities and limitations of magnetic source imaging of methohexitonal-induced epileptiform patterns in temporal lobe epilepsy patients. *Electroencephalogr. Clin. Neurophysiol.*, **102** (5), 423–436.
5. Llinas, R.R., Ribary, U., Jeanmonod, D., Kronberg, E., and Mitra, P.P. (1999) Thalamocortical dysrhythmia: a neurological and neuropsychiatric syndrome characterized by magnetoencephalography. *Proc. Natl. Acad. Sci. U.S.A.*, **96** (26), 15222–15227.
6. Garolera, M. et al. (2007) Amygdala activation in affective priming: a magnetoencephalogram study. (Translated from eng). *Neuroreport*, **18** (14), 1449–1453 (in eng).
7. Sperling, W., Vieth, J., Martus, M., Demling, J., and Barocka, A. (1999) Spontaneous slow and fast MEG activity in male schizophrenics treated with clozapine. *Psychopharmacology (Berl)*, **142** (4), 375–382.

8. Osipova, D. *et al.* (2003) Effects of scopolamine on MEG spectral power and coherence in elderly subjects. *Clin. Neurophysiol.*, **114** (10), 1902–1907.
9. Nikulin, V.V., Nikulina, A.V., Yamashita, H., Rossi, E.M., and Kahkonen, S. (2005) Effects of alcohol on spontaneous neuronal oscillations: a combined magnetoencephalography and electroencephalography study. *Prog. Neuropsychopharmacol. Biol. Psychiatry*, **29** (5), 687–693.
10. Virji-Babul N, Cheung T, Weeks D, Herdman AT, & Cheyne D (2007) Magnetoencephalographic analysis of cortical activity in adults with and without down syndrome. *J. Intellect. Disabil. Res.* **51**(Pt. 12):982–987.
11. Berendse, H.W., Verbunt, J.P., Scheltens, P., van Dijk, B.W., and Jonkman, E.J. (2000) Magnetoencephalographic analysis of cortical activity in Alzheimer's disease: a pilot study. *Clin. Neurophysiol.*, **111** (4), 604–612.
12. Stoffers, D. *et al.* (2007) Slowing of oscillatory brain activity is a stable characteristic of Parkinson's disease without dementia. *Brain*, **130** (Pt 7), 1847–1860.
13. Canive, J.M. *et al.* (1996) Magnetoencephalographic assessment of spontaneous brain activity in schizophrenia. *Psychopharmacol. Bull.*, **32** (4), 741–750.
14. Rutter, L. *et al.* (2009) Magnetoencephalographic gamma power reduction in patients with schizophrenia during resting condition. *Hum. Brain Mapping*, **30**, 3254–3264.
15. Chen, Y., Ding, M., and Kelso, J.A. (2003) Task-related power and coherence changes in neuromagnetic activity during visuomotor coordination. *Exp. Brain Res.*, **148** (1), 105–116.
16. Boonstra, T.W., Daffertshofer, A., Peper, C.E., and Beek, P.J. (2006) Amplitude and phase dynamics associated with acoustically paced finger tapping. *Brain Res.*, **1109** (1), 60–69.
17. Cover, K.S., Stam, C.J., and van Dijk, B.W. (2004) Detection of very high correlation in the alpha band between temporal regions of the human brain using MEG. *Neuroimage*, **22** (4), 1432–1437.
18. Poza, J., Hornero, R., Abasolo, D., Fernandez, A., and Garcia, M. (2007) Extraction of spectral based measures from MEG background oscillations in Alzheimer's disease. *Med. Eng. Phys.*, **29** (10), 1073–1083.
19. Liu, C., Gaetz, W., and Zhu, H. (2010) *Pseudo-Differential Operators: Complex Analysis and Partial Differential Equations. Operator Theory, Advances and Applications*, vol. 205, Springer, Basel, pp. 277–291.
20. Blank, H. *et al.* (1993) Dimension and entropy analyses of MEG time series from human alpha rhythm. *Z. Phys. B*, **91** (2), 251–256.
21. Fell, J., Roschke, J., Grozinger, M., Hinrichs, H., and Heinze, H. (2000) Alterations of continuous MEG measures during mental activities. (Translated from English). *Neuropsychobiology*, **42** (2), 99–106 (in English).
22. Gomez, C., Hornero, R., Abasolo, D., Fernandez, A., and Escudero, J. (2007) Analysis of MEG recordings from Alzheimer's disease patients with sample and multiscale entropies. (Translated from English). *Conf. Proc. IEEE Eng. Med. Biol. Soc.*, **2007**, 6184–6187 (in English).
23. Vakorin, V. (2010) Complexity analysis of source activity underlying the neuromagnetic somatosensory steady-state response. *Neuroimage*, **51**, 83–90.
24. Cohen, D. (1972) Magnetoencephalography: detection of the brain's electrical activity with a superconducting magnetometer. *Science*, **175** (22), 664–666.
25. Robinson, S.E. and Vrba, J. (1999) in *Recent Advances in Biomagnetism* (ed. T. Yoshimoto), Tohoku University Press, Sendai, pp. 105–108.
26. Vrba, J. and Robinson, S.E. (1990–2011) Signal Processing in the MEG. ed. CSPort Coquitlam, Canada.
27. Vrba, J. and Robinson, S.E. (2000) Differences between synthetic aperture magnetometry, SAM, and linear beamformers. *Biomagnetism 2000*, 12th International Conference on Biomagnetism.

28. Radler, K.H. (1980) Mean field approach to spherical dynamo models. *Astron. Nachr.*, **301** (H.3), 101–129.
29. Bayly, B. and Childress, S. (1987) Fast-dynamo action in unsteady flows and maps in three dimensions. *Phys. Rev. Lett.*, **59**, 1573–1576.
30. Ott, E. (1998) Chaotic flows and kinematic magnetic dynamos; a tutorial review. *Phys. Plasmas*, **5** (5), 1636–1646.
31. Alfvén, H. (1942) The existence of electromagnetic-hydrodynamic waves. *Nature*, **150**, 405–407.
32. Mandell, A.J., Selz, K.A., Holroyd, T., and Coppola, R. (2011) in *Neuronal Variability and its Functional Significance* (eds D. Glanzman and M. Ding), Oxford University Press, New York, pp. 328–390.
33. Mandell, A.J. (1987) Dynamical complexity and pathological order in the cardiac monitoring problem. *Physica D*, **27**, 235–242.
34. Robinson, S.F. (2004) Localization of even-related activity by SAM(erf). 14th International Conference on Biomagnetism, Boston, MA, pp. 583–584.
35. Robinson, S.E., Mandell, A.J., and Coppola, R. (2012) Imaging complexity. BioMag 2012.
36. Eckmann, J.P. (1981) Roads to turbulence in dissipative dynamical systems. *Rev. Mod. Phys.*, **53**, 643–654.
37. Eckmann, J.P. and Ruelle, D. (1985) Ergodic theory of chaos and strange attractors. *Rev. Mod. Phys.*, **57**, 617–656.
38. Mandell, A.J., Selz, K.A., Aven, J., and Holroyd, T.C. (2011) in *International Conference on Applications in Nonlinear Dynamics (ICAN II)* (eds V. In, P. Longhini, and A. Palacios), American Institute of Physics, pp. 7–24.
39. Mandell, A., Selz, K., Holroyd, T., Rutter, L., and Coppola, R. (2011) in *The Dynamic Brain* (eds M. Ding and D. Glanzman), Oxford University Press, Oxford, pp. 296–337.
40. Mandell, A.J., Russo, P.V., and Knapp, S. (1982) *Strange Stability in Hierarchically Coupled Neuropsychobiological Systems*, Springer-Verlag, New York, pp. 270–286.
41. Englander, S.W., Downer, N.W., and Teitelbaum, H. (1972) Hydrogen exchange. *Annu. Rev. Biochem.*, **41**, 903–924.
42. Wagner, G.C., Colvin, J.T., Allen, J.P., and Stapleton, H.J. (1985) Fractal models of protein structure, dynamics and magnetic relaxation. *J. Am. Chem. Soc.*, **107**, 5589–5594.
43. Mandell, A.J., Stewart, K.D., Knapp, S., and Russo, P.V. (1980) Protein fluctuations and time-space asymmetries in brain [proceedings]. *Psychopharmacol. Bull.*, **16** (4), 47–50.
44. Liebovitch, L.S. and Sullivan, J.M. (1987) Fractal analysis of a voltage-dependent potassium channel from cultured mouse hippocampal neurons. *Biophys. J.*, **52** (6), 979–988.
45. Mandell, A.J. (1983) From intermittency to transitivity in neuropsychobiological flows. *Am. J. Physiol. (Reg. Integ. Compar. Physiol.)*, **245** (14), R484–R494.
46. Paulus, M., Gass, S., and Mandell, A.J. (1989) A realistic, minimal “middle layer” for neural networks. *Physica D*, **40**, 135–155.
47. Beggs, J. and Plenz, D. (2005) Neuronal avalanches are diverse and precise activity patterns that are stable for many hours in cortical slices. *J. Neurosci.*, **24**, 5216–5519.
48. Faber, D.S. and Korn, H. (1989) Electric field effects: their relevance in central neural networks. *Physiol. Rev.*, **69**, 821–863.
49. Mandell, A.J., Selz, K.A., and Shlesinger, M. (1991) in *Chaos in the Brain* (eds D.W. Duke and W. Pritchard), World Scientific Press, Singapore, pp. 137–155.
50. Frolich, F. and McCormick, D.A. (2010) Endogenous electric fields may guide neocortical network activity. *Neuron*, **67**, 129–143.
51. de Munck, J., Huijzen, H., Waldorp, L., and Heethaar, R. (2002) Estimating stationary dipoles from MEG/EEG data contaminated with spatially and temporally correlated background noise. *IEEE Speech Signal Process. Mag.*, **50** (7), 1565–1572.

52. de Munck, J.C., Vijn, P.C., and Lopes da Silva, F.H. (1992) A random dipole model for spontaneous brain activity. *IEEE Trans. Biomed. Eng.*, **39** (8), 791–804.
53. Sato, S. and Smith, P.D. (1985) Magnetoencephalography. *J. Clin. Neurophysiol.*, **2** (2), 173–192.
54. Childress, S. and Gilbert, A. (1995) *Stretch, Twist, Fold: The Fast Dynamo Problem*, Springer, Berlin.
55. Soward, A.M. (1987) Fast dynamo action in a steady flow. *J. Fluid Mech.*, **180**, 267–295.
56. Mandell, A.J., Selz, K.A., Aven, J., Holroyd, T., and Coppola, R. (2011) in *International Conference on Applications in Nonlinear Dynamics, ICAND II* (eds V. In, P. Longhini, and A. Palacios), American Institute of Physics Conference Proceedings, Lake Louise, pp. 7–24.
57. Heisenberg, W. (1948) On the theory of statistical and isotropic turbulence. *Proc. Roy. Soc. (London)*, **195**, 402–406.
58. Chandrasekhar, S. (1961) *Hydrodynamic and Hydromagnetic Stability*, Oxford University Press, Oxford.
59. Nunez, M.J. and Srinivasan, R. (2006) *Electric Fields of the Brain; The Neurophysics of the EEG*, Oxford University Press, Oxford.
60. Moffatt, H.K. (1989) Stretch, twist and fold. *Nature*, **341**, 285–286.
61. Finn, J.M. and Ott, E. (1988) Chaotic flows and magnetic dynamos. *Phys. Rev. Lett.*, **60**, 760–763.
62. Ott, E., Du, Y., Sreenivasan, K.R., Jumea, A., and Suri, A.K. (1992) Sing-singular measures: fast magnetic dynamos and high Reynolds-number fluid turbulence. *Phys. Rev. Lett.*, **69**, 2654–2657.
63. Maruoka, H., Kubota, K., Kurokawa, R., Tsuruno, S., and Hosoya, T. (2011) Periodic organization of major subtype of pyramidal cell neurons in neocortical layer V. *J. Neurosci.*, **31**, 18522–16542.
64. Gurnett, D. and Bhattacharjee, A. (2005) *Introduction to Plasma Physics: With Space and Laboratory Applications*, Cambridge University Press, Cambridge.
65. Griffiths, D.J. (1999) *Introduction to Electrodynamics*, Prentice Hall, Saddle River, NJ.
66. Aven, J.L., Mandell, A.J., Holroyd, T., and Coppola, R. (2011) Complexity of the taskless mind at different time scales.an emperically weighted approach to decomposition and measurement. *AIP Conf. Proc.*, **1339**, 275–281.
67. Smale, S. (1967) Differentiable dynamical systems. *Bull. AMS*, **73**, 747–817.
68. Bowen, R. (1978) *On Axiom A Diffeomorphisms*, A.M.S. Publications.
69. Mandell, A.J. and Selz, K.A. (1997) Entropy conservation as topological entropy = leading Lyapounov exponent times the capacity dimension. *Chaos*, **7**, 67–81.
70. Galaburda, A.M., LeMay, M., Kemper, T.L., and Geschwind, N. (1978) Right-left asymmetries in the brain. *Science*, **199** (4331), 852–856.
71. Cowling, T.G. (1933) Axisymmetry in Static Magnetic Fields, MNRAS 94, Monthly Notice of the Royal Astronomical Society.
72. Novikov, E., Novikov, A., Shannahoff-Khalsa, D., Schwartz, B., and Wright, J. (1997) Scale-similar activity in the brain. *Phys. Rev. E*, **56**, R2387–R2389.
73. DeFelice, L.J. (1977) Fluctuation analysis in neurobiology. *Int. Rev. Neurobiol.*, **20**, 169–208.
74. Conti, F., Neumcke, B., Nonner, W., and Stampfli, R. (1980) Conductance fluctuations from the inactivation process of sodium channels in myelinated nerve fibres. (Translated from English). *J. Physiol.*, **308**, 217–239 (in English).
75. Sigworth, F.J. (1981) Interpreting power spectra from nonstationary membrane current fluctuations. (Translated from English). *Biophys. J.*, **35** (2), 289–300 (in English).
76. Ornstein, D.S. (1974) *Ergodic Theory, Randomness and Dynamical Systems*, Yale University Press, New Haven, CT.
77. Adler, R.L. and Weiss, B. (1967) Entropy, a complete metric invariant for automorphisms of the torus. *Proc. Natl. Acad. Sci. U.S.A.*, **57**, 1573–1576.

78. Cornfield, I., Fomin, V., and Sinai, Y. (1982) *Ergodic Theory*, Springer-Verlag, Berlin.
79. Mandell, A., Selz, K.A., and Shlesinger, M.F. (1991) in *Chaos in the Brain* (eds D.W. Duke and W.S. Pritchard), World Scientific Press, Hong Kong, pp. 174–190.
80. Mandell, A.J. and Selz, K.A. (1995) Nonlinear dynamical patterns as personality theory for neurobiology and psychiatry. *Psychiatry*, **58** (4), 371–390.
81. Mandell, A.J. and Shlesinger, M.F. (1990) *Lost Choices; Parallelism and Topological Entropy Decrements in Neurobiological Aging*, American Association for the Advancement of Science, Washington, DC, pp. 10–22.
82. Smotherman, W.P., Selz, K.A., and Mandell, A.J. (1996) Dynamical entropy is conserved during cocaine-induced changes in fetal rat motor patterns. *Psychoneuroendocrinology*, **21** (2), 173–187.
83. Bowen, R. and Ruelle, D. (1975) The ergodic theory of Axiom A flows. *Invent Math.*, **29**, 181–202.
84. Frisch, U. (1995) *Turbulence: The Legacy of A.N. Kolmogorov*, Cambridge University Press, Cambridge.
85. Manneville, P. and Pomeau, Y. (1980) Different ways to turbulence in dissipative dynamical systems. *Physica D*, **1**, 219–232.
86. Berge, P., Pomeau, Y., and Vidal, C. (1984) *Order and Chaos*, Chapter IX. Intermittency , John Wiley & Sons, Inc./Hermann, New York/Paris, pp. 223–247.
87. Segundo, J.P., Sugihara, G., Dixon, P., Stiber, M., and Bersier, L.F. (1998) The spike trains of inhibited pacemaker neurons seen through the magnifying glass of nonlinear analyses. *Neuroscience*, **87** (4), 741–766.
88. Mandell, A.J. and Selz, K.A. (1993) Brain stem neuronal noise and neocortical “resonance”. *J. Stat. Phys.*, **70**, 355–373.
89. Mandell, A. and Selz, K.A. (1991) in *Self-Organization, Emerging Properties and Learning* (ed. A. Babloyantz), Plenum Press, New York, pp. 255–266.
90. Novikov, A. (1990) The effects of intermittency on statistical characteristics of turbulence and scale similarity of breakdown coefficients. *Phys. Fluids*, **2**, 614–620.
91. Eckmann, J.P., Kamhorst, S., and Ruelle, D. (1987) Recurrence plots of dynamical systems. *Europhys. Lett.*, **4**, 973–977.
92. Mandell, A.J. and Selz, K.A. (1997) Entropy conservation as *Topological entropy = Lyapounov*Capacity Dimension* in neurobiological dynamical systems. *J. Chaos*, **7**, 67–91.
93. Pesin, Y. (1977) Characteristic Lyapounov exponents and smooth ergodic theory. *Russ Math. Surv.*, **32**, 55–114.
94. Paulus, M.P., Geyer, M.A., Gold, L.H., and Mandell, A.J. (1990) Application of entropy measures derived from the ergodic theory of dynamical systems to rat locomotor behavior. *Proc. Natl. Acad. Sci. U.S.A.*, **87** (2), 723–727.
95. Broomhead, D.S. and King, G.P. (1986) Extracting qualitative dynamics from experimental data. *Physica D*, **20**, 217–236.
96. Broomhead, D.S., Jones, R., and King, G.P. (1987) Addenda and correction. *J. Phys. A*, **20**, L563–L569.
97. Mandell, A.J., Selz, K.A., Owens, M.J., and Shlesinger, M.F. (2003) in *Unsolved Problems of Noise and Fluctuations* (ed. S.M. Bezrukov), American Institute of Physics Press, Melville, New York, pp. 553–559.
98. Singer, J.L. (1966) *Daydreaming: A Introduction to the Experimental Study of Inner Experience*, Random House, New York.
99. Antrobus, J.S., Singer, J.L., and Greenberg, S. (1966) Studies in the stream of consciousness:experimental enhancement and suppression of spontaneous cognitive processes. *Percept. Mot. Skills*, **23**, 399–417.
100. Petermann, T. et al. (2009) Spontaneous cortical activity in awake monkeys composed of neuronal avalanches. *Proc. Natl. Acad. Sci. U.S.A.*, **106**, 15921–15926.
101. Stauffer, D. and Aharony, A. (1994) *Introduction to Percolation Theory*, 2nd edn, CRC Press, Florence, KY.

102. Kolmogorov, A.N. (1957) General theory of dynamical systems and classical mechanics. *Proc. Internat. Cong. Math.*, 1, 315–333.
103. Arnold, V.I. and Avez, A. (1968) *Ergodic Problems of Classical Mechanics*, Addison-Wesley, Reading.
104. Arnold, V.I. (1983) *Geometrical Methods in the Theory of Ordinary Differential Equations*, Springer-Verlag, New York.
105. Sinai, Y. (1970) Dynamical systems with countably-multiple Lebesgue spectrum. *Trans. AMS*, 68, 34–88.
106. Weiss, B. (1995) *Single Orbit Dynamics* (Reg. Conf. # 95), American Mathematical Society, Providence, RI.
107. Robinson, S.E., Mandell, A.J., and Coppola, R. (2012) Imaging complexity. BioMag 2012.
108. Wikswo, J. (1989) in *Advances in Biomagnetism* (eds S.J. Williamson, M. Hoke, G. Stroink, and M. Kotani), Plenum, New York, pp. 1–18.
109. Williamson, S.J., Lu, Z.L., Karron, D., and Kaufman, L. (1991) Advantages and limitations of magnetic source imaging. *Brain Topogr.*, 4 (2), 169–180.
110. Babiloni, F. et al. (2001) Linear inverse source estimate of combined EEG and MEG data related to voluntary movements. (Translated from English). *Hum. Brain Mapp.*, 14 (4), 197–209, (in English).
111. Vrba, J. and Robinson, S.E. (2000) *IEEE Proceeding of the 34th Asimilar Conference on Signals, Systems and Computers*, Omnipress, Madison, WI, pp. 313–317.
112. Scherg, M. and von Cramon, D. (1985) A new interpretation of the generators of BAEP waves I-V: Results of a spatio-temporal dipole model. *EEG Clin. Neurophys.*, 62, 290–299.
113. Vrba, J. and Robinson, S.E. (2002) SQUID sensor array configurations for magnetoencephalography applications. *Supercond. Sci. Technol.*, 15, R51–R89.
114. Mandell, A. and Selz, K.A. (1992) in *Proceedings of the First Experimental Conference on Chaos* (eds S. Vohra, M.L. Spano, M. Shlesinger, L. Pecora, and W. Ditto), World Scientific Press, Singapore, pp. 175–191.
115. van Veen, B.D. and Buckley, K.M. (1988) Beamforming: a versatile approach to spatial filtering. *IEEE Acoust. Speech Signal Process. Mag.*, 5, 4–24.
116. Vrba, J. and Robinson, S. (2001) Signal processing in magnetoencephalography. *Methods(Duluth)*, 25, 249–271.
117. Kolmogorov, A.N. (1941) The local structure of turbulence in viscous incompressible fluid at very large Reynold's numbers. *Dokl. Akad. Nauk SSSR*, 30, 301–305.
118. Morse, M. and Hedlund, G.A. (1938) Symbolic dynamics. *Am. J. Math.*, 60, 815–866.
119. Adler, R.L., Goodwyn, L.W., and Weiss, B. (1977) Equivalence of Markoff shifts. *Isr. J. Math.*, 27, 49–63.
120. Shannon, C.E. (1948) A mathematical theory of communication. *Bell. Syst. Tech. J.*, 27, 379–423.
121. Kolmogorov, A.N. (1958) A new metric invariant of transitive dynamical systems and automorphisms in Lebesgue spaces. *Dokl. Acad. Nauk. SSSR*, 119, 861–882.
122. Basar, E., Flohr, H., Haken, H., and Mandell, A.J. (1983) *Synergetics Brain*, Springer-Verlag, Berlin.
123. Basar, E. (1980) *EEG-Brain Dynamics; Relations Between EEG and Brain Evoked Potentials*, Elsevier, Amsterdam.
124. Basar, E., Basar-Eroglu, C., Karakas, S., and Schurmann, M. (2000) Brain oscillations in perception and memory. *J. Psychophysiol.*, 35, 95–124.
125. Roach, B. and Mathalon, D. (2008) Event-related time-frequency analysis: an overview of measures and an analysis of early gamma band phase locking in schizophrenia. *Schizophr. Bull.*, 34, 907–926.
126. Makeig, S. et al. (2002) Dynamic brain sources of visual evoked responses. *Science*, 295, 690–694.
127. Kopell, N., Ermentrout, G., Whittington, M., and Traub, R.D. (2000) Gamma rhythms and beta rhythms have different synchronization properties. *Proc. Natl. Acad. Sci. U.S.A.*, 97, 1867–1872.

128. Ehlers, C., Wills, D.N., and Havstad, J. (2012) Ethanol reduces the phase locking of neural activity inn human and rodent brain. *Brain Res.*, **1450**, 67–79.
129. Ehlers, C. (1992) The new physics of chaos: can it help us to understand the effects of alcohol. *Alcohol Health Res. World*, **16**, 267–272.
130. Ehlers, C., Havstad, J., Pritchard, D., and Theiler, J. (1998) Low doses of ethanol reduce evidence for nonlinear structure in brain activity. *J. Neurosci.*, **18**, 7474–7486.
131. Donchin E, Ritter W, & McCallum C (1978) in *Brain-Event Related Potentials in Man*, eds Callaway E, Tueting P, & Koslow S Academic Press, pp. 349-411.
132. Faber, D.S. and Korn, H. (1973) A neuronal inhibition mediated electrically. *Science*, **179**, 577–578.
133. Pare, D., Shink, E., Gaudreau, H., and Destexhe, A. (1998) Impact of spontaneous synaptic activity on the resting properties of cat neocortical pyramidal neurons in vivo. *J. Neurophysiol.*, **79**, 1450–1460.
134. Palay, S.L. and Chan-Palay, V. (1974) *Cerebellar Cortex, Cytology and Organization*, Springer-Verlag, Berlin.
135. Liboff, A.R., Thomas, J.R., and Schrot, J. (1988) Intensity threshold for 60 Hz magnetically induced behavioral changes in rats. *Bioelectromagnetics*, **10**, 1–3.
136. McLeod, B. and Liboff, A.R. (1986) Dynamic characteristics of membrane ions in multifield configurations of low-frequency electromagnetic radiation. *Bioelectromagnetics*, **7**, 177–189.
137. Liboff, A. and McLeod, B.R. (1988) Kinetics of channelized membrane ions in magnetic fields. *Bioelectromagnetics*, **9**, 39–51.
138. Black Man, C., Benane, S.G., Elliott, D.J., House, D.E., and Pollock, M.M. (1988) Influence of electromagnetic fields on the efflux of calcium ions from brain tissue. *Bioelectromagnetics*, **9**, 215–227.
139. Lednev, V.V. (1991) Possible mechanism for the influence of weak magnetic fields on biological systems. *Bioelectromagnetics*, **12**, 71–75.
140. Knapp, S., Mandell, A.J., and Bullard, W.P. (1975) Calcium activation of brain tryptophan hydroxylase. *Life Sci.*, **16** (10), 1583–1593.
141. Ledda, F., De Carlo, F., Grimaldi, S., and Lisi, A. (2010) Calcium ion cyclotron resonance, ICR, at 7.0 Hz, 9.2 micro-Tesla magnetic field exposure initiates differentiation of pituitary corticotrope-derived AtT20 D16V cells. *Electromagn. Biol. Med.*, **29**, 63–71.
142. Black Man, C., Benane, S.G., Rabinowitz, J., House, D.E., and Joines, W. (1985) A role for the magnetic field in the radiation-induced efflux of calcium ions from brain tissue *in vitro*. *Bioelectromagnetics*, **6**, 327–337.
143. Hausdorff, J.M., Herman, T., Baltadjieva, R., Gurevich, T., and Giladi, N. (2003) Balance and gait in older adults with systemic hypertension. *Am. J. Cardiol.*, **91** (5), 643–645.
144. Mackey, M. and Glass, L. (1977) Oscillations and chaos in physiological control systems. *Science*, **197**, 287–289.
145. George, M. (2003) Stimulating the brain: the emerging new science of electrical brain stimulation. *Sci. Am.*, **289**, 66–73.
146. George, M.S. and Belmaker, R.H. (2007) *Transcranial Magnetic Stimulation in Clinical Psychiatry*, American Psychiatric Publishing, Washington, DC.
147. Mandell, A.J., Russo, P.V., and Blomgren, B.W. (1987) Geometric universality in brain allosteric protein dynamics; complex hydrophobic transformation predicts mutual recognition by polypeptides and proteins. *Ann. N.Y. Acad. Sci.*, **504**, 88–117.

7

Thermodynamic Model of Criticality in the Cortex Based on EEG/ECoG Data

Robert Kozma, Marko Puljic, and Walter J. Freeman

Prologue ... Thus logics and mathematics in the central nervous system, when viewed as languages, must structurally be essentially different from those languages to which our common experience refers. ... whatever the system is, it cannot fail to differ considerably from what we consciously and explicitly considered as mathematics, von Neumann [1].

7.1

Introduction

Von Neumann emphasized the need for new mathematical disciplines in order to understand and interpret the language of the brain [1]. He has indicated the potential directions of such new mathematics through his work on self-reproducing cellular automata and finite mathematics. Owing to his early death in 1957, he was unable to participate in the development of relevant new theories, including morphogenesis pioneered by Turing [2] and summarized by Katchalsky [3]. Prigogine [4] developed this approach by modeling the emergence of structure in open chemical systems operating far from thermodynamic equilibrium. He called the patterns *dissipative structures*, because they emerged by the interactions of particles feeding on energy with local reduction in entropy. Haken [5] developed the field of synergetics, which is the study in lasers of pattern formation by particles, whose interactions create order parameters by which the particles govern themselves in circular causality.

Principles of self-organization and metastability have been introduced to model cognition and brain dynamics [6–8]. Recently, the concept of self-organized criticality (SOC) has captured the attention of neuroscientists [9]. There is ample empirical evidence of the cortex conforming to the self-stabilized, scale-free dynamics of the sandpile during the existence of quasi-stable states [10–12]. However, the model cannot produce the emergence of orderly patterns within a domain of criticality [13–14]. In 15 SOC is described as “pseudocritical” and it is suggested that self-organization be complemented with more elaborate, adaptive approaches.

Extending on previous studies, we propose to treat cortices as dissipative thermodynamic systems that by homeostasis hold themselves near a critical level of

activity far from equilibrium but steady state, a pseudoequilibrium. We utilize Freeman's neuroscience insights manifested in the hierarchical brain model: the K (Katchalsky)-sets [3, 16]. Originally, K-sets have been described mathematically using ordinary differential equations (ODEs) with distributed parameters and with stochastic differential equations (SDEs) using additive and multiplicative noise [17, 18]. This approach has produced significant results, but certain shortcomings have been pointed out as well [19–21]. Calculating stable solutions for large matrices of nonlinear ODE and SDE closely corresponding to chaotic electrocorticography (ECoG) activity are prohibitively difficult and time consuming on both digital and analog platforms [22]. In addition, there are unsolved theoretical issues in constructing solid mathematics with which to bridge the difference across spatial and temporal scales between microscopic properties of single neurons and macroscopic properties of vast populations of neurons [23, 24].

In the past decade, the neuropercolation approach has proved to be an efficient tool to address these shortcomings by implementing K-sets using concepts of discrete mathematics and random graph theory (RGT) [25]. Neuropercolation is a thermodynamics-based random cellular neural network model, which is closely related to cellular automata (CA), the field pioneered by von Neumann, who anticipated the significance of CA in the context of brain-like computing [26]. This study is based on applying neuropercolation to systematically implement Freeman's principles of neurodynamics. Brain dynamics is viewed as a sequence of intermittent phase transitions in an open system, with synchronization–desynchronization effects demonstrating symmetry breaking demarcated by spatiotemporal singularities [27–30].

This work starts with the description of the basic building blocks of neurodynamics. Next, we develop a hierarchy on neuropercolation models with increasing complexity in structure and dynamics. Finally, we employ neuropercolation to describe critical behavior of the brain and to interpret experimentally observed ECoG/EEG (electroencephalography) dynamics manifesting learning and higher cognitive functions. We conclude that criticality is a key aspect of the operation of the brain and it is a basic attribute of intelligence in animals and in man-made devices.

7.2

Principles of Hierarchical Brain Models

7.2.1

Freeman K-Models: Structure and Functions

We propose a hierarchical approach to spatiotemporal neurodynamics, based on K-sets. Low-level K-sets were introduced by Freeman in the 1970s, named in honor of Aharon Kachalsky, an early pioneer of neural dynamics [16]. K-sets are multiscale models, describing the increasing complexity of structure and dynamical behaviors. K-sets are mesoscopic models, and represent an intermediate

level between microscopic neurons and macroscopic brain structures. The basic K0 set describes the dynamics of a cortical microcolumn with about 10^4 neurons. K-sets are topological specifications of the hierarchy of connectivity in neuron populations. When first introduced, K-sets were modeled using a system of nonlinear ODEs; see [16, 21]. K-dynamics predict the oscillatory waveforms that are generated by neural populations. K-sets describe the spatial patterns of phase and amplitude of the oscillations. They model observable fields of neural activity comprising EEG, local field potential (LFP), and magnetoencephalography (MEG). K-sets form a hierarchy for cell assemblies with the following components [31]:

- K0 sets represent noninteractive collections of neurons with globally common inputs and outputs: excitatory in K0e sets and inhibitory in K0isets. The K0 set is the basic module for K-sets.
- KI sets are made of a pair of interacting K0 sets, both either excitatory or inhibitory in positive feedback. The interaction of K0e sets gives excitatory bias; that of K0i sets sharpens input signals.
- KII sets are made of a KIe set interacting with a KII set in negative feedback, giving oscillations in the gamma and high beta range (20–80 Hz). Examples include the olfactory bulb and the prepyriform cortex.
- KIII sets are made up of multiple interacting KII sets. Examples include the olfactory system and the hippocampal system. These systems can learn representations and do match–mismatch processing exponentially fast by exploiting chaos.
- KIV sets made up of interacting KIII sets are used to model multisensory fusion and navigation by the limbic system.
- KV sets are proposed to model the scale-free dynamics of neocortex operating on and above KIV sets in mammalian cognition.

K-sets are complex dynamical systems modeling the classification in various cortical areas, having typically hundreds or thousands of degrees of freedom. KIII sets have been applied to solve various classification and pattern recognition problems [21, 32, 33]. In early applications, KIII sets exhibited extreme sensitivity to model parameters, which prevented their broad use in practice [32]. In the past decade, systematic analysis has identified regions of robust performance and stability properties of K-sets have been derived [34, 35]. Today, K-sets are used in a wide range of applications, including detection of chemicals [36], classification [32, 37], time series prediction [38], and robot navigation [39, 40].

7.2.2

Basic Building Blocks of Neurodynamics

The hierarchical K-model-based approach is summarized in the *10 Building Blocks of Neurodynamics*; see [16, 23, 24]:

- 1) Nonzero point attractor generated by a state transition of an excitatory population starting from a point attractor with zero activity. This is the function of the KI set.

- 2) Emergence of damped oscillation through negative feedback between excitatory and inhibitory neural populations. This is the feature that controls the beta–gamma carrier frequency range and it is achieved by KII having low feedback gain.
- 3) State transition from a point attractor to a limit cycle attractor that regulates steady-state oscillation of a mixed E-I KII cortical population. It is achieved by KII with sufficiently high feedback gain.
- 4) The genesis of broad-spectral, aperiodic/chaotic oscillations as background activity by combined negative and positive feedback among several KII populations; achieved by coupling KII oscillators with incommensurate frequencies.
- 5) The distributed wave of chaotic dendritic activity that carries a spatial pattern of amplitude modulation (AM) in KIII.
- 6) The increase in nonlinear feedback gain that is driven by input to a mixed population, which results in the destabilization of the background activity and leads to emergence of an AM pattern in KIII as the first step in perception.
- 7) The embodiment of meaning in AM patterns of neural activity shaped by synaptic interactions that have been modified through learning in KIII layers.
- 8) Attenuation of microscopic sensory-driven noise and enhancement of macroscopic AM patterns carrying meaning by divergent–convergent cortical projections in KIV.
- 9) Gestalt formation and preaffection in KIV through the convergence of external and internal sensory signals, leading to the activation of the attractor landscapes and from there to intentional action.
- 10) Global integration of frames at the theta rates through neocortical phase transitions representing high-level cognitive activity in the KV model.

Principles 1 through 7 describe the steps toward basic sensory processing, including pattern recognition, classification, and prediction, which is the function of KIII models. Principles 8 and 9 reflect the generation of basic intentionality using KIV sets. Principle 10 expresses the route to high-level intentionality and ultimately consciousness. The greatest challenge in modeling cortical dynamics is posed by the requirement to meet two seemingly irreconcilable requirements. One is to model the specificity of neural action even to the level that a single neuron can be shown to have the possibility of capturing brain output. The other is to model the generality by which neural activity is synchronized and coordinated throughout the brain during intentional behavior. Various sensory cortices exhibit great similarity in their temporal dynamics, including the presence of spontaneous background activity, power-law distribution of spatial and temporal power spectral densities, repeated formation of AM spatial patterns with carrier frequencies in the beta and gamma ranges, and frame recurrence rates in the theta range.

Models based on ODE and SDE have been used successfully to describe the mesoscopic dynamics of cortical populations for autonomous robotics [40, 41]. However, such approaches suffered from inherent shortcomings. They falter in attempts to model the entire temporal and spatial range including the transitions between levels, which appear to take place very near to criticality. Neuropercolation

and RGT offer a new approach to describe critical behavior and related phase transitions in the brain. It is shown that criticality in the neuropil is characterized by a critical region instead of a singular critical point, and the trajectory of the brain as a dynamical systems crosses the critical region from a less organized (gaseous) phase to more organized (liquid) phase during input-induced destabilization and vice versa [42–44]. Neuropercolation is able to simulate these important results from mesoscopic ECoG/EEG recording across large spacial and temporal scales, as is introduced in this chapter.

7.2.3

Motivation of Neuropercolation Approach to Neurodynamics

We utilize the powerful tools of RGT developed over the past 50 years [45–47] to establish rigorous models of brain networks. Our model incorporates CA and percolation theory in random graphs that are structured in accordance with cortical architectures. We use the hierarchy of interactive populations in networks as developed in Freeman K-models [16], but replace differential equations with probability distributions from the observed random graph that evolve in time. The corresponding mathematical object is called *neuropercolation* [25]. Neuropercolation theory provides a suitable mathematical approach to describe phase transitions and critical phenomena in large-scale networks. It has potential advantage compared to ODEs and partial differential equations (PDEs) when modeling spatiotemporal transitions in the cortex, as differential equations assume some degree of smoothness in the described phenomena, which may not be very suitable to model the observed sudden changes in neurodynamics. The neural percolation model is a natural mathematical domain for modeling collective properties of brain networks, especially near critical states, when the behavior of the system changes abruptly with the variation of some control parameters.

Neuropercolation considers populations of cortical neurons that sustain their metastable state by mutual excitation, and its stability is guaranteed by the neural refractory periods. Nuclear physicists have used the concept of criticality to denote the threshold for ignition of a sustained nuclear chain reaction, that is, fission. The critical state of nuclear chain reaction is achieved by a delicate balance between the material composition of the reactor and its geometrical properties. The criticality condition is expressed as the identity of geometrical curvature (buckling) and material curvature. Chain reactions in nuclear processes are designed to satisfy strong linear operational regime conditions, in order to assure stability of the underlying chain reaction. That usage fails to include the self-regulatory processes in systems with nonlinear homeostatic feedback that characterize cerebral cortices.

A key question is how the cortex transits between gas-like randomness and liquid-like order near the critical state. We have developed thermodynamic models of the cortex [43, 44], which postulate two phases of neural activity: vapor-like and liquid-like. In the vapor-like phase, the neurons are uncoupled and maximally individuated, which is the optimal condition for processing microscopic sensory information at low density. In the liquid-like phase, the neurons are strongly

coupled and thereby locked into briefly stable macroscopic activity patterns at high density, such that every neuron transmits to and receives from all other neurons by virtue of small-world effects [48, 49]. Local $1/f$ fluctuations have the form of phase modulation (PM) patterns that resemble droplets in vapor. Large-scale, spatially coherent AM patterns emerge from and dissolve into this random background activity but only on receiving conditioned stimulus (CS). They do so by spontaneous symmetry breaking [42] in a phase transition that resembles condensation of a raindrop, in that it requires a large distribution of components, a source of transition energy, a singularity in the dynamics, and a connectivity that can sustain interaction over relatively immense correlation distances. We conclude that the background activity at the pseudoequilibrium state conforms to SOC, that the fractal distribution of phase patterns corresponds to that of avalanches, that the formation of a perception from sensory input is by a phase transition from a gas-like, disorganized, low-density phase to a liquid-like high-density phase [43].

7.3

Mathematical Formulation of Neuropercolation

7.3.1

Random Cellular Automata on a Lattice

In large networks, such as the cortex, organized dynamics emerges from the noisy and chaotic behavior of a large number of microscopic components. Such systems can be modeled as graphs, in which neurons become vertices. The activity of every vertex evolves in time depending on its own state, the states of its neighbors, and possibly some random influence. This leads us to the general formulation of random CA. In a basic two-state cellular automaton, the state of any lattice point $x \in \mathbb{Z}^d$ is either active or inactive. The lattice is initialized with some (deterministic or random) configuration. The states of the lattice points are updated (usually synchronously) on the basis of some (deterministic or probabilistic) rule that depends on the activations of their neighborhood. For related general concepts, see CA such as Conway's Game of Life, cellular neural network, as well as thermodynamic systems like the Ising model [50–53]. Neuropercolation models develop neurobiologically motivated generalizations of CA models and incorporate the following major conditions:

- *Interaction with noise:* The dynamics of the interacting neural populations is inherently nondeterministic due to dendritic noise and other random effects in the nervous tissue and external noise acting on the population. Randomness plays a crucial role in neuropercolation models and there is an intimate relationship between noise and the system dynamics, because of the excitable nature of the neuropil.
- *Long axon effects (rewiring):* Neural populations stem ontogenetically in embryos from aggregates of neurons that grow axons and dendrites and form synaptic connections of steadily increasing density. At some threshold, the density allows

neurons to transmit more pulses than they receive, so that an aggregate undergoes a state transition from a zero point attractor to a nonzero point attractor, thereby becoming a population. In neural populations, most of the connections are short, but there are a relatively few long-range connections mediated by long axons. The effects of long-range axons are similar to small-world phenomena [48] and it is part of the neuropercolation model.

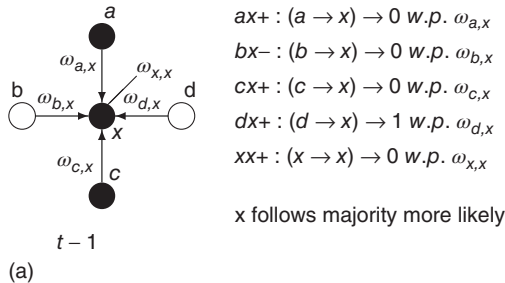
- *Inhibition:* An important property of neural tissue is that it contains two basic types of interactions: excitatory and inhibitory ones. Increased activity of excitatory populations positively influence (excite) their neighbors, while highly active inhibitory neurons negatively influence(inhibit) the neurons they interact with. Inhibition is inherent in cortical tissues and it controls stability and metastability observed in brain behaviors [7, 35]. Inhibitory effects are part of neuropercolation models.

7.3.2 Update Rules

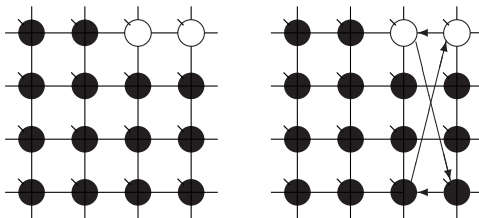
A vertex $v_i \in V$ of a graph $G(V, E)$ is in one of two states, $s(v_i)$, and influenced via the edges by $d(v_i)$ neighbors. An edge from v_i to v_j , $v_i, v_j \in E$, either excites and inhibits. Excitatory edges project the states of neighbors and inhibitory edges project the opposite states of neighbors, 0 if the neighbor's state is 1, and 1 if it is 0. The state of the vertex, influenced by edges, is determined by the majority rule; the more neighbors are active, the higher the chance for the vertex to be active; and the more neighbors are inactive, the higher the chance for the vertex to be inactive. At time $t = 0$ $s(v_i)$ is randomly set to 0 or 1. Then, for $t = 1, 2, \dots, T - 1$, a majority rule is applied simultaneously over all vertices. A vertex v_i is influenced by a state of its neighbor $v_j \in N(v_i)$, whenever a random variable $R(v_i, t)$ is less than the influencing excitatory edge $v_j v_i$ strength, $\omega_{j,i}$, else the vertex v_i is influenced by an opposite state of neighbor v_j . If the edge $v_j v_i$ is inhibitory, the vertex v_j sends 0 when $s(v_j) = 1$, and 1 when $s(v_j) = 0$. Then, a vertex v_i gets a state of the most common influence, if there is one such; otherwise, a vertex state is randomly set to 0 or 1, Figure 7.1a.

Formula for the majority rule:

$$s(v_i, t) = \begin{cases} 0 & \text{if } \sum_{v_j \in N(v_i)} f(v_j, t) < \frac{d(v_i)}{2} \\ 1 & \text{if } \sum_{v_j \in N(v_i)} f(v_j, t) > \frac{d(v_i)}{2} \\ 0 \text{ or } 1 & \text{if } \sum_{v_j \in N(v_i)} f(v_j, t) = \frac{d(v_i)}{2} \end{cases} \quad (7.1)$$



(a)



(b)

Figure 7.1 Illustration of update rules in 2D lattice. (a) An example of how majority function works. bx edge inhibits with strength $\omega_{b,x}$, so it sends 0 when $s(b, t-1) = 1$. Given the scenario, $s(x, t)$ is 0 most likely.

First row/column is connected with last row/column. Each vertex has a self-influence. Right: 2D torus after the basic random rewiring strategy. Two out of 80 (16×5) edges are rewired or 2.5%.

(b): Example of 2D torus of order 4×4 .

$$f(v_j, t) = \begin{cases} 0 & \text{if } \omega_{j,i}(s(v_j, t-1) = 0) \geq R(v_i, t); \text{ else } 1 \\ 1 & \text{if } \omega_{j,i}(s(v_j, t-1) = 1) \geq R(v_i, t); \text{ else } 0 \end{cases}$$

$$s(v_j, t-1) = \begin{cases} 0 & \text{if } \omega_{j,i}(s(v_j, t-1) = 0) \text{ excites; else } 1 \\ 1 & \text{if } \omega_{j,i}(s(v_j, t-1) = 1) \text{ excites; else } 0 \end{cases}$$

$$0 \leq R(v_i, t) \leq 1$$

$$0.5 \leq \omega_{j,i}(s(v_j)) \leq 1$$

7.3.3

Two-Dimensional Lattice with Rewiring

Lattice-like graphs are built by randomly reconnecting some edges in the graphs set on a regular two-dimensional grid and folded into tori. In the applied basic random rewiring strategy, n directed edges from $n \times 2$ vertices are plugged out from a graph randomly. At that point, the graph has n vertices lacking an incoming edge and n vertices lacking an outgoing edge. To preserve the vertex degrees of the original graph, the set of plugged-out edges is returned to the vertices with the missing edges in random order. An edge is pointed to the vertex missing

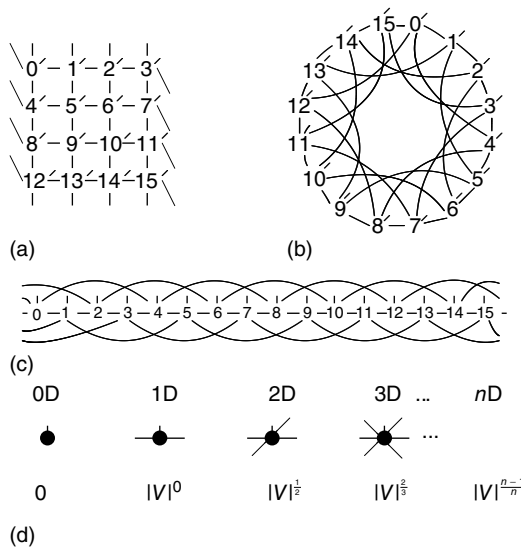


Figure 7.2 (a) Example of a labeled 4×4 torus in two-dimension. (b) Conversion of the 2D lattice approximately into a 2D torus where vertices are set in a circle. (c) 4×4 2D torus cut an unfolded into a linear band. (d) Illustration of the neighborhoods in higher dimensions.

the incoming edge and is projected from the vertex missing the outgoing edge, Figure 7.1b. Such a two-dimensional graph models a KI set with a homogeneous population of excitatory and inhibitory neurons.

It will be useful to reformulate the basic subgraph on a regular grid, as shown in Figure 7.2. We list all vertices along a circle and connect the corresponding vertices to obtain the circular representation on Figure 7.2b. This circle is unfolded into a linear band by cutting it up at one location, as shown in Figure 7.2c. Such a representation is very convenient for the design of the rewiring algorithm. Note that this circular representation is not completely identical to the original lattice, owing to the different edges when folding the lattice into a torus. We have conducted experiments to compare the two representations and obtained that the difference is minor and does not affect the basic conclusions. An important advantage of this band representation that it can be generalized to higher dimensions by simply adding suitable new edges between the vertices. For example, in 2D we have four direct neighbors and thus four connecting edges; in 3D, we have six connecting edges, and so on. Generalization to higher dimensions is not used in this work as the 2D model is a reasonable approximation of the layered cortex.

7.3.4 Double-Layered Lattice

We construct a double-layered graph by connecting two lattices (see Figure 7.3(a)). The top layer G_0 is excitatory, while the bottom layer G_1 is inhibitory. The excitatory

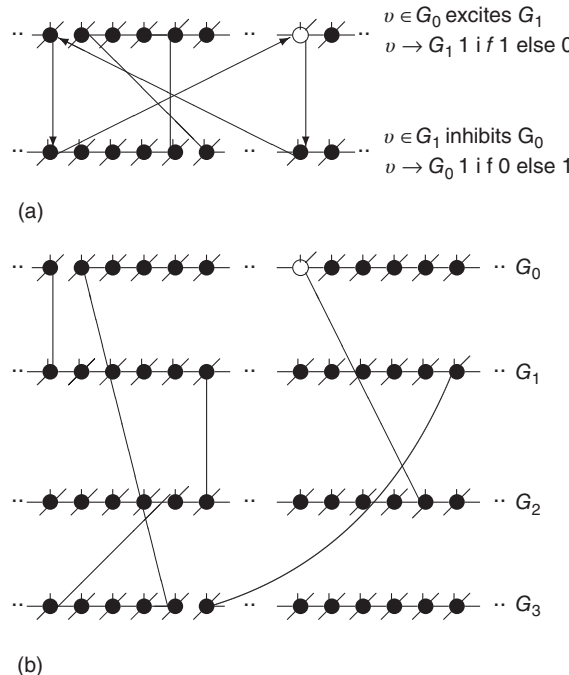


Figure 7.3 Illustration of coupled layers with randomly selected connection weights between them. (a) :Example of a double-layer coupled system that includes an excitatory layer G_0 and an inhibitory layer G_1 . Within the layers the edges are excitatory; edges from G_0 to G_1 are excitatory and edges from G_1 to G_0 are inhibitory. (b): Example

of two coupled double layers, all together four coupled layers: G_0 and G_2 are excitatory layers, while G_1 and G_3 denote inhibitory layers. Each subgraph has three edges rewired. Edges from G_1 to G_0 and edges from G_3 to G_2 are inhibitory; the other edges are excitatory.

subgraph G_0 projects to the inhibitory subgraph G_1 through edges that excite, while the G_1 inhibitory layer projects toward G_0 with edges that inhibit. An excitatory edge from G_0 influences the vertex of G_1 with 1 when active and with 0 when inactive. Conversely, an inhibitory edge from G_1 influences the vertex of G_0 with 0 when active and with 1 when inactive.

7.3.5

Coupling Two Double-Layered Lattices

By coupling two double-layered graphs, we have four subgraphs interconnected to form a graph $G = G_0 \cup G_1 \cup G_2 \cup G_3$. Subgraph G_0 and G_1 are coupled into one double layer and G_2 and G_3 into the other. There are several excitatory edges between G_0 and G_2 , G_0 and G_3 , G_1 and G_2 , G_1 and G_3 , respectively, which are responsible for coupling the two double-layered lattices (Figure 7.3(b)).

7.3.6

Statistical Characterization of Critical Dynamics of Cellular Automata

The most fundamental parameter describing the state of a finite graph G at time t is its overall activation level $S(G, t)$ defined as follows:

$$S(G, t) = \sum_{i=0}^{|V|-1} s(v_i) \quad (7.2)$$

It is useful to introduce the normalized activation per vertex, $a(G, t)$, which is zero if all sites are inactive and 1 if all sites are active. In general, $a(G, t)$ is between 0 and 1:

$$a(G, t) = \frac{S(G, t)}{|V|} \quad (7.3)$$

The average normalized activation over time interval T is given as

$$\langle a \rangle = \frac{\sum_{t=0}^{T-1} a(G, t)}{T} \quad (7.4)$$

$$\langle a^* \rangle = \frac{\sum_{t=0}^{T-1} |a(G, t) - 0.5|}{T} \quad (7.5)$$

The latter quantity can be interpreted as the average magnetization in terms of statistical physics. Depending on their structure, connectivity, update rules, and initial conditions, probabilistic automata can display very complex behavior as they evolve in time. Their dynamics may converge to a fixed point, to limit cycles, or to chaotic attractors. In some specific models, it is rigorously proved that the system is bistable and exhibits critical behavior. For instance, it spends a long time in either low- or high-density configurations, with mostly 0 or 1 activation values at the nodes, before a very rapid transition to the other state [54, 55]. In some cases, the existence of phase transitions can be shown mathematically. For example, the magnitude of the probabilistic component ω of the random majority update rule in Figure 7.1a is shown to have a critical value, which separates the region with a stable fixed point from the bistable regime [25].

In the absence of exact mathematical proofs, Monte Carlo computer simulations and methods of statistical physics provide us with detailed information on the system dynamics. The critical state of the system is studied using the statistical moments. On the basis of the finite-size scaling theory, there are statistical measures that are invariant to system size at the state of criticality [56]. Evaluating these measures, the critical state can be found. It has been shown that in addition to the system noise, which acts as a temperature measure in the model, there are other suitable control parameters that can drive the system to critical regimes, including the extent of rewiring and the inhibition strength [57].

Denote this quantity as ω , which will be a control parameter; it can be the noise, rewiring, connection strength, or other suitable quantity. In this work,

ω describes noise effects and is related to the system noise level $\varepsilon = 1 - \omega$. Distributions of $a(G, \omega)$ and $a^*(G, \omega)$ depend on ω . At a critical value of ω_i , the probability distribution functions of these quantities suddenly change. ω_i values are traditionally determined by evaluating the fourth-order moments (kurtosis, peakedness measure) u_4 , [56, 58–61], but they can also be measured using the third-order moments (skewness measure) or u_3^* :

$$u_4(G) = \frac{\langle (a - \langle a \rangle)^4 \rangle}{\langle (a - \langle a \rangle)^2 \rangle^2} \quad (7.6)$$

$$u_3^*(G) = \frac{\langle (a^* - \langle a^* \rangle)^3 \rangle}{\langle (a^* - \langle a^* \rangle)^2 \rangle^{3/2}} \quad (7.7)$$

According to the finite-size scaling theory, for two structurally equivalent finite graphs G and G' of different sizes, $u_4(G) \neq u_4(G')$ and $u_3^*(G) \neq u_3^*(G')$ for $\omega \neq \omega_i$. However, for $\omega = \omega_i$, $u_4(G) = u_4(G')$, and $u_3^*(G) = u_3^*(G')$. In this study, we use both the third- and fourth-order momentums to determine the critical points of the system.

7.4

Critical Regimes of Coupled Hierarchical Lattices

7.4.1

Dynamical Behavior of 2D Lattices with Rewiring

Two-dimensional lattices folded into tori have been thoroughly analyzed in [55]; the main results are summarized here. In the absence of rewiring, the lattice is in one of two possible states: ferromagnetic or paramagnetic, depending on the noise strength ω . The following states are observed:

- For $\omega < \omega_0$, states 0 and 1 are equiprobable across the graph and a distribution is unimodal. This state corresponds to paramagnetic regime.
- For $\omega > \omega_0$, one state dominates; vertex states are mostly 0 or mostly 1, and the graph's a distribution is bimodal. This is the ferromagnetic condition.
- In the close neighborhood of the critical point ω_0 , the lattice dynamics is unstable. Immediately above ω_0 , the vertex mostly follows its majority influences.

For $\omega > \omega_0$, the vertices cease to act individually and become a part of a group. Their activity level is determined by the population. This regime is defined by the condition that the vertices project more common activation than they receive, in the probabilistic sense. This transition is the first building block of neurodynamics and it corresponds to KI level dynamics. Figure 7.4 illustrates critical behavior of a 2D torus with $\omega_0 \approx 0.866$; no rewiring. Calculations show that for the same torus having 5.00% edges rewired, the critical probability changes to $\omega_0 \approx 0.830$. Rewiring leads to a behavior of paramount importance for future discussions: the critical condition is manifested as a *critical region*, instead of a singular *critical point*. We will show various manifestations of such principles in the brain. In the case of

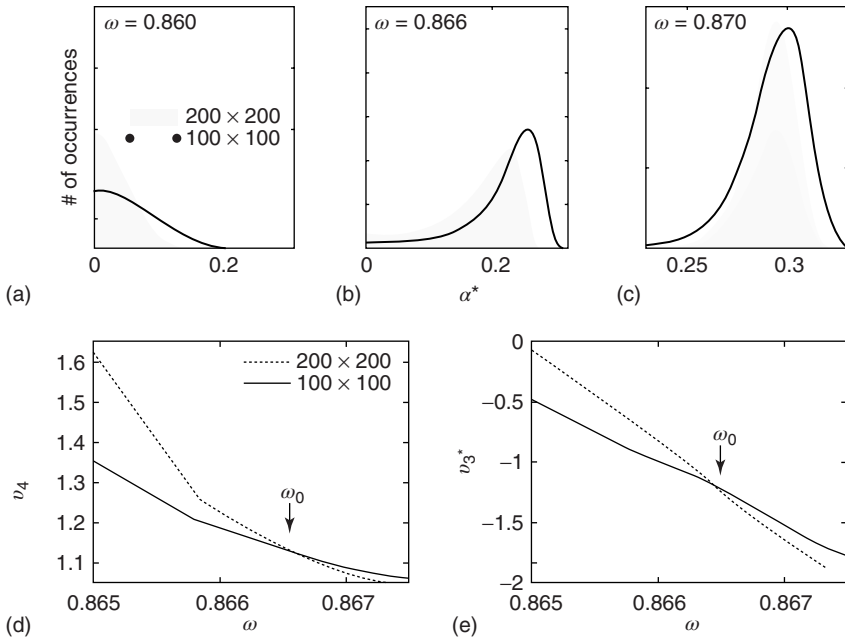


Figure 7.4 Illustration of the dynamics of the 2D torus; the case of KI architecture. There are two distinct dynamic regimes; (a) unimodal pdf with a zero average activation (paramagnetic regime); (b,c) the

case of the bimodal pdf with a positive activation level (ferromagnetic regime). (d,e) $v_4 = \langle (a - \langle a \rangle)^4 \rangle / \langle (a - \langle a \rangle)^2 \rangle^2$ and v_3^* around ω_0 for two graphs of different orders.

the rewiring discussed in this section, the emergence of a critical region is related to the fact that same amount of rewiring can be achieved in multiple ways. For example, it is possible to rewire all edges with equal probability, or select some vertices that are more likely rewired, and so on. In real life, as in the brain, all these conditions happen simultaneously. This behavior is illustrated in Figure 7.5 and it has been speculated as a key condition guiding the evolution of the neuropil in the infant's brain in the months following birth [54, 55, 62] giving rise to a robust, broadband background activity as a necessary condition of the formation of complex spatiotemporal patterns during cognition.

7.4.2

Narrow Band Oscillations in Coupled Excitatory–Inhibitory Lattices

Inhibitory connections in the coupled subgraph $G = G_0 \cup G_1$ can generate oscillations and multimodal activation states [57]. In an oscillator, there are three possible regimes demarcated by two critical points ω_0 and ω_1 :

- ω_0 is the transition point where narrow-band oscillations start.
- ω_1 is the transition point where narrow-band oscillations terminate.

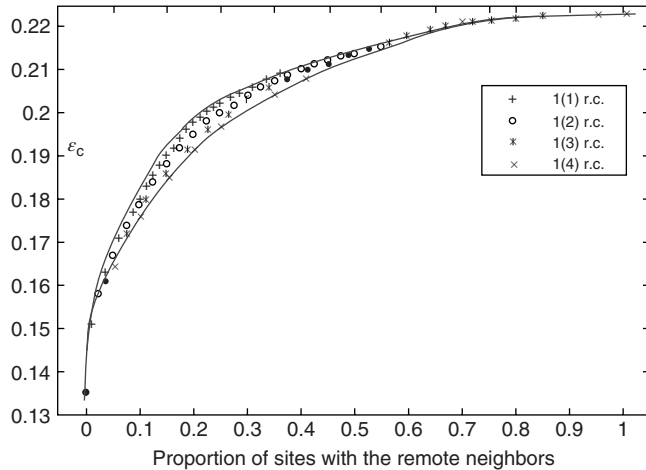


Figure 7.5 Integrated view of the relationship between the proportion of rewired edges and critical noise $\varepsilon_c = 1 - \omega_0$. Notations 1(1), 1(2), 1(3), and 1(4) mean that a vertex can have 1, 2, 3, or 4 remote connections.

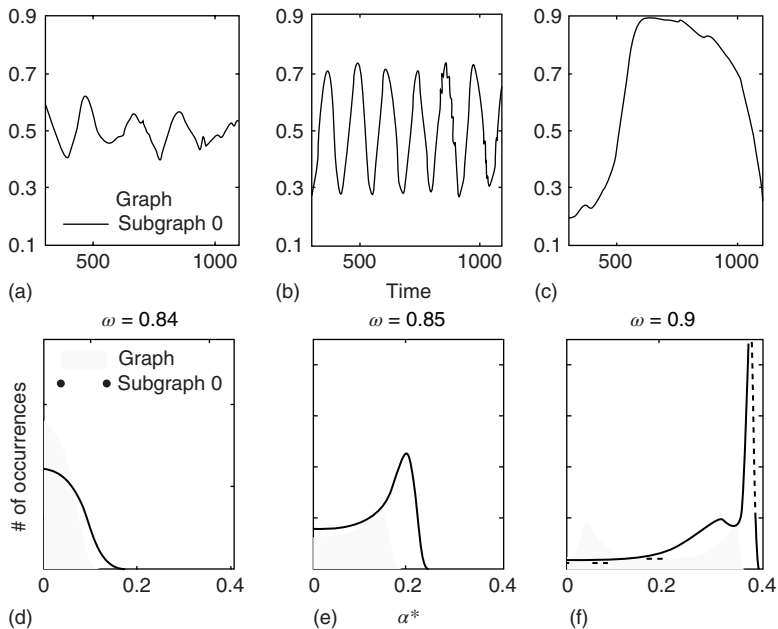


Figure 7.6 Illustration of the dynamics of coupled excitatory-inhibitory layers; the case of KII architecture. There are three modes of the oscillator $G(5\%, 3.75\%)$ made of two 2D layers G_0 and G_1 of order 96×96 . (a–c) $a(G, \omega)$ of the whole graph (gray line) and

of subgraph G_0 (black line) at three different ω values, which produce three different dynamic modes. (d–e) Distributions of a^* at three different ω values for graphs of orders 100×100 and 200×200 ; only one side of the symmetric a^* distribution is shown.

Under appropriately selected graph parameters, $a(G, \omega)$ distribution is unimodal when $\omega < \omega_0$, bimodal when $\omega_0 < \omega < \omega_1$, and quadromodal when $\omega > \omega_1$, Figure 7.6. Each subgraph has 2304 (5%) edges rewired within the layer and 1728 (3.75%) edges rewired toward the other subgraph. Just below ω_0 , vertices may oscillate if they are excited. $a(G, \omega)$ values of temporarily excited graph oscillate, but return to the basal level in the absence of excitation. This form of oscillation is the second building block of neuron-inspired dynamics. When ω is further increased, that is, $\omega_0 < \omega < \omega_1$, $a(G, \omega)$ exhibits sustained oscillations even in the absence of external perturbation. When the double layer is temporarily excited, it returns to the basal oscillatory behavior. Self-sustained oscillation is the third building block of neuron-inspired dynamics and it corresponds to KII hierarchy.

7.5

BroadBand Chaotic Oscillations

7.5.1

Dynamics of Two Double Arrays

Two coupled layers with inhibitory and excitatory nodes exhibit narrow-band activity oscillations. These coupled lattices with appropriate topology can model any frequency range with oscillations occurring between ω_0 and ω_1 . For example, an oscillator $G(5\%, 2.5\%) = G_0 \cup G_1$ has 2.5% edges rewired across the two layers and 5% edges are rewired within each layer. $G(5\%, 2.5\%)$ has $\omega_0 \approx 0.840$ and $\omega_1 \approx 0.860$, Figure 7.7b. Similarly, oscillator $G(5\%, 3.75\%)$ has $\omega_0 \approx 0.845$ and $\omega_1 \approx 0.865$. Each of the coupled lattices in this example is of size 100×100 . When coupling two such oscillators together, we have a total of four layers (tori) coupled into a unified oscillatory system. Clearly, the two oscillators coupled together may or may not agree on a common frequency. We will show that under specific conditions, various operational regimes may occur, including narrow band oscillations, broadband (chaotic) oscillations, intermittent oscillations, and various combinations of these. One of the multiple ways to couple two oscillators is to rewire excitatory edges between subgraphs G_0 - G_2 , G_0 - G_3 , G_1 - G_2 , and G_1 - G_3 , respectively. Two coupled oscillators have additional behavioral regimes. When oscillators $G(5\%, 2.5\%)$ and $G(5\%, 3.75\%)$ are coupled with 0.625% edges into a new graph $G(5\%, 2.5\%, 3.75\%, 0.625\%)$, ω_0 is shifted to lower level, Figure 7.8. Every parameter describing a graph influences the critical behavior under appropriate conditions. If two connected oscillators with different frequencies cannot agree on a common mode, together they can generate large-scale synchronization or chaotic background activity.

In the graph made of two oscillators, there are four critical points $\omega_0 < \omega_1 < \omega_2 < \omega_3$, separating five possible major operational regimes.

- Case of $\omega < \omega_0$: The aggregate activation distribution is unimodal and it represents the paramagnetic regime in lattice dynamics analogy.

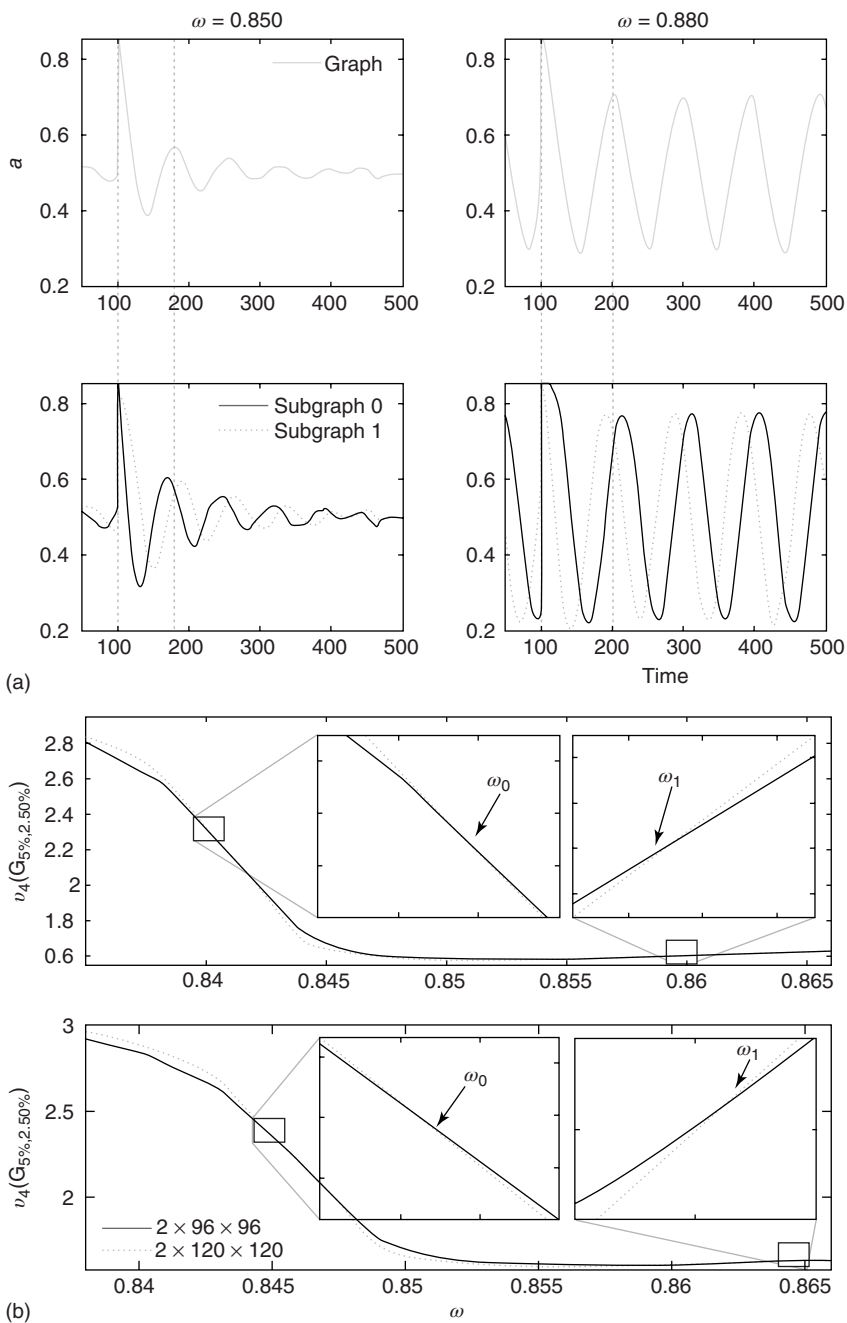


Figure 7.7 Critical states obtained by coupling two double layers of oscillators with rewiring (case of KIII). (a): Left: The graph starts to oscillate after an impulse, but the oscillation decays and returns to the basal level; right: oscillation is sustained even after the input is removed, if $\omega_0 < \omega < \omega_1$. (b): Critical behavior and ω_0 and ω_1 values for two different oscillators, $G(5\%, 2.5\%)$ (up) and $G(5\%, 3.75\%)$ (bottom).

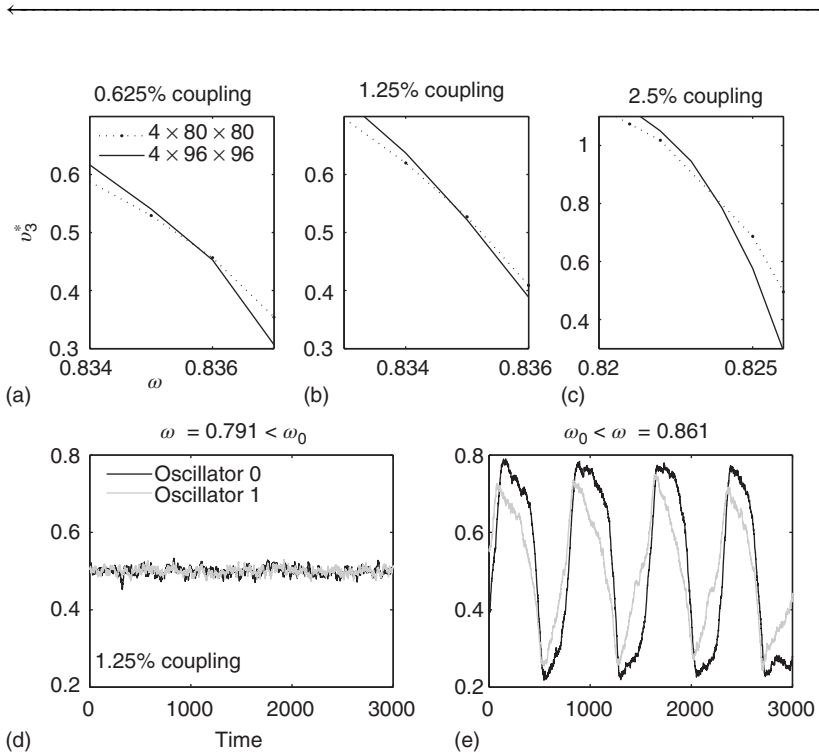


Figure 7.8 Coupling two KII oscillators into KIII, lowers ω_0 , the point above which large-scale synchronous oscillations are formed. (a–c) u_3^* values for

$G(5\%, 2.5\%, 3.75\%, 0.625\%)$, $G(5\%, 2.5\%, 3.75\%, 1.25\%)$, and $G(5\%, 2.5\%, 3.75\%, 2.5\%)$. (d,e) Typical activation of graph for ω below and above ω_0 .

- $\omega_0 < \omega < \omega_1$: The two coupled oscillators exhibit large-scale synchronization and the activation distribution is bimodal.
- $\omega_1 < \omega < \omega_2$: The two coupled oscillators with different frequencies cannot agree on a common mode, so together they generate aperiodic background activity.
- $\omega_2 < \omega < \omega_3$: Only one oscillator oscillates in a narrow band and the activation distribution is oktamodal.
- $\omega > \omega_3$: None of the components exhibit narrow-band oscillation and the activation distribution is a hexamodal. This corresponds to ferromagnetic state.

These regimes correspond to the fourth building block of neurodynamics, as described by KIII sets.

7.5.2

Intermittent Synchronization of Oscillations in Three Coupled Double Arrays

Finally, we study a system made of three coupled oscillators, each with its own inherent frequency. Such a system produces broadband oscillations with intermittent synchronization–desynchronization behavior. In order to analyze quantitatively the synchronization features of this complex system with over 60 000 nodes in six layers, we merge the channels into a single two-dimensional array at the readout. These channels will be used to measure the synchrony among the graph components. First, we find the dominant frequency of the entire graph using Fourier transform after ensemble averaging across the $\approx 10\,000$ channels for the duration of the numeric experiment. We set a time window W for the duration of two periods determined by the dominant frequency. We calculate the correlation between each channel and the ensemble average over this time window W . At each time step, each channel is correlated with the ensemble over the window W . Finally, we determine the dominant frequency of each channel and for the ensemble average at time t and the phase shifts are calculated. The difference in phases of dominant frequencies measures the phase lag between the channel and the ensemble.

We plot the phase lags across time and space to visualize the synchrony between graph components (see Figure 7.9). We can observe intermittent synchronization spatiotemporal patterns as the function of the ω , which represents the noise component of the evolution rule. For low ω values, the phase pattern is unstructured (see Figure 7.9(a)). At a threshold ω value, intermittent synchronization occurs Figure 7.9b. Further increasing ω , we reach a regime with highly synchronized channels. Intermittent synchronization across large cortical areas has been observed in ECoG and EEG experiments as well [27–30]. The correspondence between our theoretical/computational results and experimental data is encouraging. Further detailed studies are needed to identify the significance of the findings.

7.5.3

Hebbian Learning Effects

According to principles of neurodynamics, learning reinforces Hebbian cell assemblies, which respond to known stimuli [16, 23, 24] by destabilizing the broadband chaotic dynamics and lead to an attractor basin through a narrow-band oscillation using gamma band career frequency. To test this model, we implemented learning in the neuropercolation model. We use Hebbian learning, that is, the weight from node i to node j is incrementally increased if these two nodes have the same state ($1 - 1$ or $0 - 0$). The weight from i to j incrementally decreases if the two nodes have different activations ($0 - 1$ or $1 - 0$). Learning has been maintained during the 20-step periods when input was introduced.

In the basal mode without learning, the three double layers can generate broadband chaotic oscillations; see Figure 7.10a where the lower row is a zoomed-in version of the top row. The spikes in Figure 7.10a indicate the presence of input signals. Inputs have been implemented by flipping a small percentage of

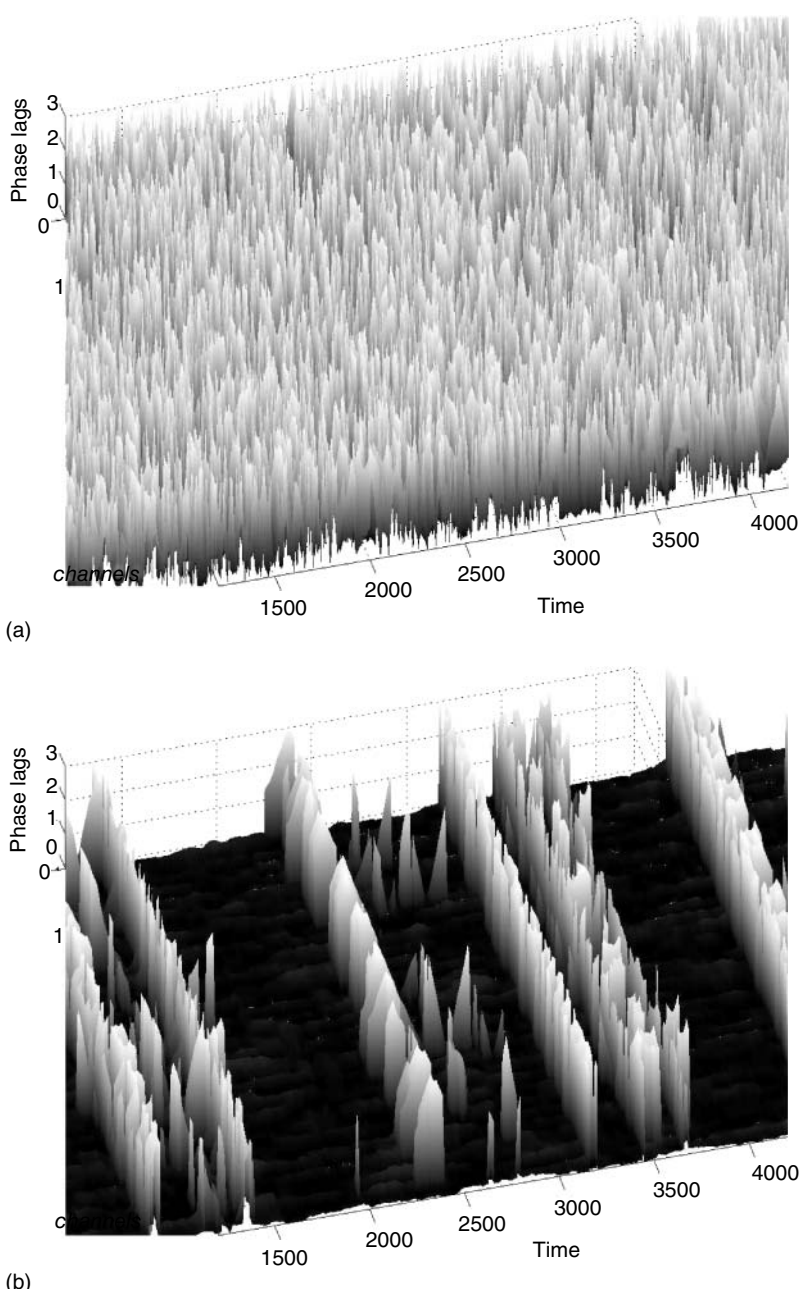


Figure 7.9 Desynchronization to synchronization transitions; (a) at ω below critical value there is no synchronization; (b) when ω exceeds a critical value, the graph exhibits intermittent large-scale synchronization.

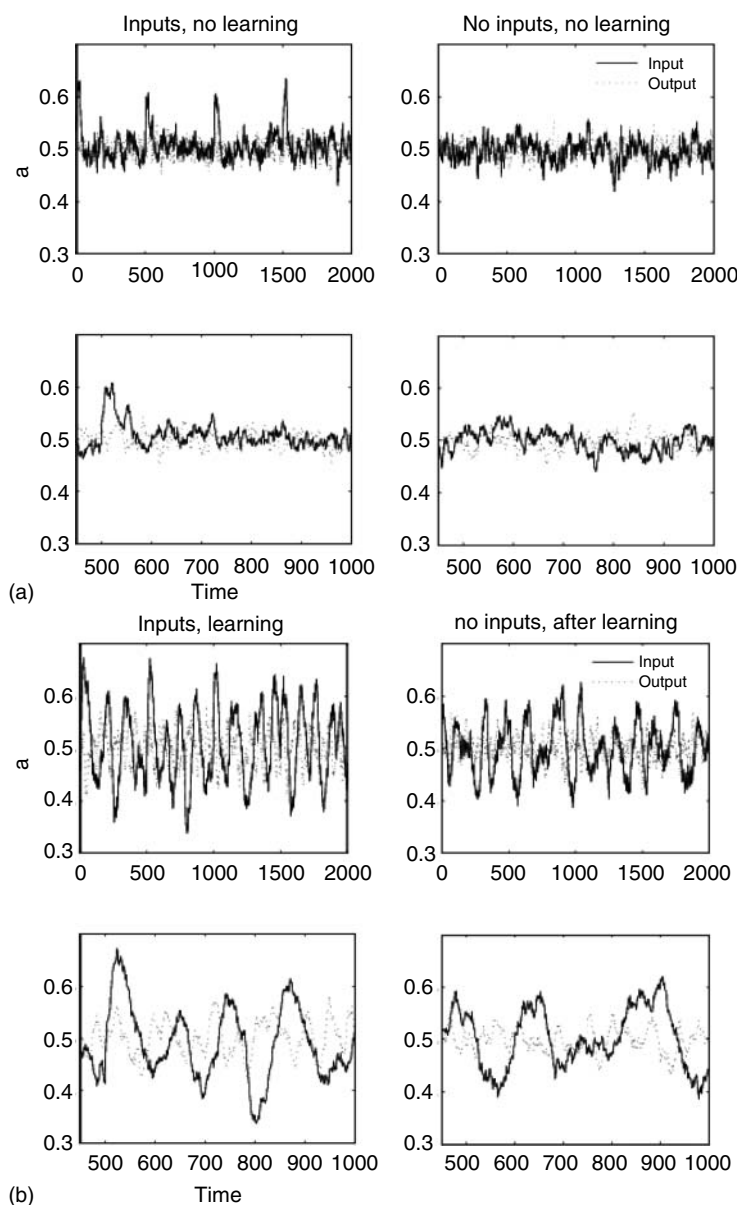


Figure 7.10 Learning effect in coupled oscillators. (a) Activity levels without learning; the first row contains extended time series plots, the second row has zoomed in sections. Input spike is shown at every 500 steps. The

activity returns to base level after the input ceases. (b): Activity levels with learning; the oscillations are prominent during learning and maintained even after the input step is removed (decayed).

the input layer nodes to state “1” (active) for the duration of 20 iteration steps. During the learning stage, inputs are introduced 40 times (20 steps each), at regular intervals of 500 iteration steps. Without learning, the activity returns to the low-level chaotic state soon after the input ceases. Figure 7.10b shows that a narrow-band oscillation becomes prominent during learning, when a specific input is presented. After learning, the oscillatory behavior of the lattice dynamics is more prominent, even without input, but the learnt input elicits much more significant oscillations. This is the manifestation of the sixth and seventh principles of Freeman’s neurodynamics, and it can be used to implement classification and control tasks using the neuropercolation model.

Further steps, toward the eighth and ninth principles, involve the analysis of the AM pattern, which is converted to a feature vector of dimension n . Here, n is the number of nodes in our lattice, which, after some coarse graining, corresponds to the EEG/ECoG electrodes. They provide our observation window into the operation of the cortex or cortex simulation. The feature vector is used to describe or label the cortical state at any moment. The AM pattern is formed by a low-dimensional, quasi-limit cycle attractor after synaptic changes with learning. The synaptic weights are described in a matrix, and the combination of different modalities to form Gestalts is done by concatenation of feature vectors. Research in this direction is in progress.

7.6 Conclusions

We employed the neuropercolation model to demonstrate basic principles of neurodynamics. Neuropercolation is a family of stochastic models based on the mathematical theory of probabilistic CA on lattices and random graphs and motivated by structural and dynamical properties of neural populations. The existence of phase transitions has been demonstrated in probabilistic CA and percolation models. Neuropercolation extends the concept of phase transitions to large interactive populations of nerve cells near criticality. Criticality in the neuropil is characterized by a critical region instead of a singular critical point. The trajectory of the brain as a dynamical system crosses the critical region from a less organized (gaseous) phase to a more organized (liquid) phase during input-induced destabilization and vice versa. Neuropercolation simulates these important results from mesoscopic ECoG/EEG recording across large spatial and temporal scales.

We showed that neuropercolation is able to naturally model input-induced destabilization of the cortex and the consequent phase transitions due to sensory input and learning effects. Broadband activity with scale-free power spectra is observed for unlearnt conditions. On the other hand, Hebbian learning results in the onset of narrow-band oscillations, indicating the selection of specific learnt inputs. These observations demonstrate the operation of the first seven building blocks of neurodynamics. Our results indicate that the introduced Hebbian learning effect can be used to identify and classify inputs. Considering that our model has

six coupled lattices, each with up to 10 000 nodes, massive computational resources have been involved in the simulations. Parallel chip implementation may be a natural way to expand the research in the future, especially when extending the work for multisensory Gestalt formation in the cortex.

References

1. von Neumann, J. (1958) *The Computer and the Brain*, Yale University Press, New Haven, CT.
2. Turing, A. (1954) The chemical basis of morphogenesis. *Philos. Trans. R. Soc. London, Ser. B*, **237**, 37–94.
3. Katchalsky, A. (1971) Biological flow structures and their relation to chemodiffusional coupling. *Neurosci. Res. Progr. Bull.*, **9**, 397–413.
4. Prigogine, I. (1980) *From Being to Becoming: Time and Complexity in the Physical Sciences*, WH Freeman, San Francisco, CA.
5. Haken, H. (1983) *Synergetics: An Introduction*, Springer-Verlag, Berlin.
6. Haken, H., Kelso, J., and Bunz, H. (1985) A theoretical model of phase transitions in human hand movements. *Biol. Cybern.*, **51**, 347–356.
7. Kelso, J. (1995) *Dynamic Patterns: The Self-Organization of Brain and Behavior*, MIT Press, Cambridge, MA.
8. Haken, H. (2002) *Brain Dynamics: Synchronization and Activity Patterns in Pulse-Coupled NeuralNets with Delays and Noise*, Springer-Verlag, Heidelberg.
9. Beggs, J.M. and Plenz, D. (2003) Neuronal avalanches in neocortical circuits. *J. Neurosci.*, **23** (35), 11 167.
10. Bak, P. (1996) *How Nature Works: The Science of Self-Organized Criticality*, Springer-Verlag, New York.
11. Beggs, J. (2008) The criticality hypothesis: how local cortical networks might optimize information processing. *Philos. Trans. R. Soc. A Math. Phys. Eng. Sci.*, **366** (1864), 329–343.
12. Petermann, T., Thiagarajan, T.C., Lebedev, M.A., Nicolelis, M.A.L., Chialvo, D.R., and Plenz, D. (2009) Spontaneous cortical activity in awake monkeys composed of neuronal avalanches. *Proc. Natl. Acad. Sci. U.S.A.*, **106** (37), 15 921.
13. Kozma, R. and Puljic, M. (2005) Phase transitions in the neuropercolation model of neural populations with mixed local and non-local interactions. *Biol. Cybern.*, **92**, 367–379.
14. Freeman, W. and Zhai, J. (2009) Simulated power spectral density (PSD) of background electrocorticogram (ECoG). *Cogn. Neurodyn.*, **3** (1), 97–103.
15. Bonachela, J.A., de Franciscis, S., Torres, J.J., and Munoz, M.A. (2010) Self-organization without conservation: are neuronal avalanches generically critical? *J. Stat. Mech.: Theory Exp.*, **2010** (02), P02015.
16. Freeman, W.J. (1975) *Mass Action in the Nervous System*, Academic Press, New York.
17. Chang, H. and Freeman, W. (1998a) Biologically modeled noise stabilizing neurodynamics for pattern recognition. *Int. J. Bifurcation Chaos*, **8** (2), 321–345.
18. Chang, H. and Freeman, W. (1998b) Local homeostasis stabilizes a model of the olfactory system globally in respect to perturbations by input during pattern classification. *Int. J. Bifurcation Chaos*, **8** (11), 2107–2123.
19. Freeman, W. (1987) Simulation of chaotic EEG patterns with a dynamic model of the olfactory system. *Biol. Cybern.*, **56** (2-3), 139–150.
20. Freeman, W. (1991) The physiology of perception. *Sci. Am.*, **264** (2), 78–85.
21. Freeman, W. (1995) Chaos in the brain: possible roles in biological intelligence. *Int. J. Intell. Syst.*, **10** (1), 71–88.
22. Principe, J., Tavares, V., Harris, J., and Freeman, W. (2001) Design and implementation of a biologically realistic olfactory cortex in analog VLSI. *Proc. IEEE*, **89**, 1030–1051.
23. Freeman, W. (1992) Tutorial on neurodynamics. *Int. J. Bifurcation Chaos*, **2**, 451.

24. Freeman, W. (1999) *How Brains Make Up Their Minds*, Weidenfeld & Nicolson, London.
25. Kozma, R. (2007) Neuropercolation. *Scholarpedia*, 2 (8), 1360.
26. Neumann, J.V. and Burks, A. (1966) *Theory of Self-Reproducing Automata*, University of Illinois Press, Urbana, IL.
27. Freeman, W. (2004) Origin, structure, and role of background EEG activity. Part 1. analytic amplitude. *Clin. Neurophysiol.*, 115 (9), 2077–2088.
28. Kozma, R. and Freeman, W. (2008) Interdispl Intermittent spatio-temporal desynchronization and sequenced synchrony in ECoG signals. *Interdispl. J. Chaos*, 18, 037131.
29. Freeman, W. and Kozma, R. (2010) Freeman's mass action. *Scholarpedia*, 5 (1), 8040.
30. Freeman, W. and Quiroga, Q. (2013) *Imaging Brain Function with EEG and ECoG*, Springer-Verlag, New York.
31. Freeman, W. and Erwin, H. (2008) Freeman k-set. *Scholarpedia*, 3 (2), 3238.
32. Chang, H. and Freeman, W. (1998c) Optimization of olfactory model in software to give power spectra reveals numerical instabilities in solutions governed by aperiodic (chaotic) attractors. *Neural Networks*, 11, 449–466.
33. Kozma, R. and Freeman, W. (2001) Chaotic resonance - methods and applications for robust classification of noisy and variable patterns. *Int. J. Bifurcation & Chaos*, 11 (6), 1607–1629.
34. Xu, D. and Principe, J. (2004) Dynamical analysis of neural oscillators in an olfactory cortex model. *IEEE Trans. Neural Netw.*, 5 (5), 1053–1062.
35. Ilin, R. and Kozma, R. (2006) Stability of coupled excitatory-inhibitory neural populations and application to control of multi-stable systems. *Phys. Lett. A*, 360 (1), 66–83.
36. Gutierrez-Osuna, R. and Gutierrez-Galvez, A. (2003) Habituation in the KII olfactory model with chemical sensor arrays. *IEEE Trans. Neural Netw.*, 14 (6), 1565–1568.
37. Freeman, W., Kozma, R., and Werbos, P. (2001) Biocomplexity: adaptive behavior in complex stochastic systems. *BioSystems*, 59, 109–123.
38. Beliaev, I. and Kozma, R. (2007) Time series prediction using chaotic neural networks: case study of cats benchmark test. *Neurocomputing*, 7 (13), 2426–2439.
39. Harter, D. and Kozma, R. (2005) Chaotic neurodynamics for autonomous agents. *IEEE Trans. Neural Netw.*, 16 (3), 565–579.
40. Kozma, R., Aghazarian, H., Huntsberger, T., Tunstel, E., and Freeman, W. (2007) Computational aspects of cognition and consciousness in intelligent devices. *IEEE Comput. Intell. Mag.*, 2 (3), 53–64.
41. Kozma, R., Huntsberger, T., Aghazarian, H., Tunstel, E., Ilin, R., and Freeman, W. (2008) Intentional control for planetary rover SRR2K. *Adv. Robot.*, 21 (8), 1109–1127.
42. Freeman, W. and Vitiello, G. (2008) Dissipation and spontaneous symmetry breaking in brain dynamics. *J. Phys. A: Math. Theory*, 41, 304042.
43. Freeman, W., Kozma, R., and Vitiello, G. (2012a) Adaptation of the generalized carnot cycle to describe thermodynamics of cerebral cortex. International Joint Conference on Neural Networks IJCNN2012, 10-15 June, 2012, Brisbane, QLD.
44. Kozma, R. and Puljic, M. (2013) Hierarchical Random Cellular Neural Networks for System-Level Brain-Like Signal Processing. *Neural Networks*, 45, pp. 101–110.
45. Erdős, P. and Rényi, A. (1959) *On Random Graphs I*, Publicationes Mathematicae, pp. 290–297.
46. Bollobás, B. (1984) The evolution of random graphs. *Trans. Am. Math. Soc.*, 286 (1), 257–274.
47. Bollobas, B. and Riordan, O. (2006) *Percolation*, Cambridge University Press, New York.
48. Watts, D. and Strogatz, S. (1998) Collective dynamics of “small-world” networks. *Nature*, 393, 440–442.
49. Sporns, O. (2006) Small-world connectivity, motif composition, and complexity of fractal neuronal connections. *BioSystems*, 85, 55–64.

50. Berlekamp, E., Conway, J., and Guy, R. (1982) *Winning Ways for Your Mathematical Plays: Games in General*, Vol. 1, Academic Press, New York.
51. Cipra, A. (1987) An introduction to the Ising model. *Am. Math. Mon.*, **94** (10), 937–959.
52. Marcq, P., Chaté, H., and Manneville, P. (1997) Universality in ising-like phase transitions of lattices of coupled chaotic maps. *Phys. Rev. E*, **55** (3), 2606–2627.
53. Wolfram, S. (2002) *A New Kind of Science*, Wolfram Media, Champaign, IL.
54. Balister, P., Bollobás, B., and Kozma, R. (2006) Large deviations for mean field models of probabilistic cellular automata. *Random Struct. Algor.*, **29** (3), 399–415.
55. Kozma, R., Puljic, M., Bollobás, B., Balister, P., and Freeman, W. (2005) Phase transitions in the neuropercolation model of neural populations with mixed local and non-local interactions. *Biol. Cybern.*, **92** (6), 367–379.
56. Binder, K. (1981) Finite size scaling analysis of ising model block distribution functions. *Z. Phys. B: Condens. Matter*, **43** (2), 119–140.
57. Puljic, M. and Kozma, R. (2008) Narrow-band oscillations in probabilistic cellular automata. *Phys. Rev. E*, **78** (026214), 6.
58. Ferrenberg, A. and Swendsen, R. (1988) New Monte Carlo technique for studying phase transitions. *Phys. Rev. Lett.*, **61** (23), 2635–2638, doi: 10.1103/PhysRevLett.61.2635.
59. Li, Z., L, S., and B, Z. (1995) Dynamic monte carlo measurement of critical exponents. *Phys. Rev. Lett.*, **74** (17), 3396–3398, doi: 10.1103/PhysRevLett.74.3396.
60. Loison, D. (1999) Binder's cumulant for the Kosterlitz–Thouless transition. *Journal of Physics: Condensed Matter*, **11** (34), 10.1088/0953-8984/11/34/101.
61. Hasenbusch, M. (2008) The binder cumulant at the Koesterlitz–Thouless transition. *Journal of Statistical Mechanics: Theory and Experiment*, **2008** (08), P08 003.
62. Kozma, R., Puljic, M., Balister, P., Bollobás, B. and Freeman, W. (2004) Neuropercolation: A random cellular automata approach to spatio-temporal neurodynamics. *Lecture Notes in Computer Science*, **3305**, 435–443.

8

Neuronal Avalanches in the Human Brain

Oren Shriki and Dietmar Plenz

8.1

Introduction

Neuronal avalanches are cascades of activity whose sizes obey a power-law distribution with a specific exponent of $\alpha = -3/2$ [1]. The demonstration of neuronal avalanches in cortical cultures as well as in anesthetized and awake animals [2] suggests that cortical dynamics in the brain is critical. By establishing critical dynamics, cortical networks maintain a balance of excitatory and inhibitory forces, which allows for the millisecond-precise propagation of neural activity without premature termination or explosive growth. These studies were based on recordings with microelectrode arrays on the scale of 1–10 mm with millisecond temporal resolution, leaving it unclear whether neuronal avalanches also appear in large-scale brain activity with similar temporal precision.

Here, we studied neuronal avalanches in large-scale human brain activity recorded using magnetoencephalography (MEG). The MEG signal is generated mainly by local, synchronous neuronal activity in the cortex. It has a temporal resolution that matches the millisecond timescale of neural activity propagation, which is advantageous over the relatively slow timescale of the blood-oxygen-level-dependent (BOLD) signal in functional magnetoresonance imaging (fMRI), an alternative noninvasive technique to study human brain activity. Compared to electroencephalography (EEG), the MEG signal is less distorted by the meninges and skull and is less affected by the activations of deeper brain structures [3]. The MEG also correlates well with the local field potential (LFP) [4], a measure preferentially used for invasive neuronal avalanche studies [1, 5–7].

Here we describe the main steps in applying the avalanche analysis to human brain data and present evidence for neuronal avalanches in large-scale human brain activity. A major aspect of our study is the description of neuronal avalanches in terms of a critical branching process [1, 2, 8]. For an introduction to critical branching processes, see Chapter 2 in this book. Briefly, in branching processes, activity propagates from one active group of neurons to another in a cascade. The ratio between the number of activations in consecutive time steps

is termed the *branching parameter*, σ . When $\sigma = 1$, the system is critical, producing a power-law size distribution with exponent $\alpha = -3/2$ [8]. For a given fixed inter-sensor sampling distance, the values of σ and α depend on the timescale at which the analysis is performed (see Chapter 1 for a detailed explanation). Here, we demonstrate that ongoing MEG resting activity in the human brain fulfills the minimal criterion for a fixed sensor sampling distance, that is, there is a timescale at which σ is close to 1 and α is indeed $-3/2$.

Several recent studies investigated the idea of critical dynamics in the human brain, but they did not address the critical branching process model in a rigorous quantitative manner. For example, a variation of the neuronal avalanche metric with events defined as moments of rapid amplitude transitions was applied to EEG data, but yielded poorer power-law fits and α close to -1.9 and steeper than $-3/2$ [9]. A recent study showed that avalanche exponents derived from resting-state MEG are correlated with exponents derived from a sensory-motor task [10]. In a recent resting-state human fMRI study [11] (see also Chapter 3), spatiotemporal contiguous clusters of activations in the BOLD signal also exhibited power-law behavior, but the exponents were not assessed.

Our major findings on neuronal avalanches in the resting MEG of humans first appeared in [12] in which we combined both positive and negative signal deflections for detecting events that constitute neuronal avalanches. Here, we show that similar results are obtained with either positive or negative signal deflections. We also present another analysis which shows that the area of the deflections is preserved in the course of an avalanche, providing another line of support for an underlying critical branching process.

8.2

Data and Cascade-Size Analysis

We analyzed resting-state activity from a total of $n = 104$ healthy subjects (38 males; 66 females; 31.8 ± 11.8 years). Recordings were done at the MEG core facility of the NIMH using 273 axial gradiometer sensors. Activity was recorded for 4 min with eyes closed at a sampling rate of 600 Hz and was band-pass filtered (1–80 Hz). In addition, we used independent component analysis (ICA) to remove components associated with the magnetocardiogram (MCG). We note that [12] also includes analysis of data sets from the MEG facility at Cambridge. Here, for clarity, we focus on the NIMH data sets.

Following previous studies of neuronal avalanches [1], we first detected discrete events in the continuous MEG signal. In each sensor, we examined positive and negative excursions beyond a threshold of ± 3 SD, and identified a single event per excursion, at the most extreme value (maximum for positive excursions and minimum for negative excursions; Figure 8.1a). The choice of threshold was motivated by observing the amplitude distribution and comparing it to the best-fit Gaussian distribution (Figure 8.1b). As indicated in the figure, the amplitude distributions start to differ from the Gaussian fit for values larger than ± 2.7 SD. A

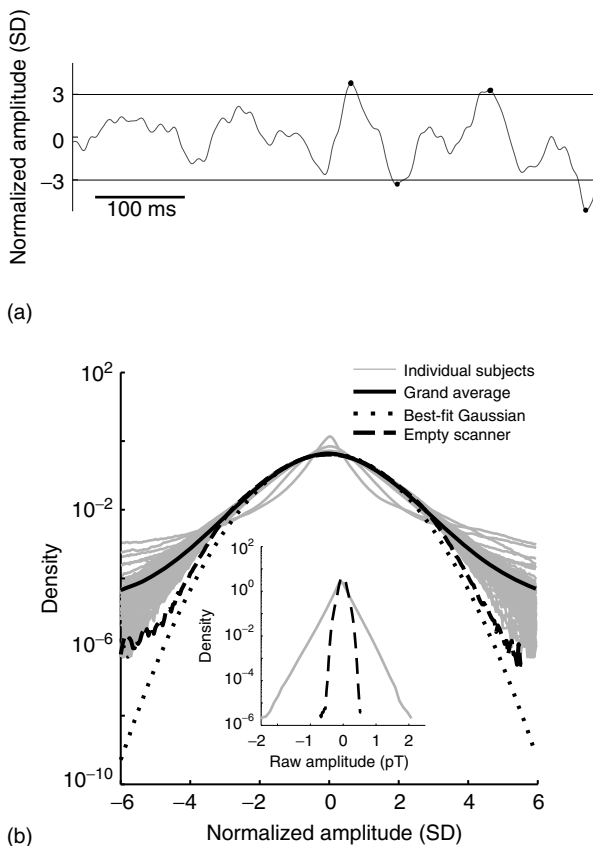


Figure 8.1 Detection of discrete events in the continuous MEG signal. (a) Continuous MEG signal of neuronal resting-state activity of the human brain (single sensor). The most extreme point in each excursion beyond a threshold of ± 3 SD (horizontal lines) was treated as a discrete event in the signal. Black dots mark positive and negative suprathreshold events. (b) Signal amplitude distributions. The gray curves in the background are the signal amplitude distributions of all individual subjects (based on all channels and all time points). Note that the signal from each sensor was z-normalized by subtracting its mean and dividing by the

standard deviation (SD). The solid black curve depicts the grand average over all subjects. The dotted line depicts the best-fit Gaussian distribution for the grand average for the range between ± 6 SD. The grand average and the Gaussian fit start deviating from one another around ± 2.7 SD. The broken line curve depicts the signal distribution of an empty scanner recording. For clarity, a logarithmic scale is used for the ordinate. The inset depicts the distributions of a single subject (solid line) and an empty scanner (broken line) recording using the raw amplitude in pico Tesla $10^{(-12)}$ Tesla.

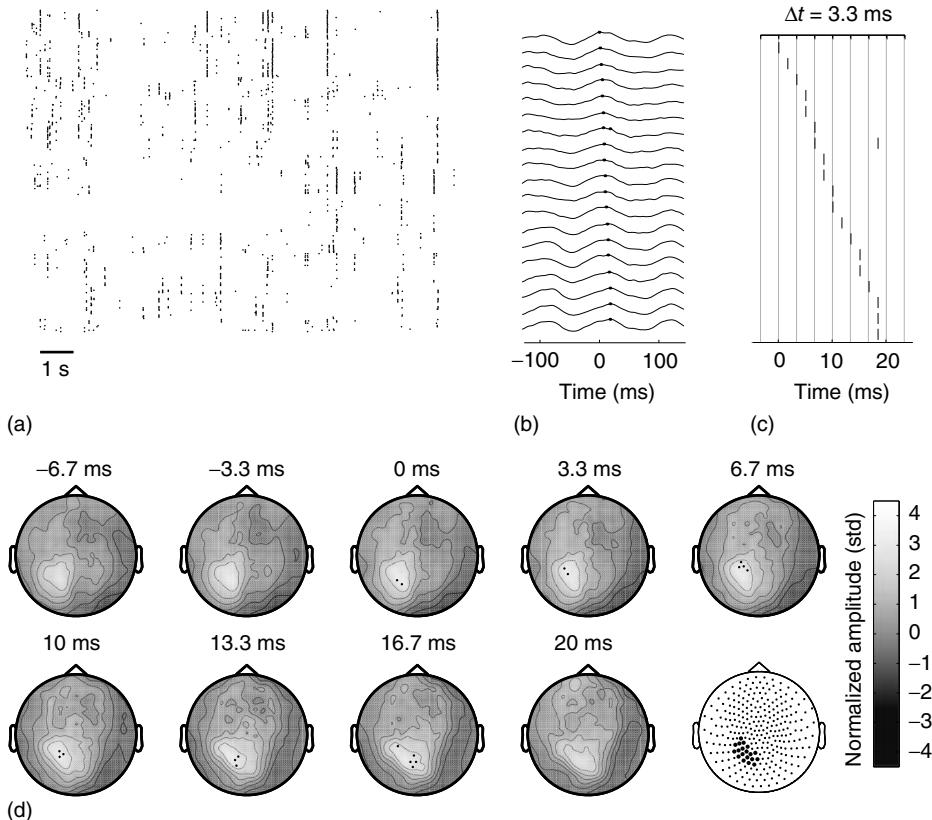


Figure 8.2 Identification and visualization of spatiotemporal cascades formed by discrete MEG events on the sensor array. (a) Raster of events on all sensors ($n=273$) in a 10 s segment of recording. (b-d) An example avalanche with cascade size of 20 events, lasting 20 ms and encompassing 19 different sensors. The original time series with identified events (b) leads to the raster of the cascade (c). For visualization, sensors are ordered according to the order of events.

A cascade was defined as a series of time bins in which at least one event occurred, ending with a silent time bin. Here, the time bin duration was 3.3 ms, twice the sampling time step (1.67 ms; 600 Hz). This cascade is visible as a positive-signed propagation in the lower left part of the sensor array (d). In each panel of (d), the black dots mark which sensors were active in that time bin. The last panel depicts the set of all sensors that participated in the cascade.

threshold of 3 SD ensures that most detected events reflect signal and not noise, but similar results were also obtained with other threshold values albeit with reduced rate of events when using higher thresholds [12].

A typical event raster (Figure 8.2a) reveals that events tend to cluster in time across subgroups of sensors. To quantify these clusters, each sensor's time series of events was individually time binned with bins of duration Δt . A cascade was defined as a continuous sequence of time bins in which there was an event on any sensor, ending with a time bin with no events on any sensor (Figure 8.2b,c).

Event clusters frequently engaged spatially contiguous sensors (Figure 8.2d). The number of events on all sensors in a cascade was defined as the cascade size. For each subject, the analysis was repeated for several bin durations, Δt (in multiples of $\Delta t_{\min} = 1.67$ ms, the inverse of the data acquisition sampling rate).

8.3

Cascade-Size Distributions are Power Laws

Figure 8.3a depicts the distribution of cascade sizes from a single subject analyzed at $\Delta t = 3.3$ ms. A maximum likelihood-based analysis [13, 14] demonstrates a significantly better fit to a power law compared to an exponential function [12]. Similar results were obtained for over 95% of the 104 NIH subjects and Δt ranging from the minimal time step of 1.67 up to 10 ms ($P < 0.05$ for all Δt). Phase shuffling of the original continuous signal destroys the correlations among brain sites as well as the power law (Figure 8.3a; broken line). It is important to note that the phase shuffling maintains the power spectrum density function. Thus, the shape of the power spectrum alone cannot account for the observed power-law distribution of cascade sizes.

As another control, we tested the effect of scaling the array size on the cutoff of the power law. To this end, we divided the original sensor array into subarrays of different sizes (Figure 8.3b, the upper right inset refers to the illustrations of the sensor arrays above the curve.) and recalculated the cascade size distributions (Figure 8.3b). As the sensor array increases in size, the power-law cutoff also increases. The mean estimated power-law cutoff across all subjects increased linearly with the size of the sensor array ($R^2 = 0.999$; $n = 104$; $\Delta t = 3.3$ ms). We also tested the effect of coarse-graining the sensor array by grouping clusters of neighboring sensors and combining their event rasters with a logical OR operation (i.e., multiple events observed during the same time bin for any sensor group were counted as one event). The resulting distributions maintained the power law behavior (Figure 8.3c).

8.4

The Data are Captured by a Critical Branching Process

In previous studies, the propagation of neuronal activity that results in a neuronal avalanche pattern was well described by a critical branching process [1, 2, 8]. The branching parameter σ was estimated by calculating the ratio of the number of events in the second time bin of an avalanche pattern to that in the first time bin. This ratio was averaged across all avalanche patterns for each subject (with no selection criteria). While critical dynamics are scale invariant in both space and time, the experimental necessity of a sensor array with characteristic spacing between sensors imposes a characteristic timescale on the observed events in the system. This relationship between timescale and sensor spacing was demonstrated previously for neuronal avalanches [1] and follows from the average speed of activity propagation in cortical tissue; as the sensor spacing increases, the time period Δt

required for activity to propagate across sensors will increase (see also Chapter 1). Because the folding of the cortex makes exact prediction of the relevant timescale difficult, we systematically examined multiple timescales for evidence of a critical branching process.

Using different timescales, that is, values of Δt , we found that both α and σ increased with longer Δt for all subjects (Figure 8.4a) in line with previous findings on neuronal avalanches *in vitro* [1]. Importantly, at the value of Δt where $\sigma = 1$, α was close to $-3/2$ (Figure 8.4a,b), consistent with a critical branching process. This

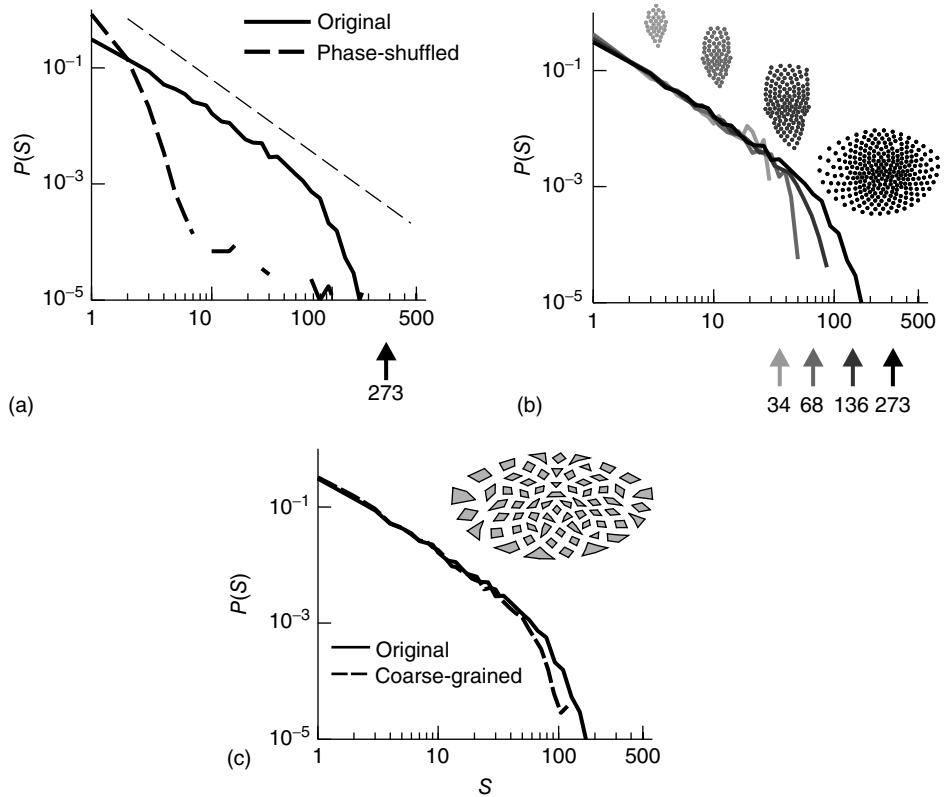


Figure 8.3 Cascade size distributions follow a power law with finite size cutoff as expected for neuronal avalanches. (a–c) Cascade size distributions for a single subject using $\Delta t = 3.3$ ms. (a) Solid black line depicts original data and thick broken line corresponds to phase-shuffled data. Thin broken line represents a power law with an exponent of $-3/2$. Arrow indicates the number of sensors N in the analysis (system size). (b) The cutoff of the size distribution changes

with array size as predicted for finite-size scaling. Cascade size distributions for subsamples of the sensor array. Gray values and arrows indicate the number of sensors N in the analysis. Upper right inset: Diagrams of the subregions of the sensor array used for analysis. (c) Cascade size distributions for the coarse-grained array. Black line: original data. Broken line: coarse-grained data. Inset: Diagram of coarse-grained sensor array with sensors grouped in clusters of ~ 4 sensors.

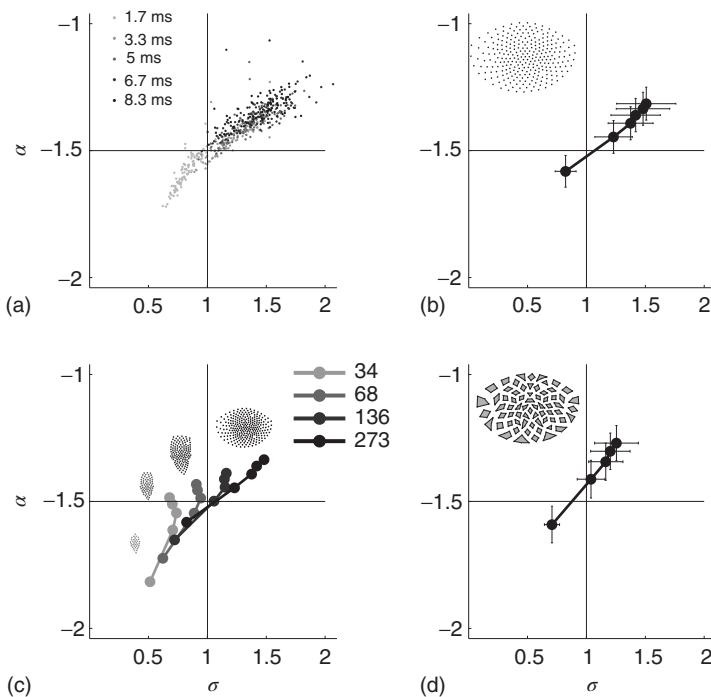


Figure 8.4 Neuronal avalanches in human MEG reveal power-law exponent of $\alpha = -3/2$ at critical branching parameter $\sigma = 1$. (a) Phase plots of the power-law exponent, α , versus the branching parameter, σ , for the several array types examined. Vertical and horizontal bars denote standard deviation. Solid vertical and horizontal lines denote the point $\sigma = 1$, $\alpha = -3/2$. Insets depict the corresponding sensor arrays. (b) All sensors. (c) Subsamples of the array. Error bars were omitted for clarity of presentation. (d) Coarse-grained array.

the branching parameter, σ , for the several array types examined. Vertical and horizontal bars denote standard deviation. Solid vertical and horizontal lines denote the point $\sigma = 1$, $\alpha = -3/2$. Insets depict the corresponding sensor arrays. (b) All sensors. (c) Subsamples of the array. Error bars were omitted for clarity of presentation. (d) Coarse-grained array.

Δt value was 3.3 ms, and at that timescale the avalanche rate across all NIH subjects was 18.3 ± 4.1 avalanches per second (mean \pm SD). The intersection of the critical values $\sigma = 1$, $\alpha = -3/2$ persisted when taking subarrays (Figure 8.4c) or coarse-graining the array (Figure 8.4d). We also found that subjects had well-correlated results between the first half and the second half of the recording (Figure 8.5a,b; α : $R^2 = 0.83$; σ : $R^2 = 0.72$).

In the analysis presented thus far, both positive and negative deflections in the MEG signal were used for identifying discrete events. However, similar results were also obtained when considering only positive or only negative events. In particular, cascade size distributions displayed power-law behavior (Figure 8.6a,b) and at $\sigma = 1$, α was close to $-3/2$ (Figure 8.6c,d). We also found that the exponents obtained using only positive or only negative events were correlated with the exponent obtained

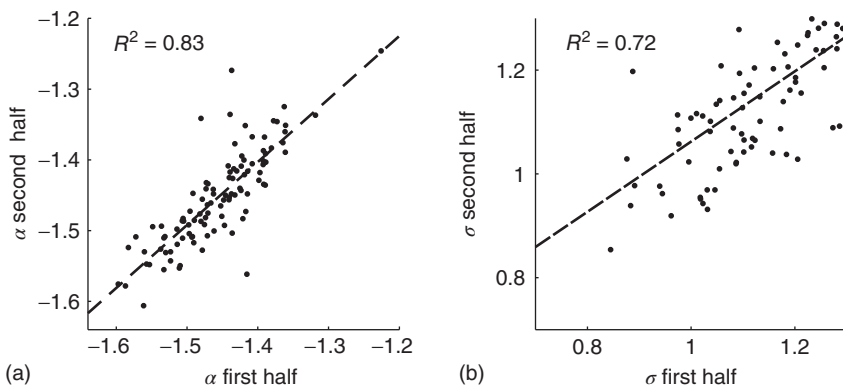


Figure 8.5 Power-law exponent and branching parameter are robust over time. Correlation of the power-law exponent, α , (a) and branching parameter, σ , (b) for all subjects ($N=104$), comparing the first 2 min of each 4 min recording to the last 2 min.

using both positive and negative events (Figure 8.6e,f; $R^2 = 0.95$ and $R^2 = 0.96$, respectively). Furthermore, the exponent obtained using only positive events was correlated with the one obtained using only negative events (Figure 8.6g; $R^2 = 0.89$). The branching parameters were correlated as well. For example, the branching parameter obtained using only positive events was correlated with the one obtained using only negative events (Figure 8.6h; $R^2 = 0.72$).

Another characteristic of critical behavior is the conservation of the level of activity within an avalanche. At criticality, the size of the activated group of neurons in each step of a cascade should reflect the size of the neuronal group that initiated that cascade. One approach to quantify this is to measure the area of the deflection associated with each event and then normalize it by the area associated with the first event (Figure 8.7a,b). This ratio is expected to be narrowly distributed around 1, or alternatively the log of this ratio should be narrowly distributed around 0 (Figure 8.7b). This was indeed demonstrated for LFP data [2], where the area of the deflection is proportional to the number of spiking neurons (see also Chapter 1). Although the relationship between the area of deflection in the MEG signal and the underlying neuronal activity is less clear, we performed this analysis and obtained similar results. Using the z-normalized waveforms (after subtracting the mean and dividing by the SD), we calculated for each identified event the area of the deflection between the two adjacent zero crossings. We normalized this by the mean area of the first identified event in the avalanche. The distributions of the log of the normalized areas for each time bin are presented in Figure 8.7c (solid curves; see legend). These distributions are the grand average from the distributions of all individual subjects ($n=104$). For comparison, we also generated shuffled data by randomly shuffling the areas among all events in a dataset. The distributions generated from these data have the same shape in different time bins and can therefore be averaged across time bins. The grand average distribution from the shuffled data (across time bins and subjects) is also presented in Figure 8.7c. This

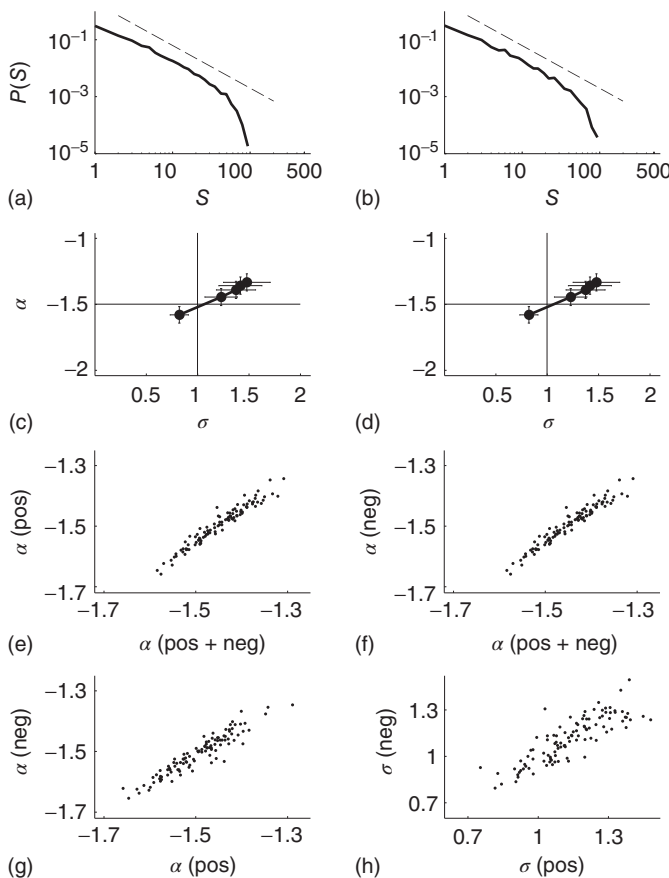


Figure 8.6 Similar results are obtained when using only positive or only negative events. (a,b) Cascade size distributions obtained using only positive (a) or only negative (b) events display power-law behavior. (c,d) Average phase plots of the exponent, α , versus the branching parameter, σ , using only positive (c) or only negative (d) events, show that for $\sigma=1$, α is close to $-3/2$. (e,f) The exponents obtained using

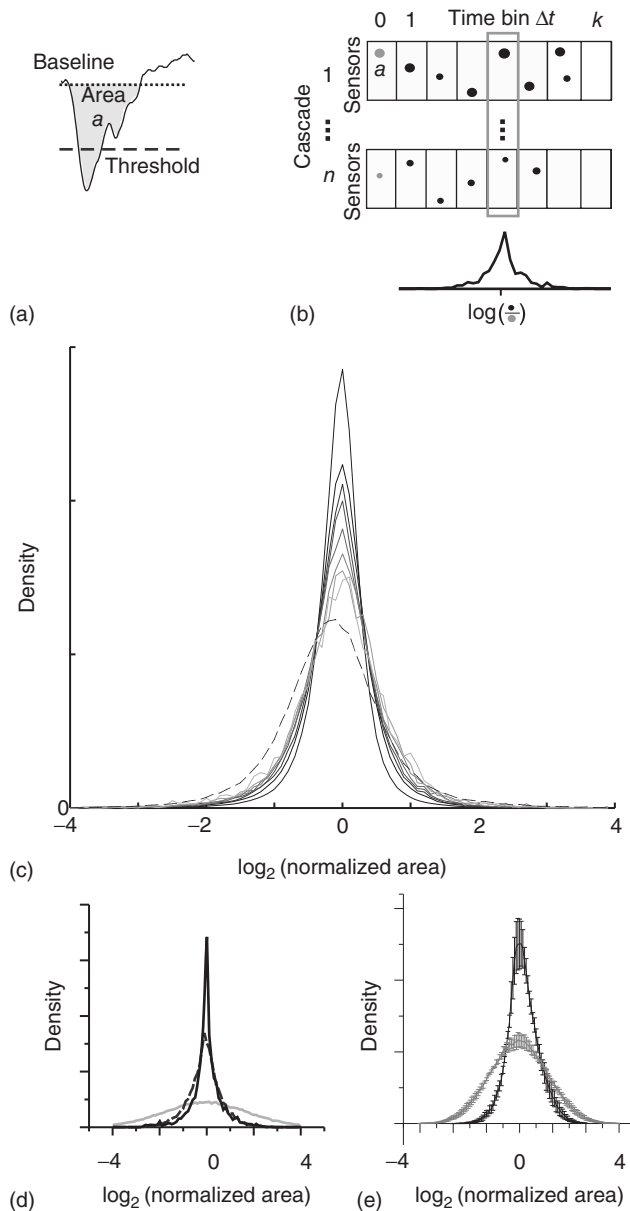
only positive (e) or only negative (f) events is correlated with the exponent obtained using both positive and negative events.

(g) The exponent obtained using only positive events is correlated with the exponent obtained using only negative events. (h) The branching parameter obtained using only positive events is correlated with the branching parameter obtained using only negative events.

distribution is also centered at 0 but is wider than the original distributions, most prominently in the earlier time bins. Similar results were obtained for positive-only or negative-only avalanches. For reference, Figure 8.7d,e depicts the results obtained from *in vitro* data (Figure 8.7d) and monkey *in vivo* data (Figure 8.7e) ([2]; see also Chapter 2).

8.5 Discussion

We studied resting-state activity in normal human subjects using MEG. We z-normalized the 273 MEG sensor signals and extracted discrete sequences of significant events by simple thresholding. The raster of significant events on the



sensor array revealed cascades of events, which we quantified further at different timescales. We found that the distribution of cascade sizes followed a power law and that the cutoff of the power law increased with the size of the sensor array, demonstrating clear finite-size scaling. At the timescale when the branching parameter σ was 1, the power-law exponent α was $-3/2$. The results were also robust to using either positive or negative deflections for event identification. In addition, we demonstrated that the area of signal deflections tends to be preserved in an avalanche, more than what would be expected by chance. Our results show that resting-state activity of the human brain as measured by MEG is well described by a critical branching process that produces scale-invariant neuronal avalanches. These findings represent neuronal avalanches previously identified at smaller spatial scales in *in vitro* and *in vivo*, for example, in the awake monkey, implying a universality of cortical activity [1, 5, 7].

Previous evidence for scale invariance and criticality in human brain activity was largely based on temporal measurements, such as long-range temporal correlations [15] and power-law power spectra [16]. Other ways to probe for scale-invariant behavior in human resting state activity have been based on dynamical synchronization. For example, Gong *et al.* [17] showed that the durations of transient synchronization events in the alpha band of the EEG obey a power-law distribution with an exponent close to -1.8 . This measure is more directly related to the lifetime of avalanches, which has been shown to follow a power law with exponent close to -2 [1], in line with expectations for critical branching processes. Similar results were later obtained by Kitzbichler *et al.* [18] for MEG and fMRI in several frequency bands, and, based on modeling work, it was proposed that they reflect critical dynamics.

An important aspect of the present study was the systematic investigation of a range of timescales and the use of the branching parameter to identify a particular timescale at which both $\sigma=1$ and power-law exponent $\alpha=-3/2$ were satisfied in line with predictions for the dynamics of a critical branching process, that is, neuronal avalanches. A power-law size distribution of cascade sizes was also recently reported in [10] based on human MEG. The analysis was performed by preselecting a single timescale that seemed consistent with previous reports on neuronal avalanches in the literature. The avalanche exponents of individual subjects were found to be correlated with exponents derived from a behavioral

Figure 8.7 Area of MEG deflections is conserved within cascades. (a) The area associated with an MEG event was defined as the area a of the deflection relative to the baseline. Here, we used the MEG waveform after subtracting the mean and dividing by the SD and for each event we calculated the area between the two adjacent zero crossings. (b) Illustration of estimating the change in a during cascades. At each time bin k , the log-values of $a(k)$ normalized to initial area, $a(0)$, (light gray) are calculated

for all cascades (box) and collected into a histogram. Dot diameter indicates area size. (c) Distributions of the log of the normalized areas for each time bin (solid curves; darker colors denote earlier time bins) and of shuffled data (broken line). (d,e) Similar distributions are obtained using neuronal avalanches in organotypic cortex cultures (d) and awake nonhuman primate (e) (for details, see [2]; light curves are shuffled controls).

power law (see also Chapter 5), further demonstrating the importance of neuronal avalanche dynamics for human brain function.

Theory and experiment have shown that systems at criticality maximize various information processing features (e.g., [19, 20]). Our results suggest that the human cortex realizes these information processing advantages and maintains its dynamics at the critical branching parameter of $\sigma = 1$. Some disorders in information processing, such as schizophrenia and autism, are thought to be associated with imbalance of excitatory and inhibitory forces [21, 22], reflecting deviations from the critical state [19]. These disorders may be probed using the framework of criticality and methodological approaches presented here.

8.6

Summary

Systems poised at criticality show scale-invariant dynamics, that is, similar types of activity can be observed at very different spatial and temporal scales. In the brain, critical dynamics have been associated with neuronal avalanches, intermittent cascades of neuronal activity that unfold with millisecond precision and which are characterized by a power law in cascade sizes and a critical branching parameter. Neuronal avalanches have been previously identified at millimeter scales in *in vitro* and *in vivo* animal studies. Here, we identified neuronal avalanches noninvasively in the human on a much larger spatial scale using MEG. We showed that avalanches can be obtained from positive as well as negative significant MEG deflections. We further demonstrated that MEG deflections remain relatively constant throughout an avalanche in line with a critical branching parameter and finding from LFP-based avalanche studies in the awake nonhuman primate and *in vitro*. Our findings suggest that the temporal and spatial precision of cortical dynamics is captured by neuronal avalanches and represents the normal human cortex operating at criticality.

Acknowledgements

This research was supported by the Division of Intramural Research Program of the National Institute of Mental Health, NIH, USA.

References

1. Beggs, J.M. and Plenz, D. (2003) Neuronal avalanches in neocortical circuits. *J. Neurosci.*, **23** (35), 11167–11177.
2. Plenz, D. (2012) Neuronal avalanches and coherence potentials. *Eur. Phys. J. Spec. Top.*, **205** (1), 259–301.
3. Hansen, P.C., Kringselbach, M.L., and Salmelin, R. (2010) *MEG: An Introduction to Methods*, Oxford University Press, Oxford, New York.
4. Zhu, Z. *et al.* (2009) The relationship between magnetic and electrophysiological responses to complex tactile stimuli. *BMC Neurosci.*, **10** (1), 4.
5. Gireesh, E.D. and Plenz, D. (2008) Neuronal avalanches organize as nested theta- and beta/gamma-oscillations during development of cortical layer 2/3. *Proc. Natl. Acad. Sci. U.S.A.*, **105** (21), 7576–7581.

6. Hahn, G. *et al.* (2010) Neuronal avalanches in spontaneous activity in vivo. *J. Neurophysiol.*, **104** (6), 3312–3322.
7. Petermann, T. *et al.* (2009) Spontaneous cortical activity in awake monkeys composed of neuronal avalanches. *Proc. Natl. Acad. Sci. U.S.A.*, **106** (37), 15921–15926.
8. Harris, T.E. (1989) *The Theory of Branching Processes*, Dover Publications, New York.
9. Allegrini, P., Paradisi, P., Menicucci, D., and Gemignani, A. (2010) Fractal complexity in spontaneous EEG metastable-state transitions: new vistas on integrated neural dynamics. *Front. Physiol.*, **1**, 128.
10. Palva, J.M. *et al.* (2013) Neuronal long-range temporal correlations and avalanche dynamics are correlated with behavioral scaling laws. *Proc. Natl. Acad. Sci. U.S.A.*, **110** (9), 3585–3590.
11. Tagliazucchi, E., Balenzuela, P., Fraiman, D., and Chialvo, D.R. (2012) Criticality in large-scale brain fMRI dynamics unveiled by a novel point process analysis. *Front. Physiol.*, **3**, 15.
12. Shriki, O. *et al.* (2013) Neuronal avalanches in the resting MEG of the human brain. *J. Neurosci.*, **33** (16), 7079–7090.
13. Klaus, A., Yu, S., and Plenz, D. (2011) Statistical analyses support power law distributions found in neuronal avalanches. *PLoS One*, **6** (5), e19779.
14. Clauset A, Shalizi CR, and Newman MEJ (2007) Power-law distributions in empirical data, arXiv:0706.1062v2.
15. Linkenkaer-Hansen, K., Nikouline, V.V., Palva, J.M., and Ilmoniemi, R.J. (2001) Long-range temporal correlations and scaling behavior in human brain oscillations. *J. Neurosci.*, **21** (4), 1370–1377.
16. He, B.J., Zempel, J.M., Snyder, A.Z., and Raichle, M.E. (2010) The temporal structures and functional significance of scale-free brain activity. *Neuron*, **66** (3), 353–369.
17. Gong, P., Nikolaev, A.R., and van Leeuwen, C. (2003) Scale-invariant fluctuations of the dynamical synchronization in human brain electrical activity. *Neurosci. Lett.*, **336** (1), 33–36.
18. Kitzbichler, M.G., Smith, M.L., Christensen, S.R., and Bullmore, E. (2009) Broadband criticality of human brain network synchronization. *PLoS Comput. Biol.*, **5** (3), e1000314.
19. Shew, W.L., Yang, H., Petermann, T., Roy, R., and Plenz, D. (2009) Neuronal avalanches imply maximum dynamic range in cortical networks at criticality. *J. Neurosci.*, **29** (49), 15595–15600.
20. Shew, W.L., Yang, H., Yu, S., Roy, R., and Plenz, D. (2011) Information capacity and transmission are maximized in balanced cortical networks with neuronal avalanches. *J. Neurosci.*, **31** (1), 55–63.
21. Insel, T.R. (2010) Rethinking schizophrenia. *Nature*, **468** (7321), 187–193.
22. Rubenstein, J. and Merzenich, M. (2003) Model of autism: increased ratio of excitation/inhibition in key neural systems. *Genes Brain Behav.*, **2** (5), 255–267.

9**Critical Slowing and Perception**

Karl Friston, Michael Breakspear, and Gustavo Deco

9.1**Introduction**

It is generally assumed that criticality and metastability underwrite the brain's dynamic repertoire of responses to an inconstant world. From perception to behavior, the ability to respond sensitively to changes in the environment – and to explore alternative hypotheses and policies – seems inherently linked to self-organized criticality. This chapter addresses the relationship between perception and criticality – using recent advances in the theoretical neuroscience of perceptual inference. In short, we will see that (Bayes) optimal inference – on the causes of sensations – necessarily entails a form of criticality – critical slowing – and a balanced synchronization between the sensorium and neuronal dynamics. This means that the optimality principles describing our exchanges with the world may also account for dynamical phenomena that characterize self-organized systems such as the brain.

This chapter considers the formal basis of self-organized instabilities that enable perceptual transitions during Bayes-optimal perception. We will consider the perceptual transitions that lead to conscious *ignition* [1] and how they depend on dynamical instabilities that underlie chaotic itinerary [2, 3] and self-organized criticality [4–6]. We will try to understand these transitions using a dynamical formulation of perception as approximate Bayesian inference. This formulation suggests that perception has an inherent tendency to induce dynamical instabilities that enable the brain to respond sensitively to sensory perturbations. We review the dynamics of perception, in terms of Bayesian optimization (filtering), present a formal conjecture about self-organized instability, and then test this conjecture, using neuronal simulations of perceptual categorization.

9.1.1**Perception and Neuronal Dynamics**

Perceptual categorization speaks to two key dynamical phenomena: transitions from one perceptual state to another and the dynamical mechanisms that permit

this transition. In terms of perceptual transitions, perception can be regarded as the selection of a single hypothesis from competing alternatives that could explain sensations [7]. This selection necessarily entails a change in the brain's representational or perceptual state – that may be unconscious in the sense of Helmholtz's unconscious inference or conscious. The implicit transition underlies much of empirical neuroscience (e.g., event-related potentials and brain activation studies) and has been invoked to understand how sensory information “goes beyond unconscious processing and gains access to conscious processing, a transition characterized by the existence of a reportable subjective experience” [1]. Dehaene and Changeux review converging neurophysiological data, acquired during conscious and unconscious processing, that speaks to the neural signatures of conscious access: late amplification of relevant sensory activity, long-distance cortico-cortical synchronization, and *ignition* of a large-scale prefrontoparietal network. The notion of ignition calls on several dynamical phenomena that characterize self-organization, such as distributed processing in coupled nonlinear systems, phase transitions, and metastability: see also [8]. In what follows, we ask whether the underlying dynamical mechanisms that lead to perceptual transitions and consequent ignition can be derived from basic principles; and, if so, what does this tell us about the self-organized brain.

9.1.2

Overview

We focus on a rather elementary form of self-organized criticality; namely, the self-destruction of stable dynamics during (Bayes-optimal) perception. In brief, if neuronal activity represents the causes of sensory input, then it should represent uncertainty about those causes in a way that precludes overly confident representations. This means that neuronal responses to stimuli should retain an optimal degree of instability that allows them to explore alternative hypotheses about the causes of those stimuli. To formalize this intuition, we consider neuronal dynamics as performing Bayesian inference about the causes of sensations, using a gradient descent on a (variational free energy) bound on the surprise induced by sensory input. This allows us to examine the stability of this descent in terms of Lyapunov exponents and how local Lyapunov exponents should behave. We see that the very nature of free energy minimization produces local Lyapunov exponents that fluctuate around small (near-zero) values. In other words, Bayes-optimal perception has an inherent tendency to promote critical slowing, which may be necessary for perceptual transitions and consequent categorization.

This chapter comprises five sections. The first section reviews the mechanisms that lead to itinerant and critical dynamics, noting that they all rest upon some form of dynamical instability – that can be quantified in terms of local Lyapunov exponents. The next section then turns to Bayes-optimal inference in the setting of free energy minimization to establish the basic imperatives for neuronal activity. In the third section, we look at neuronal implementations of free energy minimization, in terms of predictive coding, and how this relates to the anatomy and physiology

of message passing in the brain. In the fourth section, we consider the dynamics of predictive coding in terms of generalized synchronization and the Lyapunov exponents of the first section. This section establishes a conjecture that predictive coding will necessarily show self-organized instability. The conjecture is addressed numerically using neuronal simulations of perceptual categorization in the final section. We conclude with a brief discussion of self-organization, over different scales, in relation to the optimality principles on which this approach is based.

9.2 Itinerant Dynamics

One ubiquitous (and paradoxical) feature of self-organizing and *autopoietic* systems [9] is their predisposition to destroy their own fixed points. We have referred to this as *autovitiation* to emphasize the crucial role that self-induced instabilities play in maintaining peripatetic or itinerant (wandering) dynamics [10, 11]. The importance of itinerancy has been articulated many times in the past [12], particularly from the perspective of computation and autonomy [13]. Itinerancy provides a link between exploration and foraging in ethology [14] and dynamical systems theory approaches to the brain [15] that emphasize the importance of chaotic itinerancy [2] and self-organized criticality [6, 16, 4]. Itinerant dynamics also arise from metastability [17] and underlie important phenomena such as winnerless competition [18].

The vitiation of fixed points or attractors is a mechanism that appears in several guises and has found important applications in a number of domains. For example, it is closely related to the notion of autopoiesis and self-organization in situated (embodied) cognition [9]. It is formally related to the destruction of gradients in synergetic treatments of intentionality [19]. Mathematically, it finds a powerful application in universal optimization schemes [20] and, indeed, as a model of perceptual categorization [21]. In what follows, we briefly review the scenarios that give rise to itinerant dynamics: namely, *chaotic itinerancy*, *heteroclinic cycling*, and *multistable switching*.

9.2.1 Chaotic Itinerancy

Chaotic itinerancy refers to the behavior of complicated (usually coupled nonlinear) systems that possess weakly attracting sets – *Milnor attractors* – with basins of attraction that are very close to each other. Their proximity destabilizes the Milnor attractors to create *attractor ruins*, which allow the system to leave one attractor and explore another, even in the absence of noise. A Milnor attractor is a chaotic attractor onto which the system settles from a set of initial conditions with positive measure (volume). However, another set of initial conditions (also with positive measure) that belong to the basin of another attractor can be infinitely close; this is called *attractor riddling*. Itinerant orbits typically arise from unstable periodic orbits that connect to another attractor, or just wander out into state space and

then back onto the attractor, giving rise to *bubbling*. This is a classic scenario for *intermittency* – in which the dynamics are characterized by long periods of orderly behavior – as the system approaches a Milnor attractor – followed by brief turbulent phases, when the system approaches an unstable orbit. If the number of orbits is large, then this can happen indefinitely, because the Milnor attractor is *ergodic*. Ergodicity is an important concept and is also a key element of the free energy principle we will call upon later. The term *ergodic* is used to describe a dynamical system that has the same behavior averaged over time as averaged over its states. The celebrated ergodic theorem is credited to Birkhoff [22], and concerns the behavior of systems that have been evolving for a long time: intuitively, an ergodic system forgets its initial states, such that the probability a system is found in any state becomes – for almost every state – the proportion of time that state is occupied. See [23] for further discussion and illustrations. See [24] for discussion of chaotic itinerancy and power law residence times in attractor ruins.

The notion of Milnor attractors underlies much of the technical and cognitive literature on itinerant dynamics. For example, one can explain “a range of phenomena in biological vision, such as mental rotation, visual search, and the presence of multiple time scales in adaptation” using the concept of weakly attracting sets [21]. The common theme here is the induction of itinerancy through the destabilization of attracting sets or the gradients causing them [19]. The ensuing attractor ruins or relics [25] provide a framework for heteroclinic orbits that are ubiquitous in electrophysiology [26], cognition [27], and large-scale neuronal dynamics [28].

9.2.2

Heteroclinic Cycling

In heteroclinic cycling there are no attractors, not even Milnor ones – only saddles connected one to the other by heteroclinic orbits. A saddle is a point (invariant set) that has both attracting (stable) and repelling (unstable) manifolds. A heteroclinic cycle is a topological circle of saddles connected by heteroclinic orbits. If a heteroclinic cycle is asymptotically stable, the system spends longer and longer periods of time in a neighborhood of successive saddles; producing a peripatetic wandering through state space. The resulting heteroclinic cycles have been proposed as a metaphor for neuronal dynamics that underlie cognitive processing [18] and exhibit important behaviors such as winnerless competition, of the sort seen in central pattern generators in the motor system. Heteroclinic cycles have also been used as generative models in the perception of sequences with deep hierarchical structure [29]. Both chaotic itinerancy and heteroclinic cycling can arise from deterministic dynamics, in the absence of noise or random fluctuations. This contrasts with the final route to itinerancy that depends on noise.

9.2.3

Multistability and Switching

In multistability, there are typically a number of classical attractors – stronger than Milnor attractors in the sense that their basins of attraction not only have

positive measure but are also open sets. Open sets are just sets of points that form a neighborhood: in other words, one can move a point in any direction without leaving the set – similar to the interior of a ball, as opposed to its surface. These attractors are not connected, but rather separated by a basin boundary. However, they are weak in the sense that the basins are shallow (but topologically simple). System noise can then drive the system from attractor one to another to produce a succession of distinct trajectories – this is called *switching*. Multistability underlies much of the work on attractor network models of perceptual decisions and categorization; for example, binocular rivalry [30].

Notice that noise is required for switching among multistable attractors; however, it is not a prerequisite for chaotic itinerancy or heteroclinic cycling. In chaotic itinerancy, the role of noise is determined by the geometry of the instabilities. In heteroclinic cycles, noise acts to settle the time it takes to go around the cycle onto some characteristic time scale. Without noise, the system will gradually slow as it gets closer and closer (but never onto) the cycle.

9.2.4

Itinerancy, Stability, and Critical Slowing

All three scenarios considered rest on a delicate balance between dynamical stability and instability: chaotic itinerancy requires weakly attracting sets that have unstable manifolds; heteroclinic cycles are based on saddles with unstable manifolds and switching requires classical attractors with shallow basins. So how can we quantify dynamical stability? In terms of linear stability analysis, dynamical instability requires the principal Lyapunov exponent – describing the local exponential divergence of flow – to be greater than zero. Generally, when a negative principal Lyapunov exponent approaches zero from below, the systems approach a phase transition and exhibit critical slowing.

Lyapunov exponents are based on a local linear approximation to flow and describe the rate of exponential decay of small fluctuations about the flow. As the Lyapunov exponents approach zero, these fluctuations decay more slowly. However, at some point very near the instability, the local linearization breaks down and higher order nonlinear terms from the Taylor series expansion dominate (or at least contribute). At this stage, the system's memory goes from an exponential form to a power law and the fluctuations no longer decay exponentially but can persist, inducing correlations over large distances and timescales [31]. For example, in the brain, long-range cortico-cortical synchronization may be evident over several centimeters and show slow fluctuations [32]. This phenomenon is probably best characterized in continuous phase transitions in statistical physics, where it is referred to as *criticality*. The possibility that critical regimes – in which local Lyapunov exponents fluctuate around zero – are themselves attracting sets leads to the notion of *self-organized criticality* [33].

In this chapter, *critical slowing* is taken to mean that one or more local Lyapunov exponents approach zero from below [34]. Note that critical slowing does not imply the dynamics *per se* are slow; it means that unstable modes of behavior decay

slowly. Indeed, as the principal Lyapunov exponent approaches zero from below, the system can show fast turbulent flow as in intermittency. In what follows, we explore the notion that any self-organizing system that maintains a homeostatic and ergodic relationship with its environment will tend to show critical slowing. In fact, we conjecture that critical slowing is mandated by the very processes that underwrite ergodicity. In this sense, the existence of a self-organizing (ergodic) system implies that it will exhibit critical slowing. Put another way, self-organized critical slowing may be a necessary attribute of open ergodic systems.

In the context of self-organized neuronal activity, this leads to the conjecture that perceptual inference mandates critical slowing and is therefore associated with phase transitions and long-range correlations – of the sort that may correspond to the ignition phenomena considered in [1]. So what qualifies the brain as ergodic? Operationally, this simply means that the probability of finding the brain in a particular state is proportional to the number of times that state is visited. In turn, this implies that neuronal states are revisited over sufficiently long periods of time. This fundamental and general form of homeostasis is precisely what the free energy principle tries to explain.

9.3

The Free Energy Principle

This section establishes the nature of Bayes-optimal perception in the context of self-organized exchanges with the world. It may seem odd to consider, in such detail, a specific function as perception to understand generic behaviors such as critical slowing. However, to understand how the brain is coupled to the sensorium, we need to carefully distinguish between the hidden states of the world and internal states of the brain. Furthermore, we need to understand the basic nature of this coupling to see how key dynamical phenomena might arise.

We start with the basic premise that underlies free energy minimization; namely, that self-organizing systems minimize the dispersion of their sensory (interoceptive and exteroceptive) states to ensure a homeostasis of their (internal and external) milieu [35]. In this section, we see how action and perception follow from this premise and the central role of minimizing free energy. This section develops the ideas in a rather compact and formal way. Readers who prefer a nonmathematical description could skip to the summary at the end of this section.

Notation and set up: We will use $X : \Omega \rightarrow \mathbb{R}$ for real-valued random variables and $x \in X$ for particular values. A probability density will be denoted by $p(x) = \Pr\{X = x\}$ using the usual conventions and its entropy $H[p(x)]$ by $H(X)$. The tilde notation $\tilde{x} = (x, x', x'', \dots)$ denotes variables in generalized coordinates of motion, using the LaGrange notation for temporal derivatives [36]. Finally, $E[\cdot]$ denotes an expectation or average. For simplicity, constant terms will be omitted.

In what follows, we consider free energy minimization in terms of active inference: active inference rests on the tuple $(\Omega, \Psi, S, A, R, q, p)$ that comprises the following:

- A sample space Ω or nonempty set from which random fluctuations or outcomes $\omega \in \Omega$ are drawn;
- Hidden states $\Psi : \Psi \times A \times \Omega \rightarrow \mathbb{R}$ that constitute the dynamics of states of the world that cause sensory states and depend on action;
- Sensory states $S : \Psi \times A \times \Omega \rightarrow \mathbb{R}$ that correspond to the agent's sensations and constitute a probabilistic mapping from action and hidden states;
- Action $A : S \times R \rightarrow \mathbb{R}$ that corresponds to action emitted by an agent and depends on its sensory and internal states;
- Internal states $R : R \times S \times \Omega \rightarrow \mathbb{R}$ that constitute the dynamics of states of the agent that cause action and depend on sensory states;
- Conditional density $q(\tilde{\psi}) := q(\tilde{\psi}|\tilde{\mu})$ – an arbitrary probability density function over hidden states $\tilde{\psi} \in \Psi$ that is parameterized by internal states $\tilde{\mu} \in R$;
- Generative density $p(\tilde{s}, \tilde{\psi}|m)$ – a probability density function over external (sensory and hidden) states under a generative model denoted by m . This model specifies the Gibbs energy of any external states: $G(\tilde{s}, \tilde{\psi}) = -\ln p(\tilde{s}, \tilde{\psi}|m)$.

We assume that the imperative for any biological system is to minimize the dispersion of its sensory states, with respect to action: mathematically, this dispersion corresponds to the (Shannon) entropy of the probability density over sensory states. Under ergodic assumptions, this entropy is equal to the long-term time average of surprise (almost surely):

$$\begin{aligned} H(S) &= E_t[\mathcal{L}(\tilde{s}(t))] \\ \mathcal{L} &= -\ln p(\tilde{s}(t)|m) \end{aligned} \quad (9.1)$$

Surprise (or more formally surprisal or self-information) $\mathcal{L}(\tilde{s})$ is defined by the generative density or model. This means that the entropy of sensory states can be minimized through action:

$$a(t) = \arg \min_{a \in A} \{\mathcal{L}(\tilde{s}(t))\} \quad (9.2)$$

When Eq. (9.2) is satisfied, the variation of entropy in Eq. (9.1) with respect to action is zero, which means sensory entropy has been minimized (at least locally). From a statistical perspective, surprise is called *negative log evidence*, which means that minimizing surprise is the same as maximizing the Bayesian model evidence for the agent's generative model.

9.3.1

Action and Perception

Action cannot minimize sensory surprise directly (Eq. (9.2)) because this would involve an intractable marginalization over hidden states (an impossible averaging over all hidden states to obtain the probability density over sensory states) – so surprise is replaced with an upper bound called *variational free energy* [37]. This free energy is a functional of the conditional density or a function of the internal states that parameterize the conditional density. The conditional density is a key concept in inference and is a probabilistic representation of the unknown or hidden states.

It is also referred to as the *recognition density*. Unlike surprise, free energy can be quantified because it depends only on sensory states and the internal states that parameterize the conditional density. However, replacing surprise with free energy means that internal states also have to minimize free energy, to ensure it is a tight bound on surprise:

$$\begin{aligned} a(t) &= \arg \min_{a \in A} \{F(\tilde{s}(t), \tilde{\mu}(t))\} \\ \tilde{\mu}(t) &= \arg \min_{\tilde{\mu} \in R} \{F(\tilde{s}(t), \tilde{\mu})\} \\ F &= E_q[G(\tilde{s}, \tilde{\psi})] - H[q(\tilde{\psi}|\tilde{\mu})] \\ &= \mathcal{L}(\tilde{s}) + D[q(\tilde{\psi})||p(\tilde{\psi}|\tilde{s}, m)] \geq \mathcal{L}(\tilde{s}) \end{aligned} \quad (9.3)$$

This induces a dual minimization with respect to action and the internal states. These minimizations correspond to *action* and *perception*, respectively. In brief, the need for perception is induced by introducing free energy to finesse the evaluation of surprise, where free energy can be evaluated by an agent fairly easily, given a Gibbs energy or generative model. Gibbs energy is just the surprise or improbability associated with a combination of sensory and hidden states. This provides a probabilistic specification of how sensory states are generated from hidden states. The last equality here says that free energy is always greater than surprise because the second (Kullback–Leibler divergence) term is nonnegative. This means that when free energy is minimized with respect to the internal states, free energy approximates surprise and the conditional density approximates the posterior density over hidden states:

$$D[q(\tilde{\psi})||p(\tilde{\psi}|\tilde{s}, m)] \approx 0 \Rightarrow \begin{cases} F(\tilde{s}, \tilde{\mu}) \approx \mathcal{L}(\tilde{s}) \\ q(\tilde{\psi}) \approx p(\tilde{\psi}|\tilde{s}, m) \end{cases} \quad (9.4)$$

This is known as *approximate Bayesian inference*, which becomes exact when the conditional and posterior densities have the same form [38]. The only outstanding issue is the form of the conditional density adopted by an agent.

9.3.2

The Maximum Entropy Principle and the Laplace Assumption

If we admit an encoding of the conditional density up to second-order moments, then the maximum entropy principle [39] implicit in the definition of free energy (Eq. (9.3)) requires $q(\tilde{\psi}|\tilde{\mu}) = \mathcal{N}(\tilde{\mu}, \Sigma)$ to be Gaussian. This is because a Gaussian density has the maximum entropy of all forms that can be specified with two moments. Assuming a Gaussian form is known as the *Laplace assumption* and enables us to express the entropy of the conditional density in terms of its first moment or expectation. This follows because we can minimize free energy with

respect to the conditional covariance as follows:

$$\begin{aligned} F &= G(\tilde{s}, \tilde{\mu}) + \frac{1}{2} \text{tr}(\Sigma \cdot \partial_{\tilde{\mu}\tilde{\mu}} G) - \frac{1}{2} \ln|\Sigma| \Rightarrow \partial_\Sigma F = \frac{1}{2} \partial_{\tilde{\mu}\tilde{\mu}} G - \frac{1}{2} \Pi \\ \partial_\Sigma F &= 0 \Rightarrow \begin{cases} \Pi = \partial_{\tilde{\mu}\tilde{\mu}} G \\ F = G(\tilde{s}, \tilde{\mu}) + \frac{1}{2} \ln|\partial_{\tilde{\mu}\tilde{\mu}} G| \end{cases} \end{aligned} \quad (9.5)$$

Here, the conditional precision $\Pi(\tilde{s}, \tilde{\mu})$ is the inverse of the conditional covariance $\Sigma(\tilde{s}, \tilde{\mu})$. In short, free energy is a function of the conditional expectations (internal states) and sensory states.

9.3.3 Summary

To recap, we started with the assumption that biological systems minimize the dispersion or entropy of sensory states to ensure a sustainable and homeostatic exchange with their environment [35]. Clearly, this entropy cannot be measured or changed directly. However, if agents know how their action changes sensations (e.g., if they know contracting certain muscle fibers will necessarily excite primary sensory afferents from stretch receptors), then they can minimize the dispersion of their sensory states by countering surprising deviations from their predictions. Minimizing surprise through action is not as straightforward as it might seem, because surprise *per se* is an intractable quantity to estimate. This is where free energy comes in – to provide an upper bound that enables agents to minimize free energy instead of surprise. However, in creating the upper bound, the agent now has to minimize the difference between surprise and free energy by changing its internal states. This corresponds to perception and makes the conditional density an approximation to the true posterior density in a Bayesian sense [7, 40–44]. See Figure 9.1 for a schematic summary. We now turn to neurobiological implementations of this scheme, with a special focus on hierarchical message passing in the brain and the associated neuronal dynamics.

9.4

Neurobiological Implementation of Active Inference

In this section, we take the above-mentioned general principles and consider how they might be implemented in the brain. The equations in this section may appear a bit complicated; however, they are based on just three assumptions:

- The brain minimizes the free energy of sensory inputs defined by a generative model.
- The generative model used by the brain is hierarchical, nonlinear, and dynamic.
- Neuronal firing rates encode the expected state of the world, under this model.

The first assumption is the free energy principle, which leads to active inference in the embodied context of action. The second assumption is motivated easily by

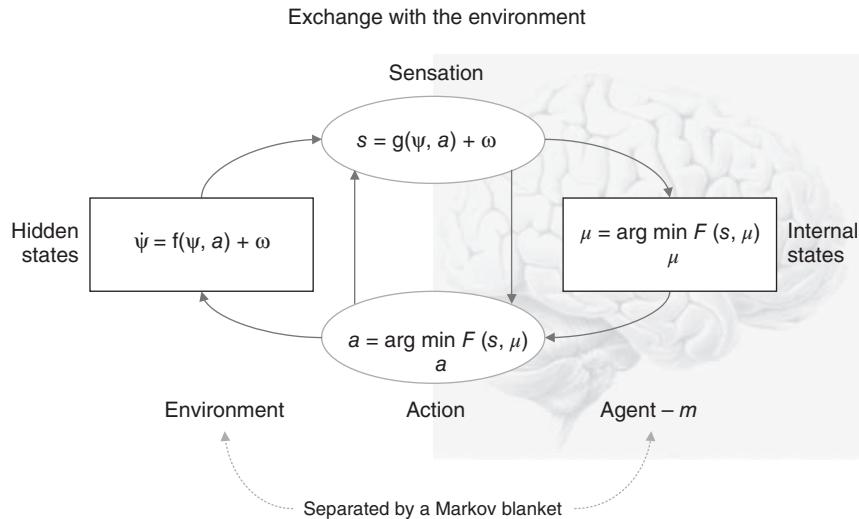


Figure 9.1 This schematic shows the dependencies among various quantities modeling exchanges of a self-organizing system such as the brain with the environment. It shows the states of the environment and the system in terms of a probabilistic dependency graph, where connections denote directed dependencies. The quantities are described within the nodes of this graph, with exemplar forms for their dependencies

on other variables (see main text). Here, hidden and internal states are separated by action and sensory states. Both action and internal states encoding a conditional density minimize free energy. Note that hidden states in the real world and the form of their dynamics are different from that assumed by the generative model; this is why hidden states are in bold. See main text for details.

noting that the world is both dynamic and nonlinear and that hierarchical causal structure emerges inevitably from a separation of temporal scales [45, 46]. The final assumption is the Laplace assumption that, in terms of neural codes, leads to the *Laplace code*, which is arguably the simplest and most flexible of all neural codes [47].

Given these assumptions, one can simulate a whole variety of neuronal processes by specifying the particular equations that constitute the brain's generative model. The resulting perception and action are specified completely by these assumptions and can be implemented in a biologically plausible way as described subsequently (see Table 9.1 for a list of previous applications of this scheme). In brief, these simulations use differential equations that minimize the free energy of sensory input using a generalized gradient descent [48].

$$\begin{aligned}\dot{\tilde{\mu}}(t) &= \mathcal{D} \tilde{\mu}(t) - \partial_{\tilde{\mu}} F(\tilde{s}, \tilde{\mu}) \\ \dot{a}(t) &= -\partial_a F(\tilde{s}, \tilde{\mu})\end{aligned}\quad (9.6)$$

These coupled differential equations describe perception and action, respectively, and just say that internal brain states and action change in the direction that reduces free energy. The first is known as (*generalized*) *predictive coding* and has the same form as Bayesian (e.g., Kalman–Bucy) filters used in time series analysis; see

Table 9.1 Processes and paradigms that have been modeled using generalized filtering.

Domain	Process or paradigm
Perception	Perceptual categorization (bird songs) [49] Novelty and omission-related responses [49] Perceptual inference (speech) [29]
Illusions	The Cornsweet illusion and Mach bands [50]
Sensory learning	Perceptual learning (mismatch negativity) [51]
Attention	Attention and the Posner paradigm [52] Attention and biased competition [52]
Motor control	Retinal stabilization and oculomotor reflexes [53] Orienting and cued reaching [53] Motor trajectories and place cells [54]
Sensorimotor integration	Bayes-optimal sensorimotor integration [53]
Visual search	Saccadic eye movements [55]
Behavior	Heuristics and dynamical systems theory [11] Goal-directed behavior [56]
Action observation	Action observation and mirror neurons [54]
Action selection	Affordance and sequential behavior [57]

also [58]. The first term in Eq. (9.6) is a prediction based on a matrix differential operator \mathcal{D} that returns the generalized motion of conditional expectations, such that $\mathcal{D}\tilde{\mu} = (\mu', \mu'', \mu''', \dots)$. The second term is usually expressed as a mixture of prediction errors that ensures the changes in conditional expectations are Bayes-optimal predictions about hidden states of the world. The second differential equation says that action also minimizes free energy. The differential equations are coupled because sensory input depends on action, which depends upon perception through the conditional expectations. This circular dependency leads to a sampling of sensory input that is both predicted and predictable, thereby minimizing free energy and surprise.

To perform neuronal simulations using this generalized descent, it is only necessary to integrate or solve Eq. (9.6) to simulate neuronal dynamics that encode the conditional expectations and ensuing action. Conditional expectations depend on the brain's generative model of the world, which we assume has the following (hierarchical) form

$$\begin{aligned}
s &= g^{(1)}(x^{(1)}, v^{(1)}, u^{(i)}) + \omega_v^{(1)} \\
\dot{x}^{(1)} &= f^{(1)}(x^{(1)}, v^{(1)}, u^{(i)}) + \omega_x^{(1)} \\
&\vdots \\
v^{(i-1)} &= g^{(i)}(x^{(i)}, v^{(i)}, u^{(i)}) + \omega_v^{(i)} \\
\dot{x}^{(i)} &= f^{(i)}(x^{(i)}, v^{(i)}, u^{(i)}) + \omega_x^{(i)} \\
&\vdots
\end{aligned} \tag{9.7}$$

This equation is just a way of writing down a model that specifies the generative density over the sensory and hidden states, where the hidden states $\Psi = X \times V$ have been divided into hidden dynamic states and causes. Here, $(g^{(i)}, f^{(i)})$ are nonlinear functions of hidden states that generate sensory inputs at the first (lowest) level, where for notational convenience, $v^{(0)} := s$.

Hidden causes $V \subset \Psi$ can be regarded as functions of hidden dynamic states; hereafter, hidden states $X \subset \Psi$. Random fluctuations $(\omega_x^{(i)}, \omega_v^{(i)})$ on the motion of hidden states and causes are conditionally independent and enter each level of the hierarchy. It is these that make the model probabilistic – they play the role of sensory noise at the first level and induce uncertainty about states at higher levels. The (inverse) amplitudes of these random fluctuations are quantified by their precisions $(\Pi_x^{(i)}, \Pi_v^{(i)})$, which we assume to be fixed in this chapter (but see Section 9.7). Hidden causes link hierarchical levels, whereas hidden states link dynamics over time. Hidden states and causes are abstract quantities that the brain uses to explain or predict sensations (similar to the motion of an object in the field of view). In hierarchical models of this sort, the output of one level acts as an input to the next. This input can produce complicated (generalized) convolutions with a deep (hierarchical) structure.

9.4.1

Perception and Predictive Coding

Given the form of the generative model (Eq. (9.7)), we can now write down the differential equations (Eq. (9.6)) describing neuronal dynamics in terms of (precision-weighted) prediction errors on the hidden causes and states. These errors represent the difference between conditional expectations and predicted values, under the generative model (using $A \cdot B := A^T B$ and omitting higher order terms):

$$\begin{aligned}\tilde{\mu}_x^{(i)} &= \mathcal{D} \tilde{\mu}_x^{(i)} + \frac{\partial \tilde{g}^{(i)}}{\partial \tilde{\mu}_x^{(i)}} \cdot \xi_v^{(i)} + \frac{\partial \tilde{f}^{(i)}}{\partial \tilde{\mu}_x^{(i)}} \cdot \xi_x^{(i)} - \mathcal{D}^T \xi_x^{(i)} \\ \dot{\tilde{\mu}}_v^{(i)} &= \mathcal{D} \dot{\tilde{\mu}}_v^{(i)} + \frac{\partial \tilde{g}^{(i)}}{\partial \tilde{\mu}_v^{(i)}} \cdot \xi_v^{(i)} + \frac{\partial \tilde{f}^{(i)}}{\partial \tilde{\mu}_v^{(i)}}^T \cdot \xi_x^{(i)} - \xi_v^{(i+1)} \\ \xi_x^{(i)} &= \Pi_x^{(i)} (\mathcal{D} \tilde{\mu}_x^{(i)} - \tilde{f}^{(i)}(\tilde{\mu}_x^{(i)}, \tilde{\mu}_v^{(i)})) \\ \xi_v^{(i)} &= \Pi_v^{(i)} (\tilde{\mu}_v^{(i-1)} - \tilde{g}^{(i)}(\tilde{\mu}_x^{(i)}, \tilde{\mu}_v^{(i)}))\end{aligned}\quad (9.8)$$

Equation (9.8) can be derived fairly easily by computing the free energy for the hierarchical model in Eq. (9.7) and inserting its gradients into Eq. (9.6). This gives a relatively simple update scheme, in which conditional expectations are driven by a mixture of prediction errors, where prediction errors are defined by the equations of the generative model.

It is difficult to overstate the generality and importance of Eq. (9.8): its solutions grandfather nearly every known statistical estimation scheme, under parametric assumptions about additive or multiplicative noise [36]. These range from ordinary

least squares to advanced variational deconvolution schemes. The resulting scheme is called *generalized filtering* or *predictive coding* [48]. In neural network terms, Eq. (9.8) says that error units receive predictions from the same level and the level above. Conversely, conditional expectations (encoded by the activity of state units) are driven by prediction errors from the same level and the level below. These constitute bottom-up and lateral messages that drive conditional expectations toward a better prediction to reduce the prediction error in the level below. This is the essence of the recurrent message passing between hierarchical levels to optimize free energy or suppress prediction error (see [49] for a more detailed discussion). In neurobiological implementations of this scheme, the sources of bottom-up prediction errors, in the cortex, are thought to be superficial pyramidal cells that send forward connections to higher cortical areas. Conversely, predictions are conveyed from deep pyramidal cells, by backward connections, to target (polysynaptically) the superficial pyramidal cells encoding prediction error [59, 51]. Figure 9.2 provides a schematic of the proposed message passing among

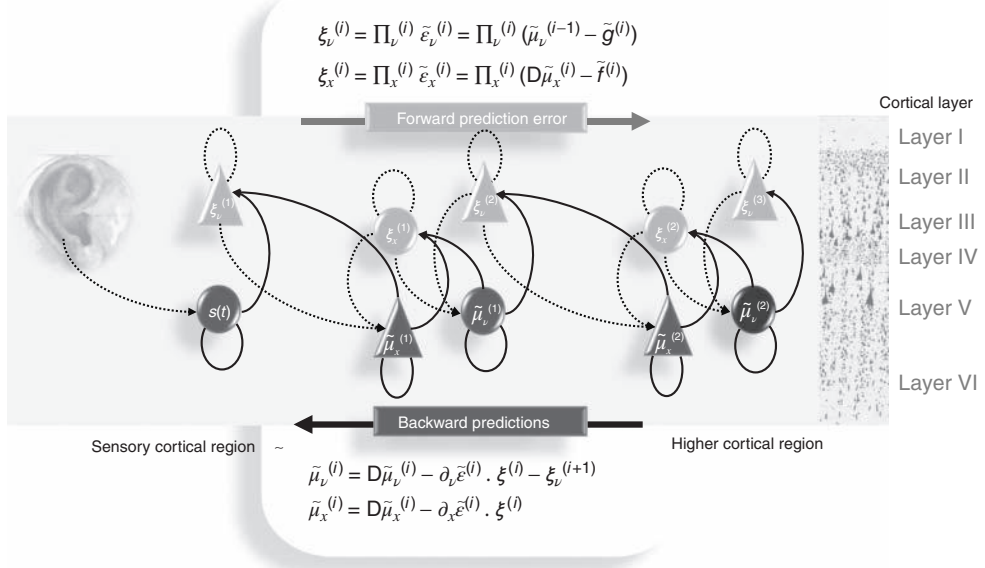


Figure 9.2 Schematic detailing a neuronal architecture that might encode conditional expectations about the states of a hierarchical model. This shows the speculative cells of origin of forward driving connections that convey prediction error from a lower area to a higher area and the backward connections that construct predictions [59]. These predictions try to explain away prediction error in lower levels. In this scheme, the sources of forward and backward connections are

superficial and deep pyramidal cells respectively. The equations represent a generalized descent on free energy under the hierarchical model described in the main text: see also [36]. State units are in black and error units are in gray. Here, neuronal populations are deployed hierarchically within three cortical areas (or macrocolumns). Within each area, the cells are shown in relation to cortical layers: supragranular (I–III), granular (IV), and infragranular (V–VI) layers.

hierarchically deployed cortical areas. Although this chapter focuses on perception, for completeness we conclude this section by looking at the neurobiology of action.

9.4.2

Action

In active inference, conditional expectations elicit behavior by sending top-down predictions down the hierarchy that are unpacked into proprioceptive predictions at the level of the cranial nerve nuclei and spinal cord. These engage classical reflex arcs to suppress proprioceptive prediction errors and produce the predicted motor trajectory

$$\dot{a} = -\frac{\partial}{\partial a} F = -\frac{\partial \tilde{s}}{\partial a} \cdot \xi_v^{(1)} \quad (9.9)$$

The reduction of action to classical reflexes follows because the only way that action can minimize free energy is to change sensory (proprioceptive) prediction errors by changing sensory signals; compare the equilibrium point formulation of motor control [60]. In short, active inference can be regarded as equipping a generalized predictive coding scheme with classical reflex arcs: see [53, 56] for details. The actual movements produced clearly depend on top-down predictions that can have a rich and complex structure, due to perceptual optimization based on the sampling of salient exteroceptive and interoceptive inputs.

9.4.3

Summary

In summary, we have derived equations for the dynamics of perception and action using a free energy formulation of adaptive (Bayes-optimal) exchanges with the world and a generative model that is both generic and biologically plausible. Intuitively, all we have done is to apply the principle of free energy minimization to a particular model of how sensory inputs are caused. This model is called a *generative model* because it can be used to generate sensory samples and thereby predict sensory inputs for any given set of hidden states. By requiring hidden states to minimize free energy, they become Bayes-optimal estimates of hidden states in the real world – because they implicitly maximize Bayesian model evidence. One simple scheme – that implements this minimization – is called *predictive coding* and emerges when random effects can be modeled as additive Gaussian fluctuations. Predictive coding provides a neurobiological plausible scheme for inferring states of the world that reduces, essentially, to minimizing prediction errors; namely, the difference between what is predicted – given the current estimates of hidden states – and the sensory inputs actually sampled.

In what follows, we use Eq. (9.6), Eq. (9.7), and Eq. (9.8) to treat neuronal responses in terms of predictive coding. A technical treatment of the above-mentioned material is found in [48], which provides the details of the generalized descent or filtering used to produce the simulations in the last section. Before

looking at these simulations, we consider the nature of generalized filtering and highlight its curious but entirely sensible dynamical properties.

9.5

Self-Organized Instability

This section examines self-organization in the light of minimizing free energy. These arguments do not depend in any specific way on predictive coding or the neuronal implementation of free energy minimization – they apply to any self-organizing system that minimizes the entropy of the (sensory) states that drive its internal states; either exactly by minimizing (sensory) surprise or approximately by minimizing free energy. In what follows, we first look at the basic form of the dynamics implied by exposing a self-organizing system to sensory input in terms of skew product systems. A skew product system comprises two coupled systems, where the states of one system influence the flow of states in the other – in our case, hidden states in the world influence neuronal dynamics. These coupled systems invoke the notion of (generalized) synchronization as quantified by conditional Lyapunov exponents (CLEs). This is important because the dynamics of a generalized descent on free energy have some particular implications for the CLEs. These implications allow us to conjecture that the local Lyapunov exponents will fluctuate around small (near-zero) values, which is precisely the condition for chaotic itinerancy and critical slowing. By virtue of the fact that this critical slowing is self-organized, it represents an elementary form of self-organized criticality; namely, self-organized critical slowing. In the next section, we test this conjecture numerically with simulations of perception, using the predictive coding scheme of the previous section.

9.5.1

Conditional Lyapunov Exponents and Generalized Synchrony

CLEs are normally invoked to understand synchronization between two systems that are coupled, usually in a unidirectional manner, so that there is a *drive* (or master) system and a *response* (or slave) system. The conditional exponents are those of the response system, where the drive system is treated as a source of a (chaotic) drive. Synchronization of chaos is often understood as a behavior in which two coupled systems exhibit identical chaotic oscillations – referred to as *identical synchronization* [61, 62]. The notion of chaotic synchronization has been generalized for coupled nonidentical systems with unidirectional coupling or a *skew product structure* [63]:

$$\begin{aligned}\dot{\tilde{\psi}} &= G_{\Psi}(\tilde{\psi}) \\ \tilde{\mu} &= G_{\mathcal{R}}(\tilde{\mu}, \tilde{\psi})\end{aligned}\tag{9.10}$$

Crucially, if we ignore action, neuronal dynamics underlying perception have this skew product structure, where $G_{\Psi}(\tilde{\psi})$ corresponds to the flow of hidden states and

$G_R = \mathcal{D} \tilde{\mu} - \partial_{\tilde{\mu}} F(\tilde{s}(\tilde{\psi}), \tilde{\mu})$ corresponds to the dynamical response. This is important because it means one can characterize the coupling of hidden states in the world to self-organized neuronal responses, in terms of generalized synchronization.

Generalized synchronization occurs if there exists a map $\Phi : \Psi \rightarrow R$ from the trajectories of the (random) attractor in the driving space to the trajectories of the response space, such that $\tilde{\mu}(t) = \Phi(\tilde{\psi}(t))$. Depending on the properties of the map $\Phi : \Psi \rightarrow R$, generalized synchronization can be of two types: weak and strong. Weak synchronization is associated with a continuous C^0 but nonsmooth map, where the synchronization manifold $M = \{(\Psi, R) : \Phi(\Psi) = R\}$ has a fractal structure and the dimension $D_{\Psi \times R}$ of the attractor in the full state space $\Psi \times R$ is larger than the dimension of the attractor D_Ψ in the driving Ψ subspace – that is $D_{\Psi \times R} > D_\Psi$.

Strong synchronization implies a smooth map (C^1 or higher) and arises when the response system does not inflate the global dimension, $D_{\Psi \times R} = D_\Psi$. This occurs with identical synchronization, which is a particular case $\Phi(\Psi) = \Psi$ of strong synchronization. The global and driving dimensions can be estimated from the appropriate Lyapunov exponents $\lambda_1 \geq \lambda_2 \geq \dots$ using the Kaplan–Yorke conjecture [64]

$$D = k + \sum_{i=1}^k \frac{\lambda_i}{|\lambda_{k+1}|} \quad (9.11)$$

Here, $\lambda_1 \geq \dots \geq \lambda_k$ are the k largest exponents for which the sum is nonnegative. Strong synchronization requires the principal Lyapunov exponent of the response system (neuronal dynamics) to be less than the k th Lyapunov exponent of the driving system (the world), while weak synchronization just requires it to be < 0 .

The Lyapunov exponents of a dynamical system characterize the rate of separation of infinitesimally close trajectories and provide a measure of contraction or expansion of the state space occupied. For our purposes, they can be considered as the eigenvalues of the Jacobian that describes the rate of change of flow, with respect to the states. The *global Lyapunov exponents* correspond to the long-term time average of *local Lyapunov exponents* evaluated on the attractor (the existence of this long-term average is guaranteed by Oseledets theorem). Lyapunov exponents also determine the stability or instability of the dynamics, where negative Lyapunov exponents guarantee Lyapunov stability (of the sort associated with fixed point attractors). Conversely, one or more positive Lyapunov exponents imply (local) instability and (global) chaos. Any (negative) Lyapunov exponent can also be interpreted as the rate of decay of the associated eigenfunction of states, usually referred to as *(Oseledeps) modes*. This means as a (negative) Lyapunov exponent approaches zero from below, perturbations of the associated mode decay more slowly. We will return to this interpretation of Lyapunov exponents in the context of stability later. For skew product systems, the CLE correspond to the eigenvalues of the Jacobian $\partial_{\tilde{\mu}} G_R(\tilde{\mu}, \tilde{\psi})$ mapping small variations in the internal states to their motion.

9.5.2

Critical Slowing and Conditional Lyapunov Exponents

This characterization of coupled dynamical systems means that we can consider the brain as being driven by sensory fluctuations from the environment. The resulting skew product system suggests that neuronal dynamics should show weak synchronization with the sensorium, which means that the maximal (principal) CLE should be <0 . However, if neuronal dynamics are generating predictions, by modeling the causes of sensations, then these dynamics should themselves be chaotic – because the sensations are caused by itinerant dynamics in the world. So, how can generalized synchronization support chaotic dynamics when the principal CLE is negative?

In skew product systems of the above-mentioned sort, it is useful to partition the Lyapunov exponents into those pertaining to *tangential* flow within the synchronization manifold and *transverse* flow away from the manifold [23]. In the full state space, the tangential Lyapunov exponents can be positive such that the motion on the synchronization manifold is chaotic, as in the driving system, while the transverse Lyapunov exponents are negative (or close to zero) so that the response system is weakly synchronized with the drive system. See Figure 9.3 for a schematic illustration of tangential and transverse stability. In short, negative transverse Lyapunov exponents ensure the synchronization manifold $M \subset \Psi \times R$ is transversely stable or (equivalently), while negative CLEs ensure the synchronized manifold

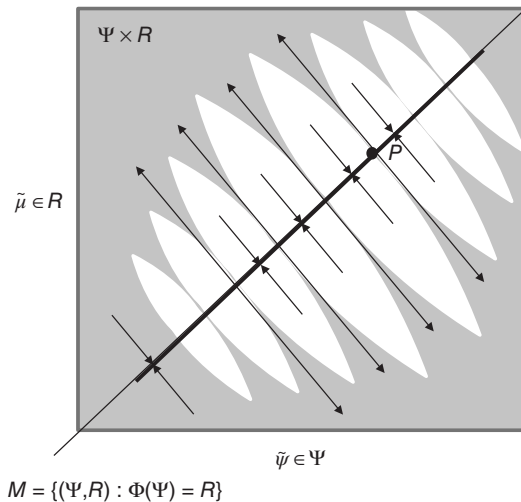


Figure 9.3 Schematic representation of synchronization manifold with weak transverse stability (Adapted from [3].): A Milnor attractor (dotted line) is contained within a synchronization manifold – here, an identity mapping. Unstable saddle points such as P

are repelling in the transverse direction and create narrow tongues of repelling regions (gray regions). Other orbits are attracted toward the chaotic attractor contained within the synchronization manifold.

$R = \Phi(\Psi)$ is stable [63]. In the present setting, this means that the sensorium enslaves chaotic neuronal responses. See [3] for a treatment of chaotic itinerancy and generalized synchronization as the basis of olfactory perception: by studying networks of Milnor attractors, [3] shows how different sensory perturbations can evoke specific switches between various patterns of activity.

Although generalized synchronization provides a compelling metaphor for perception, it also presents a paradox: if the CLE are negative and the synchronized manifold is stable, there is no opportunity for neuronal dynamics (conditional expectations) to jump to another attractor and explore alternative hypotheses. This dialectic is also seen in system identification, where the synchronization between an observed dynamical system and a model system is used to optimize model parameters by maximizing synchronization. However, if the coupling between the observations and the model is too strong, the variation of synchronization with respect to the parameters is too small to permit optimization. This leads to the notion of *balanced synchronization* that requires that the CLE “remain negative but small in magnitude” [65]. In other words, we want the synchronization between the causes of sensory input and neuronal representations to be strong but not too strong. Here, we resolve this general dialectic with the conjecture that Bayes-optimal synchronization is inherently balanced:

Conjecture: Dynamical systems that minimize variational free energy dynamically show self-organized critical slowing, with local CLEs $\lambda(t) \in \mathbb{R}$ that fluctuate around small (near-zero) values, where

$$\begin{aligned}\lambda &= \text{eig}(\partial_{\tilde{\mu}} G_R) \\ G_R &= \mathcal{D} \tilde{\mu} - \partial_{\tilde{\mu}} F(\tilde{s}(t), \tilde{\mu}(t))\end{aligned}\quad (9.12)$$

Proof: Let $0 \leq \gamma_1 \leq \gamma_2 \leq \dots$ be the real-valued positive eigenvalues of the curvature of Gibbs energy or conditional precision. From Eq. (9.5), the free energy can be expressed in terms of these Gibbs exponents

$$\begin{aligned}F &= G + \frac{1}{2} \ln |\partial_{\tilde{\mu}\tilde{\mu}} G| \\ &= G + \frac{1}{2} \sum_i \ln \gamma_i \Rightarrow \frac{\partial F}{\partial \gamma_i} = \frac{1}{2\gamma_i} \geq 0\end{aligned}\quad (9.13)$$

This shows that the greatest contribution ($\ln \gamma_1 \ll 0$) to free energy comes from the smallest exponent – and changes in free energy, with respect to the Gibbs exponents, are greater for smaller values. Therefore, all other things being equal, a generalized descent on free energy will reduce small Gibbs exponents toward zero. So how are the Lyapunov and Gibbs exponents related? By ignoring third and higher derivatives of Gibbs energy, we can approximate the curvature of the free energy with the curvature of the Gibbs energy: from Eq. (9.5) and Eq. (9.6)

$$\begin{aligned}\partial_{\tilde{\mu}\tilde{\mu}} F &= \partial_{\tilde{\mu}\tilde{\mu}} G + \partial_{\tilde{\mu}\tilde{\mu}} \frac{1}{2} \ln |\partial_{\tilde{\mu}\tilde{\mu}} G| \\ &\Rightarrow \\ \partial_{\tilde{\mu}} G_R &\approx \mathcal{D} - \partial_{\tilde{\mu}\tilde{\mu}} G\end{aligned}\quad (9.14)$$

The relationship between the Lyapunov exponents (eigenvalues of $\mathcal{D} - \partial_{\tilde{\mu}\tilde{\mu}} G$) and Gibbs exponents (eigenvalues of $\partial_{\tilde{\mu}\tilde{\mu}} G$) is not simple; however, if we assume that $\partial_{\tilde{\mu}\tilde{\mu}} G$ is approximately diagonal, then

$$\lambda = \text{eig}(\mathcal{D} - \partial_{\tilde{\mu}\tilde{\mu}} G) \approx \text{eig}(-\partial_{\tilde{\mu}\tilde{\mu}} G) = -\gamma \quad (9.15)$$

In other words, the Lyapunov exponents approximate the negative Gibbs exponents. This means that a generalized descent on free energy will be attracted to inherently unstable minima, with a low curvature and small local CLE. ■

Remarks: More intuitively, from Eq. (9.6), one can see that the Jacobian can be decomposed into prediction and update terms

$$\partial_{\tilde{\mu}} G_R = \mathcal{D} - \partial_{\tilde{\mu}\tilde{\mu}} F(\tilde{s}(t), \tilde{\mu}(t)) \quad (9.16)$$

The contribution of the second (update) depends on the curvature of the variational free energy. This will always have negative eigenvalues, because the curvature is positive definite (near a minimum). Conversely, the first (prediction) term has eigenvalues of zero. This means, as the free energy curvature decreases, the eigenvalues of the Jacobian will get smaller (and can indeed become positive for small but finite curvatures). This is important for two reasons; first, because the free energy changes with time, the local CLE will fluctuate. Second, because the system is minimizing free energy, it is implicitly minimizing its curvature (conditional precision) and is therefore driving some local CLE toward zero (and possibly positive) values. In short, free energy minimization will tend to produce local CLE that fluctuate at near-zero values and exhibit self-organized instability or slowing.

We could motivate the diagonal approximation of the curvature by noting diagonal forms of the conditional covariance minimize free energy. However, off-diagonal terms are usually quite pronounced and indicate conditional dependencies among representations. The associated off-diagonal terms in the curvature mean that $\lambda \approx -\gamma$ only holds for large exponents, while small Lyapunov exponents are greater than their corresponding (negative) Gibbs exponents. This means that a generalized descent on free energy can become transiently chaotic with positive Lyapunov exponents. We will see an example of this later.

Heuristically, this self-organized instability follows from the principle of maximum entropy (that generalizes Laplace's principle of indifference) and reflects the intuition that, while being faithfully responsive to sensory information, it is important to avoid very precise and particular interpretations. From a dynamical perspective, it implies an active maintenance of critically slow (Oseledets) modes, whose CLE are close to zero. In summary, dynamical (approximate) Bayesian inference schemes are inherently self-destabilizing because they search out explanations for data that have the largest margin of error (smallest conditional precision). This produces instability and a critical slowing of the implicit gradient descent. In the

next section, we use a heuristic measure of this slowing:

$$C = \sum_i \exp(\tau \cdot \lambda_i) \quad (9.17)$$

This is simply a sum of the exponential CLE that discounts large negative values. It can be thought of, roughly, as the number of small CLE, where smallness is controlled by a scale parameter τ . Alternatively, the components of the sum in Eq. (9.17) can be regarded as the relative amplitude of a perturbation to the associated mode after τ units of time. In systems with a large number of small negative CLE, these relative amplitudes will be preserved and critical slowing will be large. For systems that show generalized synchronization (where all the CLE are negative), the critical slowing in Eq. (9.17) is upper bounded by the number of CLE.

9.5.3

Summary

In summary, we have reviewed the central role of Lyapunov exponents in characterizing dynamics, particularly in the context of generalized (weak or strong) synchronization. This is relevant from the point of view of neuronal dynamics because we can cast neuronal responses to sensory drive as a skew product system, where generalized synchronization requires the CLE of the neuronal system to be negative. However, generalized synchronization is not a complete description of how external states entrain the internal states of self-organizing systems: entrainment rests upon minimizing free energy that, we conjecture, has an inherent instability. This instability or self-organized critical slowing is due to the fact that internal states with a low free energy are necessarily states with a low free energy curvature. Statistically, this ensures that conditional expectations maintain a conditional indifference or uncertainty that allows for a flexible and veridical representation of hidden states in the world. Dynamically, this low curvature ameliorates dissipation by reducing the (dissipative) update, relative to the (conservative) prediction. In other words, the particular dynamics associated with variational free energy minimization may have a built-in tendency to instability.

It should be noted that this conjecture deals only with dynamical (gradient descent) minimization of free energy. One could also argue that chaotic itinerancy may be necessary for exploring different conditional expectations to select the one with the smallest free energy. However, it is interesting to note that – even with a deterministic gradient descent – there are reasons to conjecture a tendency to instability. The sort of self-organized instability is closely related to, but is distinct from, chaotic itinerancy and classical self-organized criticality. Chaotic itinerancy deals with itinerant dynamics of deterministic systems that are reciprocally coupled to each other [2]. Here, we are dealing with systems with a skew product (master–slave) structure. However, it may be that both chaotic itinerancy and critical slowing share the same hallmark, namely, fluctuations of the local Lyapunov exponents around small (near-zero) values [66].

Classical self-organized criticality usually refers to the intermittent behavior of skew product systems in which the drive is constant. This contrasts with the current situation, where we consider the driving system (the environment) to show chaotic itinerancy. In self-organized criticality, one generally sees intermittency with characteristic power laws pertaining to macroscopic behaviors. It would be nice to have a general theory linking the organization of microscopic dynamics in terms of CLE to the macroscopic phenomena studied in self-organized criticality. However, work in this area is generally restricted to specific systems. For example, [67] discuss Lyapunov exponents in the setting of the Zhang model of self-organized criticality. They show that small CLE are associated with energy transport and derive bounds on the principal negative CLE in terms of the energy flux dissipated at the boundaries per unit of time. Using a finite-size scaling ansatz for the CLE spectrum, they then relate the scaling exponent to quantities such as avalanche size and duration. Whether generalized filtering permits such an analysis is an outstanding question. For the rest of this chapter, we focus on illustrating the more limited phenomena of self-organized critical slowing using simulations of perception.

9.6

Birdsong, Attractors, and Critical Slowing

In this section, we illustrate perceptual ignition and critical slowing using neuronal simulations based on the predictive coding scheme of previous sections. Our purpose here is simply to illustrate self-organized instability using numerical simulations: these simulations should be regarded as a proof of principle but should not be taken to indicate that the emergent phenomena are universal or necessary for perceptual inference. In brief, we created sensory stimuli corresponding to bird songs, using a Lorenz attractor with variable control parameters (similar to the Raleigh number). A synthetic bird then heard the song and used a hierarchical generative model to infer the control parameters and thereby categorize the song. These simulations show how the stimulus induces critical slowing in terms of changes in the CLE of the perceptual dynamics. We then systematically changed the generative model by changing the precision of the motion on hidden states. By repeating the simulations, we could then examine the emergence of critical slowing (averaged over peristimulus time) in relation to changes in variational free energy and categorization performance. On the basis of the conjecture of the previous section, we anticipated that there will be a regime in which critical slowing was associated with minimum free energy and veridical categorization. In what follows, we describe the stimuli and generative model. We then describe perceptual categorization under optimal prior beliefs about precision and finally characterize the perceptual responses under different (suboptimal) priors.

9.6.1

A Synthetic Avian Brain

The example used here deals with the generation and recognition of bird songs [68, 69]. We imagine that bird songs are produced by two time-varying hidden causes that modulate the frequency and amplitude of vibrations of the syrinx of a song bird (Figure 9.4). There has been an extensive modeling effort using attractor

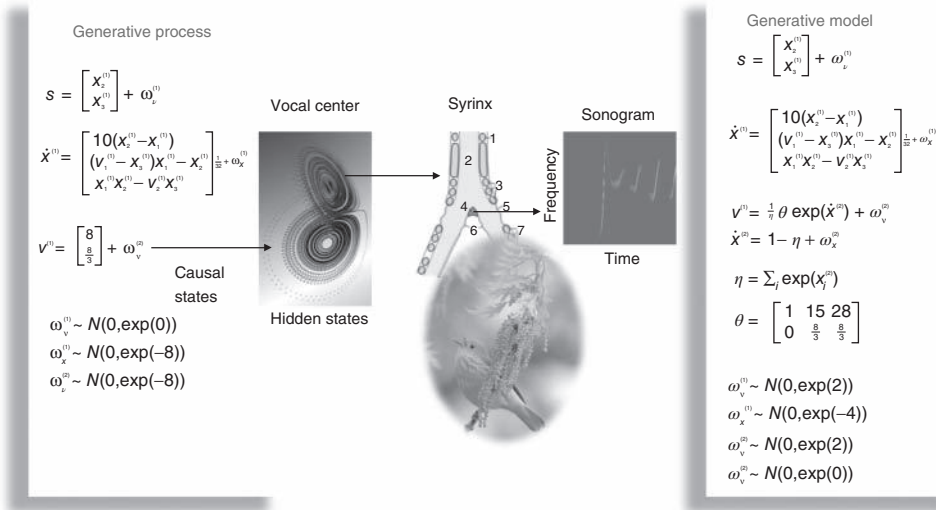


Figure 9.4 This is a schematic of stimulus generation and the generative model used for the simulations of bird song perception. In this setup, the higher vocal center of a song bird has been modeled with a Lorenz attractor from which two states have been borrowed, to modulate the amplitude and frequency of chirps by its voice box or syrinx. Crucially, the sequence of chirps produced in this way depends on the shape of the attractor, which is controlled by two hidden causes. This means that we can change the category of song by changing the two hidden causes. This provides a way of generating songs that can be mapped to a point in a two-dimensional perceptual space. The equations on the left describe the production of the stimulus, where the equations of motion for the hidden states correspond to the equations of motion with a Lorenz attractor. These hidden causes were changed smoothly after 32 (16 ms) time bins to transform the attractor from a fixed point

attractor (silence) to a chaotic attractor (bird song). The resulting stimulus is shown in sonogram format with time along the x-axis and frequency over the y-axis. The equations on the right constitute the generative model. The generative model is equipped with hidden states at a higher (categorical) level that model the evolution of the hidden causes that determine the attractor manifold for the hidden (attractor) states at the first level. The function-generating hidden causes uses a softmax function of the hidden categorical states to select one of three hidden causes. The associated categories of songs correspond to silence, a quasiperiodic song, and a chaotic song. The amplitudes of the random fluctuations are determined by their variance or log precisions and are shown in the lower part of the figure. Using this setup, we can produce some fairly realistic chirps that can be presented to a synthetic bird to see if it can recover the hidden causes and implicitly categorize the song.

models at the biomechanical level to understand the generation of birdsong [68]. Here, we use the attractors at a higher level to provide time-varying control over the resulting sonograms [29]. We drive the syrinx with two states of a Lorenz attractor, one controlling the frequency (between 2 and 5 kHz) and the other (after rectification) controlling the amplitude or volume. The parameters of the Lorenz attractor were chosen to generate a short sequence of chirps every second or so. These parameters correspond to hidden causes ($\mathbf{v}_1^{(1)}, \mathbf{v}_2^{(1)}$) that were changed as a function of peristimulus time to switch the attractor into a chaotic state and generate stimuli. Note that these hidden causes have been written in boldface. This is to distinguish them from the hidden causes ($v_1^{(1)}, v_2^{(1)}$) inferred by the bird hearing the stimuli.

The generative model was equipped with prior beliefs that songs could come in one of three categories; corresponding to three distinct pairs of values for the hidden causes. This was modeled using three hidden states to model the Lorenz attractor dynamics at the first level and three hidden states to model the category of the song at the second level. The hidden causes linking the hidden states at the second level to the first were a weighted mixture of the three pairs of values corresponding to each category of song. The bird was predisposed to infer one and only one category by weighting the control values with a softmax function of the hidden states. This implements a winner-takes-all-like behavior and enables us to interpret the softmax function as a probability over the three song categories (softmax probability).

This model of an avian brain may seem a bit contrived or arbitrary; however, it was chosen as a minimal but fairly generic model for perception. It is generic because it has all the ingredients required for perceptual categorization. First, it is hierarchical and accommodates chaotic dynamics in the generation of sensory input. Here, this is modeled as a Lorenz attractor that is subject to small random fluctuations. Second, it has a form that permits categorization of stimuli that extend over (frequency) space and time. In other words, perception or model inversion maps a continuous, high-dimensional sensory trajectory onto a perceptual category or point in some perceptual space. This is implemented by associating each category with a hidden state that induces particular values of the hidden causes. Finally, there is a prior that induces competition or winner-takes-all interactions among categorical representations, implemented using a softmax function. This formal prior (a prior induced by the form of a generative model) simply expresses the prior belief that there is only one cause of any sensory consequence at any time. Together, this provides a generative model based on highly nonlinear and chaotic dynamics that allows competing perceptual hypotheses to explain sensory data.

9.6.2

Stimulus Generation and the Generative Model

Figure 9.4 shows a schematic of stimulus generation and the generative model used for categorization. The equations on the left describe the production of the stimulus, where the equations of motion for the hidden states $\mathbf{x}^{(1)} \in \mathbb{R}^3$ correspond

to the equations of motion with a Lorenz attractor. In all the simulations that follow, the hidden causes were changed smoothly from $v^{(1)} = (1, 0)$ to $v^{(1)} = \left(28, \frac{8}{3}\right)$ after 32 (16 ms) time bins. This changes the attractor from a fixed point attractor to a chaotic attractor and produces the stimulus onset.

The equations on the right constitute the generative model and have the form of Eq. (9.7). Notice that the generative model is slightly more complicated than the process generating stimuli – it is equipped with hidden states at a higher hierarchical level $x^{(2)} \in \mathbb{R}^3$ that determine the values of the hidden causes, which control the attractor manifold for the hidden states $x^{(1)} \in \mathbb{R}^3$ at the first level. Also note that these hidden states decay uniformly until the sum of their exponentials is equal to 1. The function-generating hidden causes implement a softmax mixture of three potential values for the hidden causes $v^{(1)} \in \mathbb{R}^2$ encoded in the matrix $\theta \in \mathbb{R}^{2 \times 3}$. The three categories of songs correspond to silence, a quasiperiodic song, and a chaotic song. This means that the stimulus changes from silence (the first category) to a chaotic song (the third category). The amplitudes of the random fluctuations are determined by their variance or log precisions and are shown in the lower part of Figure 9.4. Given the precise form of the generative model and a stimulus sequence, one can now integrate or solve Eq. (9.8) to simulate neuronal responses encoding conditional expectations and prediction errors.

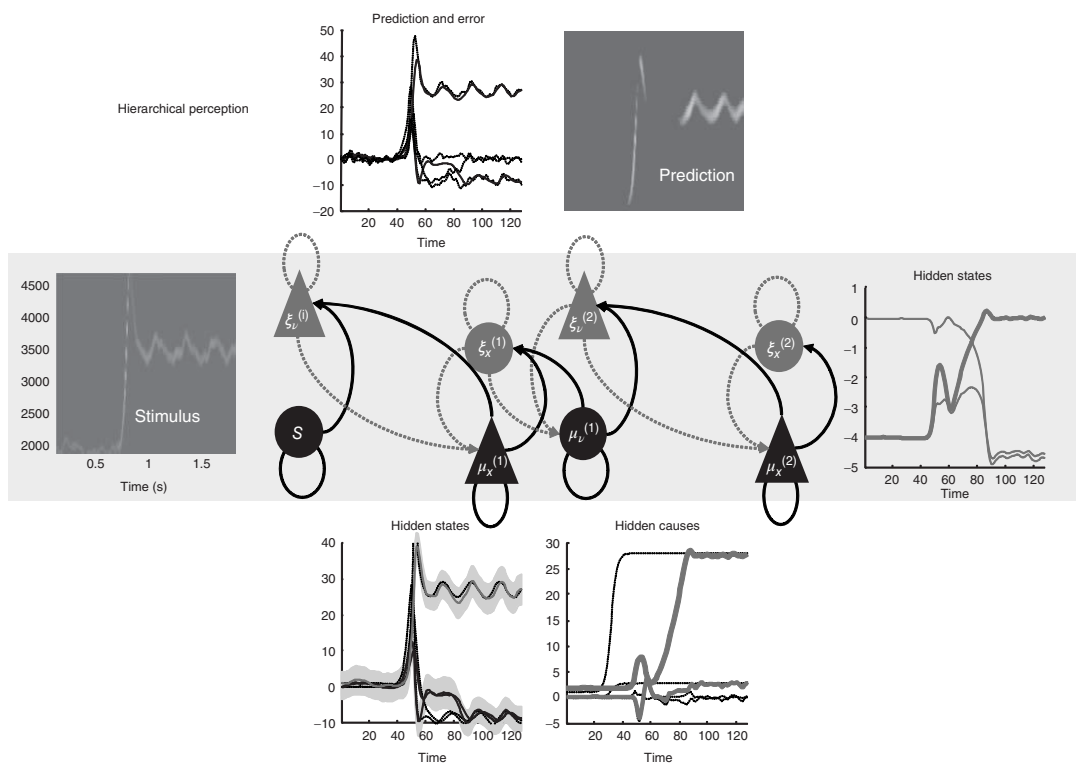
9.6.3

Perceptual Categorization

Figure 9.5 shows an example of perceptual categorization using the format of Figure 9.2. The panel on the left shows the stimulus in sonogram format, while the corresponding conditional predictions and errors (dotted lines) are shown as functions of time (respectively a sonogram) in the upper left (respectively right) panel. These predictions are based on the expected hidden states at the first level shown on the lower left. The gray areas correspond to conditional confidence intervals of 90%. It can be seen that the conditional estimate of the hidden state modulating frequency is estimated reasonably accurately (upper gray line);

Figure 9.5 This reports an example of perceptual categorization following the format of Figure 9.2. The panel on the left shows the stimulus in sonogram format, while the corresponding conditional predictions and errors (dotted lines) are shown as functions of time (respectively a sonogram) in the upper left (respectively right) panel. These predictions are based on the expected hidden states at the first level shown on the lower left. The gray areas correspond to 90% conditional confidence intervals. It can be seen that the conditional estimate of the

hidden state modulating frequency is estimated reasonably accurately (upper gray line); however, the corresponding modulation of amplitude takes a couple of chirps before it finds the right level (lower black line). This reflects changes in the conditional expectations about hidden causes and the implicit category of the song. The correct category is only inferred after about 80 time bins (thick line in the right panel), when expectations of the second level hidden states are driven by ascending prediction errors to their appropriate values.



however, the corresponding modulation of amplitude takes a couple of chirps before it finds the right level (lower black line). This reflects changes in the conditional expectations about hidden causes and the implicit category of the song. The correct (third) category is only inferred after about 80 time bins (thick line in the right panel), when expectations of the second level hidden states are driven by ascending prediction errors to their appropriate values.

Figure 9.6 shows the same results with conditional confidence intervals on all hidden states and causes and the implicit softmax probabilities based on the categorical hidden states at the second level (lower right panel). Note the high degree of uncertainty about the first hidden attractor state, which can only be inferred on the basis of changes (generalized motion) in the second and third states that are informed directly by the frequency and amplitude of the stimulus. These results illustrate perceptual ignition of dynamics in higher levels of the hierarchical model that show an almost categorical switch from the first to the third category (see the lower right panel). This ignition occurs after a period of exposure to the new song and enables it to be predicted more accurately. These dynamics can also be regarded as a generalized synchronization of simulated neuronal activity, with the true hidden states generating the stimulus. So, is there any evidence for critical slowing?

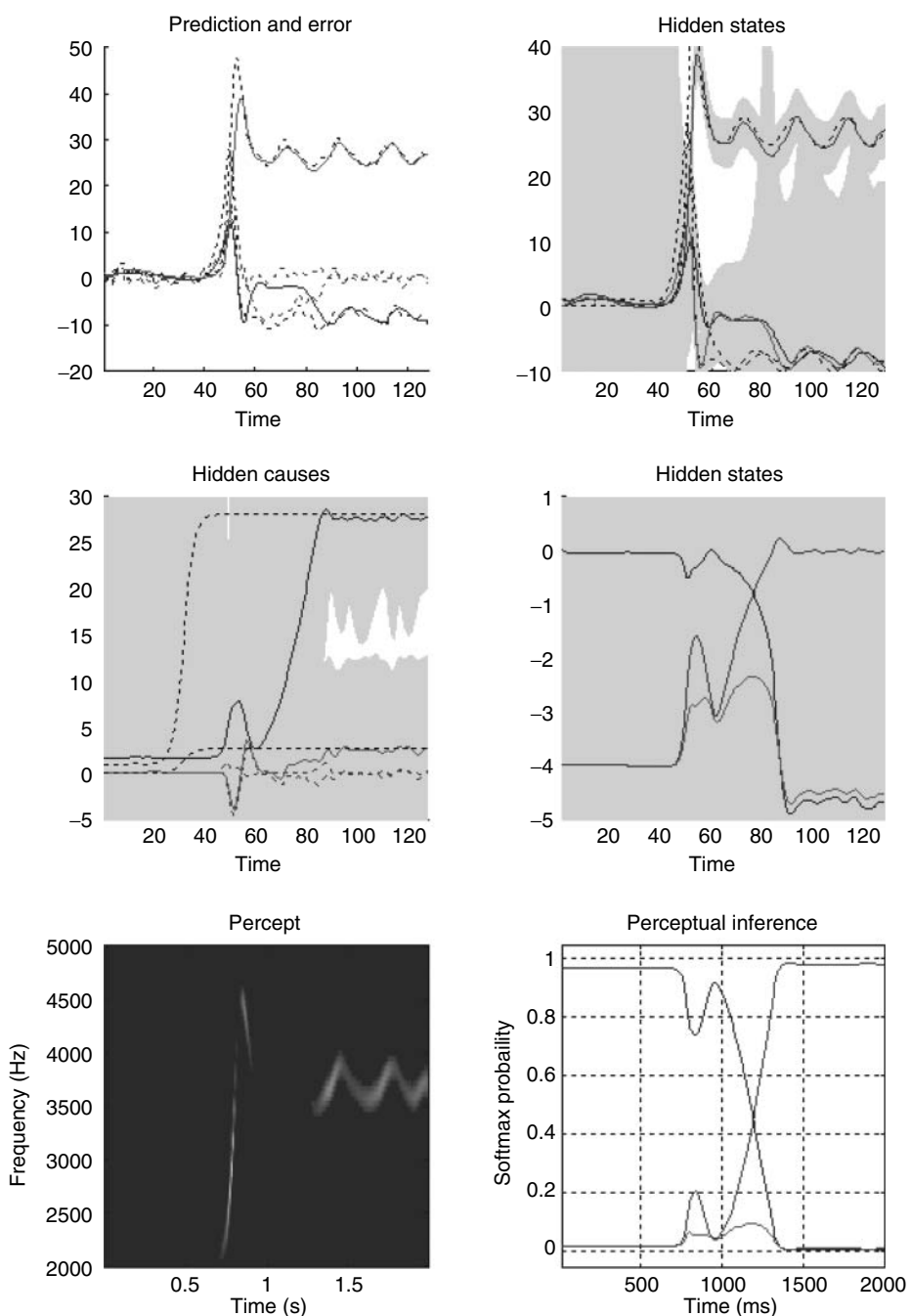
9.6.4

Perceptual Instability and Switching

Figure 9.7 shows the evolution of free energy and CLE as a function of peristimulus time. Figure 9.7a shows a phasic excess of free energy at the stimulus onset (first chirp or frequency glide). This is resolved quickly by changes in conditional expectations to reduce free energy to prestimulus levels. This reduction changes the flow and Jacobian of the conditional expectations and the local CLEs as shown on Figure 9.7b. Remarkably, there is pronounced critical slowing, as quantified by Eq. (9.17) (using $\tau = 8$ time bins or 128 ms), from the period of stimulus onset to the restoration of minimal free energy. The panels on the right show the underlying changes in the CLE – in their raw form (Figure 9.7b) and their exponentials (Figure 9.7d). The measure of critical slowing is simply the sum of these exponential CLE. It can be seen that many large negative CLE actually decrease their values, suggesting that some subspace of the generalized descent becomes more stable. However, the key change is in the CLE with small negative values, where several move toward zero (highlighted). These changes dominate the measure of critical slowing and reflect self-organized instability following stimulus

Figure 9.6 This shows the same results as in Figure 9.5, with conditional confidence intervals on all hidden states and causes and the implicit softmax probabilities based on the hidden states at the second level (lower right panel). These results illustrate switching from the first (silence) to the third (bird song)

category. This switch occurs after a period of exposure to the new song and enables the stimulus to be predicted more accurately. These dynamics can also be regarded as generalized synchronization between simulated neuronal activity and the true hidden states generating the stimulus.



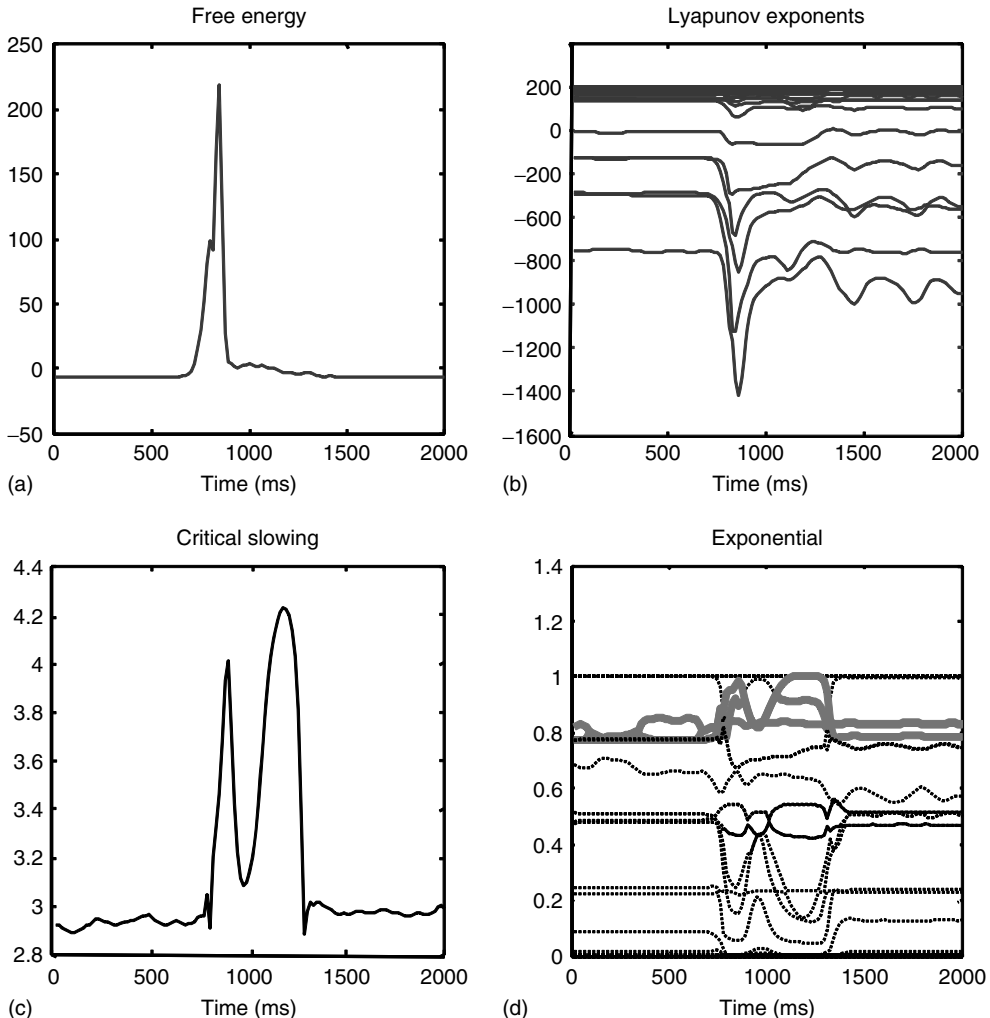


Figure 9.7 This shows the evolution of free energy and CLE over peristimulus time. (a) A phasic excess of free energy at the stimulus onset (first chirp or frequency glide). This is quickly resolved by changes in conditional expectations to reduce free energy to prestimulus levels. This reduction changes the Jacobian of the motion of internal states (conditional expectations) and the local conditional Lyapunov exponents (CLE), as shown in (b). (c) A pronounced critical slowing, as quantified by Eq. (9.17) (using $\tau = 8$ time bins or 128 ms) from stimulus onset

to the restoration of minimal free energy. The panels on the right show the underlying changes in the CLE (b) and their exponentials (d). The measure of critical slowing is the sum of exponential CLE. It can be seen that several CLE with small negative values move toward zero (highlighted). These changes dominate the measure of critical slowing and reflect self-organized instability following stimulus onset – an instability that coincides with the perceptual switch to the correct stimulus category (see previous figure).

onset – an instability that coincides exactly with the perceptual switch to the correct category of stimulus (see previous figure).

9.6.5

Perception and Critical Slowing

The changes described are over peristimulus time and reflect local CLE. Although we will not present an analysis of global CLE, we can average the local values over the second half of peristimulus time during which the chaotic song is presented. To test our conjecture that free energy minimization and perceptual inference induce critical slowing, we repeated the earlier simulations while manipulating the (prior beliefs about) precision on the motion of hidden attractor states.

Bayes-optimal inference depends on a delicate balance in the precisions assumed for the random fluctuations at each level of hierarchical models. These prior beliefs are encoded by the log precisions in Eq. (9.8). When intermediate levels are deemed too precise, top-down empirical priors overwhelm sensory evidence, resulting in illusory predictions. Furthermore, they predominate over the less precise prior beliefs at higher levels in the hierarchy. This can lead to false inference and a failure to recognize the high-level causes of sensory inputs. Conversely, when intermediate precisions are too low, the prediction errors from intermediate levels are insufficiently precise to change higher level conditional expectations. This again can lead to false perception, even if low-level attributes are represented more accurately. These failures of inference are illustrated in Figure 9.8, using the same format as Figure 9.6. The left panels show the results of decreasing the log precision on the motion of hidden states from 4 to 1, while the right panels show the equivalent results when increasing the log precision from 4 to 7. These simulations represent perceptual categorization with under- and overconfident beliefs about the chaotic motion of the hidden attractor states. In both instances, there is a failure of perception of all but the frequency glide at the onset of the song (compare the sonograms in Figure 9.8 with that in Figure 9.6). In both cases, this is due to a failure of inference about the hidden categorical states that would normally augment the predictions of hidden attractor states and subsequent sensations. In the underconfident condition, there is a slight deviation of predictions about amplitude from baseline (zero) levels – but this is not sufficiently informed by top-down empirical priors to provide a veridical prediction. Conversely, in the overconfident condition, the amplitude predictions remain impervious to sensory input and reflect top-down prior beliefs that the bird is listening to silence. Notice the shrinkage in conditional uncertainty about the first hidden attractor state in the upper right panels. This reflects the increase in precision on the motion of these hidden states.

Finally, we repeated the above-mentioned simulations for 64 values of precision on the motion of hidden attractor states from a log precision of 0 (a variance of 1) to a log precision of 7. At each value, we computed the time average of free energy, the softmax probability of the correct stimulus category, and critical slowing. In addition, we recorded the principal local CLE for each simulation.

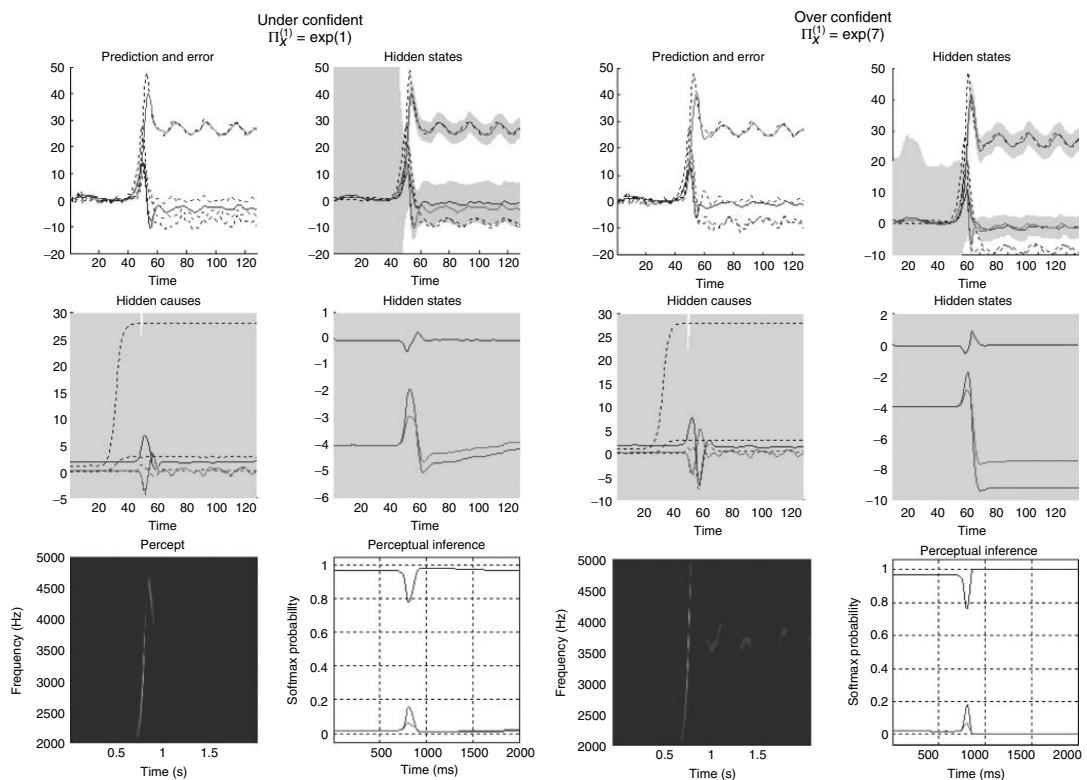


Figure 9.9 shows the interrelationships among these characterizations: Figure 9.9a shows the average probability of correctly identifying the song, which ranges from 0 in the low and high precision regime, to about 70% in the intermediate regime. The two vertical lines correspond to the onset and offset of nontrivial categorization, with a softmax probability of >0.05 . The variation in these average probabilities is due to the latency of the perceptual switch to the correct song. This can be seen in Figure 9.9b, which shows the principal CLE in image format as a function of peristimulus time (columns) and precision (rows). It can be seen that the principal CLE shows fluctuations in, and only, in the regime of veridical categorization. Crucially, these fluctuations appear earlier when the categorization probabilities were higher, indicating short latency perceptual switches. Note that the principal CLE attains positive values for short periods of time. This does not necessarily mean a loss of generalized synchronization; provided the long-term time average is zero or less, when evaluated over long stimulus presentation times. Given that we are looking explicitly at stimulus responses or transients, these positive values could be taken as evidence for transient chaos.

Figure 9.9c shows the average free energy as a function of precision. As one might anticipate, this exhibits a clear minimum around the level of precision that produces the best perceptual categorization. The key results, from the point of view of this chapter, are presented in Figure 9.9d. This shows a very clear critical slowing in, and only in the regime of correct categorization. In short, these results are entirely consistent with the conjecture that free energy minimization induces instability or critical slowing and thereby provides a more veridical representation of hidden states in the world.

9.6.6 Summary

In summary, these simulations of perceptual transitions affirm the notion that a sensitive response to sensory perturbations from the environment is accompanied by critical slowing of representational dynamics – of the sort that would be predicted

Figure 9.8 Failures of perceptual inference illustrated using the same format as Figure 9.6. The left panels show the results of decreasing the log precision on the notion of hidden states from 4 to 1; while the right panels show the equivalent results when increasing the log precision from 4 to 7. These simulations represent perceptual categorization with under- and overconfident beliefs about the motion of hidden attractor states. In both instances, there is a failure of perception of all but the frequency

glide at the onset of the song (compare the sonograms in Figure 9.8 with that in Figure 9.6). In the underconfident condition, there is a slight deviation of predictions about amplitude from baseline (zero) levels – but this is not sufficiently informed by (imprecise) top-down empirical priors to provide a veridical prediction. Conversely, in the overconfident condition, the amplitude predictions are impervious to sensory input and reflect top-down prior beliefs that the bird is listening in silence.

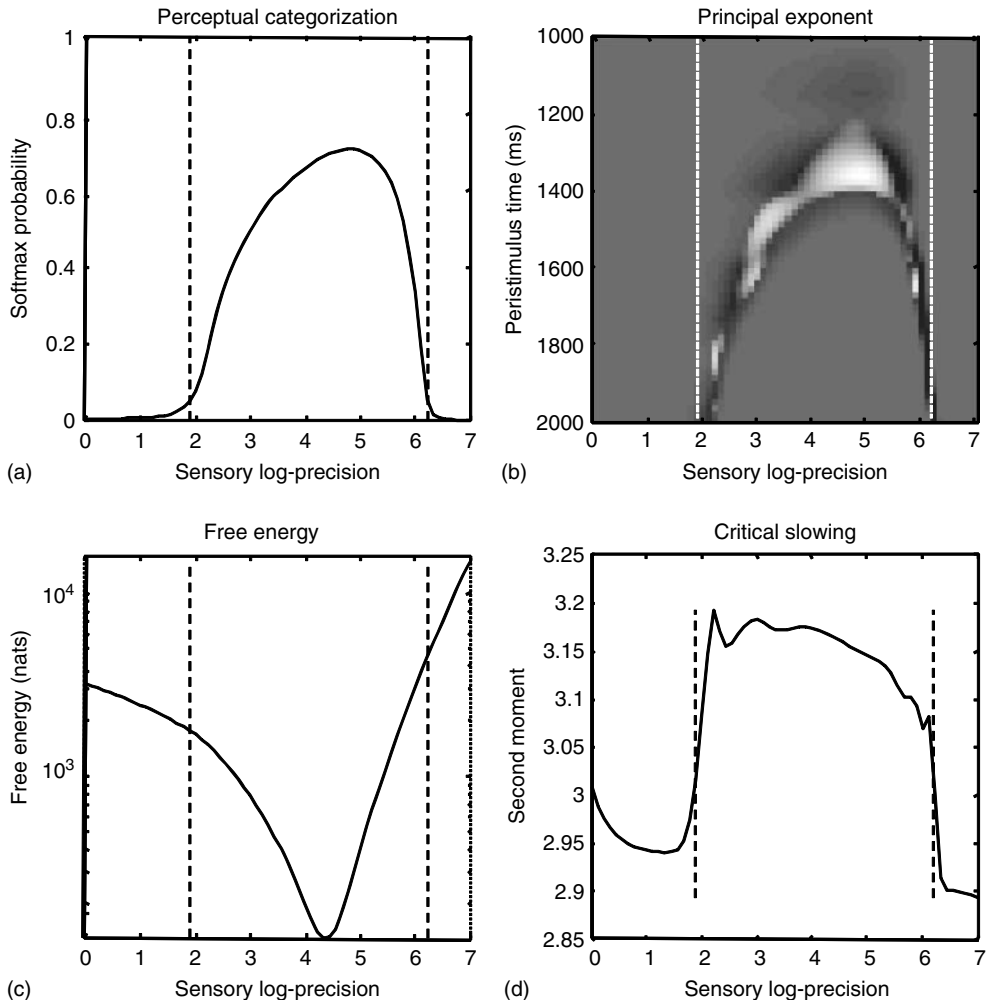


Figure 9.9 (a) The average probability (following stimulus onset) of correctly identifying a song over 64 values of precision on the motion of hidden attractor states. The two vertical lines correspond to the onset and offset of nontrivial categorization – a softmax probability of >0.05 . The variation in these average probabilities is due to the latency of the perceptual switch to the correct song. This can be seen in (b) that shows the principal CLE in image format as a function of peristimulus time (columns) and precision (rows). It can be seen that the principal CLE shows fluctuations in, and only, in the regime of veridical

categorization. Crucially, these fluctuations appear earlier when the categorization probabilities were higher, indicating short latency perceptual switches. (c) The time-averaged free energy as a function of precision. As one might anticipate, this exhibits a clear minimum around the level of precision that produces the best perceptual categorization. (d) Seen here is a very clear critical slowing in, and only in, the regime of correct categorization. In short, these results are consistent with the conjecture that free energy minimization can induce instability and thereby provide a more responsive representation of hidden states in the world.

by Bayes-optimal perception and the implicit maximum entropy principle. Although we have focused on perception, the imperative to minimize free energy, in the larger setting of active inference, may mean that any self-organizing system that resists a dispersion of its (sensory) states should show the same sort of critical slowing. The perceptual categories used in this chapter to illustrate perceptual transitions were very distinct. One might imagine that the role of critical slowing and transitions may become more important when discriminating between more ambiguous stimuli; for example, those used to elicit bistable perception. In future work, we hope to look at bistable perception (binocular rivalry) and revisit our recent work in this area, in terms of critical slowing. In these models, the system works at the border of a Hopf bifurcation, where noise is more efficient in provoking perceptual transitions [30].

9.7 Conclusion

We have addressed self-organization at a number of levels. First, we have looked at self-organization in terms of the selective sampling of the environment to minimize surprise (free energy) and therefore maintain a homeostasis in the sense of Ashby [35]. Because surprise is negative log evidence in statistics, free energy minimization can also be understood as accumulating evidence for generative models of the world in a Bayes-optimal manner. Second, we have considered free energy minimization in self-organizing systems as a dynamical process that performs a (generalized) gradient descent. Statistically speaking, this corresponds to a generalized (Bayesian) filtering or deconvolution that discovers the underlying causes of sensory states. This form of dynamics has the rather curious property of self-destabilization, in the sense that the internal states of a system (as in the brain) will seek out regions of low free energy that, by definition, have a low curvature and invite relatively unstable (slow) dynamics. This form of self-organizing instability was demonstrated using neuronal simulations of perceptual categorization and a fairly minimal, but generic generative model. These demonstrations provided an example of Bayes-optimal perceptual categorization that was associated with self-organized instability or critical slowing that may be an integral part of perceptual switching or ignition. Finally, there is an important third level of self-organization that is implicit in the final simulations: at the beginning, we established that the internal states of a self-organizing system will minimize free energy. *This includes posterior beliefs about (estimates of) the precision of random fluctuations.* This means that had we allowed the precision on the motion of hidden attractor states to minimize free energy, it would have found the value that is in the center of the region showing critical slowing. In other words, if the system chose the level of uncertainty or confidence in its prior beliefs, it would choose a critical regime. Figure 9.9 is a good illustration of how criticality can induce self-organization in a subtle and recursive manner.

References

1. Dehaene, S. and Changeux, J.-P. (2011) Experimental and theoretical approaches to conscious processing. *Neuron*, **70**, 200–227.
2. Tsuda, I. (2001) Toward an interpretation of dynamic neural activity in terms of chaotic dynamical systems. *Behav. Brain Sci.*, **24** (5), 793–810.
3. Breakspear, M. (2001) Perception of odors by a nonlinear model of the olfactory bulb. *Int. J. Neural Syst.*, **11** (2), 101–124.
4. Shew, W.L., Yang, H., Yu, S., Roy, R., and Plenz, D. (2011) Information capacity and transmission are maximized in balanced cortical networks with neuronal avalanches. *J. Neurosci.*, **31** (1), 55–63.
5. Plenz, D. and Thiagarajan, T.C. (2007) The organizing principles of neuronal avalanches: cell assemblies in the cortex? *Trends Neurosci.*, **30** (3), 101–110.
6. Beggs, J.M. and Plenz, D. (2003) Neuronal avalanches in neocortical circuits. *J. Neurosci.*, **23** (35), 11167–11177.
7. Gregory, R.L. (1980) Perceptions as hypotheses. *Philos. Trans. R. Soc. London, Ser. B*, **290**, 181–197.
8. Fisch, L., Privman, E., Ramot, M. et al. (2009) Neural ignition: enhanced activation linked to perceptual awareness in human ventral stream visual cortex. *Neuron*, **64**, 562–574.
9. Maturana, H.R. and Varela, F. (1980) Autopoiesis: the organization of the living, in *Autopoiesis and Cognition* (eds H.R. Maturana and F. Varela), Reidel, Dordrecht.
10. Friston, K. (2010) The free-energy principle: a unified brain theory? *Nat. Rev. Neurosci.*, **11** (2), 127–138.
11. Friston, K. and Ao, P. (2012) Free-energy, value and attractors. *Comput. Math. Meth. Med.*, **2012**, 937860.
12. Nara, S. (2003) Can potentially useful dynamics to solve complex problems emerge from constrained chaos and/or chaotic itinerancy? *Chaos*, **13** (3), 1110–1121.
13. van Leeuwen, C. (2008) Chaos breeds autonomy: connectionist design between bias and baby-sitting. *Cogn. Process.*, **9** (2), 83–92.
14. Ishii, S., Yoshida, W., and Yoshimoto, J. (2002) Control of exploitation-exploration meta-parameter in reinforcement learning. *Neural Netw.*, **15** (4-6), 665–687.
15. Freeman, W.J. (1994) Characterization of state transitions in spatially distributed, chaotic, nonlinear, dynamical systems in cerebral cortex. *Integr. Physiol. Behav. Sci.*, **29** (3), 294–306.
16. Pasquale, V., Massobrio, P., Bologna, L.L., Chiappalone, M., and Martinoia, S. (2008) Self-organization and neuronal avalanches in networks of dissociated cortical neurons. *Neuroscience*, **153** (4), 1354–1369.
17. Jirsa, V.K., Friedrich, R., Haken, H., and Kelso, J.A. (1994) A theoretical model of phase transitions in the human brain. *Biol. Cybern.*, **71** (1), 27–35.
18. Rabinovich, M., Huerta, R., and Laurent, G. (2008) Neuroscience. Transient dynamics for neural processing. *Science*, **321** (5885), 48–50.
19. Tschacher, W. and Haken, H. (2007) Intentionality in non-equilibrium systems? The functional aspects of self-organized pattern formation. *New Ideas Psychol.*, **25**, 1–15.
20. Tyukin, I., van Leeuwen, C., and Prokhorov, D. (2003) Parameter estimation of sigmoid superpositions: dynamical system approach. *Neural Comput.*, **15** (10), 2419–2455.
21. Tyukin, I., Tyukina, T., and van Leeuwen, C. (2009) Invariant template matching in systems with spatiotemporal coding: a matter of instability. *Neural Netw.*, **22** (4), 425–449.
22. Birkhoff, G.D. Proof of the ergodic theorem. *Proc. Natl. Acad. Sci. U.S.A.*, **17** (1931), 656–660.
23. Breakspear, M. (2004) Dynamic connectivity in neural systems – theoretical and empirical considerations. *Neuroinformatics*, **2** (2), 205–225.
24. Namikawa, J. (2005) Chaotic itinerancy and power-law residence time distribution in stochastic dynamical systems. *Phys. Rev. E*, **72** (2), 026204.

25. Gros, C. (2009) Cognitive computation with autonomously active neural networks: an emerging field. *Cognit. Comput.*, **1**, 77–99.
26. Breakspear, M. and Stam, C.J. (2005) Dynamics of a neural system with a multiscale architecture. *Philos. Trans. R. Soc. Lond. B Biol. Sci.*, **360** (1457), 1051–1074.
27. Bressler, S.L. and Tognoli, E. (2006) Operational principles of neurocognitive networks. *Int. J. Psychophysiol.*, **60** (2), 139–148.
28. Werner, G. (2007) Brain dynamics across levels of organization. *J. Physiol. Paris*, **4-6**, 273–279.
29. Kiebel, S.J., Daunizeau, J., and Friston, K.J. (2009) Perception and hierarchical dynamics. *Front. Neuroinf.*, **3**, 20.
30. Theodoni, P., Panagiotaropoulos, T.I., Kapoor, V., Logothetis, N.K., and Deco, G. (2011) Cortical microcircuit dynamics mediating binocular rivalry: the role of adaptation in inhibition. *Front. Hum. Neurosci.*, **5**, 145.
31. Aburn, M.J., Holmes, C.A., Roberts, J.A., Boonstra, T.W., Breakspear, M. (2012) Critical fluctuations in cortical models near instability. *Front. Physio.* **3**, 331. doi: 10.3389/fphys.2012.00331
32. Breakspear, M., Heitmann, S., and Daffertshofer, A. (2010) Generative models of cortical oscillations: neurobiological implications of the kuramoto model. *Front. Hum. Neurosci.*, **4**, 190.
33. Bak, P., Tang, C., and Wiesenfeld, K. (1987) Self-organized criticality: an explanation of 1/f noise. *Phys. Rev. Lett.*, **59** (4), 381–384.
34. Kelso, J.A.S. (2010). Instabilities and phase transitions in human brain and behavior. *Front. Hum. Neurosci.* 4:23.10.3389/fnhum.2010.00023
35. Ashby, W.R. (1947) Principles of the self-organizing dynamic system. *J. Gen. Psychol.*, **37**, 125–128.
36. Friston, K. (2008) Hierarchical models in the brain. *PLoS Comput. Biol.*, **4** (11), e1000211.
37. Feynman, R.P. (1972) *Statistical Mechanics*, Benjamin, Reading, MA.
38. Beal, M.J. (2003) Variational algorithms for approximate bayesian inference. PhD Thesis, University College London.
39. Jaynes, E.T. (1957) Information theory and statistical mechanics. *Phys. Rev. Ser. II*, **106** (4), 620–630.
40. Helmholtz, H. (1866/1962) Concerning the perceptions in general, in *Treatise on Physiological Optics*, Dover Publications, New York.
41. Ballard, D.H., Hinton, G.E., and Sejnowski, T.J. (1983) Parallel visual computation. *Nature*, **306**, 21–26.
42. Dayan, P., Hinton, G.E., and Neal, R.M. (1995) The Helmholtz machine. *Neural Comput.*, **7**, 889–904.
43. Friston, K. (2005) A theory of cortical responses. *Philos. Trans. R. Soc. Lond. B Biol. Sci.*, **360** (1456), 815–836.
44. Yuille, A. and Kersten, D. (2006) Vision as Bayesian inference: analysis by synthesis? *Trends Cogn. Sci.*, **10** (7), 301–308.
45. Ginzburg, V.L. and Landau, L.D. (1950) On the theory of superconductivity. *Zh. Eksp. Teor. Fiz.*, **20**, 1064.
46. Haken, H. (1983) *Synergetics: An Introduction. Non-Equilibrium Phase Transition and Self-Selforganisation in Physics, Chemistry and Biology*, Springer-Verlag, Berlin.
47. Friston, K. (2009) The free-energy principle: a rough guide to the brain? *Trends Cogn. Sci.*, **13** (7), 293–301.
48. Friston, K., Stephan, K., Li, B., and Daunizeau, J. (2010) Generalised filtering. *Math. Prob. Eng.*, **2010**, 621670.
49. Friston, K. and Kiebel, S. (2009) Cortical circuits for perceptual inference. *Neural Networks*, **22** (8), 1093–1104.
50. Brown, H. and Friston, K.J. (2012) Free-energy and illusions: the cornsweet effect. *Front. Psychol.*, **3**, 43.
51. Friston, K.J. and Kiebel, S.J. (2009) Predictive coding under the free-energy principle. *Philos. Trans. R. Soc. B*, **364**, 1211–1221.
52. Feldman, H. and Friston, K.J. (2010) Attention, uncertainty, and free-energy. *Front. Hum. Neurosci.*, **4**, 215.
53. Friston, K.J., Daunizeau, J., Kilner, J., and Kiebel, S.J. (2010) Action and behavior: a free-energy formulation. *Biol. Cybern.*, **102** (3), 227–260.
54. Friston, K., Mattout, J., and Kilner, J. (2011) Action understanding and active inference. *Biol. Cybern.*, **104**, 137–160.

- 55. Friston, K., Adams, R., Perrinet, L., and Breakspear, M. (2012) Perceptions as hypotheses: saccades as experiments. *Front. Psychol.*, **3**, 151.
- 56. Friston, K.J., Daunizeau, J., and Kiebel, S.J. (2009) Active inference or reinforcement learning? *PLoS One*, **4** (7), e6421.
- 57. Friston, K.J., Shiner, T., Fitzgerald, T., Galea, J.M. et al. (2012) Dopamine, affordance and active inference. *PLoS Comput. Biol.*, **8** (1), e1002327.
- 58. Rao, R.P. and Ballard, D.H. (1999) Predictive coding in the visual cortex: a functional interpretation of some extra-classical receptive-field effects. *Nat. Neurosci.*, **2** (1), 79–87.
- 59. Mumford, D. (1992) On the computational architecture of the neocortex. II. *Biol. Cybern.*, **66**, 241–251.
- 60. Feldman, A.G. and Levin, M.F. (1995) The origin and use of positional frames of reference in motor control. *Behav. Brain Sci.*, **18**, 723–806.
- 61. Hunt, B., Ott, E., and Yorke, J. (1997) Differentiable synchronisation of chaos. *Phys. Rev. E*, **55**, 4029–4034.
- 62. Barreto, E., Josic, K., Morales, C.J., Sander, E., and So, P. (2003) The geometry of chaos synchronization. *Chaos*, **13**, 151–164.
- 63. Pyragas, K. (1997) Conditional Lyapunov exponents from time series. *Phys. Rev. E*, **56** (5), 5183–5187.
- 64. Kaplan, J. and Yorke, J. (1979) Chaotic behavior of multidimensional difference equations, in *Functional Differential Equations and Approximation of Fixed Points* (eds H.O. Peitgen and H.O. Walther), Springer, New York.
- 65. Abarbanel, H.D.I., Creveling, D.R., and Jeanne, J.M. (2008) Estimation of parameters in nonlinear systems using balanced synchronization. *Phys. Rev. E*, **77**, 016208.
- 66. Tsuda, I. and Fujii, H. (2004) *Computational Neuroscience: Cortical Dynamics*, Lecture Notes in Computer Science, ISSU, vol. 3146, Springer, Berlin, Heidelberg, pp. 109–128.
- 67. Cessac, B., Blanchard, P., and Krüger, T. (2001) Lyapunov exponents and transport in the Zhang model of self-organized criticality. *Phys. Rev. E Stat. Nonlinear Soft Matter Phys.*, **64** (1 Pt 2), 016133.
- 68. Perl, Y.S., Arneodo, E.M., Amador, A., Goller, F., and Mindlin, G.B. (2011) Reconstruction of physiological instructions from Zebra finch song. *Phys. Rev. E*, **84**, 051909.
- 69. Zeigler, P. and Marler, P. (2008) *Neuroscience of Birdsong*. Cambridge University Press, Cambridge.

10

Self-Organized Criticality in Neural Network Models

Matthias Rybarsch and Stefan Bornholdt

10.1 Introduction

Information processing by a network of dynamical elements is a delicate matter: avalanches of activity can die out if the network is not connected enough or if the elements are not sensitive enough; on the other hand, activity avalanches can grow and spread over the entire network and override information processing as observed in epilepsy.

Therefore, it has long been argued that neural networks have to establish and maintain a certain intermediate level of activity in order to keep away from the regimes of chaos and silence [1–4]. Similar ideas were also formulated in the context of genetic networks, where Kauffman postulated that information processing in these evolved biochemical networks would be optimal near the “edge of chaos,” or criticality, of the dynamical percolation transition of such networks [5].

In the wake of self-organized criticality (SOC), it was asked if neural systems were also self-organized to some form of criticality [6]. In addition, actual observations of neural oscillations within the human brain were related to a possible SOC phenomenon [7]. An early example of a SOC model that had been adapted to be applicable to neural networks is the model by Eurich *et al.* [8]. They show that their model of the random neighbor Olami – Feder – Christensen universality class exhibits (subject to one critical coupling parameter) distributions of avalanche sizes and durations, which they postulate could also occur in neural systems.

Another early example of a model for self-organized critical neural networks [4, 9] drew on an alternative approach to SOC based on adaptive networks [10]. Here, networks are able to self-regulate toward and maintain a critical system state, via simple local rewiring rules that are plausible in the biological context.

After these first model approaches, indeed strong evidence for criticality in neural systems has been found in terms of spatiotemporal activity avalanches, first in the seminal work of Beggs and Plenz [11]. Much further experimental evidence has been found since, which we briefly review below. These experimental findings sparked intense research on dynamical models for criticality and avalanche dynamics in neural networks, which we also give a brief overview subsequently.

While most models emphasized biological and neurophysiological detail, our path here is different:

The purpose of this review is to pick up the thread of the early self-organized critical neural network model [4] and test its applicability in the light of experimental data. We would like to keep the simplicity of the first spin model in the light of statistical physics, while lifting the drawback of a spin formulation with respect to the biological system [12]. We will study an improved model and show that it adapts to criticality exhibiting avalanche statistics that compare well with experimental data without the need for parameter tuning [13].

10.2

Avalanche Dynamics in Neuronal Systems

10.2.1

Experimental Results

Let us first briefly review the experimental studies on neuronal avalanche dynamics. In 2003, Beggs and Plenz [11] published their findings about a novel mode of activity in neocortical neuron circuits. During *in vitro* experiments with cortex slice cultures of the rat, where neuronal activity in terms of local field potentials was analyzed via a 8×8 multielectrode array, they found evidence of spontaneous bursts and avalanche-like propagation of activity followed by silent periods of various lengths. The observed power-law distribution of event sizes indicates the neuronal network is maintained in a critical state. In addition, they found that the precise spatiotemporal patterns of the avalanches are stable over many hours and also robust against external perturbations [14]. They concluded that these neuronal avalanches might play a central role for brain functions like information storage and processing. Also, during the developmental stages of *in vitro* cortex slice cultures from newborn rats, neuronal avalanches were found, indicating a homeostatic evolution of the cortical network during postnatal maturation [15]. Moreover, cultures of dissociated neurons were also found to exhibit this type of spontaneous activity bursts in different kinds of networks, as for example in rat hippocampal neurons and leech ganglia [16], as well as dissociated neurons from rat embryos [17].

Aside from these *in vitro* experiments, extensive studies *in vivo* have since been conducted. The emergence of spontaneous neuronal avalanches has been shown in anesthetized rats during cortical development [18] as well as in awake rhesus monkeys during ongoing cortical synchronization [19].

The biological relevance of the avalanche-like propagation of activity in conjunction with a critical state of the neuronal network has been emphasized in several works recently. Such network activity has proved to be optimal for maximum dynamical range [20–22], maximal information capacity, and transmission capability [23], as well as for a maximal variability of phase synchronization [24].

10.2.2

Existing Models

The experimental studies with their rich phenomenology of spatiotemporal patterns sparked a large number of theoretical studies and models for criticality and self-organization in neural networks, ranging from very simple toy models to detailed representations of biological functions. Most of them try to capture self-organized behavior with emerging avalanche activity patterns, with scaling properties similar to the experimental power-law event size or duration distributions.

As briefly mentioned earlier, early works as [10] and [4, 9] focus on simple mechanisms for self-organized critical dynamics in spin networks, which also have been discussed in a wider context [25]. These models represent an approach aiming at utmost simplicity of the model, quite similar to the universality viewpoint of statistical mechanics, rather than faithful representations of neurobiological and biochemical detail. Nevertheless, they are able to self-regulate toward and maintain a critical system state, manifested in features as a certain limit cycle scaling behavior, via simple local rewiring rules that are still plausible in the biological context. We take a closer look at these models in Section 10.3, because they provide some of the groundwork for current models.

Regarding neuronal avalanches, a 2002 work by Eurich *et al.* investigates networks of globally coupled threshold elements that are related to integrate-and-fire neurons. They present a model that, after proper parameter tuning, exhibits avalanche-like dynamics with distinctive distributions of avalanche sizes and durations as expected at a critical system state [8].

It is notable that these models came up even before experimental evidence was found for the existence of neuronal avalanches in [11]. Understandably, extensive studies have been done on avalanche models following their discovery. Again, most models have their mechanisms of self-organization motivated by brain plasticity.

A 2006 model proposed by de Arcangelis *et al.* consists of a model electrical network on a square lattice, where threshold firing dynamics, neuron refractory inhibition, and activity-dependent plasticity of the synaptic couplings, represented by the conductance of the electrical links, serve as the basis for self-organization. Neuron states are characterized by electrical potentials, which may be emitted as action potentials to neighboring nodes once a certain threshold has been reached. With these incoming currents, the neighbor sites can eventually also reach their activation threshold and thus activity avalanches can propagate through the network. Avalanches are triggered by external currents to specific input sites. Following the activation of a node, the coupling conductances are increased by a small value for each link, which has carried a firing current. On the other hand, after completing a whole avalanche, all couplings in the network have their conductance reduced by the average of the increase that has taken place before, during the avalanche propagation. This way, those couplings that carry many signals will effectively get stronger connections, while the rather inactive connections will be reduced and subsequently pruned from the network. Indeed, the model evolves to a critical state with power-law scaling of avalanche sizes [26]. In a subsequent work,

the same behavior of such an adaptive model could also be observed on a class of scale-free networks (namely *Apollonian networks*), which is argued to be more appropriate as an approach to real neuronal networks than a lattice would be [27].

A related model (in terms of insertion of links or facilitation of weights where signals have been passed) has been proposed by Meisel and Gross [28]. The authors focus on the interplay between activity-driven vs. spike-time-dependent plasticity and link their model to a phase transition in synchronization of the network dynamics. The temporal sequence of node activations serves as the key criterion for the topological updates. While they do not specifically discuss avalanche-like activity patterns, one observes power-law distributed quantities as for example correlation measures or synaptic weights in the self-organized states which point to dynamical criticality.

While the last three models mentioned are set up to strengthen those couplings over which signals have been transmitted, a kind of opposite approach was proposed by Levina *et al.* [29]. In their model, synaptic depression after propagation of activity over a link – biologically motivated by the depletion of neurotransmitter resources in the synapse – is the key mechanism that drives their model to a critical behavior. The network consists of fully connected integrate-and-fire neurons whose states are described by a membrane potential. This potential is increased by incoming signals from other sites or by random external input, and may cause the site to emit signals when the activation threshold is exceeded. Following such a firing event, the membrane potential is reduced by the threshold value. Again, a single neuron starting to fire after external input, may set off an avalanche by passing its potential to other sites, which in turn can exceed their activation threshold, and so on. The couplings in this model take nondiscrete values, directly related to the biologically relevant amount of neurotransmitter available in each synapse. In short, whenever a signal is passed by a synapse, its value will be decreased. The coupling strength is, on the other hand, recovering slowly toward the maximum value in periods when no firing events occur. The authors also extend the model to consider leaky integrate-and-fire neurons, and find a robust self-organization toward a critical state, again with the characteristic power-law distribution of avalanche sizes. In a later work [30], the authors further investigate the nature of the self-organization process in their model and discuss the combination of first- and second-order phase transitions with a self-organized critical phase.

Meanwhile, field-theoretic approaches to fluctuation effects helped shed light on the universality classes to expect in critical neural networks [31] and the presence of SOC in nonconservative network models of leaky neurons were linked to the existence of alternating states of high versus low activity, so-called up- and down-states [32]. It has been shown that anti-Hebbian evolution is generally capable of creating a dynamically critical network when the anti-Hebbian rule affects only symmetric components of the connectivity matrix. The anti-symmetric component remains as an independent degree of freedom and could be useful in learning tasks [33]. Another model highlights the importance of synaptic plasticity for a phase transition in general and relates the existence of a broad critical regime to a hierarchical modularity [34]. The biological plausibility of activity-dependent

synaptic plasticity for adaptive self-organized critical networks has further been stressed recently [35]. Also, the robustness of critical brain dynamics to complex network topologies has been emphasized [36].

The relevance of the critical state in neuronal networks for a brain function as learning was underlined in [37], where the authors find that the performance in learning logical rules as well as time to learn are strongly connected to the strength of plastic adaptation in their model, which at the same time is able to reproduce critical avalanche activity. In a more recent work [38], the same authors present a new variant of their electrical network model. They again use facilitation of active synapses as their primary driving force in the self-organization, but now focus more on activity correlation between those nodes that are actually active in consecutive time steps. Here, they investigate the emergence of critical avalanche events on a variety of different network types, as, for example, regular lattices, scale-free networks, small-world networks, or fully connected networks.

Also, most recently, [39] investigate the temporal organization of neuronal avalanches in real cortical networks. The authors find evidence that the specific waiting time distribution between avalanches is a consequence of the above-mentioned up- and down-states, which in turn is closely linked to a balance of excitation and inhibition in a critical network.

While the proposed organization mechanisms strongly differ between the individual models (see Figure 10.1 for a cartoon representation of the various mechanisms), the resulting evolved networks tend to be part of only a few fundamental universality classes, exhibiting, for example, avalanche statistics in a similar way as in the experimental data, as power-law distributions at an exponent of $-3/2$. With the recent, more detailed models in mind, we are especially interested in the underlying universality of self-organization, also across other fields. Considering the enormous interest in neuronal self-organization, we here come back to our older spin models [4, 10] and develop a new basic mechanism in the light of better biological plausibility of these models.

10.3

Simple Models for Self-Organized Critical Adaptive Neural Networks

10.3.1

A First Approach: Node Activity Locally Regulates Connectivity

In the very minimal model of a random threshold network [10], a simple local mechanism for topology evolution based on node activity has been defined, which is capable of driving the network toward a critical connectivity of $K_c = 2$. Consider a network composed of N randomly and asymmetrically connected spins ($\sigma_i = \pm 1$), which are updated synchronously in discrete time steps via a threshold function of the inputs they receive:

$$\sigma_i(t+1) = \text{sgn}(f_i(t)) \quad (10.1)$$

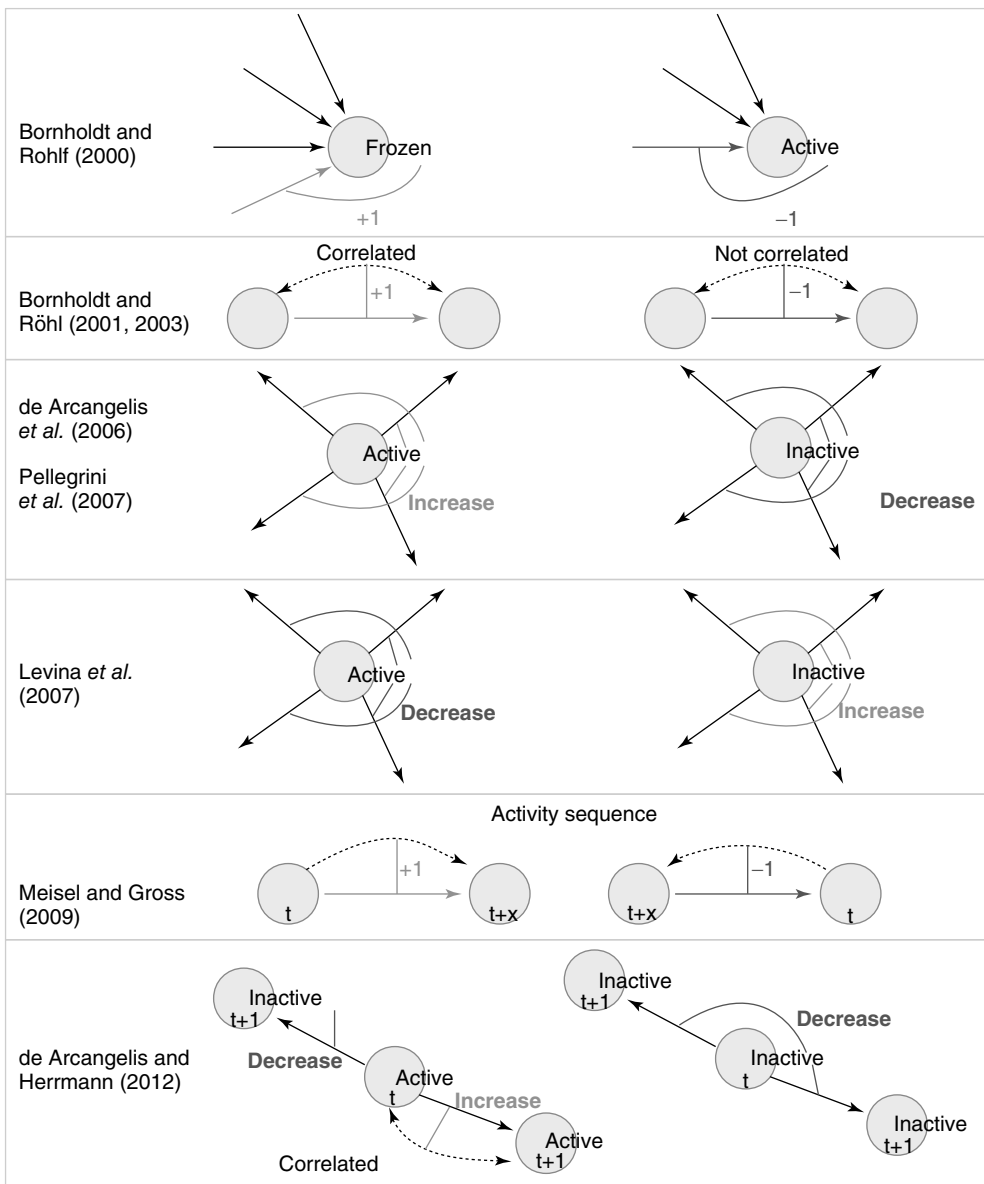


Figure 10.1 Schematic illustration of some of the different approaches to self-organization in neural network models. Rows 1 – 2: Links are either added (denoted by +1; green link) or removed (denoted by -1; red link) as a function of node activity or correlation between nodes. Rows 3 - 4: Here, activity or inactivity of a node affects all outgoings links (thin lines). All weights of the outgoing links from a node are decreased (red) or increased (green) as a function

of node activity. Row 5: Links are created and facilitated when nodes become active in the correct temporal sequence. Links directed against the sequence of activation are deleted. Row 6: Positive correlation in the activity between two nodes selectively increases the corresponding link, whereas there is non-selective weight decrease for links between uncorrelated or inactive nodes. (Please find a color version of this figure on the color plates.)

using

$$\text{sgn}(x) = \begin{cases} +1, & x \geq 0 \\ -1, & x < 0 \end{cases}$$

and

$$f_i(t) = \sum_{j=1}^N c_{ij} \sigma_j(t) + h \quad (10.2)$$

where the link weights have discrete values $c_{ij} = \pm 1$ (or $c_{ij} = 0$ if node i does not receive input from node j). In the minimal model, activation thresholds are set to $h = 0$ for all nodes. A network run is started with random initial configuration and iterated until either a fixed point attractor or a limit cycle attractor is reached. The attractor of a network is where its dynamics ends up after a while, which is either a fixed point of the dynamics (all nodes reach a constant state) or a limit cycle of the whole network dynamics. A limit cycle in these discrete dynamical models is a cyclic sequence of a finite number of activation patterns.

For the topological evolution, a random node i is selected and its activity during the attractor period of the network is analyzed. The network is observed until such an attractor is reached; and afterwards, activity of the single node during that period is measured. In short, if node i changes its state σ_i at least once during the attractor, a random one of the existing nonzero in-links c_{ij} to that node is removed. If, vice versa, σ_i remains constant throughout the attractor period, a new nonzero in-link c_{ij} from a random node j is added to the network.

In one specific among several possible realizations of an adaptation algorithm, the average activity $A(i)$ of node i over an attractor period from T_1 to T_2 is defined as

$$A(i) = \frac{1}{T_2 - T_1} \sum_{t=T_1}^{T_2} \sigma_i(t) \quad (10.3)$$

Topological evolution is now imposed in the following way:

- 1) A random network with average connectivity K_{ini} is created and node states are set to random values.
- 2) Parallel updates according to Eq. (10.1) are executed until a previous state reappears (i.e., until a dynamical attractor is reached).
- 3) Calculate $A(i)$ for a randomly selected node i . If $|A(i)| = 1$, node i receives a new in-link of random weight $c_{ij} = \pm 1$ from a random other node j . Otherwise (i.e., if the state of node i changes during the attractor period), one of the existing in-links is set to zero.
- 4) Optional: a random nonzero link in the network has its sign reversed.

A typical run of this algorithm will result in a connectivity evolution as shown in Figure 10.2 for a network of $N = 1024$ nodes. Independent of the initial connectivity K_{ini} , the system evolves toward a statistically stationary state with an average evolved connectivity of $K_{\text{ev}}(N = 1024) = 2.55 \pm 0.04$. With increasing

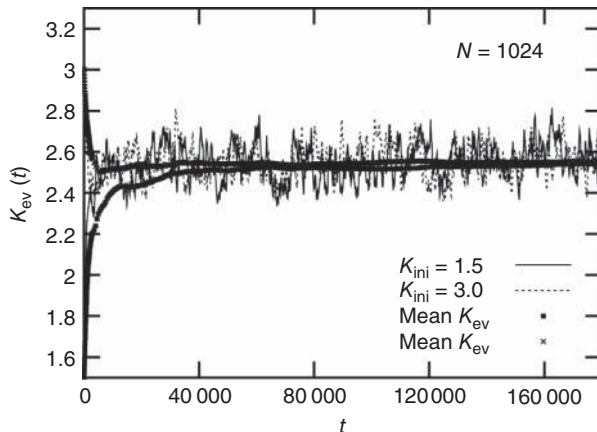


Figure 10.2 Evolution of the average connectivity K_{ev} with an activity-driven rewiring, shown for two different initial connectivities. Independent of the initial conditions chosen

at random, the networks evolve to an average connectivity, $K_{ev} = 2.55 \pm 0.04$. Time t is in simulation steps.

system size N , K_{ev} converges toward $K_c = 2$ for the large system limit $N \rightarrow \infty$ with a scaling relationship

$$K_{ev}(N) = 2 + cN^{-\delta} \quad (10.4)$$

with $c = 12.4 \pm 0.5$ and $\delta = 0.47 \pm 0.01$ (compare Figure 10.3).

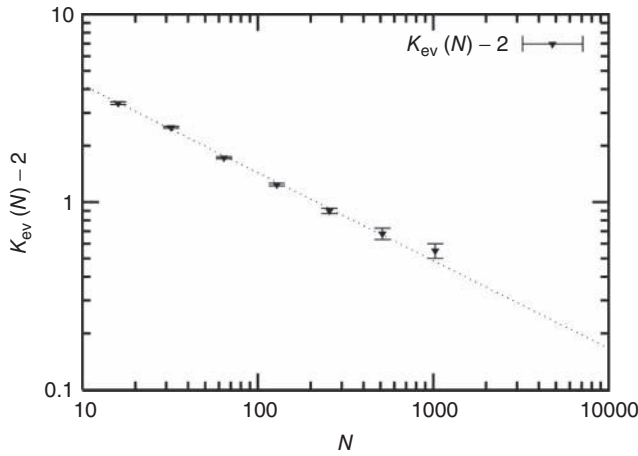


Figure 10.3 A finite-size scaling of the evolved average connectivity K_{ev} as a function of network size N reveals that for large N , the mean K_{ev} converge toward the critical connectivity $K_c = 2$. For systems with

$N \leq 256$, the average was taken over 4×10^6 time steps, for $N = 512$ and $N = 1024$ over 5×10^5 and 2.5×10^5 time steps respectively.

The underlying principle that facilitates self-organization in this model is based on the activity $A(i)$ of a node being closely connected to the frozen component of the network – the fraction of nodes which do not change their state along the attractor – which also undergoes a transition from a large to a vanishing frozen component at the critical connectivity. At low network connectivity, a large fraction of nodes will likely be frozen, and thus receive new in-links once they are selected for rewiring. On the other hand, at high connectivity, nodes will often change their state and in turn lose in-links in the rewiring process. Figure 10.4 shows the above-mentioned transition as a function of connectivity for two different network sizes. With a finite-size scaling of the transition connectivities at the respective network sizes, it can be shown that for large $N \rightarrow \infty$, the transition occurs at the critical value of $K_c = 2$.

10.3.2

Correlation as a Criterion for Rewiring: Self-Organization on a Spin Lattice Neural Network Model

The models described in the following section and originally proposed in [4, 9] capture self-organized critical behavior on a two-dimensional spin lattice via a simple correlation-based rewiring method. The motivation behind the new approach was to transfer the idea of self-organization from [10] to neural networks, thus creating a first self-organized critical neural network model.

In contrast to the activity-regulated model [10] discussed earlier, now:

- the topology is constrained to a squared lattice;
- thermal noise is added to the system;

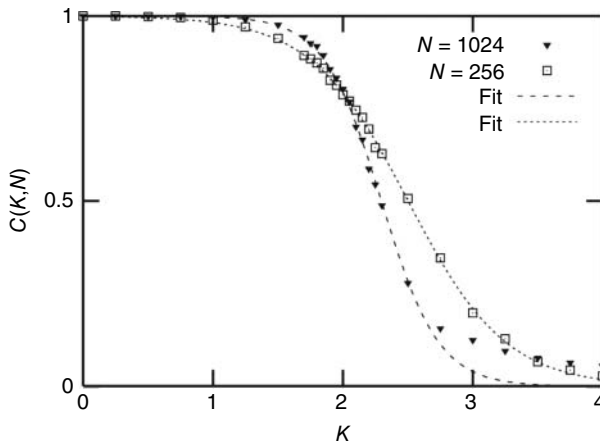


Figure 10.4 The frozen component $C(K,N)$ of random threshold networks, as a function of the networks' average connectivities K , shown for two different network sizes. Sigmoid function fits can be used for a

finite-size scaling of the transition connectivity from active to frozen networks. The results indicate that this transition takes place at $K_c = 2$ for large N , details can be found in the original work [10].

- link weights take nondiscrete values; and
- activation thresholds may vary from 0.

The model consists of a randomly and asymmetrically connected threshold network of N spins ($\sigma_i = \pm 1$), where links can only be established among the eight local neighbors of any lattice site. The link weights w_{ij} can be activating or inhibiting and are chosen randomly from a uniform distribution $w_{ij} \in \{-1, +1\}$. The average connectivity K denotes the average number of nonzero incoming weights. All nodes are updated synchronously via a simple threshold function of their input signals from the previous time step:

$$\begin{aligned}\text{Prob}[\sigma_i(t+1) = +1] &= g_\beta(f_i(t)) \\ \text{Prob}[\sigma_i(t+1) = -1] &= 1 - g_\beta(f_i(t))\end{aligned}\quad (10.5)$$

with

$$f_i(t) = \sum_{j=1}^N w_{ij} \sigma_j(t) + \Theta_i \quad (10.6)$$

and

$$g_\beta(f_i(t)) = \frac{1}{1 + \exp(-2\beta f_i(t))} \quad (10.7)$$

where β denotes the inverse temperature and Θ_i is the activation threshold of node i . Thresholds are chosen as $\Theta_i = -0.1 + \gamma$, where γ is a small random Gaussian noise of width ϵ . The model *per se* exhibits a percolation transition under variation of K or Θ , changing between a phase of ordered dynamics, with short transients and limit cycle attractors, and a chaotic phase with cycle lengths scaling exponentially with system size.

On a larger time scale, the network topology is changed by a slow local rewiring mechanism according to the following principle: if the dynamics of two neighboring nodes is highly correlated or anticorrelated, they get a new link between them. Otherwise, if their activity shows low correlation, any present link between them is removed, which is reminiscent of the Hebbian learning rule. In this model, the correlation $C_{ij}(\tau)$ of nodes i, j over a time interval τ is defined as

$$C_{ij}(\tau) = \frac{1}{\tau + 1} \sum_{t=t_0}^{t_0+\tau} \sigma_i(t) \sigma_j(t) \quad (10.8)$$

The full model is constructed as follows:

- 1) Start with a randomly connected lattice of average connectivity K_{ini} , random initial node configuration, and random individual activation thresholds Θ_i .
- 2) Perform synchronous updates of all nodes for τ time steps. (Here, the choice of τ is not linked to any attractor period measurement, but should be chosen large enough to ensure a separation of time scales between network dynamics and topology changes.)

- 3) Choose a random node i and random neighbor j and calculate $C_{ij}(\tau/2)$ over the last $\tau/2$ time steps (a first $\tau/2$ time steps are disregarded to exclude a possible transient period following the previous topology change.)
- 4) If $|C_{ij}(\tau/2)|$ is larger than a given threshold α , a new link from node j to i is inserted with random weight $w_{ij} \in \{-1, +1\}$. If else $|C_{ij}(\tau/2)| \leq \alpha$ the weight w_{ij} is set to 0.
- 5) Use the current network configuration as new initial state and continue with step 2.

Independent of the initial average connectivity K_{ini} , one finds a slow convergence of K toward a specific mean evolved connectivity K_{ev} , which is characteristic for the respective network size N (Figure 10.5) and shows a finite-size scaling according to

$$K_{\text{ev}}(N) = aN^{-\delta} + b \quad (10.9)$$

with $a = 1.2 \pm 0.4$, $\delta = 0.86 \pm 0.07$, and $b = 2.24 \pm 0.03$, where b can be interpreted as the evolved average connectivity for the large system limit $N \rightarrow \infty$:

$$K_{\text{ev}}^{\infty} = 2.24 \pm 0.03 \quad (10.10)$$

In addition, it is shown that the proposed adaptation mechanism works robustly toward a wide range of thermal noise β , and also the specific choice of the correlation threshold α for rewiring only plays a minor role regarding the evolved K_{ev} (Figure 10.6).

Having a closer look at a finite-size scaling of the evolved average attractor length, one finds a scaling behavior close to criticality. While attractor lengths normally scale exponentially with system size in the supercritical, chaotic regime and sublinearly in the subcritical, ordered phase, this model exhibits relatively short attractor cycles also for large evolved networks in the critical regime (Figure 10.7).

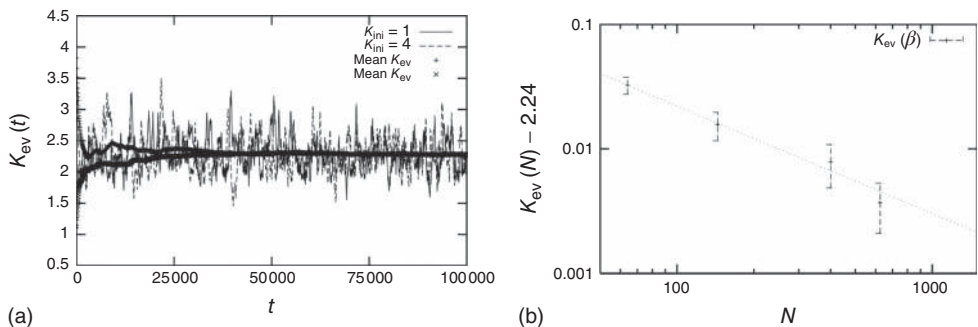


Figure 10.5 (a) Evolution of the average connectivity with a correlation-based rewiring, shown for two different initial connectivities. Again, connectivity evolves to a specific average depending on network size, but independent of the initial configuration. (b) Finite-size scaling of the evolved average connectivity. The best fit is obtained for a large system limit of $K_{\text{ev}}^{\infty} = 2.24 \pm 0.03$. Averages are taken over 4×10^5 time steps.

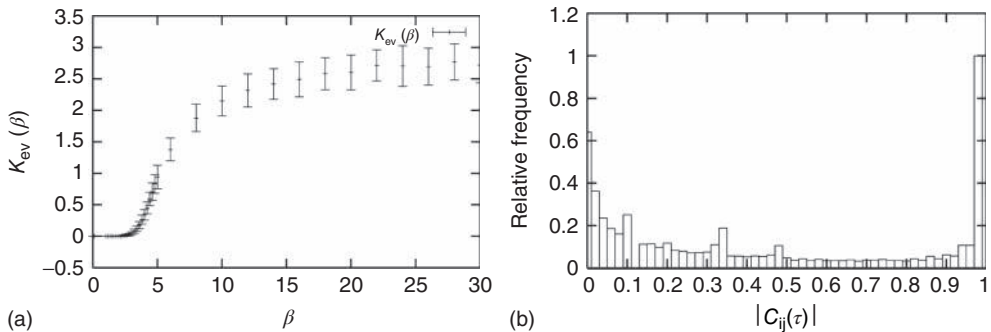


Figure 10.6 (a) Evolved average connectivity $K_{ev}(\beta)$ as a function of the inverse temperature β . The behavior is robust over a wide range of β . (b) Histogram of the average correlation $|C_{ij}(\tau)|$ for a network evolving in time

with $N = 64$ and $\beta = 10$. As very low and very high correlations dominate, the exact choice of the correlation threshold during the rewiring process is of minor importance.

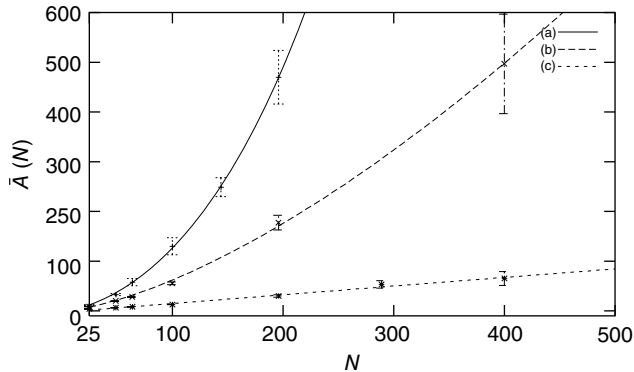


Figure 10.7 Finite-size scaling of the evolved average attractor period $\bar{A}(N)$ for networks of different sizes N (b). Also shown for comparison is the corresponding

scaling of the attractor lengths of a supercritical random network (a) with $K = 3.8$ and a subcritical one (c) with $K = 1.5$.

10.3.3

Simplicity versus Biological Plausibility – and Possible Improvements

10.3.3.1 Transition from Spins to Boolean Node States

In the earlier sections, we have seen that already basic toy models, neglecting a lot of details, can reproduce some of the observations made in real neuronal systems. We now want to move these models a step closer toward biological plausibility and at the same time construct an even simpler model.

One major shortcoming of both models discussed earlier is the fact that they are constructed as spin models. In some circumstances, however, when faithful representation of certain biological details is important, the exact definition matters. In the spin version of a neural network model, for example, a node with

negative spin state $\sigma_j = -1$ will transmit nonzero signals through its outgoing weights c_{ij} , despite representing an inactive (!) biological node. In the model, such signals arrive at target nodes i , for example, as a sum of incoming signals $f_i = \sum_{j=1}^N c_{ij} \sigma_j$. However, biological nodes, as genes or neurons, usually do not transmit signals when inactive. Also, in other contexts such as biochemical network models, each node represents whether a specific chemical component is present ($\sigma = 1$) or absent ($\sigma = 0$). Thus, the network itself is mostly in a state of being partially absent as, for example, in a protein network where for every absent protein all of its outgoing links are absent as well. In the spin state convention, this fact is not faithfully represented. A far more natural choice would be to construct a model based on Boolean state nodes, where nodes can be truly “off” ($\sigma_i = 0$) or “on” ($\sigma_i = 1$) – which is precisely what we are going to do in the following sections.

Another example of an inaccurate detail is the common practice of using the standard convention of the Heaviside step function as an activation function in discrete dynamical networks (or the sign function in the spin model context). The convention $\Theta(0) = 1$ is not a careful representation of biological circumstances. Both for genes and neurons, a silent input frequently maps to a silent output. Therefore, we use a redefined threshold function defined as

$$\Theta_0(x) = \begin{cases} 1, & x > 0 \\ 0, & x \leq 0 \end{cases} \quad (10.11)$$

Most importantly, in our context here, the choice of Boolean node states and the redefined threshold function are vital when we discuss mechanisms of self-organization. For instance, the correlation-based approach presented in the older spin model [4] in Section 10.3.2 explicitly measures contributions by pairs of nodes that could be constantly off ($\sigma_{i,j} = -1$) and still treat them as highly correlated (because $(-1) \cdot (-1) = +1$) even though there is no activity involved at all. In the later Section 10.3.4, we therefore present a new approach for a network of Boolean state nodes, which does not rely on nonactivity correlations anymore.

10.3.3.2 Model Definitions

Let us consider randomly wired threshold networks of N nodes $\sigma_i \in \{0, 1\}$. At each discrete time step, all nodes are updated in parallel according to

$$\sigma_i(t+1) = \Theta_0(f_i(t)) \quad (10.12)$$

using the input function

$$f_i(t) = \sum_{j=1}^N c_{ij} \sigma_j(t) + \theta_i \quad (10.13)$$

In particular, we choose $\Theta_0(0) := 0$ for plausibility reasons (zero input signal will produce zero output). While the weights take discrete values $c_{ij} = \pm 1$ with equal probability for connected nodes, we select the thresholds $\theta_i = 0$ for the following discussion. For any node i , the number of incoming links $c_{ij} \neq 0$ is called the *in-degree* k_i of that specific node. K denotes the average connectivity of the whole

network. With randomly placed links, the probability for each node to actually have $k_i = k$ incoming links follows a Poissonian distribution:

$$p(k_i = k) = \frac{K^k}{k!} \cdot \exp(-K) \quad (10.14)$$

10.3.3.3 Exploration of Critical Properties – Activity-Dependent Criticality

To analytically derive the critical connectivity of this type of network model, we first study damage spreading on a local basis and calculate the probability $p_s(k)$ for a single node to propagate a small perturbation, that is, to change its output from 0 to 1 or vice versa after changing a single input state. The calculation can be done closely following the derivation for spin-type threshold networks in Ref. [40], but one has to account for the possible occurrence of “0” input signals also via nonzero links. The combinatorial approach yields a result that directly corresponds to the spin-type network calculation via $p_s^{\text{bool}}(k) = p_s^{\text{spin}}(2k)$.

However, this approach does not hold true for our Boolean model in combination with the defined theta function $\Theta_0(0) := 0$ as it assumes a statistically equal distribution of all possible input configurations for a single node. In the Boolean model, this would involve an average node activity of $b = 0.5$ over the whole network (where b denotes the average fraction of nodes which are active, i.e., $\sigma_i = 1$). Instead we find (Figure 10.8) that the average activity on the network is significantly below 0.5. At $K = 4$ (which will turn out to be already far in the supercritical regime), less than 30% of all nodes are active on average. Around $K \approx 2$ (where we usually expect the critical connectivity for such networks), the average activity is in fact below 10%. Thus, random input configurations of nodes in this network will more likely consist of a higher number of “0” signal contributions than of ± 1 inputs.

Therefore, when counting input configurations for the combinatorial derivation of $p_s(k)$, we need to weight all relevant configurations according to their realization probability as given by the average activity b – the detailed derivation can be found in [12]. With the average probability of damage spreading, we can further compute the branching parameter or sensitivity $\lambda = K \cdot \langle p_s \rangle(K)$ and apply the annealed approximation [10, 41] to obtain the critical connectivity K_c by solving

$$\lambda_c = K_c \cdot \langle p_s \rangle(K_c) = 1 \quad (10.15)$$

However, K_c now depends on the average network activity, which in turn is a function of the average connectivity K itself as shown in Figure 10.8.

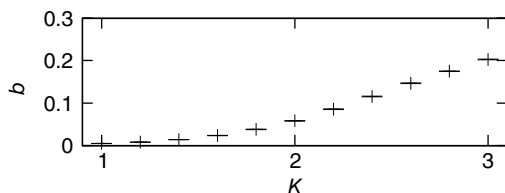


Figure 10.8 Average node activity b as function of connectivity K measured on attractors of 10 000 sample networks each, 200 nodes.

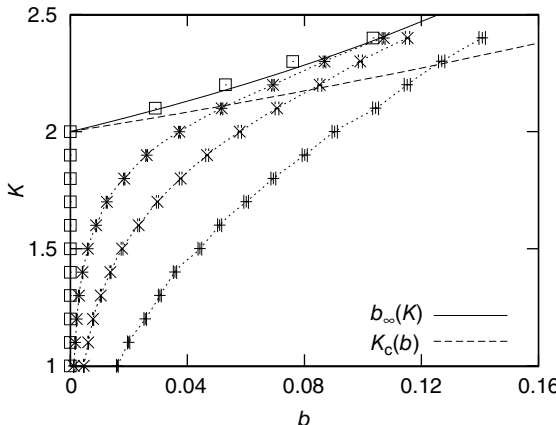


Figure 10.9 Average activity b on attractors of different network sizes (right to left: $N = 50, 200, 800$, ensemble averages were taken over 10 000 networks each). Squares indicate activity on an infinite system determined by finite-size scaling, which is in good

agreement with the analytic result (solid line). The dashed line shows the analytic result for $K_c(b)$ from Eq. (10.15). The intersections represent the value of K_c for the given network size.

From the combined plot in Figure 10.9, we find that both curves intersect at a point where the network dynamics – as a result of the current connectivity K – exhibit an average activity, which in turn yields a critical connectivity K_c that exactly matches the given connectivity. This intersection thus corresponds to the critical connectivity of the present network model.

However, the average activity still varies with different network sizes, which is obvious from Figure 10.9. Therefore, the critical connectivity is also a function of N . For an analytic approach to the infinite size limit, it is possible to calculate the average network activity at the next time step b_{t+1} in an iterative way from the momentary average activity b_t . Again, the details can be found in [12]. We can afterwards distinguish between the different dynamical regimes by solving $\langle b_{t+1} \rangle = b_t(K)$ for the critical line. The solid line in Figure 10.9 depicts the evolved activity in the long time limit. We find that for infinite system size, the critical connectivity is at

$$K_c(N \rightarrow \infty) = 2.000 \pm 0.001$$

while up to this value all network activity vanishes in the long time limit ($b_\infty = 0$). For any average connectivity $K > 2$, a certain fraction of nodes remains active. In finite-size systems, both network activity evolution and damage propagation probabilities are subject to finite-size effects, thus increasing K_c to a higher value.

Finally, let us have a closer look on the average length of attractor cycles and transients. As shown in Figure 10.10, the behavior is strongly dependent on the dynamical regime of the network. As expected and in accordance with early works on random threshold networks [42] as well as random Boolean networks [43], we find an exponential increase of the average attractor lengths with network size N in

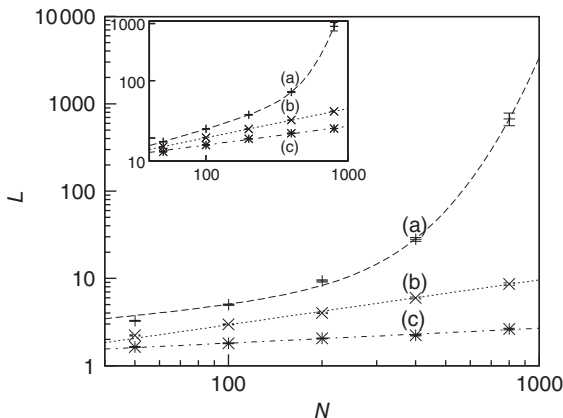


Figure 10.10 Average attractor length at different network sizes. Ensemble averages were taken over 10 000 networks each at (a) $K = 2.4$, (b) $K = 2.0$, (c) $K = 1.6$. Inset figure shows the scaling behavior of the corresponding transient lengths.

the chaotic regime ($K > K_c$), whereas we can observe a power-law increase in the frozen phase ($K < K_c$). We find similar behavior for the scaling of transient lengths (inset of Figure 10.10).

10.3.3.4 Extension of the Model: Thermal Noise

As is clear from Eq. (10.12), nodes in our model will only switch to active state if they get a positive input from *somewhere*. Thus, to get activity into the system, we could either define certain nodes to get an additional external input, but this would at the same time create two different kinds of nodes, those with and those without external activity input, which would in turn diminish the simplicity of our model. That is why we will alternatively use thermal noise to create activity, using a Glauber update of the nodes in the same way as it was discussed in the spin model [4] in Section 10.3.2, with one slight modification. We define a probability for the activation of a node, which is a sigmoid function of the actual input sum, but also leaving room for a spontaneous activation related to the inverse temperature β of the system.

$$\begin{aligned} \text{Prob}[\sigma_i(t+1) = +1] &= g_\beta(f_i(t)) \\ \text{Prob}[\sigma_i(t+1) = 0] &= 1 - g_\beta(f_i(t)) \end{aligned} \quad (10.16)$$

with

$$f_i(t) = \sum_{j=1}^N c_{ij} \sigma_j(t) + \Theta_i \quad (10.17)$$

and

$$g_\beta(f_i(t)) = \frac{1}{1 + \exp(-2\beta(f_i(t) - 0.5))} \quad (10.18)$$

You will note the similarity to the older spin model [4], but be aware that in Eq. (10.18) we shift the input sum f_i by -0.5 , and we will explain now why this is necessary. Remember that we use binary coupling weights $c_{ij} = \pm 1$ for existing links in our model. The input sum f_i to any node will therefore be an integer value. If we would not shift the input sum, a node with an input $f_i = 0$ (which should always be inactive in the deterministic model without thermal noise), would, after the introduction of the Glauber update rule with nonzero temperature, always have a probability of $\text{Prob}[\sigma_i(t+1) = +1] = 0.5$ to be activated, regardless of the actual inverse temperature β . Figure 10.11 illustrates this problem. A simple shift of -0.5 will now give us the desired behavior: Nodes with input $f_i = 0$ will stay off in most cases, with a slight probability to turn active depending on temperature, and, on the other hand, nodes with activating input $f_i = +1$ will be on in most cases, with slight probability to remain inactive. With this modification of the original basic model [12], we can now continue to make our network adaptive and critical.

10.3.4

Self-Organization on the Boolean State Model

We now want to set up an adaptive network based on the model discussed earlier, which is still capable of self-regulation toward a critical state despite being simplified to the most minimal model possible. Particularly, we want it to

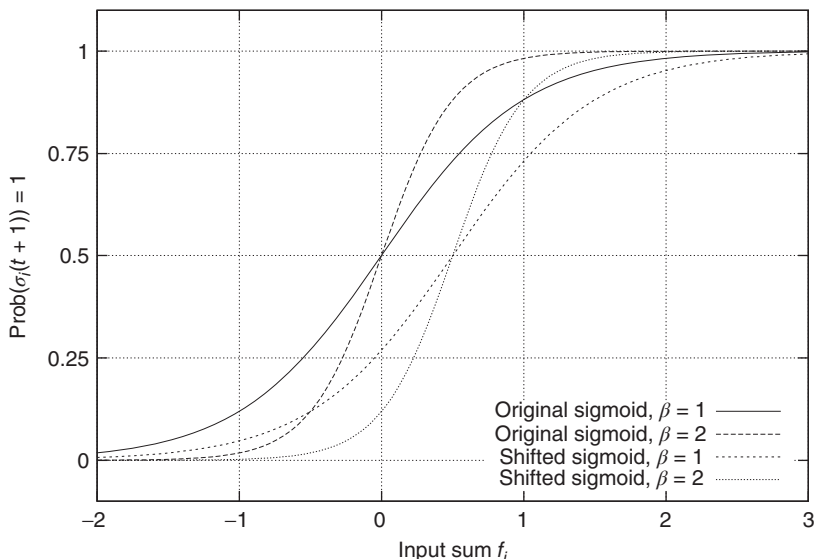


Figure 10.11 With integer input sum values, such that the transition between off and on nodes without input would turn active with probability 0.5 regardless of temperature. To prevent this, we shift the input sum by -0.5 so that the state happens exactly in the middle between input sums 0 respectively 1.

- have a simple, yet biologically plausible rewiring rule, which only uses local information accessible to individual nodes;
- work independently from a special topology as a lattice.

We have already pointed out the problems of a spin formulation of neural network models similar to [4], and possible ways out with the Boolean state model. As a major advantage of the latter, activity avalanches intrinsically occur in this type of network, whereas spin networks typically exhibit continuous fluctuations with no avalanches directly visible. However, the old correlation-based rewiring mechanism will no longer work when inactive nodes are now represented by “0” instead of “−1.” A solution is presented below.

A second aspect that needs to be addressed concerning the self-organization mechanism is topological invariance of the algorithm. The older, correlation-based mechanism from the spin model relies on randomly selecting neighboring sites on a lattice for the rewiring processes. On a lattice, the number of possible neighbors is strictly limited, but on a large random network near critical connectivity, there are far more unconnected pairs of nodes than there are connected pairs. Thus, randomly selecting pairs of nodes for rewiring would introduce a strong bias toward connecting nodes that were previously unconnected. This results in a strong increase of connectivity and makes a self-organized adaptation toward a critical state practically impossible. If we want to overcome the restriction of, for example, a confined lattice topology in order to improve biological applicability of the model, we have to adapt the rewiring mechanism such that this bias no longer exists.

Of course, the new model shall inherit several important features from the older spin models, which already underline the applicability to biological networks: in particular, it must be capable of self-regulation toward a critical state despite being simplified to the most minimal model possible. The organization process, however, should be based on a simple, yet biologically plausible rewiring rule, which only uses local information accessible to individual nodes like pre- and postsynaptic activity and correlation of such activity.

This section is directly based on our recent work [13].

10.3.4.1 Model Definitions

Consider a randomly connected threshold network of the type discussed in Section 10.3.3. The network consists of N nodes of Boolean states $\sigma_i \in \{0, 1\}$, which can be linked by asymmetric directed couplings $c_{ij} = \pm 1$. Node pairs that are not linked have their coupling set to $c_{ij} = 0$, and links may exist between any two nodes; so, there is no underlying spatial topology in this model.

All nodes are updated synchronously in discrete time steps via a simple threshold function of their input signals with a little thermal noise introduced by the inverse temperature β , in the same way as in the model of Bornholdt and Roehl (Section 10.3.2), but now with an input shift of −0.5 in the Glauber update, representing

the new Θ_0 function as discussed in Section 10.3.3.4:

$$\begin{aligned}\text{Prob}[\sigma_i(t+1) = +1] &= g_\beta(f_i(t)) \\ \text{Prob}[\sigma_i(t+1) = 0] &= 1 - g_\beta(f_i(t))\end{aligned}\quad (10.19)$$

with

$$f_i(t) = \sum_{j=1}^N c_{ij} \sigma_j(t) + \Theta_i \quad (10.20)$$

and

$$g_\beta(f_i(t)) = \frac{1}{1 + \exp(-2\beta(f_i(t) - 0.5))} \quad (10.21)$$

For the simplicity of our model, we first assume that all nodes have an identical activation threshold of $\Theta_i = 0$.

10.3.4.2 Rewiring Algorithm

The adaptation algorithm is now constructed in the following way: we start the network at an arbitrary initial connectivity K_{ini} and do parallel synchronous updates on all nodes according to Eq. (10.16). All activity in this model originates from small perturbations by thermal noise, leading to activity avalanches of various sizes. In this case, we set the inverse temperature to $\beta = 5$. On a larger time scale, that is, after $\tau = 200$ updates, a topology rewiring is introduced at a randomly chosen, single node. The new element in our approach is to test whether the addition or the removal of one random in-link at the selected node will increase the average dynamical correlation to all existing inputs of that node. By selecting only one single node for this procedure, we effectively diminish the bias of selecting mostly unconnected node pairs – but retain the biologically inspired idea for a Hebbian, correlation-based rewiring mechanism on a local level.

Now, we have to define what is meant by *dynamical correlation* in this case. We here use the Pearson correlation coefficient to first determine the dynamical correlation between a node i and one of its inputs j :

$$C_{ij} = \frac{\langle \sigma_i(t+1)\sigma_j(t) \rangle - \langle \sigma_i(t+1) \rangle \langle \sigma_j(t) \rangle}{S_i \cdot S_j} \quad (10.22)$$

where S_i and S_j in the denominator depict the standard deviation of states of the nodes i and j , respectively. In case one or both of the nodes are frozen in their state (i.e., yield a standard deviation of 0), the Pearson correlation coefficient would not be defined, we will assume a correlation of $C_{ij} = 0$. Note that we always use the state of node i at one time step later than node j , thereby taking into account the signal transmission time of one time step from one node to the next one. Again, as in the model of [4], the correlation coefficient is only taken over the second half of the preceding τ time steps in order to avoid transient dynamics. Finally, we define the average input correlation C_i^{avg} of node i as

$$C_i^{\text{avg}} = \frac{1}{k_i} \sum_{j=0}^N |c_{ij}| C_{ij} \quad (10.23)$$

where k_i is the in-degree of node i . The factor $|c_{ij}|$ ensures that correlations are only measured where links are present between the nodes. For nodes without any in-links ($k_i = 0$), we define $C_i^{\text{avg}} := 0$.

In detail, the adaptive rewiring is now performed in the following steps:

- Select a random node i and generate three clones of the current network topology and state:
 - [Network 1:] This copy remains unchanged.
 - [Network 2:] In this copy, node i will get one additional in-link from a randomly selected other node j which is not yet connected to i in the original copy (if possible, i.e., $k_i < N$). Also, the coupling weight $c_{ij} \pm 1$ of the new link is chosen at random.
 - [Network 3:] In the third copy, one of the existing in-links to node i (again if possible, i.e., $k_i > 0$) will be removed.
- All three copies of the network are individually run for $\tau = 200$ time steps.
- On all three networks, the average input correlation C_i^{avg} of node i to all of the respective input nodes in each network is determined.
- We accept and continue with the network which yields the highest absolute value of C_i^{avg} , the other two clones are dismissed. If two or more networks yield the same highest average input correlation such that no explicit decision is possible, we simply continue with the unchanged status quo.
- A new random node i is selected and the algorithm starts over with step 1.

It is worth noting that this model – in the same way as the earlier work by Bornholdt and Röhl [4] – uses locally available information at synapse level and takes into account both pre- and postsynaptic activity (Figure 10.12). This is a fundamental difference to approaches discussed, for example, by de Arcangelis *et al.* [26–29], where only presynaptic activity determines changes to the coupling weights. Note that the non-locality of running three network copies in parallel

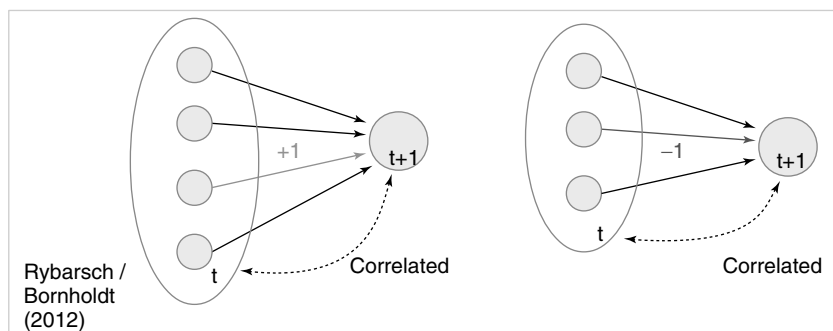


Figure 10.12 Schematic illustration of the rewiring mechanism based on average input correlation. In this example, the target node initially has three in-links. Left: If the addition of a fourth input increases the average

input correlation C_i^{avg} , a link will be inserted. Right: If removal of an existing in-link increases C_i^{avg} , the link will be deleted. (Please find a color version of this figure on the color plates.)

that we use here is not critical. A local implementation is straightforward, locally estimating the order parameter (here the average input correlation C_i^{avg}) as time average, with a sufficient time scale separation towards the adaptive changes in the network. A local version of the model will be studied in the published version of [13].

10.3.4.3 Observations

In the following, we take a look at different observables during numerical simulations of network evolution in the model presented earlier. Key figures include the average connectivity K and the branching parameter (or sensitivity) λ . Both are closely linked to and influenced by the ratio of activating links p , which is simply the fraction of positive couplings $c_{ij} = +1$ among all existing (non-zero) links.

Figure 10.13a shows an exemplary run of the topology evolution algorithm, where we start with completely isolated nodes without any links. Trivially, the “network” is subcritical at this stage, which can be seen from the branching parameter which is far below 1. As soon as rewiring takes place, the network starts to insert new links, obviously because these links enable the nodes to pass signals and subsequently act in a correlated way. With increasing connectivity, the branching parameter also rises, indicating that perturbations start to spread from their origin to other nodes. When the branching parameter approaches 1, indicating that the network reaches a critical state, the insertion of new links is cut back. The processes of insertion and depletion of links tend to be balanced against each other, regulating the network close to criticality.

If we, on the other hand, start with a randomly interconnected network at a higher connectivity like $K_{\text{ini}} = 4$ as shown in Figure 10.13b, we find the network in the supercritical regime ($\lambda > 1$) at the beginning. When above the critical threshold, many nodes will show chaotic activity with very low average correlation to their respective inputs. The rewiring algorithm reacts in the appropriate way by deleting links from the network, until the branching parameter approaches 1.

In both the above-mentioned examples, the evolution of the ratio of activating links p (which tends toward 1) shows that the rewiring algorithm in general favors the insertion of activating links and, vice versa, the deletion of inhibitory couplings. This appears indeed plausible if we remind ourselves that the rewiring mechanism optimizes the inputs of a node toward high correlation, on average. Also, nodes will only switch to active state $\sigma_i = 1$ if they get an overall positive input. As we had replaced spins by Boolean state nodes, this can only happen via activating links – and that is why correlations mainly originate from positive couplings in our model. As a result, we observe the connectivity evolving toward one in-link per node, with the ratio of positive links also tending toward one.

For a richer pattern complexity, we might later want to introduce a second mechanism that balances out positive via negative links, and with a first approach we can already test how the rewiring strategy would fit to that situation: if after each rewiring step, we change the sign of single random links as necessary to obtain a ratio of e.g. 80% activating links (i.e. $p = 0.8$), keeping the large majority of present links unchanged, the branching parameter will again stabilize close

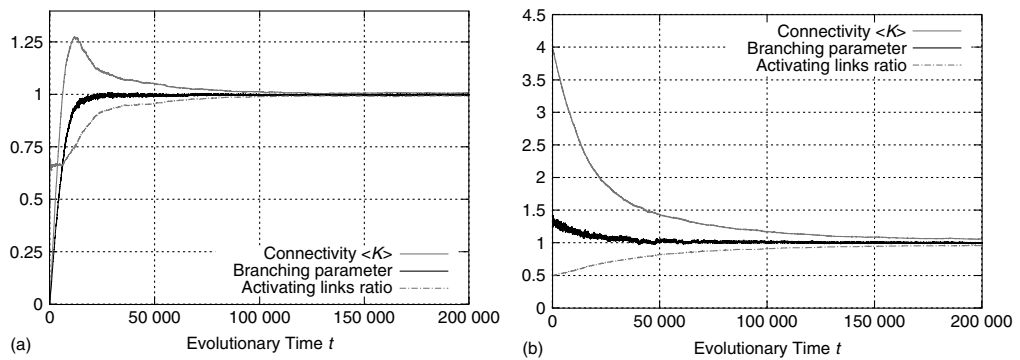


Figure 10.13 Regardless of initial connectivity and sensitivity, the network evolves to a critical configuration. (a) Starting with completely disconnected nodes and obviously subcritical “network.” (b) Starting with a supercritical network.

to the critical transition, while the connectivity is maintained at a higher value. Figure 10.14 shows that the self-organization behavior is again independent from the initial conditions. This result does not depend on the exact choice of the activating links ratio p ; similar plots can easily be obtained for a large range starting at $p = 0.5$, where the connectivity will subsequently evolve towards a value slightly below $K = 2$, which is the value we would expect as the critical connectivity for a randomly wired network with balanced link ratio according to the calculations made in Section 10.3.3 for the basic network model [12].

In addition to the branching parameter measurement, we also take a look at some dynamical properties of the evolved networks to further verify their criticality. As stated in section 10.1, we are especially interested in the resulting activity avalanches on the networks. Figure 10.15a shows the cumulative distribution of avalanche sizes in an evolved sample network of $N = 1024$ nodes. We observe a broad distribution of avalanche sizes and a power-law-like scaling of event sizes with an exponent close to $-1/2$, corresponding to an exponent of $-3/2$ in the probability density – which is characteristic of a critical branching process. At the same time, this is in perfect agreement with the event size distribution observed by Beggs and Plenz in their *in vitro* experiments.

In our most recent version of [13] we were also able to quantify the scaling behavior of avalanche durations in addition to the size distributions, as well as the relations between durations and spatial sizes of avalanches. We find good agreement of the corresponding scaling exponents with relations predicted by universal scaling theory [44], and observe avalanche statistics and collapsing avalanche profiles compatible with recent results from biological experiments by Friedman *et al* [45].

If we randomly activate small fractions of nodes in an otherwise silent network (single nodes up to $\approx 5\%$ of the nodes) to set off avalanches, we can also see (Figure 10.15b) that the resulting transient length shows a power-law scaling with network size right up to network snapshots taken after an evolution run at the final average branching parameter of 1. Intermediate networks taken from within an evolution process at a higher branching parameter instead show a superpolynomial increase of transient lengths with system size, which is precisely what we expect.

10.3.5

Response to External Perturbations

In recent *in vitro* experiments, Plenz [46] could further demonstrate that cortical networks can self-regulate in response to external influences, retaining their functionality, while avalanche-like dynamics persist – for example, after neuronal excitability has been decreased by adding an antagonist for fast glutamatergic synaptic transmission to the cultures.

To reproduce such behavior in our model, we can include variations in the activation thresholds Θ_i of the individual nodes, which had been set to zero in the above-mentioned discussions for maximum model simplicity. Assume that we start our network evolution algorithm with a moderately connected, but subcritical network, where all nodes have a higher activation threshold of $\Theta_i = 1$. According to

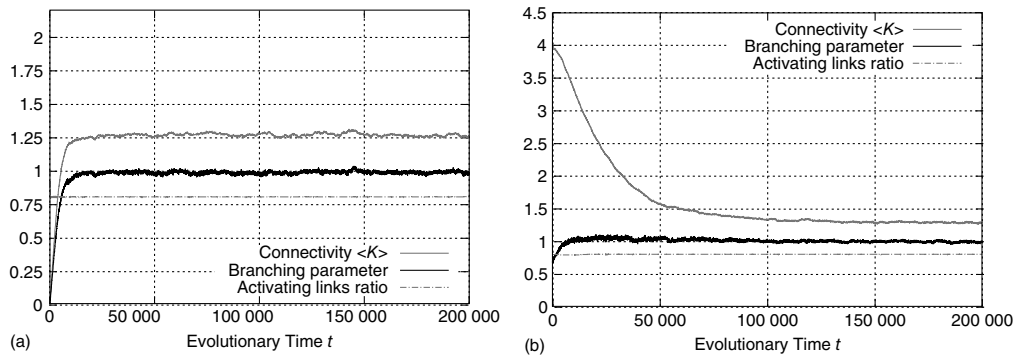


Figure 10.14 Network evolution with activating links ratio kept at $p = 0.8$.

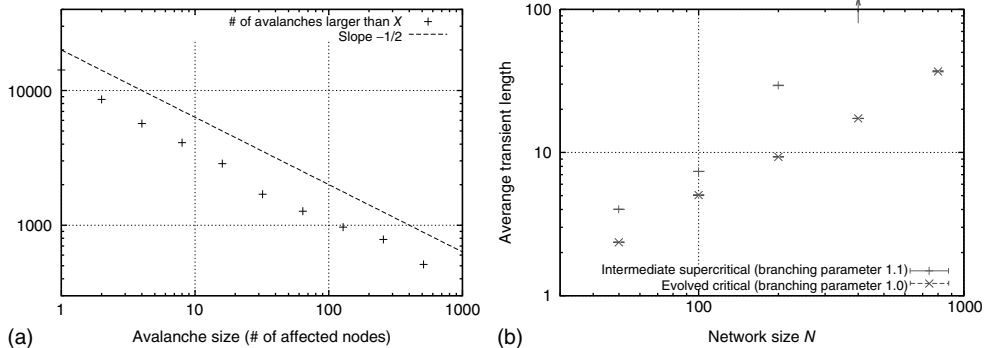


Figure 10.15 (a) Cumulative distribution of avalanche sizes in an evolved sample network of $N = 1024$ nodes. We find a broad, near power-law distribution comparable to a slope of $-1/2$, indicative of a critical

branching process and corresponding well to the experimental results of Beggs and Plenz. (b) Scaling of average transient lengths at different network sizes, 50 evolved networks each.

the update rule 10.6, now at least two positive inputs are necessary to activate a single node. As the rewiring algorithm is based on propagation of thermal noise signals, the inverse temperature β needs to be selected at a lower value than before. (As a general rule, β should be selected in a range where thermal activation of nodes occur at a low rate, such that avalanches can be triggered, but are not dominated by noise.)

Figure 10.16 shows that, same as earlier, the subcritical network starts to grow new links, thereby increasing the average branching parameter. Again, this process is stopped after the supercritical regime is reached. While the system does not

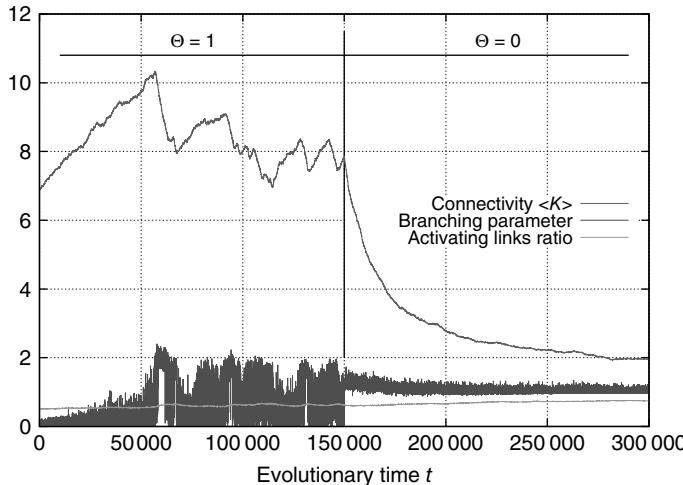


Figure 10.16 Rewiring response to a sudden decrease of activation thresholds. All Θ_i were set from 1 to 0 in the same time step. (Please find a color version of this figure on the color plates.)

approach to a phase transition as well as shown above for activation thresholds of 0 (in fact, the branching fluctuates much more around the target value of 1), the general tendency remains: the rewiring mechanism reacts properly as the network drifts too far off from criticality. At one time step in the center of Figure 10.16, we suddenly reset all nodes to an activation threshold of $\Theta_i = 0$, simulating the addition of a stimulant. As we can expect, this immediately puts the network into a supercritical, chaotic state. This is reflected by the branching parameter, which now constantly stays above 1 and does not fluctuate below anymore. It is clearly visible that the rewiring mechanism promptly reacts and drives back the connectivity, until the branching parameter slowly converges toward 1 again. A similar behavior is also found if thresholds Θ_i are not changed all at once, but gradually during network evolution.

10.4

Conclusion

We have seen that very minimalistic binary neural network models are capable of self-organized critical behavior. While older models show some drawbacks regarding biological plausibility originating directly from their nature as spin networks, we subsequently presented a possible transition to a self-organized critical, randomly wired network of Boolean node states with emerging dynamical patterns, namely, activity avalanches, reminiscent of activity modes as observed in real neuronal systems. This is possible via a simple, locally realizable, rewiring mechanism that uses activity correlation as its regulation criterion, thus retaining the biologically inspired rewiring basis from the spin version. While it is obvious that there are far more details involved in self-organization of real neuronal networks – some of which are reflected in other existing models – we here observe a fundamental organization mechanism leading to a critical system that exhibits statistical properties pointing to a larger class of universality, regardless of the details of a specific biological implementation.

Acknowledgments

For the presentation of the earlier work from our group (Sections 10.3.1 and 10.3.2), excerpts from the text and figures of the original publications [4, 10] were used, as well as from [12, 13] for our recent work.

References

1. Langton, C.G. (1990) Computation at the edge of chaos. *Physica D*, **42**, 12–37.
2. Herz, A.V.M. and Hopfield, J.J. (1995) Earthquake cycles and neural reverberations: collective oscillations in systems with pulse-coupled threshold elements. *Phys. Rev. Lett.*, **75** (6), 1222–1225.
3. Bak, P. and Chialvo, D.R. (2001) Adaptive learning by extremal dynamics and negative feedback. *Phys. Rev. E*, **63** (3), 031912.

4. Bornholdt, S. and Röhl, T. (2003) Self-organized critical neural networks. *Phys. Rev. E*, **67** (066118).
5. Kauffman, S. (1993) *The Origins of Order: self-Organization and Selection in Evolution*, Oxford University Press.
6. Bak, P., Tang, C., and Wiesenfeld, K. (1988) Self-organized criticality. *Phys. Rev. A*, **38** (1), 364.
7. Linkenkaer-Hansen, K., Nikouline, V.V., Palva, J.M., and Ilmoniemi, R.J. (2001) Long-range temporal correlations and scaling behavior in human brain oscillations. *J. Neurosci.*, **21** (4), 1370–1377.
8. Eurich, C.W., Herrmann, J.M., and Ernst, U.A. (2002) Finite-size effects of avalanche dynamics. *Phys. Rev. E*, **66**, 066137.
9. Bornholdt, S. and Röhl, T. (2001) Self-organized critical neural networks. arXiv:cond-mat/0109256v1.
10. Bornholdt, S. and Röhl, T. (2000) Topological evolution of dynamical networks: Global criticality from local dynamics. *Phys. Rev. Lett.*, **84** (26), 6114–6117.
11. Beggs, J.M. and Plenz, D. (2003) Neuronal avalanches in neocortical circuits. *J. Neurosci.*, **23** (35), 11167–11177.
12. Rybarsch, M. and Bornholdt, S. (2012) Binary threshold networks as a natural null model for biological networks. *Phys. Rev. E*, **86**, 026114.
13. Rybarsch, M. and Bornholdt, S. (2012) A minimal model for self-organization to criticality in binary neural networks. arXiv:1206.0166.
14. Beggs, J.M. and Plenz, D. (2004) Neuronal avalanches are diverse and precise activity patterns that are stable for many hours in cortical slice cultures. *J. Neurosci.*, **24**, 5216–5229.
15. Stewart, C.V. and Plenz, D. (2007) Homeostasis of neuronal avalanches during postnatal cortex development in vitro. *J. Neurosci. Methods*, **169** (2), pp. 405–416.
16. Mazzoni, A., Broccard, F.D., Garcia-Perez, E., Bonifazi, P., Ruaro, M.E., and Torre, V. (2007) On the dynamics of the spontaneous activity in neuronal networks. *PLoS One*, **2** (5), Article e439.
17. Pasquale, V., Massobrio, P., Bologna, L.L., Chiappalone, M., and Martinoia, S. (2008) Self-organization and neuronal avalanches in networks of dissociated cortical neurons. *Neuroscience*, **153** (4), 1354–1369.
18. Gireesh, E.D. and Plenz, D. (2008) Neuronal avalanches organize as nested theta- and beta/gamma-oscillations during development of cortical layer 2/3. *Proc. Natl. Acad. Sci. U.S.A.*, **105** (21), 7576–7581.
19. Petermann, T., Thiagarajan, T.C., Lebedev, M.A., Nicolelis, M.A.L., Chialvo, D.R., and Plenz, D. (2009) Spontaneous cortical activity in awake monkeys composed of neuronal avalanches. *Proc. Natl. Acad. Sci. U.S.A.*, **106** (37), 15921–15926.
20. Kinouchi, O. and Copelli, M. (2006) Optimal dynamical range of excitable networks at criticality. *Nat. Phys.*, **2**, 348–352.
21. Shew, W.L., Yang, H., Petermann, T., Roy, R., and Plenz, D. (2009) Neuronal avalanches imply maximum dynamic range in cortical networks at criticality. *J. Neurosci.*, **29** (49), 15595–15600.
22. Larremore, D.B., Shew, W.L., and Restrepo, J.G. (2011) Predicting criticality and dynamic range in complex networks: Effects of topology. *Phys. Rev. Lett.*, **106** (5), 058101.
23. Shew, W.L., Yang, H., Yu, S., Roy, R., and Plenz, D. (2011) Information capacity and transmission are maximized in balanced cortical networks with neuronal avalanches. *J. Neurosci.*, **31** (1), 55–63.
24. Yang, H., Shew, W.L., Roy, R., and Plenz, D. (2012) Maximal variability of phase synchrony in cortical networks with neuronal avalanches. *J. Neurosci.*, **32** (3), 1061–1072.
25. Gross, T., and Blasius, B., (2008) Adaptive coevolutionary networks: a review. *J. R. Soc. Interface*, **5** (20), 259–271.
26. de Arcangelis, L., Perrone-Capano, C., and Herrmann, H.J. (2006) Self-organized criticality model for brain plasticity. *Phys. Rev. Lett.*, **96** (2), 028107.
27. Pellegrini, G.L., de Arcangelis, L., Herrmann, H.J., and Perrone-Capano, C. (2007) Activity-dependent neural

- network model on scale-free networks. *Phys. Rev. E*, **76** (1 Pt 2), 016107.
28. Meisel, C., and Gross, T. (2009) Adaptive self-organization in a realistic network model. *Phys. Rev. E*, **80** (2), 061917.
 29. Levina, A., Herrmann, J.M., and Geisel, T. (2007) Dynamical synapses causing self-organized criticality in neural networks. *Nat. Phys.*, **3**, 857–860.
 30. Levina, A., Herrmann, J.M., and Geisel, T. (2009) Phase transitions towards criticality in a neural system with adaptive interactions. *Phys. Rev. Lett.*, **102** (11), 118110.
 31. Buice, M.A. and Cowan, J.D. (2007) Field-theoretic approach to fluctuation effects in neural networks. *Phys. Rev. E*, **75** (5 Pt 1), 051919.
 32. Millman, D., Mihalas, S., Kirkwood, A., and Niebur, E. (2010) Self-organized criticality occurs in non-conservative neuronal networks during ‘up’ states. *Nat. Phys.*, **6**, 801–805.
 33. Magnasco, M.O., Piro, O., and Cecchi, G.A. (2009) Self-tuned critical anti-hebbian networks. *Phys. Rev. Lett.*, **102**, 258102.
 34. Rubinov, M., Sporns, O., Thivierge, J.-P., and Breakspear, M. (2011) Neurobiologically realistic determinants of self-organized criticality in networks of spiking neurons. *PLoS Comput. Biol.*, **7** (6), e1002038.
 35. Droste, F., Do, A.-L., and Gross, T. (2013) Analytical investigation of self-organized criticality in neural networks. *J. R. Soc. Interface.*, **10** (78).
 36. Larremore, D.B., Carpenter, M.Y., Ott, E., and Restrepo, J.G. (2012) Statistical properties of avalanches in networks. *Phys. Rev. E*, **85**, 066131.
 37. de Arcangelis, L. and Herrmann, H.J. (2010) Learning as a phenomenon occurring in a critical state. *Proc. Natl. Acad. Sci. U.S.A.*, **107** (9).
 38. de Arcangelis, L. and Herrmann, H.J. (2012) Activity-dependent neuronal model on complex networks. *Front. Physio.*, **3** (62).
 39. Lombardi, F., Herrmann, H.J., Perrone-Capano, C., Plenz, D., and de Arcangelis, L. (2012) The balance between excitation and inhibition controls the temporal organization of neuronal avalanches. *Phys. Rev. Lett.*, **108**, 228703.
 40. Rohlf, T. and Bornholdt, S. (2002) Criticality in random threshold networks: annealed approximation and beyond. *Physica A*, **310**, 245–259.
 41. Derrida, B. and Pomeau, Y. (1986) Random networks of automata: a simple annealed approximation. *Europhys. Lett.*, **1**, 45–49.
 42. Kürten, K. (1988) Critical phenomena in model neural networks. *Phys. Lett. A*, **129** (3), 157–160.
 43. Bastolla, U. and Parisi, G. (1996) Closing probabilities in the kauffman model: an annealed computation. *Physica D*, **98**, 1–25.
 44. Sethna, J.P., Dahmen, K.A., and Myers, C.R. (2001) Crackling Noise. *Nature*, **410**, 242–250.
 45. Friedman, N., Ito, S., Brinkman, B.A.W., Shimono, M., DeVille, R.E.L., Dahmen, K.A., Beggs, J.M., and Butler, T.C. (2012) Universal critical dynamics in high resolution neuronal avalanche data. *Phys. Rev. Lett.*, **108**, 208102.
 46. Plenz, D. (2012) Neuronal avalanches and coherence potentials. *Eur. Phys. J. Special Topics*, **205**, pp. 259–309.

11

Single Neuron Response Fluctuations: A Self-Organized Criticality Point of View

Asaf Gal and Shimon Marom

Criticality and self-organized criticality (SOC) are concepts often used to explain and think about the dynamics of large-scale neural networks. This is befitting, if one adopts, as common, the description of neural networks as large ensembles of interacting elements. The criticality framework provides an attractive (but not unique) explanation of the abundance of scale-free statistics and fluctuations in the activity of neural networks both *in vitro* and *in vivo*, as measured by various means [1–3]. While similar phenomena, including scale-free fluctuations and power-law-distributed event sizes, are observed also at the level of single neurons [4–8], the application of criticality concepts to single neuron dynamics seems less natural. Indeed, in modern theoretical neuroscience, single neurons are mostly taken as the fundamental, simple “atomic” elements of neural systems. These elements are usually attributed with stereotypical dynamics, with the fine details being stripped away in favor of “computational simplicity,” thus off-loading the emergent complexity to the population level. On the other hand, “detailed” modeling approaches fit neuronal dynamics using extremely elaborated, high-dimensional, multiparameter, spatiotemporal mathematical models. In this chapter, we demonstrate that using concepts borrowed from the physics of critical phenomena offers a different, intermediate, approach (introduced in [9]) abstracting the details on the one hand, while doing justice to the dynamic complexity on the other. Treating a neuron as a heterogeneous ensemble of numerous interacting ion-channel proteins and using statistical mechanics terms, we interpret neuronal response fluctuations and excitability dynamics as reflections of self-organization of the ensemble that resides near a critical point.

11.1

Neuronal Excitability

Cellular excitability is a fundamental physiological process, which plays an important role in the function of many biological systems. An excitable cell produces an all-or-none event, termed action potential (AP), in response to a strong enough (but small compared to the response) perturbation or input. Excitability, as a measurable

biophysical property of a membrane, is thus defined as its susceptibility to such a perturbation, or, alternatively, as the minimal input required to generate an AP. In their seminal work, Hodgkin and Huxley [10] have explained the dynamics of the AP and its dependence on various macroscopic conductances of the membrane. In later years, these conductances were shown to result from the collective action of numerous quantized conductance elements, namely proteins functioning as transmembrane ion channels.

Excitability in the Hodgkin-Huxley (HH) model is determined by a set of maximal conductance parameters G_i , with i designating each of the relevant conductances. The effect of these parameters on the excitability of a neuron can be demonstrated by changing the maximal sodium conductance, G_{Na} (Figure 11.1). As the sodium conductance decreases, so does the excitability, as measured by the response threshold, or by the corresponding response latency to a supra-threshold input. For a critically low G_{Na} , the neuron becomes unexcitable and stops responding altogether. The existence of a sharp transition between “excitable” and

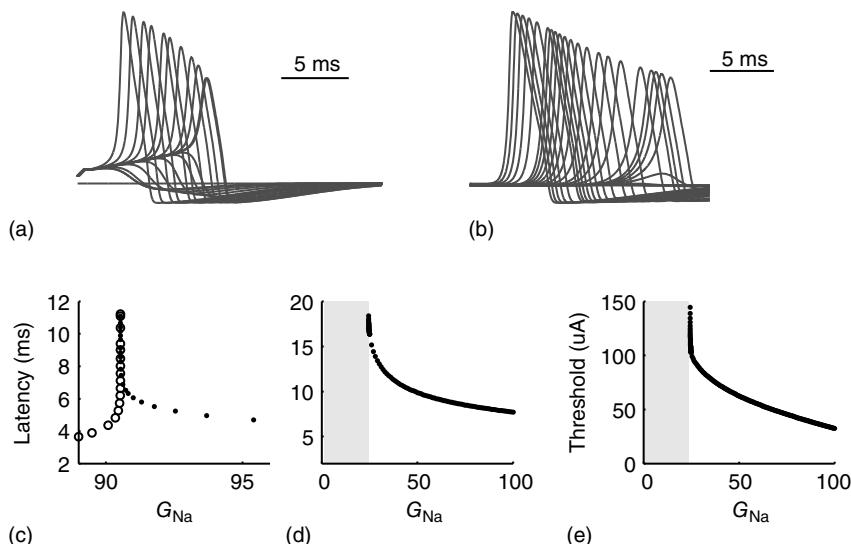


Figure 11.1 Excitability in a Hodgkin-Huxley (HH) neuron (adapted from [9]). (a) The effect of modulating G_{Na} on the voltage response of an isopotential HH neuron to a short (500 μ s) current pulse. As G_{Na} decreases, the AP is delayed. Below a certain critical conductance, no AP is produced. (b) The effect of modulating G_{Na} on the voltage response of an HH axon with 50 compartments expressed at the fiftieth compartment, to a short (500 μ s) current pulse given at the first compartment. The delayed latency effect is enhanced (due to reduced conduction velocity), and below the critical level

the response is flattened (the subthreshold response is not transmitted from the first to the fiftieth compartment). (c) AP latency in (a) as a function of G_{Na} , demonstrating the existence of a sharp threshold. Above-threshold APs are marked with filled circles, and non-AP events are marked with empty circles. (d) AP latency in (b) as a function of G_{Na} . Shaded area is a regime where no event was propagated. (e) The stimulation threshold (minimal current to elicit an AP) is plotted as a function of G_{Na} for the fiftieth compartment neuron.

“non-excitatory” membrane states is even more pronounced when one looks at the conduction of the AP along a fiber, for example, an axon. Of course, excitability is determined by more than one conductance, and its phase diagram is consequently richer, but the general property holds: the excitable and non-excitatory states (or phases) are separated by a sharp boundary in the parameter space.

In the short term (about 10 ms) which is accounted for by the HH model, maximal conductances can safely assumed to be constant, justifying the parameterization of G_i . However, when long-term effects are considered, the maximal conductance can (and indeed should) be treated as a macroscopic system variable governed by stochastic, activity-dependent transitions of ion channels into and out of long-lasting *unavailable* states (reviewed in [11]). In an unavailable state, ion channels are “out of the game” as far as the short-term dynamics of the AP generation is concerned, and the corresponding values of G_i are effectively reduced. Viewed as such, excitability has the flavor of an order parameter, reflecting population averages of availability of ion channels to participate in the generation of APs. In what follows, we describe a set of observations that characterize the dynamics of excitability over extended durations, and interpret these observations in the framework of SOC.

11.2

Experimental Observations on Excitability Dynamics

In a series of experiments, detailed in a previous publication [8], the intrinsic dynamics of excitability over time scales longer than that of an AP was observed by monitoring the responses of single neurons to series of pulse stimulations. In brief, cortical neurons from newborn rats were cultured on multielectrode arrays, allowing extracellular recording and stimulation for long, practically unlimited, durations. The neurons were isolated from their network by a pharmacological synaptic blockage to allow the study of intrinsic excitability dynamics, with minimal interference by synaptically coupled cells. Neurons were stimulated with sequences of short, identical electrical pulses. For each pulse, the binary response (AP produced or not) was registered, marking the neuron as being either in the *excitable* or the *unexcitable* state. For each AP recorded, the *latency* from stimulation to the AP was also registered, quantifying the neuron’s excitability. The amplitude of the stimulating pulses was constant throughout the experiment and well above threshold, such that neurons responded in a 1 : 1 manner (i.e., every stimulation pulse produces an AP) under low rate (1 Hz) stimulation conditions. Various control measures were used to verify experimental stability, see [8] for details.

When the stimulation rate r is increased beyond 1 Hz, and the neuron is allowed to reach a steady-state response, one of two distinct response regimes can be identified: a *stable* regime, in which each stimulation elicits an AP, and an *intermittent* regime, in which the spiking is irregular. The response of a neuron following a change of stimulation rate is demonstrated in Figure 11.2, as well

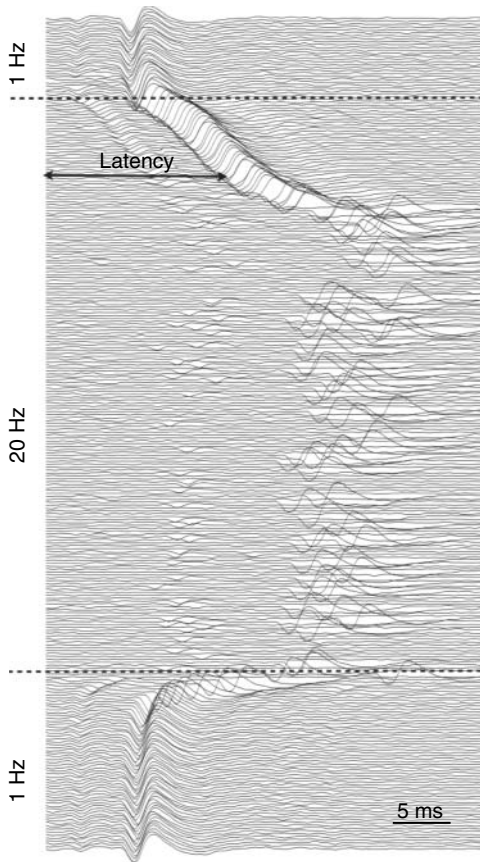


Figure 11.2 Experimental study of excitability dynamics. An isolated neuron is stimulated with a sequence of short ($400\ \mu\text{s}$) electrical pulses. Shown are extracellular voltage response traces, each 20 ms long. The traces are ordered from top to bottom, and temporally aligned to the stimulation time. For visual clarity, only every other trace is plotted. In the example shown, the neuron is stimulated with a 1-Hz sequence for 1 min (top section of the figure, 60 traces). For this stimulation protocol, the response latency is stable (arrow shows the time between stimulation and spike)

and the response is reliable, implying constant excitability. The stimulation rate is then abruptly increased to 20 Hz for 2 min (middle section). After a transient period, in which latency is gradually increased (excitability decreases), the neuron reaches an intermittent steady state, in which it is barely excitable, spiking failures occur, and the response is irregular. When the stimulation rate is decreased back to 1 Hz (bottom section), the latency (excitability) recovers, and the stable steady-state response is restored.

as in [8]: When the stimulation rate is abruptly increased, the latency gradually becomes longer and stabilizes at a new, constant value (as is evident in the first two blocks, where the rate is increased to 5 and 7 Hz). For a sufficiently high stimulation rate (above a critical value r_0), the 1:1 response mode breaks down and becomes intermittent (the 20-Hz block in the example shown). All transitions

are fully reversible. The steady-state properties of the two response regimes may be observed by slowly changing the stimulation rate, so its response properties can be safely assumed to reflect an excitability steady state. As seen in the result of the “adiabatic” experiment (Figure 11.3a), the stable regime is characterized by a 1 : 1 response (no failures), stable latency (low jitter), and monotonic dependence of latency on stimulation rate. In contrast, the intermittent regime is characterized by a failure rate that increases with stimulation rate, unstable latency (high jitter),

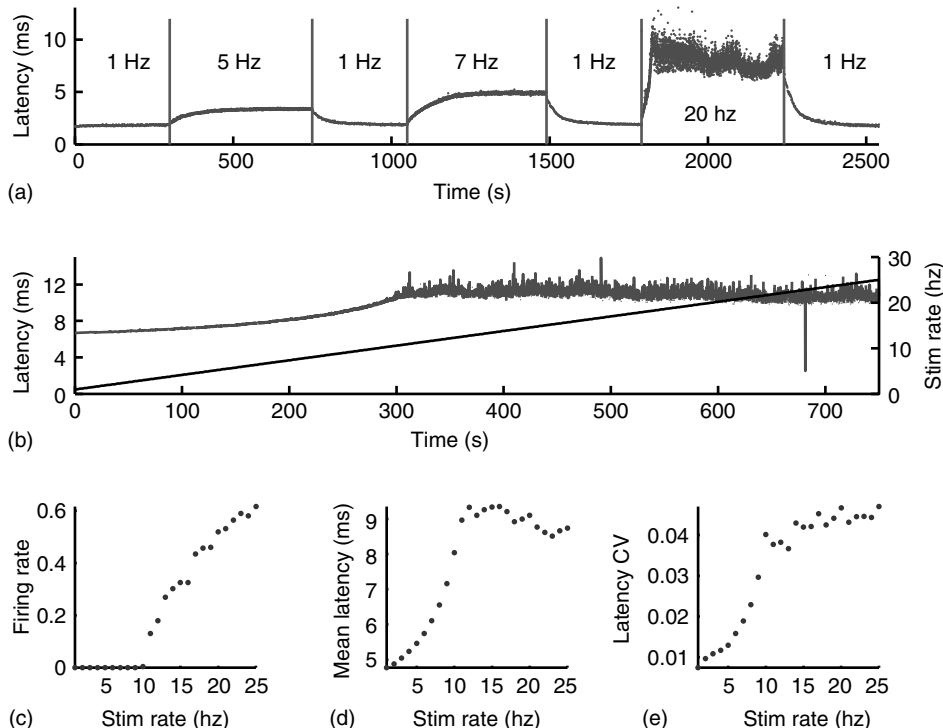


Figure 11.3 Steady-state characterization of the response (adapted from [9]). (a) The AP latency plotted as a function of time in an experiment where the stimulation rate is changed in an adiabatic manner, meaning slow enough so that the response can be assumed to reflect steady-state properties. For low stimulation rates, the excitability (quantified as the latency from stimulation to AP) stabilizes at a constant above-threshold value (threshold on excitability resources, as exemplified with G_{Na} in Figure 11.1). When the stimulation rate is increased, the steady-state excitability is accordingly decreased (latency increased). For high stimulation

rates (>10 Hz), excitability reaches the threshold, and the neuron responds intermittently, with strong fluctuations. (b) Response latencies (solid line) in response to a stimulation sequence with slowly increasing stimulation rate (dashed line). (c) Fail (no spike) probability as a function of stimulation rate. A critical stimulation rate is clearly evident. (d) Mean response latency as a function of stimulation rate. The increase of the latency accelerates as the stimulation rate approaches the critical point. (e) The jitter (coefficient of variation) of the latency as a function of the stimulation rate.

and independence of the mean latency on the stimulation rate. The existence of a critical (or threshold) stimulation rate is reflected in measures of the failure rate (Figure 11.3b), mean latency (Figure 11.3c), and latency coefficient of variation (Figure 11.3d). The exact value of r_0 varies considerably between neurons, but its existence is observed in practically all measured neurons (see details in [8]).

Within the intermittent regime, the fluctuations of excitability (as defined by the excitable/unexcitable state sequence) are characterized by scale-free long-memory statistics. Its power spectral density (PSD) exhibits a power law ($1/f^\beta$) in the low-frequency range. The characteristic exponent of this power law does not depend on the stimulation rate as long as the latter is kept above r_0 (Figure 11.4a). The typical exponent of the rate PSD is $\beta = 1.26 \pm 0.21$ (mean \pm SD, calculated over 16 neurons). Moreover, within the intermittent regime, the distributions of the lengths of consecutive response sequences (i.e., periods during which the neuron is fully excitable, responding to each stimulation pulse) and consecutive no-response sequences (periods when the neuron is not responding) are qualitatively different (Figure 11.4b, 11.4c). The consecutive response sequence length

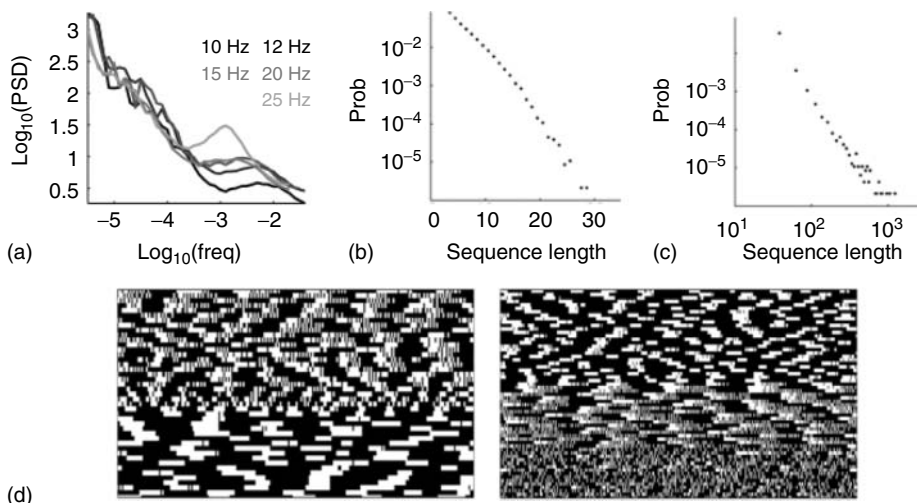


Figure 11.4 Scale-free fluctuations in the intermittent regime (adapted from [8]). (a) Periodograms of the failure rate fluctuations, at five different stimulation rates above r_0 . (b) Length distribution of spike-response sequences, on a semilogarithmic plot, demonstrating exponential behavior. Example from one neuron stimulated at 20 Hz for 24 h. (c) Length distribution of no-spike response sequences from the same neuron, on a double-logarithmic plot, demonstrating a power-law-like behavior. (d) Pattern

modes in binary response sequences. Extracts (approximately 10 min long) from the response pattern of two neurons to long 20-Hz stimulation. A white pixel represents an interval with a spike response, and black represents an interval with no-spike response. The response sequence is wrapped. Spontaneous transitions between distinct temporal pattern modes occur while the neuron is in the intermittent response regime, visible as different textures of the black/white patterns.

histogram is strictly exponential, having a characteristic duration; the consecutive no-response sequence length histogram is wide, to the point of scale-freeness (power law distribution). Likelihood ratio tests for power law distribution fit to the empirical histogram (containing more than 90,000 samples) yielded significantly higher likelihood compared with fits to exponential, log normal, stretched exponential and linear combination of two exponential distributions (normalized log likelihood ratios $R > 10$, $p < 0.001$, see [12]). This suggests that the fluctuations are dominated by widely distributed excursions into an unexcitable state¹⁾. Moreover, as shown in Figure 11.4d, during the intermittent regime, the response of the neuron is characterized by transitions between periods characterized by different typical quasi-stable temporal response patterns that dominate the response sequence. It is important to emphasize that the instability observed in the intermittent regime is activity dependent. Whenever the stimulation stops for a while, allowing the neuron to recover, its response properties return to its original form.

11.3 Self-Organized Criticality Interpretation

The above experimental observations are difficult to interpret within the conventional framework of neuronal dynamics, which relies on extensions of the original formalism of the Hodgkin and Huxley approach. Given that the observed dynamics is intrinsic [8], this formalism dictates integration of many processes into a mathematical model, each with its own unique time scale, to allow reconstructing and fitting the complex scale-free dynamics. When the temporal range of the observed phenomena extends over many orders of magnitudes, such an approach yields large intractable models, the conceptual contribution of which is limited. As we have already discussed previously, we suggest here to take a more abstract direction, viewing the neuron in statistical mechanics terms, as a large ensemble of interacting elements. Under this conjecture, the transition between excitable and unexcitable states of the cell is naturally interpreted as a second-order phase transition. This interpretation is further supported by the described experimental results, which exhibit critical-like fluctuations in the barely excitable regime (around the threshold of excitability). Further motivation for this interpretation can be drawn from mathematical analysis of macroscopic, low dimensional models of excitability, which also exhibit critical behavior near the spiking bifurcation point [15,16].

1) Such distribution are analogous to the distributions of residence times in the open and closed states, observed in single-channel recordings [13]. Such an asymmetry can be accounted for by a Markovian model, where two types of states exist: responsive (excitable) and nonresponsive (unexcitable). A compact

representation for the responsive subspace will lead to an exponential distribution of residence times in this subspace, while an extended, possibly infinite, representation of the nonresponsive subspace will lead to heavy-tailed distribution of residence times [14].

However, in this picture the control parameter (“temperature”)²⁾ that moves the membrane between excitable and unexcitable phases is elusive. One immediate candidate is the experimental parameter – the stimulation rate. However, in such a scenario one would expect to observe the critical characteristics within a limited range of stimulation rates; higher values of stimulation rate should shut down excitability altogether. Our experimental results show that this is not the case. For example, the experiments show that the response latency (Figure 11.3c) as well as the characteristic exponent of the PSD (Figure 11.4a) are insensitive to the stimulation rate. The reason for this apparent inconsistency is that the stimulation rate does not directly impact the dynamics of the underlying ionic channels. Rather, the relevant control parameter is in fact the *activity* rate, which itself is a dynamic variable of the system. This is consistent with the known biophysics of ion channels, in which transition rates are dependent on the output of the system – the membrane voltage or neuronal activity. This picture implies that a form of *self-organization* is at work here.

The concept of SOC [17] designates a cluster of physical phenomena characterizing systems that reside near a phase transition. What makes SOC unique is the fact that residing near a phase transition is not the result of a fine-tuned control parameter; rather, in SOC the system posits itself near a phase transition as a natural consequence of the underlying internal dynamic process that drives toward the critical value. Such systems exhibit many complex statistical and dynamical features that characterize their behavior near a phase transition, without these features being sensitive to system parameters. The most well-known canonical example for such a system is the sandpile model, in which the relevant parameter is the number of its grains (or equivalently, the steepness of its slope). This parameter is characterized by a critical value that separates the stable and unstable phases. However, in the context of SOC sandpile models, this “control” parameter is not externally set but is a dynamical variable of the system. When the system is stable, grains are added onto the pile, and while it is unstable, grains are lost via its margins. The most prominent property of a system in a state of SOC is the *avalanche*: an episode of instability that propagates through the system, with size and lifetime distributions that follow a power law form.

The sandpile model of Bak, Tang, and Wiesenfeld (BTW) is a cellular automaton with an integer variable z_i (“energy”), defined on a finite d -dimensional lattice. At each time step, an energy grain is added to a randomly chosen site. When the energy of a certain site reaches a threshold z_c , the site relaxes as $z_i \rightarrow z_i - z_c$, and the energy is distributed between the nearest neighbors of the active site. This relaxation can induce threshold crossings at the neighboring sites, potentially propagating through the lattice until all sites relax. Grains that “fall off” the boundary are dissipated out of the system. The sequence of events from the initial excitation until full relaxation constitutes an avalanche. The model requires that

2) Temperature is the standard control parameter in statistical mechanical models, such as the Ising model, and is often used as a generic term for control parameters in the context of phase transitions.

grain addition will occur only when the system is fully relaxed. Under these conditions, the size and lifetime of the avalanches will follow a power law distribution, and order parameters such as the total energy in the pile will fluctuate with a $1/f^\beta$ spectral density.

The BTW model, as well as its later variants, is nonlocal in the sense that events in a certain point in the lattice (grain addition) depend on the state of the entire lattice (full relaxation). Dickman, Vespignani and Zapperi [18, 19] have shown that this model can be made to conform to the “conventional” phase-transition model by introducing periodic boundary conditions (thereby preventing dissipation) and stopping the influx of grains, while retaining the local dynamic rule of the original model. In such a model, the number of grains in the pile is conserved and serves as the relevant control parameter. This model is known as the *activated random walk model*: walkers (or grains) are moved to adjacent cells if they are pushed by another walker (in the version with $z_c = 2$), otherwise they are paralyzed. This is an example of a model with an absorbing state (AS): if all walkers are inactive (i.e., none is above threshold), the dynamics of the model freezes. When the number of walkers on the lattice is low, the model is guaranteed to reach an AS within a finite time. If, on the other hand, the number of walkers is high, the probability of reaching the AS becomes so low that the expected time to reach it becomes infinite. The transition between the two phases is a second-order phase transition. In the sandpile model, the number of walkers on the lattice becomes a dynamic variable of the system, with a carefully designed dynamics: as long as the system is super-critical, with constantly moving walkers, grains will keep on falling off the edge of the pile, until an absorbing state will be reached. Once the pile is quiescent, new grains will be added. In such a way, the number of grains is guaranteed to converge to the critical value. Dickman *et al.* [18, 19] have shown that many of the popular SOC models can be viewed as an AS model with a feedback from the system state onto the control parameter, which effectively pushes it to the critical value.

This picture intuitively maps excitability dynamics, where neural activity serves as a temperature-like parameter, and the single AP serves as a drive (quantal influx of energy, or small increase in temperature). In the absence of activity, the neuron reaches an excitable phase, while increased activity reduces excitability, and (when high enough) pushes the membrane into the unexcitable phase. While the system is in the unexcitable phase, neural activity is decreased, leading to restoration of excitability. As a result, the neuron resides in a state where it is “barely excitable,” exhibiting characteristics of SOC. Of course, not all classes of neurons follow this simple process, but the general idea holds: activity pushes excitability toward a threshold state, while the longer time scale regulatory feedback reigns in the system.

11.4

Adaptive Rates and Contact Processes

This interpretation of excitability in SOC terms may also be theoretically supported, within certain limits, by considering the underlying biophysical machinery. The

state of the membrane is a function of the individual states of a large population of interacting ion-channel proteins. A single ion channel can undergo transformations between uniquely defined conformations, which are conventionally modeled as states in a Markov chain. The faster transition dynamics between states is the foundation of the HH model, which describes the excitation event itself – the AP. But, as explained previously, for the purpose of modeling the dynamics of excitability, rather than the generative dynamics of the AP itself, it is useful to group these conformations into two sets [11, 20–22]: the *available*, in which channels can participate in generation of APs, and the *unavailable*, in which channels are deeply inactivated and are “out of the game” of AP generation. The microscopic details of the single-channel dynamics in this state space, and definitely the collective dynamics of the interacting ensemble, are complex [13, 20] and no satisfactory comprehensive model exists to date. There are several approaches for modeling channel dynamics, the most widespread is the Markov chain approach, in which a channel moves in a space of conformations, with topology and parameters fitted to experimental observations. Such a model can, in general, be very large, containing many states and many parameters [14, 21]. Another approach advocates a more compact representation, mostly containing functionally defined states, but with dynamics that are non-Markovian, meaning that transition probabilities can be history-dependent [13, 23, 24]. These two approaches are focused on the single-channel dynamics. However, it has been suggested recently [11, 22] that the transition dynamics between the available and unavailable states may be expressed in terms of an “adaptive rate” logistic-function-like model of the general form

$$\dot{x} = -f(\gamma)x + g(x)(1-x) \quad (11.1)$$

where f is a function of the neural activity measure γ , and $g(x)$ is a monotonically increasing function of the system state x .

Following the lead of the above adaptive rate approach, one can consider, for instance, a model in which x represents the availability of a restoring (e.g., potassium) conductance.³⁾ The state of the single channel is represented by a binary variable σ_i , where $\sigma_i = 0$ is the unavailable state and $\sigma_i = 1$ is the available state. Unavailable channels are recruited with a rate of x , while available channels are lost with a rate of $2 - \gamma$. This picture gives rise to a dynamical mean-field-like equation

$$\dot{x} = (\gamma - 1)x - x^2 \quad (11.2)$$

The model is a variant of a globally coupled contact process, which is a well-studied system exhibiting an AS phase transition [26]. Here, $x = 0$ is the AS, representing the excitable state of the system. In the artificial case of taking γ as an externally modified control parameter, for $\gamma < 1$ (low activity) the system will always settle into this state, and the neuron will sustain this level of activity. For $\gamma > 1$, the

3) For example, the small conductance calcium dependent potassium channel [25] is an excitability inhibitor, having a calcium-mediated positive interaction that gives rise to a form similar to Eq. 11.1.

system will settle on $x^* = \gamma - 1$, which is an unexcitable state, and the neuron will not be able to sustain activity. Feedback is introduced into the system by specifying the state dependency of γ : An AP is fired if and only if the system is excitable (i.e., in the absence of restoring conductance, $x = 0$), giving rise to a small increase in γ . When $x > 0$, the system is unexcitable, APs are not fired, and γ is slowly decreased. This is an exact implementation of the scheme proposed in Dickman *et al.* [18, 19]: an absorbing state system, where the control parameter (activity, γ) is modified by a feedback from the order parameter (excitability, a function of x). As always with SOC, the distinction between order and control parameters becomes clear only when the conservative, open-loop version of the model is considered.

Note that the natural dependency of the driving event (the AP) on the system state in our neural context resolves a subtlety involved in SOC dynamics: the system must be driven slowly enough to allow the AS to be reached before a new quantum of energy is invested. In most models, this condition is met by assuming the rate to be infinitesimally small.

Numerical simulation of the model (Eq. 11.2), together with the closed-loop dynamics of γ , qualitatively reproduces the power law statistics observed in the experiment, including the existence of a critical stimulation rate r_0 (Figure 11.5a), the $1/f^\beta$ behavior for $r > r_0$, with exponent independent of r (Figure 11.5b), and the distributions of sequence durations (Figures 11.5c and 11.5D). The critical stimulation rate r_0 is adjustable by the kinetics of γ , its increase and decrease during times of activity, and inactivity of the neuron. While this simplistic model does capture the key observed properties, others are not accounted for. The latency transient dynamics when switching between stimulation rates (Figure 11.2b) and the multitude of stable latency values for $r < r_0$ (Figure 11.3) suggest that a model with a single excitable state is not sufficient. Sandpile models (and more generally activated random walk models, see Dickman *et al.* [18, 19]) do exhibit such multiplicity, arising out of a continuum of stable subcritical values of pile height (or slope). In this analogy, adding grains to the pile increases its height up to the critical point, where SOC is observed. Another experimentally observed property that is not accounted for by the model is the existence of *pattern modes* in the intermittent response regime as described in Figure 11.4d, implying temporal correlations between events of excitability and unexcitability. Also, the fact that the $1/f^\beta$ relation of the PSD extends to a time scale much longer than the maximal avalanche duration suggests that these correlations have a significant contribution for the observed temporal dynamics. While such correlations and temporal patterns can be generated in SOC models [27] and while they characterize the dynamics in other (non-self-organizing) critical systems, they are still largely unexplored.

11.5 Concluding Remarks

In this chapter, we have focused on SOC as a possible framework to account for temporal complexity in neuronal response variations. The motivation for this

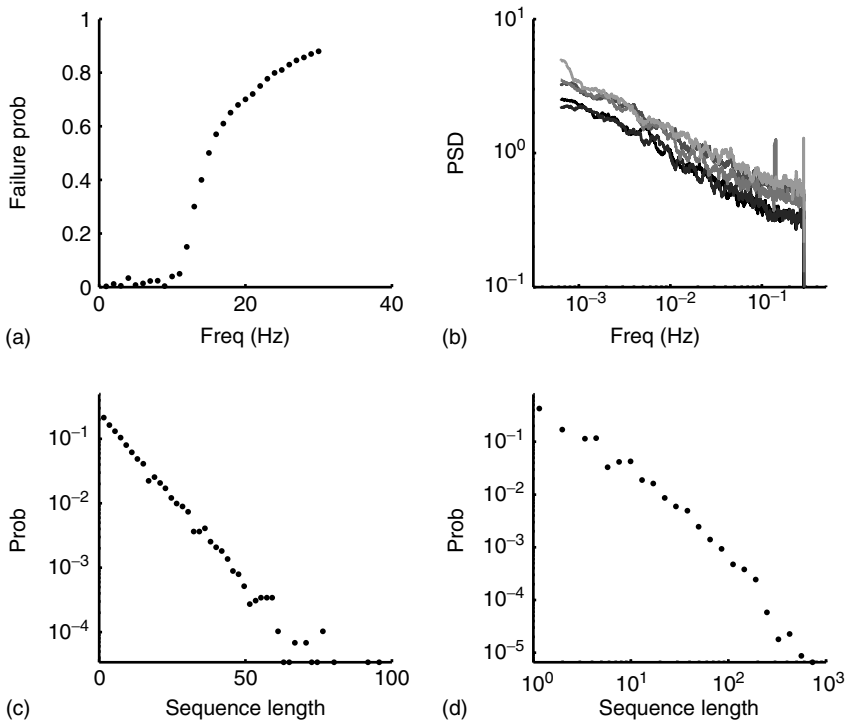


Figure 11.5 Model simulation results (adapted from [9]). All simulations were performed using an ensemble of 10 000 channels. The loop on neuronal activity γ was closed as follows: for each AP fired, a single channel was inactivated, and γ was increased by a value of $d\gamma = 0.005$. Between APs, γ decayed exponentially with a rate of 0.001/s. (a) Dependence of the spike failure probability on the stimulation rate, analogous to Figure 11.3b. Each point in the graph was estimated from 1-h simulated time. (b) Power spectral densities of the response fluctuations at different frequencies

above r_0 . Each PSD was computed from a period of 12 h of simulated time. (c) Length distribution of spike-response sequences, on a semilogarithmic plot, demonstrating an exponential behavior. Analogous to Figure 11.4b. The distribution was estimated from 24-h simulated time, with stimulation at a constant, above r_0 , stimulation rate. (d) Length distribution of no-spike response sequences from the same neuron, on a double-logarithmic plot, demonstrating a power-law-like behavior. Analogous to Figure 11.4c.

approach stems from the macroscopic behavior of the neuron in the experiments of Gal *et al.* [8], which can be mapped to the macroscopic behavior of many models exhibiting SOC. In the neuron, excitability is slowly reduced from the initial level as a result of activity; this reduction continues until excitability drops below a threshold level, leading to a pause in activity. Excitability is then restored following an avalanche-like period of unexcitability, and so forth. For comparison, in the canonical SOC model of the sandpile, grains are added continuously to the top of the pile. The pile's height and slope slowly increase until they reach a critical level, where the pile loses stability. Stability is then restored by an avalanche, which

decreases the slope back to a subcritical level, from where the process starts again. This analogy is supported by the critical-like behavior of excitability fluctuations around its threshold.

In addition to the macroscopic behavior, we have offered a microscopic “toy model,” based on known ion-channel dynamics, that might reproduce this behavior. This model is built upon an approach called *adaptive rates* [11, 22], accounting for the observed dynamics of ion channels by introducing an ensemble-level interaction term. We have shown how variants of this general scheme might result in formal SOC. It is important to stress, however, that the instantiation used here is not unique, and is not intended to represent any specific ion channel. It is merely a demonstration that the emergence of the self-organized critical behavior is not alien to theoretical formulations of excitability. This said, candidate ionic channels with similar properties to those used in the model do exist. For example, the calcium-dependent potassium SK channel [25] is an excitability inhibitor, which has a calcium-mediated positive interaction, not unlike the one used in the model suggested here. Also, note that the formulation chosen here does not give rise to an exact reproduction of the observed phenomenology. Not only do the exponents of the critical behavior not match (in the language of critical phenomena this means that the experiment and the model are not in the same universality class), but the model family used here produces uncorrelated avalanche sizes, while in the experiments the response breaks are clearly correlated and form complex patterns and distinct quasi-stable patterns. However, this is not a general property of critical behavior, and other models (e.g., [27]) can produce correlated, complex temporal patterns.

As attractive as the SOC interpretation might be, it is acknowledged that this framework is highly controversial. Many physicists question the relevance of this approach to the natural world, and in spite of the many candidate phenomena that have been suggested as reflecting SOC (e.g., forest fires, earthquakes, and, of course, pile phenomena such as sand and snow avalanches), no sound models have been suggested to account for these phenomena to date. One of the obstacles is the subtlety inherent to the involved feedback loop, because the driving of the model must depend on its state. In the case of excitability, this loop seems natural: the occurrence of an AP is directly dependent on the macroscopic state of the membrane – its excitability.

The mapping between SOC and excitability suggested here is only a first step, which can be regarded as an instigation of a research program. This program should include both experimental and theoretical efforts, to support and validate the SOC interpretation in the context of neuronal excitability. Specific issues should be addressed: First, is the transition of the membrane between the excitable and the unexcitable states a genuine second-order phase transition? Ideally, this question should be addressed using carefully designed experiments that enable investigation of the approach to the transition point, from both sides. Care must be taken to define and manipulate the excitability of the neuron (the relevant control parameter). This can be achieved, for example, by the well-controlled application of channel blockers (e.g., tetrodotoxin, charybdotoxin), which have a

direct impact on excitability (Figure 11.1). Second, the existence of this phase transition should also be demonstrated by manipulating the neuronal level of activity. A possibly useful technique here is the so-called response clamp method, recently introduced by Wallach and colleagues [28,29], which clamps neuronal activity to a desired level by controlling stimulation parameters. Third, careful characterization of the critical phenomena around this phase transition should be made, in order to point to plausible theoretical models. It should be emphasized that these suggested experiments are in a regime where the feedback loop of the SOC is broken, by enforcing fixed excitability/activity levels. On the theoretical side, the space of possible models should be explored, portraying the scope of phenomena accountable by SOC, and hopefully should converge on a biophysical plausible model that reproduces as much of the observed data as possible. Finally, the ultimate challenge for SOC is for it to account for aspects of neuronal dynamics beyond critical statistics (with the usual power law characteristics), with emphasis on functional aspects.

SOC constitutes one hardly explored framework for understanding response fluctuations in single neurons. It can be considered as a niche inside the larger class of stochastic modeling. Such models can lead to temporal complexity in compact formalisms with several possible stochastic mechanisms (e.g., [6, 21, 23]). A further theoretical investigation of these modeling approaches might provide useful representations of temporal complexity in neurons, other than SOC. Such an investigation was recently carried out by Soudry and Meir, [30, 31]. They conducted a study that draws the boundaries for the range of phenomena that may be generated by conductance-based stochastic models (i.e., with channel noise) and discusses the extent to which such models can explain the data presented here. Deterministic chaotic models are also an attractive paradigm that is able to generate temporal complexity, and was explored in several past studies (for review see [32, 33]).

Self-organization is an important concept in the understanding of biological systems, including the study of excitable systems. Many studies have demonstrated how excitability is “self-organized” into preferable working points following perturbations or change in conditions [34–39]. These and related phenomena are conventionally classified under homeostasis, and are shown to depend on mechanisms such as calcium dynamics or ion channel inactivation. While a connection between SOC and activity homeostasis was hypothesized in the context of a neural network [40], it still awaits extensive explorations, both theoretically and experimentally.

In summary, we provided several arguments, experimental and theoretical, in support of a plausible connection between the framework of SOC and the dynamics underlying response fluctuations in single neurons. This interpretation succeeds in explaining critical-like fluctuations of neuronal responsiveness over extended time scales, which are not accounted for by other more common approaches. Acknowledging the limitations of the simplified approach presented here, and respecting the gap between theoretical models and biological reality, we submit that SOC seems to capture the core phenomenology of fluctuating neuronal

excitability, and has a potential to enhance our understanding of physiological aspects of excitability dynamics.

References

1. Beggs, J.M. and Plenz, D. (2003) Neuronal avalanches in neocortical circuits. *J. Neurosci.*, **23** (35), 11 167.
2. Chialvo, D. (2010) Emergent complex neural dynamics. *Nat. Phys.*, **6** (10), 744–750.
3. Beggs, J.M. and Timme, N. (2012) Being critical of criticality in the brain. *Front. Physiol.*, **3**, 163, doi: 10.3389/fphys.2012.00163. <http://www.ncbi.nlm.nih.gov/article/2369250?tool=pmcentrez&rendertype=abstract> (accessed 10 December 2013).
4. Lowen, S.B. and Teich, M.C. (1996) The periodogram and Allan variance reveal fractal exponents greater than unity in auditory-nerve spike trains. *J. Acoust. Soc. Am.*, **99** (6), 3585–3591.
5. Teich, M.C., Heneghan, C., Lowen, S.B., Ozaki, T., and Kaplan, E. (1997) Fractal character of the neural spike train in the visual system of the cat. *J. Opt. Soc. Am. A*, **14** (3), 529–546.
6. Soen, Y. and Braun, E. (2000) Scale-invariant fluctuations at different levels of organization in developing heart cell networks. *Phys. Rev. E*, **61** (3), R2216-R229.
7. Lowen, S.B., Ozaki, T., Kaplan, E., Saleh, B.E., and Teich, M.C. (2001) Fractal features of dark, maintained, and driven neural discharges in the cat visual system. *Methods*, **24** (4), 377–394, doi: 10.1006/meth.2001.1207.
8. Gal, A., Eytan, D., Wallach, A., Sandler, M., Schiller, J., and Marom, S. (2010) Dynamics of excitability over extended timescales in cultured cortical neurons. *J. Neurosci.*, **30** (48), 16-332-16-342, doi: 10.1523/JNEUROSCI.4859-10.2010. <http://www.ncbi.nlm.nih.gov/pubmed/21123579>; <http://www.jneurosci.org/cgi/content/abstract/30/48/16332> (accessed 10 December 2013).
9. Gal, A. and Marom, S. (2013). Self-organized criticality in single-neuron excitability. *Physical Review E*, **88** (6), 062717. doi:10.1103/PhysRevE.88.062717.
10. Hodgkin, A. and Huxley, A. (1952) A quantitative description of membrane current and its application to conduction and excitation in nerve. *J. Physiol.*, **117**, 500–544.
11. Marom, S. (2010) Neural timescales or lack thereof. *Prog. Neurobiol.*, **90** (1), 16–28, doi: 10.1016/j.pneurobio.2009.10.003. <http://www.ncbi.nlm.nih.gov/pubmed/19836433> (accessed 10 December 2013).
12. Clauset, A., Shalizi, C.R., and Newman, M.E.J. (2009) Power-law distributions in empirical data. *SIAM Review*.
13. Liebovitch, L.S., Fischbarg, J., Koniarek, J.P., Todorova, I., and Wang, M. (1987) Fractal model of ion-channel kinetics. *Biochim. Biophys. Acta*, **896** (2), 173–180, doi: 10.1016/0005-2736(87)90177-5. [http://dx.doi.org/10.1016/0005-2736\(87\)90177-5](http://dx.doi.org/10.1016/0005-2736(87)90177-5).
14. Millhauser, G.L., Salpeter, E.E., and Oswald, R.E. (1988) Diffusion models of ion-channel gating and the origin of power-law distributions from single-channel recording. *Proc. Natl. Acad. Sci. U.S.A.*, **85** (5), 1503–1507, <http://www.ncbi.nlm.nih.gov/article/2795800?tool=pmcentrez&rendertype=abstract> (accessed 10 December 2013).
15. Roa, M., Copelli, M., Kinouchi, O., and Caticha, N. (2007) Scaling law for the transient behavior of type-II neuron models. *Physical Review E*, **75** (2), 021911, doi:10.1103/PhysRevE.75.021911.
16. Steyn-Ross, D., Steyn-Ross, M., Wilson, M., and Sleigh, J. (2006) White-noise susceptibility and critical slowing in neurons near spiking threshold. *Physical Review E*, **74** (5), 051920, doi:10.1103/PhysRevE.74.051920.

17. Bak, P., Tang, C., and Wiesenfeld, K. (1987) Self-organized criticality: an explanation of 1/f noise. *Phys. Rev. Lett.*, **59** (4), 381–384.
18. Dickman, R., Vespignani, A., and Zapperi, S. (1998) Self-organized criticality as an absorbing-state phase transition. *Phys. Rev. E*, **57** (5), 5095–5105, doi: 10.1103/PhysRevE.57.5095. <http://pre.aps.org/abstract/PRE/v57/i5/p5095> (accessed 10 December 2013).
19. Dickman, R., Muñoz, M., Vespignani, A., and Zapperi, S. (2000) Paths to self-organized criticality. *Braz. J. Phys.*, **30** (1), 27–41, <http://www.scielo.br/scielo.php?pid=S0103-97332000000100004&%script=sci%arttext> (accessed 10 December 2013).
20. Toib, A., Lyakhov, V., and Marom, S. (1998) Interaction between duration of activity and time course of recovery from slow inactivation in mammalian brain Na⁺ channels. *J. Neurosci.*, **18** (5), 1893–1903.
21. Gilboa, G., Chen, R., and Brenner, N. (2005) History-dependent multiple-time-scale dynamics in a single-neuron model. *J. Neurosci.*, **25** (28), 6479–6489, doi: 10.1523/JNEUROSCI.0763-05.2005.
22. Marom, S. (2009) Adaptive transition rates in excitable membranes. *Front. Comput. Neurosci.*, **3**, 2. doi: 10.3389/neuro.10.002.2009.
23. Lowen, S.B., Liebovitch, L.S., and White, J.A. (1999) Fractal ion-channel behavior generates fractal firing patterns in neuronal models. *Phys. Rev. E*, **59** (5 Pt B), 5970–5980.
24. Soudry, D. and Meir, R. (2010) History-dependent dynamics in a generic model of ion channels - an analytic study. *Front. Comput. Neurosci.*, **4**, 1–19, doi: 10.3389/fncom.2010.00003. <http://www.pubmedcentral.nih.gov/articlerender.fcgi?artid=291%6672&tool=pmcentrez&rendertype=abstract> (accessed 10 December 2013).
25. Adelman, J.P., Maylie, J., and Sah, P. (2012) Small-conductance Ca²⁺-activated K⁺ channels: form and function. *Annu. Rev. Physiol.*, **74**, 245–69, doi: 10.1146/annurev-physiol-020911-153336. <http://www.ncbi.nlm.nih.gov/pubmed/21942705> (accessed 10 December 2013).
26. Harris, T. (1974) Contact interactions on a lattice. *Ann. Probab.*, **2** (6), 969–988, <http://www.jstor.org/stable/10.2307/2959099> (accessed 10 December 2013).
27. Davidsen, J. and Paczuski, M. (2002) Noise from correlations between avalanches in self-organized criticality. *Phys. Rev. E*, **66** (5), 050 101, 1/F doi: 10.1103/PhysRevE.66.050101. <http://link.aps.org/doi/10.1103/PhysRevE.66.050101> (accessed 10 December 2013).
28. Wallach, A., Eytan, D., Gal, A., Zrenner, C., and Marom, S. (2011) Neuronal response clamp. *Front. Neuroeng.*, **4**, 3. doi: 10.3389/fneng.2011.00003. <http://www.pubmedcentral.nih.gov/articlerender.fcgi?artid=307%68750&tool=pmcentrez&rendertype=abstract> (accessed 10 December 2013).
29. Wallach, A. (2013) The response clamp: functional characterization of neural systems using closed-loop control. *Front. Neural Circ.*, **7**, 5, doi: 10.3389/fncir.2013.00005. <http://www.pubmedcentral.nih.gov/articlerender.fcgi?artid=355%68724&tool=pmcentrez&rendertype=abstract> (accessed 10 December 2013).
30. Soudry, D. and Meir, R. (2012) Conductance-based neuron models and the slow dynamics of excitability. *Front. Comput. Neurosci.*, **6**, 4, doi: 10.3389/fncom.2012.00004. <http://www.pubmedcentral.nih.gov/articlerender.fcgi?artid=328%60430&tool=pmcentrez&rendertype=abstract> (accessed 10 December 2013).
31. Soudry, D. and Meir, R. (2013) The neuron's response at extended timescales. arXiv preprint arXiv:1301.2631
32. Korn, H. and Faure, P. (2003) Is there chaos in the brain? II. Experimental evidence and related models. *C. R. Biol.*, **326** (9), 787–840, doi: 10.1016/j.crvi.2003.09.011. <http://linkinghub.elsevier.com/retrieve/pii/S1631069103002002%> (accessed 10 December 2013).
33. Faure, P. and Korn, H. (2001) Is there chaos in the brain? I. Concepts of nonlinear dynamics and methods of investigation. *C. R. Acad. Sci. Sér. III, Sci.*, **324** (9), 773–93,

- <http://www.ncbi.nlm.nih.gov/pubmed/11558325> (accessed 10 December 2013).
34. Prinz, Aa., Billimoria, C.P., and Marder, E. (2003) Alternative to hand-tuning conductance-based models: construction and analysis of databases of model neurons. *J. Neurophysiol.*, **90** (6), 3998–4015, doi: 10.1152/jn.00641.2003. <http://www.ncbi.nlm.nih.gov/pubmed/12944532> (accessed 10 December 2013).
35. Turrigiano, G., Abbott, L.F., and Marder, E. (1994) Activity-dependent changes in the intrinsic properties of cultured neurons. *Science*, **264** (5161), 974–977, <http://www.sciencemag.org/content/264/5161/974.short> (accessed 10 December 2013).
36. LeMasson, G., Marder, E., and Abbott, L.F. (1993) Activity-dependent regulation of conductances in model neurons. *Science*, **259** (5103), 1915–1917.
37. Liu, Z., Golowasch, J., Marder, E., and Abbott, L.F. (1998) A model neuron with activity-dependent conductances regulated by multiple calcium sensors. *J. Neurosci.*, **18** (7), 2309–2320.
38. Marom, S., Toib, A., and Braun, E. (1995) Rich dynamics in a simplified excitable system. *Adv. Exp. Med. Biol.*, **382**, 61–66.
39. Kispersky, T.J., Caplan, J.S., and Marder, E. (2012) Increase in sodium conductance decreases firing rate and gain in model neurons. *J. Neurosci.*, **32** (32), 10–995-10-1004. doi: 10.1523/JNEUROSCI.2045-12.2012. <http://www.ncbi.nlm.nih.gov/pmc/articles/PMC3429678/> (accessed 10 December 2013).
40. Hsu, D. and Beggs, J.M. (2006) Neuronal avalanches and criticality: a dynamical model for homeostasis. *Neurocomputing*, **69** (10-12), 1134–1136, doi: 10.1016/j.neucom.2005.12.060. <http://dx.doi.org/10.1016/j.neucom.2005.12.060>.

12

Activity Dependent Model for Neuronal Avalanches

Lucilla de Arcangelis and Hans J. Herrmann

Cortical networks exhibit diverse patterns of spontaneous neural activity, including oscillations, synchrony, and waves. The spontaneous activity, often, in addition exhibits slow alternations between high activity periods, or bursts, followed by essentially quiet periods. Bursts can last from a few to several hundred milliseconds and, if analyzed at a finer temporal scale, show a complex structure in terms of neuronal avalanches. As discussed in the previous chapters, neuronal avalanches exhibit dynamics similar to that of self-organized criticality (SOC), see [1–4]. Avalanches have been observed in organotypic cultures from coronal slices of rat cortex [5], where neuronal avalanches are stable for many hours [6]. The size and duration of neuronal avalanches follow power law distributions with very stable exponents, typical features of a system in a critical state, where large fluctuations are present and system responses do not have a characteristic size. The same critical dynamics has been measured also *in vivo* in rat cortical layers during early postnatal development [7], in the cortex of awake adult rhesus monkeys [8], as well as in dissociated neurons from rat hippocampus [9, 10] or leech ganglia [9]. The term “SOC” usually refers to a mechanism of slow energy accumulation and fast energy redistribution driving the system toward a critical state, where the distribution of avalanche sizes obeys a power law obtained without fine-tuning of a particular model parameter. The simplicity of the mechanism at the basis of SOC suggests that many physical and biological phenomena characterized by power laws in the size distribution might represent natural realizations of SOC. For instance, SOC has been proposed to model earthquakes [11, 12], the evolution of biological systems [13], solar flare occurrences [14], fluctuations in confined plasma [15], snow avalanches [16], and rain fall [17].

While sizes and durations of avalanches have been intensively studied in neuronal systems, the quiet periods between neuronal avalanches are much less understood. *In vitro* preparations exhibit such quiescent periods, often called *down-states* which can last up to several seconds, in contrast to periods of avalanche activity, which generally are shorter in duration. The emergence of these downstates be attributed to a variety of mechanisms: a decrease in the neurotransmitter released by each synapse, either due to the exhaustion of available synaptic vesicles or to the increase of a factor inhibiting the release [18] such as the nucleoside adenosine [19]; the

blockage of receptor channels by the presence, for instance, of external magnesium [20]; or else spike adaptation [21]. A downstate is therefore characterized by a *disfacilitation*, that is, reduction of synaptic activity, indicative of a large number of neurons with long-lasting return to their resting membrane potentials [22]. It was shown analytically and numerically, and discussed in the previous chapters, that self-organized critical behavior characterizes upstates, whereas subcritical behavior characterizes downstates [23].

Here we discuss a neural network model based on SOC ideas that takes into account synaptic plasticity. Synaptic plasticity is one of the most astonishing properties of the brain, occurring mostly during development and learning [24–26]. It is defined as the ability to modify the structural and functional properties of synapses in response to past activity in the network. Such modifications in the strength of synapses are thought to underlie memory and learning. Among the postulated mechanisms of synaptic plasticity, the activity-dependent Hebbian plasticity constitutes the most developed and influential model of how information is stored in neural circuits [27–29]. In order to get real insights into the relation between macroscopic network dynamics and the microscopic, that is, cellular, interactions inside a neural network, it is necessary to identify the basic ingredients of brain activity that could be responsible for characteristic scale-free behavior such as observed for neuronal avalanches. These insights are the basis for any further understanding of the diverse additional features, such as the interpretation by practitioners of electroencephalography (EEG) time series for diagnosis or the understanding of learning behavior. Therefore, the formulation of a neuronal network model that yields the correct scaling behavior for spontaneous activity is of crucial importance for any further progress in the understanding of the living brain.

12.1 The Model

In order to formulate a new model to study neuronal activity, we incorporated [30, 31] into a SOC framework three important neuronal ingredients, namely action potential firing after the neuronal intracellular membrane potential reaches a threshold, the refractory period of a neuron after firing an action potential, and activity-dependent synaptic plasticity. We consider a lattice of N sites where each site represents the cell body of a neuron and each bond a synaptic connection to a neighboring neuron. Each neuron is characterized by its intracellular membrane potential v_i . The number of connections from one neuron to other neurons is established by assigning to each neuron i a random outgoing connectivity degree, k_{out_i} . The distribution of the number of outgoing connections is chosen to be in agreement with the experimentally determined properties of the functional network connectivity [32] in human adults. Functional magnetic resonance imaging (fMRI) has indeed shown that this network has universal scale-free properties: that is, it exhibits a scaling behavior $n(k_{\text{out}}) \propto k_{\text{out}}^{-2}$, independent of the different tasks

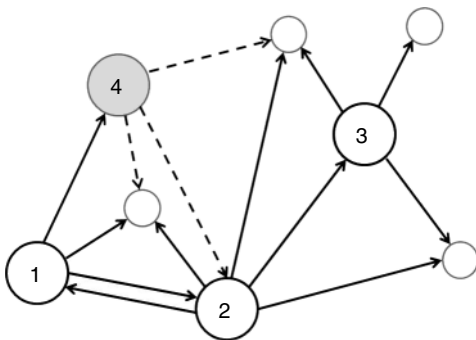


Figure 12.1 Three excitatory (white) neurons and one inhibitory (gray) neuron embedded in a larger network (neurons without number). Synaptic connections for the four neurons, indicated by arrows, can be

excitatory (continuous lines) or inhibitory (dashed lines). The connectivity degrees are $k_{\text{out}_1} = k_{\text{out}_3} = k_{\text{out}_4} = 3$, $k_{\text{out}_2} = 5$, $k_{\text{in}_1} = k_{\text{in}_3} = k_{\text{in}_4} = 1$, and $k_{\text{in}_2} = 2$.

performed by the subject. We adopt this distribution for the number of presynaptic terminals of each neuron, over the range of possible values between 2 and 100. Two neurons are then connected with a distance-dependent probability, $p(r) \propto e^{-r/r_0}$, where r is their Euclidian distance [33] and r_0 a typical edge length. Once the network of output connections is established, we identify the resulting degree of in-connections, k_{in_j} , for each neuron j . An example of a small network is shown in Figure 12.1. To each synaptic connection we then assign an initial random strength g_{ij} , where $g_{ij} \neq g_{ji}$. Moreover, synapses can have an excitatory or inhibitory character: some neurons are chosen to be inhibitory, that is, all their outgoing synapses are inhibitory, to account for a total fraction p_{in} of inhibitory synapses in the network.

Whenever at time t the value of the potential in neuron i is above a certain threshold $v_i \geq v_{\max}$, approximately equal to -55 mV for real cortical neurons, the neuron fires, that is, generates action potentials that arrive at each of the k_{out_i} presynaptic buttons and lead to a total production of neurotransmitter proportional to v_i , whose value can be larger than v_{\max} . This choice implies that the neurotransmitter production depends on the integrated stimulation received by the neuron, as it happens for real neurons where the production is controlled by the frequency of the action potential. As a consequence, the total charge that could enter into the connected neurons is proportional to $v_i k_{\text{out}_i}$. This charge is distributed among the postsynaptic neurons in proportion to the strength of the connection g_{ij} , which is implemented by the normalization $\sum_k g_{ik}(t)$, the total strength of all synapses outgoing from neuron i to the k postsynaptic neurons. The temporal evolution of the membrane voltage is therefore

$$v_j(t+1) = v_j(t) \pm \frac{v_i(t) k_{\text{out}_i}}{k_{\text{in}_j}} \frac{g_{ij}(t)}{\sum_k g_{ik}(t)} \quad (12.1)$$

where k_{in_j} is the in-degree of neuron j . This factor implies that the received charge is distributed over the surface of the soma of the postsynaptic neuron, which is proportional to the number of in-going terminals k_{in_j} . Moreover, this normalization preserves the controlled functioning of the firing cascades in networks where highly connected neurons are present, as in scale-free networks. The plus or minus sign in Eq. (12.1) is for excitatory or inhibitory synapses, respectively. After firing, a neuron is set to zero resting membrane potential and remains in a refractory state for $t_{\text{ref}} = 1$ time steps, during which it is unable to receive or transmit any charge. We wish to stress that the unit time step in Eq. (12.1) does not correspond to a real time scale; it is simply the time unit for charge propagation from one neuron to its neighbors. The synaptic strengths have initially equal value, whereas the neuron potentials are uniformly distributed random numbers between $v_{\max} - 1$ and v_{\max} . Moreover, a small random fraction (10%) of neurons are chosen to be boundary sites, with a potential fixed to 0, playing the role of sinks for the charge. An external stimulus is imposed at a random site and, if the potential reaches the firing threshold, the neuron fires and a cascade of firing neurons can evolve in the network.

12.1.1

Plastic Adaptation

As soon as a neuron is at or above the threshold v_{\max} at a given time t , it fires according to Eq. (12.1). Then the strength of all the synapses connecting to active neurons are increased in the following way:

$$g_{ij}(t+1) = g_{ij}(t) + \alpha \frac{(v_j(t+1) - v_j(t))}{v_{\max}} \quad (12.2)$$

where α is a dimensionless parameter. Conversely, the strength of all inactive synapses is reduced by the average strength increase per connection, that is,

$$\Delta g = \sum_{ij,t} \frac{\delta g_{ij}(t)}{N_b} \quad (12.3)$$

where N_b is the number of connections active in the previous avalanche. This normalization implements a sort of homeostatic regulation of plastic adaptation: the more active connections are strengthened, on average, the more inactive ones are weakened. The adaptation of synaptic strength is therefore tuned by a single parameter, α , which represents the ensemble of all possible physiological factors influencing synaptic plasticity. The quantity Δg depends on α and on the response of the network to a given stimulus. In this way, our neuronal network “memorizes” the most used paths of discharge by increasing their synaptic strengths, whereas less used synapses atrophy. Once the strength of a synaptic connection is below an assigned small value σ_t , we remove it, that is, set it equal to 0, which corresponds to what is known as *synaptic pruning*. These mechanisms correspond to a Hebbian form of activity-dependent plasticity, where the conjunction of activity at the presynaptic and postsynaptic neuron modulates the efficiency of the synapse [29].

To ensure the stable functioning of neural circuits, both strengthening and weakening of Hebbian synapses are necessary to avoid instabilities due to positive feedback [34]. However, different from short-term plasticity, such as short-term facilitation or short-term depression, in our model the change of synaptic strength does not depend on the frequency of synapse activation [24, 35, 36]. It should be also considered that, in the living brain, many synapses exhibiting plasticity are chemical synapses with functional properties different from electrical synapses. For instance, Hebbian plasticity at excitatory synapses is classically mediated by postsynaptic calcium-dependent mechanisms [37]. In our approach, the excitability of the postsynaptic neuron is simply modulated by the value of the intracellular membrane potential of the presynaptic neuron.

12.2

Neuronal Avalanches in Spontaneous Activity

We applied the plasticity rules of Eqs. 12.2 and 12.3 during a series of N_p stimuli to adapt the strengths of synapses. In fact, the more the system is actively strengthening the used synapses, the more the unused synapses will weaken. This plastic adaptation proceeds until only few connections are pruned in response to the stimuli. The system at this stage constitutes the first approximation to a trained brain, on which measurements are performed. These consist of a new sequence of stimuli, by increasing the intracellular membrane potential of a randomly selected neuron until it fires an action potential. We monitor the propagation of neuronal activity as a function of time.

After each stimulus, we measure the size distribution of the neuronal cascades (see Figure 12.2). The cascade size is defined as either the total number of firing neurons or the sum of their intracellular membrane potential variations during a cascade. This distribution exhibits a power law behavior, with an exponent equal to 1.5 ± 0.1 (see Figure 12.3). This power law identifies the cascading activity as neuronal avalanches. The avalanche activity is quite stable with respect to various parameters. The power law is also robust for densities of inhibitory synapses up to 10%, whereas it is lost for higher densities. Moreover, the distribution of avalanche durations, defined as the time period from the first spike to the last spike within an avalanche, also obeys a power law with an exponent close to -2.0 (see Figure 12.3). Both these values show excellent agreement with experimental data [5]. Extensive simulations have verified that the critical behavior of avalanche distributions does not depend on parameter values or network properties (regular, small-world, Apollonian networks) [38]. Moreover, these scaling properties do not depend on the system size, indicating that the network is in a critical state and self-regulates by adjusting synaptic strengths, thereby producing the observed scale-invariant behavior.

It is interesting to notice that recently the statistics of neuronal cascades has been measured in anesthetized rats treated with a GABA inhibitor to induce epileptic behavior [39]. Under these conditions, the size distribution shows the presence of

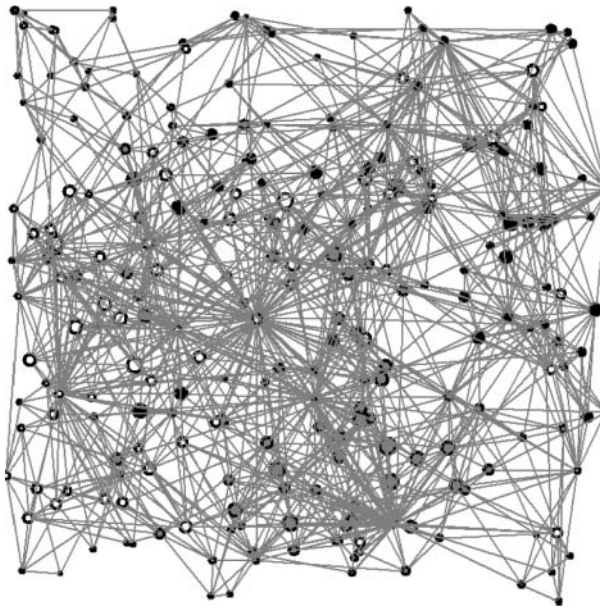


Figure 12.2 Two neuronal avalanches in the scale-free network. Two-hundred and fifty neurons are connected by directed bonds (direction indicated by the arrow at one edge), representing the synapses. The size of each neuron is proportional to the number

of in-connections, namely the number of dendrites. The two different avalanches are characterized by black and gray colors. Neurons not involved in the avalanche propagation are shown in white. (Please find a color version of this figure on the color plates.)

large events with a characteristic size in an almost periodic regime. This periodicity therefore induces a shoulder in the waiting time distribution, that is, the time between the beginning of two successive avalanches. Different is the case for slices of rat cortex that do not undergo any pharmacological treatment [5, 40, 41], where spontaneous activity is critical, that is, the size distribution obeys a power law over several orders of magnitude and no characteristic size or periodicity is detected.

12.2.1 Power Spectra

In order to compare with medical data, we calculate the power spectrum of the time series for neuronal activity, that is, the square of the amplitude of the Fourier transform as function of frequency. The average power spectrum (see Figure 12.4) exhibits a power law behavior with exponent 0.8 ± 0.1 over more than three orders of magnitude. This is the same value as that found generically for medical EEG power spectra [42, 43]. We also show in Figure 12.4 the magnetoencephalography spectra obtained from channel 17 in the left hemisphere of a male subject resting

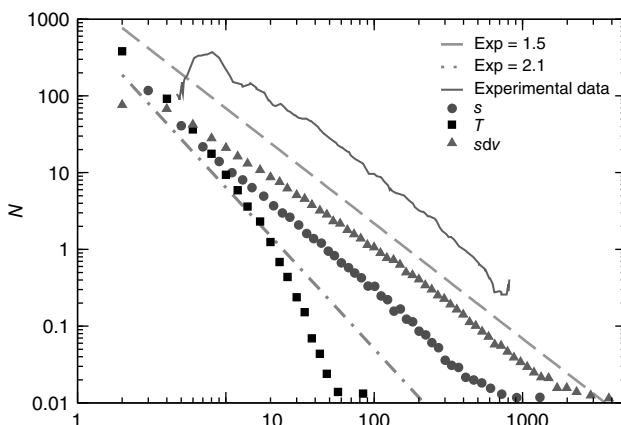


Figure 12.3 The distributions of avalanche size (circles), duration (squares), and the total potential variation during one avalanche (triangles) for 100 configurations of scale-free network with $N = 16000$ neurons ($\alpha = 0.6$, $N_p = 10000$, $p_{in} = 0.05$). The dashed line has a slope of -1.5 , whereas the dot-dashed line has a slope of -2.1 . The continuous line

represents the experimental distribution of avalanche sizes in rat cortex slices. Experimental data are shifted for better comparison, and no quantitative comparison is made between the size of experimental avalanches and the potential variation for numerical data.

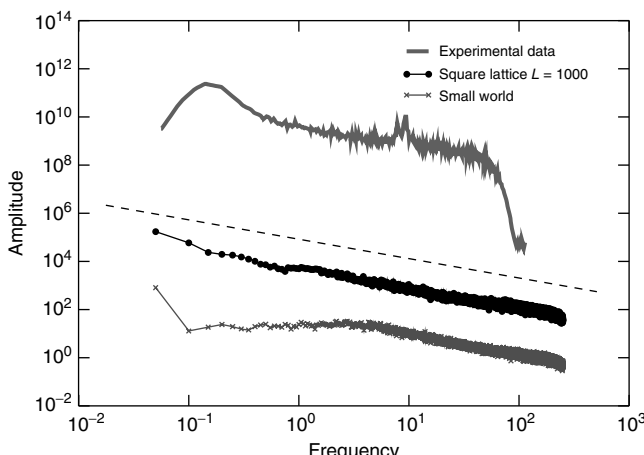


Figure 12.4 Power spectra for experimental data and numerical data ($L = 1000$, $\alpha = 0.03$, $N_p = 10$, $v_{max} = 6$) for the square lattice (middle line) and the Small-world lattice (bottom line, $L = 1000$, $\alpha = 0.05$, $N_p = 1000$, $v_{max} = 8$) with 1% rewired connections. The experimental data (top line) are from Ref. [43] and frequency is in hertz. The

numerical data are averaged over 10000 stimuli in 10 different network configurations. The dashed line has a slope 0.8. Source: Novikov *et al.* 1997 [43]. Reproduced with permission of the American Physical Society. (We gratefully thank E. Novikov and collaborators for allowing us to use their experimental data.)

with his eyes closed, as measured in Ref. [43], having an exponent equal to 0.795. This value is also found in the physiological signal spectra for other brain-controlled activities [44].

We have verified that the value of the exponent is stable against changes of the parameters α , v_{\max} , and N_p , and also for random initial bond conductances. For $\alpha = 0$, the frequency range of validity of the power law decreases by more than an order of magnitude. Figure 12.4 also shows the power spectrum for a small-world network with 1% rewired connections and a different set of the parameters α , N_p , and v_{\max} . The spectrum has some deviations from the power law at small frequencies but tends to the same universal scaling behavior at larger frequencies over two orders of magnitude. The same behavior is found for a larger fraction of rewired connections. We have also studied the power spectrum for a range of values of p_{in} , the probability of inhibitory synapses. For a density up to 10% of inhibitory synapses, the same power law behavior is recovered within error bars. For increasing density, the scaling behavior is progressively lost and the spectrum develops a complex multipike structure. These results suggest that the balance between excitatory and inhibitory synapses plays a crucial role for the overall behavior of the network, similar to what can occur in some severe neurological and psychiatric disorders [45, 46].

The scaling behavior of the power spectrum can be interpreted in terms of a stochastic process determined by multiple random inputs [47]. In fact, the output signal resulting from different and uncorrelated superimposed processes is characterized by a power spectrum with power law behavior and a crossover to white noise at low frequencies. The crossover frequency is related to the inverse of the longest characteristic time among the superimposed processes. The value of the scaling exponent depends on the ratio of the relative effect of a process of given frequency on the output with respect to other processes. $1/f$ noise corresponds to a superposition of processes of different frequencies having all the same relative effect on the output signal. In our case, the scaling exponent is smaller than unity, suggesting that processes with a high characteristic frequency are more relevant than processes with a low frequency in the superposition [47].

12.3 Learning

Next we study the learning performance of this neuronal network when it is in a critical state [48]. In order to start activity, we identify the input neurons on which the rule to be learned is applied and the output neuron on which the response is monitored. These neurons are randomly selected under the condition that they are not located at a boundary and they are separated in the network by a distance k_d . Here, k_d represents the chemical distance between two neurons, namely the number of connections in the shortest path between them, which differs from the Euclidian distance. k_d can be thought of as the number of hidden layers in a perceptron. We test the ability of the network to learn different rules: AND, OR,

XOR, and a random rule RAN that associates to all possible combinations of binary states at three inputs a random binary output. More precisely, the AND, OR and XOR rules are made of three input–output relations, whereas the RAN rule with three input sites implies a sequence of seven input–output relations. A single learning step requires the application of the entire sequence of states at the input neurons and then monitoring the state of the output neuron. For each rule, the binary value 1 is identified by the firing of the output neuron, that is, when the intracellular membrane potential of the output neuron reaches a value greater than or equal to v_{\max} at some time during the activity. Conversely, the binary state 0 at the output neuron corresponds to the state of a neuron that has been depolarized by excitatory input but failed to reach the firing threshold of the membrane potential during the entire avalanche. Once the input sites are stimulated, their activity may bring to threshold other neurons and therefore lead to avalanches of firings. We impose no restriction on the number of firing neurons, and let the avalanche evolve to its end according to Eq. (12.1). If, at the end of the avalanche, the activity did not reach the output neuron, we consider that the state of the system was unable to respond to the given stimulus and, as a consequence, to learn. We therefore increase uniformly the intracellular membrane potential of all neurons by a small quantity, $\beta = 0.01$, until the activity in the network has reached the output neuron, after which we compare the state of the output neuron with the desired output.

Plastic adaptation is applied to the system according to a nonuniform negative-feedback algorithm. That is, if the output neuron is in the correct state according to the rule, we keep the value of synaptic strengths. Conversely, if the response is incorrect, we modify the strengths of those synapses involved in the activity propagation by $\pm \alpha / d_k$, where d_k is the chemical distance of the presynaptic neuron from the output neuron. The sign of the adjustment depends on the nature of the incorrect response: if the output neuron fails to be in a firing state, we strengthen all active synapses by a small additive quantity proportional to α . Conversely, synaptic strengths are weakened if the neuron fired when it was supposed to be silent. This adaptation rule thus provides feedback in response to the incorrect answer. The feedback is applied locally to the corresponding output neuron as well as propagating backward toward the input sites triggered locally at the output site. The biological realization of such a feedback mechanism can be thought of as a binary error signal that is locally applied at the output site and diffuses toward the input site.

Next, we analyze the performance of the system to learn different input–output rules. Figure 12.5 shows the fraction of configurations learning the XOR rule versus the number of learning steps for different values of the plastic adaptation strength α . We notice that the larger the value of α , the sooner the system starts to learn the rule; however, the final percentage of learning configurations is lower. The final rate of success increases as the strength of plastic adaptation decreases. This is due to the highly nonlinear dynamics of the model, where firing activity is an all-or-none event controlled by the threshold. The result that all rules give a higher percentage of success for weaker plastic adaptation is in agreement with recent experimental findings on visual perceptual learning, where better performances

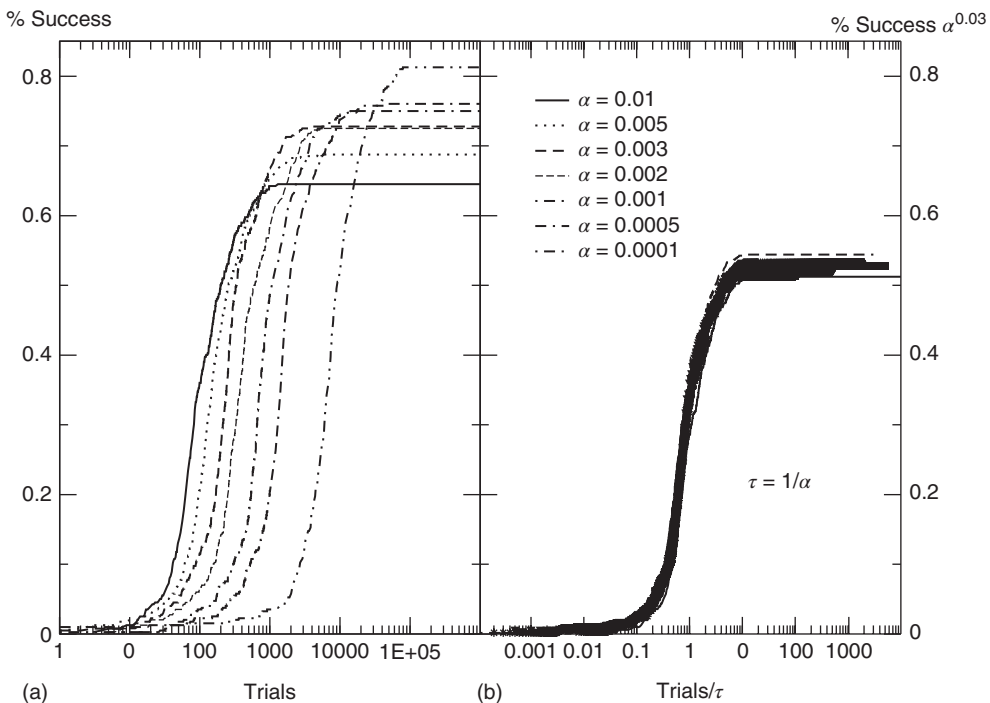


Figure 12.5 (a) Percentage of configurations learning the XOR rule as function of the number of learning steps for different plastic adaptation strengths α (decreasing from bottom to top). Data are for 400 realizations of a network with $N = 1000$ neurons,

$p_{in} = 0$, $r_0 = 15$, $k_{min} = 3$ and $k_d = 5$. (b) Collapse of the curves by rescaling the number of learning steps by the characteristic learning time $\tau = 1/\alpha$ and the percentage of success by $\alpha^{-0.03}$.

were measured when minimal changes in the functional network occurred as a result of learning [49].

We characterize the learning ability of a system for different rules by the average learning time, that is, the average number of times a rule must be applied to obtain the right answer, and the asymptotic percentage of learning configurations. This is determined as the percentage of learning configurations at the end of the teaching routine, namely after 10^6 applications of the rule. The average learning time scales as $\tau \propto 1/\alpha$ for all rules, independent of the parameter values. The asymptotic percentage of success increases by decreasing α as a very slow power law, $\propto \alpha^{-0.03 \pm 0.01}$, where the exponent is the average value over different rules. We check this scaling behavior by appropriately rescaling the axes in Figure 12.5. The curves corresponding to different α values indeed all collapse onto a unique scaling function. Similar collapse is observed for the OR, AND, and RAN rules and for different parameters k_d and p_{in} . The dynamics of the learning process shows therefore universal properties, independent of the details of the system or the specific task assigned.

Finally, we explicitly analyze the dependence of the learning performance and its scaling behavior for different model parameters. The learning behavior is sensitive to the number of neurons involved in the propagation of the signal, and therefore depends on the distance between the input and output neurons and the level of connectivity in the system. We investigate the effect of the parameters k_d and k_{\min} on the performance of the system. Systems with larger k_{\min} have a larger average number of synapses per neuron, producing a more branched network. The presence of several alternative paths facilitates information transmission from the inputs to the output site. However, the participation of more branched synaptic paths in the learning process may delay the time the system first gives the right answer. As expected, the performance of the system improves as the minimum out-connectivity degree increases, with the asymptotic percentage of success scaling as $\sim k_{\min}^{0.4}$. On the other hand, also the chemical distance between the input and output sites plays a very important role, as the number of hidden layers in a perceptron. Indeed, as k_d becomes larger, the length of each branch in a path involved in the learning process increases. As a consequence, the system needs a higher number of tests to first give the right answer, and a lower fraction of configurations learns the rule after the same number of steps. The percentage of learning configurations, as expected, decreases as $\sim k_d^{-0.3}$, and similar behavior is detected for all rules. As the system size increases, the number of highly connected neurons becomes larger. A well-connected system provides better performances, therefore we could expect that the size dependence reflects the same effect. The learning performance indeed improves with the system size, since, for the same out degree distribution, the overall level of connectivity improves for larger systems.

12.4

Temporal Organization of Neuronal Avalanches

Here we focus on the overall temporal organization of neuronal avalanches both in organotypic cultures and neuronal network simulations. Each avalanche is characterized by its size s_i , and its start and end times, t_i^s and t_i^f , respectively. The properties of temporal occurrence are analyzed by evaluating the distribution of waiting times $\Delta t_i = t_{i+1}^s - t_i^f$. This is a fundamental property of stochastic processes, widely investigated for natural phenomena [50] and used to discriminate between a simple Poisson process and a correlated stochastic process. Indeed, in the first case the distribution is an exponential, whereas it exhibits a more complex behavior with power law regime if long-range correlations are present. For a wide variety of phenomena, for example, earthquakes, solar flares, rock fracture, and so on, this distribution always shows a monotonic behavior. In some of the chapters of this book and in an article by Ribeiro *et al.* [51], this distribution has been analyzed for freely behaving and anesthetized rats. The distributions show consistently a decreasing behavior. Universal scaling features are observed when waiting times are rescaled by the average occurrence rate for freely behaving rats, whereas curves for anesthetized rats do not collapse onto a unique function.

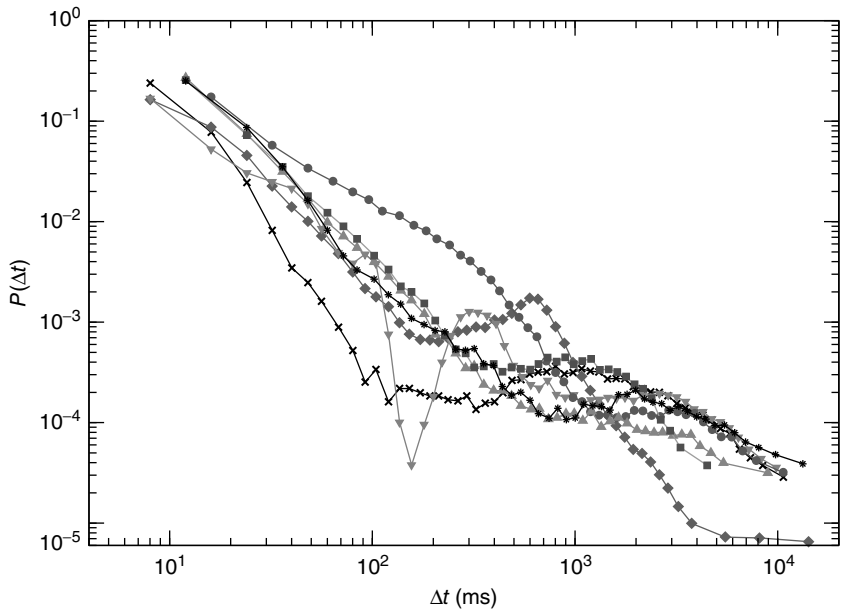


Figure 12.6 The distribution of waiting times for seven different slices of rat cortex exhibiting a non-monotonic behavior, undetected in any other stochastic process. All curves show an initial power law regime between 10 and ~ 200 ms, characterized by

exponent values between 2 and 2.3. For $\Delta t > 200$ ms curves can become quite different, with the common characteristics of a local minimum located at 200 ms $< \Delta t_{\min} < 1$ s, followed by a more or less pronounced maximum at $\Delta t \approx 1$ – 2 s.

In Figure 12.6, we show the waiting time distribution for different cultures of rat cortex slices [41]. The curves exhibit a complex non-monotonic behavior with common features: an initial power law regime and a local minimum, followed by a more or less pronounced maximum. This behavior is not usually observed in natural phenomena and suggests that the timing of avalanches in organotypic cultures is not governed by a pure Poisson process. In order to investigate the origin of this behavior, we simulate avalanche activity by our model, considering that the system slowly alternates between upstates and downstates [41]. The basic idea is that, after a large avalanche, activated neurons become hyperpolarized and the system goes into a downstate where the neuronal stimulation has a small random amplitude. Conversely, after a small avalanche, active neurons remain depolarized and the system is in an upstate, where stimulation depends on the previous avalanche activity. In order to implement these mechanisms in the numerical procedure, we fix a threshold value, $s_{\Delta v}^{\min}$, for the avalanche size measured in terms of the sum of depolarizations of all active neurons, $s_{\Delta v} = \sum \delta v_i$. More precisely, if the last avalanche is larger than a threshold, $s_{\Delta v} > s_{\Delta v}^{\min}$, the system transitions into a downstate and neurons that were active in the last avalanche become

hyperpolarized proportional to their previous activity: that is, we reset

$$v_i = v_i - h \delta v_i \quad (12.4)$$

where $h > 0$. This rule introduces a short-range memory at the level of a single neuron and models the local inhibition experienced by a neuron, due to spike adaptation, adenosine accumulation, synaptic vesicle depletion, and so on. Conversely, if the avalanche just ended had a size $s_{\Delta\nu} \leq s_{\Delta\nu}^{\min}$, the system either will remain in an upstate or will transition into an upstate. All neurons that fired in the previous avalanche are set to the depolarized value

$$v_i = v_{\max}(1 - s_{\Delta\nu}/s_{\Delta\nu}^{\min}) \quad (12.5)$$

The neuron's intracellular potential depends on the response of the whole network via $s_{\Delta\nu}$, in agreement with experimental measurements that the neuronal membrane potential remains close to the firing threshold during an upstate. $s_{\Delta\nu}^{\min}$ controls the extension of the upstate and therefore the level of excitability of the system. The high activity in the upstate must be sustained by collective effects in the network; otherwise, the depolarized potentials would soon decay to 0, and therefore the random stimulation in the upstate has an amplitude that depends on past activity. Eqs (12.4) and (12.5) represent the simplest implementation of the neuron's upstate and downstate. Each equation depends on a single parameter, h and $s_{\Delta\nu}^{\min}$, which introduce a memory effect at the level of single neuron activity and the entire system, respectively. In order to reproduce the behavior observed experimentally, the parameters $s_{\Delta\nu}^{\min}$ and h are controlled separately. However, our simulations show that the ratio $R = h/s_{\Delta\nu}^{\min}$ is the only relevant quantity controlling the temporal organization of avalanches.

Following the above procedure, the system indeed transitions between upstates and downstates, though with different temporal durations (see Figure 12.7). The distribution of upstate durations is consistent with an exponential decay, in agreement with previous numerical results [23]. Conversely, the downstates exhibit a sharply peaked distribution with a most probable value at about 200 numerical time units. Avalanches are characterized by power law distributions for the size and the temporal duration with exponents, in good agreement with experimental results.

Next we measure the waiting time distribution between successive avalanches. In the analysis of the temporal signal, we consider avalanches involving at least two neurons, whereas single spikes are considered background noise. We measure the waiting time as the time delay between the end of an avalanche and the beginning of the next one. We notice that long waiting times generally occur after large avalanches, corresponding to downstates, whereas short ones are detected during upstates (see Figure 12.8). The scatter plot of the waiting time as a function of the previous avalanche shows that experimental data are quite scattered. In order to evidence a scaling behavior, we evaluate the expectation value of the waiting time as function of the cumulated activity over a temporal bin. These data exhibit a scaling behavior that is fully reproduced by numerical data. The good agreement between experimental and numerical results confirms the validity of our approach.

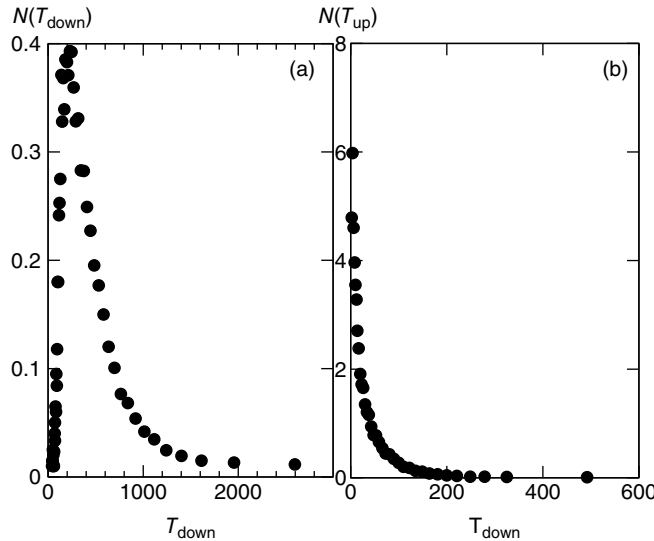


Figure 12.7 Distribution of durations of downstates (a) and upstates (b) for 100 configurations of a network of $N = 64000$ neurons with $p_{\text{in}} = 0.05$, $\alpha = 0.9$, $s_{\Delta\nu}^{\min} = 160$, $d_d = 0.15$, and $c_d = -0.65$. Data are averaged over the number of configurations.

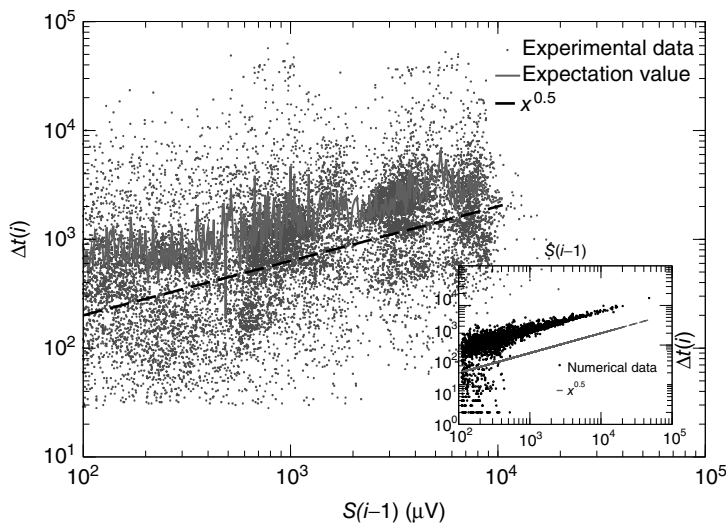


Figure 12.8 Main panel: Scatter plot of waiting time versus previous avalanche size for 15 slices of rat cortex (symbols). Expectation value of waiting time as function of the cumulated previous avalanche activity over a

temporal window of 50 ms (continuous line). Data indicate that the waiting time increases with preceding avalanche activity, in line with our model assumption. Inset: Same quantity evaluated for numerical data.

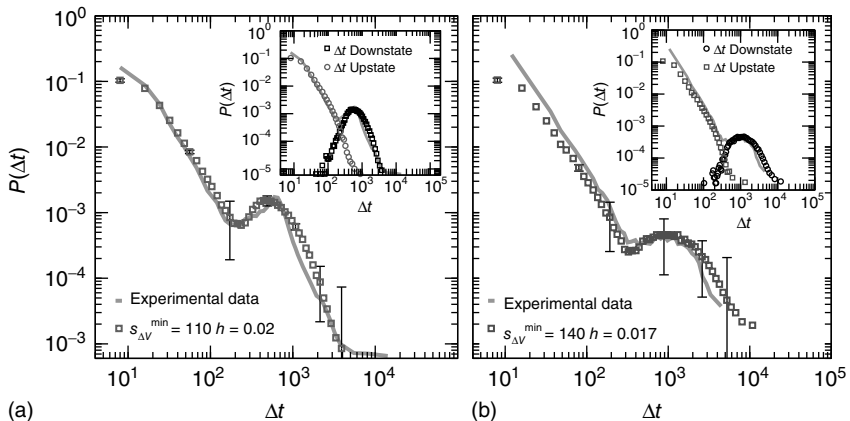


Figure 12.9 Waiting time distributions measured experimentally compared with the average numerical distributions for 100 networks with $N = 64000$ neurons. (a) Numerical curve ($s_{\Delta v}^{\min} = 110$ and $h = 0.02$). (b) Numerical curve ($s_{\Delta v}^{\min} = 140$ and $h = 0.017$). In the

inset, the numerical waiting time distributions evaluated separately in the up- and down-states for the numerical statistical error bars not shown are comparable to the symbol size.

The numerical waiting time distributions (see Figure 12.9) exhibit the non-monotonic behavior of the experimental curves, where the position of the minimum is controlled by the value of $s_{\Delta v}^{\min}$, and the power law regime scales with the same exponent ~ -2 as the experimental data. The agreement between the numerical and the experimental distributions is confirmed by the Kolmogorov–Smirnov test at the $p = 0.05$ significance level. Both distributions pass the statistical test with $p = 0.99$ (a) and $p = 0.68$ (b). The different contribution from the two states is reflected in the activity temporal scale (inset of Figure 12.9). The upstate generates strongly clustered avalanches, yielding the power law regime of the waiting time distribution, whose extension depends on $s_{\Delta v}^{\min}$. Large Δt between avalanches generated in the upstate are observed with a very small probability, which increases with decreasing h . Conversely, the waiting time distribution evaluated in the downstate has a bell-shaped behavior centered at large waiting times which depends on h , that is, for a larger disinhibition of the network, the probability to observe intermediate waiting times decreases in favor of long Δt . The presence of the minimum and the height of the relative maximum are sample dependent (Figure 12.7) and for each sample, simulations are able to reproduce the different behaviors by choosing the appropriate parameter values. However, the agreement between numerical and experimental data depends uniquely on the ratio $R = h/s_{\Delta v}^{\min} \simeq 10^{-4}$, expressing the subtle balance between excitation and inhibition. For different samples, optimal agreement is realized for the same value of the ratio R . For instance, enhancing the excitatory mechanism, by increasing the threshold value $s_{\Delta v}^{\min}$, clearly produces a major shift in the data [41]. Increasing the inhibitory mechanism, by tuning the hyperpolarization constant parameter h ,

generates the opposite effect, recovering the good agreement with experimental data. It is interesting to note that the avalanche size and duration distributions exhibit the experimental scaling behavior for the set of parameters expressing the balance between the excitatory and inhibitory components.

The abrupt transition between the upstate and the downstate, controlled by a threshold mechanism, produces the minimum observed experimentally. However, this mechanism alone is not sufficient to reproduce the non-monotonic behavior. Indeed, simulations of upstates and downstates only in terms of different drives, without the dependence of the single neuron state on upstate and downstates, provide a monotonic behavior [41]. The initial power law regime is followed by a plateau and a final exponential decay. The power law regime is still observed in this case, since this is mainly controlled by the drive in the upstate which introduces correlations between successive avalanches. Therefore, the introduction of inhibitory mechanisms following activity, that is, the hyperpolarizing currents in the downstate and the neuron disfacilitation, are crucial ingredients to fully reproduce the dynamics of the transition between the different activity states.

12.5

Conclusions

Several experimental evidences suggest that the brain behaves as a system acting at a critical point. This statement implies that the collective behavior of the network is more complex than the functioning of the single components. Moreover, the emergence of self-organized neuronal activity, with the absence of a characteristic scale in the response, unveils similarities with other natural phenomena exhibiting scale-free behavior, such as earthquakes or solar flares. For a wide class of these phenomena, SOC has indeed become a successful interpretive scheme. However, it is important to stress that the observation of a scale-free response is not a sufficient indication for temporal correlations among events. For instance, the waiting time distribution for the original sand pile model is a simple exponential [2] because avalanches are temporally uncorrelated. Several natural stochastic phenomena, characterized by temporal correlations and clustering, provide similar nonexponential distributions, all with a monotonic functional behavior.

Our model inspired by SOC is able to capture the scaling behavior of avalanches in spontaneous activity and to reproduce the underlying power law behavior measured by EEG in human patients. Besides reproducing neuronal activity, the network is able to learn Boolean rules via plastic modification of synaptic strengths. The implemented learning dynamics is a cooperative mechanism where all neurons contribute to select the right answer and negative feedback is provided in a nonuniform way. Despite the complexity of the model and the high number of degrees of freedom involved at each step of the iteration, the system can learn successfully even complex rules. In fact, since the system acts in a critical state, the response to a given input can be highly flexible, adapting more easily to different inputs. The analysis of the dependence of the performance of the system on the

average connectivity confirms that learning is a truly collective process, where a high number of neurons may be involved and the system learns more efficiently if more branched paths are possible. The role of the plastic adaptation strength, considered as a constant parameter in most studies, provides a striking new result: the neuronal network has a “universal” learning dynamics, and even complex rules can be learned provided that the plastic adaptation is sufficiently slow.

Moreover, the temporal organization of avalanches exhibits a complex non-monotonic behavior of the waiting time distribution. Avalanches are temporally correlated in the upstate, whereas downstates are long-term recovery periods where memory of the past activity is erased. The model suggests that the crucial feature of this temporal evolution is the different single neuron behavior in the two phases. This result provides new insights into the mechanisms necessary to introduce complex temporal correlations within the framework of SOC. The good agreement with experimental data indicates that the transition from an upstate to a downstate has a high degree of synchronization. Moreover, it confirms that alternation between up- and downstates is the expression of a homeostatic regulation which, during periods of high activity, is activated to control the excitability of the system, driving it into the downstate, and avoiding pathological behavior. Network mechanisms in the upstate, where neurons mutually sustain the activity, act as a form of short-term memory. This is the crucial effect giving rise to the initial power law regime in the waiting time distribution, which is a clear sign of temporal correlations between avalanches occurring close in time in the upstate. Conversely, in the downstate, the system slowly goes back to the active state, with no memory of past activity.

These collective effects must be supported by the single neuron behavior, which toggles between two preferential states, a depolarized one in the upstate and a hyperpolarized one in the downstate. The model suggests that the depolarized neuron state is a network effect: the avalanche activity itself determines how close to the firing threshold a neuron stays in the upstate. Conversely, the hyperpolarized state is a form of temporal auto-correlation in the neuron state: the higher the neuron response during the previous avalanche, the lower is its membrane potential. The hyperpolarizing currents act as a form of memory of past activity for the single neuron. The critical state of the system is therefore the one that realizes the correct balance between excitation and inhibition via self-regulating mechanisms. This balance ensures the scale-free behavior of the avalanche activity and bursts of correlated avalanches in the upstate.

References

1. Bak, P. (1996) *How Nature Works: The Science of Self-Organized Criticality*, Springer, New York.
2. Jensen, H.J. (1998) *Self-Organized Criticality: Emergent Complex Behavior in Physical and Biological Systems*, Cambridge University Press, New York.
3. Maslov, S., Paczuski, M., and Bak, P. (1994) Avalanches and 1/f noise in evolution and growth models. *Phys. Rev. Lett.*, **73** (16), 2162–2165.

4. Davidsen, J. and Paczuski, M. (2002) $1/f\{\alpha\}$ noise from correlations between avalanches in self-organized criticality. *Phys. Rev. E*, **66** (5), 050 101.
5. Beggs, J.M. and Plenz, D. (2003) Neuronal avalanches in neocortical circuits. *J. Neurosci.*, **23** (35), 11 167.
6. Beggs, J. and Plenz, D. (2004) Neuronal avalanches are diverse and precise activity patterns that are stable for many hours in cortical slice cultures. *J. Neurosci.*, **24** (22), 5216–5229.
7. Gireesh, E.D. and Plenz, D. (2008) Neuronal avalanches organize as nested theta-and beta/gamma-oscillations during development of cortical layer 2/3. *Proc. Natl. Acad. Sci. U.S.A.*, **105** (21), 7576.
8. Petermann, T., Thiagarajan, T.C., Lebedev, M.A., Nicolelis, M.A.L., Chialvo, D.R., and Plenz, D. (2009) Spontaneous cortical activity in awake monkeys composed of neuronal avalanches. *Proc. Natl. Acad. Sci. U.S.A.*, **106** (37), 15 921.
9. Mazzoni, A., Broccard, F., Garcia-Perez, E., Bonifazi, P., Ruaro, M., and Torre, V. (2007a) On the dynamics of the spontaneous activity in neuronal networks. *PLoS One*, **2** (5), e439.
10. Pasquale, V., Massobrio, P., Bologna, L., Chiappalone, M., and Martinoia, S. (2008) Self-organization and neuronal avalanches in networks of dissociated cortical neurons. *Neuroscience*, **153** (4), 1354–1369.
11. Bak, P. and Tang, C. (1989) Earthquakes as a self-organized critical phenomenon. *J. Geophys. Res.*, **94** (B11), 15 635–15.
12. Sornette, A. and Sornette, D. (1989) Self-organized criticality and earthquakes. *EPL Europhys. Lett.*, **9**, 197.
13. Bak, P. and Sneppen, K. (1993) Punctuated equilibrium and criticality in a simple model of evolution. *Phys. Rev. Lett.*, **71** (24), 4083–4086.
14. Lu, E. and Hamilton, R. (1991) Avalanches and the distribution of solar flares. *Astrophys. J.*, **380**, L89–L92.
15. Politzer, P. (2000) Observation of avalanchelike phenomena in a magnetically confined plasma. *Phys. Rev. Lett.*, **84** (6), 1192–1195.
16. Faillettaz, J., Louchet, F., and Grasso, J. (2004) Two-threshold model for scaling laws of noninteracting snow avalanches. *Phys. Rev. Lett.*, **93** (20), 208 001.
17. Peters, O., Hertlein, C., and Christensen, K. (2002) A complexity view of rainfall. *Phys. Rev. Lett.*, **88** (1), 18 701.
18. Staley, K.J., Longacher, M., Bains, J.S., and Yee, A. (1998) Presynaptic modulation of ca3 network activity. *Nat. Neurosci.*, **1**, 201–209.
19. Thompson, S., Haas, H., and Gähwiler, B. (1992) Comparison of the actions of adenosine at pre-and postsynaptic receptors in the rat hippocampus in vitro. *J. Physiol.*, **451** (1), 347–363.
20. Maeda, E., Robinson, H., and Kawana, A. (1995) The mechanisms of generation and propagation of synchronized bursting in developing networks of cortical neurons. *J. Neurosci.*, **15** (10), 6834–6845.
21. Sanchez-Vives, M., Nowak, L., and McCormick, D. (2000) Cellular mechanisms of long-lasting adaptation in visual cortical neurons in vitro. *J. Neurosci.*, **20** (11), 4286–4299.
22. Timofeev, I., Grenier, F., and Steriade, M. (2001) Disfacilitation and active inhibition in the neocortex during the natural sleep-wake cycle: an intracellular study. *Proc. Natl. Acad. Sci. U.S.A.*, **98** (4), 1924.
23. Millman, D., Mihalas, S., Kirkwood, A., and Niebur, E. (2010) Self-organized criticality occurs in non-conservative neuronal networks during Up states. *Nat. Phys.*, **6** (10), 801–805, PMCID: PMC3145974.
24. Albright, T.D., Jessell, T.M., Kandel, E.R., and Posner, M. (2000) Neural science: a century of progress and the mysteries that remain. *Neuron*, **59**, S1–S5.
25. Hensch, T. (2004) Critical period regulation. *Annu. Rev. Neurosci.*, **27**, 549–579.
26. Abbott, L. and Nelson, S. et al. (2000) Synaptic plasticity: taming the beast. *Nat. Neurosci.*, **3**, 1178–1183.
27. Hebb, D. (1949) *The Organization of Behavior*, John Wiley & Sons, Inc., New York.

28. Tsien, J. (2000) Linking hebb's coincidence-detection to memory formation. *Curr. Opin. Neurobiol.*, **10** (2), 266–273.
29. Cooper, S. (2005) Donald O. Hebb's synapse and learning rule: a history and commentary. *Neurosci. Biobehav. Rev.*, **28** (8), 851–874.
30. de Arcangelis, L., Perrone-Capano, C., and Herrmann, H. (2006b) Self-organized criticality model for brain plasticity. *Phys. Rev. Lett.*, **96** (2), 28 107.
31. Pellegrini, G.L., de Arcangelis, L., Herrmann, H., and Perrone-Capano, C. (2007) Activity-dependent neural network model on scale-free networks. *Phys. Rev. E*, **76** (1), 016 107.
32. Eguiluz, V., Chialvo, D., Cecchi, G., Baliki, M., and Apkarian, A. (2005) Scale-free brain functional networks. *Phys. Rev. Lett.*, **94** (1), 18 102.
33. Roerig, B. and Chen, B. (2002) Relationships of local inhibitory and excitatory circuits to orientation preference maps in ferret visual cortex. *Cereb. Cortex*, **12** (2), 187–198.
34. Desai, N. (2003) Homeostatic plasticity in the cns: synaptic and intrinsic forms. *J. Physiol.-Paris*, **97** (4-6), 391–402.
35. Paulsen, O. and Sejnowski, T. (2000) Natural patterns of activity and long-term synaptic plasticity. *Curr. Opin. Neurobiol.*, **10** (2), 172–180.
36. Braunewell, K. and Manahan-Vaughan, D. (2001) Long-term depression: a cellular basis for learning? *Rev. Neurosci.*, **12** (2), 121.
37. Bi, G. and Poo, M. (2001) Synaptic modification by correlated activity: Hebb's postulate revisited. *Annu. Rev. Neurosci.*, **24** (1), 139–166.
38. de Arcangelis, L. and Herrmann, H. (2012) Activity-dependent neuronal model on complex networks. *Front. Physiol.*, **3**, 62.
39. Osorio, I., Frei, M., Sornette, D., Milton, J., and Lai, Y. (2010) Epileptic seizures: quakes of the brain?. *Phys. Rev. E*, **82** (2), 021 919.
40. Stewart, C. and Plenz, D. (2006) Inverted-u profile of dopamine-nmda-mediated spontaneous avalanche recurrence in superficial layers of rat prefrontal cortex. *J. Neurosci.*, **26** (31), 8148–8159.
41. Lombardi, F., Herrmann, H., Perrone-Capano, C., Plenz, D., and de Arcangelis, L. (2012) Balance between excitation and inhibition controls the temporal organization of neuronal avalanches. *Phys. Rev. Lett.*, **108** (22), 228 703.
42. Freeman, W., Rogers, L., Holmes, M., and Silbergeld, D. (2000) Spatial spectral analysis of human electrocorticograms including the alpha and gamma bands. *J. Neurosci. Methods*, **95** (2), 111–121.
43. Novikov, E., Novikov, A., Shannahoff-Khalsa, D., Schwartz, B., and Wright, J. (1997) Scale-similar activity in the brain. *Phys. Rev. E*, **56** (3), 2387–2389.
44. Hausdorff, J., Ashkenazy, Y., Peng, C., Ivanov, P., Stanley, H., and Goldberger, A. (2001) When human walking becomes random walking: fractal analysis and modeling of gait rhythm fluctuations. *Physica A*, **302** (1), 138–147.
45. Rubenstein, J. and Merzenich, M. (2003) Model of autism: increased ratio of excitation/inhibition in key neural systems. *Genes, Brain Behav.*, **2** (5), 255–267.
46. Powell, E., Campbell, D., Stanwood, G., Davis, C., Noebels, J., and Levitt, P. (2003) Genetic disruption of cortical interneuron development causes region- and gaba cell type-specific deficits, epilepsy, and behavioral dysfunction. *J. Neurosci.*, **23** (2), 622–631.
47. Hausdorff, J. and Peng, C. (1996) Multi-scaled randomness: a possible source of 1/f noise in biology. *Phys. Rev. E*, **54** (2), 2154.
48. de Arcangelis, L. and Herrmann, H. (2010) Learning as a phenomenon occurring in a critical state. *Proc. Natl. Acad. Sci. U.S.A.*, **107** (9), 3977–3981.
49. Lewis, C., Baldassarre, A., Committeri, G., Romani, G., and Corbetta, M. (2009) Learning sculpts the spontaneous activity of the resting human brain. *Proc. Natl. Acad. Sci. U.S.A.*, **106** (41), 17–558–17–563.
50. de Arcangelis, L., Godano, C., Lippiello, E., and Nicodemi, M. (2006a) Universality in solar flare and earthquake

- occurrence. *Phys. Rev. Lett.*, **96** (5), 51 102.
51. Ribeiro, T., Copelli, M., Caixeta, F., Belchior, H., Chialvo, D., Nicolelis, M., and Ribeiro, S. (2010) Spike avalanches exhibit universal dynamics across the sleep-wake cycle. *PLoS One*, **5** (11), e14 129.

13

The Neuronal Network Oscillation as a Critical Phenomenon

Richard Hardstone, Huibert D. Mansvelder, and Klaus Linkenkaer-Hansen

13.1

Introduction

When investigating nature we often discard the observed variation and describe its properties in terms of an average, such as the mean or median [1]. For some objects or processes, however, the average value is a poor description, because they do not have a typical or “characteristic” scale. Such systems are broadly referred to as *scale-free* [2]. There is growing evidence that physiological processes can exhibit fluctuations without characteristic scales and that this scale-free dynamics is important for their function [2–8]. Heuristically, one may reason that scale-free dynamics implies a wide range of functional states, which is characteristic for physiological systems in general and neuronal networks in particular.

Synchronous brain activity is thought to be crucial for neural integration, cognition, and behavior [9, 10]. The multiscale properties of synchronous cell assemblies, however, remain poorly understood. While probing activity at different scales, several investigators have begun to consider self-organized criticality (SOC) as an overriding neuronal organizing principle [7, 11–22]. The SOC theory holds that slowly driven, interaction-dominated threshold systems will be attracted to a critical point, with the system balanced between order and disorder [3, 23, 24].

This critical state is characterized by scale-free probability distributions. In cortical slices, “neuronal avalanches” of local field potential activity are governed by a power-law (i.e., scale-free) distribution of event sizes with an exponent of -1.5 , as expected for a critical branching process [12]. Similar results have also been found *in vivo* [19]. This finding inspired the development of computational models that were capable of producing power-law-distributed neuronal avalanches through a process of self-organization, thereby providing theoretical support for SOC in neuronal systems [15, 21, 22]. Models have shown that networks in a critical state display differing responses to the widest input range [14], with the largest repertoire of metastable patterns [13], and maximal information and transmission capacity [25, 26]. Scale-free dynamics have been observed on many levels of neuronal organization. Power-law scaling is, for example, found in the decay of temporal

correlations in behavioral performance [1], and in the phase-locking intervals between brain regions [27, 28].

Interestingly, ongoing oscillations measured with electroencephalography (EEG) or magnetoencephalography (MEG) exhibit power-law-scaled temporal (auto-)correlations in their amplitude modulation, also known as *long-range temporal correlations* (LRTCs) [11, 29]. Given that neuronal avalanches and oscillations depend on balanced excitation and inhibition [12, 26, 30], it is plausible that their scale-free dynamics are related. In this chapter, we explain the methods used for studying scale-free dynamics of neuronal oscillations and provide examples of these analyses applied to the amplitude dynamics in health and disease. Further, we describe the concept of multilevel criticality as a state where scale-free behavior emerges jointly on different levels of network dynamics: the short-time-scale spreading of activity in the form of avalanches, with an upper bound at the characteristic timescale of the dominant oscillation, and the long-time-scale modulation of the oscillatory amplitude.

13.2

Properties of Scale-Free Time Series

Detrended fluctuation analysis (DFA) is widely used for quantifying LRTCs and scaling behavior in neuronal time series, because it provides a more reliable estimate of scaling exponents than the autocorrelation function or the power-spectrum density [31–33]. The signal-processing steps in DFA have often been reported [11, 34]; however, the concepts of self-affinity and stationarity are fundamental to understanding why DFA provides a measure of correlations over time and, therefore, we shall first explain these.

13.2.1

Self-Affinity

Self-affinity is a property of fractal time series [35, 36]. It is a special case of self-similarity, according to which a small part of a fractal structure is similar to the whole structure. When this small part is an exact replica of the whole then the fractal is exact, which is the case for purely mathematical and geometrical fractals (e.g., the van Koch curve and the Mandelbrot tree) [37]. When the self-similarity is expressed in terms of statistical properties (e.g., the mean and standard deviation for a portion of a fractal are scaled versions of the mean and standard deviation of the whole), then the fractal is a statistical fractal. While the self-similarity property is isotropic and applies along all the dimensions of a fractal object, self-affinity describes anisotropic scaling, where statistical properties of the fractal scale differently along different dimensions. In the case of a time series, the time dimension is rescaled.

Nature hosts some intriguing examples of self-similar structures, such as the Roman cauliflower (*Romanesco broccoli*), in which almost exact copies of the entire flower may be recognized on multiple smaller scales (Figure 13.1A). Physiological

time series may exhibit statistical self-affine properties [38, 39]. Self-affine processes and self-similar structures have in common that the statistical distribution of the measured quantity follows a power-law function, which is the only mathematical function without a characteristic scale. Self-affine and self-similar phenomena are therefore called *scale-free*.

Considering again the example of the *Romanesco broccoli*, we can say that it is a “scale-free” structure, because there is no typical size of flower on the cauliflower, with the frequency of a certain size of flower being inversely proportional to its size. A scale-free time series will in a similar manner be composed of sine waves with amplitudes inversely proportional to their frequency (Figure 13.1B), seen as a straight line when the power spectrum is plotted on a double-logarithmic axis. This is in contrast to the wide variety of objects that have a typical scale, for example, the size of the apples on a tree (Figure 13.1C). None of them will be very small or very large; rather, they will form a Gaussian distribution centered on some characteristic size, which is well represented by the mean of the distribution. Qualitatively, the characteristic scale is present at the expense of rich variability. Similarly, a time series in which all frequencies are represented with the same characteristic amplitude will lack the rich variability of the scale-free time series and is referred to as *white noise* (Figure 13.1D). Phenomena with characteristic scales are well defined by their mean and standard deviation (Figure 13.1C,D), whereas scale-free phenomena are better described by the exponent of a power-law function, because it captures the relationship between objects or fluctuations on different scales (Figure 13.1A,B).

Let us now introduce the mathematical definitions:

A nonstationary stochastic process is said to be *self-affine* in a statistical sense, if a rescaled version of a small part of its time series has the same statistical distribution as the larger part. For practical purposes, it is sufficient to assess the standard deviation. Thus, the process, Y , is self-affine if for all windows of length t [40]:

$$Y(Lt) \equiv L^H Y(t) \quad (13.1)$$

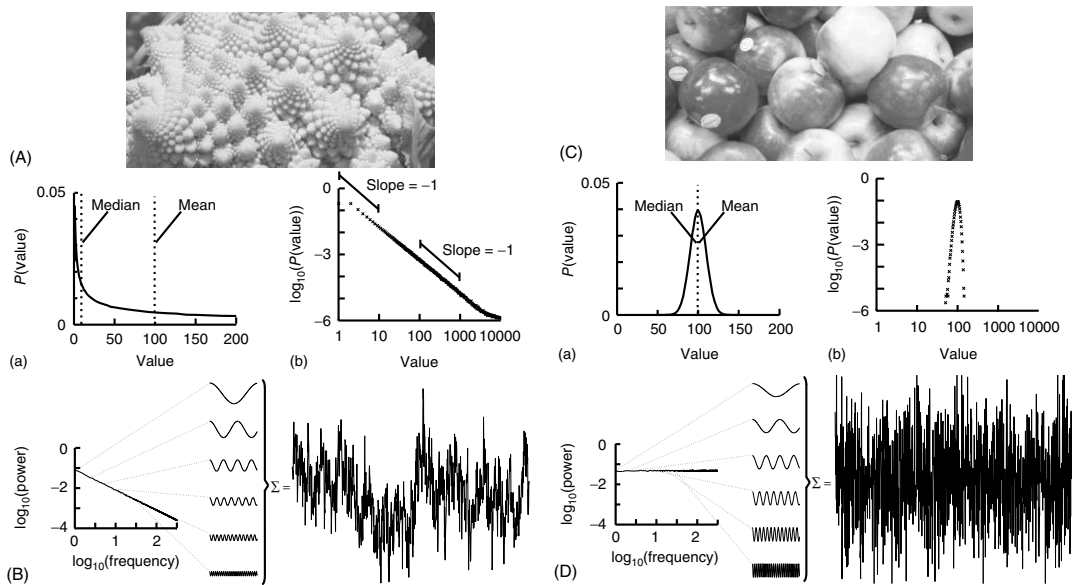
where:

- “ $Y(Lt)$ ” and “ $Y(t)$ ” are values of a process at time windows of length Lt and t , respectively
- “ L ”: window-length factor
- “ H ”: Hurst exponent, dimensionless estimator of self-affinity
- “ \equiv ”: the standard deviation on both sides of the equation are identical.

To illustrate the implications of this definition for the property of a self-affine process, we consider a Hurst exponent of 0.75 and derive the standard deviation for two and three times the length of the timescale. To double the timescale, we set $L = 2$:

$$Y(2t) \equiv 2^{0.75} Y(t)$$

$$Y(2t) \equiv 1.68 Y(t)$$



Therefore, the standard deviation of a signal twice the length of $Y(t)$ is 1.68 times larger than that of the original signal $Y(t)$.

Tripling the window size with $L = 3$ gives:

$$Y(3t) \equiv 3^{0.75} Y(t)$$

$$Y(3t) \equiv 2.28 Y(t)$$

The standard deviation increases by a factor of 2.28. In other words, with a Hurst exponent $H = 0.75$, the standard deviation grows with increasing window size according to the power law, L^H , as indicated in Eq. (13.1). This mathematical formulation shows another property of self-affine processes, which is scale invariance: the scaling of the standard deviation is not dependent on the absolute scale. A signal exhibiting the described behavior is also said to exhibit “scale-free” fluctuations with a “power-law scaling exponent” H . H is the Hurst exponent [41] and ranges between 0 and 1. For signals with H approaching 1, the appearance is smooth, typically meaning that high values are followed by high values (or low values are followed by low values). This lack of independency over time implies that the time series is temporally correlated. In contrast, for signals with H close to 0, the appearance is rough and “hairy,” which typically means faster switching between high and low values.

Figure 13.1 The Roman cauliflower is a striking example of self-similarity in nature. (A) The cauliflower is composed of flowers that are similar to the entire cauliflower. These smaller flowers, in turn, are composed of flowers that are similar to the entire cauliflower or the intermediate flowers. The self-similarity is apparent on at least four levels of magnification, thereby illustrating the scale-free property that is a consequence of self-similarity. (a) A hypothetical distribution of the likelihood of flowers on a cauliflower having a certain size. This property is captured by the power-law function. The mean or median of a power law, however, provides a poor representation of the scale-free distribution (and in a mathematical sense is not defined). (b) The power-law function makes a straight line in double-logarithmic coordinates. The slope of this line is the exponent of the power law, which captures an important property of scale-free systems, namely, the relationship between the size of objects or fluctuations on different scales, that is, the slope between 1 and 10 is the same as the

slope between 100 and 1000 (both -1). (B) Time signals can also be viewed as self-affine as they can be transformed into a set of sine waves of different frequencies. In a $1/f$ signal, the lower frequency objects have larger amplitude than the higher frequency objects, which we can compare with there being fewer large cauliflowers than there are small cauliflowers. (C) As the size of apples shows smaller variation, they are well described by taking an average value such as the mean or median. (a) Hypothetical distribution showing the likelihood of apples having a certain size. Both the mean and median are good statistics to convey the size of the apples. (b) Plotting the normal distribution on double-logarithmic coordinates has little effect on the appearance of the distribution, which still shows a characteristic scale. (D) A white-noise signal is also self-affine, but now the lower frequency objects have the same amplitude as the higher frequency objects, meaning that only the high-frequency fluctuations are visible in the signal. (Modified from [33].)

The estimation of the scaling exponent is particularly interesting for neuronal oscillation dynamics, because it can reveal the presence of LRTCs in neuronal network oscillations [11]. In the following sections, we show you how.

13.2.2

Stationary and Nonstationary Processes

Definition: A process $X(t)$ is stationary if the distribution of $X(t)$ is independent of t , the joint distribution of $X(t_1 + \tau)$ and $X(t_2 + \tau)$ is independent of τ and similarly – for all k – for the joint distributions of $X(t_1 + \tau) \dots X(t_k + \tau)$ [42].

When performing scale-free analysis of a time series, it is essential to have a model of whether the underlying process is stationary. This is because many of the methods used on a time series to estimate H make assumptions about whether the process is stationary or not. For example, self-affinity as described only applies to nonstationary processes, because by definition the variance of a stationary process does not alter with the amount of time looked at [40].

Nevertheless, scale-free processes that are stationary also exist and can be modeled as so-called fractional Gaussian noise (fGn), whereas nonstationary processes are modeled as fractional Brownian motion (fBm). There is an important relationship, however, between these two types of processes in that, by definition, the increments of a fBm process are modeled as an fGn process with the same Hurst exponent; for more details on these models, see [38, 42]. This relationship allows us to apply the definition of self-affinity given here to a stationary fGn process, by first converting it into its nonstationary fBm equivalent as follows. Given the time series $y(t)$, we define the *signal profile* as the cumulative sum of the signal:

$$x(t) = \sum_{k=1}^t y(k) - \langle y \rangle \quad (13.2)$$

where $\langle y \rangle$ is the mean of the time series. The subtraction of the mean eliminates the global trend of the signal. The advantage of applying scaling analysis to the signal profile instead of the signal is that it makes no *a priori* assumptions about the stationarity of the signal. When computing the scaling of the signal profile (as explained subsequently), the resulting scaling exponent, α , is an estimation of H . If α is between 0 and 1, then x was produced by a stationary process, which can be modeled as an fGn process with $H=\alpha$. If α is between 1 and 2, then x was produced by a nonstationary process, and $H=\alpha-1$ [38].

13.2.3

Scaling of an Uncorrelated Stationary Process

We now show that the scaling of a so-called random-walk process can be used to infer whether a time series is uncorrelated. A random walk is a nonstationary probabilistic process derived from the cumulative sum of independent random variables, where each variable has equal probability to take a value of 1 or -1 .

Imagine a walker that at each time step can either take one step left (-1) or right ($+1$) with equal probabilities. The sequence of the steps representing independent random variables forms a stationary time series as it can only take two values, which do not depend on time. If we calculate the standard deviation of this time series for differently sized time windows, we will not see a scaling effect as there will always on average be an equal number of 1 's and -1 's. As the probability of taking either action does not depend on any previous actions, the process is said to be “*memory-less*.”

Now, if we compute the cumulative sum of this time series, using Eq. (13.2) to obtaining the random walk, we can calculate the distance that the walker deviates from the zero line where it started (following a given number of steps). This distance changes with the number of steps that the walker has taken. Therefore, it is possible to calculate how the standard deviation of distance from the origin (referred to as *random-walk fluctuations*) changes depending on the number of steps that the walker has taken.

We can calculate this by working out the relationship between the displacement, x , at time t and time $t + 1$. If at time t the walker is at position x_t then at time $t + 1$ the walker will be at position $x_t - 1$ or $x_t + 1$ with equal likelihood. Therefore, we can calculate the mean square displacement at time $t + 1$:

$$\begin{aligned}\langle x_{t+1}^2 \rangle &= \frac{\langle (x_t + 1)^2 + (x_t - 1)^2 \rangle}{2} = \frac{\langle x_t^2 + 2x_t + 1 + x_t^2 - 2x_t + 1 \rangle}{2} \\ \langle x_{t+1}^2 \rangle &= \frac{2\langle x_t^2 \rangle + 2}{2} = \langle x_t^2 + 1 \rangle\end{aligned}\tag{13.3}$$

Let us define the starting position to be 0, that is, the mean square displacement at time 0 is

$$\langle x_0^2 \rangle = 0$$

Now, we can calculate the mean square displacement after an arbitrary number of steps by applying Eq. (13.3) iteratively:

$$\begin{aligned}\langle x_1^2 \rangle &= \langle x_0^2 \rangle + 1 = 0 + 1 = 1 \\ \langle x_2^2 \rangle &= \langle x_1^2 \rangle + 1 = 1 + 1 = 2 \\ \langle x_3^2 \rangle &= \langle x_2^2 \rangle + 1 = 2 + 1 = 3 \\ &\vdots \\ \langle x_L^2 \rangle &= L\end{aligned}$$

Thus, the mean square displacement after a walk of L steps is L , or equivalently, the root-mean-square displacement after L steps is the square root of L :

$$(\langle x_L^2 \rangle)^{0.5} = L^{0.5}\tag{13.4}$$

For a zero-mean signal, x , the root-mean-square displacement is the standard deviation. Thus, the cumulative sum of a randomly fluctuating zero-mean signal will have the standard deviation growing with window length, L , according to a

power law with the exponent of 0.5. Now, recall from Eq. (13.1) that if the standard deviation of a signal scales by a factor L^H according to the length of the signal, L , then the process exhibits self-affinity with Hurst exponent H . Thus, we have derived that a stationary randomly fluctuating process has a signal profile, which is self-affine with a scaling exponent $\alpha = 0.5$.

13.2.4

Scaling of Correlated and Anticorrelated Signals

What happens to the self-affinity of a process when we add memory in the sense that the probability of an action depends on the previous actions that the walker has made? Different classes of processes with memory exist. Let us focus on those with positive correlations and those with anticorrelations. Anticorrelations can be seen as a stabilizing mechanism: any action the walker makes means that when taking future actions the walker will be more likely to take the opposite action (Figure 13.2A-a). This leads to smaller fluctuations on longer timescales than seen by chance (Figure 13.2B). Positive correlations have the opposite effect: Any action the walker takes makes it more likely to take that action in the future (Figure 13.2A-c). This leads to large fluctuations in the integrated signal (Figure 13.2B). We define a fluctuation function as the standard deviation of the signal profile:

$$f(L) = (\langle x_L^2 \rangle)^{0.5} = L^\alpha \quad (13.5)$$

We note from Eq. (13.4) that this function grows as a power law with scaling exponent $\alpha = 0.5$ for a stationary random signal. Using Eq. (13.5) – and as shown in Figure 13.2C – it follows that if the fluctuations scale according to time with:

- $0 < \alpha < 0.5$ then the process has a memory, and it exhibits anticorrelations (can be modeled by fGn with $H = \alpha$).
- $0.5 < \alpha < 1$ then the process has a memory, and it exhibits positive correlations (can be modeled by fGn with $H = \alpha$).
- $\alpha = 0.5$ then the process is indistinguishable from a random process with no memory (can be modeled by fGn with $H = \alpha$).
- $1 < \alpha < 2$ then the process is nonstationary (can be modeled as a fBm with $H = \alpha - 1$).

For short-range correlations, the scaling exponent will deviate from 0.5 only for short window sizes, because the standard deviation of the integrated signal in long windows will be dominated by fluctuations that have no dependence on each other. Thus, it is important to report the range where the scaling is observed. We return to the practical issues of identifying the scaling range in the section on “Insights from the application of DFA to neuronal oscillations.”

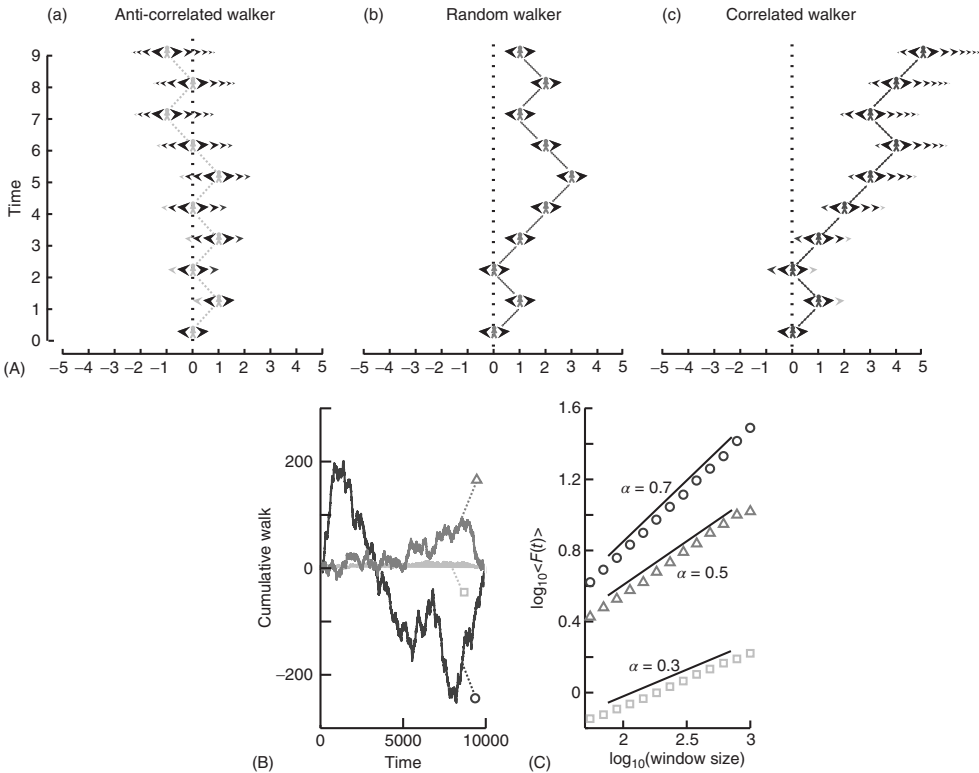


Figure 13.2 Processes with a memory produce qualitatively, and quantitatively, different fluctuations compared to a random-walk process. (A) Correlations occur when the “walker’s” decision to follow a certain direction is influenced by its past actions. (a) Path of an anticorrelated walker shown over time. At each time step, the walker makes a decision based on a weighted choice between left and right. The weighted choice can be seen by the sum of the areas of the arrows pointing left and right. Each action the walker takes continues to influence future actions, with the walker being more likely to take the opposite action. This is illustrated as a gradual accumulation of arrows that refer to past actions, but also decrease in size over time, because the bias contributions of those actions decay over time. The light gray arrows show how the first action the walker takes (going right) persists over time, with the influence getting smaller as time goes on seen by the dark arrow size decreasing. (b) Path of a random walker shown

over time. The random walker is not influenced by previous actions and so always has equal probability of going left or right. (c) Path of a correlated walker shown over time. Here, each action the walker takes influences future actions by making the walker more likely to take that action. The light gray shows that by taking the action of going right at time 0, the walker is more likely to go right in future time steps with the influence getting smaller as time goes on. (B) Cumulative signal for a positively correlated process (dark gray, circle) shows larger fluctuations over time than a random walker (gray, triangle). An anticorrelated signal (light gray, square) shows smaller fluctuations over time. (C) By looking at the average fluctuations for these different processes at different timescales, we can quantify this difference. A random walker shows a scaling exponent of 0.5, with the positively correlated process having a larger exponent, and the anticorrelated process having a smaller exponent. (Modified from [33].)

13.3

The Detrended Fluctuation Analysis (DFA)

We have seen that calculating the fluctuation of signal profiles in windows of different sizes can be used to quantify the scale-free nature of time series. However, calculating the fluctuations at a certain timescale is strongly influenced by whether the signal has a steady trend on longer timescales. This trend is unlikely to be part of a process on the timescale of that window and may be removed by subtracting the linear trend in the window, and then calculating the standard deviation. This way we know that processes on scales larger than the given window size will only marginally influence the fluctuation function, Eq. (13.5).

The idea to remove the linear trend was introduced by Peng *et al.* [43] as DFA with less strict assumptions about the stationarity of the signal than the autocorrelation function. Since then, the algorithm has been applied in more than a 1000 studies, and it is one of the most commonly used methods to quantify the scale-free nature of physiological time series and their alteration in disease [34, 44, 45]. The DFA is based on the rationale described in the sections presented so far, and can be summarized as follows:

- 1) Compute the cumulative sum of the time series (Figure 13.3a) to create the signal profile (Figure 13.3b).
- 2) Define a set of window sizes, T , which are equally spaced on a logarithmic scale between the lower bound of four samples [43] and the length of the signal.
 - a. For each window length $\tau \in T$
 - (i) Split the signal profile into a set (W) of separate time series of length t , which have 50% overlap.
 - (ii) For each window $w \in W$
 - A. Remove the linear trend (using a least-squares fit) from the time series (Figure 13.3c) to create w^{detrend} (Figure 13.3d)
 - B. Calculate the standard deviation of the detrended signal, $\sigma(w^{\text{detrend}})$
 - (iii) Compute fluctuation function as the mean standard deviation of all identically sized windows: $\langle F(t) \rangle = \text{mean}(\sigma(W))$
 - 3) Plot the fluctuation function for all window sizes, T , on logarithmic axes (Figure 13.3e).
 - 4) The DFA exponent, α , is the slope of the trend line in the range of timescales of interest and can be estimated using linear regression (Figure 13.3e).

Here, we have chosen logarithmically spaced window sizes, because it gives equal weight to all timescales when we fit a line in log–log coordinates using linear regression. The lower end of the fitting range is at least four samples, because linear detrending will perform poorly with less points [43]. For the high end of the fitting range, DFA estimates for window sizes $>10\%$ of the signal length are more noisy because of a low number of windows available for averaging (i.e., less than 10 windows). Finally, the 50% overlap between windows is commonly used to increase the number of windows, which can provide a more accurate estimate of the fluctuation function especially for the long-time-scale windows.

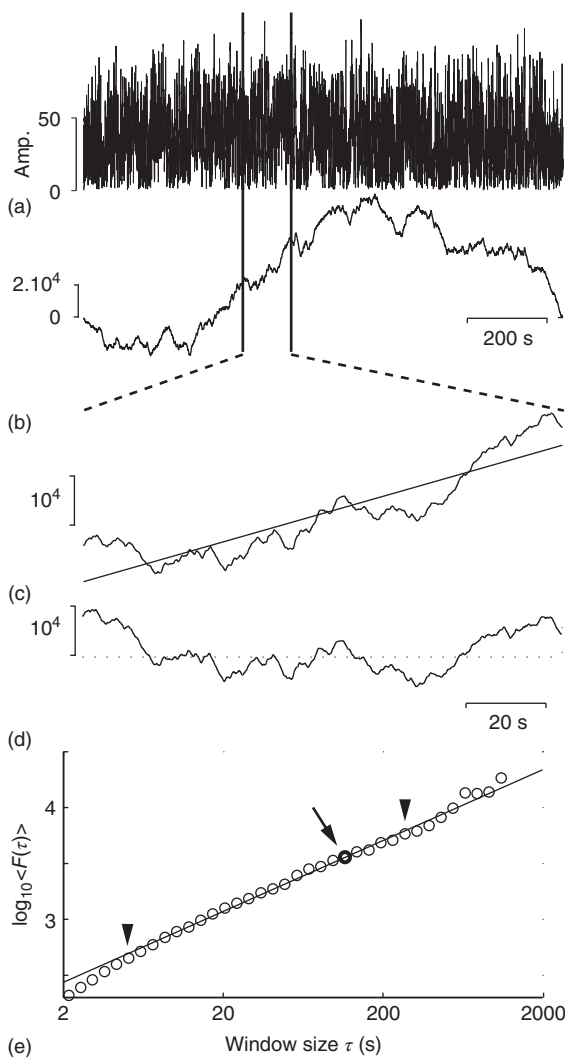


Figure 13.3 Step-wise explanation of detrended fluctuation analysis. (a) Time series with a sampling rate of 300 Hz and a duration of 1200 s. (b) Cumulative sum of signal shows large fluctuations away from the mean. (c) For each window looked at, calculate the linear trend (straight line). (d)

Fluctuation is calculated on the window after removing the linear trend. (e) Plot the mean fluctuation per window size against window size on logarithmic axes. The DFA exponent is the slope of the best-fit line. (Modified from [11].)

The DFA exponent is interpreted as an estimation of the Hurst exponent, as explained with the random-walker example, that is, the time series is uncorrelated if $\alpha = 0.5$. If $0.5 < \alpha < 1$, then there are positive correlations present in the time series as you are getting larger fluctuations on longer timescales than expected by chance. If $\alpha < 0.5$, then the time series is anticorrelated, which means that fluctuations are smaller in larger time windows than expected by chance.

Since DFA was first introduced, several papers have validated the robust performance of DFA in relation to trends [46], nonstationarities [47], preprocessing such as artifact rejection [47], and coarse graining [48].

13.4

DFA Applied to Neuronal Oscillations

Synchronized activity between groups of neurons occurs in a range of frequencies spanning at least four orders of magnitude from 0.01 to 100 Hz [10]. The power spectral density plotted on double-logarithmic axes roughly follows a power-law distribution, but there may also be several “peaks” seen along it, corresponding to the classical frequency bands (e.g., θ , α , β , etc.). In this section, we describe how to apply DFA analysis to the amplitude modulation in these frequency bands, and show how they have been utilized in quantifying healthy and pathological conditions. We cannot apply DFA directly to the band-pass-filtered signal, because it will appear as a strongly anticorrelated signal because of the peaks and troughs averaging out when computing the cumulative sum. Instead, we focus on the amplitude envelope of oscillations.

The method consists of four steps:

- 1) *Preprocess the signals.*
- 2) *Create band-pass filter* for the frequency band of interest.
- 3) *Extract the amplitude envelope and perform DFA.*
- 4) *Determine the temporal integration effect of the filter* to choose the window sizes for calculating the DFA exponent.

13.4.1

Preprocessing of Signals

Sharp transient artifacts are common in EEG signals. These large jumps in the EEG signal on multiple channels are, for example, caused by electrode movement. Leaving these in the signal is likely to affect the DFA estimates, whereas removing them has little effect on the estimated exponent [47]. Other artifacts from, for example, eye movement, respiration, and heartbeat are also likely to disturb the estimate and are better removed. Another factor that can influence the DFA estimate is the signal-to-noise ratio (SNR) of the signal. The lower this ratio, the more biased the estimated scaling is toward an uncorrelated signal. Simulations indicated that a $\text{SNR} > 2$ is sufficient to accurately determine LRTC [32].

13.4.2 Filter Design

To filter the EEG/MEG data (Figure 13.4A), we use a band-pass finite-impulse-response (FIR) filter. This is used instead of an infinite impulse response (IIR) filter to avoid introducing long-range correlations in the signal before calculating the fluctuation function. The filter order for the FIR filter is recommended to be set to two cycles of the lowest frequency in order to accurately detect the oscillations while also limiting the temporal integration caused by the filter. In Figure 13.4B we can see a clear peak in the α -band frequency range (8–13 Hz) and, therefore, we would band-pass filter in this frequency range with a filter order set to two cycles of 8 Hz.

13.4.3 Extract the Amplitude Envelope and Perform DFA

When applying DFA to neuronal oscillations, we are interested in how the amplitude of an oscillation changes over time. To calculate this, we extract the amplitude envelope from the filtered signal by taking the absolute value of the Hilbert transform (Figure 13.4C) [49]. The Hilbert transform is easily accessible in most programming languages (e.g., `scipy.signal.Hilbert` in Python (Scipy), `Hilbert` in Matlab). Wavelet transforms, however, have also been used to extract the amplitude envelope [11]. Once you have the amplitude envelope, you can perform DFA on it (Figure 13.4E). However, to decide which window sizes to calculate the exponent from, you first need to follow step 4.

13.4.4 Determining the Temporal Integration Effect of the Filter

Filtering introduces correlation in the signal between the neighboring samples (e.g., owing to the convolution in case of FIR filtering). Thus, including very small window sizes in the fitting range of the fluctuation function will lead to an overestimation of temporal correlations (Figure 13.4D). The effect of a specific filter on the DFA may be estimated using white-noise signals (where a DFA exponent of 0.5 is expected) [50]:

13.5 Insights from the Application of DFA to Neuronal Oscillations

The discovery of LRTCs in the amplitude envelope of ongoing oscillations was based on 20 min recordings of EEG and MEG during eyes-closed and eyes-open rest [11]. In both conditions, amplitude envelopes of α and β oscillations exhibited power-law scaling behavior on timescales of 5–300 s with DFA exponents significantly higher than for band-pass-filtered white noise. These results were further validated

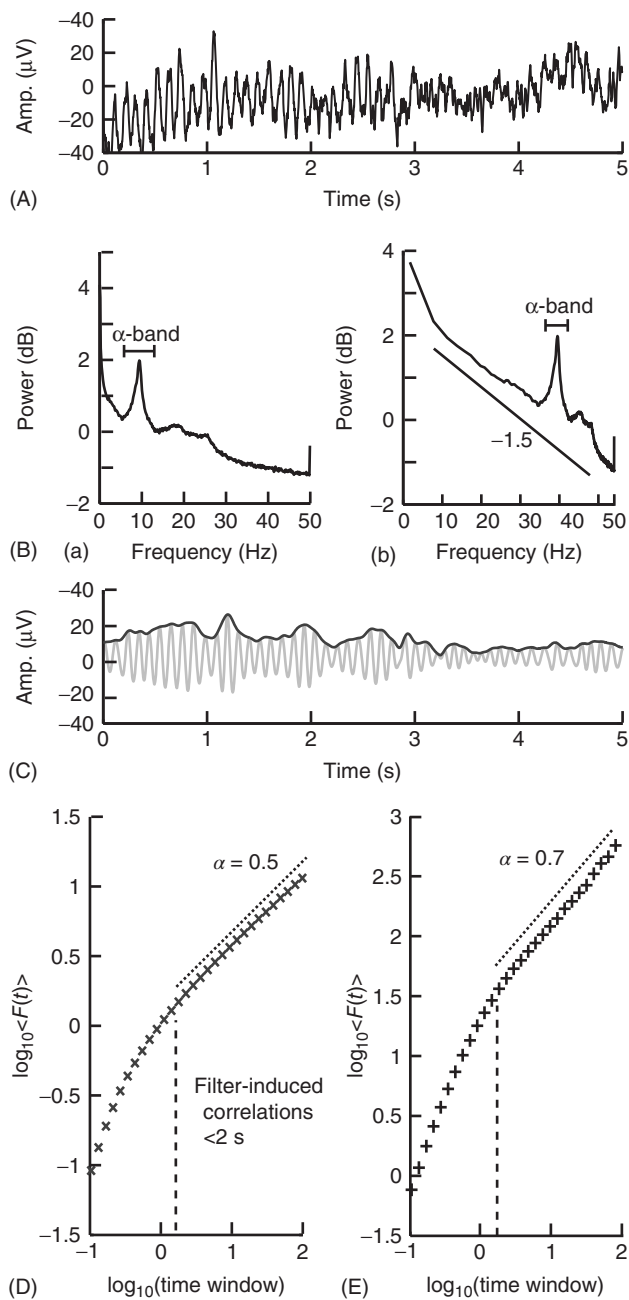


Figure 13.4 Step-wise explanation of applying DFA to neuronal oscillations. (A) EEG recording from electrode Oz shows clear oscillations during a 15 min eyes-closed rest session. Data were recorded at 250 Hz and band-passed filtered between 0.1 and 200 Hz. (B) Power spectrum (Welch method, zero padded) shown in logarithmic (a) and double-logarithmic axes (b), shows clear peak in the α band. (C) Signal in (A) filtered in the α band (8–13 Hz) using an FIR filter with an order corresponding to

the length of two 8 Hz cycles (light gray). Amplitude envelope (black) calculated using the Hilbert transform. (D) DFA applied to the amplitude envelope of white-noise signal filtered using the same filter as in (C). At time windows <2 s, filter-induced correlations are visible through a bend away from the 0.5 slope. (E) DFA applied to the amplitude envelope of the α -band-filtered EEG signal shows long-range temporal correlations between 2 and 90 s with exponent $\alpha = 0.71$. (Modified from [33].)

by showing $1/f$ power spectra and a power-law decay in the autocorrelation function.

The robustness of LRTC in ongoing oscillations has been confirmed in several follow-up studies, albeit often based on shorter experiments and scaling analysis in the range of about 1–25 s [29, 32, 51, 52]. The power-law scaling behavior in the θ band is reported less often [52], and, to our knowledge, LRTC in the delta band have only been investigated in subdural EEG [29]. LRTC have also not been reported often in the gamma band owing to the low SNR obtained from EEG/MEG recordings in this band. Invasive recordings in nonhuman primates, however, have reported $1/f$ spectra for the amplitude modulation in both low and high gamma bands [53]. Recordings from the subthalamic nucleus in Parkinson patients even show prominent LRTC in the very high-frequency gamma range (>200 Hz), especially when treated with the dopamine-precursor drug Levodopa [54].

To gain validity for LRTC, it has been shown that LRTC have a link to the underlying genetics of the subject. This link was provided in [32] where the scaling of eyes-closed rest EEG from monozygotic and dizygotic twin subjects ($n = 368$) showed that ~60% of the variance of DFA exponents in the α - and β -frequency bands is attributable to genetic factors (Figure 13.5a–e). This was an important result as it clearly showed that the nonrandom patterns of fluctuations in the ongoing oscillations are governed by low-level biological factors as opposed to uncontrolled experimental variables during the recording sessions. The finding also provides an explanation of the significant test-retest reliability of DFA exponents [50].

Several studies have reported that DFA exponents of neuronal oscillations are independent of oscillation power for a given frequency band, both when the oscillations are recorded with subdural EEG [29] and scalp EEG [32, 52] (Figure 13.5f). These results together indicate that the DFA can be used as a robust measure of oscillatory dynamics, which captures features of brain activity different from those seen in classical analysis such as power in a frequency band.

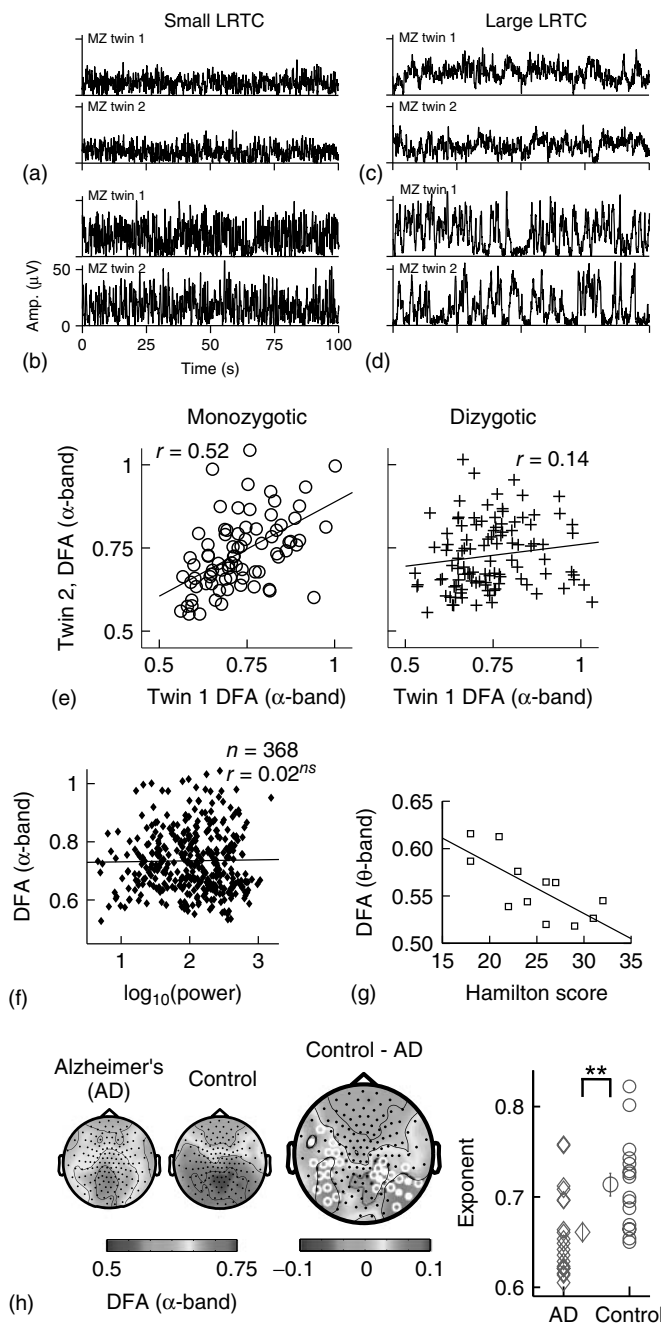


Figure 13.5 Results of applying DFA to neuronal oscillations. (a–d) Individual differences in long-range temporal correlations in α oscillations are, to a large extent, accounted for by genetic variation, which can be seen qualitatively by looking at four sets of monozygotic twins. (Figure modified from [32].) (e) The effect of genetic variation on LRTC can be quantified by the difference in correlations of DFA exponents between monozygotic and dizygotic twins. (Figure modified from [32].) (f) The DFA exponent is independent of oscillation power. Data were recorded using EEG on 368 subjects during a 3 min eyes-closed rest session. (Figure modified from [32].) (g) DFA exponents of θ oscillations in the left sensorimotor region correlate with the

severity of depression based on the Hamilton score. Data recorded from 12 depressed patients with MEG, during an eyes-closed rest session of 16 minutes. (Figure modified from [55].) (h) DFA of α oscillations shows a significant decrease in the parietal area in patients with Alzheimer's disease than in controls. MEG was recorded during 4 min of eyes-closed rest and the DFA exponent estimated in the time range of 1–25 s. (Right) Individual-subject DFA exponents averaged across significant channels are shown for the patients diagnosed with early-stage Alzheimer's disease ($n=19$) and the age-matched control subjects ($n=16$). (Figure modified from [56].) (Please find a color version of this figure on the color plates.)

13.5.1

DFA as a Biomarker of Neurophysiological Disorder

We have so far discussed the results of applying DFA to healthy subjects; however, some of the most exciting results have come from preclinical studies, which indicate possible functional roles for LRTC. For example, a breakdown of LRTC in the amplitude fluctuations of resting-state θ oscillations detected in the left sensorimotor region was reported for patients with major depressive disorder [55]. Interestingly, the severity of depression, as measured by the Hamilton depression rating scale, inversely correlated with the DFA exponent of the patients (Figure 13.5g). Reduction in the LRTC of oscillations has also been reported in the α band in the parietal region in patients with Alzheimer's disease [56] (Figure 13.5h). Furthermore, reduction in the α and β bands in the centroparietal and frontocentral areas has also been reported for patients with schizophrenia [57].

Interestingly, it seems as though it is not only a loss of LRTC that correlates with disorders but also elevated levels of LRTC. Monto *et al.* [29] looked at different scales of neuronal activity by using subdural EEG to record the areas surrounding an epileptic focus in five patients during ongoing seizure-free activity. They discovered that the LRTC are abnormally strong near the seizure-onset zone. Further, it was shown that administration of the benzodiazepine lorazepam to the patients leads to decreased DFA exponents in the epileptic focus, suggesting that the pharmacological normalization of seizure activity brings with it also a normalization of LRTC. Interestingly, however, DFA exponents were observed to increase in the seizure-free surrounding areas, which may correspond to the increase in LRTC observed *in vitro* after application of Zolpidem, which is also a GABAergic modulator [58].

Overall, these studies seem to indicate that there is an optimal level of temporal structure of oscillations and any deviation from this can result in a significant loss of function. Importantly, early studies have estimated the DFA exponent from the scaling of the fluctuation function across almost two orders of magnitude in time [11, 29, 59, 60], whereas most reports have used one decade of fitting range and found the DFA a very useful biomarker to study neuronal dynamics in health and disease.

13.6

Scaling Behavior of Oscillations: a Sign of Criticality?

The LRTCs in neuronal oscillations reviewed in the previous sections have often been suggested to reflect neuronal networks operating in a critical state. Critical dynamics of oscillatory networks, however, would ideally be accompanied by scale-free spatial distributions of neuronal activation patterns. To investigate this, Poil *et al.* [61] have modeled a generic network of excitatory and inhibitory neurons in which the local connectivities could be varied systematically.

13.6.1

CRitical OScillations Model (CROS)

The networks consisted of excitatory (75%) and inhibitory (25%) neurons arranged in an open grid, with local functional connectivity (Figure 13.6a). To define the local connectivity, each neuron was given a square area that marked the limits of being able to connect to other neurons. The connectivity probability for excitatory and inhibitory neurons was varied independently and is defined as the percentage of neurons that a neuron connects to within its local range. In neocortical tissue, local functional connectivity between neurons decays with distance; however, only a few empirical reports have assessed this quantitatively [62, 63]. Given the small radius of connectivity, this was implemented as an exponential decay.

Five networks were created for each combination of excitatory and inhibitory connectivity and each of these networks were simulated for 1000 s. The weights of these connections were dependent on the type (excitatory or inhibitory) of the presynaptic and postsynaptic neuron (Figure 13.6b), but were otherwise fixed in order to limit the number of free model parameters.

Neurons were modeled using a synaptic model integrating received spikes, and a probabilistic spiking model (Figure 13.6c). Each time step started with every neuron updating its synaptic model with received input. The spiking model is then updated by the synaptic model. On the basis of the spiking model, it is determined whether each neuron spikes. If a neuron spikes, the probability of spiking is reset, and this models a refractory period for the neuron. All neurons it connects to will receive an input from this neuron during the next time step.

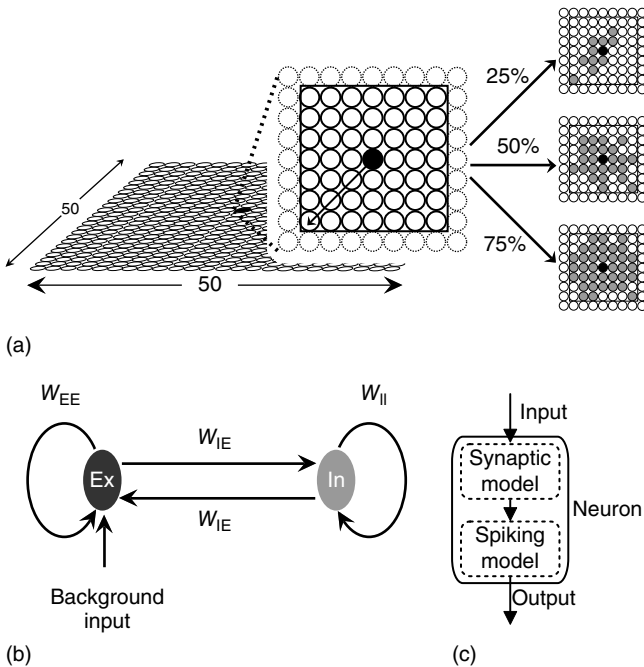


Figure 13.6 Structure of CROS model. (a) Neurons are situated in a 2D grid. A neuron (filled black circle) is connected in a local range (black box). Connectivity is defined as the percentage of connected neurons within this range. Shown in light gray to the right are the target neurons of example neurons with connectivity of 25% (top), 50%

(middle), and 75% (bottom). (b) The network contains excitatory (Ex) and inhibitory (In) neurons, with connection weights (W_{ji}) fixed depending on the type of the spiking (i) and receiving (j) neuron. (c) Each neuron consists of a synaptic model to integrate received spikes, and a spiking model. (Modified from [61].)

13.6.2

CROS Produces Neuronal Avalanches with Balanced Ex/In Connectivity

The model displayed many forms of activity propagation depending on the excitatory/inhibitory connectivity ratio (Ex/In balance). This is illustrated in Figure 13.7A, where the temporal dynamics of activity propagation can be inferred from the color scale, indicating the time since a given neuron spiked. For the networks with a low Ex/In balance, the activity was characterized by localized wavelike spreading (Figure 13.7A-a). The propagation stops because of the strong local inhibition. With increasing Ex/In balance, the waves were able to spread further until they were able to reach across the entire network. In these networks, sustained activity patterns were possible (Figure 13.7A-b), with complex patterns such as spiral waves repeating themselves several times. These patterns would eventually dissipate with the network, either going through a period of low activity similar to the low Ex/In balance case or the network would become highly active and lose any spatially

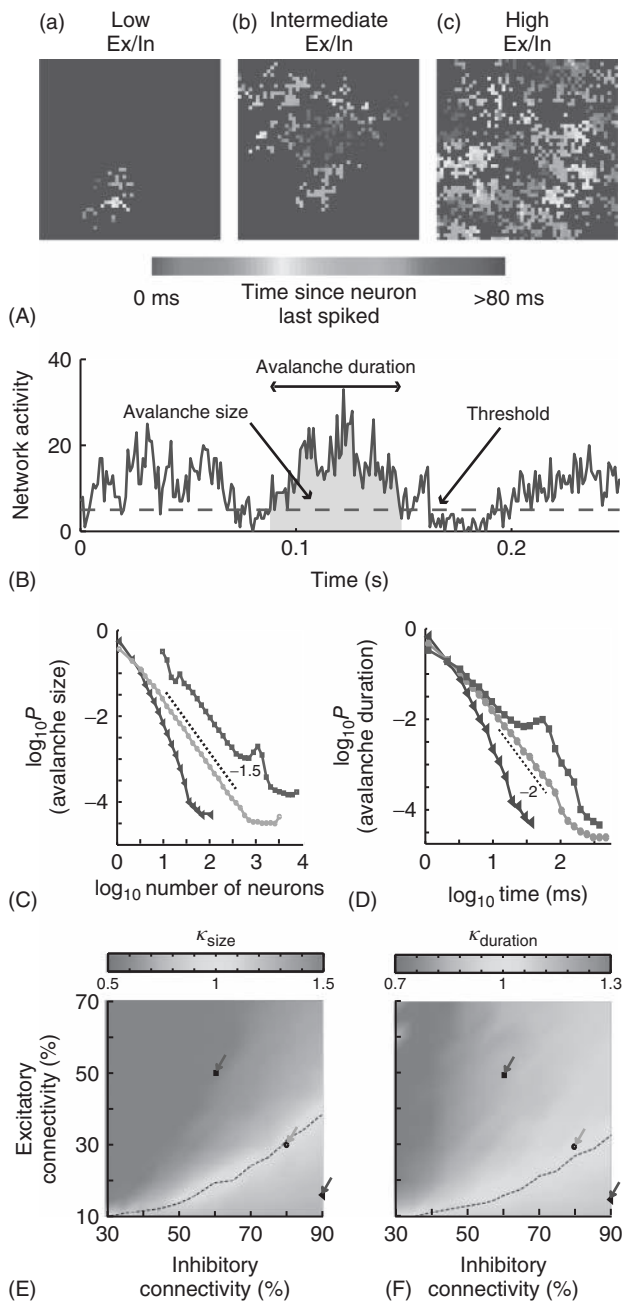


Figure 13.7 On short timescales (120 ms), activity spreads in the form of neuronal avalanches. (A) Example snapshot of network activity for three networks with different excitatory (Ex)/inhibitory (In) connectivity balance (Ex/In balance). Colors indicate the time since each neuron last spiked. (a) Networks with low Ex/In balance show wavelike propagation over short distances. (b) Networks with intermediate Ex/In balance often display patterns that are able to span the network and repeat. (c) Networks with high Ex/In balance have high network activity, but have little spatial coherence in their activity patterns. (B) An avalanche starts and ends when integrated network activity crosses a threshold value. (C) The avalanche-size distribution shows power-law scaling in the transition region (green circles) with a slope of -1.5 (dashed line). The subcritical region has an exponential distribution

(blue triangles). The supercritical region (red squares) has a clear characteristic scale. (D) The avalanche-size distribution shows power-law scaling in the transition region (green circles) with a slope of -2 (dashed line). The subcritical region has an exponential distribution (blue triangles). The supercritical region (red squares) has a clear characteristic scale. (E) The connectivity-parameter space shows a transition (dashed black line) from subcritical (blue) to supercritical (red) avalanches. Arrows indicate the connectivity parameters of networks in (C). (F) The connectivity-parameter space shows a transition (dashed black line) from subcritical (blue) to supercritical (red) avalanches. Arrows indicate the connectivity parameters of networks in (D). (Modified from [61].) (Please find a color version of this figure on the color plates.)

contiguous patterns. This highly active state is characteristic of the networks with a high Ex/In balance (Figure 13.7A-c).

The propagation of activity in the network was quantified using the concept of neuronal avalanches (Figure 13.7B), which have been reported for local field potential recordings *in vitro* [12] and *in vivo* [19]. The size of an avalanche is the total number of spikes during the avalanche, and the duration is the time spent with above-threshold activity. The size distributions were characterized using the statistical measure κ , which was developed by [64]. In agreement with visual inspection of the distributions, κ indicated that the model could produce subcritical, critical, or supercritical dynamics depending on the connectivity parameters (Figure 13.7C–F). The subcritical regime ($\kappa < 1$) had exponentially decaying avalanche sizes, the supercritical regime ($\kappa > 1$) had a characteristic scale indicated by the bump at large avalanche sizes, and power-law scaling extended up to the system size in the transition regime ($\kappa \approx 1$).

13.6.3

CROS Produces Oscillations with LRTC When there are Neuronal Avalanches

On longer timescales (>120 ms), the progression of these avalanches gave the spatially integrated network activity a distinct oscillatory character (Figure 13.8A,B), which was qualitatively similar to what is typically observed in recordings of human resting-state MEG (Figure 13.8C) [59, 18]. Most network configurations produced 8–16 Hz oscillations (Figure 13.8D). To quantitatively assess scaling behavior on the level of oscillations, the waxing and waning of the oscillations (Figure 13.8B) were analyzed on the long timescales of 2–10 s using DFA (Figure 13.8E). In the model, DFA revealed a critical regime of strong temporal correlations ($\alpha = 1.0$), whereas

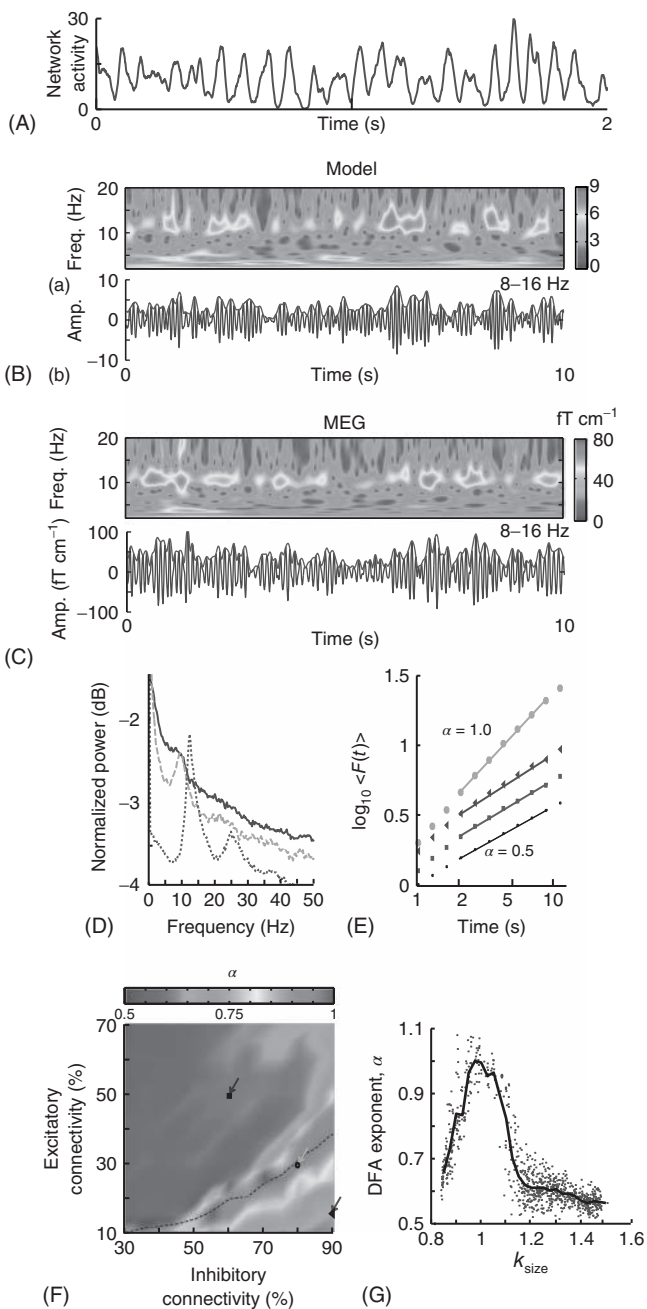


Figure 13.8 On long timescales (>2 s), the model produces oscillations qualitatively and quantitatively similar to human α -band oscillations. A: The spatially integrated network activity in a sliding window of 10 ms displays oscillatory variation. B: (a) Time-frequency plot of the integrated network activity from a network with 50% excitatory and 90% inhibitory connectivity. (b) Integrated network activity filtered at 8–16 Hz (blue), and the amplitude envelope (red). C: The same plots as in (B), but for a representative subject and MEG planar gradiometer above the parietal region. D: Power spectrum of the integrated network activity shows a clear peak frequency at ~ 10 Hz for three networks with Excitatory:Inhibitory connectivity of 50%:60% (red), 30%:80%

(green), and 15%:90% (blue), respectively. E: DFA in double-logarithmic coordinates shows power-law scaling in the critical regime with $\alpha=0.9$ (green circles). The subcritical ($\alpha=0.6$, blue triangles) and supercritical ($\alpha=0.6$, red squares) regimes display similar correlations to a random signal (black dots). F: The connectivity-parameter space shows a clear peak region with stronger long-range temporal correlations. Overlaying the transition line from Figure 13.7E indicates that peak DFA occurs at $\kappa \sim 1$. G: DFA exponents peak when the networks produce neuronal avalanches with critical exponents ($\kappa \sim 1$). (Modified from [61].) (Please find a color version of this figure on the color plates.)

a relative increase in either inhibitory or excitatory connectivity led to reduced temporal correlations ($\alpha=0.6$), similar to those of filtered white noise ($\alpha=0.5$, Figure 13.8F). Interestingly, the binned averages of DFA exponents peaked when the network produced critical avalanches, with the correlations decreasing for the more subcritical or supercritical avalanches (Figure 13.8G). Taken together, the data indicated that nontrivial scaling behavior in the modulation of oscillatory activity can emerge on much longer timescales than those implemented in the model, and that neuronal avalanches may be viewed as the building blocks of neuronal oscillations with scale-free amplitude modulation.

13.6.4

Multilevel Criticality: A New Class of Dynamical Systems?

The concept of multilevel criticality was proposed [61] to denote the phenomenon of critical behavior on multiple levels. Multilevel criticality may define a new class of dynamical systems, because it allows for criticality to emerge jointly on multiple levels separated by a characteristic scale, which is traditionally considered contradictory for critical dynamics.

The restricted spreading of activity in CRitical OScillations (CROS) seems essential for build up of temporal autocorrelations and criticality, as it allows clusters of nonexcitable and excitable neurons to form. These clusters act as memories of past activity, shaping the path of future activity analogously to a river's flow being shaped by the past flow of water [3, 65]. A recent study of model networks showed that a hierarchical topology can increase the range of parameters that give rise to critical dynamics – and thereby also the robustness of a critical state – because the modular topology limits activity spreading to local parts of the network [66]. Similarly, a localized topology is likely to support the emergence of oscillations with LRTCs.

Future research should address how multilevel criticality affects neuronal network properties such as its information processing capabilities, reactivity, ability to transiently synchronize with other networks, the importance of synaptic plasticity for these functional states to emerge and how memories are encoded, maintained, or lost in such networks.

Acknowledgment

The authors thank all the coworkers on the studies reviewed in the present chapter. In particular, Simon-Shlomo Poil, Teresa Montez, Giuseppina Schiavone, Rick Jansen, Vadim V. Nikulin, Dirk Smit, and Matias Palva.

References

1. Gilden, D.L. (2001) Cognitive emissions of 1/f noise. *Psychol. Rev.*, **108** (1), 33–56.
2. Bassingthwaite, J.B., Liebovitch, L.S. *et al.* (1994) *Fractal Physiology*, American Physiological Society by Oxford University Press, New York.
3. Bak, P. (1999) *How Nature Works: The Science of Self-Organized Criticality*, Copernicus Press, New York.
4. Goldberger, A.L., Amaral, L.A.N. *et al.* (2002) Fractal dynamics in physiology: alterations with disease and aging. *Proc. Natl. Acad. Sci. U.S.A.*, **99**, 1.
5. Stam, C. (2005) Nonlinear dynamical analysis of EEG and MEG: review of an emerging field. *Clin. Neurophysiol.*, **116** (10), 2266–2301.
6. Ghosh, A., Rho, Y. *et al.* (2008) Noise during rest enables the exploration of the brain's dynamic repertoire. *PLoS Comput. Biol.*, **4** (10), e1000196.
7. He, B.J., Zempel, J.M. *et al.* (2010) The temporal structures and functional significance of scale-free brain activity. *Neuron*, **66** (3), 353–369.
8. West, B.J. (2010) Frontiers: fractal physiology and the fractional calculus: a perspective. *Front. Fractal Physiol.*, **1**, 12.
9. Fries, P. (2005) A mechanism for cognitive dynamics: neuronal communication through neuronal coherence. *Trends Cognit. Sci.*, **9** (10), 474.
10. Buzsáki, G. (2006) *Rhythms of the Brain*, Oxford University Press, New York.
11. Linkenkaer-Hansen, K., Nikouline, V.V. *et al.* (2001) Long-range temporal correlations and scaling behavior in human brain oscillations. *J. Neurosci.*, **21** (4), 1370.
12. Beggs, J.M. and Plenz, D. (2003) Neuronal avalanches in neocortical circuits. *J. Neurosci.*, **23** (35), 11167.
13. Halderman, C. and Beggs, J.M. (2005) Critical branching captures activity in living neural networks and maximizes the number of metastable states. *Phys. Rev. Lett.*, **94** (5), 58101.
14. Kinouchi, O. and Copelli, M. (2006) Optimal dynamical range of excitable networks at criticality. *Nat. Phys.*, **2** (5), 348–351.
15. Levina, A., Herrmann, J.M. *et al.* (2007) Dynamical synapses causing self-organized criticality in neural networks. *Nat. Phys.*, **3** (12), 857–860.
16. Plenz, D. and Thiagarajan, T.C. (2007) The organizing principles of neuronal avalanches: cell assemblies in the cortex? *Trends Neurosci.*, **30** (3), 101–110.
17. Gireesh, E.D. and Plenz, D. (2008) Neuronal avalanches organize as nested theta-and beta/gamma-oscillations during development of cortical layer 2/3. *Proc. Natl. Acad. Sci. U.S.A.*, **105** (21), 7576.
18. Poil, S., van Ooyen, A. *et al.* (2008) Avalanche dynamics of human brain oscillations: relation to critical branching

- processes and temporal correlations. *Hum. Brain Mapping*, **29** (7), 770.
19. Petermann, T., Thiagarajan, T.C. *et al.* (2009) Spontaneous cortical activity in awake monkeys composed of neuronal avalanches. *Proc. Natl. Acad. Sci.*, **106** (37), 15921.
 20. Chialvo, D.R. (2010) Emergent complex neural dynamics. *Nat. Phys.*, **6** (10), 744–750.
 21. Millman, D., Mihalas, S. *et al.* (2010) Self-organized criticality occurs in non-conservative neuronal networks during/up/'states. *Nat. Phys.*, **6** (10), 801–805.
 22. Rubinov, M., Sporns, O. *et al.* (2011) Neurobiologically realistic determinants of self-organized criticality in networks of spiking neurons. *PLoS Comput. Biol.*, **7** (6), e1002038.
 23. Bak, P., Tang, C. *et al.* (1987) Self-organized criticality: an explanation of the 1/f noise. *Phys. Rev. Lett.*, **59** (4), 381.
 24. Jensen, J. (1998). *Self-Organized Criticality*, H.J. Jensen, pp. 167, ISBN: 0521483719. Cambridge University Press: Cambridge, 1998.
 25. Beggs, J. (2008) The criticality hypothesis: how local cortical networks might optimize information processing. *Philos. Trans. Ser. A, Math. Phys. Eng. Sci.*, **366** (1864), 329.
 26. Shew, W.L., Yang, H. *et al.* (2011) Information capacity and transmission are maximized in balanced cortical networks with neuronal avalanches. *J. Neurosci.: Off. J. Soc. Neurosci.*, **31** (1), 55.
 27. Gong, P., Nikolaev, A. *et al.* (2003) Scale-invariant fluctuations of the dynamical synchronization in human brain electrical activity. *Neurosci. Lett.*, **336** (1), 33.
 28. Kitzbichler, M.G., Smith, M.L. *et al.* (2009) Broadband criticality of human brain network synchronization. *PLoS Comput. Biol.*, **5** (3), e1000314.
 29. Monto, S., Vanhatalo, S. *et al.* (2007) Epileptogenic neocortical networks are revealed by abnormal temporal dynamics in seizure-free subdural EEG. *Cereb. Cortex*, **17** (6), 1386.
 30. Atallah, B.V. and Scanziani, M. (2009) Instantaneous modulation of gamma oscillation frequency by balancing excitation with inhibition. *Neuron*, **62** (4), 566–577.
 31. Rangarajan, G. and Ding, M. (2000) Integrated approach to the assessment of long range correlation in time series data. *Phys. Rev. E*, **61** (5), 4991.
 32. Linkenkaer-Hansen, K., Smit, D.J.A. *et al.* (2007) Genetic contributions to long-range temporal correlations in ongoing oscillations. *J. Neurosci.*, **27** (50), 13882–13889.
 33. Hardstone, R., Poil, S.-S. *et al.* (2012) Detrended fluctuation analysis: a scale-free view on neuronal oscillations. *Front. Physiol.*, **3**.
 34. Peng, C., Havlin, S. *et al.* (1995) Quantification of scaling exponents and crossover phenomena in nonstationary heartbeat time series. *Chaos*, **5** (1), 82–87.
 35. Mandelbrot, B. (1967) How long is the coast of Britain? Statistical self-similarity and fractional dimension. *Science*, **156** (3775), 636.
 36. Turcotte, D.L. (1997) *Fractals and Chaos in Geology and Geophysics*, Cambridge University Press, Cambridge.
 37. Peitgen, H.O., Jurgens, H. *et al.* (1992) *Chaos and Fractals: New Frontiers of Science*, Springer, Berlin.
 38. Eke, A., Hermán, P. *et al.* (2000) Physiological time series: distinguishing fractal noises from motions. *Pflügers Arch.: Eur. J. Physiol.*, **439** (4), 403.
 39. Eke, A., Herman, P. *et al.* (2002) Fractal characterization of complexity in temporal physiological signals. *Physiol. Meas.*, **23**, R1.
 40. Beran, J. (1994) *Statistics for Long-memory Processes*, Chapman & Hall/CRC Press.
 41. Mandelbrot, B.B. and Wallis, J.R. (1969) Some long-run properties of geophysical records. *Water Resour. Res.*, **5** (2), 321–340.
 42. Mandelbrot, B.B. (1982) *The Fractal Geometry of Nature*, Times Books.
 43. Peng, C.K., Buldyrev, S.V. *et al.* (1994) Mosaic organization of DNA nucleotides. *Phys. Rev. E*, **49** (2), 1685.
 44. Castiglioni, P., Parati, G. *et al.* (2010) Scale exponents of blood pressure and heart rate during autonomic blockade

- as assessed by detrended fluctuation analysis. *J. Physiol.*, **589**, 355–369.
45. Frey, U., Maksym, G. *et al.* (2011) Temporal complexity in clinical manifestations of lung disease. *J. Appl. Physiol.*, **110** (6), 1723.
46. Hu, K., Ivanov, P.C. *et al.* (2001) Effect of trends on detrended fluctuation analysis. *Phys. Rev. E*, **64** (1), 011114.
47. Chen, Z., Ivanov, P.C. *et al.* (2002) Effect of nonstationarities on detrended fluctuation analysis. *Phys. Rev. E Stat. Nonlinear Soft Matter Phys.*, **65** (4 Pt 1), 041107.
48. Xu, Y., Ma, Q.D.Y. *et al.* (2011) Effects of coarse-graining on the scaling behavior of long-range correlated and anti-correlated signals. *Physica A: Stat. Mech. Appl.*, **390**, 4057–4072.
49. Nikulin, V.V. and Brismar, T. (2005) Long-range temporal correlations in electroencephalographic oscillations: relation to topography, frequency band, age and gender. *Neuroscience*, **130** (2), 549–558.
50. Nikulin, V.V. and Brismar, T. (2004) Long-range temporal correlations in alpha and beta oscillations: effect of arousal level and test-retest reliability. *Clin. Neurophys.*, **115** (8), 1896–1908.
51. Berthonouze, L., James, L.M. *et al.* (2010) Human EEG shows long-range temporal correlations of oscillation amplitude in theta, alpha and beta bands across a wide age range. *Clin. Neurophysiol.*, **121** (8), 1187–1197.
52. Smit, D.J.A., de Geus, E.J.C. *et al.* (2011) Scale-free modulation of resting-state neuronal oscillations reflects prolonged brain maturation in humans. *J. Neurosci.*, **31** (37), 13128–13136.
53. Leopold, D.A., Murayama, Y. *et al.* (2003) Very slow activity fluctuations in monkey visual cortex: implications for functional brain imaging. *Cereb. Cortex*, **13** (4), 422.
54. Hohlfeld, F.U., Huebl, J. *et al.* (2012) Long-range temporal correlations in the subthalamic nucleus of patients with Parkinson's disease. *Eur. J. Neurosci.*, **36**, 2812–2821.
55. Linkenkaer-Hansen, K., Monto, S. *et al.* (2005) Breakdown of long-range temporal correlations in theta oscillations in patients with major depressive disorder. *J. Neurosci.*, **25** (44), 10131–10137.
56. Montez, T., Poil, S.S. *et al.* (2009) Altered temporal correlations in parietal alpha and prefrontal theta oscillations in early-stage Alzheimer disease. *Proc. Natl. Acad. Sci. U.S.A.*, **106** (5), 1614.
57. Nikulin, V.V., Jönsson, E.G. *et al.* (2012) Attenuation of long range temporal correlations in the amplitude dynamics of alpha and beta neuronal oscillations in patients with schizophrenia. *Neuroimage*, **61**, 162–169.
58. Poil, S.S., Jansen, R. *et al.* (2011) Fast network oscillations in vitro exhibit a slow decay of temporal auto-correlations. *Eur. J. Neurosci.*, **34**, 394–403.
59. Linkenkaer-Hansen, K., Nikulin, V. *et al.* (2004) Stimulus-induced change in long-range temporal correlations and scaling behaviour of sensorimotor oscillations. *Eur. J. Neurosci.*, **19** (1), 203.
60. Parish, L., Worrell, G. *et al.* (2004) Long-range temporal correlations in epileptogenic and non-epileptogenic human hippocampus. *Neuroscience*, **125** (4), 1069–1076.
61. Poil, S.-S., Hardstone, R. *et al.* (2012) Critical-state dynamics of avalanches and oscillations jointly emerge from balanced excitation/inhibition in neuronal networks. *J. Neurosci.*, **32** (29), 9817–9823.
62. Holmgren, C., Harkany, T. *et al.* (2003) Pyramidal cell communication within local networks in layer 2/3 of rat neocortex. *J. Physiol.*, **551** (Pt 1), 139.
63. Sporns, O. and Zwi, J. (2004) The small world of the cerebral cortex. *Neuroinformatics*, **2** (2), 145.
64. Shew, W., Yang, H. *et al.* (2009) Neuronal avalanches imply maximum dynamic range in cortical networks at criticality. *J. Neurosci.: Off. J. Soc. Neurosci.*, **29** (49), 15595.
65. Chialvo, D.R. and Bak, P. (1999) Learning from mistakes. *Neuroscience*, **90** (4), 1137–1148.
66. Wang, S.J. and Zhou, C. (2012) Hierarchical modular structure enhances the robustness of self-organized criticality in neural networks. *New J. Phys.*, **14** (2), 023005.

14

Critical Exponents, Universality Class, and Thermodynamic “Temperature” of the Brain

Shan Yu, Hongdian Yang, Oren Shriki, and Dietmar Plenz

14.1 Introduction

Modern science faces a major challenge with its rapid progress in monitoring complex systems with ever greater detail. Complex systems generally consist of many elements that interact weakly and, consequently, no individual element can be singled out to understand the collective behavior of the system, or in general, its dynamics [1]. This challenge is faced across different scientific fields ranging from physics to neuroscience to economy. Over several decades, statistical physics has developed a set of theories as well as methods to predict the collective behavior of a system from the interactions of the system's constituent elements [2]. In particular, the *critical* state of a system, that is, the state at equilibrium thermodynamic criticality, has attracted great interest, and has been demonstrated to be very useful in understanding a wide range of complex systems [3–5]. A system in the critical state, or in short, a critical system, resides at the border of contrasting phases where it acquires a number of interesting emergent properties such as a maximized sensitivity to external perturbations and a maximized internal diversity/complexity. These properties are at the root of numerous highly nontrivial phenomena observed in nature, for example, the existence of the Curie point and critical opalescence. Near or at the critical state, the quantitative nature of those emergent properties does not depend on the specific, microscopic realization of a system. Accordingly, a multitude of systems are categorized into a small number of “universality classes” based on only a few parameters, the so-called critical exponents. Within a universality class, the collective behavior of systems composed of apparently different elements follows identical quantitative rules [3–6].

Here, we explore the possibility that the theory of thermodynamic criticality might be applicable to understand some of the dynamics of the brain, in particular the mammalian cortex. Obviously, the cortex shares a number of important features with those systems that traditionally fall into the scope of thermodynamics. First, the cortex is made of billions of neurons that are relatively uniform in their basic operations. The trillions of relatively weak connections among these neurons lead to complex interactions at various scales ranging from local microcircuits, to cortical

areas, and even across the entire cortex that underlie various brain functions ranging from motion, to perception, to cognition [7–10]. Second, interactions between neurons are not only weak but also probabilistic, that is, transmission between neurons has a certain likelihood to fail [11], suggesting that brain activity needs to be addressed in a probabilistic (rather than deterministic) framework. By its very nature, thermodynamic equilibrium theory constitutes such a probabilistic framework. Third, cortical dynamics exhibits a number of properties reminiscent of what has been reported for critical systems. Cortical dynamics is very sensitive to external perturbations [12–14], exhibits highly complex activity patterns/dynamics even without any sensory input or cognitive task [15–17], and displays intermittent switching between macroscopic states such as transitions between sleep and wakefulness [18] or attentive and inattentive conditions [19].

In the following sections, we summarize and elaborate on our recent approach [20] in applying the theory and methods of thermodynamic criticality to a specific type of cortical dynamics – neuronal avalanches. Neuronal avalanches are intermittent cortical activity cascades that spontaneously form in the normal brain at rest, that is, in the absence of any particular motor behavior or sensory experience [21–32]. During an avalanche, spontaneous activation of one neuronal group can trigger consecutive activations of other neuronal groups within just a few milliseconds and the propagation of such activity spans both spatial and temporal domains. Studies of neuronal avalanche dynamics suggest that neuronal interactions, both at the mesoscopic level (within tens of square millimeter of cortical tissue [21–27]) and macroscopic level (across the entire cortex [28–32]), may position the cortex at or near a nonequilibrium critical state in order to optimize information processing. However, it is not clear if neuronal avalanches indicate cortical dynamics also close to a critical state in the sense of a thermodynamic equilibrium and, if so, what quantitative rules, that is, critical exponents, they obey and what would be its functional implications for neuronal information processing.

14.2

Thermodynamic Quantities at the Critical Point and Their Neuronal Interpretations

In this section, we recapitulate briefly the main concepts and methods established in statistical physics to study thermodynamic criticality in complex systems and how they can be applied to study brain activity. We start with a spin model in which the whole system consists of a large number of spins, σ , each of which can exhibit two states (up and down), labeled +1 and -1, respectively ($\sigma = 1$ or $\sigma = -1$; Figure 14.1a). There are interactions among spins, that is, the state of one spin causally influences the state of others. However, the interactions are usually local, which means if some spins are separated far away from each other (in any metric space that is properly defined for the whole system), the interactions among them are diminished. Importantly, although the interactions are local, in the critical state, there can be long-range correlations between distant spin activities. That is, for spins that are separated by a long distance, although there is no direct

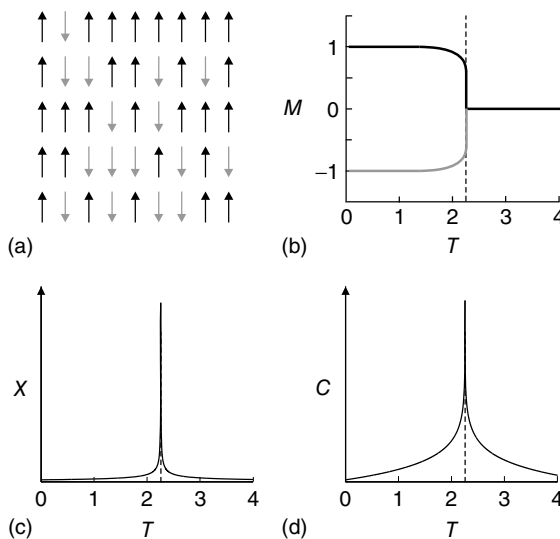


Figure 14.1 Diagram showing a spin system and how its thermodynamic properties change as a function of the temperature T . (a) Illustration of a system consisting of spins with two possible directions

(upward: 1 and downward: -1). (b-d) Diagrams showing that the order parameter M , susceptibility χ , and specific heat C change as functions of T . T_c is marked by vertical broken lines.

causal relation among them, in the critical state, their activities can be correlated, which is mediated through “chains” of local interactions. In fact, criticality is reached when the decreasing effect along any one of the chains is balanced by the increasing number of possible chains as distance increases [6]. This balance is usually quantified by a power-law decay in the correlation, G , with distance, r , that is,

$$G \sim r^{-\eta} (\eta \geq 0)^{[4]} \quad (14.1)$$

Thus, no matter how large their distance to each other is, correlations between spins will not completely diminish.

Next, we introduce the Gibbs–Boltzmann distribution, which completely characterizes the behavior of a spin system at thermodynamic equilibrium:

$$p(\sigma) = \frac{1}{Z} e^{-E(\sigma)/T} \quad (14.2)$$

where $p(\sigma)$ is the probability of the configuration or pattern $\sigma = (\sigma_1, \sigma_2, \dots, \sigma_n)$. For a system with N spins, there are 2^N different patterns that can potentially form. We define E , the “energy” associated with pattern σ as

$$E(\sigma) = - \left(\sum_i \theta_i \sigma_i + \sum_{(i < j)} \theta_{ij} \sigma_i \sigma_j + \sum_{(i < j < k)} \theta_{ijk} \sigma_i \sigma_j \sigma_k + \dots \right) \quad (14.3)$$

where θ_i , θ_{ij} , θ_{ijk} characterizes different orders of interactions among spins i , j , $k \leq N$. Thus, θ sets the internal constraint/order for specific systems [33], for example, for $\theta_i > 0$, the product of $\theta_i \sigma_i$ will be positive whenever $\sigma_i = 1$. Thus, a positive spin σ_i will lower the energy of a pattern and, therefore, will make the pattern more likely to occur. In this case, we say that the tendency of spin i is to be in the state of 1. Similarly, if $\theta_{ij} > 0$, then only when $\sigma_i = 1$ and $\sigma_j = 1$ or $\sigma_i = -1$ and $\sigma_j = -1$, the product of $\theta_{ij} \sigma_i \sigma_j$ will contribute to lower the energy of the pattern. In this case, we say that the two spins tend to assume the same state. All θ s taken together provide a complete description of spin interactions.

In Eq. (14.2), T reflects the influence of the temperature, which controls how important those internal constraints (θ s) are in terms of shaping the system's behavior. A low value of T is associated with a stronger influence of θ s, reflected by a larger heterogeneity in $p(\sigma)$, and vice versa. This role of T is commonly interpreted as the degree of randomness. For example, in the limiting case of $T \rightarrow \infty$, the randomness of the system reaches its maximum. For such a condition, the influence of the internal constraints (order) completely vanishes and all patterns are equally likely to occur. The critical state is associated with a unique value of T , that is, T_c , at which point the influence of the internal constraints and randomness reach a balance. Finally, Z is a normalization factor, which ensures that $\sum p(\sigma) = 1$.

Next, we introduce the quantities that are informative for identifying the critical state by quantifying some of the collective behavior of the system. First, the overall status of the system will be quantified by an order parameter, M , defined as

$$M = \frac{1}{N} \sum_{i=1}^{2^n} p_i \sum_{j=1}^n \sigma_j^i \quad (14.4)$$

where N is number of spins in the system, σ_j^i is the state of the j th spin when the system is at i th configuration. M measures the ensemble average of the spins and is bounded between -1 and 1 . M close to 1 or -1 means that the majority of spins exhibit state 1 or -1 most of the time and spins behave quite similar to each other, which is called an *ordered state*. In contrast, a value of M close to 0 means that there are equally many spins in opposite directions most of the time. This is usually realized in a random system, that is, when spins are equally likely to adopt the value 1 or -1 and no correlation between spins is present. Such a state is called a *disordered state*. With the increase of T from a low enough value, M moves away from the ordered state ($M = 1$ or -1) and approaches the disordered state ($M = 0$) (Figure 14.1b). At the vicinity of the critical point,

$$M \sim |t|^\beta \quad (14.5)$$

where t is the so-called reduced temperature, defined as $t = (T - T_c)/T_c$, T_c is the temperature corresponding to the critical state and β is a critical exponent. Thus, the critical exponent β will fully characterize the behavior of M as a function of T for a critical system.

The second commonly used quantity is the sensitivity to external perturbation, or the susceptibility, χ , defined as

$$\chi = \left. \frac{\partial M}{\partial H} \right|_{H=0} \quad (14.6)$$

where M is the order parameter as defined in Eq. 14.4 and H is a weak “external field,” which makes the spins more likely to be in one state (either 1 or -1 , depending on the polarity of the field), compared to when external fields are absent. Applying the external field H is equivalent to adding a term of $H\Sigma\sigma_i$ to the energy term (E). Similarly, when T is close to T_c ,

$$\chi \sim |t|^\gamma \quad (14.7)$$

The exponent γ tells us how χ changes as a function of T . At T_c , a system consisting of infinite spins, that is, at the thermodynamic limit, is usually associated with the divergence of χ , that is, it has maximized the input sensitivity (Figure 14.1c).

The last quantity studied here is the internal complexity or diversity of the system, measured by the specific heat, C , defined as

$$C = \frac{1}{N} \frac{\partial U}{\partial T} = \frac{\langle E_i^2 \rangle - \langle E_i \rangle^2}{nT^2} \quad (14.8)$$

where N is the number of spins in the system, $U \equiv \langle E_i \rangle = \sum p_i E_i$, and E_i can be calculated as $E_i = -T \log[p_i(T)Z(T)]$. As for other quantities, the specific heat exhibits power-law behavior close to the critical point T_c , which can be characterized by the exponent α :

$$C \sim |t|^\alpha \quad (14.9)$$

Exactly at T_c ($t = 0$), C diverges for infinitely large systems (Figure 14.1d).

The order parameter M , the susceptibility χ , and the specific heat C exhibit unique behavior at the critical point. Namely, M undergoes a phase transition from a value close to 1 or -1 to 0, while χ and C diverge for infinitely large system. Importantly, this behavior is characterized by three critical exponents: α, β, γ .

How can those quantities be studied in a neural system and what would be their interpretations in terms of the operation of neural networks? Clearly, the calculation of M , χ , and C can be done for any system that consists of binary elements. For a neural system, if we define the active state of the element as 1, for example, a neuron that is generating an action potential or a population of neurons that are generating a population spike, that is, spikes in synchrony, and accordingly the quiescent state as -1 , then all those quantities can be computed in a straightforward way. Moreover, M , χ , and C will also have clear meaning for a neural system. Namely, M reflects the overall activity level and χ is a measure of the sensitivity of the neuronal network to weak inputs; for example, for sensory systems it could be the ability of detecting subtle changes in the environment. The variable C quantifies the diversity of system configurations because it describes the variance of $\log(p_i)$ and can be thought of as a measure of the capacity of a neural network to represent/store information [37].

We note that the thermodynamic framework assumes symmetrical interactions (θ_{ij}) between neurons that are active or quiescent simultaneously. For example, the pair-wise condition $\sigma_i = 1$ and $\sigma_j = 1$ or $\sigma_i = -1$ and $\sigma_j = -1$, contributes the same amount of “energy” drop. Is this warranted, given that synaptic interactions only occur when at least one neuron is active, that is, fires an action potential, and no synaptic interaction occurs when both neurons are quiescent? One way to see when this assumption might hold is provided in the following concrete example. For simplicity, let us look at a system consisting of only two neurons (A and B). Without losing generality, we assume that the firing probability (per unit time window) is 0.5 for these two neurons, that is, $p(A_1) = p(A_{-1}) = p(B_1) = p(B_{-1}) = 0.5$, where 1 and -1 represent the active and quiescent state, respectively. Now we assume that owing to direct synaptic interactions between the two neurons, when neuron B is active, neuron A is more likely to be active, that is, $p(A_1|B_1) > p(A_1)$. If $p(A_1|B_1) = 0.6$, then $p(A_1B_1) = p(A_1|B_1) \times p(B_1) = 0.3$. If there are no interactions, we can compute $p(A_1B_1) = p(A_1) \times p(B_1) = 0.25$. So, the contribution of the interaction, in terms of increasing the probability of the joint active state, is $0.3 - 0.25 = 0.05$. Now let us look at the probability of the joint quiescent state. Here too, if there is no interaction, $p(A_{-1}B_{-1}) = p(A_{-1}) \times p(B_{-1}) = 0.25$. With the interaction just specified, that is, $p(A_1|B_1) = 0.6$, we can compute that $p(A_{-1}B_{-1}) = 1 - p(A_1B_1) - p(A_1B_{-1}) - p(A_{-1}B_1) = 1 - [p(A_1) - p(A_1B_1)] - [p(B_1) - p(A_1B_1)] = 0.3$. So, the interaction is reflected by the same amount of probability increase (0.05) if we look at the joint quiescence state. In general, it is easy to show that $p(A_1) \times p(B_1) - p(A_1B_1) = p(A_{-1}) \times p(B_{-1}) - p(A_{-1}B_{-1})$. That is, the effects of the interaction can be equally inferred on the basis of the joint active state or the joint quiescent state. This can also be roughly understood intuitively: if neuron A is more likely to fire as a result of the input of neuron B, it will equally more likely be quiescent because of the absence of that very input. Thus, the symmetry of θ_{ij} toward the active or quiescent state reflects this fact.

14.3 Finite-Size Scaling

Given the characteristics of those macroscopic properties at the critical state, one can straightforwardly determine T_c as well as all critical exponents. In principle, one can simply measure how these quantities change as a function of T to find out when M goes through a phase transition and C and χ diverge. The corresponding T would be T_c . Similarly, observing how M , C , and χ change as functions of T around T_c would suffice to yield the corresponding critical exponents. However, the complications arrive with the fact that actual systems are often finite in size. Thus, the so-called finite-size effect will make the finite-size systems’ behavior deviate from that of the infinitely large system, which we just described, and, consequently, renders straightforward measuring of T_c and the exponents impossible. Nevertheless, how systems of finite size behave as a function of T can still reveal important information about T_c and critical exponents.

For example, if we examine how the function of $\chi(T)$ changes with increase in system size N , we will notice very systematic alterations, for example, that the T corresponding to the maximum of χ asymptotically approaches T_c . Thus, if we know how to extrapolate such a trend for the limit of $N \rightarrow \infty$, we might be able to recover T_c for infinitely sized system. Finite-size scaling (FSS) is a procedure developed in statistical physics to do exactly that [4, 34]. By analyzing the behavior of systems with finite size, FSS is able to extrapolate the results for the thermodynamic limit ($N \rightarrow \infty$) and correctly estimate T_c as well as the critical exponents. In brief, we can choose a unique set of parameters to scale the functions of $M(T)$, $C(T)$, and $\chi(T)$ for various N . Specifically, the reduced temperature t needs to be scaled by $L^{1/\nu}$, where $L = \sqrt[d]{n}$, d is the dimensionality of the system and ν is the critical exponent associated with the correlation length. C , M , and χ are scaled by $L^{-\alpha/\nu}$, $L^{\beta/\nu}$, and $L^{-\gamma/\nu}$, respectively. The set of parameters (ν , α , β , γ , and T_c) that scales all functions and makes them collapse for different N , that is, superimpose on each other, is estimated as if the measurement was done at the thermodynamic limit (see [20] for detailed derivation of the FSS method). In this way, we can infer T_c and critical exponents for a very large or even infinite system based on a series of measurements made on much smaller systems.

14.4

Studying the Thermodynamics Properties of Neuronal Avalanches at Different Scales

Now we can lay down the steps needed to examine if cortical dynamics as reflected by neuronal avalanches are organized close to a thermodynamic critical point and, if so, what are the critical exponents that characterize it. We calculate all functions including $M(T)$, $C(T)$, and $\chi(T)$ for different system size N and then apply the FSS method to infer T_c and corresponding exponents. How far the actual brain dynamics are away from the critical point can be measured by the distance from the T of the actual dynamics to that of the estimated T_c .

The foundation of calculating various thermodynamic quantities, for example, M , C , and χ is the relation $p(\sigma) = \frac{1}{Z} e^{-E(\sigma)/T}$. To begin, we need to define the patterns or configurations σ for the system. First, the spatiotemporal clusters of synchronized neuronal activities, that is, avalanches, were detected. This was done by identifying significant negative peaks in the local field potential (nLFPs, Figure 14.2A) or negative/positive peaks in magnetoencephalography (MEG) signal for each channel. The peak times were extracted and binned (about 2–4 ms in width). Then, consecutive time bins that contained at least one significant event were concatenated to establish a spatiotemporal avalanche pattern. Thus, successive avalanches are separated by a quiescent period of at least one time bin (Figure 14.2B). We then define the configurations σ of the system by the spatial avalanche patterns, obtained by collapsing the spatiotemporal avalanche patterns along the temporal domain. More specifically, each avalanche is originally represented by an $N \times Q$ activity matrix, where N is the number of electrodes and Q is the temporal extent of the avalanche. The activity matrix is then turned into an

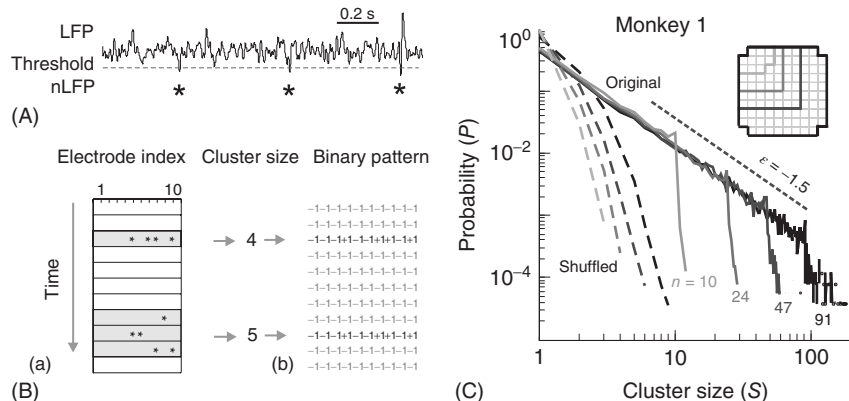


Figure 14.2 Identifying neuronal avalanches in the local field potential (LFP). (A) Example period of continuous LFP at a single electrode. The negative deflections in the LFP (nLFPs; marked by asterisks) were detected by applying a threshold of -2.5 SD (standard deviation; broken line). (B) Identification of spatiotemporal activity clusters and corresponding spatial patterns. (a): nLFPs that occur in the same time bin or consecutive bins of length Δt define a spatiotemporal cluster, whose size is given by its number of nLFPs (two clusters of size 4 and 5

shown; gray area). (b) Patterns represent the spatial information of clusters only. (C) Neuronal avalanche dynamics are identified when the sizes of activity cascades distribute according to a power law with slope close to -1.5 (monkey 1). Four distributions from the same original data set (solid line) using different areas (inset), that is, number of electrodes (N), are superimposed. The power-law distributions vanish for shuffled data (broken lines). A theoretical power law with slope of -1.5 is provided as guidance to the eye (gray, broken line). (Adapted from [20]).

N -component binary vector, where an electrode is set to 1 if it participates at least once in the avalanche and -1 otherwise (Figure 14.2B). This mapping ignores the internal temporal structure of individual avalanches and by doing so ignores the nonequilibrium aspects of neuronal cascading activities. Consequently, we found that the equilibrium framework provides a fairly good approximation for describing the ensemble of configurations defined in this way [20]. After σ is defined, next we need to measure the occurring probability $p(\sigma)$ from the data. Clearly, the most straightforward way is just trying to count how many times individual patterns occurred during the recording session and then convert it to probability. However, for a limit-length recording (about 30 min in the current experiments), such a direct measurement fails to provide enough accuracy even for small systems ($N \sim 10$). In order to estimate $p(\sigma)$ for larger N , we take advantage of a simple parametric model, the dichotomized Gaussian (DG) model [25, 35–37], which considers only the observed first-order (event rate) and second-order (pair-wise correlations) statistics. This model estimates $p(\sigma)$ more accurately than directly measuring it from the limited data [25, 20]. Owing to the exponential increase in possible configurations with increasing N , we restrict the calculation of $p(\sigma)$ to $N \leq 20$. Finally, as it is currently not clear how to empirically change the “temperature” T for the brain and see how such manipulation will change the thermodynamic properties of the system, we used a so-called single-histogram method [34, 38], developed to infer a

system's behavior for different conditions based on the measurement made at one condition. Specifically, if we set the actual T of neuronal avalanches, that is, the T at which the actual recording was taken, to be 1, it can be shown that $p_i(T) = \frac{1}{Z} p_i(1)^{1/T}$ [39, 40]. This way, we can infer $p(\sigma)$, and, consequently, all macroscopic properties for any other temperature.

The results obtained when applying these methods to study neuronal avalanches are shown next. We tested two different spatial scales. The mesoscopic scale reflects cortical population dynamics at the spatial extent of millimeters. Ongoing, or resting, neuronal population activities were recorded on the basis of local field potential (LFP) using high-density microelectrode arrays (10×10 , 0.4 mm interelectrode distance) chronically implanted in the superficial layers of premotor and prefrontal cortices of two macaque monkeys, respectively. The macroscopic scale reflects cortical population dynamics at the level of many cortical areas and extends across the whole brain. Resting-state activities were recorded using MEG in three healthy human subjects. The two scales analyzed differ from each other by orders of magnitude, yet, strikingly, they exhibited very similar results in terms of T_c as well as critical exponents. Later we use the mesoscopic scale results as examples but show comprehensive results for both.

First, we demonstrate that the recorded resting activity patterns of the cortex are neuronal avalanches by showing the power-law-distributed cluster sizes (Figure 14.2C). The system also exhibits scale-free behavior, that is, the power law and its slope were stable for different system sizes N , whereas the cutoff changed systematically with N . We then used FSS to estimate T_c as well as the critical exponents α , β , γ , and the product of v and d . To this end, we analyzed the thermodynamic quantities χ , C , and M as functions of T for system sizes $N = 12–20$ (Figure 14.3). Functions measured for different N were scaled for collapse (see preceding text for details). Achieving this collapse implies that, in the thermodynamic limit, the system has a critical point at T_c characterized by the divergence of χ , C , and the phase transition of M . We find an excellent collapse up to the maximal size examined ($N = 20$; Figure 14.3). Importantly, the values of T_c estimated by the FSS method (Table 14.1) are close to 1, suggesting that neuronal avalanche patterns emerge at the vicinity of a thermodynamic critical point. Moreover, we found strikingly similar scaling behavior for resting activities measured by LFP in nonhuman primates and measured in MEG across the entire human cortex [20]. FSS analysis again suggests that $T_c \approx 1$ for such a macroscopic system (Table 14.1) and the estimated critical exponents are very close to the ones obtained at the mesoscopic scale. The estimated $T_c \approx 1$ by FSS for cortical dynamics is nontrivial, as shown by its absence in various controls based on shuffled data sets. Using a parametric model, we show that both the collapse and $T_c \approx 1$ are reliable features for systems in a critical state [20]. Consistent with the hypothesis that neuronal avalanche dynamics reflect a critical organization of cortical dynamics, we found that the fluctuations of activity between distant cortical sites were still highly correlated (Figure 14.4). More precisely, the correlation decayed close to a power law with an exponent of -0.25 .

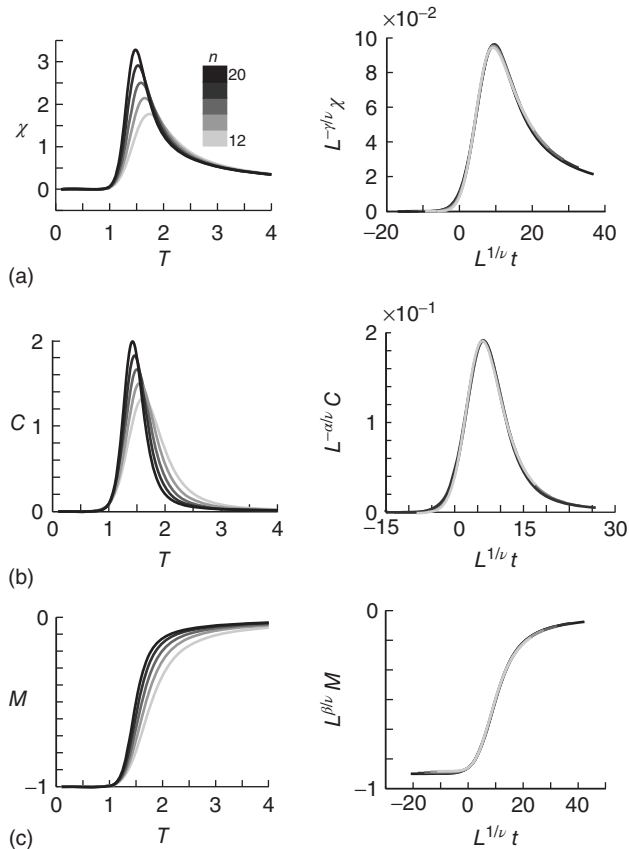


Figure 14.3 Scaling behavior of various thermodynamic properties for neuronal avalanches at the mesoscopic level, that is, recorded by LFPs. Order parameter M (a), susceptibility χ (b), and specific heat C (c) plotted as a function of T for system size

$N = 12-20$ (gray scale code). Left: Original nonscaled functions. Right: Corresponding collapse using FSS analysis. Results are shown for one subgroup of monkey 1. (Adapted from [20].)

Taken together, our results provide evidence that neuronal avalanches represent scale-invariant cortical dynamics that show the characteristic features of dynamics close to a thermodynamic critical point. By being close to a critical point, the brain might gain several functional advantages for neuronal information processing. For example, an enhanced capability of information representation and storage is demonstrated by the maximization of specific heat. A high sensitivity to detect subtle inputs is captured by the maximization of susceptibility. Both features would be highly desirable for cortical processing and are in line with previous suggestions from empirical observations [12–15]. Moreover, with the estimation of the critical exponents, our results provide a quantitative characterization of how various macroscopic properties are regulated at the vicinity of T_c (as $T_c \approx 1$, it is also the

Table 14.1 Critical temperature T_c and critical exponents νd , α , β , and γ estimated using finite-size scaling (FSS) analysis for eight 20-electrode subgroups in two monkeys (M1, M2) and six 20-sensor subgroups in three human subjects (H1–H3).

Subject	Group	$T_c (\chi)$	$\nu d (\chi)$	γ	$T_c (C)$	$\nu d (C)$	α	$T_c (M)$	$\nu d (M)$	β
M1	A	1.13	0.88	1.04	1.15	0.92	0.72	1.16	0.84	-0.028
	B	1.12	0.86	1.00	1.14	0.90	0.72	1.14	0.84	-0.021
	C	1.12	0.86	0.98	1.14	0.88	0.72	1.13	0.84	0.001
	D	1.12	0.86	1.02	1.15	0.88	0.73	1.16	0.80	-0.03
M2	A	1.10	0.82	1.05	1.14	0.84	0.71	1.16	0.76	-0.03
	B	1.11	0.90	1.10	1.13	0.96	0.71	1.13	0.84	0.001
	C	1.10	0.84	1.06	1.14	0.84	0.71	1.12	0.78	0.001
	D	1.11	0.82	1.05	1.15	0.86	0.72	1.13	0.78	0.000
H1	A	1.16	0.84	1.20	1.22	0.86	0.67	1.20	0.74	0.0006
	B	1.20	1.04	1.18	1.23	1.06	0.64	1.24	0.96	-0.02
H2	A	1.17	0.82	1.21	1.22	0.84	0.68	1.20	0.74	-0.0007
	B	1.18	0.98	1.17	1.22	1.00	0.66	1.20	0.92	-0.0003
H3	A	1.14	0.82	1.09	1.17	0.86	0.67	1.16	0.78	0.0007
	B	1.18	0.98	1.02	1.20	1.00	0.65	1.17	0.98	0.0001

Arguments in brackets indicate that T_c and νd were estimated by applying FSS to susceptibility χ , specific heat C , and order parameter M , respectively.

Adapted from [20].

vicinity of the actual physiological condition). The estimated critical exponents are highly consistent across dramatically different spatial scales, suggesting a universal organization of the cortical dynamics within the framework of thermodynamics. Specifically, neuronal avalanches at different scales fall into the same universality class but, interestingly, it seems to be a different class from the ones that have been identified before [4] (e.g., the 2D and 3D Ising models). This distinction may be related to the unique higher order interaction structure of avalanche dynamics [25] that is missing in previously studied systems. Importantly, the thermodynamic criticality demonstrated here is a new property revealed for neuronal avalanche dynamics. We also show that the power-law-distributed cluster size distribution, which is a hallmark of the nonequilibrium criticality, is neither sufficient nor necessary for the system to be critical in the equilibrium thermodynamic sense [20]. This can be clearly seen from the fact that the probability of the quiescent state (cluster size $s = 0$) is a free parameter given the power-law size distribution (because it leads to the divergence of a power law) but this probability contributes significantly to all the thermodynamic quantities that we computed, as it is the dominant pattern for $T = 1$ [20]. Thus, none of the thermodynamic properties can be inferred from the power-law distribution alone. Actually, it is possible to construct a system exhibiting power-law size distribution but without features of thermodynamics criticality, or vice versa. Thus, the current results suggest that cortical dynamics may be organized close to both a nonequilibrium critical point indicated by

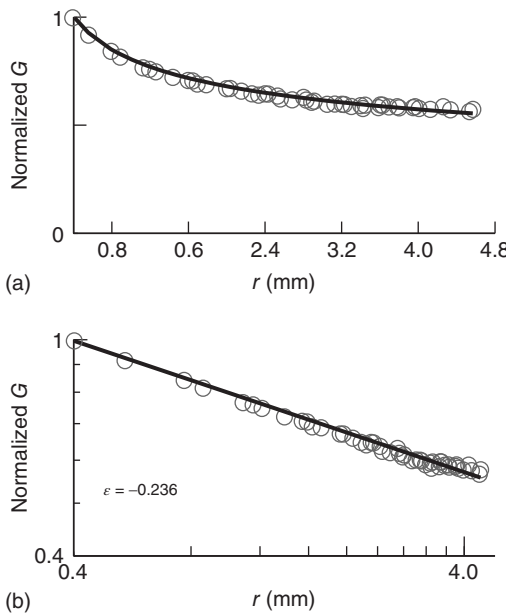


Figure 14.4 Correlation function for neuronal avalanches. Pair-wise correlation, G , defined as $G_{ij} = \langle \sigma_i \sigma_j \rangle - \langle \sigma_i \rangle \langle \sigma_j \rangle$, is plotted as a function of the Euclidean distance r between sites i and j in both linear (a) and log–log coordinates (b). G is normalized by the value of the $G(0.4)$, that is, the

covariance with the nearest neighbor. In both panels, the data are represented by circles and solid lines indicate the best power law fit. ϵ , the exponent of the best-fitting power law. Results are shown for monkey 1. (Adapted from [20].)

power-law-distributed cluster size and an equilibrium critical point indicated by $T_c \approx 1$. This may allow the brain to capitalize on possible functional advantages associated with these two types of criticality, such as, maximized dynamic range, entropy, and information transmission associated with a critical branching process (nonequilibrium criticality) and maximized sensitivity and internal complexity associated with equilibrium criticality [12, 15, 21, 37, 39, 41–44].

14.5

What Could be the “Temperature” for the Brain?

Our findings suggest that cortical dynamics are organized close to a critical state by utilizing the control parameter T , which represents temperature in thermodynamics. In or near the critical state, subtle changes of T will have significant effects on the collective behavior such as the overall activity level, information representation, and input sensitivity. A major question thus remains as to whether a control parameter similar to “temperature” is actually present in real brains. An even more interesting question would be if the brain exploits this

very feature of the critical point and adjusts T to control various collective properties in order to perform different computational tasks. We do not know the definite answers to these questions yet. However, available evidence does warrant further investigation in this direction. One intriguing possibility is that some indigenous neuromodulators may serve the function of adjusting the collective behavior of the neural network along roughly the same dimension as the temperature T . In systems studied in statistical mechanics, increasing the temperature T drives the system toward a state of higher activity and weaker effective interactions among the system components. This is reminiscent of some state changes that occur naturally in the brain, such as the sleep/awake and inattentive/attentive transitions [18, 19, 45–47]. In these physiological transitions, neuromodulators such as acetylcholine (ACh) play an important role [19, 48, 49]. Moreover, studies have reported that applying ACh to neuronal cultures with neuronal avalanche dynamics drives the system toward a high-activity, low-coupling regime [50, 51]. Similar effects have also been observed for spiking activities *in vivo* at the visual cortices [52, 53]. Future experiments that compare the network effects of precisely controlled ACh changes [52, 54, 55] and the prediction based on changing the temperature would shed light on this important issue and further support our approach of understanding macroscopic brain states in the framework of thermodynamic temperature.

Acknowledgment

This research was supported by the Intramural Research Program of the NIMH, NIH, USA.

References

1. Barabási, A.-L. (2012) The network takeover. *Nat. Phys.*, **8**, 14–16.
2. Sethna, J.P. (2006) *Statistical Mechanics: Entropy, Order Parameters and Complexity*, Oxford University Press.
3. Stanley, H.E. (1987) *Introduction to Phase Transitions and Critical Phenomena*, Oxford University Press.
4. Binney, J. (1992) *The Theory of Critical Phenomena: An Introduction to the Renormalization Group*, Clarendon Press, Oxford.
5. Sornette, D. (2006) *Critical Phenomena in Natural Sciences: Chaos, Fractals, Self-organization, and Disorder: Concepts and Tools*, Springer.
6. Stanley, H. (1999) Scaling, universality, and renormalization: three pillars of modern critical phenomena. *Rev. Mod. Phys.*, **71**, S358–S366.
7. Singer, W. (1999) Neuronal synchrony: a versatile code for the definition of relations? *Neuron*, **24** (49–65), 111–125.
8. Rodriguez, E. *et al.* (1999) Perception's shadow: long-distance synchronization of human brain activity. *Nature*, **397**, 430–433.
9. Vaadia, E. *et al.* (1995) Dynamics of neuronal interactions in monkey cortex in relation to behavioural events. *Nature*, **373**, 515–518.
10. Bullmore, E. and Sporns, O. (2009) Complex brain networks: graph theoretical analysis of structural and functional systems. *Nat. Rev. Neurosci.*, **10**, 186–198.
11. Katz, B. (1969) *The Release of Neural Transmitter Substances*, Liverpool University Press.

12. Shew, W.L., Yang, H., Petermann, T., Roy, R., and Plenz, D. (2009) Neuronal avalanches imply maximum dynamic range in cortical networks at criticality. *J. Neurosci.*, **29**, 15595–15600.
13. Houweling, A.R. and Brecht, M. (2007) Behavioural report of single neuron stimulation in somatosensory cortex. *Nature*, **451**, 65–68.
14. Huber, D. *et al.* (2008) Sparse optical microstimulation in barrel cortex drives learned behaviour in freely moving mice. *Nature*, **451**, 61–64.
15. Shew, W.L., Yang, H., Yu, S., Roy, R., and Plenz, D. (2011) Information capacity and transmission are maximized in balanced cortical networks with neuronal avalanches. *J. Neurosci.*, **31**, 55–63.
16. Hoffman, K.L. and McNaughton, B.L. (2002) Coordinated reactivation of distributed memory traces in primate neocortex. *Science*, **297**, 2070–2073.
17. Kenet, T., Bibitchkov, D., Tsodyks, M., Grinvald, A., and Arieli, A. (2003) Spontaneously emerging cortical representations of visual attributes. *Nature*, **425**, 954–956.
18. Vyazovskiy, V.V. *et al.* (2009) Cortical firing and sleep homeostasis. *Neuron*, **63**, 865–878.
19. Harris, K.D. and Thiele, A. (2011) Cortical state and attention. *Nat. Rev. Neurosci.*, **12**, 509–523.
20. Yu, S., Yang, H., Shriki, O., and Plenz, D. (2013) Universal organization of resting brain activity at the thermodynamic critical point. *Front. Syst. Neurosci.*, **7**, 42. doi: 10.3389/fnsys.2013.00042
21. Beggs, J.M. and Plenz, D. (2003) Neuronal avalanches in neocortical circuits. *J. Neurosci.*, **23**, 11167–11177.
22. Gireesh, E.D. and Plenz, D. (2008) Neuronal avalanches organize as nested theta- and beta/gamma-oscillations during development of cortical layer 2/3. *Proc. Natl. Acad. Sci. U.S.A.*, **105**, 7576–7581.
23. Petermann, T. *et al.* (2009) Spontaneous cortical activity in awake monkeys composed of neuronal avalanches. *Proc. Natl. Acad. Sci. U.S.A.*, **106**, 15921–15926.
24. Hahn, G. *et al.* (2010) Neuronal avalanches in spontaneous activity in vivo. *J. Neurophysiol.*, **104**, 3312–3322. doi: 10.1152/jn.00953.2009
25. Yu, S. *et al.* (2011) Higher-order interactions characterized in cortical activity. *J. Neurosci.*, **31**, 17514–17526.
26. Ribeiro, T.L. *et al.* (2010) Spike avalanches exhibit universal dynamics across the Sleep-wake cycle. *PLoS One*, **5**, e14129.
27. Priesemann, V., Valderrama, M., Wibral, M., and Le Van Quyen, M. (2013) Neuronal avalanches differ from wakefulness to deep sleep--evidence from intracranial depth recordings in humans. *PLoS Comput. Biol.*, **9**, e1002985.
28. Tagliazucchi, E., Balenzuela, P., Fraiman, D., and Chialvo, D.R. (2012) Criticality in large-scale brain fMRI dynamics unveiled by a novel point process analysis. *Front. Fractals Physiol.*, **3**, 15.
29. Haimovici, A., Tagliazucchi, E., Balenzuela, P., and Chialvo, D.R. (2013) Brain organization into resting state networks emerges at criticality on a model of the human connectome. *Phys. Rev. Lett.*, **110**, 178101.
30. Allegrini, P., Paradisi, P., Menicucci, D., and Gemignani, A. (2010) Fractal complexity in spontaneous EEG metastable-state transitions: new vistas on integrated neural dynamics. *Front. Fractals Physiol.*, **1**, 128.
31. Shriki, O. *et al.* (2013) Neuronal avalanches in the resting MEG of the human brain. *J. Neurosci.*, **33**, 7079–7090.
32. Palva, J.M. *et al.* (2013) Neuronal long-range temporal correlations and avalanche dynamics are correlated with behavioral scaling laws. *Proc. Natl. Acad. Sci. U.S.A.*, **110**, 3585–3590.
33. Nakahara, H. and Amari, S. (2002) Information-geometric measure for neural spikes. *Neural Comput.*, **14**, 2269–2316.
34. Newman, M.E.J. and Barkema, G.T. (1999) *Monte Carlo Methods in Statistical Physics*, Clarendon Press.
35. Amari, S.-I., Nakahara, H., Wu, S., and Sakai, Y. (2003) Synchronous firing and higher-order interactions in neuron pool. *Neural Comput.*, **15**, 127–142.

36. Macke, J.H., Berens, P., Ecker, A.S., Tolias, A.S., and Bethge, M. (2009) Generating spike trains with specified correlation coefficients. *Neural Comput.*, **21**, 397–423.
37. Macke, J.H., Opper, M., and Bethge, M. (2011) Common input explains higher-order correlations and entropy in a simple model of neural population activity. *Phys. Rev. Lett.*, **106**, 208102.
38. Ferrenberg, A.M. and Swendsen, R.H. (1988) New Monte Carlo technique for studying phase transitions. *Phys. Rev. Lett.*, **61**, 2635–2638.
39. Tkacik, G., Schneidman, E., Berry, M.J. II, and Bialek, W. (2009) Spin glass models for a network of real neurons, arXiv:0912.5409, <http://arxiv.org/abs/0912.5409>.
40. Stephens, G.J., Mora, T., Tkačik, G., and Bialek, W. (2013) Statistical thermodynamics of natural images. *Phys. Rev. Lett.*, **110**, 018701.
41. Kinouchi, O. and Copelli, M. (2006) Optimal dynamical range of excitable networks at criticality. *Nat. Phys.*, **2**, 348–351.
42. Yang, H., Shew, W.L., Roy, R., and Plenz, D. (2012) Maximal variability of phase synchrony in cortical networks with neuronal avalanches. *J. Neurosci.*, **32**, 1061–1072.
43. Mora, T. and Bialek, W. (2011) Are biological systems poised at criticality? *J. Stat. Phys.*, **144**, 268–302.
44. Deco, G. and Jirsa, V.K. (2012) Ongoing cortical activity at rest: criticality, multistability, and ghost attractors. *J. Neurosci.*, **32**, 3366–3375.
45. Cohen, M.R. and Maunsell, J.H.R. (2009) Attention improves performance primarily by reducing interneuronal correlations. *Nat. Neurosci.*, **12**, 1594–1600.
46. Mitchell, J.F., Sundberg, K.A., and Reynolds, J.H. (2009) Spatial attention decorrelates intrinsic activity fluctuations in macaque area V4. *Neuron*, **63**, 879–888.
47. Grosmark, A.D., Mizuseki, K., Pastalkova, E., Diba, K., and Buzsáki, G. (2012) REM sleep reorganizes hippocampal excitability. *Neuron*, **75**, 1001–1007.
48. Himmelheber, A.M., Sarter, M., and Bruno, J.P. (2000) Increases in cortical acetylcholine release during sustained attention performance in rats. *Brain Res. Cogn. Brain Res.*, **9**, 313–325.
49. Jones, B.E. (2005) From waking to sleeping: neuronal and chemical substrates. *Trends Pharmacol. Sci.*, **26**, 578–586.
50. Chiappalone, M., Vato, A., Berdondini, L., Koudelka-Hep, M., and Martinoia, S. (2007) Network dynamics and synchronous activity in cultured cortical neurons. *Int. J. Neural Syst.*, **17**, 87–103.
51. Pasquale, V., Massobrio, P., Bologna, L.L., Chiappalone, M., and Martinoia, S. (2008) Self-organization and neuronal avalanches in networks of dissociated cortical neurons. *Neuroscience*, **153**, 1354–1369.
52. Goard, M. and Dan, Y. (2009) Basal forebrain activation enhances cortical coding of natural scenes. *Nat. Neurosci.*, **12**, 1444–1449.
53. Thiele, A., Herrero, J.L., Distler, C., and Hoffmann, K.-P. (2012) Contribution of cholinergic and GABAergic mechanisms to direction tuning, discriminability, response reliability, and neuronal rate correlations in macaque middle temporal area. *J. Neurosci.*, **32**, 16602–16615.
54. Rokem, A. and Silver, M.A. (2010) Cholinergic enhancement augments magnitude and specificity of visual perceptual learning in healthy humans. *Curr. Biol.*, **20**, 1723–1728.
55. Ma, M. and Luo, M. (2012) Optogenetic activation of basal forebrain cholinergic neurons modulates neuronal excitability and sensory responses in the main olfactory bulb. *J. Neurosci.*, **32**, 10105–10116.

15

Peak Variability and Optimal Performance in Cortical Networks at Criticality

Hongdian Yang, Woodrow L. Shew, Rajarshi Roy, and Dietmar Plenz

15.1

Introduction

Variability and fluctuation are among the most prominent and pervasive characteristics of neural dynamics in mammalian cortex. This fact is apparent in the trial-to-trial variability of responses to a repeated stimulus as well as in the large ongoing, that is, spontaneous, fluctuations in neural activity in the absence of a particular stimulus. For example, in the visual cortex, the spike count or spike rate that a neuron generates in response to a single repeated stimulus has variability that is similar in magnitude to the average response [1–5]. Ongoing fluctuations are even greater in magnitude when no stimulus is present [6, 7]. In fact, the ongoing fluctuations immediately preceding a stimulus strongly influence the ensuing response [8, 9]. In addition to evidence from electrophysiological studies, similar findings come from human brain imaging (electroencephalography (EEG), magnetoencephalography (MEG), functional magnetic resonance imaging (fMRI)) studies. The human brain spontaneously generates activity (the so-called resting state) with huge fluctuations and variability [10–12], and a large part of the trial-to-trial variability in evoked brain responses can be explained by considering the immediately preceding spontaneous fluctuations [13, 14]. For a review, see [15], which mostly addressed fMRI-BOLD studies. Thus, better understanding of ongoing fluctuations will also entail better understanding of the variability in cortical response to input. However, the importance of understanding the origins of ongoing activity fluctuations extends beyond the questions of how it affects response to stimulus. Mounting evidence demonstrates that fluctuations of ongoing activity reflect previous experience [6, 16–19], which implicates a role for ongoing fluctuations in internal cognitive processes such as consolidation of memory. In line with this view, there are dramatic changes in the character of ongoing activity during development [20] as well as developmental changes in variability of task-evoked neural activity [21, 22].

There are numerous potential underlying mechanisms for large fluctuations and high variability in cortical network dynamics. At the synaptic level, the release of neurotransmitters is a stochastic process, which often results in total failure

of a presynaptic spike to elicit a postsynaptic response [23]. At the systems level, ongoing changes in mood, vigilance, attention, and more may influence the observed fluctuations of cortical neural populations [24, 25]. Another population-level explanation of highly variable spiking is balanced excitation and inhibition [26, 27]. Here, we focus on a source of variability of ongoing activity that has been studied less. We hypothesize that variability is the result of operating near criticality. In this chapter, we review recent experimental studies in mammals that support this hypothesis.

15.2

Fluctuations are Highest Near Criticality

The theory of criticality describes and quantifies a system's behavior when it is poised at the brink of a second-order phase transition. At criticality, systems are endowed with unusual properties that are absent when the system is away from the critical point. One of the most fundamental of such critical phenomena is the lack of a dominant length scale and, for nonequilibrium systems, the lack of a dominant time scale in the system dynamics. Rather, all scales play an important role in the system's dynamics – fluctuations may be tiny at one moment, but may span the entire system a moment later. In contrast, when systems operate in a regime far from criticality, only one or a few scales dominate the dynamics. In critical systems, correlations between different parts of the system exist at small scales, but also extend across intermediate and large scales. In fact, the correlation length is highest at criticality compared to noncritical regimes. Thus, if the cortex operates near criticality, then we expect diverse cortical dynamics with a high degree of fluctuation as the system explores the wide range of spatiotemporal scales available to it. Figure 15.1 shows examples of network dynamics generated by a model operating far from criticality (Figure 15.1a,c) and near criticality (Figure 15.1b). It is immediately apparent in this example that variability is largest near criticality.

How can this possibility be tested in experiments? It is crucial that the experimentalist be able to tune the cortex through a range of different operating regimes putatively including criticality as well as noncritical regimes. Without this ability to compare critical versus noncritical conditions, one cannot conclude that criticality gives rise to the *largest* fluctuations. Below, we review two experimental studies in which cortical networks were tuned using pharmacological agents which change the balance of excitation and inhibition [28, 29]. In both studies, the degree of variability of cortical neural activity was assessed using Shannon entropy. In the first study, spatial patterns of spontaneous and evoked activity were studied. Temporal fluctuations of spontaneous activity were examined in the second study, with a focus on phase synchrony. In both studies, entropy was found to be highest when the cortex was tuned to operate nearest to putative criticality, thus supporting the hypothesis that criticality results in maximal fluctuations of ongoing dynamics in the cortex.

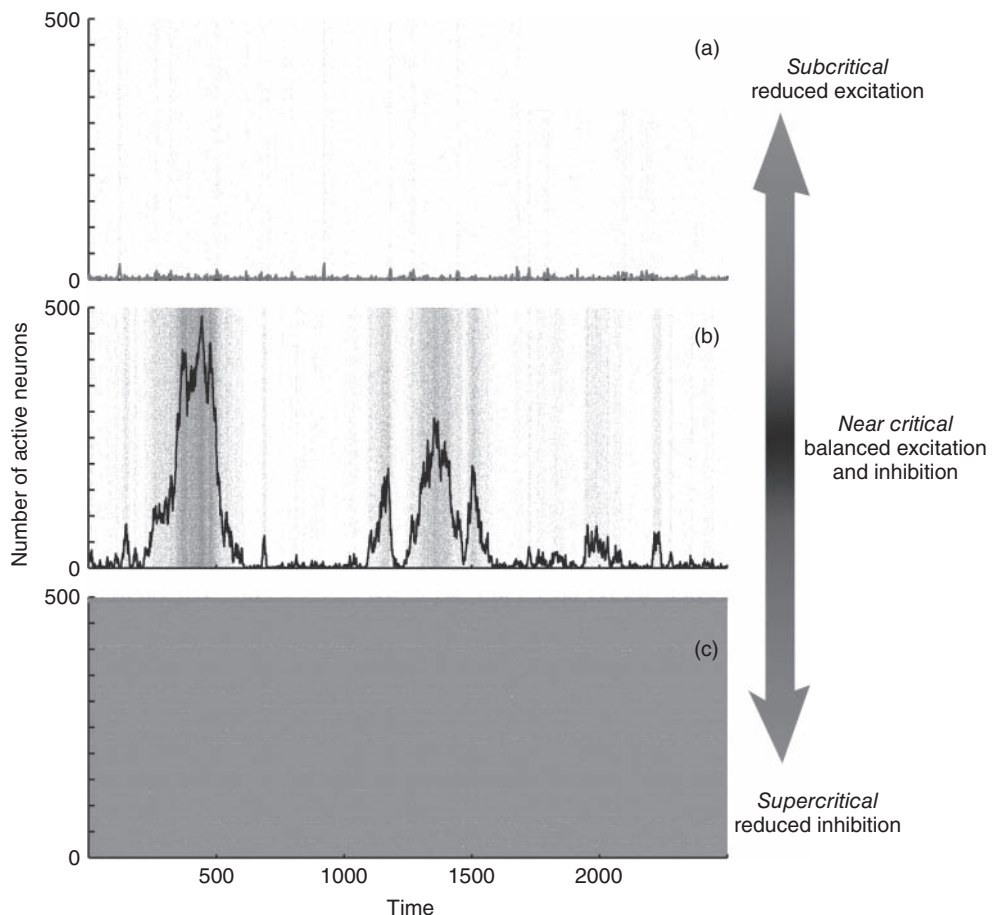


Figure 15.1 Dynamic variability is greatest at criticality. Three examples of dynamics generated by a model comprised of 500 leaky integrate-and-fire neurons. The network is all-to-all connected with 20% inhibitory neurons. When the excitatory and inhibitory connections are balanced appropriately [28], the network operates at criticality. (a) When excitation is reduced by 10%, the system is subcritical with few active neurons and very low fluctuations. The gray dots represent a spike raster. The black line represents the number of active neurons. (b) At criticality,

the inhibitory neurons balance the excitatory neurons and activity fluctuates greatly. (c) When the strengths of inhibitory connections are reduced by 10% compared to the critical case, the system is supercritical. Most neurons are active, but fluctuations are very small. For supercritical dynamics, the activity never ceases. For the subcritical and critical cases, these example time series appear ceaseless because activity was restarted whenever it came to a quiescent state by activating a randomly chosen single neuron.

15.3

Variability of Spatial Activity Patterns

The study of Shew *et al.* [29] provided the first experimental support for the hypothesis that the diversity of cortical activity patterns is maximized at criticality. They studied local field potential (LFP) dynamics in cortex slice cultures grown on the surface of multielectrode arrays [30]. The micro-electrode array provided simultaneous measurements from many recording sites arranged on an 8×8 square grid covering $1.4 \times 1.4 \text{ mm}^2$ (Figure 15.2a). The spacing between adjacent electrodes was $200 \mu\text{m}$. The electrodes were also used to deliver an electrical shock stimulus to a single location. Both spontaneous and stimulus-evoked cortical activity patterns were studied. In these slice cultures, activity (both spontaneous and stimulus-evoked) was burst-like. Bursts were diverse; some manifested as a brief fluctuating

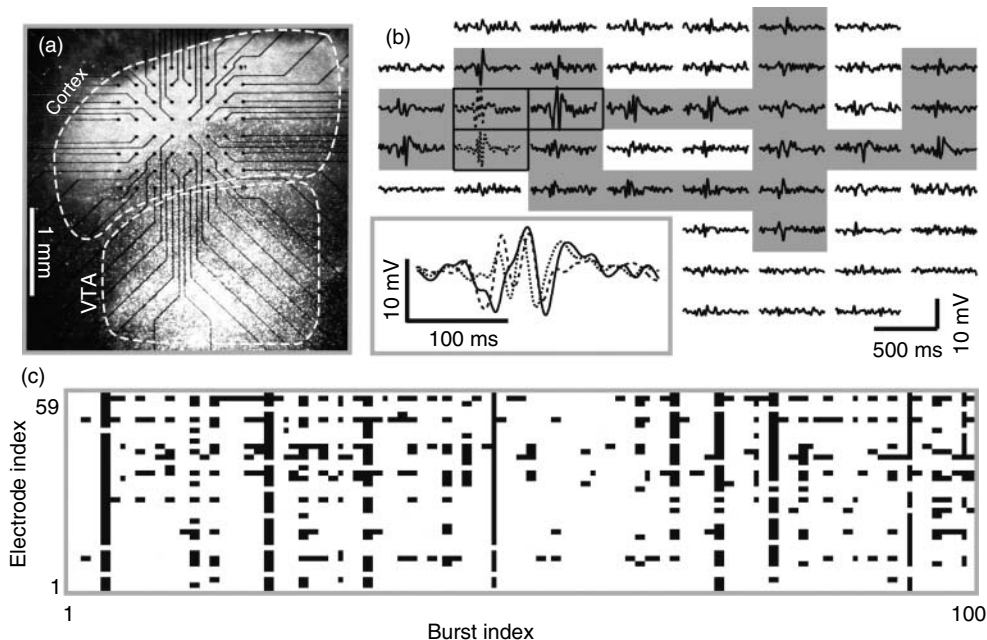


Figure 15.2 Spontaneous burst of neuronal activity in cortex organotypic cultures grown on planar **microelectrode arrays (MEAs)**. (a) Light-microscopic image of a neural culture including somatosensory cortex and ventral tegmental area (VTA) grown on a 60-channel MEA. Black dots indicate the location of the $n=59$ recording electrodes. The ground electrode is outside the imaged region. (b) Example of local field potential (LFP) traces simultaneously recorded during a burst of neural activity (no drugs applied).

The spatial arrangement of LFP traces matches that of the electrodes from which they were recorded. *Inset:* magnified view of three LFP traces. The traces with gray background are considered to be active during the burst (fluctuations >4 SD). (c) Raster displaying patterns of active recording sites for 100 consecutive bursts. Each column represents one burst, and each row represents one recording site. Black – active; white – quiescent.

signal at a single electrode, while other bursts spanned multiple electrodes and hundreds of milliseconds. An example burst is shown in Figure 15.2b. Consecutive bursts were well separated in time by clear periods of quiescence. Shew *et al.* [29] analyzed the spatial patterns of bursts. Temporal aspects of these bursts were studied later in Yang *et al.* [28] (see Section 15.4). The spatial pattern of one burst was defined, on the basis of which electrodes in the array displayed high amplitude neuronal activity during the burst (shaded recording sites in Figure 15.2b). Different spatial patterns correspond to different groups of activated neurons. After a large number of bursts were recorded, the variability of spatial patterns was assessed by computing the Shannon entropy. The diversity of different spatial patterns is illustrated in Figure 15.2c.

With the aim of tuning the cortex cultures through a range of operating regimes, potentially including criticality, Shew *et al.* [29] altered the balance of excitatory and inhibitory interactions in the cortical network using pharmacological means. Empirically, they found that reducing inhibition (partially blocking the GABA_A channels) resulted in network dynamics very similar to the supercritical dynamics observed in nonequilibrium models (e.g., directed percolation), and reducing excitation (partially blocking glutamate channels) led to dynamics similar to subcritical activity. Importantly, neuronal avalanches typically occurred when no drug was applied to the tissue, suggesting that the default operating regime of the cortex is near criticality and that the drugs push the network away from the critical state (Figure 15.3a). Consistent with this possibility, the entropy of burst patterns was also highest when no drug was applied (Figure 15.3b,c). For either reduced inhibition or reduced excitation, the entropy dropped, just as expected for subcritical and supercritical regimes. These results held for both spontaneous and stimulus-evoked bursts.

15.4

Variability of Phase Synchrony

The results of Shew *et al.* [29] were primarily concerned with variability of spatial patterns. However, the bursts of activity they studied also exhibited rich temporal dynamics (see inset in Figure 15.2b), which was not studied in Shew *et al.* [29]. To obtain a better understanding of these dynamics, Yang *et al.* [28] studied phase synchrony across different recording electrodes using exactly the same experimental dataset as studied by Shew *et al.* [29]. Across the same range of drug-altered excitation and inhibition conditions, they compared both the mean levels of synchrony and its variability.

Yang *et al.* [28] used the Hilbert transform to extract phase traces from the LFP traces of each electrode (Figure 15.4a,b). The network-level phase synchrony at any given instant was quantified using Kuramoto's order parameter [32, 33], treating each electrode as one phase oscillator. During a burst, phase signals from many different sites tended to transiently synchronize, and then desynchronize when the burst ended (Figure 15.4c). For each burst, the network-level phase synchrony was averaged over the duration of the burst to obtain a single number that quantifies

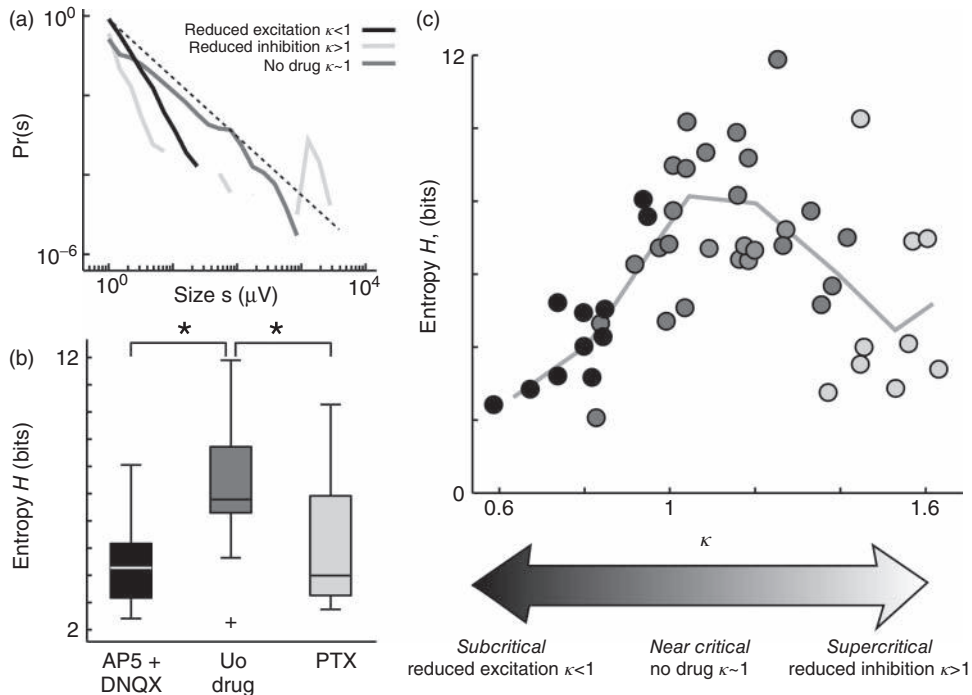


Figure 15.3 Maximized information capacity at criticality. (a) Example probability density distributions of spontaneous burst sizes for a normal (no drug, dark gray), reduced inhibition (PTX, light gray), and reduced excitation (AP5/DNQX, black). Broken line: $-3/2$ power law. Burst size s is the sum of n LFP peak amplitudes during the burst (see [29] for details). Note that the distribution is closest to a power law with $-3/2$ exponent when no drug is added, suggesting that the system operates near criticality. (b) Information capacity (entropy H) of the pattern repertoire is maximized when no drugs perturb the E/I ratio. Significant differences marked with * ($p < 0.05$). Box plot lines indicate lower quartile, median, upper quartile;

whiskers indicate range of data, excluding outliers (+, > 1.5 times the interquartile range). (c) Pattern entropy H peaks near criticality, indicated by $\kappa \approx 1$. Each point represents one recording of ongoing activity ($n = 47$, 8×8 MEA, 1 h, gray scale indicates drug condition; light gray = PTX, black = AP5 + DNQX, dark gray = no drug). Line is the binned average of points. κ is a parameter to quantify proximity to criticality based on similarity of the burst size distribution to a $-3/2$ power law. Typically, the no-drug condition would have κ close to 1, reduced inhibition $\kappa > 1$, and reduced excitation state with $\kappa < 1$. Details can be found in [28, 29, 31].

the degree of synchrony in the network during the burst. Thus, for a recording in which many thousands of bursts occurred, a distribution of burst synchrony values was obtained. The Shannon entropy of this distribution was computed to quantify the variability. In line with Shew *et al.* [29], they found that neuronal synchrony is maximally variable when no drug altered excitation and inhibition and neuronal avalanches occurred (Figure 15.5). When excitation or inhibition was altered with drugs, neuronal avalanches were abolished, and the variability

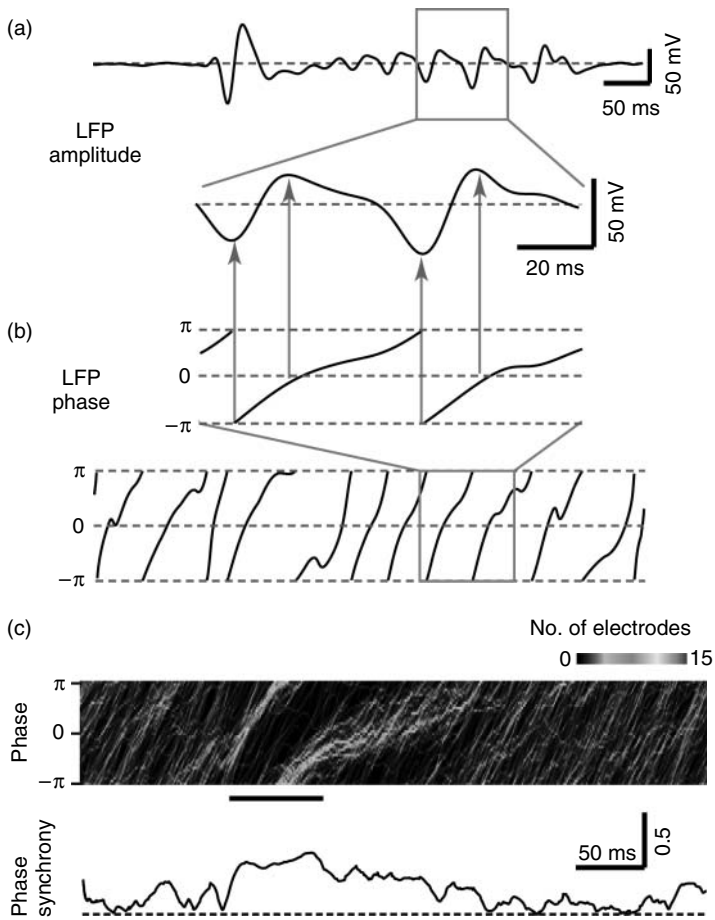


Figure 15.4 Assessing phase synchrony from multisite LFP recordings. (a) Example LFP amplitude trace recorded from a single electrode under disinhibited condition. A 100 ms period (gray box) is expanded (lower trace). (b) Using the Hilbert transform, the LFP amplitude trace is converted to a corresponding phase trace. Top: Phase corresponding to expanded LFP trace. Note that phase near $\pm\pi$ corresponds to negative LFP peaks, while phase near zero coincides with positive LFP peaks (arrows). Lower trace shows the phase for the full time period in (a). (c) Example of phase synchrony

dynamics under normal condition. Duration of the burst is indicated by the black bar. Top: Dynamic phase histogram. Gray scale indicates the number of electrodes with a given phase (vertical axis) at a given time (horizontal axis). Phase “bundles” marked by light gray/white pixels over time indicate many sites with the same phase, that is, in-phase locking. Bottom: Phase synchrony quantified with Kuramoto’s order parameter r . Dashed line indicates $r=0$. Phase synchrony r is high during periods of in-phase locking.

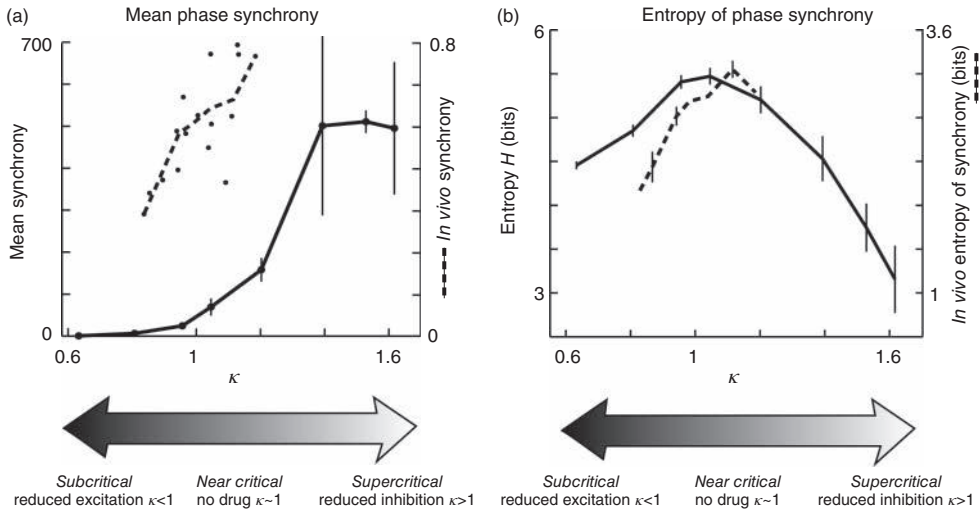


Figure 15.5 Neural synchrony attains moderate mean and maximum entropy near criticality. (a) Mean network synchrony *in vitro* (solid black) rises slowly for low κ , increases sharply near or just above $\kappa=1$, and saturates for high κ . Here, synchrony is averaged over bursts. The synchrony of one burst is the integral of r over the burst duration. Dashed black: Mean network synchrony *in vivo*. For *in vivo* data, synchrony of one burst was defined as the average of r over the

burst duration. Each point represents one recording of ongoing activity ($n=16$, Michigan probe 8×4 , 0.5 h). (b) The variation of synchrony across bursts was quantified with entropy. The entropy peaked close to $\kappa=1$. Since $\kappa=1$ is expected near criticality, these findings support the hypothesis that variability of network dynamics is highest near criticality. Findings *in vivo* (dashed black) are in line with *in vitro* results (solid black).

of synchrony dropped. Given that neuronal avalanches are expected to occur at criticality, the results of Yang *et al.* [28] constitute the first experimental evidence that network-level synchrony in the cortex is most variable near criticality.

Preliminary results *in vivo* are in line with the findings of Yang *et al.* [28]. A 32-channel probe was inserted in the barrel cortex of urethane-anesthetized rats, LFPs were recorded, and the phase signal and variability of synchrony were computed similar to the *in vitro* analysis. Despite the limited range in κ , which reflects variability between different experiments in the absence of any drug manipulation, these preliminary data are consistent with the results of Yang *et al.* [28]: that is, the variability of synchrony is highest when the cortical state is close to criticality (Figure 15.5, dashed black).

15.5

High Variability, but Not Random

Above, we have emphasized that dynamic variability is high at criticality. Here we address the question: high compared to what? From the experimentalist's point

of view, the two reviewed experiments demonstrate that systematically altering the balance of excitation and inhibition away from their “default” levels results in a reduction in variability. On comparing with models and theory, these results correspond to the fact that entropy at criticality is higher than that found in subcritical or supercritical regimes. However, the observed values of entropy were very far from the upper bounds they could theoretically reach. This upper bound would be reached if the neural activity at different electrodes was totally independent with equal probability to be active or inactive in each burst. In contrast, the observed activity near criticality was often rather correlated across distant recording sites. While the high variability at criticality is partly due to stochastic aspects of the underlying network, it should not be interpreted as totally random; criticality would not exist if not for the coordinated interactions among the neurons. Indeed, criticality is often described as a regime at the boundary between randomness and order.

15.6

Functional Implications of High Entropy of Ongoing Cortex Dynamics

Is high entropy a good thing when it comes to spatial patterns and phase synchrony of cortical network dynamics? As Shannon suggested with his use of entropy to quantify information, high entropy can be good as long as the information in question is useful. Indeed, many information theoretic studies have found that maximizing entropy of neural responses considering the statistics of the stimuli may be a common “design principle” in sensory systems [34–41]. However, in the two studies reviewed in the previous sections of this chapter, most of the entropy measurements were done on spontaneous activity. Thus, we may rephrase our question: Does spontaneous activity contain useful information? Given that spontaneous activity consumes 80% of the energy used by the brain [42], it would be surprising if the answer to this question is no. However, whether information is useful or not clearly depends on context. For example, a long-standing tradition in sensory neuroscience is to treat ongoing, spontaneous activity as a noisy hindrance to reliable encoding of sensory input (not useful information) [43]. However, this point of view was directly challenged in experiments which showed that exactly the same conditions that result in high entropy of spontaneous activity are also optimal for transfer of information from stimulus to response [29, 31]. This aspect of these studies has recently been reviewed elsewhere [44]. Similarly, variability of task-related brain activity in humans is positively correlated with task performance [21, 22]. Moreover, a growing number of studies are uncovering traces of recent experiences in spontaneous activity, implicating a more interesting role for spontaneous activity in internal cognitive processes such as memory consolidation [16–19]. In this view, the information contained in spontaneous activity is potentially important whether or not it is directly evoked by sensory input. More generally, if we consider that any given cortical microcircuit may be responsible for processing input from both the thalamus (sensory processing) and

from other cortical microcircuits (internal cognitive processing), then it is clear that this microcircuit must have a large repertoire of accessible activated states to work with. The microcircuit must switch among its different possible roles in cortical information processing. This switching is likely to manifest as high entropy ongoing dynamics. Indeed, low entropy dynamics would necessarily constrain the possible contributions to cortical information processing. Therefore, we suggest that having high entropy, whether spontaneous or stimulus-evoked, is a beneficial property of cortical network dynamics. If this is indeed true, then criticality is an optimal regime of operation for the cortex, which may contribute to explaining why so many studies have observed neuronal avalanches in the cortex.

References

1. Tolhurst, D.J., Movshon, J.A., and Dean, A.F. (1983) The statistical reliability of signals in single neurons in cat and monkey visual cortex. *Vision Res.*, **23**, 775–785.
2. Vogels, R., Spileers, W., and Orban, G.A. (1989) The response variability of striate cortical neurons in the behaving monkey. *Exp. Brain Res. (Experimentelle Hirnforschung Expérimentation cérébrale)*, **77**, 432–436.
3. Softky, W.R. and Koch, C. (1993) The highly irregular firing of cortical cells is inconsistent with temporal integration of random EPSPs. *J. Neurosci.: Off. J. Soc. Neurosci.*, **13**, 334–350.
4. Swindale, N.V. and Mitchell, D.E. (1994) Comparison of receptive field properties of neurons in area 17 of normal and bilaterally amblyopic cats. *Exp. Brain Res.*, **99**, 399–410.
5. Holt, G.R., Softky, W.R., Koch, C., and Douglas, R.J. (1996) Comparison of discharge variability in vitro and in vivo in cat visual cortex neurons. *J. Neurophys.*, **75**, 1806–1814.
6. Luczak, A., Barthó, P., and Harris, K.D. (2009) Spontaneous events outline the realm of possible sensory responses in neocortical populations. *Neuron*, **62**, 413–425.
7. Churchland, M.M. et al. (2010) Stimulus onset quenches neural variability: a widespread cortical phenomenon. *Nat. Neurosci.*, **13**, 369–378.
8. Arieli, A., Sterkin, A., Grinvald, A., and Aertsen, A. (1996) Dynamics of ongoing activity: explanation of the large variability in evoked cortical responses. *Science*, **273**, 1868–1871.
9. Azouz, R. and Gray, C.M. (1999) Cellular mechanisms contributing to response variability of cortical neurons in vivo. *J. Neurosci.: Off. J. Soc. Neurosci.*, **19**, 2209–2223.
10. Linkenkaer-Hansen, K., Nikouline, V.V., Palva, J.M., and Ilmoniemi, R.J. (2001) Long-range temporal correlations and scaling behavior in human brain oscillations. *J. Neurosci.: Off. J. Soc. Neurosci.*, **21**, 1370–1377.
11. Corbetta, M. and Shulman, G.L. (2002) Control of goal-directed and stimulus-driven attention in the brain. *Nat. Rev. Neurosci.*, **3**, 201–215.
12. Laufs, H., Krakow, K., Sterzer, P., Eger, E., Beyerle, A., Salek-Haddadi, A., and Kleinschmidt, A. (2003) Electroencephalographic signatures of attentional and cognitive default modes in spontaneous brain activity fluctuations at rest. *Proc. Natl. Acad. Sci. U.S.A.*, **100**, 11053–11058.
13. Fox, M.D., Snyder, A.Z., Zacks, J.M., and Raichle, M.E. (2006) Coherent spontaneous activity accounts for trial-to-trial variability in human evoked brain responses. *Nat. Neurosci.*, **9**, 23–25.
14. Fox, M.D., Snyder, A.Z., Vincent, J.L., and Raichle, M.E. (2007) Intrinsic fluctuations within cortical systems account for intertrial variability in human behavior. *Neuron*, **56**, 171–184.

15. Fox, M.D. and Raichle, M.E. (2007) Spontaneous fluctuations in brain activity observed with functional magnetic resonance imaging. *Nat. Rev. Neurosci.*, **8**, 700–711.
16. Tsodyks, M., Kenet, T., Grinvald, A., and Arieli, A. (1999) Linking spontaneous activity of single cortical neurons and the underlying functional architecture. *Science*, **286**, 1943–1946.
17. Kenet, T., Bibitchkov, D., Tsodyks, M., Grinvald, A., and Arieli, A. (2003) Spontaneously emerging cortical representations of visual attributes. *Nature*, **425**, 954–956.
18. Ji, D. and Wilson, M.A. (2007) Coordinated memory replay in the visual cortex and hippocampus during sleep. *Nat. Neurosci.*, **10**, 100–107.
19. Han, F., Caporale, N., and Dan, Y. (2008) Reverberation of recent visual experience in spontaneous cortical waves. *Neuron*, **60**, 321–327.
20. Berkes, P., Orban, G., Lengyel, M., Fiser, J., and Orbán, G. (2011) Spontaneous cortical activity reveals hallmarks of an optimal internal model of the environment. *Science*, **331**, 83–87.
21. McIntosh, A.R., Kovacevic, N., and Itier, R.J. (2008) Increased brain signal variability accompanies lower behavioral variability in development. *PLoS Comput. Biol.*, **4**, e1000106.
22. Garrett, D.D., Kovacevic, N., McIntosh, A.R., and Grady, C.L. (2011) The importance of being variable. *J. Neurosci.*, **31**, 4496–4503.
23. Borst, J.G.G. (2010) The low synaptic release probability in vivo. *Trends Neurosci.*, **33**, 259–266.
24. Alkire, M.T., Hudetz, A.G., and Tononi, G. (2008) Consciousness and anesthesia. *Science (New York)*, **322**, 876–880.
25. Fekete, T., Pitowsky, I., Grinvald, A., and Omer, D.B. (2009) Arousal increases the representational capacity of cortical tissue. *J. Comput. Neurosci.*, **27**, 211–227.
26. van Vreeswijk, C. and Sompolinsky, H. (1996) Chaos in neuronal networks with balanced excitatory and inhibitory activity. *Science (New York)*, **274**, 1724–1726.
27. Shadlen, M.N. and Newsome, W.T. (1998) The variable discharge of cortical neurons: implications for connectivity, computation, and information coding. *J. Neurosci.: Off. J. Soc. Neurosci.*, **18**, 3870–3896.
28. Yang, H., Shew, W.L., Roy, R., and Plenz, D. (2012) Maximal variability of phase synchrony in cortical networks with neuronal avalanches. *J. Neurosci.*, **32**, 1061–1072.
29. Shew, W.L., Yang, H., Yu, S., Roy, R., and Plenz, D. (2011) Information capacity and transmission are maximized in balanced cortical networks with neuronal avalanches. *J. Neurosci.*, **31**, 55–63.
30. Plenz, D., Stewart, C.V., Shew, W., Yang, H., Klaus, A., and Bellay, T. (2011) Multi-electrode array recordings of neuronal avalanches in organotypic cultures. *J. Visual. Exp.*, **1**, 2949.
31. Shew, W.L., Yang, H., Petermann, T., Roy, R., and Plenz, D. (2009) Neuronal avalanches imply maximum dynamic range in cortical networks at criticality. *J. Neurosci.*, **29**, 15595–15600.
32. Strogatz, S.H. (2001) Exploring complex networks. *Nature*, **410**, 268–276.
33. Arenas, A., Diazguilera, A., Kurths, J., Moreno, Y., and Zhou, C. (2008) Synchronization in complex networks. *Phys. Rep.*, **469**, 93–153.
34. Laughlin, S. (1981) A simple coding procedure enhances a neuron's information capacity. *Z. Naturforsch., C: Biosci.*, **36**, 910–912.
35. Laughlin, S.B. (2001) Energy as a constraint on the coding and processing of sensory information. *Curr. Opin. Neurobiol.*, **11**, 475–480.
36. Dong, D. and Atick, J. (1995) Statistics of natural time-varying images. *Network: Comput. Neural Syst.*, **6**, 345–358.
37. Dan, Y., Atick, J.J., and Reid, R.C. (1996) Efficient coding of natural scenes in the lateral geniculate nucleus: experimental test of a computational theory. *J. Neurosci.: Off. J. Soc. Neurosci.*, **16**, 3351–3362.
38. Li, Z. (1996) A theory of the visual motion coding in the primary visual cortex. *Neural Comput.*, **8**, 705–730.
39. Baddeley, R., Abbott, L.F., Booth, M.C., Sengpiel, F., Freeman, T., Wakeman, E.,

- and Rolls, E.T. (1997) Responses of neurons in primary and inferior temporal visual cortices to natural scenes. *Proc. R. Soc. Lond. B Biol. Sci.*, **264**, 1775–1783.
40. Bhandawat, V., Olsen, S.R., Gouwens, N.W., Schlief, M.L., and Wilson, R.I. (2007) Sensory processing in the *Drosophila* antennal lobe increases reliability and separability of ensemble odor representations. *Nat. Neurosci.*, **10**, 1474–1482.
41. Garrigan, P., Ratliff, C.P., Klein, J.M., Sterling, P., Brainard, D.H., and Balasubramanian, V. (2010) Design of a trichromatic cone array. *PLoS Comput. Biol.*, **6**, e1000677.
42. Zhang, D. and Raichle, M.E. (2010) Disease and the brain's dark energy. *Nat. Rev. Neurol.*, **6**, 15–28.
43. Lee, D., Port, N.L., Kruse, W., and Georgopoulos, A.P. (1998) Variability and correlated noise in the discharge of neurons in motor and parietal areas of the primate cortex. *J. Neurosci.: Off. J. Soc. Neurosci.*, **18**, 1161–1170.
44. Shew, W.L. and Plenz, D. (2012) The functional benefits of criticality in the cortex. *Neurosci.: Rev. Bringing Neurobiol. Neurol. Psychiatry*, **32**, 9817–9823.

16

Criticality at Work: How Do Critical Networks Respond to Stimuli?

Mauro Copelli

16.1 Introduction

Most models of critical neuronal networks have in common the theoretical ingredient of separation of time scales, according to which the interval between neuronal avalanches is much longer than their duration. This framework has proven useful for several reasons, among which are the possibilities of learning from an extensive literature on models of self-organized criticality and of comparing results with data obtained from some experimental setups. The brain of a freely behaving animal, however, is often found to operate away from this regime, thereby raising doubts about the relevance of criticality for brain function. In this chapter, two questions aimed at this direction are reviewed. From a theoretical perspective, how could criticality be harnessed by neuronal networks for processing incoming stimuli? From an experimental perspective, how could we know that the brain during natural behavior is critical?

In 2003, the idea that the brain (as a dynamical system) sits at (or fluctuates around) a critical point received compelling experimental support from Dietmar Plenz's lab: cortical slices show spontaneous activity in "bursts" with the very peculiar feature of not having a characteristic size. As described in the now-classic paper by Beggs and Plenz [1], the probability distributions of size (s) and duration (d) of these *neuronal avalanches* were experimentally measured and shown to be compatible with power laws, respectively, $P(s) \sim s^{-3/2}$ and $P(d) \sim d^{-2}$. In the following, I will briefly review how this experimental result is connected with the theoretical idea of a critical brain (a much more expanded review can be found e.g., in Ref. [2]).

16.1.1 Phase Transition in a Simple Model

In order to do that, let us consider a very simple model of activity (e.g., spike) propagation in a network of connected neurons. We will make the drastic simplification that a neuron can be modeled by a finite set of states: if $s_i(t) = 0$, neuron i is in a

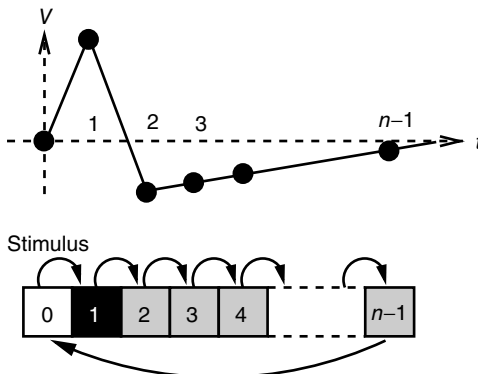


Figure 16.1 Toy model of an excitable neuron: “representative” values of the membrane potential V are replaced by the discrete values of the cellular automaton (see

text for details). Arrows denote transition probabilities, which are equal to 1 except for the $0 \rightarrow 1$ transition.

quiescent state at time t ; if $s_i(t) = 1$, neuron i is spiking; after a spike, the neuron deterministically goes through a number of refractory states, $s_i = 2, 3, \dots, n - 1$, and then returns to rest ($s_i = 0$) (see Figure 16.1). In an excitable neuron, the transition from $s_i = 0$ to $s_i = 1$ does not occur spontaneously: model neurons spike only if somehow stimulated, either by an external stimulus (say, with probability λ) or by synaptically connected neurons.

How do we model synaptic connections in such a simple model? Given a quiescent neuron i , we look at all the K_i neurons which are presynaptic to i . Let us assume that noise in the system is such that the strength of the synaptic connection between a presynaptic neuron j and postsynaptic neuron i can be represented by the probability p_{ij} (another drastic simplification): if i is quiescent ($s_i(t) = 0$) and j is the only presynaptic neuron firing at time t ($s_j(t) = 1$), then, in the absence of external stimuli ($\lambda = 0$), we have $\text{Prob}(s_i(t + \Delta t)) = p_{ij}$, where Δt is the time step of the model (usually corresponding to ~ 1 ms, about the duration of a spike). If $s_i(t) = 0$ and several presynaptic neurons are firing, then $\text{Prob}(s_i(t + \Delta t)) = 1 - (1 - \lambda) \prod_j^{K_i} [1 - p_{ij} \delta(s_j(t), 1)]$. If we subject all neurons to this dynamics and update them synchronously, the model becomes a probabilistic cellular automaton whose evolution is governed by the connection matrix $\{p_{ij}\}$ (see Figure 16.2). One of the advantages of such a simple model is that it allows one to simulate very large systems (say $\sim 10^5$ model neurons), even on a personal computer.

To render the model well defined, let us also postulate that neurons are randomly connected, that is, the network is an Erdős–Rényi random graph. If we choose a symmetric connectivity matrix (definitely not a necessary ingredient), $p_{ij} = p_{ji}$, and let $p \equiv \langle p_{ij} \rangle$ (with p_{ij} drawn from a uniform distribution) and $K \equiv \langle k_i \rangle$ be, respectively, the average values of synaptic transmission probability and number of connections upon a neuron, then a convenient control parameter of the model is the so-called branching ratio $\sigma = pK$. It can be thought of as approximately the

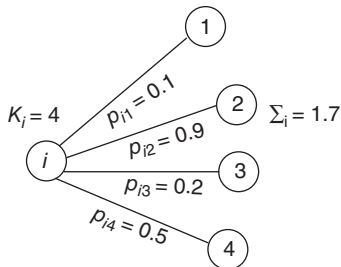


Figure 16.2 In this example, site i has $K_i = 4$ neighbors. One can define the local branching ratio $\sigma_i = \sum_{j=1}^{K_i} p_{ij}$, which gives the average number of “descendant”

spikes that site i would generate on its neighbors if they were all quiescent. The control parameter defined in the text is $\sigma = \langle \sigma_i \rangle$.

average number of spikes that the neighbors of a spiking neuron will produce in the next time step if they are all currently quiescent. This model is essentially a variant of the one introduced by Haldeman and Beggs [3].

Let us keep the network without any external stimulus for the moment, $\lambda = 0$. What happens if we initially allow a random fraction (say, 5% or 10%) of the neurons to be active, while the rest of them are quiescent? The activity of the initially active neurons will propagate (with some probability governed by σ) to their quiescent neighbors, which will then propagate to their neighbors, and so forth. If $\sigma < 1$, each spiking neuron will generate less than one spike in the subsequent time step, on average. So activity will tend to vanish with time: if all neurons become silent, the network will remain silent ever after (in the statistical physics literature, this is known as an *absorbing state* [4]). This is the so-called subcritical regime. For $\sigma > 1$, however, each spike tends to be amplified, and activity will grow up to a certain limit, which is partly controlled by the refractory period of the neurons. This regime is called *supercritical*. The difference between $\sigma < 1$ and $\sigma > 1$ is therefore the stability of self-sustained activity in the network in the absence of any stimulus. It can be characterized by an order parameter, for instance, the density F_0 of active neurons averaged over time after an appropriate transient (i.e., the average firing rate).

What happens at $\sigma = 1$? For this value of the control parameter, the system undergoes a phase transition, where the order parameter F_0 departs continuously from zero ($\sigma < 1$) to nonzero values ($\sigma > 1$). $\sigma = 1$ is the critical point at which the initial activity will also vanish but, differently from the subcritical regime, much more slowly, and without a characteristic time scale. The picture to have in mind is that of Figure 16.3.

Details of the above model can be found in Ref. [5], where one can also find simple calculations that support the above conclusions. It is important to emphasize that some of the simplifications employed in this model cannot be taken for granted. The hand-waving argument for $\sigma = 1$ being the critical value of the coupling parameter, for instance, fails if the topology of the network is more structured than a simple Erdős–Rényi random graph [6, 7]. The extension of the above results to more general topologies was put forward by Restrepo and collaborators [8, 9].

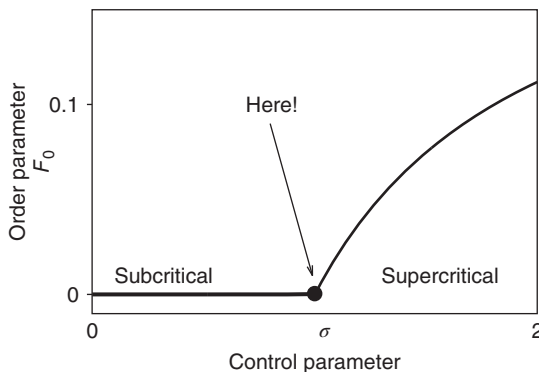


Figure 16.3 General picture of a second-order phase transition. An order parameter (here denoted by F_0) takes on nonzero values above a critical value of a control

parameter (here denoted by σ). In a second-order phase transition, the order parameter changes continuously at the critical point $\sigma = \sigma_c$.

16.1.2

What is the Connection with Neuronal Avalanches?

Now that we have a simple model which very crudely mimics collective neuronal behavior, we can play with it and try to generate neuronal avalanches. Suppose we start in the subcritical regime, $\sigma < 1$. We initially prepare the system by setting all neurons in the quiescent state. Then we randomly choose one neuron, make it fire, and see what happens. Activity will propagate to a certain extent but, since the system is subcritical, will eventually vanish. That means the avalanche we had started is over. We count the number s of neurons that fired (in the model, that is the size of the avalanche) and keep it.

Now, only after the first avalanche is over do we create another one, repeating the procedure. It is important to emphasize that one of the pivotal theoretical ingredients of avalanche models is this clear *separation of time scales*, the interval between avalanches being much longer than their duration [10, 11]. We shall come back to this point later.

Going back to the subcritical regime, if we collect many avalanches and do the statistics, what we will find out is that avalanches have characteristic sizes and durations. That is, $P(s)$ and $P(d)$ decay exponentially for sufficiently large arguments. In other words, finding unusually large or long avalanches (i.e., much larger than the characteristic size or much longer than the characteristic time) is exponentially improbable.

The supercritical case, on the other hand, is very different. Although it is possible that a single firing neuron will generate an avalanche of finite size and duration, it is very likely that activity will propagate indefinitely (or for a very long time, which grows with the number of neurons in the model). Pragmatically, one has to set a limit on the maximum number of time steps one is willing to wait for an avalanche to end [12]. Once we repeat this procedure many times, we will obtain a distribution $P(s)$ with a peak at a very large characteristic size.

At the critical point $\sigma = 1$, simulations and calculations show that both the size and the duration distributions of the model avalanches obey power laws. For a number of topologies (including the simple Erdős–Rényi random graph of our toy model), the exponents can be calculated [13, 14] and shown to be $3/2$ and 2 , respectively.¹⁾ These power laws and their exponents are in very good agreement with the experimental results obtained originally by Beggs and Plenz [1].

16.1.3

What if Separation of Time Scales is Absent?

The above-described power laws, which have been obtained at the critical point of a class of models, have been the main connection between the theory of critical phenomena and the experimental observation of neuronal avalanches. Let us recall that the connection relies heavily on the separation of time scales. In the experiments, the separation of time scales emerges naturally, not only in the original setup by Beggs and Plenz [1] but also in the cortex of anesthetized rats [19] and unanesthetized (but resting) monkeys [20]. In the models, the separation of time scales is typically imposed by hand,²⁾ that is, in the simulations one has to wait until an avalanche is over before creating another one.

But what if separation of time scales is absent? Consider, for instance, the cortical activity of a behaving animal, which typically does not display the separation of time scales seen under anesthesia or in reduced preparations. From a theoretical perspective, we could attempt to mimic such an ongoing activity by randomly stimulating our model network. In that case, how would the network respond, and what would be the role of criticality in the response? This question is addressed in Section 16.2.1.

From the perspective of an experimentalist, what would be the possible connections (if any) between the theory of critical phenomena and brain activity when there is no clear separation of time scales? A few tentative answers to this question will be reviewed in Section 16.2.2.

16.2

Responding to Stimuli

Physical stimuli impinge on our senses and get translated into neuronal activity, which is then further processed in many steps, eventually allowing us to make (some) sense of the world. In the context of the study of sensory systems, therefore, the question of how neurons respond to stimuli is natural and has a very long

1) These are the mean-field critical exponents for the models belonging to the directed percolation (DP) *universality class*. For models on this universality class running on more structured, hypercubic lattices, the exponents are different [15]. As a historical note, it is interesting that it has taken over 50 years for these DP exponents to be experimentally observed in physical systems [16–18].

2) save for a few notable exceptions, see, for example, Refs. [21–23].

history (see e.g., [24, 25]). Here we would like to explore our simple model to make the case that, in some well-defined sense, the network collectively responds optimally if it is at criticality.

16.2.1

What Theory Predicts

Let us revisit our toy model, now relaxing the condition $\lambda = 0$. If $\lambda \neq 0$, neurons can also fire “spontaneously.” We have employed this simple framework to model the interaction between physical stimuli and sensory neurons, by assuming that λ is an increasing function of the intensity of the stimulus [26–29]. In what follows, we employ $\lambda = 1 - \exp(-r\Delta t)$, where r is a Poisson rate assumed to be proportional to the stimulus intensity. Neurons are assumed to be stimulated independently.

How does that scenario compare with that in which avalanches were obtained? Once $r > 0$, separation of time scales is lost, since the network is constantly being stimulated. At every time step, a quiescent neuron may fire with nonzero probability because of an external stimulus, whether or not a spike was propagated from a spiking neighbor. One can think of this scenario as though several avalanches were being generated at every time step. Each of them then spreads out, a process that, as we have seen, is controlled by the coupling parameter σ . And they may interact nonlinearly with one another. If we look beyond the current model, in a more general scenario we are randomly generating spatio-temporal bursts of activity in an excitable medium. Loosely speaking, avalanches in this model are excitable waves in a probabilistic, excitable medium which has been tuned to its critical point.

16.2.1.1 Self-Regulated Amplification via Excitable Waves

In the context of sensory processing, how could the activity of our model network convey information about the physical stimulus impinging on it? Historically, the simplest assumption has been the so-called rate coding, namely, that the mean neuronal activity could somehow represent the stimulus rate r [25]. Let F be the mean firing rate of the network and $F(r)$ be its response function. How do we expect $F(r)$ to change as we go from subcritical ($\sigma < 1$) to critical ($\sigma = 1$) and then to a supercritical ($\sigma > 1$) regime?

Let us begin with the subcritical case, a quiescent network, and small r . For very small σ (say, $\sigma \gtrsim 0$), whenever a model neuron is externally stimulated, it generates an excitable wave which is likely to be small and to evanesce after propagating across a few synapses. So, for each instance the Poisson process happens to stimulate the network (at rate r), the average response is a small number of spikes. In the context of the rate coding mentioned above, that means that the coupling σ among the neurons manages to somehow *amplify* the signal that impinged upon a single neuron. Without the coupling ($\sigma = 0$), the same stimulus would have generated a single spike in our model excitable neuron. One can in fact define an amplification factor $A(r; \sigma) = F(r; \sigma)/F(r; \sigma = 0)$ [26].

If we increase r slightly, the process described above simply occurs more often across the network, but for sufficiently small r and σ the excitable waves essentially

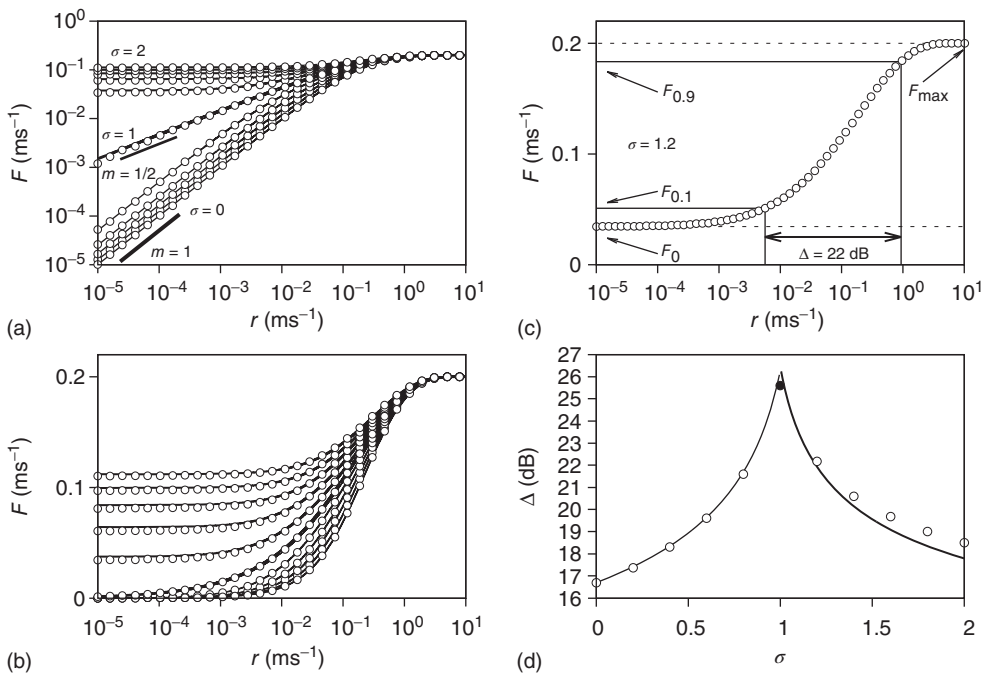


Figure 16.4 (a) Response functions $F(r)$ with σ increasing from bottom to top, in log–log scale. The exponent m shows that the low-stimulus response is linear in the subcritical case ($m = 1$) and nonlinear in the critical case ($m = 1/2$). (b) Same as

(a), except for the lin–log scale. (c) How to calculate the dynamic range of a response curve (see text for details). (d) Dynamic range as a function of coupling. (Adapted from Ref. [5].)

do not interact. This reasoning suggests that $F(r)$ increases linearly for small r and small σ , which is exactly what a simple mean-field calculation confirms [5]. Note that the larger the σ , the larger the probability of propagation and the larger the size of the resulting evanescent excitable wave. Therefore, increasing σ leads to a stronger amplification of the incoming signals. These linear response curves for low stimulus are shown in the lower curves of Figure 16.4a,b (log–log plot and lin–log plot, respectively).

On increasing r sufficiently, excitable waves will be created often and close enough so as to interact. When this happens, the nonlinearities of an excitable medium play a very interesting role. For the sake of reasoning, consider initially a one-dimensional chain of excitable neurons and two deterministic counterpropagating excitable waves on it. The site at which the waves meet is initially quiescent, but will be excited by both its left and right spiking neighbors. After that, the excitation of the collision point cannot go anywhere, because both the left and right neighbors are refractory [26]. Therefore, upon collision, excitable waves annihilate each other (differently from waves in a linear medium, such as light in vacuum). In more than one dimension, the phenomenon is not so simple, because the wave fronts can

have many different shapes (sometimes fractal) and typically intersect partially with one another. Nonetheless, the annihilation persists at whichever site they happen to bump into one another. An important consequence is, therefore, that, for large r , amplification of incoming signals by propagation of excitable waves is severely limited by the annihilation of the excitable waves. Thus for strong stimuli, the coupling among neurons does not change much the average firing rate F . This can be seen again in Figure 16.4a,b, where the curves converge to the same saturation response (including the uncoupled case $\sigma = 0$) for large r .

Therefore, we arrive at this very appealing result: for weak stimuli (small r), amplification is large (the larger the coupling σ , the larger the amplification); for strong stimuli (large r), amplification is small (i.e., the amplification factor $A(r; \sigma)$ is a decreasing function of r [26]). In other words, amplification of the incoming signals is self-regulated, a phenomenon that emerges naturally from very basic properties of excitable media.

16.2.1.2 Enhancement of Dynamic Range

Intuitively, amplifying weak stimuli while not amplifying strong stimuli looks like a good strategy for further processing of the incoming signals. The dynamic range is a standard and simple concept that somehow quantifies how good this strategy is.

Consider the response function exemplified in Figure 16.4c, which has a baseline activity F_0 for $r \rightarrow 0$ and saturates at F_{\max} for $r \rightarrow \infty$. Near those two plateau levels, the response F does not change much as we vary r . If we knew the firing rate F and had to use this knowledge to infer the intensity r of the incoming stimulus (i.e., invert the function $F(r)$), the task would be very difficult if F was close to F_0 or F_{\max} .

Let us define $F_{0.1}$ and $F_{0.9}$ according to $F_x = F_0 + x(F_{\max} - F_0)$, as shown in the horizontal lines of Figure 16.4(c). These firing rate values are sufficiently distant from the plateaus such that, for $F_{0.1} \lesssim F(r) \lesssim F_{0.9}$, it is reasonable to state that we can obtain r if we know F (the 10% and 90% levels are arbitrary but standard in the literature, see e.g., Ref. [30]). In other words, if we define r_x such that $F_x = F(r_x)$, then the stimulus rates in the interval $r \in [r_{0.1}, r_{0.9}]$ (marked by vertical lines in Figure 16.4c) are reasonably “coded by” F . The dynamic range Δ is the range of stimuli, measured in decibels, within this interval:

$$\Delta = 10 \log_{10} \left(\frac{r_{0.9}}{r_{0.1}} \right) \quad (16.1)$$

In the example of Figure 16.4c, the dynamic range covers 2.2 decades of stimulus intensity.

Note that, operationally, $r_{0.1}$ can be understood as the network sensitivity level above which stimulus intensities are “detected.” The network sensitivity depends strongly on σ , thanks to the amplification via excitable waves. The upper value $r_{0.9}$, on the other hand, is only weakly affected. We therefore conclude that the benefits of self-limited amplification discussed above are well captured by the dynamic range: as shown in the left region of Figure 16.4d, Δ increases with σ in the subcritical regime.

This result is very robust because, as mentioned previously, it depends on very few properties of excitable media. Enhancement of dynamic range has been observed in models which in their details are very different from the one described in Section 16.1.1, from deterministic excitable media (one- [26, 29], two- [27, 28, 31] and three-dimensional networks [31]) to a detailed conductance-based model of the retina [32]. In fact, one can look at a smaller scale and consider the dendritic tree of a single neuron. If the dendrites are active, dendritic spikes can propagate along the branches, a phenomenon whose significance has challenged the field of so-called dendritic computation [33]. By regarding an active dendritic tree as an excitable medium with a tree-like topology, enhancement of neuronal dynamic range emerges as a robust property, both in a simple cellular automaton [34, 35] and in a more sophisticated conductance-based model on top of morphologically reconstructed dendrites [36].

16.2.1.3 Nonlinear Collective Response and Maximal Dynamic Range at Criticality

What happens if we increase σ to its critical value? At the critical point, the theory of critical phenomena predicts that the low-stimulus response function is governed by another critical exponent [4], namely

$$F(r, \sigma_c) \xrightarrow{r \rightarrow 0} r^{1/\delta_h} \quad (16.2)$$

Our model is amenable to mean-field calculations, yielding $F(r, \sigma_c) \xrightarrow{r \rightarrow 0} r^{1/2}$ [5], a nonlinear, power-law response which is shown in Figure 16.4a,b. The exponent $1/\delta_h$ can be different for more structured topologies [15, 37] and deterministic models [31, 38], but the fact that it is always less than unity means that low-stimulus response is amplified and dynamic range is enhanced at the critical point (as compared to a linear response in the subcritical regime).

If we increase σ further and reach the supercritical regime, the benefits of low-stimulus amplification begin to deteriorate. In that regime, the same coupling that amplifies weak stimuli via propagation of excitable waves also renders those waves long-lasting, so that self-sustained activity becomes stable. The network now has a baseline activity with which the response to a weak stimulus is mixed and from which it is hard to discern. This situation is shown in the upper lines of Figure 16.4a,b. The situation is analogous to someone whispering on a microphone connected to an overamplified system dominated by audio feedback. The larger the coupling σ , the larger the network self-sustained activity (see Figure 16.3), which implies that the dynamic range Δ is a decreasing function of σ in the supercritical regime.

Figure 16.4d summarizes the above discussion: the dynamic range attains its maximum at criticality. Of all the possible values of the coupling strength, the sensory network responds optimally at $\sigma = \sigma_c$. Moreover, we can go back to our original question of Section 16.1.3: without separation of time scales in the network activity, how could one tell whether the system is at criticality? One potential fingerprint is shown in Figure 16.4b: at criticality, the low-stimulus response function is a power law, with an exponent less than unity (see Eq. (16.2)).

In hindsight, the reasoning underlying Figure 16.4d is straightforward. The ability to process stimulus intensities across several orders of magnitude is maximal at the point where stimuli are amplified as much as possible, but not so much as to engage the network in stable self-sustained activity. That result has been generalized in a number of models, including excitable networks with scale-free topology [6, 7], with signal integration where discontinuous transitions are possible [39], or with an interplay between excitatory and inhibitory model neurons [40]. In fact, the mechanism does not even need to involve excitable waves, appearing also in a model of olfactory processing where a disinhibition transition involving inhibitory units takes place [41].

16.2.2

What Data Reveals

Our simple model predicts that a system at criticality responds to stimuli (i) nonlinearly and (ii) with maximal dynamic range. Let us now briefly review how these predictions compare with experimental data.

16.2.2.1 Nonlinear Response Functions in Sensory Systems

The oldest reports of a nonlinear power law response to sensory stimuli probably come from psychophysics, a field founded in the nineteenth century. Stevens's psychophysical law states that the psychological sensation of a physical stimulus with intensity r is a power law $\sim r^m$, where m is the Stevens exponent [42]. Since the intensity of physical stimuli varies by several orders of magnitude, it is not surprising that psychophysical responses have a large dynamic range, with Stevens exponents usually taking values less than 1: $m \approx 0.5$ for light intensity of a point source, whereas $m \approx 0.6$ for the smell of heptane [42], for instance.

On the one hand, it is remarkable that the values of Stevens exponents are so close to the ones obtained from simple models, given that psychophysical responses involve a plethora of brain regions for the processing of sensory information. On the other hand, it has been argued that the nonlinear transduction of physical stimuli must be done at the sensory periphery to prevent early saturation [42], in which case the simple models would need to mimic only the first processing layers [5, 26–29, 31].

In fact, power law responses to stimuli are indeed observed at a smaller scale in early sensory processing. Odorant-evoked fluorescence activity in olfactory glomeruli of the mouse follows a power law relation with odorant concentration [43]. In the mouse retina, the spiking response of ganglion cells to visual stimulus [44] can be reasonably well fitted by a power law with exponent ~ 0.58 [29]. The highly nonlinear response observed in projection neurons of the antennal lobe of the fruit fly also seems consistent with a power law [45].

16.2.2.2 Enhanced Dynamic Range

In our simple model, the strength of the coupling between neurons j and i is simply a probability p_{ij} , a drastic simplification in which we project our ignorance

of the many mechanisms governing the propensity for the j th neuron to fire, given that the i th did. In an experiment, several mechanisms could mediate the putative amplification via excitable waves that we have described, and the enhancement of dynamic range that ensues.

One of these mechanisms could be the electrical coupling among neurons via electrical synapses (gap junctions). In the experimental setup of Deans *et al.* [44], the response of retinal ganglion cells has its dynamic range reduced from 23 dB in wild-type mice to 14 dB in connexin36 knockouts [29]. The role of lateral electrical coupling in enhancing sensitivity is also consistent with the upregulation of connexin36 in dark-adapted chicks [46] as well as with detailed simulations of the vertebrate retina [32, 36].

In the cortex, the balance between excitation and inhibition is mediated mostly by chemical synapses. Shew *et al.* [12] have recorded the activity of cortex slice cultures via microelectrode arrays. They could pharmacologically change the ratio of excitation and inhibition via the application of antagonists of glutamatergic or GABAergic synaptic transmission. After the application of an electrical pulse of variable intensity (the stimulus) in one of the electrodes, they measured the collective response of the slice. What they found is that, averaging over several slices, the dynamic range of the response function was maximal for the no-drug condition. When the system was made more insensitive (by reducing excitatory synaptic transmission) or more hyperexcitable (by reducing inhibitory synaptic transmission), in either case the dynamic range was reduced. Moreover, for each slice the dynamic range was maximal whenever the avalanche size distribution was compatible with a power law $P(s) \sim s^{-1.5}$ [12].

16.2.2.3 Scaling In Brain Dynamics

Although the dynamic range is a natural quantity to be considered in the context of sensory systems, there are many situations in which it can be very difficult to measure, or simply not relevant. Alternative fingerprints of criticality have been proposed for these cases. For instance, *nontrivial scaling* properties are predicted to appear in the distributions describing critical phenomena [47]. In this scenario, power law distributions of the size and duration of neuronal avalanches are but one example of scale invariance.

At the behavioral level, several interesting results have been obtained. For instance, sleep–wake transitions have been shown to be governed by power law distributions across mammalian species, suggesting scale-invariant features in the mechanisms of sleep control [48]. Nontrivial scaling properties have also been found in the fluctuations of the motor activity of rats, with power laws governing the distribution of time intervals between consecutive movements [49].

Ribeiro *et al.* relied on similar tools to analyze *in vivo* brain activity at the scale of a multielectrode array, with which spike avalanches were recorded from the cerebral cortex and hippocampus of rats [50]. Power law size distributions appeared only under anesthesia (a result reminiscent of those observed in dissociated neurons [51, 52]). When rats were freely behaving, no clear separation of time scales was seen in spiking activity, as shown in Figure 16.5a [50].

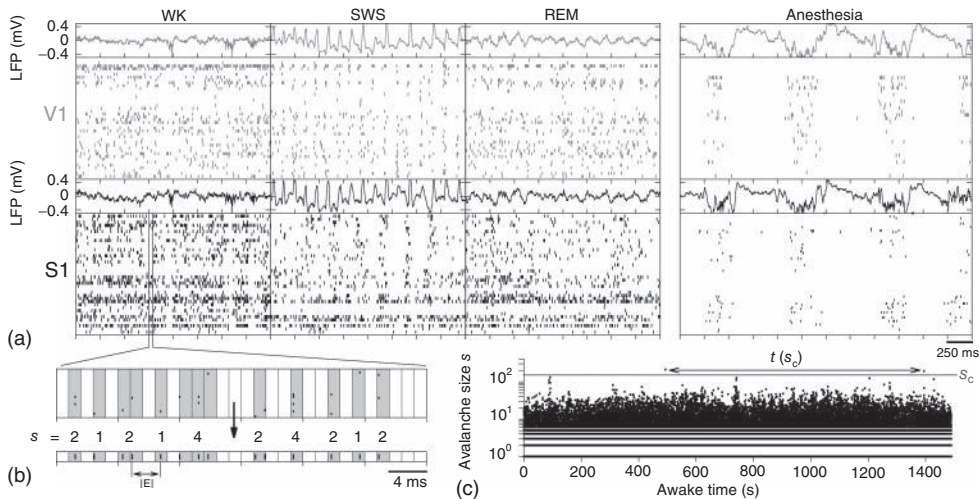


Figure 16.5 (a) Raster plot and local field potential (LFP) traces from two brain regions (V1 and S1) of a freely behaving rat during the three major behavioral states. (left panels: waking = WK, slow-wave sleep = SWS and rapid-eye-movement sleep = REM) and during anesthesia (right panel). (b) Operational definition of avalanche: the mean inter-event interval (IEI) is calculated taking

into account all neurons and then is used as the time bin. This example shows avalanches of sizes $s = 2, 1, 2, 1, 4, \dots$ (c) Time series of avalanche sizes for a WK window. $t(s_c)$ denotes one instance of the waiting time between avalanches of size $s \geq s_c$, from which the distribution of inter-avalanche intervals is then calculated (see text for details). (Adapted from Ref. [50].)

Employing an operational definition of avalanches with rate-normalized time bins (see Figure 16.5b), Ribeiro *et al.* obtained avalanche sizes spanning at least two orders of magnitude, as shown in Figure 16.5c. The size distributions were well fitted by lognormals instead of power laws, as shown in Figure 16.6 (upward triangles). In an attempt to verify whether this result necessarily invalidated the hypothesis of a critical brain, a two-dimensional cellular automaton (otherwise similar to the one described in Section 16.1.1) was simulated at the critical point, yielding a power law size distribution (Figure 16.6, circles). Then, avalanches were deliberately undersampled with a spatial structure equivalent to the multielectrode array that gave rise to the data (see inset of Figure 16.6). Even though the model was critical, the simulated avalanches exhibited size distributions compatible with lognormals when undersampled (Figure 16.6, downward triangles), in close agreement with the experimental data [50]. As had been previously shown by Priesemann *et al.*, avalanche size distributions can change considerably if a critical system is partially sampled [53]. Therefore, the lack of a power law distribution in an undersampled system does not mean that the system is not critical.

Ribeiro *et al.* also explored fingerprints of criticality in the time domain. Consider the time series of avalanche sizes shown in Figure 16.5V. First, long-range time correlations were observed in $1/f$ spectra and detrended fluctuation analysis (DFA)

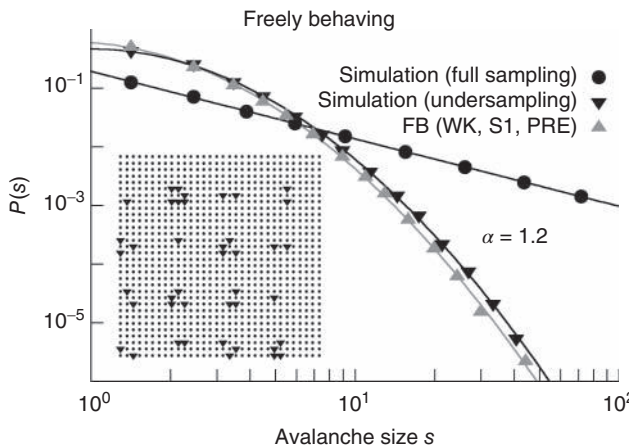


Figure 16.6 Distribution of avalanche sizes for a freely behaving rat (upward triangles) fit by a lognormal function; simulations of a two-dimensional model at criticality (circles) and a power law fit with exponent $\alpha = 1.27$;

simulations of the same model, but from avalanches measured only at a subset of the sites (downward triangles), as depicted in the inset (the underlying line is also a log-normal fit). (Adapted from Ref. [50].)

exponents close to 1 [50]. Second, the probability density function $D(t; s_c)$ of waiting times t between consecutive avalanches of size $s \geq s_c$ was well described by a scaling function. The left column of Figure 16.7a shows a family of such distributions, where each color denotes a different value of size s_c . The larger the required size s_c , the longer one typically has to wait before an avalanche occurs, leading to heavier and heavier tails as s_c increases. Let $\langle t(s_c) \rangle$ be the average waiting time for a given value of s_c . If we then plot a normalized density $D_{\text{norm}} \equiv \langle t(s_c) \rangle \times D$ versus a normalized time $t_{\text{norm}} \equiv t / \langle t(s_c) \rangle$, the family of curves for all values of s_c collapses onto a single function. As shown in Figure 16.7a, the collapse spans about six orders of magnitude. Moreover, since the rescaled axes are dimensionless, different animals could be compared. As it turns out, a single scaling function fits the data across animals, across brain regions, and across behavioral states [50]. This scaling function is a double power law, with exponents similar to those observed in other systems believed to be critically self-organized [54]. Taken together, the results suggest a universal mechanism underlying the dynamics of spike avalanches in the brain. In anesthetized animals, however, the same kind of scaling does not seem to hold (see Figure 16.7b), despite the fact that power law size distributions appear in that case [50].

16.3 Concluding Remarks

We have reviewed the basic connection between criticality in a class of simple models and the experimentally observed power law size distributions of neuronal

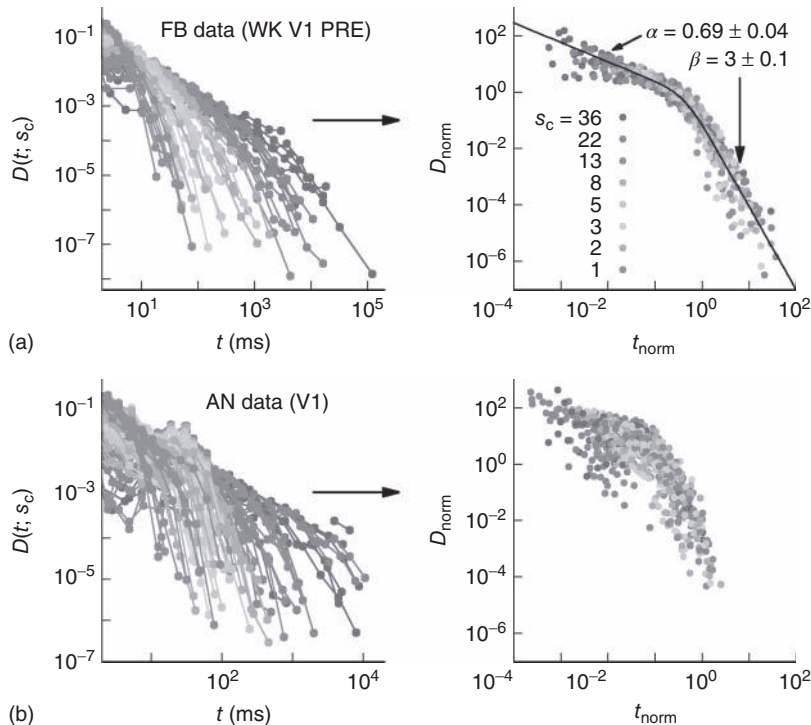


Figure 16.7 Families of distributions of inter-avalanche intervals $D(t; s_c)$ for (a) freely behaving animals and (b) anesthetized animals. Left column: regular distributions. Right column: rescaled distributions (see text

for details). Different colors denote different values of s_c . (Adapted from Ref. [50].) (Please find a color version of this figure on the color plates.)

avalanches. Separation of time scales is an important ingredient for that connection, appearing naturally in reduced preparations and being usually imposed by construction in models.

Absent that ingredient, other features emerge as potential signatures of criticality. The response function of a model network to weak stimuli has prominent features at criticality: it is nonlinear, a power law with an exponent less than 1. It also has maximal dynamic range. We have reviewed some experimental results that seem consistent with those features. It is important to emphasize that, besides the dynamic range, other interesting quantities such as information storage and transmission are maximized at criticality, as recently reviewed by Shew and Plenz [55].

The scaling properties expected at criticality have also provided a number of tools with which to analyze data. Temporal aspects, in particular, pose challenges for modeling which are now being addressed. Poil *et al.* have recently proposed a model which displays power law size distribution of avalanches as well as long-range time correlations (as measured by DFA exponents) [22]. The nonmonotonic distribution

of avalanche waiting times seen in slices has also been recently modeled by Lombardi *et al.* [23].

The simple model described in Section 16.1.1 amounts essentially to a branching process on top of a random graph. The transition in these models between an active and an absorbing phase has been very helpful in that it yields exponents for the power laws in the distributions of size and duration which are compatible with those observed experimentally. However, these are mean-field exponents, which in principle can be obtained by several other models. In other words, in the simplest scenario where separation of time scales is imposed by hand, these simple models are somewhat limited in what they can predict. Currently, we cannot be sure that the phase transition exhibited by these models (absorbing → active) is to a reasonable first approximation of the one taking place in the brain. So the search for new measures (scaling properties, adequate order parameters, etc.) with which to characterize criticality in the brain remains a fascinating challenge to be embraced by experimentalists and theoreticians alike.

Acknowledgements

This chapter is but a brief summary of work that has been performed over the years with many collaborators, with whom I am glad to share the credit and to whom I am deeply thankful. An incomplete list includes Osame Kinouchi, Sidarta Ribeiro, Paulo R. A. Campos, Antonio C. Roque and Dante R. Chialvo, as well as (and most specially) my students and former students Lucas S. Furtado, Tiago L. Ribeiro, Vladimir R. V. Assis, and Leonardo L. Gollo. I also thank Dietmar Plenz and Ernst Niebur for their efforts in organizing the wonderful conference which gave rise to this book. Financial support for the research by me reported in this chapter is gratefully acknowledged and was provided by Brazilian agencies CNPq, FACEPE and CAPES, as well as special programs PRONEX, PRONEM and INCEMaq.

References

1. Beggs, J.M. and Plenz, D. (2003) Neuronal avalanches in neocortical circuits. *J. Neurosci.*, **23** (35), 11167.
2. Chialvo, D. (2010) Emergent complex neural dynamics. *Nat. Phys.*, **6** (10), 744–750.
3. Haldeman, C. and Beggs, J.M. (2005) Critical branching captures activity in living neural networks and maximizes the number of metastable states. *Phys. Rev. Lett.*, **94** (5), 58 101.
4. Marro, J. and Dickman, R. (1999) *Nonequilibrium Phase Transition in Lattice Models*, Cambridge University Press.
5. Kinouchi, O. and Copelli, M. (2006) Optimal dynamical range of excitable networks at criticality. *Nat. Phys.*, **2**, 348–352.
6. Copelli, M. and Campos, P.R.A. (2007) Excitable scale-free networks. *Eur. Phys. J. B*, **56**, 273–278.
7. Wu, A., Xu, X., and Wang, Y. (2007) Excitable Greenberg-Hastings cellular automaton model on scale-free networks. *Phys. Rev. E*, **75** (3), 032 901.
8. Larremore, D.B., Shew, W.L., and Restrepo, J.G. (2011a) Predicting criticality and dynamic range in complex

- networks: effects of topology. *Phys. Rev. Lett.*, **106**, 058101.
9. Larremore, D.B., Shew, W.L., Ott, E., and Restrepo, J.G. (2011) Effects of network topology, transmission delays, and refractoriness on the response of coupled excitable systems to a stochastic stimulus. *Chaos*, **21** (2), 025117.
 10. Bak, P., Tang, C., and Wiesenfeld, K. (1987) Self-organized criticality: an explanation of 1/f noise. *Phys. Rev. Lett.*, **59** (4), 381–384.
 11. Bak, P. (1996) *How Nature Works: The Science of Self-Organized Criticality*, Springer, New York.
 12. Shew, W., Yang, H., Petermann, T., Roy, R., and Plenz, D. (2009) Neuronal avalanches imply maximum dynamic range in cortical networks at criticality. *J. Neurosci.*, **29**, 15 595.
 13. Harris, T. (1963) *The Theory of Branching Processes*, Springer.
 14. Larremore, D.B., Carpenter, M.Y., Ott, E., and Restrepo, J.G. (2012) Statistical properties of avalanches in networks. *Phys. Rev. E Stat. Nonlin. Soft Matter Phys.*, **85** (6).
 15. Muñoz, M.A., Dickman, R., Vespignani, A., and Zapperi, S. (1999) Avalanche and spreading exponents in systems with absorbing states. *Phys. Rev. E*, **59** (5), 6175.
 16. Hinrichsen, H. (2009) Observation of directed percolation - a class of nonequilibrium phase transitions. *Physics*, **2**, 96.
 17. Takeuchi, K.A., Kuroda, M., Chaté, H., and Sano, M. (2007) Directed percolation criticality in turbulent liquid crystals. *Phys. Rev. Lett.*, **99** (23), 234–503.
 18. Takeuchi, K.A., Kuroda, M., Chaté, H., and Sano, M. (2009) Experimental realization of directed percolation criticality in turbulent liquid crystals. *Phys. Rev. E*, **80** (5), 051–116.
 19. Gireesh, E.D. and Plenz, D. (2008) Neuronal avalanches organize as nested theta-and beta/gamma-oscillations during development of cortical layer 2/3. *Proc. Natl. Acad. Sci. U.S.A.*, **105** (21), 7576.
 20. Petermann, T., Thiagarajan, T.C., Lebedev, M.A., Nicolelis, M.A.L., Chialvo, D.R., and Plenz, D. (2009) Spontaneous cortical activity in awake monkeys composed of neuronal avalanches. *Proc. Natl. Acad. Sci. U.S.A.*, **106** (37), 15 921.
 21. Millman, D., Mihalas, S., Kirkwood, A., and Niebur, E. (2010) Self-organized criticality occurs in non-conservative neuronal networks during Up states. *Nat. Phys.*, **6** (10), 801–805.
 22. Poil, S.S., Hardstone, R., Mansvelder, H.D., and Linkenkaer-Hansen, K. (2012) Critical-state dynamics of avalanches and oscillations jointly emerge from balanced excitation/inhibition in neuronal networks. *J. Neurosci.*, **32** (29), 9817–9823.
 23. Lombardi, F., Herrmann, H., Perrone-Capano, C., Plenz, D., and de Arcangelis, L. (2012) Balance between excitation and inhibition controls the temporal organization of neuronal avalanches. *Phys. Rev. Lett.*, **108** (22), 228 703.
 24. Adrian, E.D. (1926) The impulses produced by sensory nerve endings. Part 1. *J. Physiol.*, **61**, 49–72.
 25. Rieke, F., Warland, D., de Ruyter van Stevenink, R.R., and Bialek, W. (1996) *Spikes: Exploring the Neural Code*, MIT Press.
 26. Copelli, M., Roque, A.C., Oliveira, R.F., and Kinouchi, O. (2002) Physics of Psychophysics: Stevens and Weber-Fechner laws are transfer functions of excitable media. *Phys. Rev. E*, **65** (6), 060 901.
 27. Copelli, M., Oliveira, R.F., Carlos Roque, A., and Kinouchi, O. (2005) Signal compression in the sensory periphery. *Neurocomputing*, **65**, 691–696.
 28. Copelli, M. and Kinouchi, O. (2005) Intensity coding in two-dimensional excitable neural networks. *Physica A*, **349** (3), 431–442.
 29. Furtado, L.S. and Copelli, M. (2006) Response of electrically coupled spiking neurons: a cellular automaton approach. *Phys. Rev. E*, **73** (1), 011 907.
 30. Rospars, J.P., Lánsky, P., Duchamp-Viret, P., and Duchamp, A. (2000) Spiking frequency versus odorant concentration in olfactory receptor neurons. *BioSystems*, **58** (1), 133–141.

31. Ribeiro, T.L. and Copelli, M. (2008) Deterministic excitable media under poisson drive: power law responses, spiral waves, and dynamic range. *Phys. Rev. E*, **77** (5), 051 911.
32. Publio, R., Oliveira, R.F., and Roque, A.C. (2009) A computational study on the role of gap junctions and rod ih conductance in the enhancement of the dynamic range of the retina. *PLoS One*, **4** (9), e6970.
33. Stuart, G., Spruston, N., and Häusser, M. (1999) *Dendrites*, Oxford University Press.
34. Gollo, L.L., Kinouchi, O., and Copelli, M. (2009) Active dendrites enhance neuronal dynamic range. *PLoS Comput. Biol.*, **5** (6), e1000 402.
35. Gollo, L.L., Kinouchi, O., and Copelli, M. (2012a) Statistical physics approach to dendritic computation: the excitable-wave mean-field approximation. *Phys. Rev. E*, **85** (1), 011 911.
36. Publio, R., Ceballos, C.C., and Roque, A.C. (2012) Dynamic range of vertebrate retina ganglion cells: importance of active dendrites and coupling by electrical synapses. *PLoS One*, **7** (10), e48 517.
37. Assis, V.R. and Copelli, M. (2008) Dynamic range of hypercubic stochastic excitable media. *Phys. Rev. E*, **77** (1), 011 923.
38. Ohta, T. and Yoshimura, T. (2005) Statistical pulse dynamics in a reaction-diffusion system. *Physica D*, **205** (1), 189–194.
39. Gollo, L.L., Mirasso, C., and Eguíluz, V.M. (2012b) Signal integration enhances the dynamic range in neuronal systems. *Phys. Rev. E*, **85** (4), 040 902.
40. Pei, S., Tang, S., Yan, S., Jiang, S., Zhang, X., and Zheng, Z. (2012) How to enhance the dynamic range of excitatory-inhibitory excitable networks. *Phys. Rev. E*, **86** (2), 021 909.
41. Buckley, C.L. and Nowotny, T. (2011) Multiscale model of an inhibitory network shows optimal properties near bifurcation. *Phys. Rev. Lett.*, **106** (23), 238 109.
42. Stevens, S. (1975) *Psychophysics: Introduction to its Perceptual, Neural and Social Prospects*, John Wiley & Sons, Inc., New York.
43. Wachowiak, M. and Cohen, L.B. (2001) Representation of odorants by receptor neuron input to the mouse olfactory bulb. *Neuron*, **32** (4), 723–735.
44. Deans, M.R., Volgyi, B., Goodenough, D.A., Bloomfield, S.A., and Paul, D.L. (2002) Connexin36 is essential for transmission of rod-mediated visual signals in the mammalian retina. *Neuron*, **36** (4), 703–712.
45. Bhandawat, V., Olsen, S.R., Gouwens, N.W., Schlief, M.L., and Wilson, R.I. (2007) Sensory processing in the drosophila antennal lobe increases reliability and separability of ensemble odor representations. *Nat. Neurosci.*, **10** (11), 1474–1482.
46. Kihara, A., Paschon, V., Cardoso, C., Higa, G., Castro, L., Hamasaki, D., and Britto, L. (2009) Connexin36, an essential element in the rod pathway, is highly expressed in the essentially rodless retina of gallus gallus. *J. Comp. Neurol.*, **512** (5), 651–663.
47. Sornette, D. (2000) *Critical Phenomena in Natural Sciences*, Springer.
48. Lo, C.C., Chou, T., Penzel, T., Scammell, T.E., Strecker, R.E., Stanley, H.E., and Ivanov, P.C. (2004) Common scale-invariant patterns of sleep-wake transitions across mammalian species. *Proc. Natl. Acad. Sci. U.S.A.*, **101** (50), 17545.
49. Anteneodo, C. and Chialvo, D. (2009) Unraveling the fluctuations of animal motor activity. *Chaos*, **19** (3), 033123.
50. Ribeiro, T., Copelli, M., Caixeta, F., Belchior, H., Chialvo, D., Nicolelis, M., and Ribeiro, S. (2010) Spike avalanches exhibit universal dynamics across the sleep-wake cycle. *PLoS One*, **5** (11), e14 129.
51. Mazzoni, A., Broccard, F.D., Garcia-Perez, E., Bonifazi, P., Ruaro, M.E., and Torre, V. (2007b) On the dynamics of the spontaneous activity in neuronal networks. *PLoS One*, **2** (5), e439.
52. Pasquale, V., Massobrio, P., Bologna, L., Chiappalone, M., and Martinoia, S. (2008) Self-organization and neuronal avalanches in networks of dissociated

- cortical neurons. *Neuroscience*, **153** (4), 1354–1369.
53. Priesemann, V., Munk, M.H., and Wibral, M. (2009) Subsampling effects in neuronal avalanche distributions recorded in vivo. *BMC Neurosci.*, **10** (1), 40.
54. Bak, P., Christensen, K., Danon, L., and Scanlon, T. (2002) Unified scaling law for earthquakes. *Phys. Rev. Lett.*, **88** (17), 178 501.
55. Shew, W.L. and Plenz, D. (2013) The functional benefits of criticality in the cortex. *Neuroscientist*, **19** (1), 88–100.

17

Critical Dynamics in Complex Networks

Daniel B. Larremore, Woodrow L. Shew, and Juan G. Restrepo

17.1

Introduction: Critical Branching Processes

A central concept in the preceding chapters has been that of a *critical branching process* that has been used to explain the statistics of neuronal avalanches observed *in vivo* and *in vitro*. Branching processes were first systematically studied by Galton and Watson [1] in 1874 in a context unrelated to neuroscience: their aim was to mathematically explain the extinction of aristocratic family names in Victorian England. As generations passed, the name of the patriarchs would be passed down only to their male children. Thus, the family name survives only if there is at least one male alive in each generation. Considering that each newborn child will be male with probability $1/2$, it is clear that if each male has only one child, the family name will likely die out very quickly. On the other hand, if each male has 10 children, the family name will likely carry on indefinitely. Such a process where an active node (father) may branch to other nodes (children) which are active (male) with some probability may be generalized so that the number of offspring may vary from node to node, and the probability of producing an active node may vary from branch to branch. This generalization is called a *branching process*, and finds application beyond genealogy in diverse situations including nuclear chain reactions [2] and propagation of neural activity through a network of neurons or functional units. When the number of active nodes (which will also be called *excited nodes*) neither increases nor decreases, on average, from generation to generation, the process is called a *critical branching process*. On the other hand, when the number of active nodes decreases, on average, the process is called *subcritical* and when the number active nodes increases, on average, the process is called *supercritical*. Figure 17.1 illustrates these three scenarios.

The branching process described above produces a cascade of excitations, henceforth just called an *avalanche*. Since the avalanche is a stochastic process, that is, the propagation through consecutive generations depends on chance, the duration of an avalanche (number of generations before extinction) will vary according to a distribution determined by the parameters of the process. For example, if each node that is excited at a given generation can produce M excited nodes in the

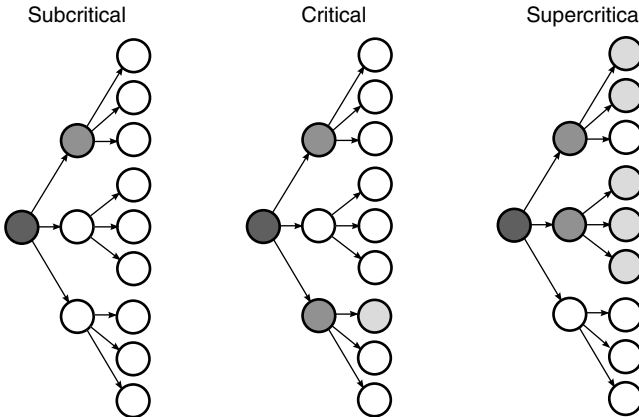


Figure 17.1 Example of subcritical, critical, and supercritical branching processes in which each ancestor produces three offspring who may possess a particular trait (filled circles) or lack it (empty circles). In a critical branching process, each ancestor possessing some trait produces *on average* one descendant who possesses the trait

(center). In a subcritical branching process, each ancestor with the trait produces on average less than one descendant with the trait (left), and in a supercritical branching process, each ancestor with the trait produces on average more than one descendant with the trait (right).

next generation with probabilities $p_1, p_2, p_3, \dots, p_M$, the process is critical when these probabilities add exactly to 1 [1, 3–5]. Defining the *branching ratio* σ to be the expected number of excitations produced by an excited node, the condition for criticality can be written as

$$\sigma = \sum_{n=1}^M p_n = 1. \quad (17.1)$$

Critical branching processes are interesting to theoreticians and experimentalists alike because of their statistical signatures: the probability that an initial excited node results in an avalanche where a total of x nodes are excited in the course of the avalanche is, for large x , a power law

$$p(x) \propto x^{-\frac{3}{2}}, \quad (17.2)$$

and the probability that an initial excited node results in a cascade that spans t generations is, for large t , also a power law

$$p(t) \propto t^{-2}, \quad (17.3)$$

a demonstration of which can be found, for example, in [5]. Remarkably, these exponents are observed in experimental distributions of neuronal avalanches in various settings. The exponent $-3/2$ for the distribution of avalanche sizes has been observed in rat cortical tissue cultures [6–10], awake monkeys [10, 11], and anesthetized mammals [10, 12, 13], while the exponent -2 for the distribution of avalanche durations has been observed in resting humans [14]. This suggests that,

at the functional level, some aspects of brain activity can be well described by a critical branching process.

The agreement between neuroscience experiments and classical theory of branching processes is surprising given the rather different structure of a neural network compared to a family tree, for example. Indeed, the network of interactions in a classical branching process is always “tree-like” – it has no loops. In contrast, in the cerebral cortex there are recurrent interactions, for example, neuron A can excite neuron B, which can in turn re-excite neuron A. More specifically, various functional brain networks have been reconstructed partially [15–19], and it has been consistently found that these reconstructed networks possess a rich structure, including in some cases a power law distribution in the number of connections per node [15], long-range connections [17], and correlations [19]. Thus, it is imperative to consider the effect that such network structural properties might have on the statistics of avalanche sizes and durations, since they are a key experimental signature of criticality.

The study of propagation of avalanches of activity in complex networks has received considerable attention recently [20–23]. Most of these studies focus on the typical behavior of avalanches in ensembles of networks sharing a certain property (e.g., the degree distribution). In contrast to these previous studies, this chapter describes a theory of avalanche sizes and durations based on [24] which explicitly accounts for networks with complex network topology. This approach allows an analysis of avalanches starting from arbitrary nodes in the network and the effect of nontrivial network structure on the distribution of avalanche sizes and durations. Some of the results presented in this chapter, such as a criterion for criticality based on the largest eigenvalue of an appropriate matrix, have counterparts in the so-called multi-type branching processes [4] if one identifies each individual node with a “particle type.” However, this chapter addresses explicitly the applicability of these results to describe avalanches in complex networks and the effect of modern network topology measures on the distribution of avalanches. Section 17.2 summarizes the terminology and concepts that will be used in subsequent analysis of branching processes in complex networks. Section 17.3 describes how the classical results for the statistics of avalanche durations and sizes mentioned above are affected by the network structure, focusing particularly on the statistics of avalanche durations. Important differences with the classical results include topology-dependent criteria for criticality, and expressions for the distribution of avalanche sizes and durations which explicitly depend on the network topology as described by an appropriate adjacency matrix. In addition, the effect of various network structural properties of interest in modern network research is discussed.

17.2

Description and Properties of Networks

Many common tools have been developed to describe and handle structural aspects of complex networks [25], and their use proves to be instrumental for analyzing

the statistics of avalanches in networks. Very generally, a network can be defined as a set of N nodes (or vertices), $V = \{1, 2, \dots, N\}$, and a set of M links (or edges), $E = \{e_1, e_2, \dots, e_M\}$, where each edge is an ordered pair of nodes and the order represents the direction of the link. For example, $e = (n, m)$ represents a link pointing from node n to node m . In the study of neuronal avalanches that follows, each node corresponds to a functional population of neurons.

17.2.1

Network Representation by an Adjacency Matrix

A network with N nodes can be conveniently represented by an $N \times N$ adjacency matrix A with entries given by

$$A_{nm} = \begin{cases} 1 & \text{if there is a link from node } n \text{ to node } m, \\ 0 & \text{otherwise.} \end{cases} \quad (17.4)$$

In many applications, links between different pairs of nodes differ in their importance and/or their effect. For this reason, it is often convenient to relax the definition above to allow any value for each entry of A :

$$A_{nm} = \begin{cases} \neq 0 & \text{if there is a link from node } n \text{ to node } m, \\ 0 & \text{otherwise.} \end{cases} \quad (17.5)$$

The nonzero entries of A are called the *link weights*, and a network is *weighted* if not all of the weights are 1. The matrix A as defined in Eq. (17.5) will be referred to as the *adjacency matrix* of the network, and the matrix A as defined in Eq. (17.4) will be referred to as the *unweighted adjacency matrix*. Undirected networks are represented by a symmetric adjacency matrix satisfying $A = A^T$, where T denotes the transpose matrix. Figure 17.2 illustrates the representation of a small network with an adjacency matrix.

17.2.2

Node Degrees

The adjacency matrix contains all the information about the network. However, often one has access only to limited information, such as local information about

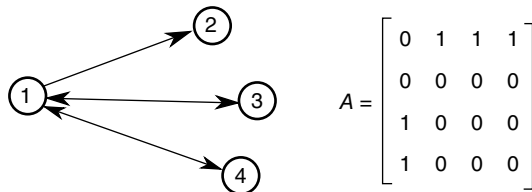


Figure 17.2 Example of an adjacency matrix for a directed network. Each node is indexed by an integer, and the connections from (to) each node are written in the corresponding row (column) of the matrix A .

a sample of nodes or links. One of the properties that can, in absence of all other information, reveal much about the network is the number of incoming and outgoing links per node. In terms of the adjacency matrix, the out-degree and in-degree of node n are

$$k_n^{\text{out}} = \sum_{m=1}^N A_{nm}, \quad k_n^{\text{in}} = \sum_{m=1}^N A_{mn}. \quad (17.6)$$

When the network is unweighted ($A_{nm} = 0$ or 1), the out- and in-degrees correspond to the number of outgoing and incoming links from and into a node. For weighted networks, the out- and in-degrees generalize this concept and represent the total strength of the outgoing and incoming links. Since every outgoing link from a given node has to be the incoming link of another node, the sum of out-degrees and in-degrees over all nodes must be the same. In fact

$$\sum_{n=1}^N k_n^{\text{out}} = \sum_{n=1}^N \sum_{m=1}^N A_{nm} = \sum_{m=1}^N \sum_{n=1}^N A_{nm} = \sum_{m=1}^N k_m^{\text{in}} \quad (17.7)$$

and the *mean degree* $\langle k \rangle$ is defined as

$$\langle k \rangle \equiv N^{-1} \sum_{n=1}^N k_n^{\text{out}} = N^{-1} \sum_{m=1}^N k_m^{\text{in}}. \quad (17.8)$$

For some networks found in applications, the in- and out-degrees of a given node can be vastly different. For example, the number of hyperlinks pointing *to* a popular web portal can number in the billions, while the number of hyperlinks pointing to other webpages *from* that web portal can be of the order of a hundred. Similarly, the directed network of *Twitter* users (Twitter is a popular microblogging platform) where a link indicates “following” also provides an example with nodes that often have vastly different in-degrees and out-degrees, although in- and out-degrees are still positively correlated in the Twitter network [26].

17.2.3

Degree Distribution

By sampling a large number of nodes from a network, one can estimate the probability that a randomly chosen node has a given in-degree and out-degree, and define the joint degree distribution

$$P(k^{\text{out}}, k^{\text{in}}) = \text{probability that a randomly chosen node has out-degree } k^{\text{out}} \text{ and in-degree } k^{\text{in}}.$$

In general, the out- and in-degrees are not independent variables. One can still define the marginal distributions

$$P_{\text{out}}(k^{\text{out}}) = \sum_{k^{\text{in}}} P(k^{\text{out}}, k^{\text{in}}) = \begin{aligned} &\text{probability that a randomly chosen} \\ &\text{node has out-degree } k^{\text{out}}, \end{aligned} \quad (17.9)$$

$$P_{\text{in}}(k^{\text{in}}) = \sum_{k^{\text{out}}} P(k^{\text{out}}, k^{\text{in}}) = \begin{aligned} &\text{probability that a randomly chosen} \\ &\text{node has in-degree } k^{\text{in}}. \end{aligned} \quad (17.10)$$

If the out-degree and the in-degree at a given node are independent variables, then

$$P(k^{\text{out}}, k^{\text{in}}) = P_{\text{in}}(k^{\text{in}})P_{\text{out}}(k^{\text{out}}).$$

As suggested by the examples mentioned above, the out-degree and in-degree distributions are not necessarily similar. As an example of a network where the out- and in-degree distributions are different, Braha and Bar-Yam studied information-sharing networks, and in particular a pharmaceutical facility development organization [27].

In addition, many real-world networks have degree distributions that are highly heterogeneous. For example, Eguíluz *et al.* [15] observed that functional magnetic resonance imaging (fMRI) networks obtained by imaging human subjects engaged in various tasks have degree distributions that follow approximately a power law, that is, $P(k) \approx Ck^{-\gamma}$, where k represents the in- or out-degree. Networks whose degree distribution follows a power law are often referred to as *scale-free networks* to indicate the absence of a typical degree, and have been the subject of extensive study in the last decade (see, e.g., [25, 28, 29]). As discussed below, heterogeneous degree distributions result in a different criterion for criticality than the classical result presented in the introduction. Another factor that can modify the classical results degree correlations, described next.

17.2.4

Degree Correlations

Two types of correlations between node degrees are often studied. The first type, *node degree correlations*, denotes correlations between the out-degree and in-degree at the same node. The presence of node degree correlations implies that knowing information about the in-degree of a randomly chosen node provides some knowledge of its out-degree, and vice versa. Mathematically, it means that the joint degree distribution does not split into a product.

$$P(k^{\text{out}}, k^{\text{in}}) \neq P_{\text{in}}(k^{\text{in}})P_{\text{out}}(k^{\text{out}})$$

Typically, one is interested not in the full form of the joint degree distribution, but in knowing whether the correlation between out- and in-degrees is positive or negative. If it is positive (negative), nodes with large out-degrees are more likely to have large (small) in-degrees. This can be quantified by the node degree correlation coefficient [30]:

$$\eta = \frac{\langle k^{\text{in}}k^{\text{out}} \rangle}{\langle k^{\text{in}} \rangle \langle k^{\text{out}} \rangle} = \frac{\langle k^{\text{in}}k^{\text{out}} \rangle}{\langle k \rangle^2} \quad (17.11)$$

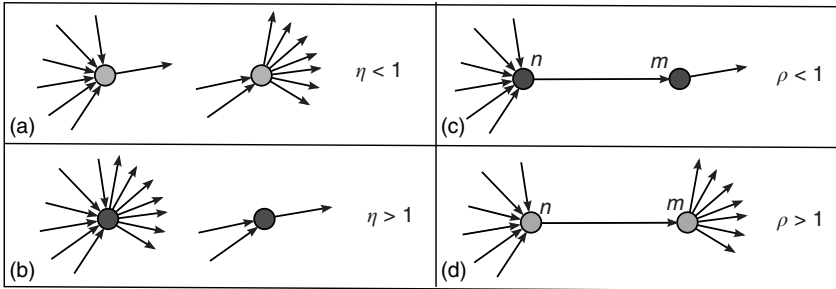


Figure 17.3 Diagram showing examples of the types of links that one might observe in networks with particular η and ρ values. (a) Node in- and out-degree are anticorrelated, (b) node in- and out-degree are correlated,

(c) in-degree at node n is anticorrelated with out-degree at node m , and (d) in-degree at node n is correlated with out-degree at node m .

where $\langle \cdot \rangle$ denotes an average over nodes. This coefficient is 1 when the out- and in-degrees are independent, is larger than 1 when they are positively correlated, and less than 1 when they are negatively correlated.

The second type of degree correlation that arises often occurs between the degrees at the ends of a randomly chosen link, referred to as *edge degree correlations*. In particular, when a link connects nodes n and m , a correlation might exist between k_n^{in} and k_m^{out} , between k_n^{out} and k_m^{out} , and so on. Since they have the most effect on network branching processes, this chapter will focus on those between k_n^{in} and k_m^{out} . This can be quantified by the edge degree correlation coefficient [30]:

$$\rho = \frac{\langle k_n^{\text{in}} k_m^{\text{out}} \rangle_e}{\langle k^{\text{in}} \rangle_e \langle k^{\text{out}} \rangle_e} \quad (17.12)$$

where $\langle \cdot \rangle_e$ denotes an average over edges, $\langle x_{nm} \rangle_e \equiv \sum_{n,m} A_{nm} x_{nm} / \sum_{n,m} A_{nm}$. As with the node degree correlation coefficient, a value of 1 indicates no correlations, and a value larger (smaller) than 1 indicates positive (negative) correlations.¹⁾ Figure 17.3 shows examples of the in- and out-degrees of typical nodes and edges in networks with positive and negative correlations: in Figure 17.3a, the in-degrees and out-degrees are negatively correlated. In Figure 17.3b, in-degrees and out-degrees are positively correlated. In Figure 17.3c, the in-degrees and out-degrees coming in and out of two connected nodes are negatively correlated, and in Figure 17.3d they are positively correlated.

Just like heterogeneity in the degree distributions, node correlations can modify the classical criterion for criticality. They affect the largest eigenvalue of the

1) A related and commonly used measure is the Pearson correlation coefficient, sometimes called the *assortativity coefficient* [31]

$$r = \frac{\langle (k'_n^{\text{out}} - \langle k'^{\text{out}} \rangle_e)(k'_m^{\text{in}} - \langle k'^{\text{in}} \rangle_e) \rangle_e}{\sqrt{\langle (k'^{\text{out}} - \langle k'^{\text{out}} \rangle_e)^2 \rangle_e} \sqrt{\langle (k'^{\text{in}} - \langle k'^{\text{in}} \rangle_e)^2 \rangle_e}}$$

where $k' = k - 1$ is the excess degree. Note that in this definition, the role of k^{out} and k^{in} is reversed.

adjacency matrix, which determines the properties of branching properties on complex networks.

17.2.5

Largest Eigenvalue and the Corresponding Eigenvector

All the properties of networks discussed above, such as the degree distribution and node correlations, are encoded in the network adjacency matrix A . While one can develop analyses of branching processes based only on knowledge of, for example, the degree distribution, the approach of this chapter is to follow [24, 32, 33] and develop an analysis technique based on the adjacency matrix A . In analyzing the propagation of avalanches in the next sections, repeated matrix–vector multiplications using the matrix A will arise, and in such cases, the resulting behavior is determined by the eigenvalue of A with largest magnitude and its corresponding right and left eigenvectors \mathbf{u} and \mathbf{v} (satisfying $A\mathbf{u} = \lambda\mathbf{u}$ and $\mathbf{v}^T A = \lambda\mathbf{v}^T$). This eigenvalue and its eigenvectors have a dominant influence on the properties of branching processes in networks, and it is therefore often possible to reduce questions about how network topology affects dynamics on networks to questions about how it affects the dominant eigenvalue λ and its eigenvectors.

The *Perron–Frobenius Theorem* [34] is fundamental when investigating the largest eigenvalue of network adjacency matrices. It states that an $N \times N$ irreducible, primitive matrix with nonnegative entries has a simple positive eigenvalue λ whose magnitude is larger than the magnitude of all other eigenvalues. Furthermore, its corresponding right and left eigenvectors have positive entries. The criterion of irreducibility, in the context of branching processes in networks, means that an avalanche has a nonzero probability to reach any node when starting from any other node. A matrix B is primitive if there is an integer $K > 0$ such that $B^K > 0$. The adjacency matrix of complex networks is typically primitive, and the subsequent analysis here assumes that this condition is satisfied.

While the theoretical results will be stated in terms of the largest eigenvalue λ and its eigenvectors \mathbf{u} and \mathbf{v} , it will be useful to present an approximation to these quantities that allows comparisons with the classical results mentioned in the introduction. When degree correlations are small, the largest eigenvalue and its eigenvectors can be approximated as [30]

$$\lambda \approx \rho\eta\langle k \rangle \quad (17.13)$$

$$u_n \approx k_n^{out} \quad (17.14)$$

$$v_n \approx k_n^{in}. \quad (17.15)$$

Note that, using the definition of η , Eqs. 17.11 and 17.13 can be rewritten as

$$\lambda = \frac{\langle k^{in}k^{out} \rangle}{\langle k \rangle} \rho. \quad (17.16)$$

One can understand these approximations for λ as follows. For random networks without correlations, one has $\rho = \eta = 1$ and thus $\lambda = \langle k \rangle$: that is, the largest eigenvalue represents the average degree (or, if one views the outgoing links from a

node as branches, the branching ratio). When there are correlations, λ generalizes the branching ratio, with positive correlations resulting in an effectively larger branching ratio.

17.3

Branching Processes in Complex Networks

This section introduces and analyzes a model of the propagation of avalanches in networks, using many of the descriptive quantities of the previous section. While this section follows [24], for simplicity of exposition only the distribution of avalanche durations is discussed in detail, while similar results for avalanche sizes are summarized.

First, a branching process in a network is defined as follows: Consider a network of N nodes labeled $m = 1, 2, \dots, N$. Each node m has a state $\tilde{x}_m = 0$ or 1 . The state $\tilde{x}_m = 0$ will be referred to as the *resting* state and $\tilde{x}_m = 1$ as the *excited* state. At discrete times $t = 0, 1, \dots$, the states of the nodes \tilde{x}_m^t are simultaneously updated as follows: (i) If node m is in the resting state, $\tilde{x}_m^t = 0$, it can be excited by an excited node n , $\tilde{x}_n^t = 1$, with probability $0 \leq A_{nm} < 1$, so that $\tilde{x}_m^{t+1} = 1$. (ii) The nodes that are excited, $\tilde{x}_n^t = 1$, will deterministically return to the resting state in the next time step, $\tilde{x}_n^{t+1} = 0$. The network of N nodes is therefore described by an $N \times N$ weighted network adjacency matrix $A = \{A_{nm}\}$, where $A_{nm} > 0$ may be thought of as the strength of the connection from node n to node m , and $A_{nm} = 0$ implies that node n does not connect to node m . It will be assumed that, given any two nodes n and m , the probability that an excitation originating at node n is able to excite node m (through potentially many intermediate nodes) is not zero. This is equivalent to saying the network is strongly connected, and therefore the matrix A is *irreducible*.

The nodes in this network should be thought of as functional units in a coarse-grained description of neuronal activity, where each unit comprises potentially many individual neurons. The probabilities A_{nm} should be thought of as an effective interaction that aggregates both excitatory and inhibitory connections. Consequently, the effect of modifying the balance of excitation and inhibition (as done experimentally, e.g., in [9]) is represented by a modification of the probabilities A_{nm} . These type of coarse-grained branching process models have been used successfully to model various aspects of information processing in neural networks (see [6, 9, 35] and other chapters in this book).

Starting from a single excited node k ($\tilde{x}_n^0 = 1$ if $n = k$ and $\tilde{x}_n^0 = 0$ if $n \neq k$), the system is allowed to evolve according to the dynamics above until there are no more excited nodes. The following definitions are introduced to analyze this process: (i) An *avalanche* is the sequence of excitations produced by a single excited node. (ii) The *duration* d of an avalanche is defined as the total number of time steps spanned by the avalanche: if the avalanche starts with $\tilde{x}_n^0 = 1$, then

$$d_n = \min_{t \geq 0} \{\tilde{x}_k^t = 0 \text{ for all } k\}. \quad (17.17)$$

An avalanche that continues indefinitely is said to have infinite duration. (iii) The size x of an avalanche starting with $\tilde{x}_n^0 = 1$ is defined as the total number of nodes excited during an avalanche, allowing nodes to be excited multiple times:

$$x_n = \sum_{t=0}^{d-1} \sum_{k=1}^N \tilde{x}_k^t. \quad (17.18)$$

Note that, by this definition, it is possible for an avalanche to have size larger than the total size of the network. The goal is to determine the probability distributions of these variables in terms of the matrix A . For simplicity of exposition, this chapter will be focused on the distribution of avalanche durations.

Since the interest is specifically in heterogeneous networks, significant differences between different nodes are expected, both in terms of their degree and their location in the network. Therefore, the distribution of avalanche durations for avalanches starting at a specific node n will be studied. To do this, the cumulative distribution of avalanche durations starting at node n is defined as

$$c_n(t) = P(d_n \leq t). \quad (17.19)$$

Note that the probability distribution of avalanche durations for avalanches starting at node n can be obtained from $c_n(t)$ by²⁾

$$P(d_n = t) = c_n(t) - c_n(t - 1). \quad (17.20)$$

By definition, $c_n(t)$ is a nondecreasing function of t which is less than or equal to 1. Therefore, as $t \rightarrow \infty$, $c_n(t)$ must approach a limiting value b_n which, from the definition of $c_n(t)$, corresponds to the probability that an avalanche starting at node n has finite duration:

$$b_n = \lim_{t \rightarrow \infty} c_n(t) = P(\text{avalanche starting at node } n \text{ is finite}). \quad (17.21)$$

The behavior of $c_n(t)$ for large t will be investigated in order to obtain information about the “tail” of the distribution of avalanche durations (i.e., the behavior of the distribution for large t). This is illustrated in Figure 17.4. The motivation for this approach stems from experimental results in which the statistics of long (and large) avalanches is claimed to reveal much about the underlying network’s critical (or noncritical) state, as discussed in the previous chapters.

While the presented framework has thus far been applicable to most networks (it has been assumed only that the matrix A is irreducible and primitive), the subsequent analysis will be restricted to a class of networks commonly referred to as *locally tree-like networks*. These networks have the property that, for most nodes, the nodes that can be reached in a relatively few number of steps form a network that can be approximately described as a tree. To make this more precise, it is

2) While the size and duration of an avalanche are, in this model, discrete random variables, terminology for continuous variables is used for the sake of self-consistency, because some of the analytical techniques utilize a continuous extension of discrete distributions, and because many experimental measurements presented in previous chapters are often not drawn from a discrete distribution.

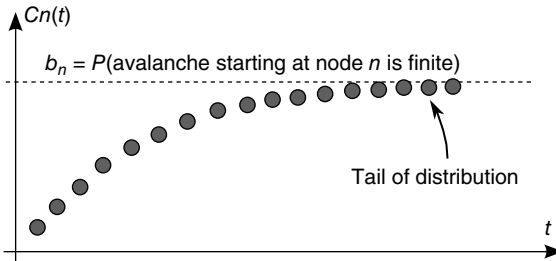


Figure 17.4 As a cumulative density function, $c_n(t)$ is an increasing function of t . The limiting behavior as $t \rightarrow \infty$, that is, how fast $c_n(t)$ approaches its limit, reveals information about the tail of the probability distribution of avalanche durations. The limit b_n is the probability that an avalanche generated at node n is finite.

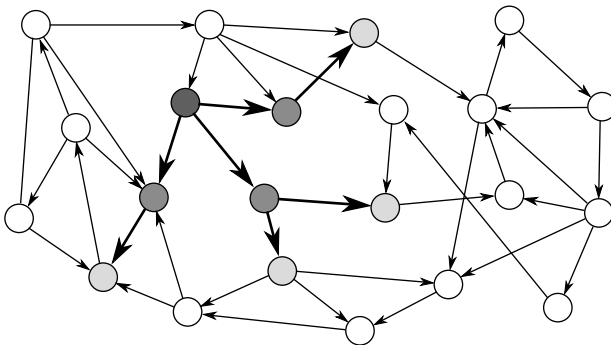


Figure 17.5 The neighborhood of the network around the black node has a tree-like structure.

assumed that for most nodes n and relatively small k , the number of different nodes reachable by paths of length k or less starting at node n , which is defined as $N_n(k)$, is close to the total number of paths of length k or less starting from node n , which is defined as $P_n(k)$. (Note that, in particular, for $k = 2$, this implies that the number of bidirectional edges is small.) Figure 17.5 illustrates this for a particular node in a small network: the number of nodes reachable from the black node by paths of length 2 or less (gray nodes) coincides with the total number of paths of length 2 or less starting at the black node, $P_n(2) = N_n(2)$. In this case, if the expected duration of the avalanches is small, avalanches starting at the dark gray nodes can be approximately treated as independent. Many networks found in applications are locally tree-like [36], and use of the locally tree-like approximation has led to theoretical insights into the behavior of various dynamical processes in networks [32, 37, 38]. Furthermore, use of the locally tree-like approximation has been observed to yield reasonable results even for networks that are not entirely tree-like [36]. Therefore, as a first step toward generalizing the classical results in branching trees to networks, the locally tree-like approximation will be assumed

hereafter. It is important to note that, even though the network is assumed to behave *locally* like a tree, this approximation still captures the effect of factors such as heterogeneous degree distributions and degree correlations.

Using the locally tree-like approximation, an equation for $c_n(t+1)$ at node n in terms of the variables $c_m(t)$ at other nodes m can be written down as follows:

$$\begin{aligned} c_n(t+1) = & P(\text{for all } m, \text{ an excitation at node } n \text{ does not propagate to node } \\ & m, \text{ or it does but then generates an avalanche that} \\ & \text{lasts less than } t \text{ steps.}) \end{aligned} \quad (17.22)$$

The left-hand side is the probability that an avalanche starting at node n lasts less than $t+1$ steps. This event is equivalent to the event that for every node m , either the excitation at node n does not propagate to node m (with probability $1 - A_{nm}$) or it propagates to node m and the avalanche that is subsequently generated at node m lasts less than t steps (with probability $A_{nm}c_m(t)$). Since the network is assumed to be locally tree-like, avalanches starting at nodes m are treated as independent events, and thus the right-hand side can be written as the product

$$c_n(t+1) = \prod_{m=1}^N [(1 - A_{nm}) + A_{nm}c_m(t)]. \quad (17.23)$$

As explained above, the behavior of $c_n(t)$ for large t , when it is approaching its limiting value b_n , is of interest. This limiting value can be obtained by taking the limit $t \rightarrow \infty$ in Eq. 17.23, and satisfies

$$b_n = \prod_{m=1}^N [(1 - A_{nm}) + A_{nm}b_m]. \quad (17.24)$$

The behavior of $c_n(t)$ as it approaches b_n can be analyzed by defining the small distance between c_n and its limit b_n as

$$f_n(t) \equiv b_n - c_n(t). \quad (17.25)$$

Inserting this quantity in Eq. 17.23, one obtains

$$b_n - f_n(t+1) = \prod_{m=1}^N [(1 - A_{nm}) + A_{nm}b_m - A_{nm}f_m(t)]. \quad (17.26)$$

This expression can be manipulated as follows:

$$b_n - f_n(t+1) = \prod_{m=1}^N [(1 - A_{nm}) + A_{nm}b_m] \left[1 - \frac{A_{nm}f_m(t)}{(1 - A_{nm}) + A_{nm}b_m} \right] \quad (17.27)$$

$$= \prod_{m=1}^N [(1 - A_{nm}) + A_{nm}b_m] \prod_{m=1}^N \left[1 - \frac{A_{nm}f_m(t)}{(1 - A_{nm}) + A_{nm}b_m} \right] \quad (17.28)$$

$$= b_n \prod_{m=1}^N \left[1 - \frac{A_{nm} f_m(t)}{(1 - A_{nm}) + A_{nm} b_m} \right] \quad (17.29)$$

$$= b_n \prod_{m=1}^N \left[1 - \frac{D_{nm}}{b_n} f_m(t) \right] \quad (17.30)$$

where D_{nm} is defined as

$$D_{nm} = \frac{A_{nm} b_n}{(1 - A_{nm}) + A_{nm} b_m}. \quad (17.31)$$

To determine the behavior when t is large and $f_n(t)$ is small, the right-hand side can be expanded in powers of f keeping only linear terms, to obtain

$$b_n - f_n(t+1) = b_n \left(1 - \sum_{m=1}^N \frac{D_{nm}}{b_n} f_m(t) + \mathcal{O}(f^2) \right). \quad (17.32)$$

After simplifying, to first order, f_n satisfies

$$f_n(t+1) = \sum_{m=1}^N D_{nm} f_m(t). \quad (17.33)$$

If an $N \times N$ matrix D with entries D_{nm} and a vector $\mathbf{f}(t) = [f_1(t), f_2(t), \dots, f_N(t)]^T$ are defined, where the superscript T denotes the transpose, the previous equation can be written as the vector equation

$$\mathbf{f}(t+1) = D\mathbf{f}(t) \quad (17.34)$$

Starting from some initial time t_0 where $f(t_0)$ is small, and iterating the previous update equation $t - t_0$ times, one has

$$\mathbf{f}(t) = D^{t-t_0} \mathbf{f}(t_0). \quad (17.35)$$

For large t , the action of the matrix D^{t-t_0} on the initial vector results in

$$\mathbf{f}(t) \propto \lambda_D^t \mathbf{u} \quad (17.36)$$

where λ_D is the eigenvalue of D with the largest magnitude, and \mathbf{u} is its corresponding right eigenvector.³⁾ In terms of the quantities $c_n(t) = b_n - f_n(t)$, for large t they satisfy

$$c_n(t) \approx b_n - C u_n \lambda_D^t \quad (17.37)$$

where C is the proportionality constant in Eq. 17.36. This analysis is valid as long as $\lambda_D < 1$, since it was assumed that f_n decays to zero as $t \rightarrow \infty$, and it was found that $f_n \propto \lambda_D^t$. It turns out that one always has $\lambda_D \leq 1$. The case $\lambda_D = 1$ must be treated separately since this analysis would conclude that $f_n(t)$ does not decay to

3) In the particular case when D is diagonalizable and a basis of eigenvectors $\{\mathbf{u}_i\}$ with eigenvalues $\{\lambda_i\}$ can be found, one can see this by decomposing $\mathbf{f}(t_0)$ into eigenvectors, $\mathbf{f}(t_0) = \sum_i \alpha_i \mathbf{u}_i$. Multiplication by D^{t-t_0} yields $D^{t-t_0} \mathbf{f}(t_0) = \sum_i \alpha_i \lambda_i^{t-t_0} \mathbf{u}_i$. As $t \rightarrow \infty$, this sum is dominated by the term with the eigenvalue of largest magnitude, λ_D , and thus $D^{t-t_0} \mathbf{f}(t_0) \propto \lambda_D^t \mathbf{u}$. In the general case, a similar argument can be made writing D in Jordan canonical form.

zero (cf. Eq. 17.36). Inclusion of the second-order terms that were neglected will confirm that $f_n \rightarrow 0$ but as a power law, $f_n \propto t^{-2}$, instead of exponentially. This will be discussed in Section 17.3.3.

17.3.1

Subcritical Regime

In the case $\lambda_D < 1$, Eq. 17.37 shows that $c_n(t)$ approaches its limit exponentially, reducing the difference to it by a factor of λ_D in each time step. Using Eq. 17.20, this implies that the probability of an avalanche starting at node n having duration t is

$$P(d_n = t) \propto u_n \lambda_D^t. \quad (17.38)$$

This result has two components that need to be interpreted: (i) the probability of an avalanche having duration t is proportional to the right eigenvector entry u_n of the matrix D , and (ii) when $\lambda_D < 1$, the probability of an avalanche having duration t decays exponentially with t . To understand these results, one needs to determine what λ_D and u_n represent, and, since the matrix D is defined in Eq. 17.31 in terms of the entries of A and of b_n , to know what b_n is. Recall that b_n is the probability that an avalanche starting at node n has finite duration and satisfies the equation

$$b_n = \prod_{m=1}^N [(1 - A_{nm}) + A_{nm} b_m]. \quad (17.39)$$

Note that $b_n = 1$ for all n is always a solution of this equation. When $b_n = 1$ in Eq. 17.31, the matrix D reduces to the matrix A , and therefore $\lambda_D = \lambda$, where λ is the eigenvalue of A with largest magnitude discussed in Section 17.2.5. Since the above argument is valid only as long as $\lambda_D = \lambda < 1$, this suggests that this solution (i.e., $b_n = 1$, $\lambda_D = \lambda$, $P(d_n = t) \propto \lambda^t v_n$) will be relevant only when $\lambda < 1$. Indeed, it can be shown that this is the *only* solution when $\lambda < 1$ (see the Appendices of [24]). Therefore one arrives at the following result: When $\lambda < 1$, all avalanches are finite, and for large t the probability of an avalanche starting at node n having duration t is proportional to $\lambda^t u_n$, where λ is the largest eigenvalue of A and \mathbf{u} its associated right eigenvector.

This result will now be interpreted and contrasted with the results from uniform branching processes and branching processes on random networks. First, consider the case of networks without correlations, such as random Erdős–Rényi networks, where links are placed with a fixed probability between any pair of nodes [39] (see also [25]). For these networks, as discussed in Section 17.2.5, one can approximate

$$\lambda \approx \langle k \rangle \quad (17.40)$$

$$u_n \approx k_n^{out}. \quad (17.41)$$

Noting that $k_n^{out} = \sum_{m=1}^N A_{nm}$ is the expected number of excited nodes produced by an excitation in node n , the mean degree $\langle k \rangle$ is equivalent to the average branching ratio σ introduced in Section 17.1. Therefore, for this type of network, $\lambda \approx \sigma$. The conclusion above then can be interpreted as saying that the distribution of

avalanche durations decays exponentially with the rate $\log(1/\sigma)$, which agrees with the classical result in critical branching processes in trees [3, 5]. Using the approximation $u_n \approx k_n^{\text{out}}$, the second part of the result above states that the probability of an avalanche starting at node n having duration t is proportional to the out-degree k_n^{out} of node n . This is very reasonable since one expects that, everything else being equal, nodes that have more outgoing links (or, more precisely, a larger sum of outgoing weights) should produce longer avalanches.

The results above generalize this intuitive result to more complex network topologies that might have correlations or heterogeneous degree distributions. For example, the largest eigenvalue of a network with a heterogeneous degree distribution, but without degree-degree correlations, can be approximated by (see Eq. 17.16)

$$\lambda \approx \eta\langle k \rangle = \frac{\langle k^{\text{in}}k^{\text{out}} \rangle}{\langle k \rangle}. \quad (17.42)$$

The largest eigenvalue λ may be interpreted as a generalization of the branching ratio σ , implying that positive node degree correlations will result in a larger effective branching ratio. Since the distribution of avalanche durations decays as λ^t , positive correlations will result in longer avalanches. In general, various other factors might affect the value of λ , and the advantage of this approach is that the study of the effect of this factor on avalanches is reduced to the study of their effect on λ .

For uncorrelated networks, the eigenvector entry u_n coincides with the *local* branching ratio k_n^{out} at node n . For more general networks, this eigenvector entry can be interpreted as a version of the branching ratio that takes into account both the expected number of nodes that the node n will generate and the location of these nodes in the network. In general, two nodes n and m that have the same out-degree, $k_n^{\text{out}} = k_m^{\text{out}}$, and can have very different values of their respective eigenvector entry, $u_n \neq u_m$. As an example, consider the networks shown in Figure 17.6, in which all the nonzero links are assumed to have the same weight: $A_{nm} = w$ if $A_{nm} \neq 0$. The network on the left has negative edge-degree correlations ($\rho < 1$): nodes with many links tend to connect mostly to nodes with few links. On the other hand, the network on the right has positive edge-degree correlations ($\rho > 1$): nodes with many links tend to connect to each other forming a highly connected core, while poorly connected nodes are in the periphery of the network. These two networks were constructed with the same degree distribution, so that, if one were to calculate the average branching ratio $\sigma = \langle k \rangle$, one would obtain $\sigma = \frac{39}{15}w$ for both networks. However, the network on the right has a larger eigenvalue λ , and avalanches are more likely to have a longer duration. Intuitively, one can imagine that an avalanche that circulates in the highly connected core will be more likely to have a long duration.

The networks in Figure 17.6 also serve to illustrate why the distribution of avalanches starting at node n is proportional to the right eigenvector entry u_n and not to the out-degree k_n^{out} . Consider the two nodes marked in black in the network on the right (one circular and the other square), and suppose that they are excited.

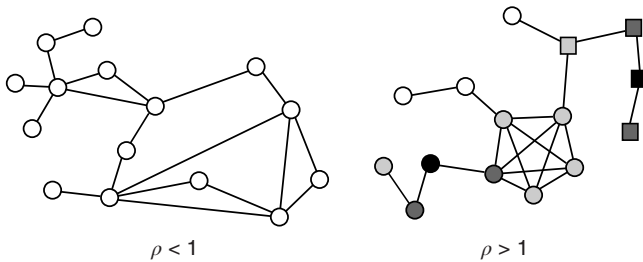


Figure 17.6 Two networks with the same degree distribution but with different edge degree correlations. The network on the left has negative edge degree correlations ($\rho < 1$), while the network on the right has positive edge degree correlations ($\rho > 1$). The number of nodes reachable in a given number of steps is different if one starts from the black circular node or from the

black square node, even though these nodes have same degree. The nodes reachable in one step are colored in dark gray, while the nodes reachable in two steps are colored in light gray. This leads to different statistics of avalanches generated at different nodes, which are captured by the eigenvector entry u_n corresponding to a given node.

The circular and square nodes colored in dark gray are those nodes that could be excited in the next time step (with probability w) by the black circular and square node, respectively, and the circular and square light gray nodes are the nodes that could be excited after two time steps by the black circular and square node, respectively. While the two black nodes have the same out-degree, $2w$, the expected size and duration of an avalanche starting at the black circular node should be much larger. The reason is that the eigenvector entry for the black circular node (0.114) is larger than that for the black square node (0.008).

The example above considered a small network, and the description was qualitative. The theory was tested quantitatively by simulating a large number of avalanches on a large network. First, an Erdős–Rényi random network [39] was constructed with $N = 2 \cdot 10^3$ nodes by assigning a directed link between any ordered pair of nodes with probability $p = 0.01$. Then, each link was assigned a weight A_{nm} uniformly chosen at random from the interval $(0, 1)$. By multiplying the resulting matrix by an appropriate number, a matrix with $\lambda = 0.95$ was obtained. Finally, links were rewired so as to decrease the edge–degree correlations (and thus decrease λ) as follows: two pairs of links $n \rightarrow m$ and $j \rightarrow k$ are chosen at random, and replaced by two links $n \rightarrow k$, $j \rightarrow m$ only if by doing so the degree–degree correlations become more negative, that is, if ρ decreases. By repeating this process multiple times, ρ can be decreased to a low enough value and thus a network with negative degree–degree correlations can be constructed (see [30, 31] for more details). Since the resulting network has degree correlations, the approximation $k_n^{\text{out}} \propto u_n$ is no longer valid and the prediction $P(d_n = t) \propto u_n$ can be verified, and it can be confirmed that, as argued above, it is in general an improvement over using $P(d_n = t) \propto k_n^{\text{out}}$.

Having constructed a network with degree correlations as described above, 2×10^6 avalanches were simulated, each one starting from a randomly chosen

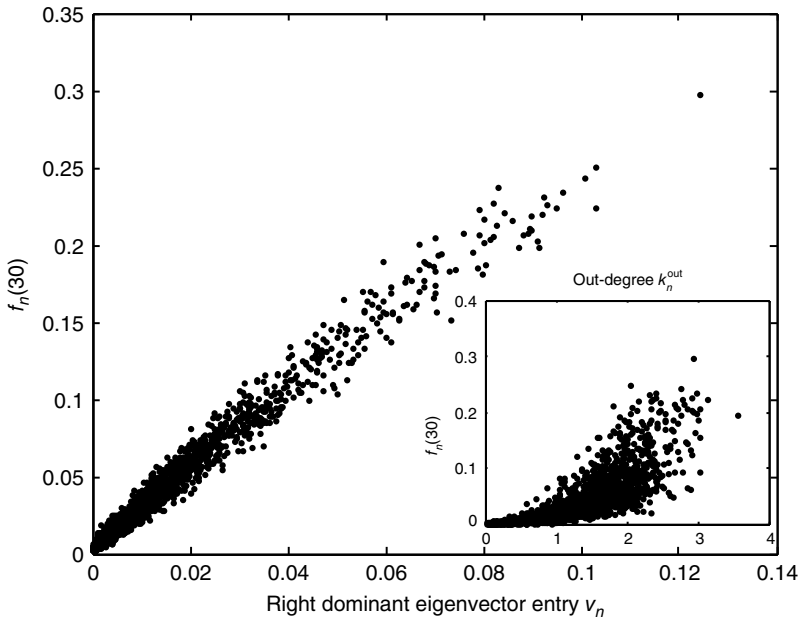


Figure 17.7 Fraction of avalanches originating at node n that last longer than 30 time steps, $f_n(30)$, versus u_n (see text for details about the network used). Theory (Eq. 17.38) predicts $f_n(30) \propto u_n$. In the inset, the same

values $f_n(30)$ are plotted against the corresponding out-degree k_n^{out} . The eigenvector entry u_n does a significantly better job than out-degree k_n^{out} of predicting the duration of avalanches originating at node n .

node. For each avalanche, its duration d_n and its starting node n were recorded. Figure 17.7 (from Ref. [24]) shows $P(d_n > 30) = f_n(30)$ versus u_n for a random sample of nodes n . As can be observed, $f_n(30)$ is well predicted by u_n , as the points lie approximately on a straight line. On the other hand, using the out-degree k_n^{out} to predict $f_n(30)$ gives bad results: the inset shows a plot of $f_n(30)$ versus k_n^{out} , and it is clear that the correlation between these two variables is significantly smaller.

17.3.2 Supercritical Regime

So far, only the case $\lambda < 1$, which results in an exponential decay in the duration of avalanches, has been discussed. The analysis of this regime was based on the fact that $b_n = 1$ is a solution of Eq. 17.24 toward which $c_n(t)$ approaches. When $\lambda > 1$, there exists another solution to Eq. 17.24 that satisfies $b_n < 1$ (see the Appendices of [24]) and toward which $c_n(t)$ converges as $t \rightarrow \infty$. Recalling that b_n is the probability that an avalanche starting at node n is finite, a solution $b_n < 1$ indicates that there is a positive probability of generating an infinite avalanche. If λ is interpreted as the branching ratio generalized to complex networks, then this conclusion is reasonable: if $\lambda > 1$, then, on average, an excited node produces

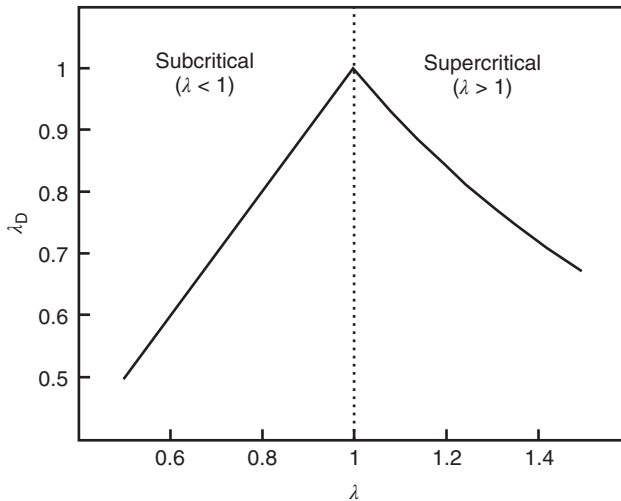


Figure 17.8 Largest eigenvalue of the matrix D with entries in Eq. 17.31, λ_D , as a function of the largest eigenvalue of the matrix A , λ . The two eigenvalues coincide for $\lambda < 1$.

The eigenvalue λ_D can be interpreted as the effective branching ratio of the avalanches that have a finite duration.

more than one excited node in the next time step and one expects that the number of excited nodes would increase and ultimately saturate. Since $c_n(t)$ describes the distribution of *finite* avalanches, Eq. 17.23 and its analysis still hold. Again, this is valid as long as $\lambda_D < 1$, since in deriving these results it was assumed that $f_n(t)$ decays to zero with increasing t . It can be shown that, if $\lambda > 1$, then $\lambda_D < 1$ (see the Appendices of [24]). The relationship between λ_D and λ is shown graphically in Figure 17.8 from Ref. [24] for an Erdős–Rényi random network. Note that when $\lambda < 1$, $\lambda_D = \lambda$, so the left half of Figure 17.8 is a straight line with slope 1. While the interpretation of λ_D in the subcritical regime is clear (i.e., $\lambda_D = \lambda$ is the effective branching ratio), it is not immediately clear how to interpret λ_D in the supercritical regime. However, recalling that the distribution of finite avalanches of duration t decays as λ_D^t , λ_D can be interpreted as the effective branching ratio of the finite avalanches. Why does this effective branching ratio decrease even as the actual branching ratio λ increases? As λ increases, finite avalanches have a shorter duration, because long-duration avalanches are more likely to become self-sustained. Therefore, the effective branching ratio of these shorter avalanches is smaller. While this is an intuitive explanation, the mathematical reason is in the derivations above.

Summarizing the results for the supercritical regime, it was found that: When $\lambda > 1$, some avalanches have infinite duration, and for large t the probability of an avalanche starting at node n having finite duration t is proportional to $u_n \lambda_D^t$, where λ_D is the largest eigenvalue of the matrix D with entries defined in Eq. 17.31 and \mathbf{u} its associated right eigenvector.

17.3.3

Critical Regime

Of particular interest is the critical regime, in which the distribution of avalanche sizes and durations obeys a power law. So far, the linear analysis of Section 17.3 has been used to analyze the subcritical and supercritical regimes. The linear approach was valid since $\lambda_D < 1$, but when $\lambda = 1$ (and thus $\lambda_D = 1$), the linear terms that were kept in Eq. 17.32 seem to imply that $f_n(t)$ does not grow or decrease with t (at least for large t). However, the terms that were neglected will be sufficient to make $f_n(t)$ decrease, albeit at a slower rate. Such behavior is not uncommon in the analysis of the stability of equilibria of nonlinear systems. When a linear stability analysis is inconclusive, the equilibrium is said to be *marginally stable* and it becomes necessary to determine the stability of the equilibrium by including higher order terms in the analysis. From this standpoint, the previous analysis is a linear stability analysis of the equilibria of the dynamical system defined by the maps Eq. 17.23, and the critical regime corresponds to marginal stability of the equilibrium $b_n = 1$. As explained above, to determine the behavior of $f_n(t)$ for large times, it is necessary to keep higher order terms in the expansion of Eq. 17.30, reproduced here for convenience with $b_n = 1$:

$$1 - f_n(t+1) = \prod_{m=1}^N [1 - A_{nm} f_m(t)]. \quad (17.43)$$

Since, as a result of the marginal stability, it is expected that $f_n(t)$ decays to zero at a slower rate than exponentially, it is proposed that the solution $f_n(t)$ is given by a function that varies slowly with t , and that can be extended to continuous values of t . Under the assumption that $f_n(t)$ varies slowly, one can approximate $f_n(t+1)$ by

$$f_n(t+1) \approx f_n(t) + f'_n(t). \quad (17.44)$$

Substituting Eq. 17.44 into Eq. 17.43, one obtains

$$1 - f_n(t) - f'_n(t) \approx \prod_{m=1}^N [1 - A_{nm} f_m(t)]. \quad (17.45)$$

Assuming $f_n(t) \ll 1$ and expanding the product to second order, one obtains, after simplification

$$f_n + f'_n \approx \sum_{m=1}^N A_{nm} f_m - \frac{1}{2} \sum_{m=1}^N \sum_{k \neq m} A_{nm} A_{nk} f_m f_k + \mathcal{O}(f^3). \quad (17.46)$$

The leading order terms as $f \rightarrow 0$ are f_n on the left-hand side and $\sum_{m=1}^N A_{nm} f_m$ on the right-hand side, so for these to balance it is required that

$$f_n = \sum_{m=1}^N A_{nm} f_m \quad (17.47)$$

which is the eigenvector equation $\mathbf{f} = A\mathbf{f}$. This means that in this limit \mathbf{f} is proportional to the eigenvector \mathbf{u} of A with eigenvalue $\lambda = 1$, implying $f_n(t) = Ku_n$,

where K is a proportionality constant. Since \mathbf{u} is independent of time, the constant of proportionality must be time dependent, $f_n(t) = K(t)u_n$. This argument was made for $f \rightarrow 0$, since the second-order terms were neglected. For finite f , it is expected that the actual solution of Eq. 17.46 deviates from $f_n(t) = K(t)u_n$ by a small error, so a reasonable *ansatz* for $f(t)$ is

$$f_n(t) = K(t)u_n/\langle u \rangle + \varepsilon_n(t) \quad (17.48)$$

where ε_n is an error term assumed to satisfy $\varepsilon_n \ll f_n(t)$ and $\varepsilon'_n \ll f'_n(t)$. The term $\langle u \rangle = \sum_{n=1}^N u_n/N$ is included to make $K(t)$ independent of the normalization of \mathbf{u} . Inserting this in Eq. 17.46, neglecting terms of order ε' , ε^2 , and $f\varepsilon$, and using the approximation $\sum_m \sum_{k \neq m} A_{nm} A_{km} u_m u_k \approx \sum_m A_{nm} u_m \sum_k A_{nm} u_k = u_n^2$ (valid when there are many links per node), one obtains

$$\varepsilon_n + K'(t)u_n/\langle u \rangle = \sum_{m=1}^N A_{nm}\varepsilon_m - \frac{1}{2}K^2(t)u_n^2/\langle u \rangle^2. \quad (17.49)$$

Besides $K(t)$, which has the desired unknown time dependence, the only unknown in this equation is the error term ε_n . To eliminate it from the equation, both sides of the equation are multiplied by v_n , where \mathbf{v} is the left eigenvector of A satisfying $\mathbf{v}^T A = \mathbf{v}^T$, or $\sum_{n=1}^N A_{nm} v_n = v_m$, and summed over n . The error terms cancel, resulting in an ordinary differential equation (ODE) for $K(t)$,

$$K'(t) = -\frac{1}{2} \frac{\langle vu^2 \rangle}{\langle vu \rangle \langle u \rangle} K^2(t) \quad (17.50)$$

where the notation $\langle xy \rangle \equiv \frac{1}{N} \sum_n x_n y_n$ is used. Solving this ODE yields

$$K(t) = \frac{1}{\beta + \frac{1}{2} \frac{\langle uv^2 \rangle}{\langle uv \rangle \langle v \rangle} t} \quad (17.51)$$

where β is an integration constant. Using $f_n(t) \approx K(t)u_n/\langle u \rangle$ and $c_n(t) = 1 - f_n(t)$, one obtains

$$c_n(t) \approx 1 - \frac{u_n/\langle u \rangle}{\beta + \frac{1}{2} \frac{\langle uv^2 \rangle}{\langle uv \rangle \langle v \rangle} t}. \quad (17.52)$$

The probability density function of the duration $p_n(t)$, in the continuous time approximation, is given by $p_n(t) = c'_n(t)$, which evaluates to

$$p_n(t) \propto \frac{u_n}{\left(\beta + \frac{1}{2} \frac{\langle uv^2 \rangle}{\langle uv \rangle \langle v \rangle} t \right)^2}. \quad (17.53)$$

For large t ,

$$p_n(t) \propto u_n t^{-2}. \quad (17.54)$$

Therefore, when $\lambda = 1$, the distribution of avalanche durations for large t is a power law with exponent -2 . As before, the dependence of the distribution on the starting

Table 17.1 Distribution of avalanche durations and sizes.

Regime	$P(d_n = t t < \infty) \propto$	$P(x_n = x x < \infty) \propto$
$\lambda < 1$ (subcritical)	$u_n \lambda^t$	$u_n x^{-3/2} e^{-x/x^*}$
$\lambda = 1$ (critical)	$u_n t^{-2}$	$u_n x^{-3/2}$
$\lambda > 1$ (supercritical)	$u_n \lambda_D^t$	$u_n x^{-3/2} e^{-x/x^*}$

node is through the right eigenvector of A corresponding to $\lambda = 1$. Thus, for the critical regime, it is found that When $\lambda = 1$, all avalanches have finite duration, and for large t the probability of an avalanche starting at node n having duration t is proportional to $u_n t^{-2}$, where λ_D is the largest eigenvalue of matrix D with entries defined in Eq. 17.31 and \mathbf{u} its associated right eigenvector.

This concludes the analysis of the distribution of avalanche durations. An analysis of the distribution of avalanche sizes can be carried out using similar techniques (see [24]), with the conclusion that the distribution of avalanche sizes for large times is a power law with exponent $-3/2$ when $\lambda = 1$ and a power law multiplied by an exponential when $\lambda \sim 1$: $p_n(x) \propto u_n x^{-3/2} e^{-x/x^*}$, where x^* is a parameter that depends on the matrix A and the vector $[b_1, b_2, \dots, b_N]$, and is proportional to $(\lambda_D - 1)^{-2}$ (for details, see [24]). The results for the distribution of avalanche sizes and durations are summarized in Table 17.1.

The predictions in the table were compared with numerical simulations of avalanches in computer-generated networks. First, heterogeneous networks with $N = 10^5$ nodes were generated by creating a sequence of N desired degrees chosen randomly from a power law degree distribution $P(k) \propto k^{-3.5}$ and then connecting pairs of nodes at random until the degree of each node reached its desired degree (i.e., the so-called configuration model [25, 29] was used). Then, each nonzero entry in the resulting unweighted adjacency matrix was replaced by a weight chosen uniformly at random from $(0, 1)$. After verifying that the resulting network was irreducible and primitive, its largest eigenvalue was adjusted by multiplying the matrix by a constant, obtaining the matrix A with largest eigenvalue λ . (This process was used for mathematical convenience, and it is not suggested that brain functional networks adjust their topology in this way. The theory above is independent of how the networks are generated.)

After creating networks as described above with $\lambda = 0.9, 1$, and 1.1 , a large number of avalanches were simulated (10^6 avalanches in the subcritical networks, and 2×10^6 avalanches in the critical network) and the starting node n , the duration d_n , and the size x_n of each avalanche were recorded. Figure 17.9 (from Ref. [24]) shows histograms of the avalanche durations (top panels) and sizes (bottom panels). The symbols indicate the number of avalanches with the duration or size in the horizontal axis, and the dashed lines show the prediction from the theory. Since the predictions above do not specify the proportionality constant, the vertical position in of the dashed curves in the plots is arbitrary. In general, the agreement between

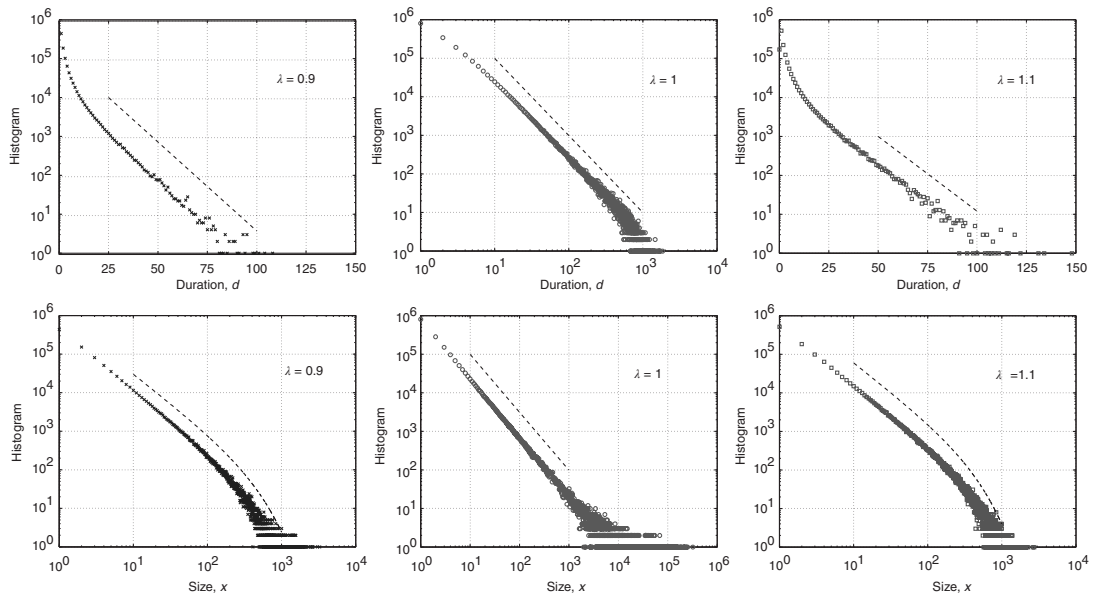


Figure 17.9 Histograms of avalanche durations (top panels) and sizes (bottom panels) for subcritical ($\lambda = 0.9$, left panels), critical ($\lambda = 1$, middle panels), and supercritical ($\lambda = 1.1$, right panels) networks. The symbols indicate the number of avalanches with the duration or size in the horizontal axis, and the dashed lines show the prediction from the theory (see the table above). The vertical position of the dashed lines is arbitrary.

the theoretical predictions and the simulations is very good. Additional quantitative comparisons can be done (see [24]) but are not shown here.

The bottom panels of Figure 17.9 show that it might be experimentally challenging to distinguish the distributions of finite avalanche sizes near criticality. These distributions have the form $P(x_n = x|x < \infty) \propto u_n x^{-3/2} e^{-x/x^*}$, where x^* is proportional to $(\lambda_D - 1)^{-2}$ and, therefore, diverges at $\lambda = 1$ (see [24]). When x/x^* is small enough, the term e^{-x/x^*} is close to 1 and the distribution appears to be a power law with exponent $-3/2$. In the examples shown in the figure, the exponential term would not be noticeable if one were to consider only avalanches of size less than $x = 10^2$, and the truncated distributions would appear critical. Only when the full range of observed avalanches is included do the distributions show the effect of the exponential term. While this suggests that it might be hard to pinpoint exactly the critical point in experiments, it also indicates that the regime in which the network is effectively critical, in the sense that its behavior is indistinguishable from the critical state for a wide range of observations, might be relatively large. For observations restricted to avalanches of size less than 10^2 , the effective range of criticality extends approximately from at least $\lambda \sim 0.9$ to ~ 1.1 . It might be worthwhile to study systematically the robustness of functional aspects such as dynamic range [9, 32, 33, 35] to variations from criticality.

17.4 Discussion

This chapter began with a discussion of critical branching processes in tree-like networks. These processes are characterized by an average branching ratio σ which characterizes the nature of the branching process as subcritical, critical, or supercritical if $\sigma < 1$, $\sigma = 1$, or $\sigma > 1$, respectively. Recent models of avalanche propagation in neural networks [6, 9, 35] have adopted a generalization of the branching ratio which is the average, over all nodes of the network, of the local branching ratio k_n^{out} , the expected number of nodes that node n will excite. Thus, the branching ratio σ generalizes to the mean degree $\langle k \rangle$. In this chapter it was shown that networks with sufficiently complex structure (such as a heterogeneous degree distribution or degree correlations between different nodes) require further generalization. In this case, the local branching ratio at node n is better approximated by u_n , the n th entry in the right eigenvector of the matrix A . This quantity accounts for the fact that not all nodes are equally effective at propagating excitations in a network with complex topology. It captures not only the expected number of nodes excited by node n but also how many nodes these will excite in turn, and so on. In short, u_n accounts for differences in local network structure. Similarly, the correct generalization of the global branching ratio in this case is given by the largest eigenvalue of the matrix A , λ . This discussion is summarized in the table below.

If the largest eigenvalue λ is used in place of σ , the main results from the theory of classical branching processes remain valid, in particular the power law form of the distribution of avalanche sizes and durations at criticality, and also the

Table 17.2 Generalization of branching parameters.

-	Local branching ratio	Global branching ratio
Uniform tree	σ	σ
Unstructured network	k_n^{out}	$\langle k \rangle$
Complex network	u_n	λ

value of the exponents in the power laws, which have been observed in various experiments of neuronal avalanches [6–13]. In this respect, there does not seem to be a difference between classical branching processes and those in networks. However, it was shown that various network properties can modify the largest eigenvalue and therefore the properties of avalanches of networks. In addition, it is possible to find the statistics of avalanches starting at a particular node, and these statistics can be related to the eigenvector entry of that particular node.

There were some limitations to the theory presented in this chapter. First, it was assumed that the network is locally tree-like. While many networks found in practice can be approximately described as locally tree-like, and a large class of computer-generated networks are also locally tree-like, this approximation might break down when the network has a significant number of short loops, as happens, for example, in networks where nodes are arranged spatially and have a strong local coupling. While it might be possible to extend these results to remove the locally tree-like assumption (which would most certainly modify the criterion for criticality), this is an open problem and left for future research. Another assumption implicit in the theory was that the largest eigenvalue λ is well separated from the next largest magnitude of the rest of the eigenvalues. While the theory, as presented above, does not rely on this fact since it was assumed that $t \rightarrow \infty$, in practice one observes avalanches up to some large but finite duration. For the approximations to be valid for finite but large t (in particular, to obtain Eq. 17.36 from Eq. 17.35) it is required that the separation between λ and the magnitude of the other eigenvalues is not small. This issue has been studied in [40] with the conclusion that this separation is typically very large, except possibly for cases where the network has strong community structure, that is, when it can be divided into groups of nodes such that connections between nodes in the same group are more likely than connections between nodes in different groups. While the analysis in this chapter could perhaps be extended to account for multiple communities, here the simplest case of one community was considered. Finally, the effect of inhibition is typically not included explicitly in branching process models of avalanche propagation, and it was not included in this chapter. It is assumed that decreased inhibition (excitation) results effectively in increased (decreased) probabilities of excitation transmission, and therefore in larger (smaller) λ .

The main motivation for the analysis above was to establish a firmer theoretical ground for the observations of criticality in neuronal avalanches in functional brain

networks. Typically, the experimentally observed critical exponents are compared with those predicted by branching processes on tree networks. However, it is known that anatomical and functional brain networks often have nontrivial and recurrent structure [15–19]. The analysis presented in this chapter offers an explanation for why the experimentally observed critical exponents match with classical branching process theory predictions in spite of such fundamental differences in the presumed underlying network topology. The analysis extends the class of networks for which one can confidently claim that the observed exponents are predicted theoretically. However, the analysis also offers a warning when interpreting the underlying causes of criticality in brain networks. For example, classical theory would suggest that an experimentally observed change from critical to supercritical dynamics is caused by a change in mean degree in the network. This is potentially misleading; the same change in dynamics could also result from changes in network topology, such as correlations, that leave the mean degree fixed.

Beyond fundamental understanding of existing observations, this chapter offers strategies for controlling avalanche dynamics in complex networks. For example, to prevent large avalanches, disabling the nodes that most contribute to their propagation would be desired. As argued in this chapter, these nodes are those with the largest eigenvector entry u_n , rather than those with the largest out-degree k_n^{out} . The two quantities can be very different, and if one used the out-degree to identify the node that produced the longest avalanches in the example used in Figure 17.7, one would identify the wrong node, as the inset shows. Since there has been tremendous progress on the identification and mapping of functional brain networks at various levels [15–19], it is essential to understand the propagation of activity in a network with a specific nontrivial structure. If advances in experimental techniques allow identification of neurons or groups of neurons with large u_n , these would likely be good targets to remove when attempting to prevent epileptic seizures. Finally, applications of this work are not restricted to critical brain dynamics, but may include other areas where branching processes in networks occur, such as power grid failure cascades [41] and epidemic propagation on networks [42–44], among others.

A power law distribution of avalanche sizes and durations is perhaps the most distinctive characteristic of critical brain dynamics, but is not the reason for criticality. As in many biological systems, the reason is likely tied to function. Critical dynamics has been observed to result in optimized information processing in neuronal networks [9, 10, 45]. An important example is the maximization of dynamic range at criticality, which was predicted for random networks in [35] and observed experimentally in [9]. Recent work by the authors [32, 33] considered the effect of complex network topology on the dynamic range, and found that, consistent with the results in this chapter, it is maximized when $\lambda = 1$. As more consequences of critical dynamics for information processing in networks are uncovered, care should be taken to understand the effect of network structure on these processes.

The authors acknowledge useful discussions with Edward Ott, Marshall Carpenter, and Dietmar Plenz. JGR acknowledges support from NSF under Grant

No. DMS-0908221. DBL acknowledges support from NSF MCTP Grant No. DMS-0602284, and was also supported by Award Number U54GM088558 from the National Institute Of General Medical Sciences. The content is solely the responsibility of the authors and editors and does not necessarily represent the official views of the National Institute of General Medical Sciences or the National Institutes of Health.

References

1. Watson, H. and Galton, F. (1874) On the probability of the extinction of families. *J. Anthropol. Inst. Great Br.*, **4**, 138–144.
2. Pázsit, I. and Pál, L. (2008) *Neutron Fluctuations: A Treatise On the Physics On Branching Processes*, Elsevier Science.
3. Harris, T. (1963) *The Theory of Branching Processes*, Springer.
4. Athreya, K.B. and Ney, P.E. (1972) *Branching Processes*, Springer Verlag.
5. Zapperi, S., Lauritsen, K., and Stanley, H. (1995) Self-organized branching processes: mean-field theory for avalanches. *Phys. Rev. Lett.*, **75** (22), 4071.
6. Beggs, J.M. and Plenz, D. (2003) Neuronal avalanches in neocortical circuits. *J. Neurosci.*, **23** (35), 11–167.
7. Beggs, J. and Plenz, D. (2004) Neuronal avalanches are diverse and precise activity patterns that are stable for many hours in cortical slice cultures. *J. Neurosci.*, **24** (22), 5216–5229.
8. Stewart, C. and Plenz, D. (2008) Homeostasis of neuronal avalanches during postnatal cortex development in vitro. *J. Neurosci. Methods*, **169** (2), 405–416.
9. Shew, W., Yang, H., Petermann, T., Roy, R., and Plenz, D. (2009) Neuronal avalanches imply maximum dynamic range in cortical networks at criticality. *J. Neurosci.*, **29**, 15–595.
10. Shew, W., Yang, H., Yu, S., Roy, R., and Plenz, D. (2011) Information capacity and transmission are maximized in balanced cortical networks with neuronal avalanches. *J. Neurosci.*, **31** (1), 55–63.
11. Petermann, T., Thiagarajan, T.C., Lebedev, M.A., Nicolelis, M.A.L., Chialvo, D.R., and Plenz, D. (2009) Spontaneous cortical activity in awake monkeys composed of neuronal avalanches. *Proc. Natl. Acad. Sci. U.S.A.*, **106** (37), 15–921.
12. Gireesh, E.D. and Plenz, D. (2008) Neuronal avalanches organize as nested theta-and beta/gamma-oscillations during development of cortical layer 2/3. *Proc. Natl. Acad. Sci. U.S.A.*, **105** (21), 7576.
13. Hahn, G., Petermann, T., Havenith, M., Yu, S., Singer, W., and Plenz, D. (2010) Neuronal avalanches in spontaneous activity in vivo. *J. Neurophysiol.*, **104** (6), 3312–3322.
14. Poil, S.S., van Ooyen, A., and Linkenkaer-Hansen, K. (2008) Avalanche dynamics of human brain oscillations: Relation to critical branching processes and temporal correlations. *Human Brain Mapping*, **29**, 770–777, doi: 10.1002/hbm.20590.
15. Eguiluz, V., Chialvo, D., Cecchi, G., Baliki, M., and Apkarian, A. (2005) Scale-free brain functional networks. *Phys. Rev. Lett.*, **94** (1), 18–102.
16. Song, S., Sjostrum, P., Reigl, M., Nelson, S., and Chklovskii, D. (2005) Highly nonrandom features of synaptic connectivity in local cortical circuits. *Public Library Sci. Biol.*, **3** (3), 507–519.
17. Pajevic, S. and Plenz, D. (2009) Efficient network reconstruction from dynamical cascades identifies small-world topology of neuronal avalanches. *PLoS Comput. Biol.*, **5** (1), e1000–271.
18. Wedeen, V.J., Rosene, D.L., Wang, R., Dai, G., Mortazavi, F., Hagmann, P., Kaas, J.H., and Tseng, T.W.Y. (2012) The geometric structure of the brain fiber pathways. *Science*, **335** (6076), 1628.
19. Pajevic, S. and Plenz, D. (2012) The organization of strong links in complex networks. *Nat. Phys.*, **8**, 429.

20. Samuelsson, B. and Socolar, J. (2006) Exhaustive percolation on random networks. *Phys. Rev. E*, **74** (3), 036–113.
21. Gleeson, J. (2008) Mean size of avalanches on directed random networks with arbitrary degree distributions. *Phys. Rev. E*, **77** (5), 057–101.
22. Benayoun, M., Cowan, J., van Drongelen, W., and Wallace, E. (2010) Avalanches in a stochastic model of spiking neurons. *PLoS Comput. Biol.*, **6** (7), e.
23. Hackett, A., Melnik, S., and Gleeson, J. (2011) Cascades on a class of clustered random networks. *Phys. Rev. E*, **83** (5), 056–107.
24. Larremore, D.B., Carpenter, M.Y., Ott, E., and Restrepo, J.G. (2012) Statistical properties of avalanches in networks. *Phys. Rev. E Stat. Nonlin. Soft Matter Phys.*, **85** (6 Pt 2), 066131, *arXiv:1204.3861v1*.
25. Newman, M. (2010) *Networks: An Introduction*, Oxford University Press.
26. Java, A., Song, X., Finin, T., and Tseng, B. (2009) Why we twitter: an analysis of a microblogging community, in *Advances in Web Mining and Web Usage Analysis*, Lecture Notes in Computer Science, Vol. 5439 (eds H. Zhang, M. Spiliopoulou, B. Mobasher, C. Giles, A., McCallum, O., Nasraoui, J., Srivastava, and J. Yen) Springer, Berlin / Heidelberg, pp. 118–138, 10.1007/978-3-642-00528-2_7.
27. Braha, D. and Bar-Yam, Y. (2004) Topology of large-scale engineering problem-solving networks. *Phys. Rev. E*, **69**, 016–113.
28. Albert, R. and Barabási, A. (2002) Statistical mechanics of complex networks. *Rev. Mod. Phys.*, **74** (1), 47.
29. Newman, M. (2003b) The structure and function of complex networks. *SIAM Rev.*, **45** (2), 167–256.
30. Restrepo, J., Ott, E., and Hunt, B. (2007) Approximating the largest eigenvalue of network adjacency matrices. *Phys. Rev. E*, **76**, 056–119.
31. Newman, M. (2003a) Mixing patterns in networks. *Phys. Rev. E*, **67**, 026–126.
32. Larremore, D., Shew, W., and Restrepo, J. (2011c) Predicting criticality and dynamic range in complex networks: Effects of topology. *Phys. Rev. Lett.*, **106**, 058–101.
33. Larremore, D., Shew, W., Ott, E., and Restrepo, J. (2011b) Effects of network topology, transmission delays, and refractoriness on the response of coupled excitable systems to a stochastic stimulus. *Chaos*, **21**, 025–117.
34. MacCluer, C. (2000) The many proofs and applications of perron's theorem. *SIAM Rev.*, **42** (3), 487–498.
35. Kinouchi, O. and Copelli, M. (2006) Optimal dynamical range of excitable networks at criticality. *Nat. Phys.*, **2**, 348–352.
36. Melnik, S., Hackett, A., Porter, M., Mucha, P., and Gleeson, J. (2011) The unreasonable effectiveness of tree-based theory for networks with clustering. *Phys. Rev. E*, **83**, 036–112.
37. Restrepo, J., Ott, E., and Hunt, B. (2008) Weighted percolation on directed networks. *Phys. Rev. Lett.*, **100**, 058–701.
38. Ott, E. and Pomerance, A. (2009) Approximating the largest eigenvalue of the modified adjacency matrix of networks with heterogeneous node biases. *Phys. Rev. E*, **79**, 056–111.
39. Erdős, P. and Gallai, T. (1960) Graphs with prescribed degrees of vertices. *Mat. Lapok.*, **11**, 264–274.
40. Chauhan, S., Girvan, M., and Ott, E. (2009) Spectral properties of networks with community structure. *Phys. Rev. E*, **80**, 056–114.
41. Dobson, I., Carreras, B.A., Lynch, V.E., and Newman, D.E. (2007) Complex systems analysis of series of blackouts: cascading failure, critical points, and self-organization. *Chaos*, **17**, 026–103.
42. Pastor-Satorras, R. and Vespignani, A. (2001) Epidemic dynamics and endemic states in complex networks. *Phys. Rev. E*, **63**, 066–117, doi: 10.1103/PhysRevE.63.066117.
43. Gomez, S., Arenas, A., Borge-Holthoefer, J., Meloni, S., and Moreno, Y. (2010) Discrete-time markov chain approach to contact-based disease spreading in complex networks. *Europhys. Lett.*, **89**, 38–009.
44. Allard, A., Noel, P., Dube, L., and Pourbohloul, B. (2009) Heterogeneous

- bond percolation on multitype networks with an application to epidemic dynamics. *Phys. Rev. E*, **79** (3), 036–113.
45. Yang, H., Shew, W., Roy, R., and Plenz, D. (2012) Maximal variability of phase synchrony in cortical networks with neuronal avalanches. *J. Neurosci.*, **32** (3), 1061–1072.

18

Mechanisms of Self-Organized Criticality in Adaptive Networks

Thilo Gross, Anne-Ly Do, Felix Drosté, and Christian Meisel

18.1

Introduction

Neural criticality, the hypothesis that the human brain may operate in a critical state, has gained much support over the past decade [1–6]. Previously, a major concern was that reaching criticality would always require the precise tuning of at least one parameter. However starting with the pioneering work of Bornholdt and Röhl [7], it has become apparent that the self-organization of adaptive networks constitutes a plausible mechanism that could generate and maintain criticality in the brain. In the present chapter, we seek to explain the underlying concepts of adaptive self-organized criticality and build up basic intuition by studying a simple toy model.

18.2

Basic Considerations

In the following, we use the term *criticality* to denote the behavior that is observed when the system is at a continuous phase transition. We also say that a system at criticality is in a *critical state*. Statistical physics defines the critical state as a point where the change of an ambient parameter (the *control parameter*) leads to a nonsmooth response from a property of the system (the *order parameter*). For *phase transitions of second order* the nonsmoothness manifests itself as a jump in the first derivative of the order parameter as a function of the control parameter. In other words, in the *phase diagram* where the order parameter is plotted as a function of a control parameter (see Figure 18.1), the critical point is marked by a sharp corner.

As an example, consider, for instance, a sample of neural tissue that is exposed to a drug that alters the excitability of neurons. Here, the concentration of the drug is the control parameter, whereas the overall activity registered in the sample constitutes a suitable order parameter. A second-order phase transition is then characterized by a nonsmooth change of the activity as the drug concentration is varied (e.g., washed out), which is often observed at the onset of activity.

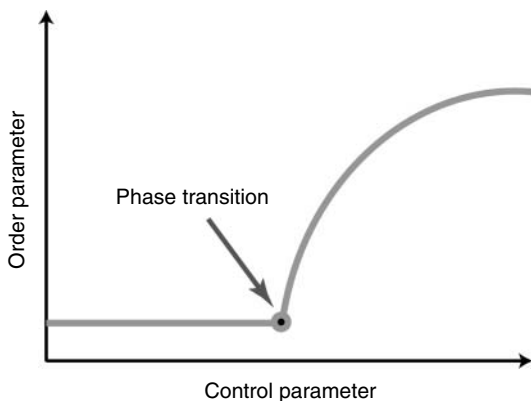


Figure 18.1 Sketch of a continuous phase transition. The critical state is found at the transition point, which appears as a sharp corner in the phase diagram.

While order and control parameters characterize the system on the macroscopic level, it is conducive for a deeper understanding to consider also the underlying microscopic dynamics. On the microscopic level, a complex system consists of many individual parts (here, neurons and their synapses). For all practical purposes, the number of these parts can be considered to be infinite. Each of the individual units is characterized by its own internal *micro-parameters*, such as, for instance, conductivities of synapses. The individual units also carry internal *micro-variables*, such as the membrane voltages of neurons, that change dynamically in time. For connecting the micro and macro levels, note that the control parameter exerts its influence on the system by altering many or all of the micro-parameters, whereas the order parameter appears as a normalized sum over the micro-variables.

In the language of nonlinear dynamics, second-order phase transitions correspond to local bifurcations of a (suitably defined) underlying dynamical system. In contrast to a phase transition, which can be considered a property of the real system, bifurcations are properties of models. Any faithful model of the system under consideration should thus exhibit the same phase transition, whereas the nature of the bifurcation may change depending on how the system is modeled. In particular, a microscopic model of the system will generally exhibit a different bifurcation than a coarse-grained macroscopic model, although both correspond to the same underlying phase transition.

When moving between different scales, the bifurcations that are observed in models cannot change arbitrarily. For instance, an important property of a bifurcation is the *codimension*. Formally, the codimension of a bifurcation is defined as the number of genericity conditions in the definition of the bifurcation [8]; however, for practical purposes the codimension denotes the number of parameters that have to be changed to find the bifurcation in a typical system. In general, the bifurcations that correspond to phase transitions will be of codimension 1, regardless of the scale of description, which tells us that we need to tune one

parameter of the system exactly right to reach the *bifurcation point*, where the system is critical.

The reasoning presented so far shows that we should not expect criticality to occur *accidentally* in any given system. Fundamentally, criticality always requires active tuning of one parameter to a precise value. Indeed, this requirement was one of the main concerns that was raised against the criticality hypothesis, as it would seem that criticality required a control circuit that measured the global state (the order parameter) of the brain and adjusted a global control parameter accordingly. The main purpose of the present chapter is to explain why such a global controller is not necessary, and discuss some implications for information processing.

In the following, we propose a basic toy model for criticality, which we subsequently expand in Section 18.4 by a mechanism that drives it robustly to criticality. We then discuss implications for information processing, first in Section 18.5, in the context of the toy model, before generalizing our findings, in Section 18.6, to more realistic neural models.

18.3 A Toy Model

In this section we formulate a toy model that is as easy as possible while containing the ingredients that are needed to build up basic intuition on self-organized criticality in the brain. Most importantly, we need criticality itself, that is, we need a model exhibiting a continuous phase transition. The simplest such system is arguably the epidemiological susceptible-infected-susceptible (SIS) model [9].

This model describes the spreading of an epidemic disease in a population of size N . Any given agent is either infected with the disease (state I) or susceptible to the disease (state S). We assume that any given agent encounters other agents at a rate c . If the focal agent is infected and the agent encountered is susceptible, then the encountered agent becomes infected with probability p . Infected agents recover at a constant rate r , and upon recovery immediately become susceptible again.

In the context of the present volume, the reader may want to consider the SIS system as a crude neural model, where the agents are neurons and infected agents represent active (firing) neurons. In this interpretation, the model may seem to be a gross oversimplification neglecting the finite duration of spikes, refractory times, and so on, but, as we show below, it still captures an important essence of neural criticality.

Let us start by considering the encounter rate c . Even without a detailed analysis, one can guess that the epidemic may go extinct such that no infected agents are left if the encounter rate c is sufficiently small. By contrast, the disease can become endemic, infecting a large fraction of the population, if c is sufficiently large. Let us now show that the transition between the endemic and the healthy state is a second-order phase transition. To illustrate the points raised in the previous section, we will compute the critical point, the so-called *epidemic threshold*, in two different ways employing microscopic and macroscopic reasoning, respectively.

We first consider the model on the micro-level. At this level of description, the system consists of a large number of individual agents that change their states in discrete stochastic events. In a sense, considering the whole system at once on this level of detail is too complicated. Thus we have to find a conceptual trick to infer the behavior of the system from the analysis of a small number of agents. For the present system, this can be accomplished by considering a state where there is a small, finite number of infected agents. Since this implies that the density of infected agents vanishes, encounters between infected agents can be neglected and every infected agent can be treated if it were the only infected in an otherwise healthy population. If such an agent causes on average less than one secondary infection before recovering, the disease must eventually go extinct. Although some infected agents may cause more than one secondary infection, the total number of infected in the population will decline exponentially in time. By contrast, if a focal infected agent causes on average more than one secondary infection before recovering, then the number of infected agents will grow exponentially (when infected agents are rare), which is sufficient to guarantee survival of the epidemic.

The average number of secondary infection from a single infected is also known as the *basic reproductive number* R_0 . It can be computed by considering that a typical infected agent will cause secondary infections at the rate pc until the focal agent itself recovers, which takes in average $1/r$ units of time. Therefore

$$R_0 = \frac{pc}{r} \quad (18.1)$$

From the condition $R_0 > 1$, we can compute the critical encounter rate $c^* = r/p$.

We can thus see that the epidemic will go extinct when $c < c^*$ and will become endemic when $c > c^*$. The critical point $c = c^*$ thus corresponds to a phase transition between a healthy phase where the dynamics is *frozen* and a dynamic endemic phase. This microscopic *branching ration* argument is often used for detecting critical avalanches of activity in neural tissue and cultures.

A similar result can be obtained by considering the system at the macroscopic level. In this case, we do not consider the states of individual agents but characterize the state of the system by a suitable order parameter. For the epidemic, such an order parameter is the prevalence I , which denotes the proportion of infected agents in the population. Given I , we know that the total number of infected agents is NI . Every one of these agents encounters other agents at a rate c such that the total rate of encounters of infected agents is cNI . The encountered agent is susceptible with probability $1 - I$ and, if susceptible, will be infected with probability p . This implies that the total rate at which agents are newly infected is $cpI(1 - I)N$. To translate the gain in numbers back to a gain in prevalence, we divide by N and find the gain of prevalence from new infections, $cpI(1 - I)$. Similarly, we know that given a number of infected agents, NI , the total rate of recovery will be rIN , which leads to a loss in prevalence of rI . We can thus write the total change in prevalence dI/dt as

$$\frac{dI}{dt} = cpI(1 - I) - rI \quad (18.2)$$

We can analyze this differential equation by computing the stationary levels of prevalence, I^* , for which $dI/dt = 0$. One can immediately see that this condition is met for $I = 0$ such that $I^* = 0$ is a stationary solution; in other words, the healthy state is always stationary. Dividing the right-hand side of the differential equation by I , we find the condition for a stationary solution $cp(1 - I^*) - r = 0$ or, equivalently, the nontrivial solution $I^* = 1 - r/(cp)$.

Considering the nontrivial solution, we observe that this solution is negative and therefore irrelevant if $cp/r < 1$. For $cp/r > 1$, the second solution corresponds to a finite prevalence of the epidemic and is thus physically relevant. At $cp/r = 1$, both stationary solutions coincide at $I^* = 0$ as the second solution enters the positive space. We thus recover the transition at $c^* = r/p$, which we discovered already by microscopic reasoning. At the macroscopic scale, the transition is marked by an intersection of stationary solution branches, which is known as *transcritical bifurcation* in dynamical systems theory. In general, such a transition is accompanied by a change in stability of the stationary solutions. Indeed, it can be confirmed by a stability analysis [8] that for $c < c^*$ the trivial solution is stable, whereas for $c > c^*$ the trivial solution is unstable and the nontrivial solution is dynamically stable.

Summarizing our findings from the macro-level analysis, we can say that for $c < c^*$ the system approaches the healthy state, whereas for $c > c^*$ a small perturbation (i.e., the introduction of some initial infected) is sufficient to drive the system to an endemic state of finite prevalence.

18.4

Mechanisms of Self-Organization

In previous section, we showed by both micro-level and macro-level reasoning that the proposed toy model has a continuous phase transition. Let us now discuss whether and how the toy model has to be extended to self-organize robustly to the critical state associated with this transition. While we will continue to use the epidemiological vocabulary to avoid confusion, this model is now interpreted mainly as a crude model of neural activity.

To enable self-organization to the critical state, at least one of the control parameters must be able to change dynamically in time. For the purpose of illustration, we focus on the parameter c . In this section, this parameter becomes a variable that follows its own equation of motion. We then ask under which conditions this equation of motion drives c robustly to the critical values c^* . The presentation thus follows a spirit of inverse engineering, where one asks how one would construct a system with given properties, not for the purpose of actual construction but for understanding how the biological system that already has these properties might work. Below, we sometimes say that the agents in the toy model want to organize a critical state. We emphasize that this is done in a physicist's way of speaking and is not meant to imply intentionality of individual neurons or synapses.

The first obstacle that we have to overcome to achieve self-organized criticality is philosophical in nature: Recall that the defining feature of a critical state is the phase transition and therefore the existence of a phase diagram as the one shown in Figure 18.1. However, in order to draw this diagram we must have control over the parameter c . If there were some internal dynamics that quickly tuned c to the critical value, we would be unable to draw the diagram and hence unable to detect that c^* corresponded to a phase transition. Indeed, deeper analysis reveals that such fast tuning to the critical state would not only obscure the critical nature of the transition point but also would destroy many of its special properties. Roughly speaking, if c approaches c^* on the same timescale as the dynamics in the system, it can no longer be considered a tuned parameter but becomes a full-fledged dynamical variable. In the bigger system which now includes this variable, the point c^* is no longer a special transition point but merely the steady-state value of c .

For avoiding the problem above, c must change on a slower timescale than the internal variables of the system. In this case, the equation governing I forms the so-called slow subsystem, in which c^* is still a transition point. In other words, if the dynamics of c is sufficiently slow, one can still draw the phase diagram from Figure 18.1 by setting c to desired values. We then have sufficient time to observe the value to which I settles before c changes noticeably.

The second obstacle that we have to overcome relates to information sensing. The critical value c^* to which we want to tune is not a fundamental constant, but rather depends sensitively on other properties of the systems such as the parameters r and p in the toy model (cf. Eq. (18.1)). This is a particular concern in biological systems such as the brain, where we need self-organized criticality to work robustly despite ongoing changes to the system in the course of development, aging, and so on. To be able to reach criticality, the system must therefore be able to sense whether the current value of c is too low or too high, and adjust it accordingly.

The current hypothesis is that the brain does not have a centralized controller that ensures criticality. Instead, criticality is achieved through synaptic plasticity on every synapse. Such delocalized control implies that at least approximate information about the global state of the brain must be available at every single neuron. The solution to this sensing problem is again timescale separation. The works of Bornholdt and others [7, 10] have shown that this information can be extracted if the local dynamics is observed for a sufficiently long time.

Let us consider the toy model again. In this system, an agent that becomes infected with the disease can tell that the system is in the endemic phase, so $c > c^*$ (also, for $c < c^*$, there might be localized outbreaks; however, these only affect a finite number of agents, a negligible fraction of the system). The agents who become infected thus know that c is too high and can thus decisively decrease their personal encounter rate, which on the macro-level leads to a reduction of c . By contrast, an agent that is not infected cannot tell whether the whole system is in the healthy phase or she is just lucky while agents elsewhere are infected. If these agents were to increase their personal encounter rate quickly, the system would overshoot the critical point. However, there are two possible strategies that the agents can employ. First, agents could observe their state for a long time; if they

do not become infected during this time, it is safe to conclude that the system is in the healthy phase and the encounter rate can be increased. Second, the healthy agents can increase their encounter rates on a slower timescale; then, they would lower it when infected, and thus avoid to overshoot.

Both of the strategies outlined above require a second timescale separation: in the first case, between observing and acting, in the second case between raising and lowering c . It has been pointed out that such a timescale separation is always necessary to achieve decentralized self-organized criticality [11]. The first choice, namely observing then acting, is used in many simple models such as in [7]. The second choice, namely decisive decrease, slow increase was used in a simple model in [12] and also occurs naturally in systems that use biologically motivated rules such as spike-timing-dependent plasticity (STDP) [13].

Combining the toy model introduced in Section 18.3 with a suitable plasticity rule following Section 18.4 leads to a system that self-organizes robustly to a critical state. This is shown explicitly for a related but more realistic neural model in [12].

18.5 Implications for Information Processing

The critical state is optimal for information processing because it can react sensitively to inputs and retain information for a long time. Let us illustrate this again by the example of the toy model. In this model, we can represent internal input by artificially infecting some agents. If $c < c^*$, then infecting a small number of agents will only cause a localized outbreak, which disappears exponentially (cf. Eq. (18.2)). If $c > c^*$, then there is an ongoing epidemic, but introducing additional infected agents will only have a small and (exponentially) short-lived effect on the ongoing dynamics. By contrast, for $c = c^*$, introducing some infected agents can cause a system-level outbreak in an otherwise healthy system. Further, this response decays only geometrically in time and can thus persist for a long time, because of an effect known as *critical slowing down*.

We note that the nature of a phase transition has direct implication for the code in which information can be fed into the system. In the toy model considered so far, the phase transition can be characterized as a percolation transition where activity starts to spread through the system. Correspondingly, the critical state is sensitive to inputs of activity. In the toy model, we chose to focus on this transition because it is most intuitive. However, for information processing in the brain, other phase transitions such as the synchronization phase transition are probably more relevant.

Our simple toy model cannot sustain synchronized dynamics. But, already somewhat more realistic models of neural dynamics are capable of showing synchronized activity between neurons [13, 14]. If the parameters in such a model are tuned to the synchronization phase transition, which marks the onset of synchronization, then information can be encoded using a synchronization code. Some evidence suggests that the brain is close to both activity [1] and

synchronization [2] phase transitions, potentially enabling it to process information using both activity and synchronization codes.

Furthermore, it is interesting to note that the critical state is primarily a resting state. Considering the toy model again, we expect some activity even in absence of external inputs. In the critical state, this activity shows the characteristic power laws that are often used as indicators of criticality [1]. However, subjecting the system to external inputs easily induces large-scale outbreaks and is thus similar to increasing c away from the critical state. One would therefore not expect to observe clean power laws during phases of strong information processing.

In the real brain, inputs are never totally absent. We can speculate that the brain compensates for these inputs by tuning to a correspondingly lower value of c . In the toy model, this is certainly true because the mechanism of plasticity of the type discussed above would lead to a lower value of c . It is thus conceivable that processing inputs slowly detunes the system from criticality and thus impairs further information processing, such that phases of reduced inputs are eventually necessary for retuning the system. This necessity for retuning might be the primary reason for sleep.

18.6

Discussion

In the present chapter, we used a very simple toy model to discuss some properties of plausible mechanisms for self-organized criticality in the brain. Using this model, we were able to gain basic intuition on the requirements and implications of adaptive self-organized criticality. While the real brain and even most models of the brain are much more complex, this basic intuition should remain valid in more complex models. Let us therefore discuss some of the simplifying assumptions that we have made above.

Instead of focusing on a neural model, we discussed a toy model inspired by epidemiology because it allowed an easier representation of some key concepts. While the propagation of the infection in the model can be seen as a crude representation of the propagation of action potentials, it does not include many properties of real neural dynamics, including travel-time delays, refractory times, real-valued action potential, and so on. As a consequence, the toy model is a poor information processor. However, it exhibits the continuous phase transition that we needed for the subsequent discussion of self-organized criticality. The properties of this phase transition do not depend crucially on the underlying model and are therefore independent of the simplifying assumptions.

Furthermore, some idealizations were necessary to draw a clean picture. For instance, we implied that perfect timescale separation is necessary to cleanly define criticality, and a second perfect timescale separation is necessary to reach the critical point precisely. In the real world, the timescale separation between neural dynamics and the relevant mechanisms of synaptic plasticity is certainly large but not infinite. This means that criticality is not reached precisely. However, in practice this is of little consequence. Both the presence of non-negligible noise due

to spontaneous activity and the finite number of neurons in the brain imply that the phase transition is not a sharp transition in the real world. In practice, that means that, on close inspection, the phase diagram does not have a sharp corner but a bend with high but finite curvature. In effect, the transition is blurred, becoming a transition region rather than a transition point. While no real system (neural or otherwise) can thus be truly critical, many of the advantageous properties of criticality are found if the system is reasonably close to the transition region.

In summary, we conclude that adaptive self-organized criticality is a plausible mechanism for driving the brain to a critical state where information processing is highly efficient. In the future, this insight may lead to a deeper understanding of neural dynamics and functioning and could potentially lead to new diagnostic and therapeutic tools. For instance, Meisel *et al.* [6] have shown that the characteristic power laws associated with neural criticality disappear during epileptic seizures. Furthermore, insights into neural information processing may inspire the design of future computers, which consist of randomly assembled active nano-elements that tune themselves to a critical state where information can be processed.

References

1. Beggs, J.M. and Plenz, D. (2003) Neuronal avalanches in neocortical circuits. *J. Neurosci.*, **23** (35), 11–167.
2. Kitzbichler, M., Smith, M., Christensen, S., and Bullmore, E. (2009) Broadband criticality of human brain network synchronization. *PLoS Comput. Biol.*, **5** (3), e1000–314.
3. Chialvo, D. (2010) Emergent complex neural dynamics. *Nat. Phys.*, **6** (10), 744–750.
4. Expert, P., Lambiotte, R., Chialvo, D., Christensen, K., Jensen, H., Sharp, D., and Turkheimer, F. (2011) Self-similar correlation function in brain resting-state functional magnetic resonance imaging. *J. R. Soc. Interface*, **8** (57), 472–479.
5. Tetzlaff, C., Okujeni, S., Egert, U., Wörgötter, F., and Butz, M. (2010) Self-organized criticality in developing neuronal networks. *PLoS Comput. Biol.*, **6** (12), e1001–013.
6. Meisel, C., Storch, A., Hallmeyer-Elgner, S., Bullmore, E., and Gross, T. (2012) Failure of adaptive self-organized criticality during epileptic seizure attacks. *PLoS Comput. Biol.*, **8** (1), e1002–312.
7. Bornholdt, S. and Röhl, T. (2000) Topological evolution of dynamical networks: global criticality from local dynamics. *Phys. Rev. Lett.*, **84**, 6114–6117. 10.1103/PhysRevLett.84.6114.
8. Kuznetsov, I. (1998) *Elements of Applied Bifurcation Theory*, Vol. 112, Springer-Verlag.
9. Anderson, R., May, R., and Anderson, B. (1992) *Infectious Diseases of Humans: Dynamics and Control*, Vol. 28, Wiley Online Library.
10. Bornholdt, S. and Röhl, T. (2003) Self-organized critical neural networks. *Phys. Rev. E*, **67** (6), 066–118.
11. Vespignani, A. and Zapperi, S. (1998) How self-organized criticality works: a unified mean-field picture. *Phys. Rev. E*, **57** (6), 6345.
12. Droske, F., Do, A.-L., and Gross, T. (2013) Analytical investigation of self-organized criticality in neural networks. *J. R. Soc. Interface*, **78**, 20120558.
13. Meisel, C. and Gross, T. (2009) Adaptive self-organization in a realistic neural network model. *Phys. Rev. E*, **80** (6), 061–917.
14. Levina, A., Herrmann, J.M., and Geisel, T. (2007b) Dynamical synapses causing self-organized criticality in neural networks. *Nat. Phys.*, **3** (12), 857–860.

19

Cortical Networks with Lognormal Synaptic Connectivity and Their Implications in Neuronal Avalanches

Tomoki Fukai, Vladimir Klinshov, and Jun-nosuke Teramae

19.1

Introduction

Much effort has been made to clarify the connectivity structure of cortical networks which is of fundamental importance for information processing in cortex [1–4]. These anatomical or electrophysiological studies have shown many interesting features of neuronal wiring in a local area of the cortex. Previously, we derived a plausible wiring pattern of cortical pyramidal neurons by asking, theoretically, what explicit network structure may underlie “neuronal avalanches” and their characteristic power-law statistics [5]. This approach led us to a hypothesis that was somewhat different from the conventional one that neuronal avalanches are critical states of neural dynamics. In our approach, neuronal avalanches reflected the topology of cortical neuronal wiring and their power law statistics resulted from a critical branching process in the development of neuronal wiring in a large ensemble of cortical neurons, rather than a critical branching process in spike propagation. In Section 19.2, we will give a brief account of this approach. A different approach to neuronal avalanches, which is also based on cortical circuit development can be found in Vogels *et al.* [6].

Then, in Sections 19.3 and 19.4 we will introduce our recent study of spontaneous cortical activity based on recurrent network models with long-tailed distributions of excitatory postsynaptic potential (EPSP). Recent electrophysiological studies have revealed that the EPSPs evoked by synaptic input are not distributed as Gaussian; rather, their distribution often displays a long tail of a small number of extremely large EPSPs. Actually, such EPSP distributions are well described as lognormal distributions [7, 8]. Our model incorporates this nontrivial feature of the weighting of neuronal wiring to explain the genesis and emergent functional roles of noise in the brain [9, 10]. We suggest that the local cortical circuit is a network of stochastic resonance units driven by optimal internal noise arising from synaptic reverberation. We will demonstrate how such distributions are advantageous over conventional Gaussian weight distributions for efficient spike communication between neurons and how the dynamics of recurrent neuronal networks may optimize such efficacy.

In Section 19.5, we will demonstrate how the nonrandom features of the connectivity in local cortical networks change the dynamics of recurrent networks with long-tailed synaptic connections. Interestingly, spike propagation in these networks exhibits power-law statistics along the main streams of spike routing, which may indicate the potential relevance of our model to neuronal avalanches [11–13].

19.2

Critical Dynamics in Neuronal Wiring Development

Neuronal avalanches represent temporally precise, spontaneous synchronous activity and have been recorded in slice cultures of rat layer 2/3 cortex by multielectrode arrays [11, 12]. They have significantly varied sizes and lifetimes that are power-law-distributed with an exponent of $-3/2$ or -2 , respectively. Neuronal avalanches have been suggested to represent a critical branching process [14, 15] in activity propagation through a cascade of cell assemblies. This view, however, assumes that the individual cell assemblies behave as independent dynamical variables. In addition, the dissipative nature of neural dynamics, or the fact that neurons are leaky integrators, makes it difficult to achieve a critical branching process in neural networks although potential solutions to this problem have been recently shown [16, 17].

Below, we briefly present the stochastic procedure to develop synaptic connections in a population of pyramidal neurons and interneurons (for details, see [5]). Consider a large pool of N excitatory and $N/4$ inhibitory neurons which initially have no synaptic connections between any neuron pair. We arrange excitatory and inhibitory neurons into cell layers, allowing each neuron to participate in more than one layer. The procedure is started by randomly choosing m ($\ll N$) excitatory neurons from the neuron pool. These neurons are defined as the initial layer. Successive layers are constructed by randomly selecting n_k excitatory and $n_k/4$ inhibitory neurons for the k th layer from the neuron pool. In doing so, n_k is determined according to a probability distribution $P(n_k|n_{k-1} = n)$, which depends on the number of neurons set in the preceding layer. Typically, $P(n_k|n_{k-1} = n)$ is a Gaussian distribution with mean n and variance $\sigma^2 n$. However, the following gamma distribution

$$\begin{aligned} P(n_k; \alpha|n_{k-1} = n) &= P_\Gamma(n_k - n + \sigma\sqrt{\alpha n}; \alpha, \sigma\sqrt{n/\alpha}) \\ P_\Gamma(x; \alpha, \beta) &= x^{\alpha-1} \exp(-x/\beta)/\beta^\alpha \Gamma(\alpha), \end{aligned} \quad (19.1)$$

better accounts for the known properties of neuronal avalanches, where the parameters are typically set as $\alpha = 0.1$ and $\sigma = 4.0$. If n_k does not satisfy $m < n_k < M$ ($m < M \ll N$) at some layer, the chain is terminated at the $(k-1)$ th layer, and a new chain is started with a new initial layer of m excitatory neurons. This procedure is repeated to construct sufficiently many chains. The lower bound m ensures a sufficient number of presynaptic spikes for spike propagation, and the upper

bound M keeps synaptic connections sufficiently sparse. The typical values are $m = 20$ and $M = 200$ in the present simulations.

We then introduce excitatory synaptic connections in successive layers. For each excitatory neuron in a succeeding layer, we randomly select m presynaptic excitatory neurons in the preceding layer. Similarly, each inhibitory neuron belonging to a layer receives synaptic inputs from m randomly chosen excitatory neurons in the preceding layer. However, unlike excitatory neurons that project selectively to neurons in the succeeding layer, inhibitory neurons project nonselectively to 5% of all excitatory neurons in the entire neuron pool.

Since the above wiring rule allows individual neurons to participate in more than one cell layer, the resultant network model is much more complicated than a mere collection of mutually independent, purely feed-forward neuronal networks, that is, the simplest form of “synfire chains” [18, 19]. In short, the wiring procedure results in an entangled ensemble of predominantly feed-forward subnetworks comprising mutually overlapping cell assemblies (Figure 19.1a). As expected from the critical branching process in neuronal wiring, the resultant neuronal network stably propagates avalanche-like activity consistent with the power law statistics characteristic for neuronal avalanches (Figure 19.1b). Synfire chains were originally proposed to account for precise spike sequences observed in the monkey frontal cortex [18] and were recently revived in the avian neuronal circuits engaged in song learning [20–22]. Our model generalizes a synfire-chain-like structure in a particular way that is consistent with neuronal avalanches, and hence the network dynamics per se is not critical. Interestingly, our wiring rule sets an upper bound for the number of cell assemblies embeddable in a neuron pool of given size [5].

The entangled synfire chain model successfully accounts for the power law statistics of neuronal avalanches (Figure 19.1c) and hence should be included in the list of candidate mechanisms for the phenomena. However, the biological reality of the model depends significantly on the reality of the wiring process shown in Eq. (19.1), for which direct experimental evidence is currently not available. Recently, many interesting features of synaptic connections have been revealed in cortical networks, and we have proposed a cortical network model in the general context of modeling spontaneous cortical activity or noise in the brain [9]. Below, we present various dynamical properties of this network model.

19.3

Stochastic Resonance by Highly Inhomogeneous Synaptic Weights on Spike Neurons

Recent electrophysiological recordings indicate that a minority of EPSPs between cortical pyramidal cells can be as large as several millivolts, while the majority is weak (< 1 mV), and the corresponding EPSP distributions obey long-tailed, typically lognormal, distributions [7, 8]. Therefore, the weight structure of local cortical networks is not random (Gaussian). We may regard them as networks with sparse-strong and weak-dense links (hereafter, we call such networks “SSWD networks”). We explored the implications of SSWD networks for network computation by

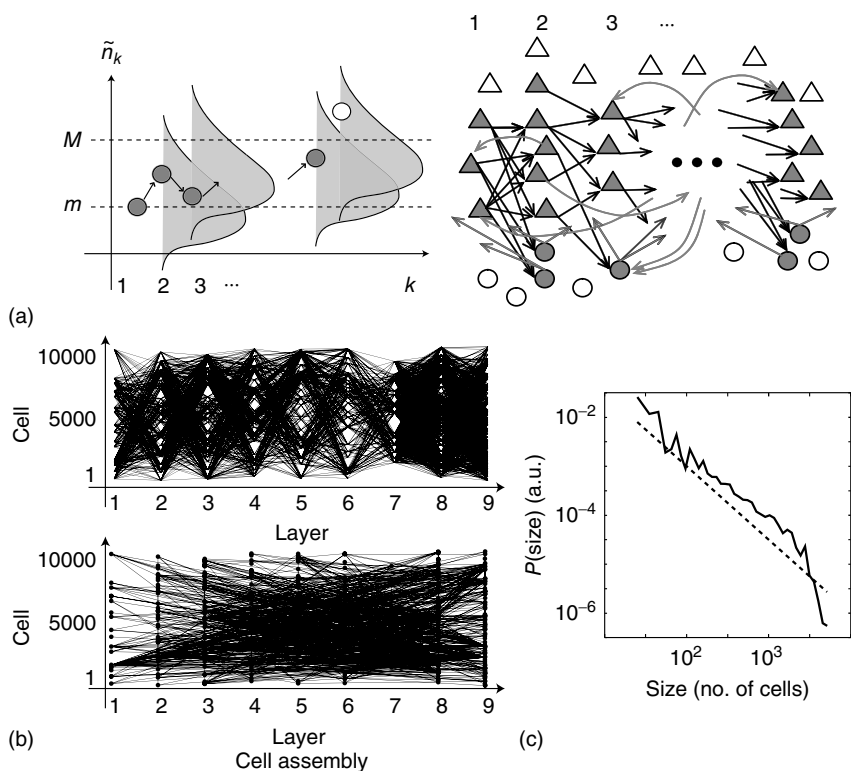


Figure 19.1 The developmental rule and structure of neuronal wiring in the entangled chain model. Parameters are $m = 20$, $\sigma = 4$ and $M = 200$. (a) The Markov process for grouping and wiring neurons is schematically illustrated. Excitatory neurons (*triangles*) in the consecutive layers are connected in a feedforward manner. Each inhibitory neuron (*circle*) receives input from a specific layer, and projects to excitatory neurons randomly chosen from the entire neuron pool. (b) A nine-layer chain is exemplified in a

10 000-neuron network. *Upper*: Solid lines represent feedforward connections between consecutive cell layers in the chain. *Lower*: The same chain also involves a considerable number of feedback connections as well as feedforward connections between distant layers. These connections come from adjacent feedforward connections in other chains, and typically constitute to about 10% of all connections in a chain. (c) Synchronized spike propagation shows a power-law distribution with the exponent of $-3/2$.

modeling single neurons receiving random inputs at AMPA synapses obeying the lognormal EPSP distribution observed experimentally. The neural dynamics are described by a leaky integrate-and-fire model:

$$\frac{dv}{dt} = \frac{1}{\tau_m}(v - V_L) - g_E(v - V_E) - g_I(v - V_I) \quad (19.2)$$

where v is the intracellular membrane potential and the second and third terms in the right-hand side represent conductance-based excitatory and inhibitory synaptic inputs, respectively. The excitatory and inhibitory synaptic conductances g_E and g_I

are normalized by the membrane capacitance and obey

$$\frac{dg_X}{dt} = -\frac{g_X}{\tau_s} + \sum_j G_{X,j} \sum_{s_j} \delta(t - s_j - d_j), \quad X = E, I \quad (19.3)$$

where $\delta(t)$ is the delta function, G_j , d_j , s_j are the weight, delay, and spike timing of synaptic input from the j th neuron, respectively. The values of G_i are distributed such that the corresponding EPSPs measured from the resting potential x obey a lognormal distribution

$$p(x) = \frac{\exp[-(\log x - \mu)^2 / 2\sigma^2]}{\sqrt{2\pi}\sigma x} \quad (19.4)$$

(Figure 19.2a). We found that the EPSP distribution achieves aperiodic stochastic resonance for spike sequences in a single neuron (Figure 19.2b). Stochastic resonance refers to a phenomenon wherein a specific level of noise enhances the response of a nonlinear system to a weak periodic or aperiodic stimulus [23, 24] and has been observed in many physical and biological systems [25]. If we vary the average membrane potential of the neuron by changing the rate of presynaptic spikes at the many weak synapses, the cross-correlation coefficients (CCs) between output spikes and inputs to the strongest synapses are maximized for a subthreshold membrane potential value roughly at the mid-point of the resting potential and firing threshold. At more hyperpolarized levels, even an extremely strong EPSP (~ 10 mV) cannot evoke a postsynaptic spike, whereas at more depolarized levels the neuron can fire without strong inputs. Importantly, stochastic resonance does not work for a Gaussian distribution with the same mean and variance of the lognormal distribution (dot-dashed line in Figure 19.2b), which demonstrates the advantage of SSWD connections.

We can analytically calculate the CC coefficient between input spike at strong synapses and output spike trains of the corresponding postsynaptic neurons as

$$\begin{aligned} CC &= \frac{\langle x_{in}(t)x_{out}(t) \rangle - \langle x_{in}(t) \rangle \langle x_{out}(t) \rangle}{\sqrt{(\langle x_{in}^2(t) \rangle - \langle x_{in}(t) \rangle^2)(\langle x_{out}^2(t) \rangle - \langle x_{out}(t) \rangle^2)}} \\ &\approx \text{Pr}(x_{out}|x_{in}) \sqrt{r_{in}/r_{out}} \end{aligned} \quad (19.5)$$

by assuming that spike trains obey a low-rate Poisson process. Here, r_{in} and r_{out} are the firing rate of input and output sequences, respectively, and $\text{Pr}(x_{out}|x_{in})$ is the conditional probability of an output spike for a given input spike at strong synapses. In numerical simulation, we evaluated $\text{Pr}(x_{out}|x_{in})$ by detecting a postsynaptic spike within the epoch of the EPSP rise time from the arrival of an input spike. Analytically, we can calculate $\text{Pr}(x_{out}|x_{in})$ from the stationary probability density of the membrane potential $P(v)$ obtained by solving the Fokker–Planck equation of the membrane potential driven by the noise generated by many weak synapses. Namely, the conditional probability P_i of having an output spike given input to the i th strong synapse is equal to the area of the stationary density function satisfying $v + F_{e,i}(v) \geq v_{thr}$, where the effective amplitude of the EPSP measured from the

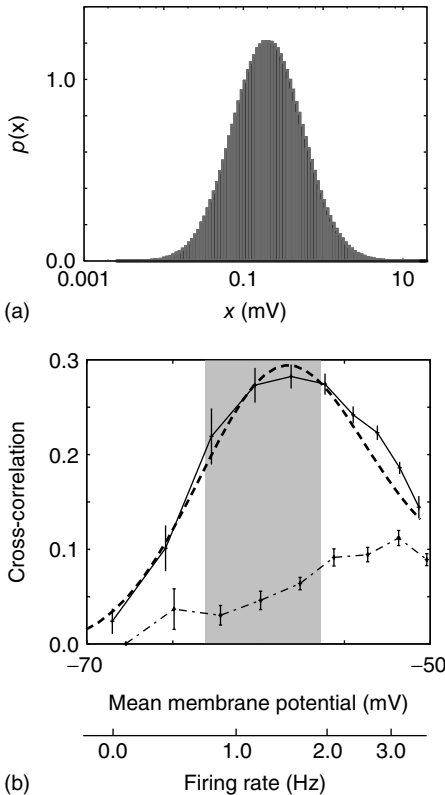


Figure 19.2 Stochastic resonance in single neuron responses to lognormally distributed EPSPs. (a) The long-tailed EPSP distribution used in the simulation was taken from experiment [7]. (b) Coherence between output and input to the strongest synapse was

calculated by numerical (solid) or analytical (dashed) methods as a function of input spike rate or the mean membrane potential. A similar curve was also obtained also for the strongest input in Gaussian distributed EPSPs (dot-dashed).

average membrane potential is given as

$$E_{e,i}(v) = \frac{(V_E - v)\tau_s^{\tau_e/(\tau_e - \tau_s)}\tau_e^{-\tau_s/(\tau_e - \tau_s)}}{(V_E - V_L)\tau_s^{\tau_m/(\tau_m - \tau_s)}\tau_m^{-\tau_s/(\tau_m - \tau_s)}} E_i \equiv \frac{(V_E - v)}{(V_E - V_L)} \beta E_i \quad (19.6)$$

in terms of the EPSP amplitude E_i measured from the resting potential. By solving the lower bound for the integration, we obtain

$$P_i = \int_{\frac{(V_E - V_L)V_{\text{thr}} - \beta E_i V_E}{(V_E - V_L) - \beta E_i}}^{V_{\text{thr}}} P(v) dv \quad (19.7)$$

The theoretical curve (dashed line in Figure 19.2b) was obtained by substituting P_i of the strongest synapse into $P(x_{\text{out}}|x_{\text{in}})$ in Eq. (19.5). The theoretical curve best coincided with numerical results when we divided excitatory synapses into the five strongest synapses and the remaining weak synapses.

19.4

SSWD Recurrent Networks Generate Optimal Intrinsic Noise

The above stochastic resonance effect on single neurons is by itself an interesting example of the benefit of noise in biological systems. However, whether cortical neurons are set at the optimal noise level in a recurrent network remains to be examined. We can show that this is indeed the case in SSWD neural networks. To see this, we conduct numerical simulations of a recurrent network model of 10 000 excitatory and 2000 inhibitory neurons that are randomly connected with coupling probabilities of excitatory and inhibitory connections being 0.1 and 0.5, respectively. Excitatory-to-excitatory connections obey the EPSP distribution shown in Eq. (19.4). We have to briefly apply external Poisson spike trains to all neurons to activate the network from a trivial resting state in which all neurons are silent. Then, the model sustains stable asynchronous firing even in the absence of external input (Figure 19.3a). This spontaneous network activity emerges purely from reverberating synaptic input, is stable in a very low-frequency regime (typically, 1–2 Hz), and is highly irregular (the average coefficient of variation ~ 1). All these properties are consistent with spontaneous activity observed in cortical neurons [26]. Importantly, reverberating synaptic input generated in the SSWD network maintains the average values of the membrane potentials of excitatory neurons at around -60 mV (Figure 19.3b), at which spike transmission

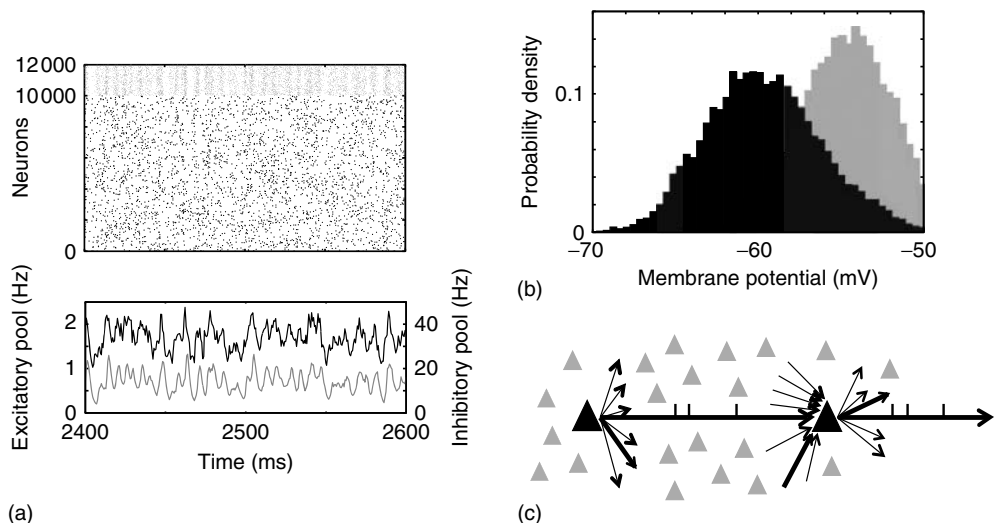


Figure 19.3 Spontaneous activity in the SSWD network. (a) Spike raster (*upper*) is shown for simulations of 10 000 excitatory (black) and 2000 inhibitory (gray) cells. The lower panel shows the mean firing rates of neural populations. Excitatory-to-excitatory connections obey the lognormal distribution

show in Figure 19.2a. (b) The distributions of the time-averaged average membrane potentials are shown for excitatory (black) and inhibitory (gray) neurons. (c) The SSWD network consists of multiple synaptic pathways gated by stochastic resonance.

at strong-sparse synapses becomes most reliable (Figure 19.2a, shaded area). This is possible because massive inputs to weak-dense synapses depolarize the average subthreshold membrane potential, on top of which inputs to strong-sparse synapses induce sparse spiking. Therefore, SSWD synapses play different roles in stochastic neural dynamics, although they distribute continuously.

In fact, both categories of synapses cooperate for the genesis of spontaneous activity and efficient spike routing (Figure 19.3c). Input to strong-sparse synapses, which may define multiple information pathways in the recurrent neural network, is absolutely necessary to evoke a postsynaptic spike from each neuron. However, the optimal efficiency of spike firing is achieved when the postsynaptic membrane potentials are maintained at the subthreshold depolarized level by massive inputs to the many weak synapses. Owing to the stochastic resonance effect at these synapses, spike sequences are routed reliably along the pathways defined by strong synapses. However, the same spikes contribute as noise source to optimizing spike routing along the “strong pathways.” We note that this noise source can be optimal only when the majority of neurons show sparse firing in the recurrent network. This provides a possible explanation for the experimental finding of spontaneous firing at relatively low frequency in real cortical networks (typically, 1–2 Hz).

19.5

Incorporation of Local Clustering Structure

While the model presented above incorporated the highly inhomogeneous nature of synaptic weights in local cortical networks, it does not take into account nonrandom features of their connectivity. The highly nonrandom structure of synaptic connections between cortical neurons or the presence of an excessive amount of local neuron clusters was reported in a number of recent experimental studies [4, 7, 8, 28, 29]. Below, we briefly present a theoretical framework that accounts for both long-tailed weight distributions and nonrandom connectivity features of cortical networks, and demonstrate the dynamical consequence and functional implications of such clustering structure.

We extend the previous random network approach to take into account the experimentally observed characteristics of the clustering of synaptic connections [7]. Experimental observations suggest that a local cortical network within a small volume (of $100 \mu\text{m}^3$) already includes a certain number of clusters, in which the connection probability is higher than in the rest of the network. For instance, the clustering structure is inferred from overrepresentations of reciprocal connections between pairs and certain network motifs such as triangles. To take these features into account, we assume that the probability of finding a synaptic connection from neuron i to neuron j is c_2 if they belong to the same cluster and $c_1 (< c_2)$ if they belong to different clusters. Then, the statistical properties of the network are completely determined by the constants c_1 and c_2 , the total number of neurons N ,

the number of clusters K in the network, and the number of neurons M in each cluster. All other characteristics can be calculated on the basis of these parameters.

Now we turn to the long-tailed distribution of synaptic weights within the clustered network. Experimental results suggests that stronger connections are more clustered than weaker ones. A simple hypothesis is to use different distributions of synaptic weights outside and within the clusters (Figure 19.4a). Namely, we introduce two different cumulative distribution functions F_1 and F_2 for the distributions of nonzero synaptic weights outside and within clusters, respectively: $F_{1,2}(w) = \text{Prob}(\text{synaptic weight} < w)$. Then, the distribution of synaptic weights in the entire network is given as

$$F(w) = F_1(w) + \frac{\alpha c_2}{c} (F_2(w) - F_1(w)) \quad (19.8)$$

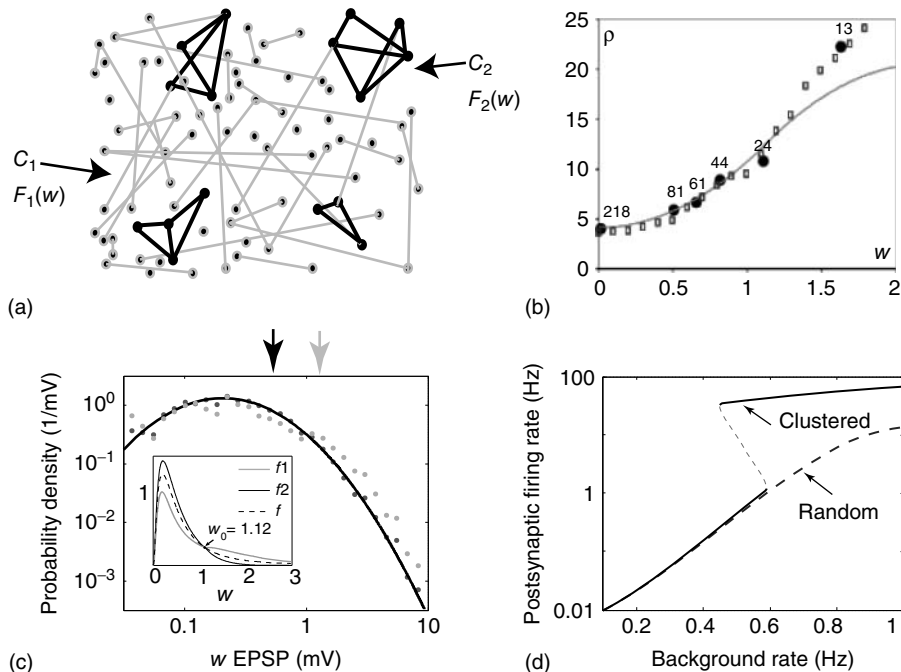


Figure 19.4 The properties of the clustered network model. (a) The model has different connection probabilities and weight distributions for excitatory synapses within and outside clusters. (b) The coefficients of overrepresentation of reciprocal connections were calculated from Eq. (19.9) (solid line) and numerically in the model network (squares). Experimental data (filled circles) were adopted from Song *et al.* [7]. (c) The long-tailed distributions for all connections (black circles) and for clustered connections

(gray circles) generated by the model. The black and gray arrows indicate the average weights of all and clustered connections, respectively. The solid line is a lognormal fit. The inset shows the weight distributions (i.e., the derivatives of the cumulative functions F) for non-clustered, clustered, and all connections. (d) The bifurcation diagram obtained for the clustered network model (solid) shows bistable firing states, whereas the random network (dashed) with the same mean connectivity does not show bistability.

and the overrepresentation of reciprocal connections as

$$\rho(w) = \frac{\kappa_1^2(w)(1 - \alpha) + \kappa_2^2(w)\alpha}{\kappa^2} \quad (19.9)$$

where $c = c_1 + \alpha(c_2 - c_1)$, $\alpha = KM^2/N^2$, and $\kappa_{1,2}(w) = c_{1,2}(1 - F_{1,2}(w))$. Using the threshold-depended statistics for reciprocal connections from Song *et al.* [7] and Eqs. (19.8) and (19.9), we can determine the cumulative distribution functions that give the same characteristics. These parameters are $K=1$, $M/N=0.222$, $c_1=0.07$, and $c_2=1$, indicating that at most a single cluster exists within the cortical volume of $100 \mu\text{m}^3$ and that neurons are all-to-all connected in this cluster ($c_2=1$) and only sparsely connected with the rest of the network ($c_1=0.07$). Our connectivity framework exhibits an excellent agreement with the experimentally observed statistics of clustered connections and long-tailed distribution of synaptic weights (Figure 19.4b,c). In particular, strong connections are more popular inside the cluster, while weaker ones are more likely to be found outside, and the total probability density of synaptic weights is a lognormal distribution.

Surprisingly, our model of connectivity well accounts for the overrepresentation of triangular network motifs (data not shown) despite that this topological metric was not used for parameter fitting. This further suggests that our connectivity scheme is biologically plausible.

19.6

Emergence of Bistable States in the Clustered Network

The small region of cortex under consideration will involve about 100 pyramidal cells and about 20 inhibitory neurons. To see the dynamical features arising from the clustering of connections, we performed numerical simulations of the dynamics of the clustered network with the parameters described above. The network consists of only 80 excitatory neurons and, for simplicity, does not contain inhibitory neurons. Since our clustered network is too small to self-sustain neuronal firing, we apply Poisson spike inputs to all neurons as weak background noise. The network contains a cluster of $M=18$ neurons that are fully connected to one another, and the mean connection probability $c \approx 0.12$ for the entire network.

Owing to external background noise, the network exhibits sustained activity at a relatively low firing rate (“low state”), as shown in Figure 19.4d. Interestingly, as the intensity of background noise is increased, the network develops another stable firing state (“high state”) in which clustered neurons fire at a much higher mean frequency of about several tens of spikes per second and the rest of the network fires at low frequencies. Therefore, the distribution of firing rates becomes bimodal in the high state. The low state, in which all neurons fire at low firing rates, coexists with the high state if the external input is not too strong. This bistability and the high state appear only in the clustered network, but are not observed in a randomly connected network having the same average connectivity without clusters. Thus, the major dynamical effect of clustered connections is the emergence of bistable

firing states. We also constructed a clustered network involving inhibitory neurons to find that they significantly reduce the average firing rate of the high state without spoiling the bistability of network dynamics.

Transitions from the low state to the high state can also be caused by an excessive correlation between inputs to the clustered neurons. For example, we found that introducing 40% correlation between these inputs for 300 ms is sufficient to cause the transition. Note that the network remains in the high state even when we remove the correlated component from the external input. Since bistable firing states are of significant functional importance in, for example, working memory [29, 30] and temporal integration [31, 32], our results imply that the basic element of cortical information processing can be as small as an ensemble of several tens of clustered neurons within $100 \mu\text{m}^3$ of cortical volume. Interestingly, this roughly coincides with the size of cortical “minicolumns” [33, 34].

19.7

Possible Implications of SSWD Networks for Neuronal Avalanches

Now we discuss possible implications of the SSWD network model for neuronal avalanches. We return to the SSWD network without clustered connections. We show that spike propagation in the spontaneous activity of the network exhibits a power law distribution of the size (the total number of neurons activated downstream of a spike) if we make a partial observation of the spikes that propagate only through the strongest synapses. Figure 19.5 displays an example of such power law distributions when we take into account the top 10 strongest synapses from

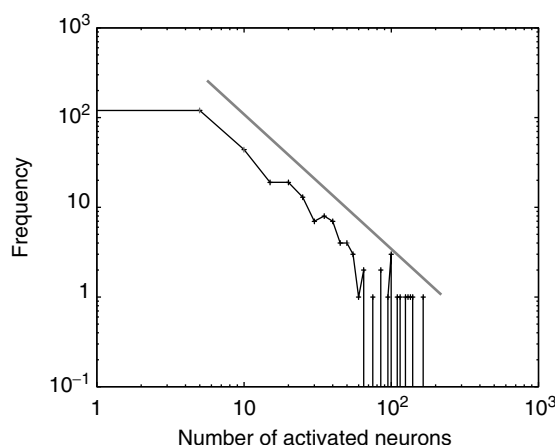


Figure 19.5 Power laws in the size distributions of propagating spikes. We measured how many spikes are generated in the downstream of a spike initiated in one neuron. The distribution (black line) obeys a power law of exponent $-3/2$ (gray line). Only the downstream spikes propagating through the top strongest synapses are measured.

each presynaptic neuron. Interestingly, the exponent of the power law is about $-3/2$, which is consistent with the experimentally observed value for neuronal avalanches [11]. Though this coincidence per se does not necessarily prove that the spike propagation is a critical branching process, the results may have significant implications for the genesis and function of neuronal avalanches in the brain, as discussed below.

The measurement of local field potential (LFP) might be governed by large amplitude EPSPs as the LFP picks up activity from more synchronized neurons in a local cortical volume around the recording electrode. In large networks with many small synapses, those synchronized groups might be a likely carrier of pulsatile, propagated activity. On the other hand, in smaller networks, with highly inhomogeneous synaptic weights, propagation is more likely realized through a few strong synaptic inputs. If strong synapses of a neuron mainly target spatially localized neurons in the vicinity of the presynaptic neuron, the electric signal recorded by a nearby electrode may be dominated by the strong inputs. Such a spatial configuration seems to be likely in the presence of the clustering structure discussed in the previous section. Therefore, it is possible that the $-3/2$ power law observed in Figure 19.5 is related to critical branching in the general sense that the cascades are probably balanced – they do not die out right away nor do they blow up in a way rendering the network globally refractory. We also speculate that these balanced cascades may naturally separate “informative spikes,” or signals, from “non-informative spikes,” or noise. This separation might be less clear in the SSWD network where synaptic weights are distributed continuously. All these points require further theoretical clarifications.

19.8

Summary

We conjoined two fundamental principles in signal processing and complex phenomena observed in cortical neural networks: stochastic resonance and noisy internal brain states. The key of this link is the coexistence of a spectrum of SSWD connections that provides a mechanism by which excitable networks generate and maintain an optimal noise level for efficient spike communication. These results have implications for the role of noise in networks with a broad spectrum of coupling strengths, such as the gating of specific signal pathways with the probabilities of pathway selection modulated by the dynamics of internal noise generation.

Acknowledgment

This work was partially supported by the JST, CREST, and PRESTO programs, KAKENHI 24120524, 25430028 (to JT), and 22115013 (to TF). VK was supported by a fellowship of the JSPS.

The authors declare that they have no competing financial interests.

References

1. Holmgren, C., Harkany, T., Svennnenfors, B., and Zilberman, Y. (2003) Pyramidal cell communication within local networks in layer 2/3 of rat neocortex. *J. Physiol.*, **551**, 139–153.
2. Stepanants, A., Tamás, G., and Chklovskii, D.B. (2004) Class-specific features of neuronal wiring. *Neuron*, **43**, 251–259.
3. Kalisman, N., Silberberg, G., and Markram, H. (2005) The neocortical microcircuit as a tabula rasa. *Proc. Natl. Acad. Sci. U.S.A.*, **102**, 880–885.
4. Yoshimura, Y., Dantzker, J.L.M., and Callaway, E.M. (2005) Excitatory cortical neurons form fine-scale functional networks. *Nature*, **433**, 868–873.
5. Teramae, J. and Fukai, T. (2007) Local cortical circuit model inferred from power-law distributed neuronal avalanches. *J. Comput. Neurosci.*, **22**, 301–312.
6. Vogels, T.P., Rajan, K., and Abbott, L.F. (2005) Neural network dynamics. *Annu. Rev. Neurosci.*, **28**, 357–376.
7. Song, S., Sjöström, P.J., Reigl, M., Nelson, S.B., and Chklovskii, D.B. (2005) Highly nonrandom features of synaptic connectivity in local cortical circuits. *PLoS Biol.*, **3** (3), e68.
8. Lefort, S., Tomm, C., Floyd Sarria, J.C., and Petersen, C.C.H. (2009) The excitatory neuronal network of the C2 barrel column in mouse primary somatosensory cortex. *Neuron*, **61**, 301–316.
9. (a) Teramae, J. and Fukai, T. (2010) A Log-Normal EPSP Distribution Accounts for the UP State, Low-Rate Asynchronous Firings, and Precise Firing Sequences in Cortical Networks, Abstract of Society for Neuroscience, San Diego, CA.
10. Teramae, J., Tsubo, Y., and Fukai, T. (2012) Optimal spike-based communication in excitable networks with strong-sparse and weak-dense links. *Sci. Rep.*, **2**, 485.
11. Beggs, J.M. and Plenz, D. (2003) Neuronal avalanches in neocortical circuits. *J. Neurosci.*, **23**, 11167–11177.
12. Beggs, J.M. and Plenz, D. (2004) Neuronal avalanches are diverse and precise activity patterns that are stable for many hours in cortical slice cultures. *J. Neurosci.*, **24**, 5216–5229.
13. Petermann, T., Thiagarajan, T.C., Lebedev, M.A., Nicolelis, M.A., Chialvo, D.R., and Plenz, D. (2009) Spontaneous cortical activity in awake monkeys composed of neuronal avalanches. *Proc. Natl. Acad. Sci. U.S.A.*, **106**, 15921–15926.
14. Harris, T.E. (1989) *The Theory of Branching Processes*, Dover, New York.
15. Zapperi, S., Baekgaard, L.K., and Stanley, H.E. (1995) Self-organized branching processes: mean-field theory for avalanches. *Phys. Rev. Lett.*, **75**, 4071–4074.
16. Levina, A., Herrmann, J.M., and Geisel, T. (2007) Dynamical synapses causing self-organized criticality in neural networks. *Nat. Phys.*, **3**, 857–860.
17. Millman, D., Mihalas, S., Kirkwood, A., and Niebur, E. (2010) Self-organized criticality occurs in non-conservative neuronal networks during ‘up’ states. *Nat. Phys.*, **6** (10), 801–805.
18. Abeles, M. (1991) *Corticonics: Neural Circuits of the Cerebral Cortex*, Cambridge University Press, Cambridge.
19. Diesmann, M., Gewaltig, M., and Aertsen, A. (1999) Stable propagation of synchronous spiking in cortical neural networks. *Nature*, **402**, 529–533.
20. Hahnloser, R.H., Kozhevnikov, A.A., and Fee, M.S. (2002) An ultra-sparse code underlies the generation of neural sequences in a songbird. *Nature*, **419**, 65–70.
21. Kimpo, R.R., Theunissen, F.E., and Doupe, A.J. (2003) Propagation of correlated activity through multiple stages of a neural circuit. *J. Neurosci.*, **23**, 5750–5761.
22. Long, M.A., Jin, D.Z., and Fee, M.S. (2010) Support for a synaptic chain model of neuronal sequence generation. *Nature*, **468**, 394–399.
23. Wiesenfeld, K. and Moss, F. (1995) Stochastic resonance and the benefits of noise: from ice ages to crayfish and SQUIDS. *Nature*, **373**, 33–36.
24. Collins, J.J., Chow, C.C., Capela, A.C., and Imhoff, T.T. (1996) Aperiodic

- stochastic resonance. *Phys. Rev. E*, **54** (5), 5575–5584.
25. McDonnell, M.D. and Ward, L.M. (2011) The benefits of noise in neural systems: bridging theory and experiment. *Nat. Rev. Neurosci.*, **12**, 415–426.
26. Destexhe, A., Rudolph, M., and Paré, D. (2003) The high-conductance state of neocortical neurons in vivo. *Nat. Rev. Neurosci.*, **4**, 739–751.
27. Thomson, A.M. and Lamy, C. (2007) Functional maps of neocortical local circuitry. *Front. Neurosci.*, **1**, 19–42.
28. Perin, R., Berger, T.K., and Markram, H. (2011) A synaptic organizing principle for cortical neuronal groups. *Proc. Natl. Acad. Sci. U.S.A.*, **108**, 5419–5424.
29. Compte, A., Brunel, N., Goldman-Rakic, P.S., and Wang, X.J. (2000) Synaptic mechanisms and network dynamics underlying spatial working memory in a cortical network model. *Cereb. Cortex*, **10**, 910–923.
30. Durstewitz, D., Seamans, J.K., and Sejnowski, T.J. (2000) Neurocomputational models of working memory. *Nat. Neurosci. Suppl.*, **3**, 1184–1191.
31. Koulakov, A.A., Raghavachari, S., Kepes, A., and Lisman, J.E. (2002) Model for a robust neural integrator. *Nat. Neurosci.*, **5** (8), 775–782.
32. Okamoto, H. and Fukai, T. (2009) Recurrent network models for perfect temporal integration of fluctuating correlated inputs. *PLoS Comput. Biol.*, **5** (6), e1000404.
33. Jones, E.G. (2000) Microcolumns in the cerebral cortex. *Proc. Natl. Acad. Sci. U.S.A.*, **97**, 5019–5021.
34. Ichinohe, N. (2012) Small-scale module of the rat granular retrosplenial cortex: an example of the minicolumn-like structure of the cerebral cortex. *Front. Neuroanat.*, **5**, 69. doi: 10.3389/fnana.2011.00069

20

Theoretical Neuroscience of Self-Organized Criticality: From Formal Approaches to Realistic Models

Anna Levina, J. Michael Herrmann, and Theo Geisel

20.1

Introduction

Self-organized criticality (SOC) is a common phenomenon in nature [1] and became a fascinating research subject for neuroscience when critical avalanches were predicted theoretically and observed experimentally to occur in networks of neurons [2–4]. Models of SOC in neural network evolve from early sandpile-like models [5, 6] on a lattice to large-scale realistically connected networks [7, 8]. In this chapter we will present a model of criticality in the brain which identifies a number of contributing factors such as short-term synaptic dynamics and homeostatic plasticity in the synapses. This model is but one approach among an ever-increasing number of other studies on the subject. We were aiming for a family of models that are simple enough to permit an analytical solution but can still account for several biological principles that are known to be relevant here.

As we try to identify the components of a neuronal network that can make it self-organized critical or, at least, bring it closer to a critical state, we have to be aware that criticality (in the sense of the existence of full-fledged power law event distributions) does not exist in finite systems. This emphasizes the importance of analytical treatments for infinite systems, while a theory of finite-size effects is also required to relate precisely to biological experiments. Such a theory exists only for the simplest abstract models (see Section 20.2), which forces us to apply a combination of analytical and numerical work on models including dynamic synapses (Section 20.3) and homeostatic adaptation (Section 20.4).

20.2

The Eurich Model of Criticality in Neural Networks

In 2002, Eurich *et al.* [2] presented a model of a globally coupled neural network that exhibits critical avalanches. In contrast to earlier work on criticality [5, 6, 9–11], here an explicit analytical derivation of the distribution of sizes of neural avalanches was given not only for the idealization of very large networks but

also for networks of any size. This work also predicted the correct critical exponent as well as various extra-critical dynamical phenomena that were later confirmed in neurophysiological experiments [3].

The analytical solvability of the model required a certain degree of simplicity which seems justified, however, by the predictive power of the model. Moreover, details of the model assumptions do not influence the qualitative behavior, which is characteristic of critical phenomena.

20.2.1

Model Description

The model consists of a set of N identical neurons each of which is characterized by a single state variable h representing the neural membrane potential. Depending on the state of the system at time t , a neuron, say neuron i , receives external input $I_i^{\text{ext}}(t)$ or internal input $I_i^{\text{int}}(t)$ from other elements. If the potential h exceeds a threshold θ , the neuron emits an action potential and returns to its resting value h_{rest} which we set for convenience to be equal to 1. The action potential serves as input to the other neurons and increases their membrane potentials by a fixed amount, which in turn may or may not surpass the threshold, thus causing further action potentials. Such a shorter or longer sequence of neural firings forms a neural avalanche in the model. It stops if no neuronal potential is above threshold after the transmitted action potentials have arrived. Time is measured in discrete steps, $t = 0, 1, 2, \dots$, and action potentials are assumed to travel for a single time step only. The system is initialized by arbitrary values h_i , $i = 1, \dots, N$, in the interval $[h_{\text{rest}}, \theta]$ which we choose conveniently as $[0, 1)$. We can describe the dynamics of the membrane potential as an accumulation of input that is occasionally interrupted by resets to the resting level after firing.

$$h_i(t+1) = \begin{cases} h_i(t) + I_i^{\text{int}}(t) + I_i^{\text{ext}}(t) & \text{if } h_i(t) + I_i^{\text{int}}(t) + I_i^{\text{ext}}(t) < 1 \\ h_i(t) + I_i^{\text{int}}(t) + I_i^{\text{ext}}(t) - 1 & \text{otherwise} \end{cases} \quad (20.1)$$

The internal input $I_i^{\text{int}}(t)$ is the product of the synaptic strength α and the number $\xi(t)$ of action potentials generated in the current time step, $I_i^{\text{int}}(t) = \alpha \xi(t)/N$, where we use the assumption of identical synapses for all neurons. The interaction strength $\alpha \geq 0$ is the only adjustable parameter in the model. It determines the synaptic efficacy between any two neurons. The scale $1/N$ ensures that a neuron receives comparable amounts of input independently of the size of the network.

The external input effects a “charging” of the neural elements and is realized by randomly selecting a single neuron in each time step and adding a small increment $I_i^{\text{ext}}(t) = \Delta h$ to its membrane potential. Another option would be spontaneous activity, that is, setting the potential of a random neuron to a superthreshold value.

We assume that avalanches start always with a single firing event, that is, $\xi(t_0) = 1$. Other neurons may be incited to fire as well, but it is also possible that no other neurons join in. Thus the avalanche always has a size greater than or equal to 1. Formally, the avalanche size L is the sum over the sets of active

neurons, $L = \sum_{k=0}^{D-1} \xi(t_0 + k)$ over the duration D of the avalanche. The duration is the smallest integer for which the stopping condition $\xi(t_0 + D) = 0$ is satisfied.

One of the important advantages of the model [2] is that the probability $P(L, N, \alpha)$ of an avalanche of size L in a network of N neurons can be calculated explicitly for each coupling parameter α .

$$P(L, \alpha, N) = L^{L-2} \left(\frac{N-1}{L-1} \right) \left(\frac{\alpha}{N} \right)^{L-1} \left(1 - L \frac{\alpha}{N} \right)^{N-L-1} \frac{N(1-\alpha)}{N-(N-1)\alpha} \quad (20.2)$$

This probability distribution has been introduced by Eurich *et al.* [2] and was analyzed by Levina [12], where also the name *Abelian distribution* was proposed because of the fact that an Abelian sum is involved. In the following section, we will compare the results of the analysis of the model based on Eq. 20.2 with numerical simulations [2].

20.2.2 Simulations and Analysis

Depending on the connection strength α , the network can produce a rich repertoire of behaviors, see Figure 20.1. For small values of α , the behavior is subcritical, that is, the avalanche size distribution decays exponentially and the number of avalanches that extend to the size of the system is negligible. If α equals the critical value α_{cr} , the system has an approximate power law avalanche distribution with an exponent close to $-3/2$ for avalanche sizes almost up to the system size where an exponential cutoff takes place. The distributions become nonmonotonous in the region $\alpha_{\text{cr}} < \alpha < 1$. For α just below 1, neurons can fire more than once per

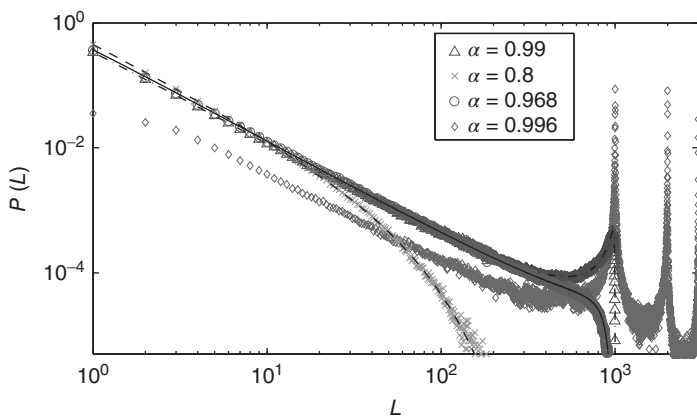


Figure 20.1 Probability distributions of avalanche sizes, $P(L, \alpha, N)$, in the subcritical (stars, $\alpha = 0.8$), critical (circles, $\alpha = 0.968$), supercritical (triangle, $\alpha = 0.99$), and multi-peaked (diamonds, $\alpha = 0.996$) regime. Thin

lines denote the analytical results for the avalanche size distributions. The symbols show temporal averages from simulations of 10^6 avalanches with $N = 1000$ and $\Delta h = 0.02$.

avalanche such that avalanche sizes larger than N are possible. Finally, if $\alpha \geq 1$, then the activity in the network will never terminate once an avalanche of size at least N has occurred.

The exact formula (20.2) allows us to determine the critical connection strength in the thermodynamic limit. Note that here several limits are involved: First, the limit of large system size $N \rightarrow \infty$ is taken. Then we let $\alpha \rightarrow 1$, and, finally, in order to justify the power law

$$P(L) \propto L^{-\frac{3}{2}}$$

we need also to consider large L because Stirling's approximation implies a small correction for small L .

The case $\alpha = 1$ is special because it implies the conservation of the neural activity in the thermodynamic limit. Numerous authors have presented arguments against the existence of nonconservative SOC models [10, 13–15] or proposed variants that were claimed to be critical in nonconservative cases [8, 16, 17]. For example, for the Abelian sandpile (i.e., a system where dynamics does not depend on the order of the update of the nodes) it was proven that conservation is necessary for SOC [18], but so far there is no final conclusion of this discussion, although the known SOC systems are conservative. In this context, it is interesting that, in the Eurich model, for $N < \infty$, the distributions that are closest to a power law occur at $\alpha_{\text{cr}} < 1$.

The restrictions of this model do not allow for a functional description of biological neuronal avalanches [3] because the parameter α needs to be tuned appropriately and, with increasing system size, more and more precisely. In real neural systems, however, critical behavior appears to be typical [19–21], and is assumed to arise from some form of feedback, which has been indicated to be essential for SOC in a general context [22]. In the next section we will introduce an extension of the model that includes such a feedback mechanism.

20.3

LHG Model: Dynamic Synapses Control Criticality

In this section we will describe an extension of the Eurich model which includes an activity-dependent dynamics of the synaptic weights. It was proposed by the present authors [23] and is sometimes referred to as the *LHG model* [24, 25].

20.3.1

Model Description

The essential difference to the previous model is that the synaptic strengths are no longer kept fixed but are allowed to follow now an activity-dependent dynamics. The synapses are described by individual variables, while α sets the scale for the maximal synaptic strength or, more biologically, the total amount of neurotransmitter in a synapse. After a presynaptic spike, the increase of the potential of the postsynaptic neuron is given by $u J_{ij}(t)$, where $J_{ij}(t)$ stands for the amount of synaptic resources

that are available at time t in a synapse between neurons j and i , and u is the fraction of these resources that is actually used for a transmission. Avalanches and model details are defined in the same way as before, and the dynamics of the membrane potential is described analogous to Eq. 20.1, but in differential form and with ζ denoting the random driving inputs and with a synaptic delay τ_d .

$$\dot{h}_i = \delta_{i,\zeta(t)} I^{\text{ext}} + \frac{1}{N} \sum_{j=1}^N u J_{ij} \delta\left(t - t_{\text{sp}}^j - \tau_d\right) \quad (20.3)$$

The dynamics of the variables J_{ij} represents the effect of synaptic depression [26]

$$\dot{J}_{ij} = \frac{1}{\tau_j} \left(\frac{\alpha}{u} - J_{ij} \right) - u J_{ij} \delta\left(t - t_{\text{sp}}^j\right) \quad (20.4)$$

and combines two effects. First, a synapse decreases in strength by a fraction u when activated because of a depletion of the resources of synaptic transmitters. Second, it slowly recovers and reapproaches the scaled maximal value $\frac{\alpha}{u}$ when the neuron is silent. Thus, if the firing frequency is low (e.g., less than one spike in 50 time steps), then the synapse has enough time to return close to the maximal value. If the frequency is higher, then the synaptic strength at firing is smaller than maximally possible [26]. If a neuron spikes rarely, the synaptic strength J_{ij} approaches α . The fraction u is fixed here, but it may as well be affected by the neural activity (cf. Section 20.3.4). Here we should include a remark relating to the separation of time scales in the model. Between avalanches, the network receives external inputs at a rate $1/\tau_s$: that is, each neuron receives on average an external input every $N\tau_s$ milliseconds. In the simulation we are free to rescale the time during these intervals and choose conveniently τ_s as a discretization step. The timescale τ_j in Eq. 20.4 is related to this rate by $\tau_j = vN \cdot \tau_s$, which gives rise to another parameter of the model, v , which is chosen to maintain a compromise between the timescale separation and the continuity of the physiological processes underlying the synaptic dynamics (Eq. (20.4)).

Just as in Section 20.2, finite networks show different avalanche size distributions for different values of α (see Figure 20.2), ranging from subcritical at small values of α to supercritical for large α . Near α_{cr} , the system has an approximate power law distribution of avalanche sizes. Here, however, the situation is more interesting as the range of near-criticality changes with the number of neurons (see Figure 20.3) and becomes dominant in the limit of large N as we will show in Section 20.3.2. To verify this claim numerically, we have used the method of finite-size scaling [27–29], details of which are given by Levina [12]. In order to quantify the difference between the models, we define a threshold $\vartheta = 0.005$ describing a “very good fit”¹⁾ and compare the parameter regions that deliver a critical distribution with at least this quality. The difference between the static model and the dynamic model is one order of magnitude (see inset in Figure 20.3). The result does not depend on the particular value of ϑ as long as it is not too large. In contrast to the static case, the

1) Meant in the sense of a linear regression of the logarithms, but other estimates have been tested as well.

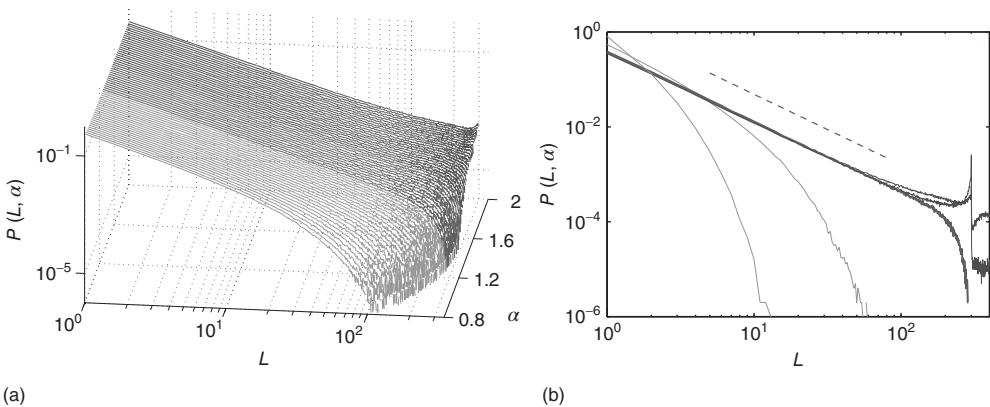


Figure 20.2 Distribution of avalanche sizes for different values of the connection parameter α . (a) At $\alpha < 1.3$, the distribution is subcritical (green). It becomes critical in an interval around $\alpha = 1.4$ (red). For $\alpha > 1.6$, the distribution is supercritical (blue). (Figure first published in Ref. [23].) (b) Characteristic

examples of all three kinds of distributions with the same color code. Results are obtained for $N = 300$, $v = 10$, $u = 0.2$, $I^{\text{ext}} = 0.025$ (Figure adapted from Ref. [39].) <http://www.nature.com/reprints/permission-requests.html>. (Please find a color version of this figure on the color plates.)

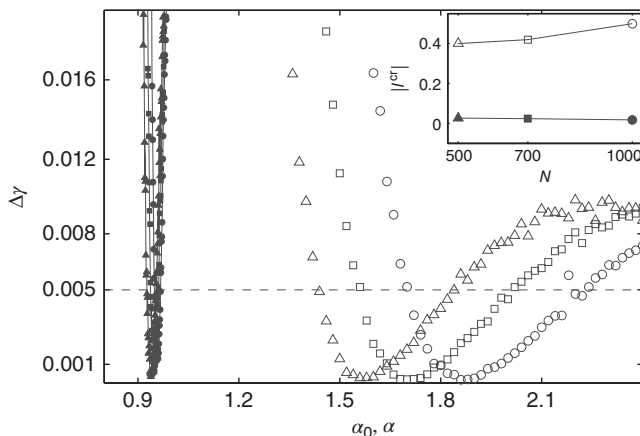


Figure 20.3 The range of connectivity parameters where critical events extend to the system size. The mean-squared deviation ΔY is plotted as a function of α . Empty circles, squares, and triangles stand for networks with dynamic synapses and system sizes $N = 500$, 700, and 1000, respectively. The

results are based on a number of avalanches that scale with N^2 . Filled symbols represent the static model. The inset (same symbols) shows the lengths of the parameter intervals where the deviation from the best matching power law is smaller than 0.005. (Figure first published in Ref. [23].)

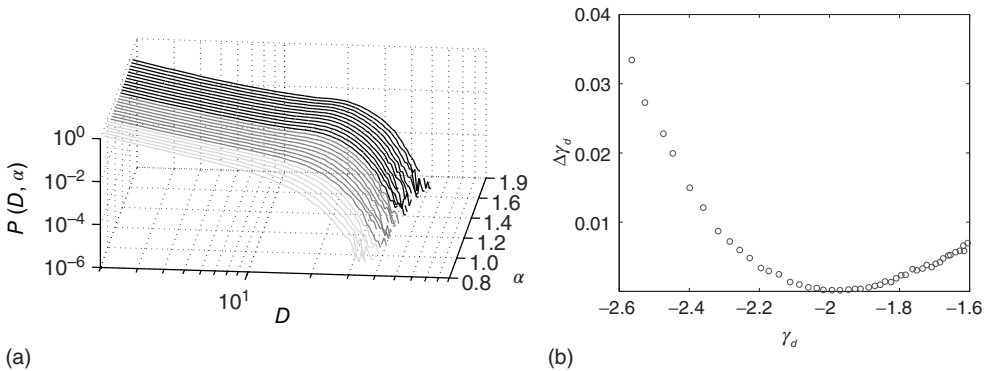


Figure 20.4 (a) Avalanche duration distribution for different values of the connectivity parameter α . (b) Power law exponent γ_d fitted for small avalanche durations as a function of the goodness of the power law fit to the avalanche size distribution.

$N = 100$, $v = 10$, $u = 0.2$. In (a), green gray traces correspond to subcritical distributions of avalanche sizes, red gray traces critical and blue ones supercritical. For details see Figure 20.2. (Please find a color version of this figure on the color plates.)

critical region with dynamic synapses apparently increases with the system size. The power law exponent at criticality for finite networks has a smaller modulus than -1.5 , but it approaches this value in the limit.

The avalanche duration distributions deviate strongly from a power law for durations larger than 10 , that is, they consist mainly of the exponential cutoff (cf. Figure 20.4(a)). We determined the slope of the power law by fitting the region of short durations where a power law is still applicable. Similar to the experimental findings [3], the exponent for the critical duration distribution is found to be -2 (cf. Figure 20.4(b)).

20.3.2

Mean-Field Approximation

The above discussion, as well as biological evidence, suggests that the synaptic strength is an important factor for the avalanche size. We will now consider a relation between α and the effective synaptic strength and derive a large N approximation for the resulting avalanche size distribution in the critical case.

The mean-field assumption stipulates that we can consider the mean $u\langle J_{ij} \rangle$ instead of the full distribution of synaptic strengths across the network. Obviously, the dynamic network is now comparable to a static model with $\alpha = u\langle J_{ij} \rangle$, which is also evident from numerical simulations [23]. We can thus rely on the results from the static case (Eq. (20.2)), but have to take into account that $\langle J_{ij} \rangle$ is no longer a free parameter but depends in turn on the avalanche distribution.

In order to express the average synaptic strength analytically, we refer to the average inter-spike interval Δ^{ISI} of a neuron (which is usually larger than the inter-avalanche interval). The relation between Δ^{ISI} and $\langle J_{ij} \rangle$ involves a form of regulation: If the inter-spike intervals are short, then the synapses have a short

time to recover and the average synaptic strength resides at a low level, while large synaptic strengths lead more often to long avalanches and to large inputs to neurons during the avalanches, which tends to shorten inter-spike intervals. This trade-off determines the effective synaptic strengths and the inter-spike intervals that are realized by the dynamics of the network. In order to express this formally, we solve the dynamical equations (20.3) and (20.4) and obtain the following equations [12, 23]:

$$\langle J_{ij} \rangle = G(\langle \Delta^{ISI} \rangle) \quad (20.5)$$

$$\langle \Delta^{ISI} \rangle = F(\langle J_{ij} \rangle) \quad (20.6)$$

The above equations must hold simultaneously and represent a self-consistency requirement in our approach. Because both F and G are increasing functions, the solution is unique; it agrees perfectly with numerical simulations [23].

With increasing N , the stationary distribution becomes less and less sensitive to changes of the parameter α near the critical value, which brings about the large critical region for the LHG model. The growth of the “critical interval” with the system size (Figure 20.3) can be rigorously shown in the thermodynamic limit. For $N \rightarrow \infty$, the region extends from $\alpha = 1$ to infinity while the deviation from an ideal power law vanishes.

The stability of the solution of the self-consistency equations (20.5) and (20.6) can be demonstrated based on the following idea. Applying a positive perturbation $\Delta J > 0$ to all synapses at time t_p leads to a temporary increase of the avalanche size. The average size of a few avalanches following t_p will be larger than in the unperturbed case. This leads, on average, to a decrease of the inter-spike intervals, which affects the average synaptic activity. The average synaptic strength at the time of the second spike after perturbation can be found from Eq. (20.4), and it can be shown that positively perturbed synapses decrease their strength to return to the equilibrium state. The same argument shows that negatively perturbed synapses increase their strength thus counteracting the perturbation.

20.3.3

Toward a Realistic Model: Network Structure, Leakage, and Inhibition

The analysis in the previous sections was considerably simplified by the restrictive model assumptions. As a side effect, this allowed us also to separate certain effects from each other. For example, for complete connectivity, effects due to the internal neural adaptation are distinguishable from network effects. See, for example, the work by Lin and Chen [30] and Teramae and Fukai [31], where often small-world connectivity is found to contribute to criticality.

We will ask here how the combination of specific connectivity and depressive synapses shapes the statistics of the network dynamics. To start with, let us consider a simple random connectivity scheme. Each neuron is connected to $p_1 N$ randomly selected neurons. Such a random network is statistically homogeneous and connected if p_1 is large enough (e.g., $p_1 \approx 0.2$). Therefore, the mean-field

approximation is still valid. The critical regime can be identified by rescaling α , where the new critical connectivity strength is now $\alpha_{\text{cr}}(N)/p_1$, where $\alpha_{\text{cr}}(N)$ is the critical parameter of a fully connected network of size N .

We will also consider another type of a random network where the degree of the nodes is not restricted. Instead of the above neuron-based procedure, we connect any pair of neurons with the same probability p_2 .

As a more general setup, we study the avalanche dynamics in a small-world network [32] which can be tuned by a parameter in between the extreme cases of a regular nearest-neighbor connectivity and a purely random network.

Comparing the four types of connectivity (nearest neighbors, two random networks, and small-world connectivity, each with appropriately rescaled parameters), we find significant differences (see Figure 20.5). Although the dependence of the critical exponent on the maximal synaptic strength α has a similar shape, the slopes are different and are steepest for the nearest-neighbor connectivity. This is reflected also in the deviation from the best matching power law, which again is largest for the regular network. Independently of the particular choice of the criterion for criticality in a finite system, the region corresponding to the random

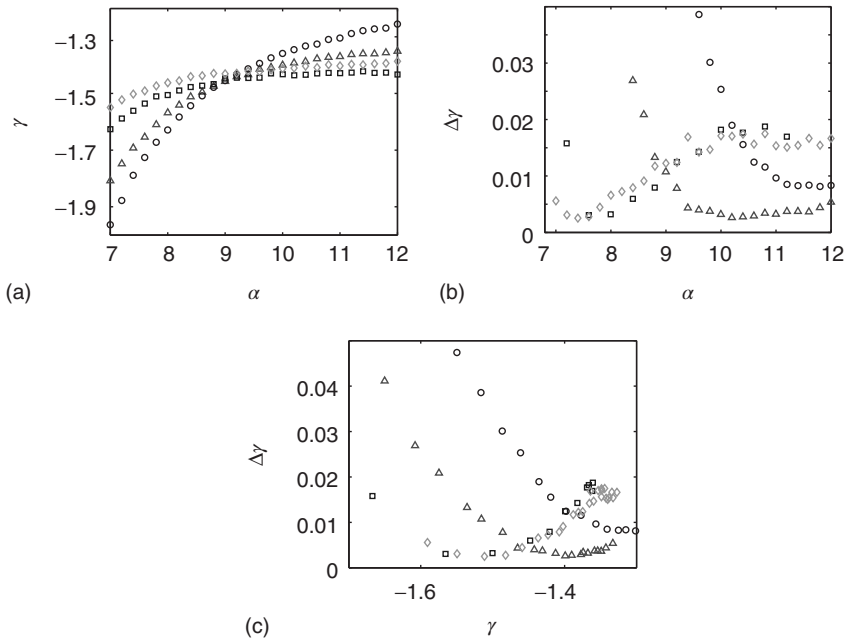


Figure 20.5 Comparison of different connectivity schemes. (a) Exponent of the best matching power law for different α s. (b) Deviation from the best matching power law for different α s. (c) Deviation from the best matching power law as a function of the matched exponent. Different symbols

stand for different connectivities: circles – nearest neighbors, triangular – small-world, squares – random connectivity with fixed number of connection per neuron, diamonds – random connectivity. Parameters are $N = 500$, $\nu = 10$, $u = 0.2$, average connectivity is always 20%.

network with a fixed number of connections per neuron is smaller than for the unrestricted random network, which in turn is smaller than the critical region for the small-world network. Small-world networks show thus a tendency to “improve” the power law in the sense that the deviation between the observed distribution and the best matching power law decreases (Figure 20.5).

Another assumption in the LHG model is the perfect integration, that is, the neurons are nonleaky integrators. In contrast to the examples where the introduction of an arbitrarily small leakage to the model neurons destroys the results for a leak-free system (see, e.g., [33, 34]), small leakage does not destroy the power law avalanches. Instead of Eq. (20.3), we now use the following dynamics for the membrane potentials:

$$\dot{h}(t) = -\frac{1}{\tau} h(t) + C + I^{\text{ext}} + I^{\text{int}}$$

where the variable C stands for an active process, for example, a dynamic threshold, that compensates the leak currents. In this way, the neurons can remain close to the threshold and the network remains conservative.

The avalanche size distribution (Figure 20.6) does not change when a moderate leakage is introduced. The power law exponent becomes larger in magnitude, reaching approximately -1.9 . Strong leakage, however, suppresses power laws in the present model.

Finally, we want to consider the effect of inhibitory synapses in the model which was so far all-excitatory. It is known that inhibition often leads to synchronization in neuronal networks, which in turn could interfere with critical behavior. It is natural to introduce inhibition according to Dale’s principle (which states that neurons release the same set of transmitters at all of their synapses) [35, 36]. Accordingly, we select a fraction of neurons [37] and change the signs of their synaptic strengths. After integrating both excitatory and inhibitory inputs to a neuron, we require that the membrane potential remains positive, that is, we set $h = 0$ if the inhibition

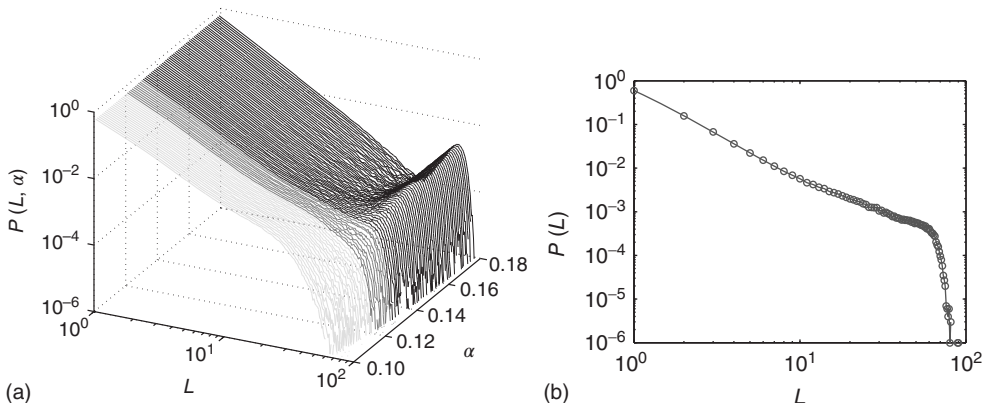


Figure 20.6 Distribution of avalanche sizes in a network with leaky neurons for different values of the connectivity parameter α (a) and for the critical case ($\alpha = 0.125$) (b) $N = 100$, $C = 0.98$, $\tau = 40$ ms.

dominates. In addition, we will also model inhibition by a randomization of the signs of synaptic strengths without enforcing Dale's principle. In both cases, a portion of 0.2 of all synapses will have negative sign [37].

Figure 20.7 shows the avalanche size distributions for the two types of inhibition. If Dale's principle holds, an externally activated neuron is inhibitory with probability of 0.2, such that avalanches of size 1 are relatively more frequent, a fact which violates the power law at small avalanche sizes but is irrelevant for the critical behavior because only the asymptotics is relevant and the inhibition has no effect for larger avalanches. In both cases, the power law exponents are approximately -1.5 in the critical regime (with Dale's principle about -1.47 , without about -1.52). We thus conclude that inhibition does not interfere with the critical behavior.

20.3.4 Synaptic Facilitation

Depressing synapses can regulate the network dynamics toward criticality. Some synapses experience also an activity-dependent facilitation at a shorter timescale than the depression. We show, that criticality is achieved in the network with facilitatory synapses in a self-organized way [38, 39].

Facilitation enters the model via the “usage” parameter u in Eq. (20.4). The synaptic model [40, 41] posits an activity-related increase of the fraction of synaptic resources that are used in the transmission. In the scheme adopted here, an action potential causes the respective individual usage variables u_{ij} to increase. After the spike, they decrease again with a time constant τ_u . The corresponding kinetic equation

$$\dot{u}_{ij} = \frac{1}{\tau_u}(u_0 - u_{ij}) + (1 - u_{ij})u_0\delta(t - t_{sp}^j) \quad (20.7)$$

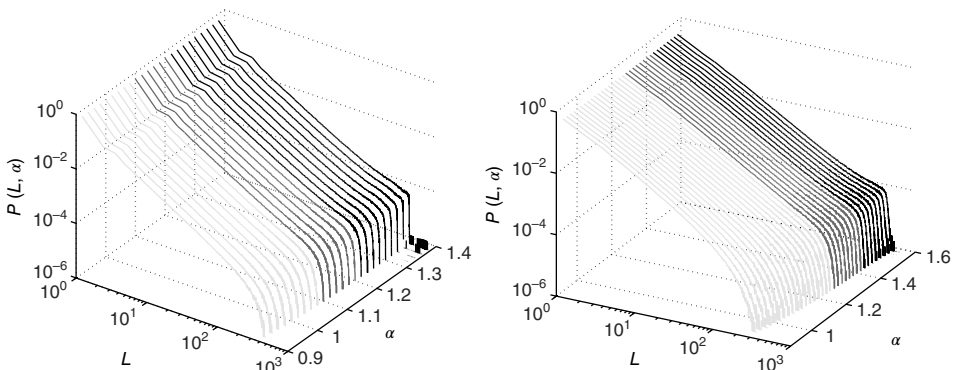


Figure 20.7 Network with 20% inhibitory connections (a) with and (b) without Dale's principle. The avalanche size distribution is plotted for different α s. For the plot on

the left, only avalanches of size 6 or larger were used in the estimation of the power law exponent. $N = 500$, $v = 10$, $u = 0.2$.

describes the dynamics of the parameter u in Eq. (20.4) for each synapse individually. The parameter u_0 in Eq. (20.7) denotes the minimal fraction of the synaptic resources that are used for a spike. The two equations (20.4) and (20.7) together with the membrane potential dynamics equation (20.3) govern the behavior of this model neural network.

The size distributions for finite networks show again subcritical, critical, and supercritical regimes for different values of α (Figure 20.8). Below a first critical value α_{cr} , the network is always subcritical, and above a second critical value $\alpha^{\text{cr}} > \alpha_{\text{cr}}$, supercritical behavior can be observed. In between the two critical values, the system has an approximate power law avalanche distribution for a large volume of initial conditions. The subcritical branch persists as well in the interval $[\alpha_{\text{cr}}, \alpha^{\text{cr}}]$ (Figure 20.8). This implies a hysteretic behavior, which is illustrated by Figure 20.9.

If α is smaller than α_{cr} , there is only one solution of the self-consistency equation. At $\alpha = \alpha_{\text{cr}}$, a saddle-node bifurcation creates a stable and an unstable branch in addition to the existing stable branch. In between α_{cr} and α^{cr} , three solutions coexist, of which two are stable; Finally, at $\alpha = \alpha^{\text{cr}}$, a second bifurcation occurs where the subcritical branch and the unstable branch annihilate such that for larger α only a single solution remains (Figure 20.9). The simulations indicate that the range of criticality increases with system size, and eventually all values of $\alpha > \alpha_{\text{cr}}$ are critical. This can be shown analytically in a similar way as for the purely depressive network. The lower boundary of the critical region for an infinite network is given by $2\sqrt{u_0 - u_0^2} \leq 1$, that is, facilitatory synapses extend the critical region toward lower synaptic strengths.

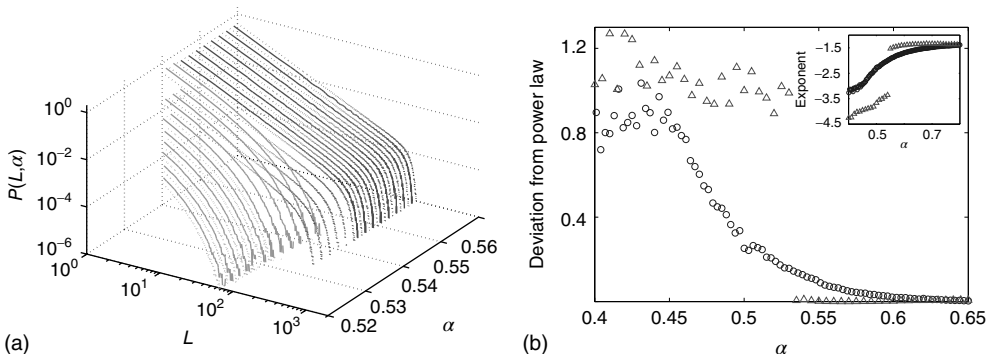


Figure 20.8 (a) Distribution of avalanche sizes for different values of α . Below $\alpha < 0.543$, a subcritical distribution exists (green). Critical behavior can be observed above $\alpha = 0.53$ (blue/red). The picture indicates a hysteresis with respect to α , which is illustrated by the section through the 3-D plot and shown in the inset. For large networks, all distributions of the upper branch are critical, while the lower branch remains subcritical. See also Figure 20.9.

(b) Deviation of avalanche size distribution from a power law for different α . Triangles represent facilitatory synapses, while circles represent depressing synapses. The inset shows the exponent of the nearest power law distribution. For both, $N = 300$, $v = 10$, $u_0 = 0.1$, $I_0 = 7.5$ [39]. (Copyright 2009 by The American Physical Society.) (Please find a color version of this figure on the color plates.)

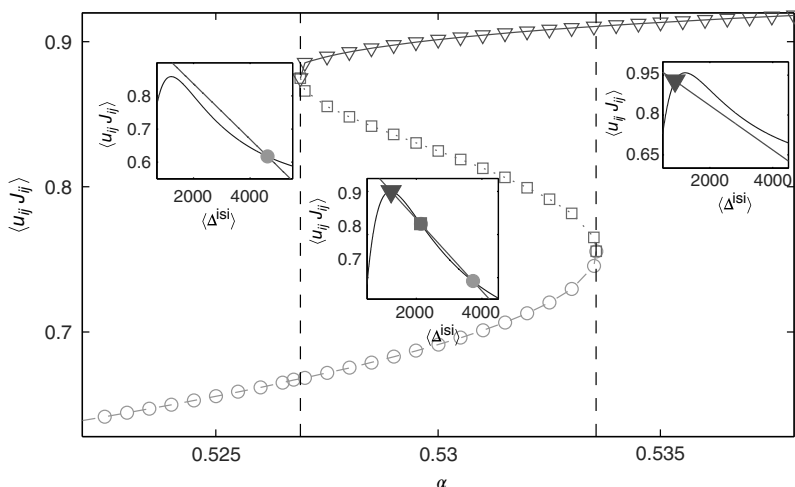


Figure 20.9 Bifurcation diagram representing the solutions of the self-consistency equation for the model with facilitating and depressing synapses. The average interaction strength $\langle u_{ij} J_{ij} \rangle$ is plotted against the interaction parameter α . The insets show the graphical solutions of the self-consistency

equation which may have one or three solutions here, in contrast to the purely depressive case (Eqs. (20.5) and (20.6)) where a unique solution exists. $N = 300$, $v = 10$, $u_0 = 0.1$, $I_0 = 7.5$. The bifurcation points are at $\alpha_{cr} = 0.534$ and $\alpha^{cr} = 0.547$. Modified from [39].

We have proposed [39] that the coexistence of a critical and a subcritical phase in this model may be related to the phenomenon of “up” and “down” states in the prefrontal cortex, an idea that was later elaborated by Millman *et al.* [8].

20.4

Criticality by Homeostatic Plasticity

Neuronal avalanches are homeostatically regulated, which has been demonstrated recently by Plenz (2012) [42], where networks after being perturbed away from the critical state gradually, within hours, return to criticality. This suggests a slow adaptation process which we will study in this section.

20.4.1

Branching Processes

The Galton–Watson branching processes were introduced in 1874 to explain the disappearance of some of the British family names [43]. Since then, they were extensively studied in mathematics [44, 45] and applied in biology and physics [46].

A branching process generates tree-like structures where each node produces i descendants with a probability p_i . The fact that the probability does not depend on the events in earlier generations differs from the situation in neural networks

where the effectiveness of a spike depends on their recent activity. Nevertheless, it was shown that branching processes provide a good approximation for data obtained from multielectrode recordings [47].

The evolution of an avalanche can be described, similar to a branching process, by the temporal sequence $\{\xi_t\}$ of the activity levels in the network. The neural connectivity parameter α corresponds to the branching parameter α_{br} of a Galton–Watson process, which describes the average number $\sum_i ip_i$ of offspring per node. The stochasticity of the process is brought forth by the randomness of the external inputs in between the avalanches. But, since the driving is assumed to halt during avalanches, the sequence ξ_t is deterministic for all $t < D$.

The sequence of neural activity $\{\xi_t\}$ is still different from a branching process because it does not share the Markov property of branching processes. That is, because of the condition $\xi_t \leq N - \sum_{s=1}^{t-1} \xi_s$, the value of ξ_t depends not only on the preceding value ξ_{t-1} but also on all previous activations during the avalanche.

Interestingly, for large networks this difference becomes irrelevant: that is, if the network size tends to infinity, then the distribution of the neural firings $\{\xi_t\}_{t=1}^\infty$ approaches the distribution of a Galton–Watson branching process [12, 48]. This asymptotic relation requires, however, that the membrane potentials are evenly spread across the phase space of the system, that is, the states of the neurons become more and more uniformly distributed independent of the initialization and in spite of the partially synchronizing effects of the ongoing avalanches. Such mixing properties can be shown by simulations, and the related analytical results have been obtained [12].

In this way, we can use the results from branching theory for control of the network. In particular, it is known [49] that the avalanche sizes in a critical branching process, that is, for $\alpha_{\text{br}} = 1$, are distributed as $P(\xi = L) \propto L^{-\frac{3}{2}}$, which can be used to derive a local learning rule that induces criticality.

20.4.2

Self-Organization by Long-Term Plasticity

A learning rule for criticality can be obtained by enforcing conservation of neural activity and thereby generating an approximation of a branching process. In particular, for the beginning of an avalanche we will require that on average only one more neuron gets activated:

$$E_i(t) = \begin{cases} \frac{1}{2} \left(\sum_j S_j(t) - 1 \right)^2 & \text{if } S_i(t-1) = 1 \\ 0 & \text{otherwise} \end{cases} \quad (20.8)$$

The criterion is not implausible because in a globally or randomly coupled network the total activity $\sum_i S_i(t)$ can be estimated locally from the internal input at the next time step. Eq. (20.8) gives rise to a learning rule for the synaptic strength [48]:

$$\alpha^{t+1} = \alpha^t + \varepsilon_{\text{homeo}} \left(1 - l - N^{-\frac{1}{2}} \right) \quad (20.9)$$

where l is the activity at the following time step and $\varepsilon_{\text{homeo}} \ll 1$ is a learning rate. Eq. (20.9) reduces the synaptic weight if the activity tends to increase and reduces

it otherwise: that is, learning according to Eq. (20.9) is *homeostatic* [50] because it tends to stabilize the flow of neural activity. A similar learning rule has been studied in Boolean networks [51], where also deviations from the ideally critical behaviors were noticed. Here they may be caused by the difference to a branching process for finite networks.

Because the number of neurons that respond to a single spike is bounded, the branching parameter tends to be underestimated. To compensate for this effect, we include a finite-size correction into Eq. (20.9). As a result (see Figure 20.10), the synaptic weights converge to the value that was identified as the critical value for finite system sizes of a network with static synapses (Eq. (20.2)).

The avalanche dynamics together with the slow homeostatic learning drives the system to a critical state independently of the initial conditions such that the neuronal network with this learning rule is indeed self-organized critical.

20.4.3

Effects of Spike-Time-Dependent Plasticity and Network Structure

The structure of neural networks is a product of developmental processes as well as activity-dependent learning (spike-time dependent plasticity, STDP, see [52]), which in combination with the short-term synaptic dynamics and homeostatic effects determines the activity dynamics. This raises the question how the complex interaction of these contributions interferes with criticality. The following sections present some evidence for cooperativity: that is, the effects are found to support each other in the maintenance of a critical regime.

We now consider a network with synaptic weights that are composed of three factors, each of which evolves on a different timescale.

$$w_{ij} = u J_{ij} w_{ij}^{\text{STDP}} w_{ij}^h \quad (20.10)$$

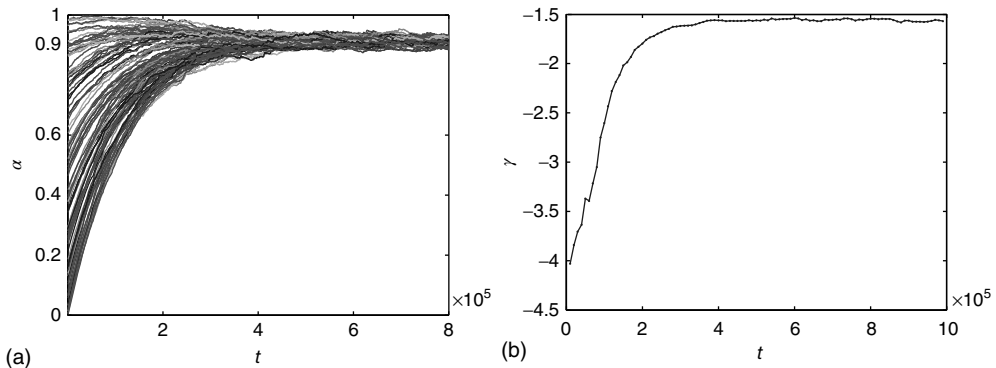


Figure 20.10 (a) Homeostatic learning of individual synapses. Shown are trajectories of the synaptic strengths of a single neuron during the initial learning phase. (b) The exponent of the power law fit

to the avalanche size distribution during homeostatic learning clearly approaches the critical value of $-3/2$. $N = 100$, $T \leq 2 \cdot 10^6$, $\epsilon_{\text{homeo}} = 10^{-4}$ [48].

The variables J_{ij} follow the short-term dynamics (Eq. (20.4)), w_{ij}^h are governed by the homeostatic learning rule (20.9), and w_{ij}^{STDP} are subject to STDP learning:

$$\Delta w_{ij}^{\text{STDP}} = \begin{cases} \varepsilon_{\text{STDP}} \left(1 - \frac{w_{ij}^{\text{STDP}}}{W_{\max}} \right) e^{t_j^{\text{sp}} - t_i^{\text{sp}}} & \text{if } t_i^{\text{sp}} > t_j^{\text{sp}} \\ -\varepsilon_{\text{STDP}} \frac{w_{ij}^{\text{STDP}}}{W_{\max}} e^{t_j^{\text{sp}} - t_i^{\text{sp}}} & \text{otherwise} \end{cases} \quad (20.11)$$

Here, t_i^{sp} denotes the time of the last spike of neuron i . The form of Eq. (20.10) is reasonable because homeostatic learning is known to be multiplicative [50] and the STDP rule is used in a multiplicative form. The results do not change if we combine the STDP term w^{STDP} additively, that is, $w_{ij} = u J_{ij} w_{ij}^h + w_{ij}^{\text{STDP}}$.

Figure 20.11 presents the results for the individual contributions for a random network with connection probability $p = 0.3$. The network with STDP has a slightly increased critical region which is shifted to the right due to pruning. Homeostatic regulation again produces criticality independently of the parameter α .

To evaluate the impact of the combination of STDP and homeostatic learning, we compare three different scenarios: A network with STDP and homeostatic learning where synaptic dynamics described by Eq. (20.10); a network with homeostatic learning only; and a network with homeostatic learning that was also corrected for pruning to simplify comparison with STDP. In the last case, we measure how many synapses were pruned in the STDP simulation and then delete randomly the same number of synapses from the network before starting with the homeostatic regulation. The results of this comparison are represented in Figure 20.12. The

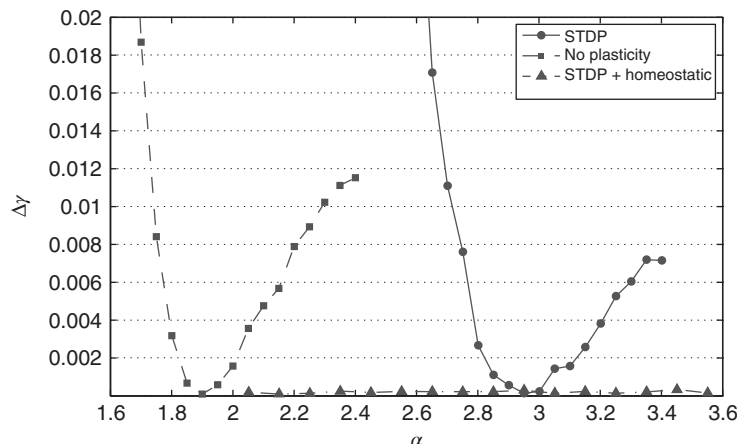


Figure 20.11 Deviation from the best matching power law for different combinations of plasticity rules. Squares: only depressing synapses, circles: depressing

synapses and STDP, triangles: depressing synapses and STDP as well as homeostatic regulation. $N = 100$, $W_{\max} = 1.5$, $\varepsilon_{\text{homeo}} = 0.01$, $\varepsilon_{\text{STDP}} = 0.08$.

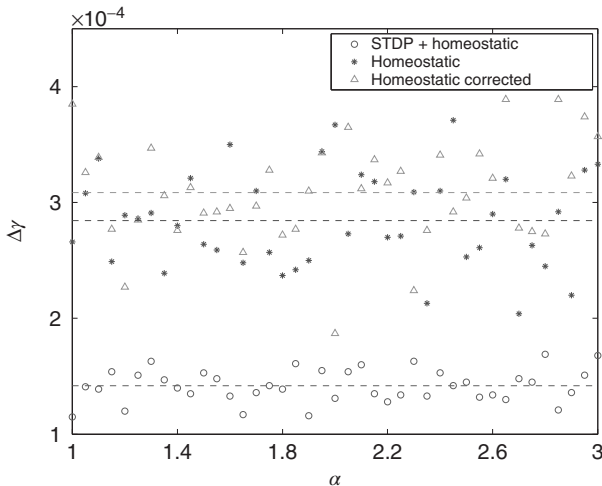


Figure 20.12 Deviation from the nearest power law with and without STDP. Circles: homeostatic plasticity combined with STDP, stars: homeostatic plasticity, asterisks: homeostatic plasticity corrected for pruning. Dashed lines represent averages. $N = 100$, $W_{\max} = 1.5$, $\epsilon_{\text{homeo}} = 0.01$, $\epsilon_{\text{STDP}} = 0.08$.

network with the combination of rules is closer to the critical state independently of the correction for pruning. This result supports the hypothesis that the specific structures that are selected by STDP learning are beneficial for criticality in the network. Similar effects might be responsible for the closeness of the network to a critical state in the models including STDP such as [7].

20.5 Conclusion

The complex dynamics underlying information processing in neural systems is under study from a multitude of approaches. Many phenomena are caused by actively acquired sensory stimuli, feedback from the body, or nonstationary interaction among brain areas. The study of criticality in this context cannot unravel the information processing aspects of brain function, but it can show that the brain has the means to maintain a regime that optimally supports the higher processes. Criticality has been shown to optimize several aspects of brain function such as sensitivity to input, information transmission, and information capacity, for example, by Shew *et al.* [53]. To a physicist, this characterization is reminiscent of the discussion of ground states of physical systems: if the brain was not excited by any internal or external inputs, it would still be critical whenever criticality describes the default behavior of a complex neural system. The fact that the clearest evidence for criticality has been obtained in *in vitro* experiments supports this view.

In addition to some recent results, we have presented the highlights of a journey that took us through the realms of critical systems for more than a decade. While highly simplified systems, such as the Eurich model, may turn out to allow for relevant predictions, most of our work was devoted to a more comprehensive understanding of the function of critical phenomena in physiologically realistic neural systems. Interestingly, the more biological details were included into the series of models, the more closely we arrived to such a functional description of criticality, which in turn represents also a justification of the original approach. Although a large part of the results covered here are due to numerical simulations, it was the analytical study, which we could touch here only briefly, that provided us with the orientation for the development of the models.

Acknowledgment

The authors wish to thank Udo Ernst, Christian Eurich, Tomoki Fukai, Georg Martius, Dietmar Plenz, and Marius Usher for valuable comments, help, and support. They also acknowledge the contributions from Victor Hernandes-Urbina, Sakyasingha Dasgupta, and Maximilian Uhlig. This work was supported by the Federal Ministry of Education and Research (BMBF), Germany, under Grant No. 01GQ1005B.

References

1. Bak, P. (1996) *How Nature Works: The Science of Self-Organized Criticality*, Springer, New York.
2. Eurich, C.W., Herrmann, M., and Ernst, U. (2002) Finite-size effects of avalanche dynamics. *Phys. Rev. E*, **66**, 066–137-06-1–15.
3. Beggs, J.M. and Plenz, D. (2003) Neuronal avalanches in neocortical circuits. *J. Neurosci.*, **23** (35), 11–167.
4. Petermann, T., Lebedev, M., Nicolelis, M., and Plenz, D. (2006) Neuronal avalanches in vivo. *Soc. Neurosci. Abstr.*, **32**, 539.
5. Chen, D., Wu, S., Guo, A., and Yang, Z.R. (1995) Self-organized criticality in a cellular automaton model of pulse-coupled integrate-and-fire neurons. *J. Phys. A: Math. Gen.*, **28**, 5177–5182.
6. Herz, A.V.M. and Hopfield, J.J. (1995) Earthquake cycles and neural reverberations: collective oscillations in systems with pulse-coupled threshold elements. *Phys. Rev. Lett.*, **75**, 1222–1225.
7. Rubinov, M., Sporns, O., Thivierge, J.P., and Breakspear, M. (2011) Neuropathologically realistic determinants of self-organized criticality in networks of spiking neurons. *PLoS Comput. Biol.*, **7** (6), e1002038.
8. Millman, D., Mihalas, S., Kirkwood, A., and Niebur, E. (2010) Self-organized criticality occurs in non-conservative neuronal networks during Up states. *Nat. Phys.*, **6** (10), 801–805. PMCID: PMC3145974.
9. Dunkelmann, S. and Radons, G. (1994) Neural networks and abelian sandpile models of self-organized criticality, in *Proceedings of International Conference Artificial Neural Networks* (eds M. Marinaro and P. Morasso), Springer-Verlag, 867–870.
10. Corral, Á., Perez, C.J., Diaz-Guilera, A., and Arenas, A. (1995) Self-organized criticality and synchronization in a lattice model of integrate-and-fire oscillators. *Phys. Rev. Lett.*, **74**, 118–121.

11. Eurich, C.W., Conradi, T., and Schwegler, H. (1999) Critical and non-critical avalanche behavior in networks of integrate-and-fire neurons, *European Symposium on Artificial Neural Networks*, D-Facto public, Bruges (Belgium), pp. 411–416.
12. Levina, A. (2008) A mathematical approach to self-organized criticality in neural networks. Nieders. Staats-u. Universitätsbibliothek Göttingen. Dissertation (Ph.D. thesis), webdoc.sub.gwdg.de/diss/2008/levina/levina.pdf.
13. Grassberger, P. (1994) Efficient large-scale simulations of a uniformly driven system. *Phys. Rev. E*, **49** (3), 2436–2444, doi: 10.1103/PhysRevE.49.2436.
14. Kinouchi, O., Pinho, S.T.R., and Prado, C.P.C. (1998) Random-neighbor Olami-Feder-Christensen slip-stick model. *Phys. Rev. E*, **58**, 3997–4000.
15. Broker, H.M. and Grassberger, P. (1997) Random neighbor theory of the Olami-Feder-Christensen earthquake model. *Phys. Rev. E*, **56** (4), 3944–3952, doi: 10.1103/PhysRevE.56.3944.
16. Olami, Z., Feder, H., and Christensen, K. (1992) Self-organized criticality in a continuous, nonconservative cellular automaton modeling earthquakes. *Phys. Rev. Lett.*, **68** (8), 1244–1247.
17. Lise, S. and Jensen, H.J. (1996) Transitions in nonconserving models of self-organized criticality. *Phys. Rev. Lett.*, **76**, 2326–2329.
18. Tsuchiya, T. and Katori, M. (2000) Proof of breaking of self-organized criticality in a nonconservative abelian sandpile model. *Phys. Rev. E*, **61** (2), 1183–1188, doi: 10.1103/PhysRevE.61.1183.
19. Gireesh, E.D. and Plenz, D. (2008) Neuronal avalanches organize as nested theta-and beta/gamma-oscillations during development of cortical layer 2/3. *Proc. Natl. Acad. Sci. U.S.A.*, **105** (21), 7576.
20. Stewart, C. and Plenz, D. (2008) Homeostasis of neuronal avalanches during postnatal cortex development in vitro. *J. Neurosci. Methods*, **169** (2), 405–416.
21. Tetzlaff, C., Okujeni, S., Egert, U., Worgötter, F., and Butz, M. (2010) Self-organized criticality in developing neuronal networks. *PLoS Comput. Biol.*, **6** (12), e1001013.
22. Sornette, D. (1992) Critical phase transitions made self-organized: a dynamical system feedback mechanism for self-organized criticality. *J. Phys. I France*, **2**, 2065–2073.
23. Levina, A., Herrmann, J.M., and Geisel, T. (2007b) Dynamical synapses causing self-organized criticality in neural networks. *Nat. Phys.*, **3** (12), 857–860.
24. Bonachela, J.A., de Franciscis, S., Torres, J.J., and Munoz, M.A. (2010) Self-organization without conservation: are neuronal avalanches generically critical? *J. Stat. Mech.: Theory Exp.*, (02), P02015 <http://iopscience.iop.org/1742-5468/2010/02/P02015/fulltext/>.
25. Choi, H., Maeng, S., and Lee, J. (2012) Self-organized criticality of a simple integrate-and-fire neural model. *J. Korean Phys. Soc.*, **60**, 657–659, doi: 10.3938/jkps.60.657.
26. Markram, H. and Tsodyks, M. (1996) Redistribution of synaptic efficacy between neocortical pyramidal neurons. *Nature*, **382**, 807–810.
27. Kadanoff, L.P., Nagel, S.R., Wu, L., and Zhou, S. (1989) Scaling and universality in avalanches. *Phys. Rev. A*, **39** (12), 6524–6537, doi: 10.1103/PhysRevA.39.6524.
28. Christensen, K. and Olami, Z. (1992) Scaling, phase transitions, and nonuniversality in a self-organized critical cellular automaton model. *Phys. Rev. A*, **46**, 1829–1838.
29. Cardy, J. (ed.) (1996) *Scaling and Renormalization in Statistical Physics*, Cambridge Lecture Notes in Physics, Vol. 5, Cambridge University Press.
30. Lin, M. and Chen, T.L. (2005) Self-organized criticality in a simple model of neurons based on small-world networks. *Phys. Rev. E*, **71**, (016133).
31. Teramae, J. and Fukai, T. (2007) Local cortical circuit model inferred from power-law distributed neuronal avalanches. *J. Comput. Neurosci.*, **22** (3), 301–312.
32. Watts, D. and Strogatz, S. (1998) Collective dynamics of “small-world” networks. *Nature*, **393**, 440–442.

33. Gerstner, W. (2000) Population dynamics of spiking neurons: fast transients, asynchronous states, and locking. *Neur. Comput.*, **12**, 43–89.
34. Timme, M., Wolf, F., and Geisel, T. (2002) Prevalence of unstable attractors in networks of pulse-coupled oscillators. *Phys. Rev. Lett.*, **89** (15), 154 105.
35. Dale, H. (1935) Pharmacology and nerve-endings. *Proc. R. Soc. Med.*, **28**, 319–332.
36. Kandel, E., Schwartz, J., and Jessel, T.M. (1991) *Principles of Neural Science*, 3rd edn, Elsevier, New York.
37. Abeles, M. (ed.) (1991) *Corticonics – Neural Circuits of the Cerebral Cortex*, Cambridge University Press.
38. Levina, A., Herrmann, J.M., Geisel, T., Weiss, Y., Scholkopf, B., and Platt, J. (eds) (2006) Dynamical synapses give rise to a power-law distribution of neuronal avalanches, in *Advances in Neural Information Processing Systems 18*, MIT Press, Cambridge, MA. pp. 771–778.
39. Levina, A., Herrmann, J.M., and Geisel, T. (2009) Phase transitions towards criticality in a neural system with adaptive interactions. *Phys. Rev. Lett.*, **102** (11), 118 110.
40. Markram, H., Wang, Y., and Tsodyks, M. (1998) Differential signaling via the same axon from neocortical layer 5 pyramidal neurons. *Proc. Natl. Acad. Sci. U.S.A.*, **95**, 5323–5328.
41. Tsodyks, M., Pawelzik, K., and Markram, H. (1998) Neural networks with dynamic synapses. *Neur. Comput.*, **10**, 821–835.
42. Plenz, D. (2012) Neuronal avalanches and coherence potentials. *Eur. Phys. J.-Spec. Top.*, **205** (1), 259–301.
43. Watson, H. and Galton, F. (1874) On the probability of the extinction of families. *J. Anthropol. Inst. Great Br.*, **4**, 138–144.
44. Athreya, K.B. and Jagers, P. (1997) *Classical and Modern Branching Processes*, IMA, Vol. 84, Springer.
45. Harris, T. (1963) *The Theory of Branching Processes*, Springer.
46. Kimmel, M. and Axelrod, D.E. (2002) *Branching Processes in Biology*, Springer.
47. Beggs, J. and Plenz, D. (2004) Neuronal avalanches are diverse and precise activity patterns that are stable for many hours in cortical slice cultures. *J. Neurosci.*, **24** (22), 5216–5229.
48. Levina, A., Ernst, U., and Herrmann, J.M. (2007a) Criticality of avalanche dynamics in adaptive recurrent networks. *Neurocomputing*, **70** (10-12), 1877–1881.
49. Otter, R. (1949) The multiplicative process. *Ann. Math. Stat.*, **20**, 248–263.
50. Turrigiano, G.G., Leslie, K.R., Desai, N.S., Rutherford, L.C., and Nelson, S.B. (1998) Activity-dependent scaling of quantal amplitude in neocortical pyramidal neurons. *Nature*, **391**, 892–896.
51. Bornholdt, S. and Rohlf, T. (2000) Topological evolution of dynamical networks: global criticality from local dynamics. *Phys. Rev. Lett.*, **84**, 6114–6117. doi: 10.1103/PhysRevLett.84.6114.
52. Bi, G. and Poo, M. (1998) Synaptic modification in cultured hippocampal neurons: Dependence on spike timing, synaptic strength and postsynaptic cell type. *J. of Neurosci.*, **18** (24), 10–464–10–472.
53. Shew, W., Yang, H., Yu, S., Roy, R., and Plenz, D. (2011) Information capacity and transmission are maximized in balanced cortical networks with neuronal avalanches. *J. Neurosci.*, **31** (1), 55–63.

21

Nonconservative Neuronal Networks During Up-States Self-Organize Near Critical Points

Stefan Mihalas, Daniel Millman, Ramakrishnan Iyer, Alfredo Kirkwood, and Ernst Niebur

21.1

Introduction

Criticality refers to the state of a system in which a small perturbation can cause appreciable changes that sweep through the entire system [8]. Self-organized criticality (SOC) means that, from a finite range of initial condition, the system tends to move toward a critical state and stay there without the need for external control of systems parameters [9]. SOC systems are usually slowly driven, steady-state, nonequilibrium systems. Systems exhibiting SOC include models for earthquakes, forest fires, and avalanches of idealized grains toppling down sandpiles [10]. Necessary, but not sufficient, conditions to achieve SOC include (i) partitions of the systems into individual components that interact with each other and with the external environment, (ii) the time scale of internal interactions being much shorter than that of external influences, (iii) individual components/units responding to input only when the input exceeds a given threshold, so that SOC involves the building up of a context-dependent “energy” over long periods followed by transient redistribution of the energy to bring the system back to quiescence, and (iv) the possibility of the system existing in a multitude of metastable states as a result of the threshold.

In a system exhibiting SOC, activity propagates in “avalanche” events in which energy is dissipated intermittently. An avalanche can be characterized by the number of units that become super-threshold as a result of transient internal interactions. For example, an avalanche in a system prone to forest fires caused by lightning would consist of all trees that ultimately burn as a result of a single lightning strike. In a geological context, an avalanche is characterized by the energy released during an earthquake.

The distribution of avalanche sizes in SOC systems follows a power law

$$P(s) = s^\beta \quad (21.1)$$

where s represents the size of the avalanche and β is a scaling exponent which is typically in the range $-2.2 < \beta < -1.5$. Power laws are scale-invariant, so for a

change in scale by an arbitrary factor k

$$\frac{P(ks)}{P(s)} = \frac{(ks)^\beta}{(s)^\beta} = k^\beta = \text{constant.} \quad (21.2)$$

Another way to see this scale invariance is to note that, in the typical range for the critical exponent ($-2.2 < \beta < -1.5$), a mean avalanche size $E(s)$ does not exist (in an infinite system), that is,

$$E(s) = \int s P(s) ds = \int s \cdot s^\beta ds = \int s^{1+\beta} ds \rightarrow \infty. \quad (21.3)$$

The branching parameter σ is a measure of the propagation of excitations in a given network. It is defined as the average number of units that become super-threshold as a result of one unit going above threshold. Perturbations die off quickly for $\sigma < 1$, grow rapidly for $\sigma > 1$, and spread invariably for $\sigma = 1$. Critical systems have $\sigma = 1$ [11], while subcritical and supercritical systems have $\sigma < 1$ and $\sigma > 1$, respectively.

SOC has been observed in neuronal networks in the form of activity avalanches with a branching parameter near unity and a size distribution that obeys a power law with a critical exponent of about $-3/2$. Neuronal avalanches provide a novel means of characterizing spatiotemporal neuronal activity. By definition, a new avalanche is initiated when a background (external) input is the first input to drive the membrane potential of a neuron above threshold. If however, the membrane potential of a neuron first surpasses threshold as a result of synaptic input from an existing avalanche member, then that neuron is considered a member of the same avalanche. To maintain a common metric for both small and large avalanches, we follow the convention established by Beggs and Plenz [12] and define the branching parameter as the average number of neurons activated directly by the initiating avalanche member (i.e., the second generation of the avalanche).

In nervous systems, the seminal study by Beggs and Plenz [12] demonstrated that adult rat cortical slices and organotypic cultures devoid of sensory input are capable of self-organizing in a critical state. Local field potential (LFP) recordings using multielectrode arrays show activity characterized by brief bursts lasting tens of milliseconds followed by periods of quiescence lasting several seconds. The number of electrodes driven above a threshold during a burst is distributed approximately like a power law. Subsequent experiments in anesthetized rats [13] and in awake monkey cortex [14] have also demonstrated the occurrence of SOC in biological neuronal networks.

Another interesting phenomenon observed during sleep, under anesthesia, and *in vitro* is the fluctuation of neuronal activity between so-called up- and down-states. These two states are characterized by distinct membrane potentials and spike rates [1–5]. Usually, membrane potential fluctuations around the up-state are of higher order amplitude, whereas the down-state is relatively free of noise. *Neurons may exhibit two-state behavior either on account of their intrinsic properties or due to the properties of the network they belong to, or both.* At the network level, a high proportion of neurons in large cortical areas alternate between states at the same time [2, 15–18]. While down-states are quiescent [19], up-states have high synaptic

and spiking activity [5], resembling that of rapid eye movement (REM) sleep and wakefulness [20]. Differences in synaptic activity and neuronal responsiveness between up- and down-states suggest that the avalanche behavior differs as well.

For a system to maintain criticality, it is typically necessary that the internal state is invariant to perturbations. Neuronal networks endowed with *intrinsic* homeostatic mechanisms can maintain the critical state [21]. Modeling studies [6] have shown that criticality can be achieved in a conservative network of non-leaky integrate-and-fire neurons with short-term synaptic depression (STSD) [22]. On addition of a voltage leak, however, the networks become nonconservative and require a compensatory current to remain critical. Levina *et al.* [7] found two stable states, one critical and one subcritical, in a similar conservative network with synaptic depression and facilitation. Nonconservative networks of leaky integrate-and-fire (LIF) neurons also exhibit stable up- and down-states [23], which are obtainable with STSD alone [24].

This chapter, which is an extension of a study by Millman *et al.* [25], presents results of analytical and numerical investigations of nonconservative networks of LIF neurons with STSD. Analytically, we solve the Fokker–Planck equation for the probability density of the membrane potential in a mean-field approximation. This leads to solutions for the branching parameter in up- and down-states, which is *close to* unity in the up-state (almost critical behavior) and close to zero (subcritical) in the down-state. Simulated networks of LIF neurons, just as biological neural systems, also exhibit these properties. This behavior persists even as additional biologically realistic features, including small-world connectivity, N-methyl-D-aspartate (NMDA) receptor currents, and inhibition, are introduced. However, in all cases, although the networks get close to the critical point, they never become perfectly critical. We present an additional mechanism, namely finite-width distribution of synaptic weights in a network, that could be tuned along with STSD to obtain a critical state for a nonconservative network.

21.2 Model

The basic model consists of networks of LIF neurons with excitatory synapses and STSD (more general cases will be considered below). Each neuron forms synapses with on average n_s other neurons with uniform probability. Also, each neuron receives Poisson-distributed external input at the rate f_e . Glutamatergic synaptic currents of the α -amino-3-hydroxy-5-methyl-4-isoxazolepropionic (AMPA) type from other neurons, $I_{in}(t)$, and external inputs, $I_e(t)$, are modeled as exponentials with amplitude w and integration time constant τ_s :

$$I_{in/e}^i(t) = w_{in/e} e^{-(t-t_s^i)/\tau_s} \quad (21.4)$$

In agreement with physiology, each synapse has multiple (n_r) release sites. When a neuron fires spike i (at time t_s^i), only some sites have a docked “utilizable” vesicle. A utilizable site releases its vesicle with probability p_r , causing a postsynaptic

current, Eq. 21.4. To model STSD, p_r is scaled by a site-specific factor $U_j(t)$, which is zero immediately after a release at site j , at time t_r^j , and recovers exponentially with time constant τ_R . Neuronal membranes have potential V , resting potential V_r , resistance R , and capacitance C . Upon reaching the threshold (θ), the potential resets to V_r after a refractory period τ_{rp} . The network dynamics are therefore

$$\dot{V} = -\frac{V - V_r}{RC} + \frac{1}{C} \left(\sum_i I_e^i(t) + \sum_i \sum_j H(p_r U_j(t_s^i) - \zeta) I_{in}^i(t) \right), \quad (21.5)$$

$$U_j(t) = 1 - e^{-\frac{(t-t_r^j)}{\tau_R}}, \quad (21.6)$$

$$\text{if } V > \theta, \text{ then } V \rightarrow V_r \text{ after } \tau_{rp} \quad (21.7)$$

where ζ is a random variable uniformly distributed on $[0, 1]$, and $H(x)$ is the Heaviside step function.

21.2.1

Analytical Solution

To begin with, the time derivative of the mean synaptic utility, $u(t) = \langle U_j(t) \rangle_j$, where $\langle \cdot \rangle_j$ represents the average over all release sites, can be expressed analytically as

$$\dot{u} = \frac{1-u}{\tau_R} - u p_r f \quad (21.8)$$

where f is the output firing rate of the network. This can be shown as follows. The time derivative of the mean synaptic utility is the sum of the rate of recovery and the rate of depression, $\dot{u} = k_R + k_D$. Recovery happens between vesicle releases, and the average rate can be obtained from the time derivative of Eq. 21.6:

$$\frac{dU_j(t)}{dt} = \frac{\exp(-\frac{(t-t_r^j)}{\tau_R})}{\tau_R} = \frac{1-U_j(t)}{\tau_R} \quad (21.9)$$

$$k_R = \frac{d \langle U_j(t) \rangle}{dt} = \frac{1 - \langle U_j(t) \rangle}{\tau_R} = \frac{1-u}{\tau_R} \quad (21.10)$$

to yield the first term on the rhs of Eq. 21.8.

A release site fully depletes following a vesicle release, which happens with probability p_r for each spike, and spikes occur at rate f . Thus, the average rate of depletion is

$$k_D = -u p_r f \quad (21.11)$$

yielding the second term on the rhs of Eq. 21.8.

The probability distribution of subthreshold membrane potentials, $P(V, t)$, can be modeled as a drift-diffusion equation [26]. This can be done under the assumption that the correlations between fluctuating parts of the synaptic inputs can be neglected, as shown by Brunel [26]. The drift, with velocity $v_d(u, f, V)$, results

from the net change in potential due to synaptic inputs minus the leak. Diffusion $D(u, f)$ arises because synaptic inputs occur with Poisson-like, rather than uniform, timing. The Fokker–Planck equation for the probability density of V is

$$\frac{\partial P(V, t)}{\partial t} = D(u, f) \frac{\partial^2 P(V, t)}{\partial V^2} - \frac{\partial [v_d(u, f, V)P(V, t)]}{\partial V}, \quad (21.12)$$

$$D(u, f) = \frac{1}{2}(V_e^2 f_e + n_s u^2 V_{in}^2 f), \quad (21.13)$$

$$v_d(u, f, V) = V_e f_e + n_s u V_{in} f - \frac{V - V_r}{RC} \quad (21.14)$$

where $V_e = w_e \tau_s / C$ and $V_{in} = p_r n_r w_{in} \tau_s / C$ are, respectively, the mean changes in membrane potential resulting from a single external and internal input event.

The output firing rate is the probability current that passes through threshold:

$$f(t) = -D(u, f) \frac{\partial P(\theta, t)}{\partial V}. \quad (21.15)$$

To analyze the fixed points of the dynamical system, the time derivative of f can be calculated by numerically evolving the Fokker–Planck equation and used in conjunction with the time derivative of u , see Eq. 21.8.

21.2.2

Numerical Evolution of the Fokker–Planck Equation

Resetting of the voltage after firing is implemented by boundary conditions that reinsert the probability current through threshold at the resting potential after a refractory period τ_{rp} :

$$-D(u, f) \frac{\partial P(\theta, t)}{\partial V} = -D(u, f) \frac{\partial P(V_r, t + \tau_{rp})}{\partial V} + v_d(u, f, V_r)P(V_r, t + \tau_{rp}) \quad (21.16)$$

$$P(\theta, t) = 0. \quad (21.17)$$

An initial distribution satisfying the following conditions is first defined:

$$\int_{V_r}^{\theta} P(V)dV = 1 \quad (21.18)$$

$$P(\theta) = 0 \quad (21.19)$$

$$f(0) = -D(u, f) \frac{\partial P(\theta, 0)}{\partial V}. \quad (21.20)$$

This initial distribution is taken to be a second-order polynomial

$$P(V) = aV^2 + bV + c. \quad (21.21)$$

It is convenient to consider the membrane potential relative to the resting potential.

$$\theta_1 = \theta - V_r \quad (21.22)$$

The conditions yield the following system of equations for the coefficients of the polynomial:

$$\frac{a\theta_1^3}{3} + \frac{b\theta_1^2}{2} + c\theta_1 = 1, \quad (21.23)$$

$$a\theta_1^2 + b\theta_1 + c = 0, \quad (21.24)$$

$$2a\theta_1 + b = -\frac{f}{D(u,f)}. \quad (21.25)$$

Solving the system for the coefficients yields

$$a = \frac{3}{\theta_1^3} - \frac{3f}{2D(u,f)\theta_1}, \quad (21.26)$$

$$b = \frac{2f}{D(u,f)} - \frac{6}{\theta_1^2}, \quad (21.27)$$

$$c = \frac{3}{\theta_1} - \frac{f\theta_1}{2D(u,f)}. \quad (21.28)$$

The initial distribution is then evolved according to the partial differential equation (PDE) given by Eqs. (21.12) and (21.14) and the boundary conditions given by Eqs. (21.16) and (21.17), holding u and f constant. This yields a stationary distribution with a stationary firing rate. Thus we refer to the initial imposed firing rate $f(0)$ as f_{input} and the stationary firing rate as f_{stat} . The value of f_{stat} as a function of f_{input} is bijective; therefore, a stationary membrane potential distribution can be obtained for any desired stationary firing rate. f as a function of f can be obtained by evolving the stationary distribution where we use the stationary firing rate as the input firing rate to obtain a self-consistent solution.

At fixed points, $f_{\text{stat}} = f^*$ (since $f = 0$). From Eqs. (21.13) and (21.15), we have

$$f_{\text{stat}} = f^* = -D(u^*, f^*) \frac{\partial P(\theta, \infty)}{\partial V} = -\frac{1}{2}(V_e^2 f_e + n_s u^{*2} V_{\text{in}}^2 f^*) \frac{\partial P(\theta, \infty)}{\partial V}. \quad (21.29)$$

21.2.3

Fixed-Point Analysis

For typical parameter values of cortical neurons [27, 28], the system has two stable fixed points, a quiescent down-state with maximal synaptic utility and an up-state with depressed synaptic utility, separated by a saddle node that sends trajectories to either stable state along the unstable manifold. This is shown in Figure 21.1a.

Networks with weak synapses (small w_{in}) exhibit only a quiescent down-state ($f \approx 0$ spikes/s). An unstable up-state and a saddle node emerge with slightly stronger synapses; with even stronger synapses, the up-state becomes stable. Increasing w_{in} further decreases the firing rate of the saddle node, thereby constricting the basin of attraction for the down-state and making the up-state the dominant feature. When vesicle replenishment is fast (short τ_r), the up-state firing rate is high. As replenishment becomes slower, the up-state firing rate decreases, then the up-state becomes unstable and ultimately collides with the saddle node at a saddle node

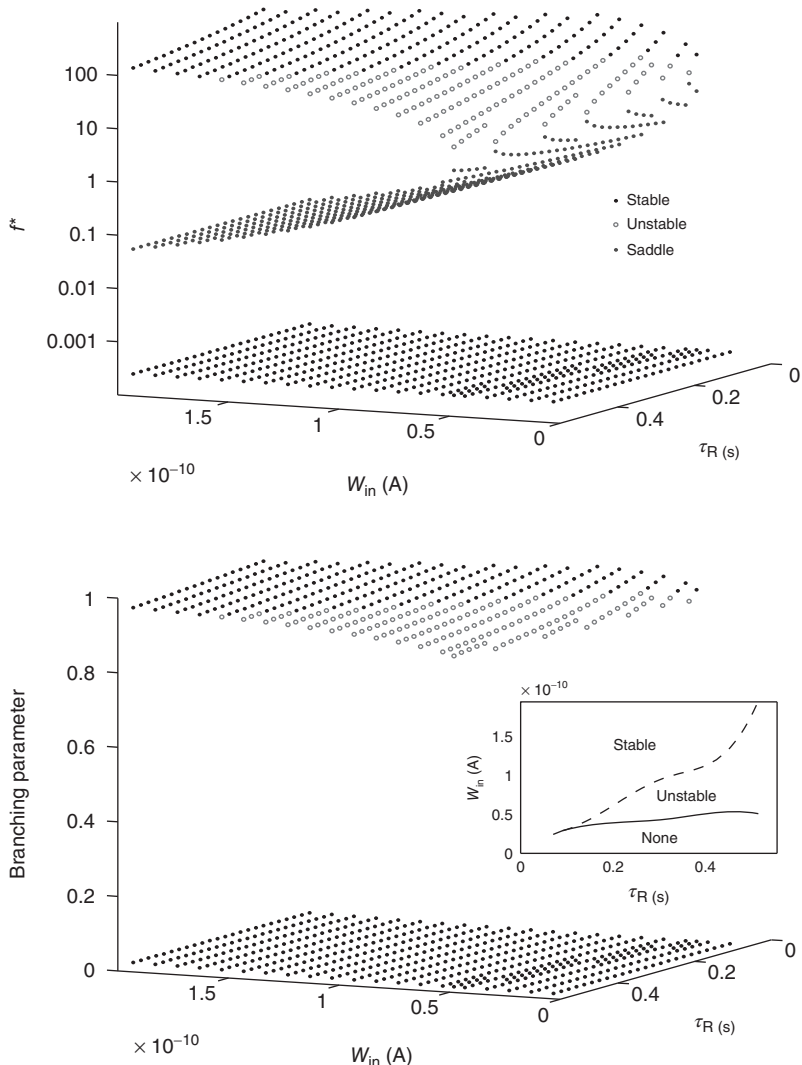


Figure 21.1 Bifurcations of mean-field approximation predict critical up-states and subcritical down-states. (a) Stable fixed points are shown as black, unstable fixed points as hollow dots, and saddle nodes as gray dots. Quiescent stable down-states are ubiquitous in the parameter region shown. When synapses are sufficiently strong and vesicle recovery is sufficiently fast, a stable or unstable high-activity up-state attractor emerges, as well as a saddle node at

an intermediate firing rate. (b) Analytical solution for the branching parameter of up- and down-states. Down-states are subcritical with a branching parameter near zero, while the up-states are critical with a branching parameter near unity. Inset: Two-dimensional view of different regions of up-state stability. Parameters: $R = 2/3 \times 10^9 \Omega$, $C = 3 \times 10^{-11} F$, $V_r = -70 \text{ mV}$, $\theta = -50 \text{ mV}$, $w_e = 95 \text{ pA}$, $f_e = 5 \text{ Hz}$, $\tau_s = 5 \text{ ms}$, $\tau_{rp} = 1 \text{ ms}$, $n_r = 6$, $n_s = 7.5$, $p_r = 0.25$.

bifurcation. Beyond the bifurcation, networks do not recover from STSD rapidly enough to sustain up-states.

The branching parameter, that is, the average number of neurons that one neuron is able to activate during an avalanche, is equal to the probability that a postsynaptic neuron's membrane potential will cross threshold due to one input times the number of postsynaptic neurons to which a neuron connects. Since the influence of any given synapse on a cortical neuron is small, the integral can be approximated by the slope near threshold.

$$\sigma = n_s \int_{\theta-\epsilon}^{\theta} P(V, \infty) dV \approx -\frac{n_s \epsilon^2}{2} \frac{\partial P(\theta, \infty)}{\partial V} \quad (21.30)$$

where $\epsilon := uV_{\text{in}} \ll (\theta - V_r)$ is the strength of a synapse. This can be expressed in terms of the firing rate at stable states f^* by solving for $\frac{\partial P(\theta, \infty)}{\partial V}$ in Eq. 21.29, using the expression for the u -nullcline u^* (in terms of f^*) obtained after setting the left hand side of Eq. 21.8 to zero and substituting in Eq. 21.30 to obtain

$$\sigma = \frac{n_s V_{\text{in}}^2 f^*}{V_e^2 f_e (1 + p_r \tau_R f^*)^2 + n_s V_{\text{in}}^2 f^*}. \quad (21.31)$$

The analytical solution shows that (quiescent) down-states are subcritical, while (active) up-states are critical (Figure 21.1b). In down-states, external input dominates the total synaptic input and the branching parameter approaches zero, indicative of subcritical networks. In up-states, input from other neurons within the network dominates synaptic input, the branching parameter approaches unity, and the network is critical.

21.3 Simulations

Networks of neurons described in Eqs. 21.5–21.7 were based on a generalized linear LIF model [29] and implemented in an event-driven simulator that is exact to machine precision [30]. Importantly, all computations in this simulation preserve causality, making it possible to trace back the unique spiking event that results in the initiation of an avalanche.

21.3.1 Up- and Down-States

The networks spontaneously alternate between two distinct levels of firing corresponding to up- and down-states (Figure 21.2a). The mean-field approximation models the synaptic inputs that contribute to diffusion and drift as instantaneous steps in the membrane potential. To test whether the mean-field approximation and simulation results converge when synaptic inputs approach steps in the membrane potential, the integration time of the excitatory AMPA currents was decreased to 0.5 ms. In this case, up- and down-state behavior is obtained, but the up-states

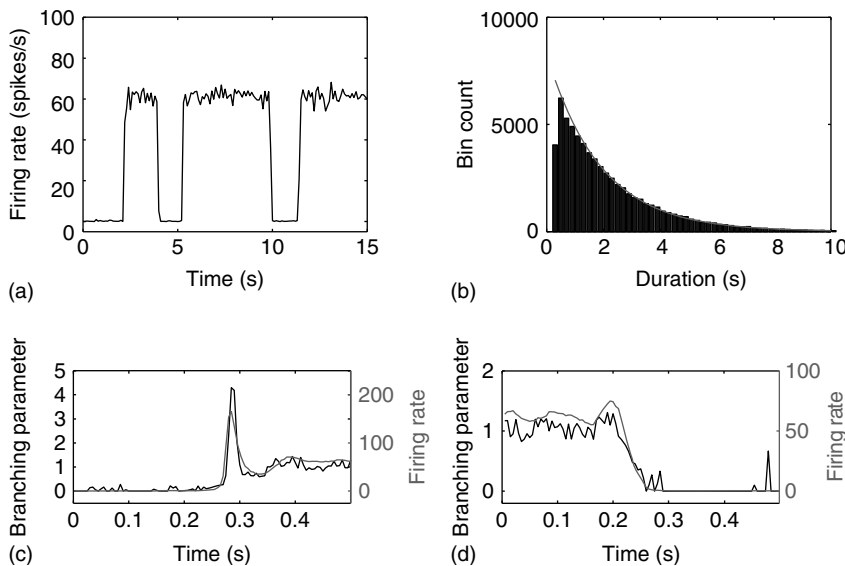


Figure 21.2 Simulated networks exhibit up- and down-state behavior. (a) Networks spontaneously alternate between a quiescent spiking (down-state) and ~ 65 spikes/s (up-state). (b) The up-state duration distribution is fitted well by an exponential (dashed line, $\tau = 1.9$ s). (c) At down-to-up transitions, the branching parameter (solid line)

increases from zero and overshoots unity before settling near unity; the firing rate (dashed line) likewise overshoots. (d) The branching parameter and firing rate decay toward zero at up-to-down transitions. Same parameters as in Figure 21.1, $\tau_R = 100$ ms, $w_{in} = 50$ pA; networks of 300 neurons.

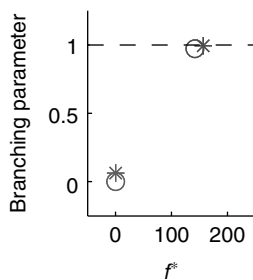


Figure 21.3 Fast excitatory currents approximate instantaneous steps in membrane potential. Firing rate and branching parameter of up- and down-states are in close agreement between mean-field approximation (circles) and simulated networks (stars). Parameters: $R = \frac{1}{1.5 \times 10^{-9}} \Omega$, $C = 3 \times 10^{-11} F$, $V_r = -70$ mV, $\theta = -50$ mV, $w_{in} = 60$ pA, $w_e = 50$ pA, $f_e = 5$ Hz, $\tau_s = 0.5$ ms, $\tau_{rp} = 1$ ms, $\tau_R = 100$ ms, $n_r = 6$, $n_s = 7.5$, $p_r = 0.25$.

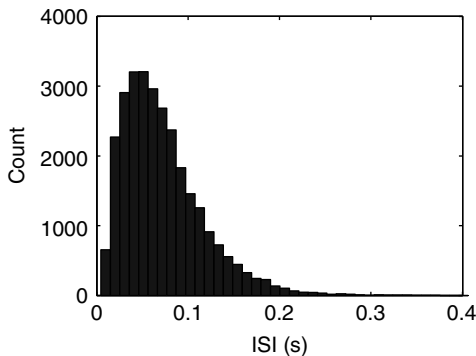


Figure 21.4 Histogram of interspike intervals during the up-state.

persist only for tens of milliseconds. Nonetheless, the up-state branching parameter is near unity, the down-state branching parameter is near zero, and the firing rates are in close agreement between simulations and the mean-field approximation, shown in Figure 21.3. Exponential synaptic currents were also modeled with a view to increasing biological realism. Consistent with findings in cortex [31], up- and down-states that persist for simulated seconds are obtained. In agreement with previous findings [2, 23], up-state durations are exponentially distributed (Figure 21.2b). The interspike interval (ISI) distribution during up-states is not exponential (Figure 21.4), leading to the conclusion that spiking during the up-state is not Poisson-distributed.

21.3.1.1 Up-/Down-State Transitions

The branching parameter follows the firing rate at state transitions. At down-to-up transitions, the branching parameter increases from zero and overshoots unity as activity spreads before finally settling near unity, Figure 21.2c. At up-to-down transitions, the branching parameter decays with the firing rate toward zero, Figure 21.2d.

These transitions can be understood as follows. In the down-state the average synaptic weight (a constant multiple of synaptic utility, u) is near-maximal (Figure 21.5a) while the average synaptic current is near zero, due to near zero firing rate. Conversely, in the up state, the synaptic utility (and hence the average synaptic weight) is low and the firing rate is high (Figure 21.5b). The external inputs have a Poisson distribution, thus having an exponential distribution of the interval between events (Figure 21.6). When external inputs, by chance, sum up to create a large enough event, with strong synaptic weights and large synaptic currents, the system moves for a very brief time in a supercritical regime, which can be observed in Figure 21.2c, as the branching parameter reaches 4 for a very short period. During this supercritical period, the firing rate is very high, resulting in a subsequent decrease in synaptic weight. In these simulations, after a damped oscillation, the system stabilizes in a new regime, the up-state, in which the synapses are weak, but neurons receive, on average, a large synaptic current because of the large stationary firing rate. Thus, external inputs have a larger probability of causing their target neurons to fire than in the down-state, leading

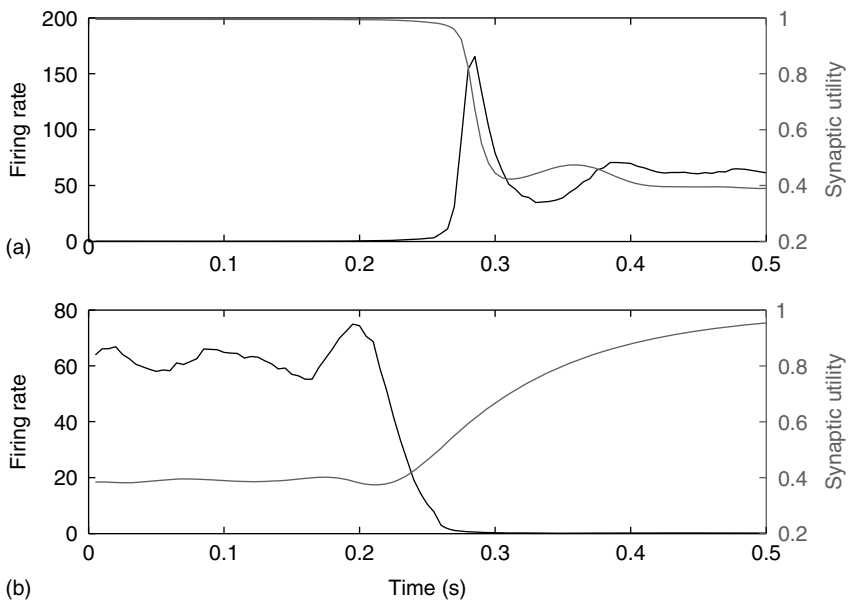


Figure 21.5 Synaptic utility (gray line) and firing rate (black line) during up-/down-state transitions. (a) At down-/up-state transitions, the synaptic utility is high initially,

but decreases upon transition to an up-state. (b) At up-/down-state transitions, the synaptic utility is partially depressed initially, but recovers upon transition to a down-state.

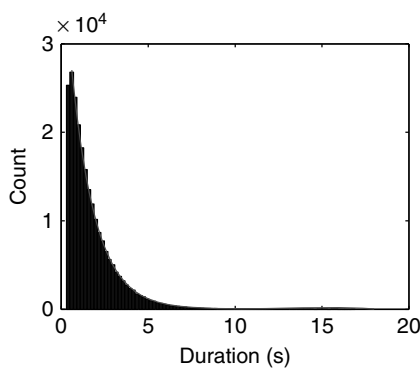


Figure 21.6 The distribution of the duration of down-states. The distribution is fitted well by an exponential with time constant $\tau = 1.4$ s.

to a high rate of avalanches. Each neuron has a probability of almost 1 to cause another neuron to fire (Figure 21.2c), driving the system to criticality. As shown in both the analytical solution and the simulation, the up-state is stable to small perturbations, as a small decrease in the firing rate would cause a compensatory increase in the synaptic weight, and vice versa. However, larger perturbations have the capacity to cause the system to switch to the down-state. An exact prediction of the frequency of the perturbations in the up-state is quite difficult, but it likely

does not deviate much from Poisson, as the distribution of the up-state length is well fitted by an exponential (Figure 21.2b).

21.3.2

Up-States are Critical; Down-States are Subcritical

Each up- or down-state is composed of hundreds or thousands of avalanches. Avalanche size and lifetime distributions in the up-state follow power laws with critical exponents near -1.5 and -2.0 (Figure 21.7a,b; maximum likelihood estimators: -1.50 and -2.03). Avalanche distributions in the down-state drop off rapidly such

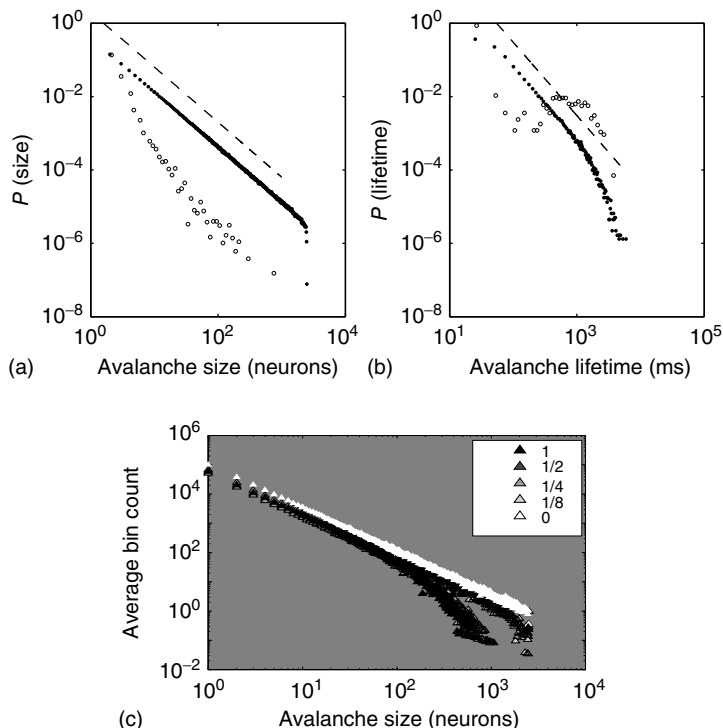


Figure 21.7 Up-states are critical, down-states are subcritical. (a) The frequency distribution of avalanche size (number of neurons) in the up-state (solid dots) follows a power law with slope -1.5 (dashed line), indicative of critical networks. In the down-state (hollow dots), the distribution is not linear and few avalanches of size > 10 occur, indicative of subcritical networks. (b) Similarly, the distribution of avalanche lifetimes follows a power law with slope -2.0 (dashed line) in the up-state but not the down-state.

Same model parameters as Figure 21.2; networks of 2500 neurons. (c) Avalanche size distributions for networks with AMPA and NMDA excitatory currents and different amplitudes of inhibitory currents. The amplitude of inhibitory to excitatory synapses (ω_{ItoE}) is given in the legend as a fraction of the excitatory current amplitude. At the highest levels of inhibition, power laws begin to break down near system size. See text for model details.

that few avalanches of size >10 occur. The method described by Clauset *et al.* [32] was used to statistically validate criticality. In brief, the maximum likelihood estimators are found under the assumption that avalanche distributions either follow a power law or an exponential. Random power law and exponential distributions are then generated given the maximum likelihood estimators to determine by bootstrap the probability of obtaining a Kolmogorov–Smirnov (KS) distance at least as great as the sample. In all cases, we fail to reject the null hypothesis that avalanche distributions are power-law-distributed (KS-test *p*-values: 0.46 and 0.29 for avalanche size and lifetime, respectively), but we do reject the null hypothesis that the distributions are exponentially distributed (*p* < 0.01 for avalanche size and lifetime).

21.3.3

More Biologically Realistic Networks

The networks can be made more biologically realistic by introducing small-world connectivity, glutamatergic synapses of the NMDA type, and inhibitory currents. While NMDA alone fails to reduce up-state firing rates to biological values, adding inhibition reduces the rates markedly (purely excitatory: 64.0 spikes/s; 1I:8E: 35.6 spikes/s; 1I:4E: 8.7 spikes/s; 1I:2E: 8.7 spikes/s; 1I:1E: 8.4 spikes/s). In all these conditions, up-states are critical and down-states are subcritical, except for the highest levels of inhibition in which the power law in avalanche size distribution begins to break down well before the system size. The models are described in greater detail below.

21.3.3.1 Small-World Connectivity

In networks with small-world connectivity, presynaptic neurons form most synapses with neighboring neurons, and a non-negligible number of connections are made with distant neurons. Figure 21.8 illustrates the connection matrix used to build such networks. The neuronal network is defined as a two-dimensional sheet of neurons. The matrix defines the probability of a synapse forming between any neuron and the neurons around it. The matrix is centered on the presynaptic neuron; note that there is zero probability of the presynaptic neuron forming a connection with itself. There is a 30% probability that the presynaptic neuron will form a connection with any one of the 8 immediately adjacent neuron, a 20% probability for any of the 16 neurons two spaces away, a 10% probability for any of the 24 neurons three spaces away, and a 1% probability for more distant neurons. This type of organization is intended to mimic that of cortical neurons.

Networks with small-world connectivity exhibit critical up-states and subcritical down-states (Figure 21.9). Different combinations of recovery time and synaptic strength were used; stronger synapses were used to balance longer recovery times. Parameters: $R = 2/3 \times 10^9 \Omega$, $C = 3 \times 10^{-11} F$, $V_r = -70$ mV, $\theta = -50$ mV, $w_e = 80$ pA, $f_e = 5$ Hz, $\tau_s = 5$ ms, $\tau_{tp} = 1$ ms, $n_r = 6$, $n_s = 8.38$, $p_r = 0.15$.

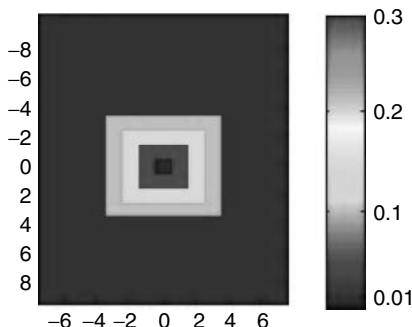


Figure 21.8 Connection matrix for small-world topology.

21.3.3.2 NMDA and Inhibition

In the model with NMDA, each synapse is composed of a 20 AMPA:3 NMDA ratio of channels [33]. The pool of NMDA channels include both NR2A (integration time of 150 ms) and NR2B (integration time of 500 ms) in 3 NR2A:1 NR2B ratio. AMPAR (α -amino-3-hydroxy-5-methyl-4-isoxazolepropionic receptor) channels have a conductance of 7.2 pS [34] and NMDAR (*N*-methyl-D-aspartate receptor) channels have a conductance of 45 pS [35], an approximate 1:6 ratio in conductance. If all channels are open, this yields a 10 AMPA: 9 NMDA ratio of total conductance. In addition, there is a voltage-dependent magnesium block of NMDAR channels. The proportion of open NMDA channels ranges from 3% to 10% and is given by the following function [36]:

$$B(V) = \left\{ 1 + \frac{e^{-0.062V[\text{Mg}^{2+}]}}{3.57} \right\}^{-1} \quad (21.32)$$

where V is in millivolts and $[\text{Mg}^{2+}]$ is in millimolars (typical value: 1.5 mM).

Since an event-driven simulator is used, conductance-based models cannot be used directly. Instead, the NMDA voltage-dependent conductance is approximated in a current-based model by multiplying the amplitude of the NMDA current by the factor $B(V)$. This factor is updated at each event the neuron experiences (synaptic input or action potential). The simulated networks remain critical in the up-state and subcritical in the down-state with the introduction of NMDA (Figure 21.7c; white triangles).

Inhibition is incorporated in the model by adding 625 inhibitory neurons to the network of 2500 excitatory neurons with AMPA and NMDA channels. Each excitatory neuron sends connections to eight other random excitatory neurons. Inhibitory neurons receive connections from eight random excitatory neurons and send back eight random inhibitory connections. Inhibitory neurons send recurrent connections to eight other random inhibitory neurons. Upon firing, inhibitory neurons induce an exponential current given by Eq. 21.4 in the postsynaptic neuron. Inhibitory (GABAergic) currents have a synaptic time constant of 25 ms, and their amplitude is varied from zero to the same level as excitatory currents. Only excitatory synapses undergo STSD. At the highest levels of inhibition, the

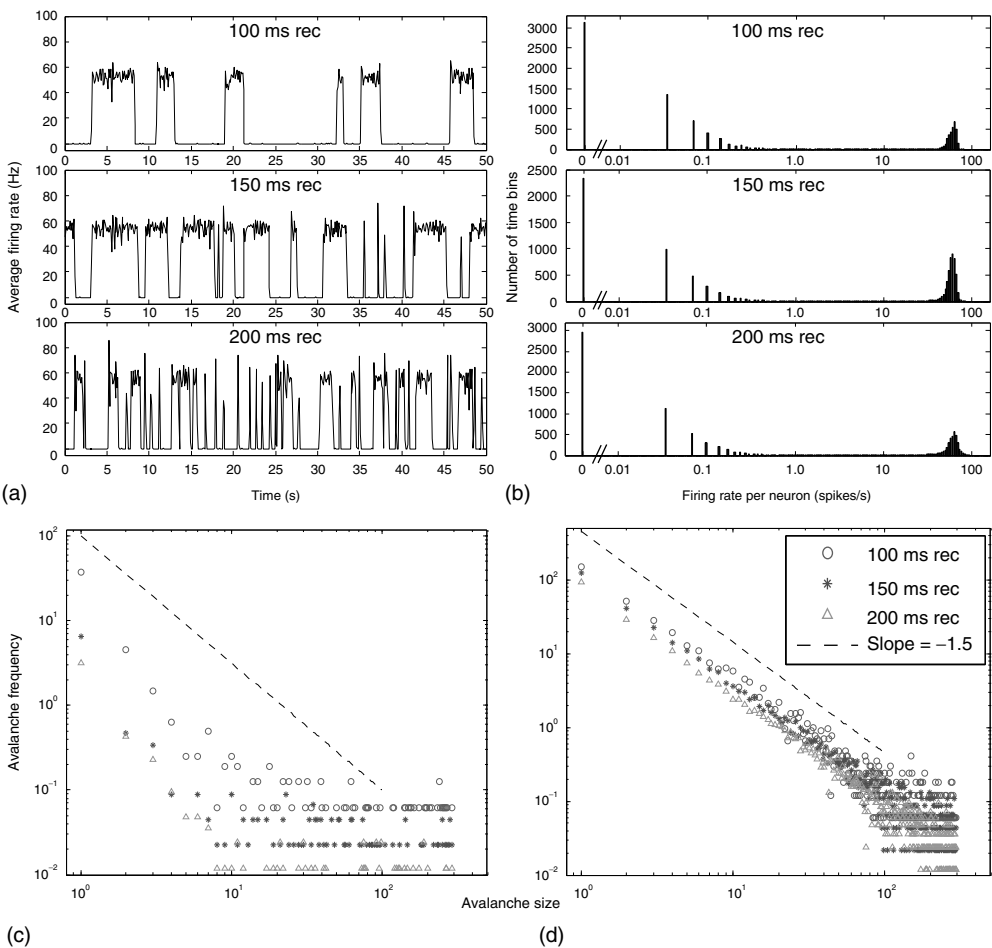


Figure 21.9 Simulation results for small-world networks. Networks with short-term synaptic depression alternate between subcritical down-states and critical up-states for different choices of recovery time and synaptic strength. In all panels, results for three parameter sets are shown, with time constants τ_r of 100, 150, and 200 ms, and input W_{in} of 6.5×10^{-11} , 7.45×10^{-11} , and 9.1×10^{-11} A. (a) Sample traces of average firing rates in networks with recovery of synaptic vesicles; results for listed parameter sets from top to bottom. (b) Histograms of firing rates by time bin for all trials. In all cases, most time is spent in a down-state

(< 1 Hz) or an up-state (50–60 Hz). The left-most firing rate in the down-state corresponds to 0 spikes per 100 ms time bin; successive firing rates correspond to additional spikes in a time bin. (c) Avalanche distributions in the down-state; they are indicative of subcritical networks. Distributions are not linear and few avalanches of size > 10 occur. The lowest avalanche frequency for networks with each recovery time constant corresponds to one occurrence. (d) Avalanche distributions in the up-state. Network behavior is critical, and power laws show critical exponent near -1.5 .

avalanche size distribution begins to deviate from a power law only near system size (Figure 21.7c). Parameters are $R = \frac{1}{1.5 \times 10^{-9}} \Omega$, $C = 3 \times 10^{-11}$ F, $V_r = -70$ mV, $\theta = -50$ mV, $w_e = 140$ pA, $f_e = 5$ Hz, $\tau_{rp} = 1$ ms, $n_r = 6$, $p_r = 0.25$, $\tau_R = 100$ ms, $w_{EtoE} = w_{ItoI} = w_{Etol} = 80$ pA.

21.3.4

Robustness of Results

Variation of crucial model parameters allows us to inspect the robustness of the results obtained thus far. Whereas the up-state firing rates change only slightly with changes in w_{in} and τ_R (Figure 21.10a), the up-state durations vary widely (Figure 21.10b). In all cases, the branching parameter remains near unity in the up-state and near zero in the down-state (Figure 21.10c), and the up-state critical exponent near -1.5 (Figure 21.10d).

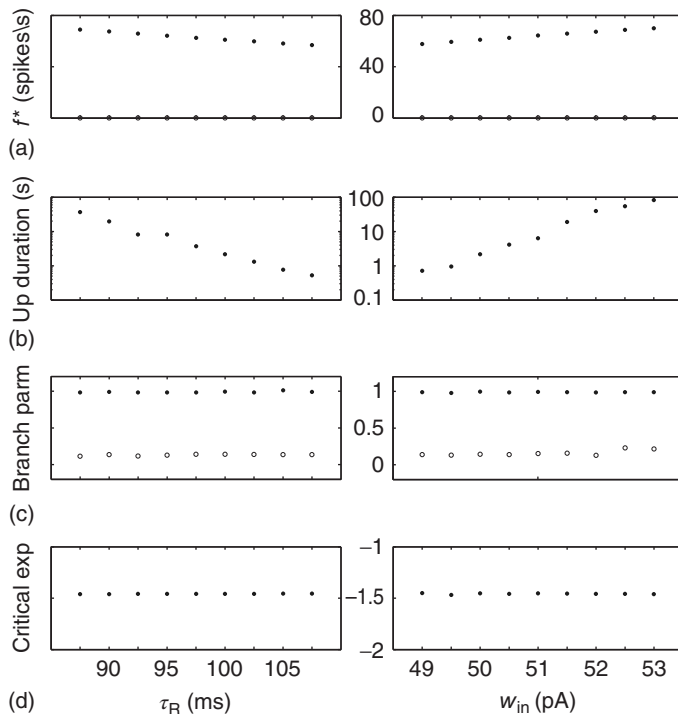


Figure 21.10 Criticality of up-states and subcriticality of down-states are robust to variations of crucial model parameters. (a) Up-state (solid dots) firing rates change slightly as τ_r and w_{in} are changed; down-states (hollow dots) remain quiescent. (b)

Up-state durations vary widely with changes in these parameters. (c) Up- and down-state branching parameters remain near unity and zero, respectively, over these parameter regions. (d) The up-state avalanche size critical exponent remains near -1.5 .

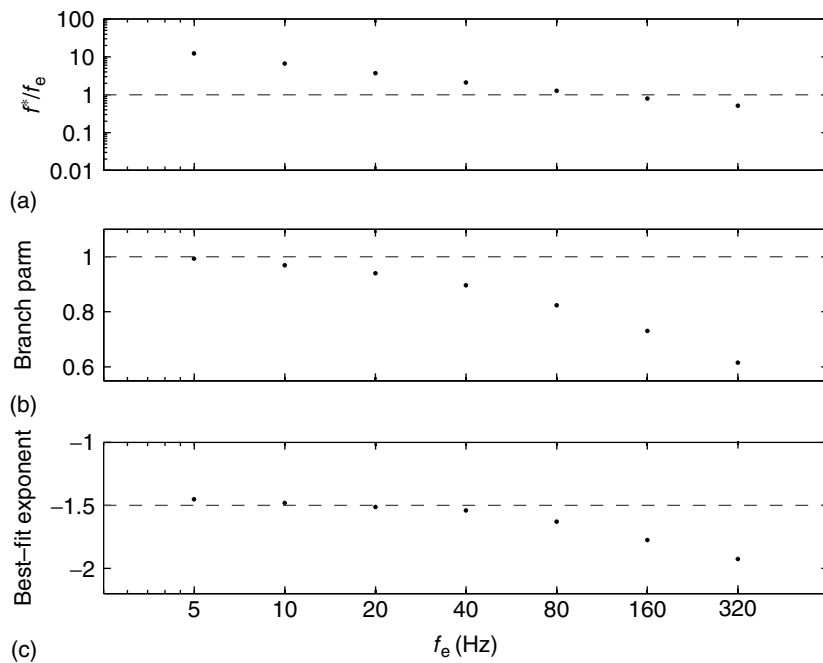


Figure 21.11 Persistent up-states become subcritical with high external input rates. The ratio of stationary firing rate to external input rate (a) as does the branching parameter (b) and best fit power law to the avalanche size distribution (c). Same parameters as in Figure 21.2.

The analytical solution for the branching parameter, given by Eq. 21.31, predicts that networks become subcritical as the external input frequency is increased. Moreover, the system undergoes a saddle-node bifurcation in which the down-state and saddle node collide, leaving only a stable up-state attractor. Figure 21.11 shows how the critical behavior varies during these persistent up-states as a function of the external input rate. As the external input rate is increased, the stationary firing rate does not increase proportionally (Figure 21.11a). In accordance with the mean-field prediction, the branching parameter decreases from unity (Figure 21.11b), while the avalanche size distribution becomes steeper (Figure 21.11c) and no longer follows a power law.

Additionally, the robustness of SOC behavior to voltage-dependent membrane resistance can also be investigated. In biological neuronal networks, a neuron's membrane resistance is dependent on its voltage. A voltage-dependent membrane resistance was implemented that resulted in a membrane time constant ($\tau_m = RC$) of 20 ms at rest and 10 ms at threshold, and varying linearly in between. Up-states are critical and down-states are subcritical even with voltage-dependent membrane resistance, as shown in Figure 21.12.

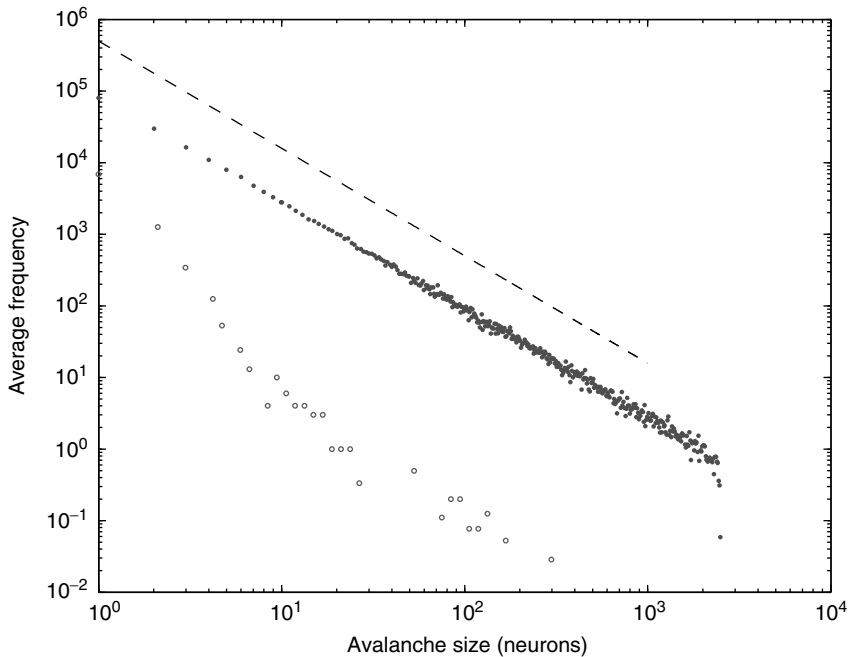


Figure 21.12 Avalanche distributions for simulated networks with voltage-dependent membrane resistance. The avalanche size distribution in the up-state (solid dots)

follows a power law with critical exponent near -1.5 (dashed line), while the distribution in the down- state (hollow dots) does not.

21.4

Heterogeneous Synapses

We have seen thus far that using a specific combination of input firing rate and average synaptic weight makes it possible for a nonconservative network to approach the critical point in the up-state very closely. The addition of STSD makes the up-state an attractor for the network dynamics. As we have seen, avalanches can effectively cause the system to shift from slightly supercritical to slightly subcritical by changing the firing rate of the up-state and the average effective synaptic weight. This causes modest changes in the relative excitability of the neurons participating in an avalanche. There are a number of biological mechanisms, in addition to STSD, that are capable of extending the range over which such excitability changes can be compensated and the system remain in, or very close to, the critical state.

21.4.1

Influence of Synaptic Weight Distributions

So far, we have made the unrealistic assumption that all synapses of a given type have identical strengths. In this section, we explore the presence of synapses that

are not necessarily identical but follow a particular distribution. Such distributions of synaptic weights provide an additional compensatory mechanism which can extend the range over which a nonconservative network becomes critical. Numerous experiments have been performed to analyze the distribution of synaptic weights [37–49]. Typically, these experiments show that the distribution of synaptic weights peaks at low amplitudes, resulting in many small-amplitude and a few large-amplitude excitatory postsynaptic potentials (EPSPs) or inhibitory postsynaptic potentials (IPSPs). Distributions have been fitted by lognormal [37], truncated Gaussian [45, 46], or highly skewed non-Gaussian [40, 42, 44, 48] distributions.

The presence of heterogeneous synapses modifies the effects of a localized increase in the firing rate. To repeat, SOC relies on an increase in excitability caused by a raised (closer to threshold) average potential which is compensated by a decrease in excitability due to a decrease in synaptic utility. To understand how heterogeneous synaptic strengths influence this balance in the recurrent networks discussed so far, we looked at a simpler system.

21.4.2

Voltage Distributions for Heterogeneous Synaptic Input

We solve the master equation for a simple network consisting of a homogeneous population of independent and identical LIF neurons with feed-forward excitation [50]. Generalizing the Fokker–Planck approach, the master equation solves for the probability $p(v, t)$ of a neuron to have a voltage v in $(-\infty, \theta)$ at time t .

$$\begin{aligned} \partial_t p(v, t) &= \partial_v(L(v)p(v, t)) - f(t)p(v, t) \\ &\quad + f(t) \int_{w_1}^{w_2} p(v - w, t)q(w)H(\theta - v + w)dw + j(v, t), \end{aligned} \quad (21.33)$$

with

$$j(v, t) = f(t) \int_{w_1}^{w_2} H(v)H(w - v)p(v + \theta - w, t)q(w)dw$$

$H(\cdot)$ is the unit step function, and θ the threshold membrane potential. $q(w)$ represents the distribution of synaptic weights, with $\int_{w_1}^{w_2} q(w)dw = 1$. w_1 and w_2 are the minimum and maximum synaptic weights, respectively. $L(v)$ represents the sum of all non-synaptic currents, which can be voltage-dependent, but not explicitly time-dependent. For the standard LIF neuron, $L(v) = -v/\tau_m$, where τ_m is the membrane time constant.

In Eq. (21.33), the first term on the rhs represents the drift due to non-synaptic currents. The second term removes the probability for neurons receiving a synaptic input while at potential v . The third term adds the probability that a neuron a distance w away in potential receives a synaptic input that changes its potential to v . The last term $j(v, t)$ represents a *probability* current injection of the neuron that previously spiked. It includes the effect of any excess synaptic input above the threshold.

The output firing rate is given by

$$f_{\text{out}}(t) = \int_{-\infty}^{\theta} j(v, t) dv \quad (21.34)$$

The stationary solution of Eq. (21.33) can be obtained as the solution to the following equation:

$$\begin{aligned} \frac{1}{f} \frac{d(L(v)p_s(v))}{dv} &= p_s(v) \\ &- \int_{w_1}^{w_2} p_s(v-w)q(w)H(\theta-v+w)dw \\ &- \int_{w_1}^{w_2} H(v)H(w-v)p_s(v+\theta-w)q(w)dw \end{aligned} \quad (21.35)$$

where $p_s(v)$ is the stationary probability distribution for the membrane potential.

Starting with a stationary state $p_s(v)$ obtained as the solution to Eq. 21.35, with input event rate $f(t)$, the response of the population to fluctuations in input can be quantified by defining

$$\mathcal{R}_\lambda = \int_0^\theta dv \int_\theta^\infty p_s(v-w)q_p^\lambda(w)dw \quad (21.36)$$

where $q_p(w)$ is related to the synaptic weight distribution $q(w)$ by

$$q_p^\eta(w) = \sum_{k=0}^{\infty} \text{Pois}(k; \eta) q(w)^{(*k)}. \quad (21.37)$$

Here, $*$ represents a convolution. $\text{Pois}(k; \eta) = \frac{\eta^k}{k!} e^{-\eta}$ represents a Poisson process with mean η and k events occurring in a time step. By definition, $q(w)^{(*0)} = \delta(w)$, $q(w)^{(*1)} = q(w)$, $q(w)^{(*2)} = q(w) * q(w)$, and so on. $q_p^\eta(w)$ thus represents the average depolarization of a single neuron, when each neuron in the population receives η excitatory inputs on average. If each neuron in the population receives λ additional inputs on average in the stationary state, then \mathcal{R}_λ represents the fraction of neurons that spike in the population starting from the stationary distribution $p_s(v)$. The relative excitability $\varepsilon(\lambda)$ of a neuronal population with a given synaptic weight distribution can then be defined as

$$\varepsilon(\lambda) = \left(\frac{d\mathcal{R}_\lambda}{d\lambda} \right) / \left(\frac{d\mathcal{R}_\lambda}{d\lambda} \right) |_{\lambda=0}. \quad (21.38)$$

21.4.3

Results for Realistic Synaptic Distributions in the Absence of Recurrence and STSD

We investigated the response to fluctuations for a purely feed-forward “network” of independent LIF neurons, with six different distributions of synaptic weights w between $w = 0$ and $w = \theta$: namely (i) δ -function (all synapses have the same weight; the case discussed so far), (ii) Gaussian, (iii) exponential, (iv) lognormal, (v) power

law with exponent -1 , and (vi) bimodal (a large fraction of synapses have a single small weight and the remaining have a single large weight). The distributions vary in the heaviness of their tails, that is, the fraction of synapses that have weights closer to the threshold θ . All these distributions have the same mean weight (1 mV), and all networks receive the same input firing rates (500 and 2000 Hz, see below), so that the mean input current is the same. The definitions for the different distributions are as follows:

- 1) δ -function: $q(w) = \delta(w - w_0)$ with $w_0 = 1$ mV.
- 2) Gaussian: $q(w) = N_g e^{-[(w-w_0)^2/2\sigma^2]}$ with $w_0 = 0.6579$ mV and $\sigma = 0.8155$ mV.
- 3) Exponential: $q(w) = N_e e^{(-w/w_0)}$ with $w_0 = 0.8963$ mV.
- 4) Lognormal: $q(w) = (\frac{N_l}{w}) e^{-(\ln w - w_0)^2/(2\sigma^2)}$ with $w_0 = -7.3265$ and $\sigma = 0.9075$.
- 5) Bimodal: $q(w) = a_1 \delta(w - w_1) + a_2 \delta(w - w_2)$ with $w_1 = 0.5$ mV, $w_2 = 15$ mV, $a_1 = 0.966$ and $a_2 = 0.034$.
- 6) Power law: $q(w) = N_p / (1 + ((w - w_0)/w_1))$ with $w_0 = \min(w)$ and $w_1 = 0.0102$ mV.

The variables N_x , where $x \in \{g, e, p\}$, are the normalization constants for Gaussian, exponential, and power law distributions, respectively. The corresponding zero-centered second moments are δ -function (1.0 mV 2), Gaussian (1.3 mV 2), exponential (1.8 mV 2), lognormal (2.2 mV 2), bimodal (8.0 mV 2), and power-law (8.7 mV 2).

The membrane time constant is fixed at $\tau_m = 20$ ms. The external input firing rates are chosen as 500 and 2000 Hz. For these choices, for all distributions, the network reaches an equilibrium firing rate approximately equal to that in a down-state for 500 Hz, and to an up-state for 2000 Hz.

For all the six synaptic weight distributions considered, the relative excitability initially rises in both the down-state (Figure 21.13a) and the up-state (Figure 21.14a). Classical definitions of the branching factor in a recurrent network do not apply for our system of independent neurons. But just as in the recurrent network, any fluctuation in this network that increases the average membrane potential carries the potential to produce a spike. Therefore, we use the relative excitability as shown in Figures 21.13a and 21.14a as a simple proxy for the branching factor. Relative excitability is unity for zero added synapses (by definition). In both the up- and down-states, excitability initially increases with added synapses and then decreases. This is consistent with the network becoming first supercritical and, in the cases where excitability falls below unity, it returning to a subcritical state. Note that over the range plotted, for some distributions the excitability does not return to unity or below, but that the range plotted already exceeds what can be expected in physiological situations (for the parameters chosen, activating additional 10 synapses would bring the neuron from rest to nearly the firing threshold). Also note that the decrease of relative excitability below unity for large numbers of added synapses is a compensatory mechanism that is needed to achieve SOC.

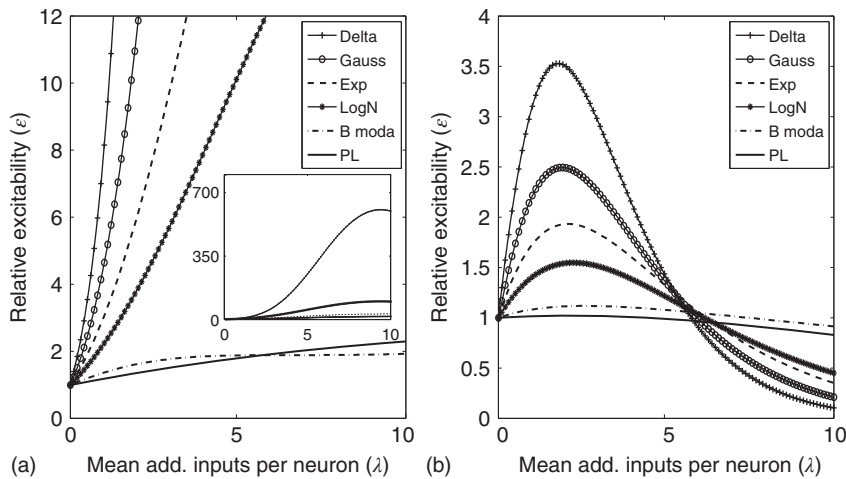


Figure 21.13 Effects of fluctuations in synaptic input due to different synaptic weight distributions in the down-state without (a) and with (b) synaptic depression, respectively. Feed-forward network with 500 Hz external Poisson input for all distributions (Delta: δ function, Gauss: Gaussian, Exp: exponential, LogN: lognormal, B moda: bimodal, PL: power law). Synaptic weight distributions are matched for mean weight = 1 mV such that drift = $0.5 \times \theta$ mV. The

relative excitability initially rises, and the rise is quickest for the distributions that are not heavy-tailed. With STSD, the relative excitability begins to decrease and eventually settles down to values that increase in order of tail-heaviness of the distributions. Note that the excitability remains relatively unchanged for the power law and bimodal distributions. The inset in (a) shows the data at a larger scale on the ordinate which allows us to see the peak of all functions.

21.4.4

Heterogeneous Synaptic Distributions in the Presence of Synaptic Depression

To push the system toward criticality, the rise in excitability can be compensated by introducing STSD. It is implemented by scaling the synaptic utility after each synaptic event, while keeping the distributions unchanged, since all synaptic weights in a distribution are depressed by the same factor. The synaptic utility does not recover and the synaptic utility after an event is decreased by a fraction p_r , which we calculate for each distribution separately, as follows. Let n^* be the number of synapses at which the relative excitability (in the absence of STSD) reaches a peak, and let ε^* be the value of this peak. To push the system toward criticality, the strength of the STSD should be such that this peak is close to unity. Therefore, the reduction of synaptic utility should be a factor of

$$p_r = \left(\frac{1}{\varepsilon^*} \right)^{1/n^*}. \quad (21.39)$$

Intuitively, this choice of p_r ensures that, after n^* extra synapses per neuron are activated on average, the relative excitability in the presence of STSD gets closer to unity.

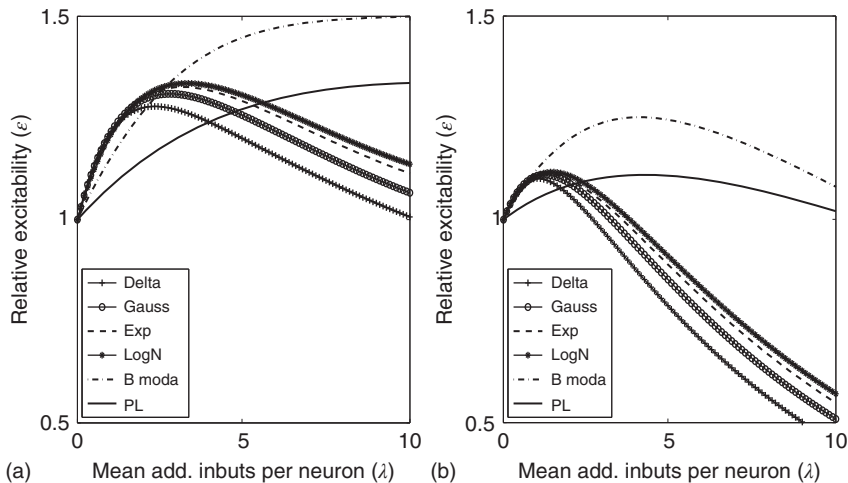


Figure 21.14 Effects of fluctuations in synaptic input due to different synaptic weight distributions in the up-state without (a) and with (b) synaptic depression, respectively. Feed-forward network with 2000 Hz external Poisson input for all distributions (see caption of Figure 21.13 for legend). Synaptic weight distributions are matched for mean weight = 1 mV such that drift $= 2 \times \theta$ mV. The relative excitability initially

rises before it starts to decrease, and the rise is fastest for the distributions that are not heavy-tailed. With STSD, the relative excitability begins to decrease even faster and eventually settles down to values that increase in order of tail-heaviness of the distributions. Note that the excitability remains relatively unchanged for the power law and bimodal distributions.

The relative excitability for the six distributions in the presence of STSD is shown for the down-state in Figure 21.13b and for the up-state in Figure 21.14b. In both states, relative excitability is unity for zero added synapses, then increases to a distribution-dependent peak, after which it falls to a value below unity. For all synaptic distributions, excitability stays closer to unity in the up-state than in the down-state, generalizing our result for the δ -function (Sections 21.2 and 21.3) to all distributions considered. The excursions from unity, both high and low, are most pronounced for the less heavy-tailed distributions. Furthermore, distributions that lack a heavy tail show much larger excursions from unity in the down-state than in the up-state, even in the presence of STSD (Figure 21.13b vs Figure 21.14b). Note that the excitability remains relatively flat around $\epsilon = 1$ for the networks that are the most influenced by extreme synaptic weights, the power law and bimodal distributions. For these distributions (only), excursions from unity are small in the down-state in the presence of STSD, indicating the possibility of critical behavior not only in the up-state but even in the down-state. In contrast, the largest excursions from unity are shown by the δ -function distribution, which was studied in Sections 21.2 and 21.3. This is the case in both up- and down-states, and both with and without STSD. The lognormal distribution which may be closest to that found in many biological systems [37, 50–55] is in between these extremes.

21.5

Conclusion

The study of complex systems is a vibrant research area and a natural avenue for understanding the behavior of highly nonlinear, densely networked structures like the nervous system. The topic of the present volume is understanding of brain states close to criticality. This state is of particular interest if it is an attractor of the network dynamics, a situation referred to as SOC. Experimental evidence discussed in this and other chapters demonstrate critical behavior in brains and other biological neuronal networks. We have also discussed theoretical work that explains SOC in networks modeled as conservative systems. In many cases, it is, however, more realistic to describe biological neurons as dissipative. We have shown in this chapter that nonconservative neuronal networks can self-organize close to a critical state. This is the case both for simplified neurons and connectivity patterns, as well as when more realism is introduced. However, the complexity of biology usually dwarfs that of the better understood physical systems. It is unlikely that the situation in biological systems is as clear-cut as that in a simulated sandpile of idealized grains. If critical behavior is needed for its efficient operation, rather than converging into an ideal state exactly at the critical point, we consider it much more likely that the biological system moves toward criticality without necessarily being pinned exactly in the critical state. It may then stay in its close vicinity, using a variety of mechanisms, some of which we have discussed here. Thus, the system behavior is better characterized as a “bag of tricks” that were acquired during long periods of evolution than by a mathematical abstraction.

Acknowledgment

This work was supported in part by Office of Naval Research, Grant N000141010278, and NIH, Grant R01EY016281.

References

1. Stern, E.A., Kincaid, A.E., and Wilson, C.J. (1997) Spontaneous subthreshold membrane potential fluctuations and action potential variability of rat corticostratial and striatal neurons *in vivo*. *J. Neurophysiol.*, **77** (4), 1697.
2. Cossart, R., Aronov, D., and Yuste, R. (2003) Attractor dynamics of network UP states in the neocortex. *Nature*, **423** (6937), 283–288.
3. Plenz, D., and Kitai, S.T. (1998) Up and down states in striatal medium spiny neurons simultaneously recorded with spontaneous activity in fast-spiking interneurons studied in cortex-striatum-substantia nigra organotypic cultures. *J. Neurosci.*, **18** (1), 266.
4. Steriade, M., Nunez, A., and Amzica, F. (1993) A novel slow (< 1 Hz) oscillation of neocortical neurons *in vivo*: depolarizing and hyperpolarizing components. *J. Neurosci.*, **13** (8), 3252.
5. Shu, Y., Hasenstaub, A., Badoual, M., Bal, T., and McCormick, D.A. (2003) Barrages of synaptic activity control the gain and sensitivity of cortical neurons. *J. Neurosci.*, **23** (32), 10–388.

6. Levina, A., Herrmann, J.M., and Geisel, T. (2007b) Dynamical synapses causing self-organized criticality in neural networks. *Nat. Phys.*, **3** (12), 857–860.
7. Levina, A., Herrmann, J.M., and Geisel, T. (2009) Phase transitions towards criticality in a neural system with adaptive interactions. *Phys. Rev. Lett.*, **102** (11), 118–110.
8. Jensen, H.J. (1998) *Self-Organized Criticality: Emergent Complex Behavior in Physical and Biological Systems*, Cambridge University Press, New York.
9. Bak, P., Tang, C., and Wiesenfeld, K. (1987) Self-organized criticality: an explanation of 1/f noise. *Phys. Rev. Lett.*, **59** (4), 381–384.
10. Bak, P. (1996) *How Nature Works: The Science of Self-Organized Criticality*, Springer, New York.
11. Christensen, K. and Olami, Z. (1993) Sandpile models with and without an underlying spatial structure. *Phys. Rev. E*, **48** (5), 3361.
12. Beggs, J.M. and Plenz, D. (2003) Neuronal avalanches in neocortical circuits. *J. Neurosci.*, **23** (35), 11–167.
13. Gireesh, E.D. and Plenz, D. (2008) Neuronal avalanches organize as nested theta-and beta/gamma-oscillations during development of cortical layer 2/3. *Proc. Natl. Acad. Sci. U.S.A.*, **105** (21), 7576.
14. Petermann, T., Thiagarajan, T.C., Lebedev, M.A., Nicolelis, M.A.L., Chialvo, D.R., and Plenz, D. (2009) Spontaneous cortical activity in awake monkeys composed of neuronal avalanches. *Proc. Natl. Acad. Sci. U.S.A.*, **106** (37), 15–921.
15. Lampl, I., Reichova, I., and Ferster, D. (1999) Synchronous membrane potential fluctuations in neurons of the cat visual cortex. *Neuron*, **22**, 361–374.
16. Watson, B.O., MacLean, J.N., and Yuste, R. (2008) UP states protect ongoing cortical activity from thalamic inputs. *PLoS One*, **3** (12), e3971.
17. MacLean, J.N., Watson, B.O., Aaron, G.B., and Yuste, R. (2005) Internal dynamics determine the cortical response to thalamic stimulation. *Neuron*, **48** (5), 811–823.
18. Hahn, T.T.G., Sakmann, B., and Mehta, M.R. (2006) Phase-locking of hippocampal interneurons' membrane potential to neocortical up-down states. *Nat. Neurosci.*, **9** (11), 1359–1361.
19. Cowan, R.L. and Wilson, C.J. (1994) Spontaneous firing patterns and axonal projections of single corticostriatal neurons in the rat medial agranular cortex. *J. Neurophysiol.*, **71** (1), 17.
20. Destexhe, A., Hughes, S.W., Rudolph, M., and Crunelli, V. (2007) Are corticothalamic Up states fragments of wakefulness? *Trends Neurosci.*, **30** (7), 334–342.
21. Hsu, D. and Beggs, J.M. (2006) Neuronal avalanches and criticality: a dynamical model for homeostasis. *Neurocomputing*, **69** (10), 1134–1136.
22. Markram, H., Lübke, J., Frotscher, M., and Sakmann, B. (1997a) Regulation of synaptic efficacy by coincidence of postsynaptic APs and EPSPs. *Science*, **275**, 213–215.
23. Parga, N. and Abbott, L.F. (2007) Network model of spontaneous activity exhibiting synchronous transitions between up and down states. *Front. Neurosci.*, **1** (1), 57.
24. Holcman, D. and Tsodyks, M. (2006) The emergence of up and down states in cortical networks. *PLoS Comput. Biol.*, **2** (3), e23.
25. Millman, D., Mihalas, S., Kirkwood, A., and Niebur, E. (2010) Self-organized criticality occurs in non-conservative neuronal networks during Up states. *Nat. Phys.*, **6** (10), 801–805.
26. Brunel, N. (2000) Dynamics of sparsely connected networks of excitatory and inhibitory spiking neurons. *J. Comput. Neurosci.*, **8** (3), 183–208.
27. Südhof, T.C. (2004) The synaptic vesicle cycle. *Annu. Rev. Neurosci.*, **27**, 509.
28. Dobrunz, L.E. and Stevens, C.F. (1997) Heterogeneity of release probability, facilitation, and depletion at central synapses. *Neuron*, **18** (6), 995–1008.
29. Mihalas, S. and Niebur, E. (2009) A generalized linear integrate-and-fire neural model produces diverse spiking behavior. *Neural Comput.*, **21** (3), 704–718.

30. Mihalas, S., Dong, Y., von der Heydt, R., and Niebur, E. (2011) Event-related simulation of neural processing in complex visual scenes. *45th Annual Conference on Information Sciences and Systems IEEE-CISS-2011*, IEEE Information Theory Society, Baltimore, MD, 1–6.
31. Amzica, F. and Steriade, M. (1995) Short-and long-range neuronal synchronization of the slow (< 1 Hz) cortical oscillation. *J. Neurophysiol.*, **73** (1), 20.
32. Clauset, A., Shalizi, C.R., and Newman, M.E. (2009) Power-law distributions in empirical data. *SIAM Rev.*, **51** (4), 661–703.
33. Franks, K.M., Bartol, T.M., and Sejnowski, T.J. (2002) A Monte Carlo model reveals independent signaling at central glutamatergic synapses. *Biophys. J.*, **83** (5), 2333–2348.
34. Jonas, P. and Sakmann, B. (1992) Glutamate receptor channels in isolated patches from CA1 and CA3 pyramidal cells of rat hippocampal slices. *J. Physiol.*, **455** (1), 143–171.
35. Keller, D.X., Franks, K.M., Bartol, T.M., and Sejnowski, T.J. (2008) Calmodulin activation by calcium transients in the postsynaptic density of dendritic spines. *PLoS One*, **3** (4), e2045.
36. Jahr, C. and Stevens, C. (1990) Voltage dependence of NMDA-activated macroscopic conductances predicted by single-channel kinetics. *J. Neurosci.*, **10**, 3178–3182.
37. Song, S., Sjostrum, P., Reigl, M., Nelson, S., and Chklovskii, D. (2005) Highly nonrandom features of synaptic connectivity in local cortical circuits. *Public Lib. Sci. Biol.*, **3** (3), 507–519.
38. Sjöström, P.J., Turrigiano, G.G., and Nelson, S.B. (2001) Rate, timing, and cooperativity jointly determine cortical synaptic plasticity. *Neuron*, **32** (6), 1149–1164.
39. Mason, A., Nicoll, A., and Stratford, K. (1991) Synaptic transmission between individual neurons of the rat visual cortex *in vitro*. *J. Neurosci.*, **11**, 72–84.
40. Lefort, S., Tomm, C., Floyd Sarria, J., and Petersen, C.C. (2009) The excitatory neuronal network of the C2 barrel column in mouse primary somatosensory cortex. *Neuron*, **61** (2), 301.
41. Frick, A., Feldmeyer, D., Helmstaedter, M., and Sakmann, B. (2008) Monosynaptic connections between pairs of L5A pyramidal neurons in columns of juvenile rat somatosensory cortex. *Cereb. Cortex*, **18** (2), 397–406.
42. Markram, H., Lübke, J., Frotscher, M., Roth, A., and Sakmann, B. (1997b) Physiology and anatomy of synaptic connections between thick tufted pyramidal neurones in the developing rat neocortex. *J. Physiol.*, **500** (Pt 2), 409.
43. Sayer, R., Friedlander, M., and Redman, S. (1990) The time course and amplitude of epsps evoked at synapses between pairs of CA3/CA1 neurons in the hippocampal slice. *J. Neurosci.*, **10** (3), 826–836.
44. Feldmeyer, D., Egger, V., Lübke, J., and Sakmann, B. (1999) Reliable synaptic connections between pairs of excitatory layer 4 neurones within a single ‘barrel’ of developing rat somatosensory cortex. *J. Physiol.*, **521** (1), 169–190.
45. Isope, P. and Barbour, B. (2002) Properties of unitary granule cell Purkinje cell synapses in adult rat cerebellar slices. *J. Neurosci.*, **22** (22), 9668–9678.
46. Brunel, N., Hakim, V., Isope, P., Nadal, J.P., and Barbour, B. (2004) Optimal information storage and the distribution of synaptic weights: perceptron versus Purkinje cell. *Neuron*, **43** (5), 745–757.
47. Ikegaya, Y., Sasaki, T., Ishikawa, D., Honma, N., Tao, K., Takahashi, N., Minamisawa, G., Ujita, S., and Matsuki, N. (2013) Interpyramidal spike transmission stabilizes the sparseness of recurrent network activity. *Cereb. Cortex*, **23** (2), 293–304.
48. Miles, R. (1990) Variation in strength of inhibitory synapses in the CA3 region of guinea-pig hippocampus *in vitro*. *J. Physiol.*, **431** (1), 659–676.
49. Holmgren, C., Harkany, T., Svennenfors, B., and Zilberman, Y. (2003) Pyramidal cell communication within local networks in layer 2/3 of rat neocortex. *J. Physiol.*, **551** (1), 139–153.
50. Iyer, R., Menon, V., Buice, M., Koch, C. and Mihalas, S. (2013) The Influence of Synaptic Weight Distribution on Neuronal Population Dynamics.

- PLoS Comput Biol*, 9 (10), e1003248.
doi:10.1371/journal.pcbi.1003248.
- 51. Beyer, H., Schmidt, J., Hinrichs, O., and Schmolke, D. (1975) A statistical study of the interspike-interval distribution of cortical neurons. *Acta Biol. Med. Ger.*, 34 (3), 409.
 - 52. Burns, B. and Webb, A. (1976) The spontaneous activity of neurones in the cat's cerebral cortex. *Proc. R. Soc. London. Ser. B Biol. Sci.*, 194 (1115), 211–223.
 - 53. Webb, A. (1976a) The effects of changing levels of arousal on the spontaneous activity of cortical neurones. I. Sleep and wakefulness. *Proc. R. Soc. London. Ser. B Biol. Sci.*, 194 (1115), 225–237.
 - 54. Webb, A. (1976b) The effects of changing levels of arousal on the spontaneous activity of cortical neurones. II. Relaxation and alarm. *Proc. R. Soc. London. Ser. B Biol. Sci.*, 194 (1115), 239–251.
 - 55. Levine, M. (1991) The distribution of the intervals between neural impulses in the maintained discharges of retinal ganglion cells. *Biol. Cybern.*, 65, 459–467.
 - 56. Bershadskii, A., Dremencov, E., Fukayama, D., and Yadid, G. (2001) Probabilistic properties of neuron spiking time-series obtained *in vivo*. *Eur. Phys. J. B*, 24 (3), 409–413.

22

Self-Organized Criticality and Near-Criticality in Neural Networks

Jack D. Cowan, Jeremy Neuman, and Wim van Drongelen

We show that an array of *E*-patches will self-organize around critical points of the directed percolation phase transition and, when driven by a weak stimulus, will oscillate between UP and DOWN states, each of which generates avalanches consistent with directed percolation. The array therefore exhibits self-organized criticality (SOC) and replicates the behavior of the original sandpile model of [1]. We also show that an array of *E/I* patches will also self-organize to a weakly stable node located near the critical point of a directed percolation phase transition, so that fluctuations about the weakly stable node will also follow a power slope with a slope characteristic of directed percolation. We refer to this as self-organized near-criticality (SONC).

22.1 Introduction

Ideas about criticality in nonequilibrium dynamical systems have been around for at least 50 years or more. Criticality refers to the fact that nonlinear dynamical systems can have local equilibria that are marginally stable, so that small perturbations can drive the system away from the local equilibria toward one of several locally stable equilibria. In physical systems, such marginally stable states manifest in several ways; in particular, if the system is spatially as well as temporally organized, then long-range correlations in both space and time can occur, and the statistics of the accompanying fluctuating activity becomes non-Gaussian, and in fact is self-similar in its structure, and therefore follows a power law. Bak *et al.* [1] introduced a mechanism whereby such a dynamical system could self-organize to a marginally stable critical point, which they called *self-organized criticality*. Their paper immediately triggered an avalanche of papers on the topic, not the least of which was a connection with $1/f$ or scale-free noise. However, it was not until another paper appeared, by Gil and Sornette [2], which greatly clarified the dynamical prerequisites for achieving SOC, that a real understanding developed of the essential requirements for SOC: (i) an *order-parameter* equation for a dynamical system with a time-constant τ_o , with stable states separated by a threshold; (ii) a

control-parameter equation with a time-constant τ_c ; and (iii) a steady *driving force*. In Bak *et al.*'s classic example, the sandpile model, the order parameter is the rate of flow of sand grains down a sandpile, the control parameter is the sandpile's slope, and the driving force is a steady flow of grains of sand onto the top of the pile. Gil and Sornette showed that, if $\tau_o \ll \tau_c$, then the resulting avalanches of sand down the pile would have a scale-free distribution, whereas if $\tau_o \gg \tau_c$, then the distribution would also exhibit one or more large avalanches.

In this chapter, we analyze two neural network models. The first is in one-to-one correspondence with the Gil–Sornette SOC model, and therefore also exhibits SOC. The second is more complex and, instead of SOC, it self-organizes to a weakly stable local equilibrium near a marginally stable critical point. We therefore refer to this mechanism as *self-organized near-criticality*, or SONC.

22.1.1

Neural Network Dynamics

Consider first the mathematical representation of the dynamics of a neocortical slab comprising a single spatially homogeneous network of N excitatory neurons. Such neurons make transitions from a quiescent state q to an activated state a at the rate σ and back again to the quiescent state q at the rate α , as shown in Figure 22.1.

It is straightforward to write down a master equation describing the evolution of the probability distribution of neural activity $P_n(t)$ in such a network. We consider n active excitatory neurons, each becoming inactive at the rate α . This causes a

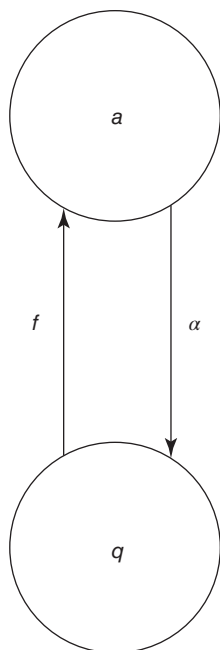


Figure 22.1 Neural state transitions. a is the activated state of a neuron, q is the inactivated or quiescent state, and α is a constant, but f depends on the number of activated neurons connected to the n th neuron and on an external stimulus h .

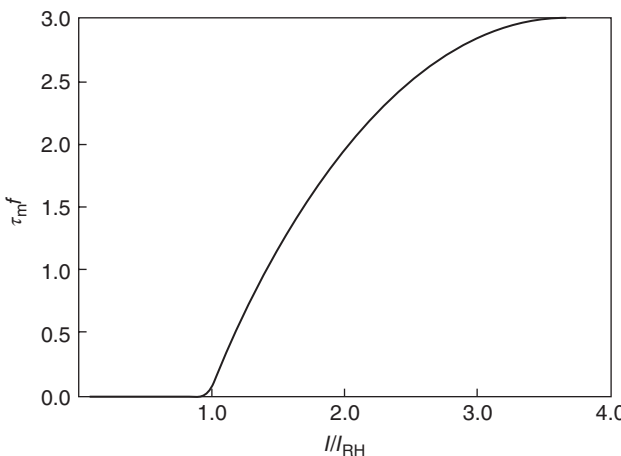


Figure 22.2 Graph of the firing rate function $f[s(l)]$. $\tau_m = 1/\alpha = 3$ is the membrane time constant (in milliseconds). $s(l) = l/l_{TH}$ is the input current, where $l_{TH} \equiv l_{RH}$ is the threshold or *rheobase* current.

flow of rate α out of the state (n) proportional to $p_n(t)$, hence a term $-\alpha n P_n(t)$. Similarly, the flow into (n) from $(n+1)$, caused by one of $n+1$ active excitatory neurons becoming inactive at rate α , gives a term $\alpha(n+1)P_{n+1}(t)$. The net effect is a contribution

$$\alpha[(n+1)P_{n+1}(t) - nP_n(t)] \quad (22.1)$$

In state (n) , there are $(N-n)$ quiescent excitatory neurons, each prepared to spike at the rate $f(s_E(n))$, leading to a term $-(N-n)f(s_E(n))P_n(t)$, where the total input is $s_E(n) = I(n)/I_{RH} = (w_{EE}n + h_E)/I_{RH}$, and $f(s_E(n))$ is the function shown in Figure 22.2.

Correspondingly, the flow into the state (n) from $(n-1)$ due to excitatory spikes is given by $(N-(n-1))f(s_E(n-1))P_{n-1}(t)$. The total contribution from excitatory spikes is then

$$(N-n+1)f(s_E(n-1))P_{n-1}(t) - (N-n)f(s_E(n))P_n(t) \quad (22.2)$$

Putting all this together, the probability $P_n(t)$ evolves according to the master equation

$$\begin{aligned} \frac{dP_n(t)}{dt} &= \alpha[(n+1)P_{n+1}(t) - nP_n(t)] \\ &\quad + [(N-n+1)f(s_E(n-1))P_{n-1}(t) - (N-n)f(s_E(n))P_n(t)] \end{aligned} \quad (22.3)$$

Using standard methods, it is easy to derive an equation for the evolution of the average number $\langle n(t) \rangle$ of active neurons in the network. The resulting equation takes the form

$$\frac{d\langle n(t) \rangle}{dt} = -\alpha\langle n(t) \rangle + (N - \langle n(t) \rangle)f(\langle s_E(n) \rangle) \quad (22.4)$$

where $\langle s_E(n) \rangle = w_{EE} \langle n \rangle + h_E$, and is the simplest form of the Wilson–Cowan equations, [3]. This mean-field equation can be obtained in several ways: in particular, it can be obtained using the van Kampen “system-size expansion” of the master equation about a locally stable equilibrium or fixed point of the dynamics, [4]. However, such an expansion breaks down at a marginally stable fixed point, which is the situation to be analyzed in this chapter, and a different method must be used to analyze such a situation.

Before proceeding further, we note that it is straightforward to extend these equations to deal with spatial effects. In such a case, the variable $n(t)/N$ is extended to $n(\mathbf{x}, t)$ which represents the *density* of active neurons at the location \mathbf{x} at time t , and the total input $s_E(n)$ becomes the current density

$$s_E(n(\mathbf{x})) = \int d^d x' w_{EE}(\mathbf{x} - \mathbf{x}') n(\mathbf{x}') + h_E(\mathbf{x}). \quad (22.5)$$

22.1.2

Stochastic Effects Near a Critical Point

To deal with the effects of fluctuations near criticality, we use the methods of statistical field theory. Essentially, we rewrite the solution of the spatial master equation in the form of a Wiener path integral. We then apply the renormalization group method [5] to calculate the statistical dynamics of the network at the marginally stable or critical points. The details of this procedure can be found in [6]. The main result is that the random fluctuations about such a critical point have the statistical signature of a certain kind of percolation process on a discrete lattice, called *directed percolation*. Such a random process is similar to isotropic percolation that occurs in the random formation of chemical bonds, except that there is a direction – in the neural network case a time direction – to the process. The statistical signature of directed percolation occurs in a large class of systems, and is independent of their various dynamical details, and is therefore taken to define a *universality class*. It is found in random contact processes, branching and annihilating random walks, predator–prey interactions in population dynamics [7], and even in bacterial colonies growing in Petri dishes [8]. Thus stochastic neural networks described by the simple Markov process we depicted in Figure 22.1 exhibit a nonequilibrium phase transition whose statistical signature is that of directed percolation [9].

In what follows, we describe how these methods and results can be used to provide insights into the nature of fluctuating neural activity found in functional magnetic resonance imaging (fMRI), electroencephalography (EEG), and local field potentials (LFPs) both in cortical slices and slabs and in the intact neocortex.

22.2

A Neural Network Exhibiting Self-Organized Criticality

We first consider a simple network comprising only excitatory neurons which exhibits SOC. We start by considering the network module shown in Figure 22.3.

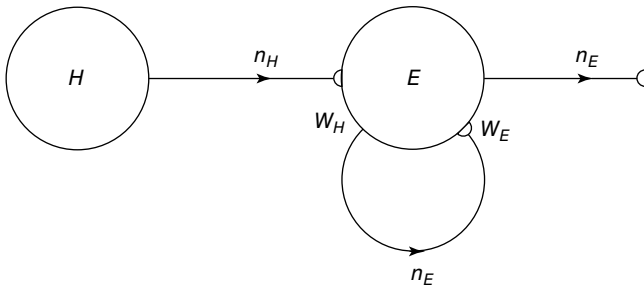


Figure 22.3 A recurrent excitatory network driven by the input H , acting through the synaptic weight w_H .

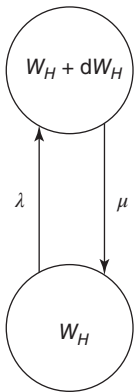


Figure 22.4 Synaptic weight transitions. Transitions from the synaptic weight w_H to $w_H + dw_H$ occur at the rate λ , and the return transition at the rate μ .

Note that this network is also spatially organized. We consider the overall system to have the geometry of a two-dimensional sheet, so that each homogeneous patch is coupled to four neighboring patches. The local dynamics of each patch is bistable. There is a stable resting state $n_E \approx 0$ for small values of n_H , and a nonzero stable state $n_E \approx 0.5 N$.

We now assume that the synaptic weight w_H is modifiable and anti-Hebbian, and makes transitions from a state w_H to a *potentiated* state $w_H + dw_H$ at the rate λ and back again (*synaptic depression*) at the rate μ , as shown in Figure 22.4

Such a Markov process satisfies the master equation

$$\begin{aligned} \frac{dP_{w_H}}{dt} = & \mu[(w_H + dw_H)P_{w_H+dw_H}(t) - w_H P_{w_H}(t)] \\ & + \lambda[(w_H - dw_H)P_{w_H-dw_H}(t) - w_H P_{w_H}(t)] \end{aligned} \quad (22.6)$$

where

$$\mu = \beta g_E \left(\frac{n_E}{w_H} + |\kappa_{H,S}| \right) n_H \quad (22.7)$$

and

$$\lambda = \beta g_E n_{E,0} n_H \quad (22.8)$$

The resulting mean-field equation takes the form

$$\frac{d\langle w_H \rangle}{dt} = \lambda - \mu \langle w_H \rangle \quad (22.9)$$

or

$$\frac{d\langle w_H \rangle}{dt} = -\beta g_E(\langle n_E \rangle - n_{E,0} + |\kappa_{H,S}| \langle w_H \rangle) \langle n_H \rangle \quad (22.10)$$

In the continuum limit, Eq. 22.10 becomes

$$\frac{d\langle w_H(x) \rangle}{dt} = -\beta g_E(x) \left(\frac{\langle n_E(x) \rangle - n_{E,0}(x)}{\rho_S} + |\kappa_{H,S}| \langle w_H(x) \rangle \right) \frac{\langle n_H(x) \rangle}{\rho_S} \quad (22.11)$$

where β is the rate constant for weight changes, ρ_S is the density of synapses at x , and g_E is the state-dependent function

$$g_E(x) \approx \frac{k(x)F'}{1/\rho - k(x)F'w_0} \quad (22.12)$$

where $F = f/(\alpha + f)$, $\langle n_{E,0}(x) \rangle$ is a constant neural activity, and $\kappa_{E,S} = L(0) < 0$ is a constant derived from the *window function* $L(\Delta t)$ of spike-time-dependent plasticity (STDP) used in [10]. The ratios $\langle n_E(x) \rangle / \rho_S$, $\langle n_{E,0}(x) \rangle / \rho_S$, and $\langle n_H(x) \rangle / \rho_S$ are zero dimensional, and represent the *mean numbers of spikes*.

In Eqs. 22.10 and 22.11, the synaptic weight $w_H(x)$ is depressed if the postsynaptic cell fires and potentiated if it does not. This is an anti-Hebbian excitatory synapse. Such an equation type was first introduced by Vogels *et al.* [10] for a purely feed-forward circuit with no loops, and a linear firing rate function f , in which the synapse was inhibitory rather than excitatory, and Hebbian rather than anti-Hebbian. The Vogels formulation has an important property: the equation can be shown to implement gradient descent to find the minimum of an energy function, the effect of which is to balance incoming excitatory and inhibitory currents to the output neuron. Equation 22.10 is an extension of the Vogels equation to the case of circuits with feedback loops, and a nonlinear firing rate function f , and incorporates modifiable synapses which are excitatory and anti-Hebbian. In fact, there is experimental evidence to support such synapses [11].

22.2.1

A Simulation of the Combined Mean-Field Equations

The combined effect of the mean-field Eqs. 22.4 and 22.10 can be easily computed. The results are shown in Figure 22.5.

It will be seen that, for low values of n_E^* , the synaptic weight w_H is potentiated until the fixed point n_E^* reaches a critical point (a *saddle-node* bifurcation), at which point the network dynamics switches to a new fixed point with a high value of n_E^* . But then the anti-Hebbian term in the w_H dynamics kicks in, and w_H depresses until n_E^* again becomes unstable at the upper critical point (another *saddle-node* bifurcation) and switches back to the lower fixed-point regime, following which the cycle starts over. This is therefore a *hysteresis* cycle, and is an exact representation of the dynamics of the sandpile model.

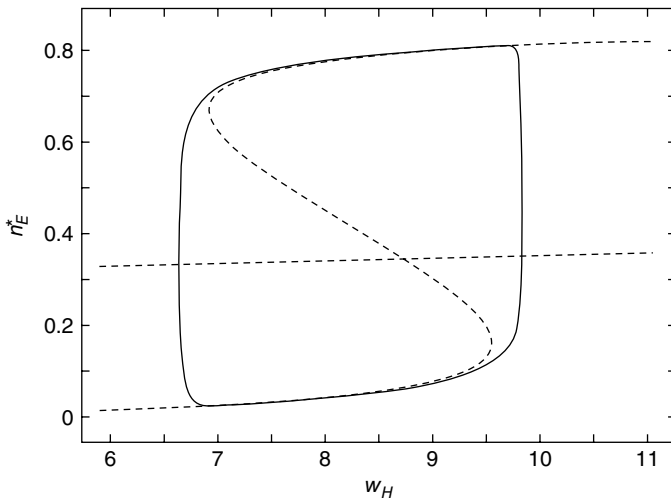


Figure 22.5 Neural state transitions between a ground state and an excited state. Parameter values: $w_E = 3$, $n_H = 3$; $\alpha = 0.2$. n_E^* is the fixed-point value of n_E , and w_H is the magnitude of the anti-Hebbian synapse in

the input path. The fast excitatory nullcline is shown as the dark grey dashed line, and the slow inhibitory nullcline as the light dashed line.

22.2.2

A Simulation of the Combined Markov Processes

The simulation above provides us with an outline of the general dynamical behavior of the coupled mean-field equations, but it provides no information about the system dynamics beyond the mean-field region. But here we can make use of the Gillespie algorithm for simulating the behavior of Markov processes in which the underlying mean-field dynamics is stable [12]. We therefore simulated the behavior of the two Markov processes introduced earlier, in which the first process describes the stochastic evolution of the firing rate n_E , driven by a weak input n_H coupled to the E -system by the modifiable anti-Hebbian weight w_H , and the second process describes the evolution of w_H driven by both the external stimulus n_H and the network variable n_E .

The network we simulated is two dimensional, and comprises 60×60 neurons with nearest neighbor connections and periodic boundary conditions, in which each neuron receives current pulses from all four nearest neighbors, and also from an external cell via the synapse w_H . The simulations are shown in Figure 22.6.

The reader is referred to [6] for all the details. However, it will be seen that the neural population behavior shown in Figure 22.6a is consistent with that shown in Figure 22.5, and the changes in w_H are also consistent with the changes shown in that figure. Figure 22.6b however, shows the burst or *avalanche-size* distribution of the underlying population spiking activity. Note that the fluctuations in spiking activity about the lower nullcline, or DOWN state, have a power law distribution

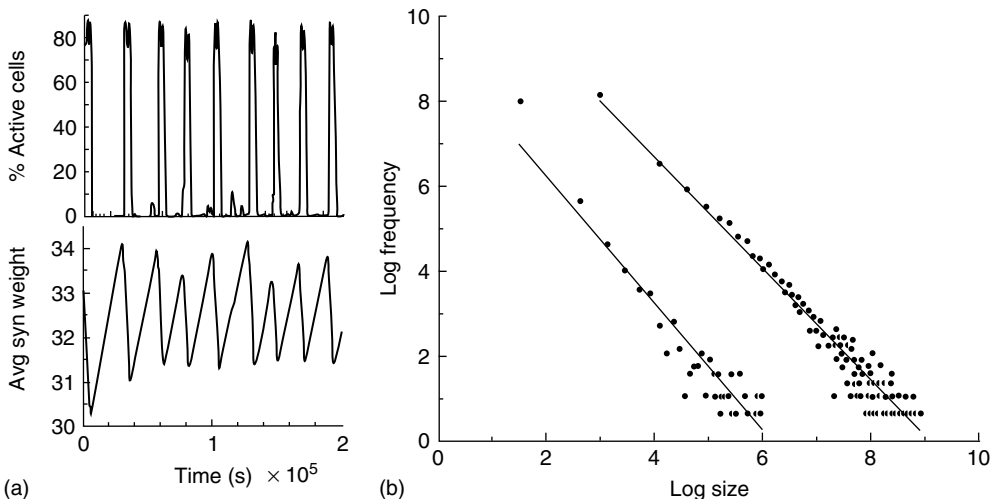


Figure 22.6 Neural state transitions between a ground state and an excited state in a two-dimensional network of 60×60 excitatory neurons with nearest neighbor connections. (a) Population activity and mean synaptic weight versus time. Activity levels display cyclic behavior with “UP”

and “DOWN” states. (b) Avalanche distribution of DOWN states (black dots) and UP states (black dots). Parameter values: $\kappa_{E,S} = 0.001$, $n_{E,0} = 0.2$, $w_E = 4$, $\alpha = 0.2$, $\beta = 0.002$, $g_E = 1$, and $I_{RH} = 1$. $f(x)$ is the function introduced in Figure 22.2.

with a slope of about -1.5 , whereas those about the higher nullcline or UP state also show a power law distribution with a slope of about -1.3 .

However, the results described above differ in certain respects from those obtained by Gil and Sornette [2]. In their simulations, they used time constants corresponding to $\alpha/\beta = 0.1$ and 100 . Both simulations produced similar power laws for small avalanche sizes, but using the larger time constant also generated isolated large system-size avalanches, 1.25 orders of magnitude greater than the smaller avalanches. In our simulations, the ratio used was $\alpha/\beta g_E = 0.2/0.002 \times 1 = 100$. The results we found are that there are two branches of power-law-distributed avalanches, corresponding to the UP and DOWN mean-field states. The UP avalanches are approximately three orders of magnitude greater than the DOWN ones.

22.3

Excitatory and Inhibitory Neural Network Dynamics

Given that about 20% of all neurons in the neocortex are inhibitory, it is important to incorporate the effects of such inhibition in changing the nature of neocortical dynamics. We therefore generalize the excitatory master equation, Eq. 22.3, to include inhibitory neurons. The result is the master equation

$$\begin{aligned}
\frac{dP(n_E, n_I, t)}{dt} = & \alpha_E[(n_E + 1) P(n_E + 1, n_I, t) - n_E P(n_E, n_I, t)] \\
& + [(N_E - n_E + 1) f_E[s_E(n_E - 1, n_I)] P(n_E - 1, n_I, t) \\
& - (N_E - n_E) f_E[s_E(n_E, n_I)] P(n_E, n_I, t)] \\
& + \alpha_I[(n_I + 1) P(n_E, n_I + 1, t) - n_I P(n_E, n_I, t)] \\
& + [(N_I - n_I + 1) f_I[s_I(n_E, n_I - 1)] P(n_E, n_I - 1, t) \\
& - (N_I - n_I) f_I[s_I(n_E, n_I)] P(n_E, n_I, t)]
\end{aligned} \tag{22.13}$$

See [13] for a derivation of this equation.

From this, it is easy to derive the mean-field $E - I$ equations in the following form:

$$\begin{aligned}
\frac{d\langle n_E(t) \rangle}{dt} = & -\alpha_E \langle n_E(t) \rangle + (N_E - \langle n_E(t) \rangle) f_E[\langle s_E(n_E) \rangle] \\
\frac{d\langle n_I(t) \rangle}{dt} = & -\alpha_I \langle n_I(t) \rangle + (N_I - \langle n_I(t) \rangle) f_I[\langle s_I(n_I) \rangle]
\end{aligned} \tag{22.14}$$

where $\langle s_E(n_E) \rangle = I_E/I_{RH}$, $\langle I_E \rangle = w_{EE}\langle n_E \rangle - w_{EI}\langle n_I \rangle + w_{EH}\langle n_H \rangle$, and $\langle s_I(n_I) \rangle = \langle I_I \rangle/I_{RH}$, $\langle I_I \rangle = w_{IE}\langle n_E \rangle - w_{II}\langle n_I \rangle + w_{IH}\langle n_H \rangle$. $\langle s_I(n_I) \rangle = \langle I_I \rangle/I_{RH}$. These are the mean-field Wilson–Cowan equations [3, 14].

22.3.1

Equilibria of the Mean-Field Wilson–Cowan Equations

A major feature of the Wilson–Cowan equations is that they support different kinds of equilibria. Figure 22.7 shows two such equilibrium patterns.

There is also another phase plane portrait in which the equilibrium is as a damped oscillation, that is, a stable *focus*. In fact, by varying the synaptic weights w_{EH} and w_{IH} or $c = w_{EE}w_{II}$ and $d = w_{IE}w_{EI}$, we can move from one portrait to another. It turns out that there is a substantial literature dealing with the way in which such changes occur. The mathematical technique for analyzing these transformations is called *bifurcation theory*, and it was first applied to neural problems 52 years ago [15], but first used systematically by Ermentrout and Cowan [16–18] in a series of papers on the dynamics of the mean-field Wilson–Cowan equations.

More detailed studies of neural bifurcation in the Wilson–Cowan equations were subsequently carried out by Borisyuk and Kirillov [20], and Hoppensteadt and Izhikevich [19]. The left panel of Figure 22.8 shows a representation of the detailed structure of such bifurcations. It will be seen that the saddle–node and Andronov–Hopf bifurcations lie quite close to the Bogdanov–Takens (BT) bifurcation. This implies that all the bifurcations of the Wilson–Cowan equations we have described are fairly close to the BT bifurcation, in the (a, b) -plane.

The BT bifurcation depends on two control parameters, and is therefore said to be of *co-dimension 2*. It has the property that an equilibrium point can simultaneously become a marginally stable saddle–node bifurcation point and an Andronov–Hopf bifurcation point. Thus at the critical point, the eigenvalues of its associated stability matrix have zero real parts.

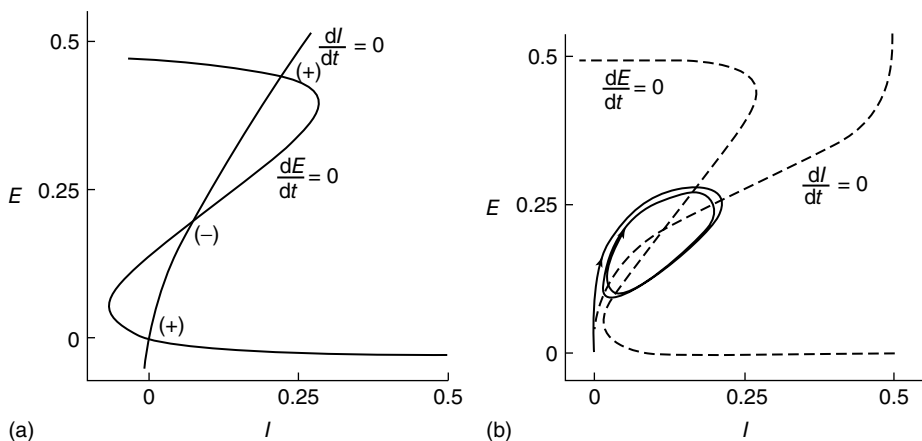


Figure 22.7 (a) E – I phase plane and nullclines of the mean-field Wilson–Cowan equations. The intersections of the two nullclines are equilibrium or fixed points of the equations. Those labeled + are stable, those labeled – are unstable. Parameters: $w_{EE} =$

$12, w_{EI} = 4, w_{IE} = 13, w_{II} = 11, n_H = 0$. The stable fixed points are nodes. (b) Equilibrium which is periodic in time. Parameters: $w_{EE} = 16, w_{EI} = 12, w_{IE} = 15, w_{II} = 3, n_H = 1.25$. In this case, the equilibrium is a limit cycle. (Redrawn from [3].)

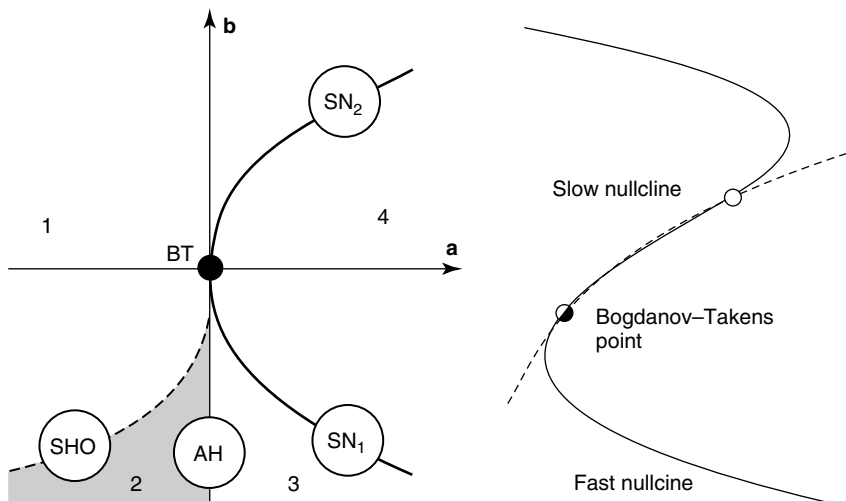


Figure 22.8 (a) Bifurcations of the Wilson–Cowan equations organized around the Bogdanov–Takens (BT) bifurcation. SN₂ and SN₁ are saddle-node bifurcations. AH is an Andronov–Hopf bifurcation, and SHO is a saddle homoclinic–orbit bifurcation. Note that a and b are control parameters,

either synaptic weights or their products, as described in the caption to Figure 22.7. (b) Nullcline structure at a Bogdanov–Takens bifurcation. At the Bogdanov–Takens point, a stable node (open circle) coalesces with an unstable point. (Redrawn from [19].)

In addition, the right panel of Figure 22.8 shows the way in which the fast E -nullcline and the slow I -nullcline intersect. The point of first contact of the two nullclines is the BT point. It will be seen that there is region of the phase plane above this point where the two nullclines remain close together. This is a defining characteristic of such a bifurcation. Interestingly, it is closely connected with the *balance* between excitatory and inhibitory currents, as was noted in Benayoun *et al.*'s study of avalanches in stochastic Wilson–Cowan equations [13]. This is another demonstration that avalanches with a power law distribution are generated in stochastic neural networks close to critical points, and therefore lie in the fluctuation-dependent region of a phase transition. In the case of stochastic neural networks, our results suggest that the phase transition belongs to the directed percolation universality class.

22.4

An E-I Neural Network Exhibiting Self-Organized Near-Criticality

We now consider the neural patch or module shown in Figure 22.9. Again, we note that this module is spatially homogeneous. We model the neocortical sheet as a two-dimensional network or array of such circuits. In such an array, note that the neighboring excitation provides the recurrent excitatory connection. This requires $\mu_j^E = 1/4$, so that the recurrent excitatory connection shown in Figure 22.9 (not labeled) has strength w_{EE} . The recurrent inhibitory connection (also unlabeled) takes the value w_{II} . The basic equations for the array thus take the form of Eqs. (22.13) and (22.14), except that the activities n_E and n_I are now functions of position, as are the excitatory and inhibitory currents I_E and I_i^I which are given by the expressions

$$I_i^E = \frac{1}{4} \sum_j w_{ij}^{EE} n_j^E - w_{ii}^{EI} n_i^I + w_{ii}^{EH} n_i^H, \quad I_i^I = w_{ii}^{IE} n_i^E - w_{ii}^{II} n_i^I + w_{ii}^{IH} n_i^H$$

where \sum_j runs over all nearest neighbor patches.

Note also that the density of inter-patch EI and II connections is very small relative to that of EE connections, so we have neglected them in calculating the excitatory and inhibitory currents I_i^E and I_i^I .

22.4.1

Modifiable Synapses

We now introduce generalized Vogels equations for the four internal synaptic weights in each patch, w_{ii}^{EE} , w_{ii}^{IE} , w_{ii}^{EI} , and w_{ii}^{II} . The excitatory synapses w_{ii}^{EE} and w_{ii}^{IE} are assumed to be *anti-Hebbian*, and the inhibitory synapses w_{ii}^{EI} and w_{ii}^{II} *Hebbian*. Mean-field equations for these weights take the following form:

$$\frac{d\langle w^{\alpha\beta} \rangle}{dt} = \lambda_{\alpha\beta} - \mu_{\alpha\beta} \langle w^{\alpha\beta} \rangle \quad (22.15)$$

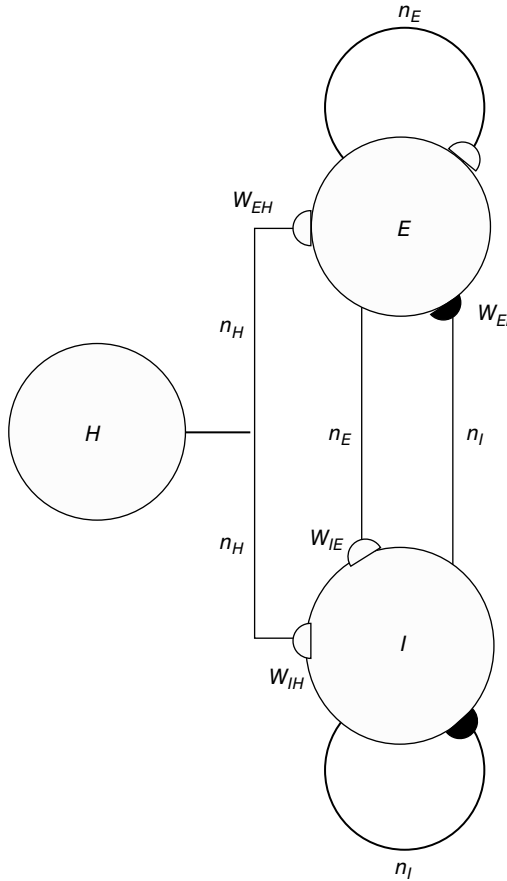


Figure 22.9 A recurrent $E - I$ network module driven by the input H , acting through the synaptic weight w_{EH} and w_{IH} .

where α and β run over the set $\{E, I\}$, and the coefficients $\lambda_{\alpha,\beta}$ and $\mu_{\alpha,\beta}$ give the transitions rates for the Markov processes governing the four weights. These take the form

$$\lambda_{\alpha E} = \beta_E g_\alpha n_{\alpha,0} n_E; \quad \mu_{\alpha E} = \beta_E g_\alpha \left(\frac{n_\alpha}{w^{\alpha E}} + |\kappa_{E,S}| \right) n_E \quad (22.16)$$

for the excitatory anti-Hebbian weights, and

$$\lambda_{\alpha I} = \beta_I g_\alpha n_\alpha n_I; \quad \mu_{\alpha I} = \beta_I g_\alpha \left(\frac{n_{\alpha,0}}{w^{\alpha E}} + \kappa_{I,S} \right) n_I \quad (22.17)$$

for the inhibitory Hebbian weights. Note that for such weights $\kappa_{E,S} < 0$, $\kappa_{I,S} > 0$.

In the continuum limit, these equations take the form

$$\frac{d\langle w_{\alpha E}(\mathbf{x}) \rangle}{dt} = -\beta_E g_\alpha(\mathbf{x}) \left(\frac{\langle n_\alpha(\mathbf{x}) \rangle - n_{\alpha,0}(\mathbf{x})}{\rho_S} + |\kappa_{E,S}| \langle w_{\alpha E}(\mathbf{x}) \rangle \right) \frac{\langle n_E(\mathbf{x}) \rangle}{\rho_S} \quad (22.18)$$

for excitatory weights, and

$$\frac{d\langle w_{\alpha I}(\mathbf{x}) \rangle}{dt} = \beta_I g_\alpha(\mathbf{x}) \left(\frac{\langle n_\alpha(\mathbf{x}) \rangle - n_{\alpha,0}(\mathbf{x})}{\rho_S} - \kappa_{I,S} \langle w_{\alpha I}(\mathbf{x}) \rangle \right) \frac{\langle n_I(\mathbf{x}) \rangle}{\rho_S} \quad (22.19)$$

for inhibitory weights.

22.4.2

A Simulation of the Combined Mean-Field E/I equations

The complete set of mean-field equations for an $E – I$ patch with modifiable weights comprises the Wilson–Cowan equations 22.14 together with the generalized Vogels Eqs. 22.18 and 22.19, supplemented by the modified current equations given above, for the full two-dimensional array. Such a system of equations can be simulated, and the results are shown in Figure 22.10.

It will be seen that a single patch self-organizes from one stable fixed point defined by the initial conditions to another stable fixed point at which $n_E = n_{E,0}$, $n_I = n_{I,0}$, as expected. We note that, in case the initial conditions are constrained so that $w_{EE} = w_{IE} = w_E$ and $w_{EI} = w_{II} = w_I$, and all the fixed parameters of the E population equal those of the I population, then the final state is also similarly constrained. We refer to this as a *symmetry* of the system. Given such a symmetry and the target condition $n_{E,0} = n_{I,0}$, it follows that $w_E - w_I \rightarrow 0$, so that

$$w_0 = w_E - w_I \ll w_E + w_I$$

Thus the combined system is *homeostatic*. It self-organizes so that the strengths of all the synaptic weights stay within a certain range. The homeostatic properties of anti-Hebbian synapses were previously noted by Rumsey and Abbott [21].

22.4.3

Balanced Amplification in E/I Patches

This inequality has a number of important consequences [13, 22]. In particular, it leads to a particular change of variables in the relevant Wilson–Cowan equations. Consider such equations for a single patch, given the symmetry described above:

$$\begin{aligned} \frac{d\langle n_E(t) \rangle}{dt} &= -\alpha \langle n_E(t) \rangle + (1 - \langle n_E(t) \rangle) f[\langle s \rangle] \\ \frac{d\langle n_I(t) \rangle}{dt} &= -\alpha \langle n_I(t) \rangle + (1 - \langle n_I(t) \rangle) f[\langle s \rangle] \end{aligned} \quad (22.20)$$

where $\langle s \rangle = w_E N_E - w_I n_I + h$, and n_E and n_I are interpreted as the fractions of activated E and I neurons in a patch.

Now introduce the change of variables

$$\Sigma = \frac{1}{2}(n_E + n_I), \quad \Delta = \frac{1}{2}(N_E - n_I) \quad (22.21)$$

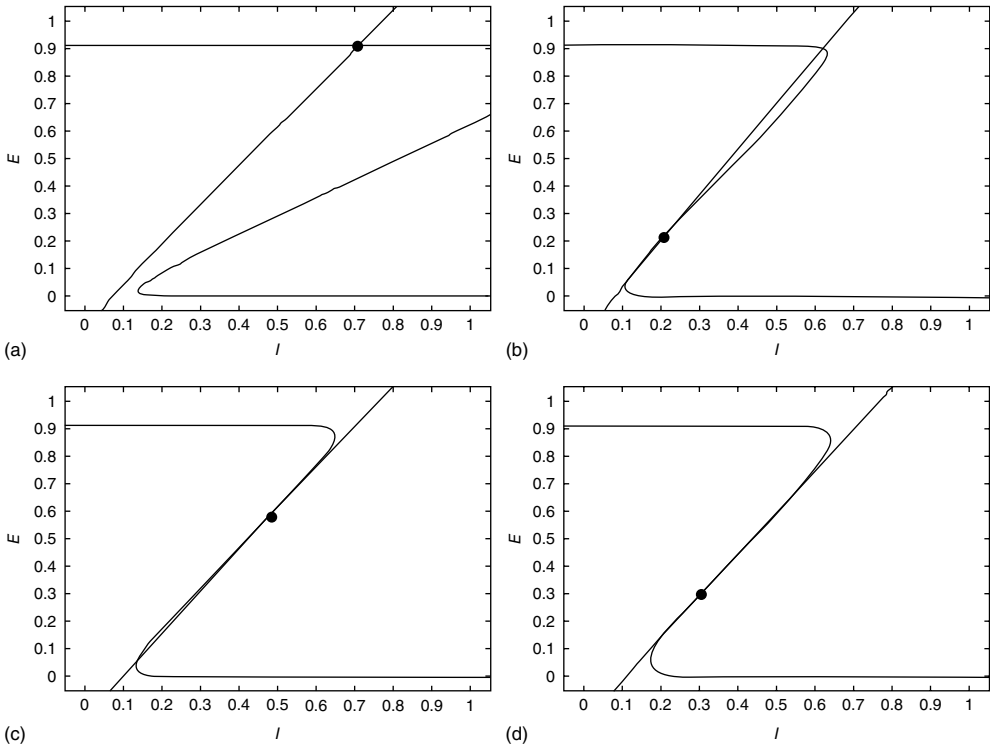


Figure 22.10 $E - I$ phase plane and nullclines of the mean-field Wilson–Cowan equations. The intersections of the two nullclines in each panel are equilibrium or fixed points of the equations. (a) Initial state at $t = 0$ s with weights $w_{EE} = 36, w_{IE} = 25, w_{EI} = 22, w_{II} = 33$. There is a stable fixed point at $n_E \approx 0.9, n_I \approx 0.7$. (b) State at $t = 1.25 \times 10^5$ s with weights $w_{EE} = 20.05, w_{IE} = 20.17, w_{EI} = 24.78, w_{II} =$

30.45. There is now a saddle point at $n_E \approx 0.2, n_I \approx 0.2$. (c) State at $t = 2.5 \times 10^5$ s, with weights $w_{EE} = 16.09, w_{IE} = 18.63, w_{EI} = 18.72, w_{II} = 24.86$, and a saddle point at $n_E \approx 0.6, n_I \approx 0.6$. (d) Final state at $t = 1 \times 10^6$ s, with weights $w_{EE} = 11.80, w_{IE} = 15.63, w_{EI} = 13.22, w_{II} = 20.83$, with a stable fixed point at $n_E = 0.3, n_I = 0.3$. The remaining fixed parameters are $w_{EH} = w_{IH} = 0, \beta_E = 1, \beta_I = 1.5$.

so that Eq. 22.20 transforms into

$$\begin{aligned} \frac{d\langle \Sigma(t) \rangle}{dt} &= -\alpha \langle \Sigma(t) \rangle + (1 - \langle \Sigma(t) \rangle) f[\langle s \rangle] \\ \frac{d\langle \Delta(t) \rangle}{dt} &= -\Delta(t)(\alpha + f[\langle s \rangle]). \end{aligned} \quad (22.22)$$

Such a transformation was first introduced into neural dynamics by Murphy and Miller [22], and followed by Benayoun *et al.* [13]. But it was actually introduced much earlier by Janssen [23] in a study of the statistical mechanics of stochastic Lotka–Volterra population equations on lattices, which are known to be closely related to stochastic Wilson–Cowan equations [24]. Interestingly, Janssen concluded that systems of interacting predator and prey populations satisfying

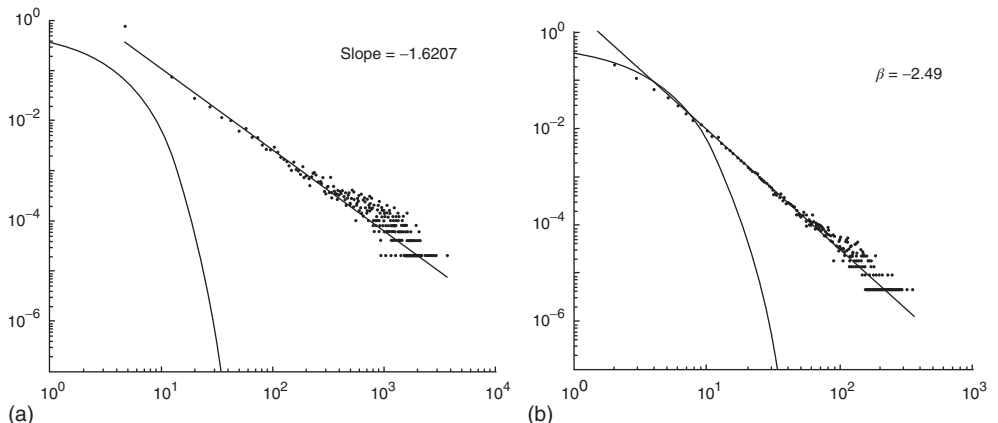


Figure 22.11 (a) Avalanche distribution in the all-to-all case. The distribution is approximately a power law with a slope $\beta = -1.62$ (blue line). For comparison, a Poisson distribution is plotted. (b) Avalanche distribution

in the sparsely connected case. The distribution is approximately another power law with a slope of $\beta = -2.5$. Note that both distributions show bulges at large avalanche sizes.

the Lotka–Volterra equations exhibited a nonequilibrium phase transition in the universality class of directed percolation, just as we later demonstrated in stochastic Wilson–Cowan equations [25]. Janssen used the transformed equations to show that, in the neighborhood of such a phase transition, only the variable Σ survives.

To show this, we note that the transformed equations are *decoupled* with the unique stable solution $(\Sigma_0, 0)$. In turn, this implies that at such a fixed point $n_E = n_I$ in the original variables. This is precisely the stable fixed point reached in the simulations shown in Figure 22.11. In addition, it also follows that the fixed-point current in the new variables is

$$s = (w_E - w_I)\Sigma + (w_E + w_I)\Delta + h = w_0\Sigma + (w_E + w_I)\Delta + h$$

So at the stable fixed point $(\Sigma_0, 0)$, $s = w_0\Sigma_0 + h$, and in fact, near such a fixed point, Δ is only weakly sensitive to changes in Σ , and Σ_0 is unchanged by varying $w_E + w_I$ while keeping w_0 constant. For all these reasons, Murphy and Miller described the decoupled equations as an *effective feed-forward system* exhibiting a balance between excitatory and inhibitory currents, and a balanced amplification of any stimulus h .

22.4.4

Analysis and Simulation of the Combined E/I Markov Processes

It remains to analyze and simulate the statistical dynamics of the coupled Markov processes introduced earlier to represent the effects of fluctuations in both neural activity and in synaptic plasticity. But the various synaptic weights have strengths that depend on neural activity. So the characteristics of such activity determine those of the weights. But we have shown for $E - I$ patches that the combined mean-field dynamics reaches a stable equilibrium in the form of a node, and that

at this node there is a balance reached between excitation and inhibition. We can obtain more information about the properties of this node by considering the effects of small deviations or fluctuations in the activity.

To do this, we now start from the fact the fixed point is a stable node. This means that we can expand the master equation directly via the van Kampen *system-size expansion* [4]. This expansion was first used in the neural context by Ohira and Cowan [26] and later by Bressloff [27] and Benayoun *et al.* [13]. Thus we do not need to use the methods of statistical field theory for this part of the analysis. The details of the system-size expansion are straightforward. Since the fixed point is stable, we can assume that small fluctuations about such a fixed point are Gaussian. Thus the fractions of activated excitatory and inhibitory neurons at time t can be written as

$$\frac{k_E}{N_E} = n_E + \frac{\xi_E}{\sqrt{N_E}}, \quad \frac{k_I}{N_I} = n_I + \frac{\xi_I}{\sqrt{N_I}} \quad (22.23)$$

where (N_E, N_I) are, respectively, the numbers of excitatory and inhibitory neurons, (n_E, n_I) are, as before, the mean fractions of activated excitatory and inhibitory neurons, and (ξ_E, ξ_I) are stochastic perturbations. The mean fractions satisfy Eq. 22.20, and the mean current is as before. The stochastic variables satisfy the (linear) Langevin equation

$$\frac{d}{dt} \begin{pmatrix} \xi_E \\ \xi_I \end{pmatrix} = A \begin{pmatrix} \xi_E \\ \xi_I \end{pmatrix} + \begin{pmatrix} \sqrt{\alpha n_E + (1 - n_E)f[s]} \eta_E \\ \sqrt{\alpha n_I + (1 - n_I)f[s]} \eta_I \end{pmatrix} \begin{pmatrix} \eta_E \\ \eta_I \end{pmatrix} \quad (22.24)$$

or in the transformed variables (Σ, Δ)

$$\frac{d}{dt} \begin{pmatrix} \xi_\Sigma \\ \xi_\Delta \end{pmatrix} = \begin{pmatrix} -\lambda_1 & w_{ff} \\ 0 & -\lambda_2 \end{pmatrix} \begin{pmatrix} \xi_\Sigma \\ \xi_\Delta \end{pmatrix} + \sqrt{\alpha \Sigma_0} \begin{pmatrix} \eta_\Sigma \\ \eta_\Delta \end{pmatrix} \quad (22.25)$$

where the eigenvalues are $\lambda_1 = (\alpha + f[s_0]) + (1 - \Sigma_0)w_0f'[s_0]$ and $\lambda_2 = (\alpha + f[s_0])$, and $w_{ff} = (1 - \Sigma_0)(w_E + w_I)f'[s_0]$. The Jacobian matrix

$$A = \begin{pmatrix} -\lambda_1 & w_{ff} \\ 0 & -\lambda_2 \end{pmatrix}$$

is upper triangular and has eigenvalues $-\lambda_1$ and $-\lambda_2$. It follows that, when w_0 is small and positive, then so are the eigenvalue magnitudes λ_1 and λ_2 . So the eigenvalues are small and negative, and the fixed point $(\Sigma_0, 0)$ is weakly stable. Evidently, A lies close to the matrix

$$B = \begin{pmatrix} 0 & w_{ff} \\ 0 & 0 \end{pmatrix} = \begin{pmatrix} 0 & 1 \\ 0 & 0 \end{pmatrix} w_{ff} = \bar{B} w_{ff}$$

But the matrix \bar{B} is the signature of the *normal form* of the BT bifurcation [19]. Thus the weakly stable node lies close to a BT bifurcation, as we have suggested. The stochastic interpretation of this is that the weakly stable node lies close to the critical point of a phase transition in the universality class of directed percolation. (Note that we cannot perform a system-size expansion of the master equation in

case the fixed point is only marginally stable, as it is at a critical point. This situation required the renormalization group treatment [9].)

To simulate the combined Markov processes described by such a stochastic system, [13] used the Gillespie algorithm to simulate the stochastic behavior of two architectures: (i) an all-to-all connected patch comprising 80 excitatory and 20 inhibitory neurons (these are the proportions of such neurons in the neocortex). The results are shown in Figure 22.11a; (ii) a sparsely connected patch in which random sparse positive matrices $W_E + W_I$ with large eigenvalues, and $W_E - W_I$ with small eigenvalues are generated so that the overall weight matrix

$$W = \begin{pmatrix} W_E & -W_I \\ W_E & -W_I \end{pmatrix}$$

is random. (The condition that the eigenvalues of $W_E + W_I$ are much greater than those of $W_E - W_I$ is equivalent to the condition $w_E - w_I \ll w_E + w_I$ in the all-to-all case.) The result is shown in the right panel of Figure 22.11. (iii) We do not yet have a finished simulation of the two-dimensional case, but we conjecture that the results will be similar in that the avalanche distribution will be approximately a power law, but with a slope of $\beta \approx -1.3$. (See also the recent paper by Magnasco *et al.* [28].)

22.5 Discussion

We have demonstrated the following properties of stochastic Wilson–Cowan equations: (i) A simple two-dimensional array comprising patches of excitatory neurons driven by a weak external stimulus acting through a modifiable anti-Hebbian synapse self-organizes into an oscillation between two stable states, an UP state of high neural activity and a DOWN state of low activity, each of which loses its stability at the critical point of a nonequilibrium phase transition in the universality class of directed percolation. Such noisy oscillations generate bursts or avalanches of neural activity whose avalanche distributions are consistent with such a phase transition. (ii) We then analyzed the properties of a array comprising patches of both excitatory and inhibitory neurons, with excitatory anti-Hebbian and inhibitory Hebbian synapses. We found that the spontaneous-fluctuation-driven activity of a single patch self-organizes to a weakly stable fixed point. However, such a fixed point lies close to a marginally stable fixed point. Thus we conclude that the effect of Hebbian inhibition is to *stabilize* the dynamics of the patch, but that the statistical dynamics of the patch remains within the fluctuation drive regime surrounding the critical point of a nonequilibrium phase transition, which again is in the universality class of directed percolation. (We are preparing a manuscript contained a detailed analysis of this situation using renormalization group techniques, along the lines of Janssen’s analysis of stochastic Lotka–Volterra equations.) (iii) We have also shown that the mean-field dynamics of the E/I case can be analyzed around the BT bifurcation, and that the generalized Vogels

equations for Hebbian and anti-Hebbian plasticity drive the patch dynamics to a weakly stable node near such a bifurcation, and in doing so reduce the E/I dynamics to the E dynamics of a single E patch.

In summary, we conclude that an array of E -patches will self-organize around critical points of the directed percolation phase transition and, when driven by a weak stimulus, will oscillate between an UP state and a DOWN state each of which generates avalanches consistent with directed percolation. The array therefore exhibits SOC and replicates the behavior of the original sandpile model of [1]. We can also conclude that an array of E/I patches will also self-organize to a weakly stable node located near the critical point of a directed percolation phase transition so that fluctuations about the weakly stable node will also follow a power slope with a slope characteristic of directed percolation. We refer to this as SONC. We note that there is some experimental evidence to support this conclusion [29, 30].

Acknowledgements

Some of the work reported in this paper was initially developed (in part) with Hugh R. Wilson, and thereafter with G.B. Ermentrout, then with Toru Ohira, and later with Michael A. Buice. The current work was supported (in part) by a grant to Wim van Drongelen from the Dr. Ralph & Marian Falk Medical Trust.

References

1. Bak, P., Tang, C., and Wiesenfeld, K. (1988) Self-organized criticality. *Phys. Rev. A*, **38**, 364–374.
2. Gil, L. and Sornette, D. (1996) Landau-ginzburg theory of self-organized criticality. *Phys. Rev. Lett.*, **76** (21), 3991–3994.
3. Wilson, H. and Cowan, J. (1972) Excitatory and inhibitory interactions in localized populations of model neurons. *Biol. Cybern.*, **12**, 1–24.
4. Van Kampen, N. (1981) *Stochastic Processes in Physics and Chemistry*. North Holland.
5. Wilson, K. (1971) Renormalization group and critical phenomena. I. renormalization group and the kadanoff scaling picture. *Phys. Rev. B*, **4** (9), 3174–3183.
6. Cowan, J., Neuman, J., Kiewiet, B., and van Drongelen, W. (2013) Self-organized criticality in a network of interacting neurons. *J. Stat. Mech.*, P04030.
7. Hinrichsen, H. (2000) Non-equilibrium critical phenomena and phase transitions into absorbing states. *Adv. Phys.*, **49** (7), 815–958.
8. Korolev, K. and Nelson, D. (2011) Competition and Cooperation in one-dimensional stepping-stone models. *Phys. Rev. Lett.*, **107** (8), 088–103.
9. Buice, M. and Cowan, J. (2007) Field theoretic approach to fluctuation effects for neural networks. *Phys. Rev. E*, **75**, 051–919.
10. Vogels, T., Sprikeler, H., Zenke, F., Clopath, C., and Gerstner, W. (2011) Inhibitory plasticity balances excitation and inhibition in sensory pathways and memory networks. *Science*, **334** (6062), 664–666.
11. Han, V.Z., Grant, K., and Bell, C. (2000) Reversible associative depression and nonassociative potentiation at a parallel fiber synapse. *Neuron*, **24**, 611–622.

12. Gillespie, D. (2000) The chemical Langevin equation. *J. Chem. Phys.*, **113** (1), 297–306.
13. Benayoun, M., Cowan, J., van Drongelen, W., and Wallace, E. (2010) Avalanches in a stochastic model of spiking neurons. *PLoS Comput. Biol.*, **6** (7), e1000846.
14. Wilson, H. and Cowan, J. (1973) A mathematical theory of the functional dynamics of cortical and thalamic nervous tissue. *Kybernetik*, **13**, 55–80.
15. Fitzhugh, R. (1961) Impulses and physiological states in theoretical models of nerve membrane. *Biophys. J.*, **1**, 445–466.
16. Ermentrout, G. and Cowan, J. (1979b) Temporal oscillations in neuronal nets. *J. Math. Biol.*, **7**, 265–280.
17. Ermentrout, G.B. and Cowan, J.D. (1979a) A mathematical theory of visual hallucinations. *Biol. Cybern.*, **34**, 137.
18. Ermentrout, G.B. and Cowan, J.D. (1980) Large scale spatially organized activity in neural nets. *SIAM J. Appl. Math.*, **38** (1), 1–21.
19. Hoppensteadt, F. and Izhikevich, E. (1997) *Weakly Connected Neural Networks*, MIT Press, Cambridge, MA.
20. Borisyuk, R. and Kirillov, A. (1992) Bifurcation analysis of a neural network model. *Biol. Cybern.*, **66** (4), 319–325.
21. Rumsey, C. and Abbott, L. (2004) Synaptic equalization by anti-STDP. *Neurocomputing*, **58**-**60**, 359–364.
22. Murphy, B. and Miller, K. (2009) Balanced amplification: a new mechanism of selective amplification of neural activity patterns. *Neuron*, **61** (4), 635–648.
23. Janssen, H. (2001) Directed percolation with codors and flabors. *J. Stat. Phys.*, **103** (5-6), 801–839.
24. Cowan, J.D. (2013) A personal account of the development of the field theory of large-scale brain activity from 1945 onward, in *Neural Field Theory* (eds S., Coombes, P., BiemGraben, R., Potthast, and J. Wright), Springer, New York.
25. Buice, M. and Cowan, J. (2009) Statistical mechanics of the neocortex. *Prog. Biophys. Theor. Biol.*, **99** (2,3), 53–86.
26. Ohira, T. and Cowan, J.D. (1997) Stochastic neurodynamics and the system size expansion, in *Proceedings of the First International Conference on the Mathematics of Neural Networks* (eds S. Ellacort and I. Anderson), Academic Press, pp. 290–294.
27. Bressloff, P. (2009) Stochastic neural field theory and the system-size expansion. *SIAM J. Appl. Math.*, **70** (5), 1488–1521.
28. Magnasco, M., Piro, O., and Cecchi, G. (2009) Self-tuned critical anti-hebbian networks. *Phys. Rev. Lett.*, **102**, 258–102.
29. Tagliazucchi, E., Balenzuela, P., Fraiman, D., and Chialvo, D. (2012) Criticality in large-scale brain fMRI dynamics unveiled by a novel point process analysis. *Front. Physiol.*, **3**, 1–12.
30. Haimovici, A., Tagliazucchi, E., Balenzuela, P., and Chialvo, D. (2013) Brain organization into reating state nnetworks emerges at crituality on a Model of the human connectiome. *Phys. Rev. Lett.*, **110**, 178–101.

23

Neural Dynamics: Criticality, Cooperation, Avalanches, and Entrainment between Complex Networks

Paolo Grigolini, Marzieh Zare, Adam Svenkeson, and Bruce J. West

23.1

Introduction

The discovery of avalanches in neural systems [1] has aroused substantial interest among neurophysiologists and, more generally, among researchers in complex networks [2–4] as well. The main purpose of this chapter is to provide evidence in support of the hypothesis that the phenomenon of *neural avalanches* [1] is generated by the same cooperative properties as those responsible for a surprising effect which we call cooperation-induced (CI) synchronization, illustrated in [5]. The phenomenon of neural entrainment [6] is another manifestation of the same cooperative property. We also address the important issue of the connection between neural avalanches and *criticality*. Avalanches are thought to be a manifestation of criticality, and especially self-organized criticality [7, 8]. At the same time, criticality is accompanied by long-range correlation [7], and a plausible model for neural dynamics is expected to account for the astounding interaction between agents separated by relatively large distances. General agreement exists in the literature that brain function rests on these crucial properties, and the phase-transition theory for physical phenomena [9] is thought to afford the most important theoretical direction for further research work on this subject. In this theory, criticality emerges at a specific single value of a control parameter, designated by the symbol K_c . In this chapter, we illustrate a theoretical model generating avalanches, long-range correlation, and entrainment, as a form of CI synchronization, over a wide range of values of the control parameter K , thereby suggesting that the form of criticality within the brain is not the ordinary criticality of physical phase transitions but is instead the *extended criticality* recently introduced by Longo and coworkers [10, 11] to explain biological processes.

Cooperation is the common effort of the elements of a network for their mutual benefit. We use the term *cooperation* in the same loose sense as that adopted, for instance, by Montroll [12] to shed light on the equilibrium condition realized by the interacting spins of the Ising model. Although the term *cooperation*, frequently used in this chapter, does not imply a network's cognition, we follow the conceptual perspective advocated by Werner [13] that cognition emerges at criticality, with the proviso that its cause may be extended criticality (EC).

The term *cooperation* suggests a form of awareness that these units do not have and must be used with caution especially because in this chapter we move from an Ising-like model to a model of interacting neurons that seems to reproduce certain experimental observations on neural networks which are thought to reflect important properties of brain dynamics, including the emergence of cognition. This is done along the lines advocated by Werner [13], who argues that consciousness is a phenomenon of statistical physics resting on renormalization group theory (RGТ) [14]. We afford additional support to this perspective, while suggesting that the form of criticality from which cognition emerges may be more complex than renormalization group criticality, thereby requiring an extension of this theory. All this must be carried out keeping in mind Werner's warning [15] against the use of metaphors of computation and information, which would contaminate the observation with meanings from the observer's mind.

We move from an Ising-like cooperative model to one of interacting neurons, which, although highly idealized, serves very well the purpose of illustrating the cooperative-induced temporal complexity of neural networks. The reason to spend time with the Ising-like cooperative model, discussed in this volume by West *et al.* [5], is the fact that dealing first with this model clarifies the difference between ordinary criticality, shared with this earlier model, and EC.

The Ising-like model that we adopt is the decision-making model (DMM) that has been used to explain the scale-free distribution of neural links recently revealed by the functional magnetic resonance imaging (fMRI) analysis of the brain [16, 17]. We examine two different weak perturbation conditions: (i) all the units are perturbed by an external low-intensity stimulus, and (ii) a small number of units are perturbed by an external field of large intensity. We show that the response of this cooperative network to extremely weak stimuli, case (i), departs from the predictions of traditional linear response theory (LRT) originally established by Green [18] and Kubo [19] and widely applied by physicists for almost 60 years. This deviation arises because cooperation generates phase-transition criticality and, at the same time, generates non-ergodic fluctuations, whereas the traditional LRT is confined to the condition of ergodic fluctuations. Condition (ii) is the source of another surprising property: although a few units are strongly perturbed, thanks to cooperation, the stimulus affects the whole network, making that response depart from either ergodic or non-ergodic LRT, thereby generating what we call *cooperation-induced* (CI) response. This form of response is the source of the perfect synchronization between a complex network and the perturbing stimulus generated by another complex network, a new phenomenon discovered by Turalska *et al.* [20], whose cooperative origin is illustrated in detail in this chapter. We term this effect *CI synchronization*. Condition (i) yields the non-ergodic extension of stochastic resonance, and the CI synchronization of condition (ii) is the cooperative counterpart of chaos synchronization.

The second step of our approach to understanding neural complexity and neural avalanches [21] rests on an *integrate-and-fire* model [22], where the firing of one unit of a set of linked neurons facilitates the firing of the other units. We refer to this model as *neural firing cooperation* (NFC). We find that, in the case

where cooperation is established through NFC, the emerging form of criticality is significantly different from that of an ordinary phase transition. In the typical case of a phase transition, temporal complexity is limited to a singular value of the control parameter, namely of the cooperation strength in the cases examined in this chapter. The NFC cooperation generates temporal complexity analogous to that generated by the DMM, but this temporal complexity, rather than being limited to a single value of the cooperation parameter, is extended to a finite interval of critical values. As a consequence, the new ways of responding to external stimuli are not limited to a singular value of the cooperation parameter either, but their regime of validity is significantly extended, suggesting this to be a manifestation of the new form of criticality which Longo and coworkers [10, 11] call *extended criticality* (EC). Adopting the EC perspective, we move within the extended critical range, from smaller to larger values of the cooperation parameter K , and we find that neural avalanches [21] emerge at the cooperation level, making the system adopt the CI response. When a neural network is driven by another neural network with the same complexity, we expect that the response of the perturbed network obeys the new phenomenon of CI synchronization. We notice that these theoretical predictions, of a close connection to neural avalanches and network entrainment, can be checked experimentally through methods of the kind successfully adopted in the University of North Texas laboratory of Gross *et al.* [23].

Finally, although the emergence of consciousness remains a mystery, we note that the assignment of cognition properties to cooperation [24] leads to temporal complexity with the same power law index as that revealed by the experimental observation of active cognition [25], thereby supporting the conjecture [14] that a close connection between cognition in action and a special form of temporal complexity exists.

The connection between neural cooperation and cognition is certainly far beyond our current understanding of emerging consciousness. Therefore, we limit ourselves to showing that the cooperation between units generates global properties, some of which are qualitatively similar to those revealed by recent analysis of the human brain.

23.2

Decision-Making Model (DMM) at Criticality

The DMM [20] is the Ising-like version of an earlier model [26] of a dynamic complex network. The DMM is based on the cooperative interaction of N units, each of which is described by the master equation

$$\frac{d}{dt}p_1^{(i)}(t) = -\frac{g_{12}^{(i)}(t)}{2}p_1^{(i)}(t) + \frac{g_{21}^{(i)}(t)}{2}p_2^{(i)}(t) \quad (23.1)$$

$$\frac{d}{dt}p_2^{(i)}(t) = -\frac{g_{21}^{(i)}(t)}{2}p_2^{(i)}(t) + \frac{g_{12}^{(i)}(t)}{2}p_1^{(i)}(t) \quad (23.2)$$

where

$$g_{12}^{(i)} \equiv g_0 \exp \left(K \frac{(N_2^{(i)} - N_1^{(i)})}{N^{(i)}} \right) \quad (23.3)$$

and

$$g_{21}^{(i)} \equiv g_0 \exp \left(K \frac{(N_1^{(i)} - N_2^{(i)})}{N^{(i)}} \right) \quad (23.4)$$

The symbol $N^{(i)}$ denotes the number of nodes linked to the i th node, with $N_1^{(i)}$ and $N_2^{(i)}$ being those in the first and second state, respectively. Of course, $N^{(i)} = N_1^{(i)} + N_2^{(i)}$.

The index i runs from 1 to N , where N is the total number of nodes of the complex network under study, thereby implying that we have to compute N pairs of equations of the kind of Eqs. (23.1) and (23.2) at each time step. The adoption of an all-to-all (ATA) coupling condition allows us to simplify the problem. In fact, in that case, all the N pairs of equations are identical to

$$\frac{d}{dt} p_1(t) = -\frac{g_{12}(t)}{2} p_1(t) + \frac{g_{21}(t)}{2} p_2(t) \quad (23.5)$$

$$\frac{d}{dt} p_2(t) = -\frac{g_{21}(t)}{2} p_2(t) + \frac{g_{12}(t)}{2} p_1(t) \quad (23.6)$$

with

$$g_{12} \equiv g_0 \exp \left(K \frac{(N_2 - N_1)}{N} \right) \quad (23.7)$$

and

$$g_{21} \equiv g_0 \exp \left(K \frac{(N_1 - N_2)}{N} \right) \quad (23.8)$$

Since normalization requires $p_1(t) + p_2(t) = 1$, it is convenient to replace the pair of equations (23.5) and (23.6) with a single equation for the difference in probabilities:

$$\Pi(t) \equiv p_1(t) - p_2(t) \quad (23.9)$$

which, after some simple algebra, becomes

$$\frac{d}{dt} \Pi = \frac{(g_{21} - g_{12})}{2} - \frac{(g_{21} + g_{12})}{2} \Pi \quad (23.10)$$

It is important to stress that the equality

$$\frac{N_1 - N_2}{N} = \Pi \quad (23.11)$$

holds true only in the limiting case $N \rightarrow \infty$. In the case of a finite network, $N < \infty$, the mean field fluctuates in time, forcing us to adopt

$$\frac{N_1 - N_2}{N} = \Pi + f(t) \quad (23.12)$$

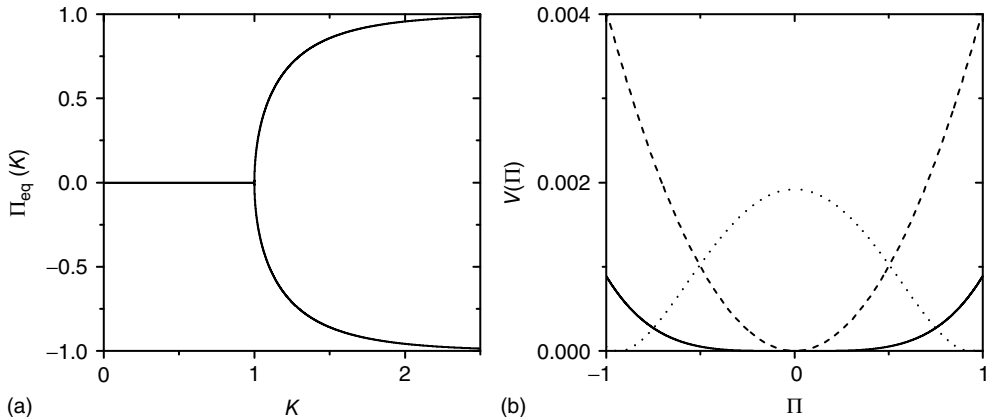


Figure 23.1 (a) The equilibrium mean field for different values of the cooperation parameter K . A bifurcation occurs at the critical point $K = K_c = 1$. (b) Potential barriers

for K subcritical (dashed line, $K = 0.2$), critical (solid line, $K = 1.0$), and supercritical (dotted line, $K = 1.8$).

where $f(t)$ is a random fluctuation, which according to the law of large numbers has an intensity proportional to $1/\sqrt{N}$. Inserting Eq. (23.12) into Eq. (23.10) yields

$$\frac{d}{dt}\Pi = \frac{g_0}{2} (e^{K\Pi} e^{Kf} - e^{-K\Pi} e^{-Kf}) - \frac{g_0}{2} (e^{K\Pi} e^{Kf} + e^{-K\Pi} e^{-Kf}) \Pi \quad (23.13)$$

and in the limiting case $N \rightarrow \infty$, the fluctuations vanish, $f = 0$, so that Eq. (23.13) generates the well-known phase-transition prediction at the critical value of the control parameter

$$K_c = 1 \quad (23.14)$$

Figure 23.1 shows that, for $K \leq 1$, the mean field has only one possible equilibrium value, $\Pi_{\text{eq}} = 0$. At the critical point $K = K_c = 1$, this vanishing equilibrium value splits into two opposite components, one positive and one negative. To understand the important role of criticality, we notice that a finite number of units generates the fluctuation f , and this, in turn, forces fluctuations in the mean field. At criticality, the fluctuations induced in $\Pi(t)$ have a relatively extended range of free evolution, as made clear in Figure 23.1. In fact, the separation between the two repulsive walls is greatest at criticality. In between them, a free diffusion regime occurs. The supercritical condition $K > K_c$ generates a barrier of higher and higher intensity with the increase of K . At the same time, the widths of the two wells shrink, bounding the free evolution regime of the fluctuating mean field to a smaller region.

23.2.1 Intermittency

Considering a large but finite number of units and expanding Eq. (23.13) to the lowest order contributions of Π and f , it is straightforward to prove that, for

either $K > 1$ or $K < 1$, due to conditions illustrated in Figure 23.1, the mean field fluctuations are driven by an ordinary Langevin equation of the form

$$\frac{d}{dt}x = -\Gamma x + \xi(t) \quad (23.15)$$

Note that, when $K > 1$

$$x(t) \equiv \Pi(t) - \Pi_{eq}(K) \quad (23.16)$$

where $\Pi_{eq}(K)$ denotes the equilibrium value for $N = \infty$. Of course, either at criticality or in the subcritical condition $\Pi_{eq}(K) = 0$, thereby making $x(t)$ coincide with $\Pi(t)$.

At the critical point $K = K_c = 1$, we find the time evolution of the mean field to be described by a nonlinear Langevin equation of the form

$$\frac{d}{dt}x = -\gamma x^3 + \xi(t) \quad (23.17)$$

The linear term that dominates in Eq. (23.15) vanishes identically, and the cooperation between units at criticality displays a remarkable change in behavior, which is characterized by the weakly repulsive walls of Fig. 23.1.

If we interpret the conditions $x > 0$ and $x < 0$ as corresponding to the light and dark states of blinking quantum dots [27], the DMM provides a satisfactory theoretical representation of this complex intermittent process. It was, in fact, noticed [27] that, if the survival probability $\Psi(t)$, namely the probability that a given state, either light or dark, survives for a time t after its birth, is evaluated beginning its observation at a time distance t_a from its birth, then its decay becomes slower (aging). Furthermore, this aging effect is not affected by randomly time-ordering the sequence of light and dark states. Notice that the aged curves of Figure 23.2 are actually doublets of survival probabilities generated by shuffled and non-shuffled sequences of states, thereby confirming the renewal nature of this process.

Figure 23.2 shows that the inverse power law region of the survival probability, corresponding to an inverse power law waiting-time distribution density with power law index $\mu = 1.5$, has a limited time range of validity. This limitation arises because Eq. (23.17) has an equilibrium distribution, generated by the confining action of the friction term. Thus, the upper time limit of the inverse power law waiting time distribution density is determined by the relation $t < T_{eq}$, with

$$T_{eq} \approx \left(\frac{1}{\gamma D} \right)^{\frac{1}{2}} \quad (23.18)$$

where the diffusion coefficient D is proportional to $1/N$. This theoretical prediction is obtained by means of straightforward dimensional arguments [28].

Notice that, in the traditional case of the ordinary Langevin equation, the restoring term $-\gamma x^3$ of Eq. (23.17) is replaced by $-\gamma x$ and $T_{eq} \approx 1/\gamma$, implying that at criticality the transient regime is $(\gamma/D)^{1/2}$ times larger than the conventional transition to equilibrium. Remember that we have assumed the number of interacting units

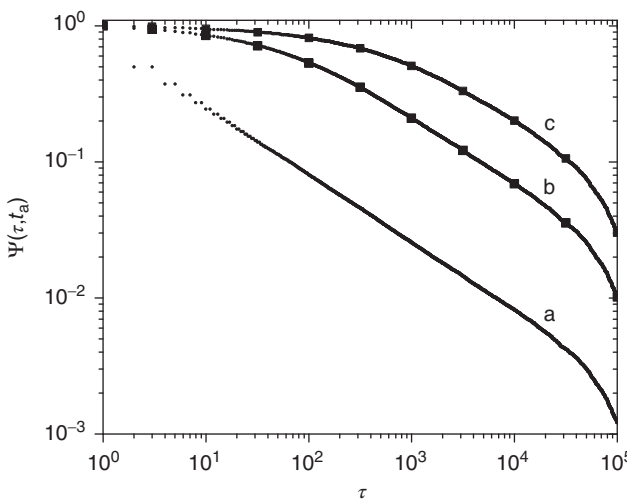


Figure 23.2 The t_a -aged survival probability of the mean field fluctuations x at criticality $K = 1$ for $N = 1000$ units and $g_0 = 0.01$. (a) $t_a = 0$, the power index $\mu - 1 = 0.5$. (b) $t_a = 100$. (c) $t_a = 1000$. The squares in (b)

and (c) correspond to the t_a -aged survival probability of randomly shuffled sequences of waiting times. Their equivalence to the non-shuffled aged survival probability indicates the fluctuations are renewal.

to be large but finite, thereby generating small fluctuations under the condition $D \ll \gamma$. As a consequence, the temporal complexity illustrated in Figure 23.2 becomes ostensible only at criticality, while remaining virtually invisible in both the subcritical and supercritical regimes.

Figure 23.3 illustrates an important dynamical property of criticality concerning the fluctuations emerging as a finite-size effect. We have to stress that the fluctuations, bringing important information about the network's complexity, are defined by Eq. (23.16). We define the equilibrium autocorrelation function of the variate x , $\Phi(\tau)$, as

$$\Phi(\tau) = \Phi(t, t') \equiv \frac{\langle x(t)x(t') \rangle}{\langle x^2 \rangle_{\text{eq}}} \quad (23.19)$$

with the time difference

$$\tau \equiv t - t' \quad (23.20)$$

Figure 23.3 shows the important property that, at criticality, the equilibrium correlation function is markedly slower than in both the supercritical and the subcritical regimes. This property has to be kept in mind to appreciate the principal difference between ordinary and extended criticality. In fact, this is an indication that, with ordinary criticality, the significant effects of cooperation correspond to a single value of K , this being the critical value $K = K_c = 1$.

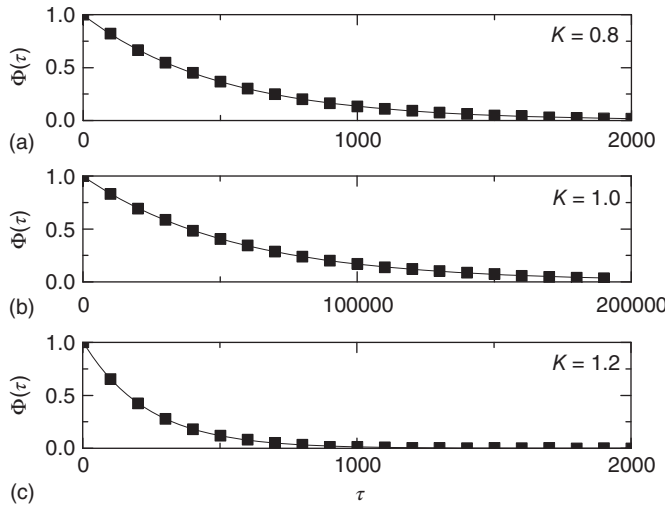


Figure 23.3 The equilibrium correlation function for the fluctuations x in the subcritical (a), critical (b), and supercritical (c) cases, each considering $N = 1000$ units with

$g_0 = 0.01$. The scale of the exponential decay is increased by two orders of magnitude at criticality.

23.2.2

Response to Perturbation

As far as the response to an external perturbation is concerned, it is important to address the issue of the connection with the phenomenon of complexity management [29]. We have noticed that, at criticality, the fluctuation in sign $\eta \equiv x/|x|$ is not ergodic for $t < T_{\text{eq}}$, thereby implying that the transmission of information from one network to another may require a treatment going beyond the traditional Green–Kubo approach. To recover the important results of Ref. [29], we should adopt a dichotomous representation fitting the nature of the DMM units that have to choose between the two states + and -. To simplify the numerical calculations, we assume that the influence of an external stimulus on the system is described by Eq. (23.21). This is a simplified picture that does not take into account that, in the case of flocks of birds [30], for instance, the single units make a decision based on the + or - sign of the stimulus rather than on its actual value. In other words, in the case of flocks [30], this would imply that the external stimulus assigns to each bird either the right or the left direction.

The perturbed time evolution of the mean field at criticality is described by

$$\frac{d}{dt}x = -\gamma x^3 + \xi(t) + \epsilon \gamma F(t) \quad (23.21)$$

where $F(t)$ is the external perturbation, and ϵ a small dimensionless number that will serve the purpose of ensuring the linear response condition. The factor of γ is introduced for dimensional reasons.

We note that, in the diffusional transient regime, which is much more extended in time than that generated by the traditional Langevin equation, Eq. (23.21) becomes

$$\frac{d}{dt}x(t) = \xi(t) + \epsilon\gamma F(t) \quad (23.22)$$

yielding the average response

$$\langle x(t) \rangle = \epsilon\gamma \int_0^t F(t') dt' \quad (23.23)$$

which, in the case where $F(t) = A\cos(\omega t)$, becomes

$$\langle x(t) \rangle = \frac{A\gamma\epsilon}{\omega} \sin(\omega t) \quad (23.24)$$

Taking into account that during the transient regime $\langle x^2(t) \rangle = 2Dt$, we immediately obtain

$$\langle \eta(t) \rangle \propto \frac{1}{t^{0.5}} A\epsilon\gamma \sin(\omega t) \quad (23.25)$$

in accordance with the experimental observation [31] that the response of a non-ergodic system to harmonic perturbation generates damped oscillations.

The rigorous treatment would lead to

$$\langle \eta(t) \rangle = \epsilon\gamma \int_0^t d\tau \chi(t, \tau) F(\tau) \quad (23.26)$$

where

$$\chi(t, \tau) = -\frac{d}{dt}\Psi(t, \tau) \quad (23.27)$$

and $\Psi(t, \tau)$ is the aged survival probability [28].

As a consequence, we predict that, at criticality, the complex network obeys the principle of complexity management [29] when all the units are weakly perturbed by an external stimulus. The chapter of West *et al.* [5] in this volume shows that, because of cooperation, a strong perturbation on a limited number of units is the source of the related phenomenon of *CI synchronization*, which in this chapter we show to emerge also at the level of neural EC, under the form of neural network entrainment.

23.3 Neural Dynamics

The cooperation of units within the DMM at criticality generates the temporal complexity illustrated by Figure 23.2, which turns out to be a source of information transport. This transfer of information is especially convenient as shown in the recent work of Vanni *et al.* [30]. This cooperation property yields the surprising effect of the crucial role of committed minorities discussed in this volume by West *et al.* [5].

In this section, we illustrate a very similar property generated by a model of neurophysiological interest, with the surprising discovery that these effects do not rest on a single value of the cooperation strength, that is, on the magnitude of the control parameter. This suggests the conjecture that a new form of criticality, called *extended criticality*, may be invoked [10, 11].

We show that the DMM leads to Plenz's avalanches [21], which are now a well-established property of neural networks. The model proposed in this chapter interprets the avalanches as a manifestation of cooperation. We also show that the amount of cooperation-generating avalanches is responsible for the phenomenon of entrainment.

23.3.1

Mittag–Leffler Function Model Cooperation

First of all, let us examine how the Mittag–Leffler function models relaxation. Metzler and Klafter [32] explain how the Mittag–Leffler function established a compromise between two apparently conflicting complexity schools, the advocates of inverse power laws and the advocates of stretched exponential relaxation, see also West *et al.* [33]. We denote with $\Psi(t)$ the survival probability, that is, the probability that no event occurs up to time t , and we assign to its Laplace transform, $\hat{\Psi}(u)$, the following form (we adopt the notation for the Laplace transform $\hat{f}(u) = \int_0^\infty dt \exp(-ut)f(\tau)$):

$$\hat{\Psi}(u) = \frac{1}{u + \lambda^\alpha(u + \Gamma_t)^{1-\alpha}} \quad (23.28)$$

with $\alpha < 1$. In the case $\Gamma_t = 0$, this is the Laplace transform of the Mittag–Leffler function [32], a generalization of the ordinary exponential relaxation which interpolates between the stretched exponential relaxation $\exp(-(\lambda t)^\alpha)$, for $t < 1/\lambda$ and the inverse power law behavior $1/t^\alpha$, for $t > 1/\lambda$.

Recent work [34] has revealed the existence of quakes within the human brain, and proved that the time interval between two consecutive quakes is well described by a survival probability $\Psi(t)$, whose Laplace transform fits very well the prescription of Eq. (23.28). The parameter $\Gamma_t > 0$ has been introduced [34, 35] to take into account the truncation which is thought to be a natural consequence of the finite size of the time series under study. As a matter of fact, when $1/\lambda$ is of the order of the time step and $1/\Gamma_t$ is much larger than the unit time step, the survival probability turns out to be virtually an inverse power law, whereas when $1/\lambda$ is of the order of $1/\Gamma_t$ and both are much larger than the unit time step, the survival probability turns out to be a stretched exponential function.

Failli *et al.* [35] illustrate the effect of establishing a cooperative interaction in the case of the random growth of surfaces. A growing surface is a set of growing columns whose height increases linearly in time with fluctuations, which, in the absence of cooperation, would be of Poisson type. The effect of cooperative interaction is to turn the Poisson fluctuations into complex fluctuations, the interval between two consecutive crossings of the mean value being described by an inverse

power law waiting time distribution $\psi(t)$, corresponding to a survival probability $\Psi(t)$, whose Laplace transform is given by Eq. (23.28). In conclusion, according to the earlier work [35], we interpret $\alpha < 1$ as a manifestation of the cooperative nature of the process.

In this section, we illustrate a neural model where the time interval between two consecutive firings, in the absence of cooperation, is described by an ordinary exponential function, thereby corresponding to $\alpha = 1$. The effect of cooperation is to make α decrease in a monotonic way, when increasing the cooperation strength, K , with no special critical value.

We note that Barabasi [36] stressed the emergence of the inverse power law behavior, properly truncated, as a consequence of the cooperative nature of human actions. Here we interpret the emergence of the Mittag-Leffler function structure as an effect of the cooperation between neurons. The emergence of a stretched exponential function confirms this interpretation if we adopt an intuitive explanation of it based on the distinction between the attempt to cooperate and to succeed. The action generator is assumed to not be fully successful, and a success rate parameter $P_S < 1$ is introduced with the limiting condition $P_S = 1$ corresponding to full success. To turn this perspective into a theory, yielding the theoretical prediction of Eq. (23.28), we assume that the time interval between two consecutive cooperative actions is described by the function $\psi^{(S)}(\tau)$, where the superscript (S) indicates that, from a formal point of view, we realize a process corresponding to subordination theory [37–41]. Here we make the assumption that the survival probability for an action, namely the probability that no action occurs up to a time t after an earlier action, has the form

$$\Psi^{(S)}(t) = \left(\frac{T_S}{t + T_S} \right)^\alpha \quad (23.29)$$

with

$$\alpha = \mu_S - 1 \quad (23.30)$$

and

$$\mu_S < 2 \quad (23.31)$$

As a consequence, the time interval between two consecutive actions has the distribution density $\psi^{(S)}(t)$ of the form

$$\psi^{(S)}(\tau) = (\mu_S - 1) \frac{T_S^{\mu_S - 1}}{(\tau + T_S)^{\mu_S}}. \quad (23.32)$$

Note that the distance between two actions is assumed to depart from the condition of ordinary ergodic statistical mechanics. In fact, the mean time distance τ between two consecutive actions emerging from the distribution density of Eq. (23.32) is

$$\langle \tau \rangle = \frac{T_S}{\mu_S - 2} \quad (23.33)$$

for $\mu_S > 2$ and diverges for $\mu_S \leq 2$. As a consequence, this process shares the same non-ergodic properties as those generated by human action [36].

It is evident that, when $P_S = 1$, the survival probability $\Psi(\tau)$ is equal to $\Psi^{(S)}(\tau) = \int_{\tau}^{\infty} \psi^{(S)}(\tau') d\tau'$. When, $P_S < 1$, using the formalism of the subordination approach [34, 35, 37–39], we easily prove that the Laplace transform of $\Psi(\tau)$ is given by

$$\hat{\Psi}(u) = \frac{1}{u + P_S \hat{\Phi}(u)} \quad (23.34)$$

where

$$\hat{\Phi}(u) = \frac{u \hat{\psi}^{(S)}(u)}{1 - \hat{\psi}^{(S)}(u)} \quad (23.35)$$

To prove the emergence of the Mittag–Leffler function of Eq. (23.28), with $\Gamma_t = 0$, from this approach, let us consider for simplicity the case where $\psi^{(S)}(\tau)$ is not truncated. In the non-ergodic case $\mu_S < 2$, using the Laplace transform method [33], we obtain that the limiting condition $u \rightarrow 0$ yields Eq. (23.28) with

$$\lambda = \left[\frac{P_S}{T_S^\alpha \Gamma(1-\alpha)} \right]^{\frac{1}{\alpha}} \quad (23.36)$$

where $\Gamma(1-\alpha)$ is the Gamma function. Note that when $P_S = 1$, the Laplace transform of Eq. (23.34) in the limit of $u \rightarrow 0$ coincides, as it must, with the Laplace transform of $\Psi^{(S)}(t)$. In conclusion, we obtain

$$\hat{\Psi}(u) = \frac{1}{u + \lambda^\alpha u^{1-\alpha}} \quad (23.37)$$

with

$$\lambda^\alpha \propto P_S \quad (23.38)$$

In the neural model illustrated here, we define a parameter of cooperation effort, denoted, as in the DMM case, by the symbol K . The success of cooperation effort is measured by the quantity

$$g(K) = \lambda(K)^{\alpha(K)} \quad (23.39)$$

We determine that the sign of success is given by the number of neurons firing at the same time. We speculate that there is a connection with the dragon kings [42, 43] and coherence potentials [8].

23.3.2

Cooperation Effort in a Fire-and-Integrate Neural Model

The NFC model refers to the interaction between N neurons, each of which has a time evolution described by

$$x(t+1) = (1 - \gamma)x(t) + S + \sigma\xi(t) \quad (23.40)$$

where t is a natural number; $\xi(t)$ is a variable getting either the value of 1 or of -1 , with equal probability, with no memory of the earlier values; and $\gamma \ll 1$

so as to make the integer time virtually continuous when $\gamma t \approx 1$. The quantity σ is the noise intensity. The quantity $S > 0$ serves the purpose of making the potential x essentially increase as a function of time. The neuron potential x moves from the initial condition $x = 0$ and, through fluctuations around the deterministic time evolution corresponding to the exact solution of the case $\sigma = 0$ [44], reaches the threshold value $x = 1$. When the threshold is reached, it fires and resets back to the initial value $x = 0$. It is straightforward to prove that the variable x can reach the threshold only when the condition

$$\frac{S}{\gamma} > 1 \quad (23.41)$$

applies. In this case, the time necessary for the neuron to reach the threshold, called T_p , is given by

$$T_p = \frac{1}{\gamma} \ln \left(\frac{1}{1 - \frac{\gamma}{S}} \right) \quad (23.42)$$

In the absence of interaction, the motion of each neuron is periodic, and the interval between two consecutive firings of the same neuron is given by T_p . The real sequence of firings looks random, as a consequence of the assumption that the initial conditions of N neurons are selected randomly. In this case, the success rate g is determined by the random distribution of initial conditions and can be very small, as we subsequently show.

The cooperative properties of the networks are determined as follows. Each neuron is the node of a network and interacts with all the other nodes linked to it. When a neuron fires, all the neurons linked to it make an abrupt step ahead of intensity K . This is the cooperation parameter, or intensity strength. An inhibition link is introduced by assuming that, when one neuron fires, all the other neurons linked to it through inhibition links make an abrupt step backward.

This model is richly structured and may allow us to study a variety of interesting conditions. There is widespread conviction that the efficiency of a network, namely its capacity to establish global cooperative effects, depends on network topology, as suggested by the brain behavior [34, 45]. The link distribution itself, rather than being fixed in time, may change according to the Hebbian learning principle [16]. It is expected [16] that such learning generates a scale-free distribution, thereby shedding light on the interesting issue of burst leaders [46].

All these properties are studied elsewhere. In this chapter, we focus on cooperation by assuming that all the links are excitatory. To further emphasize the role of cooperation, we should make the ATA assumption adopted by Mirolo and Strogatz [44]. This assumption was also made in earlier work [47]. In spite of the fact that the efficiency of the ATA model is reduced by the action of the stochastic force $\xi(t)$ which weakens the action of cooperation, thereby generating time complexity, the ATA condition generates the maximal efficiency and neuronal avalanches. However, this condition inhibits the realization of an important aspect of cooperation, namely locality breakdown. For this reason, in addition to the ATA condition, we also study the case of a regular, two-dimensional (2D) network,

where each node has four nearest neighbors and consequently four links. It is important to stress that, to make our model as realistic as possible, we should introduce a delay time between the firing of a neuron and the abrupt step ahead of all its nearest neighbors. This delay should be assumed to be proportional to the Euclidean distance between the two neurons, and it is expected to be a property of great importance to prove the breakdown of locality when the scale-free condition is adopted. The two simplified conditions studied in this chapter, ATA and 2D, would not be affected by a time delay, which should be the same for all the links. For this reason, we do not further consider time delay.

For the cooperation strength, we must assume the condition

$$K \ll 1 \quad (23.43)$$

When K is of the order of magnitude of the potential threshold $V_T = 1$, the collective nature of cooperation is lost because the firing of a few neurons causes an abrupt cascade in which all the other neurons fire. Thus, we do not consider to be important the non-monotonic behavior of network efficiency which our numerical calculations show to emerge by assigning K values of the same order as the potential threshold.

We also note that, in the case of this model, the breakdown of the Mittag–Leffler structure, at large times, is not caused by a lack of cooperation but by the excess of cooperation. To shed light on this fact, keep in mind that this model has been solved exactly by Mirollo and Strogatz when $\sigma = 0$ [44]. In this case, even if we adopt initial random conditions, after a few steps, all the neurons fire at the same time, and the time distance between two consecutive firings is given by T_p of Eq. (23.42). As an effect of noise, the neurons can also fire at times $t \ll T_p$, and consequently, setting $\sigma > 0$, a new, and much shorter timescale is generated. When we refer to this as *the timescale of interest*, the Mirollo and Strogatz time T_p plays the role of a truncation time and

$$\Gamma_t \approx \frac{1}{T_p} \quad (23.44)$$

To examine this condition, let us assign to K a value very close to $K = 0$. In this case, even if we assign to all the neurons the same initial condition, $x = 0$, because of the presence of stochastic fluctuations, the neurons fire at different times, thereby creating a spreading on the initial condition that tends to increase in time, even if initially the firing occurs mainly at times $t = nT_p$. The network eventually reaches a stationary condition with a constant firing rate G given by

$$G = \frac{N}{\langle \tau \rangle} \quad (23.45)$$

where $\langle \tau \rangle$ denotes the mean time between two consecutive firings of the same neuron. For $\sigma \ll 1$, $\langle \tau \rangle = T_{MS}$. From the condition of a constant rate G , we immediately derive the Poisson waiting-time distribution

$$\psi(\tau) = G \exp(-G\tau) \quad (23.46)$$

Consequently, this heuristic argument agrees very well with numerical results.

We consider a set of N identical neurons, each of which obeys Eq. (23.40), and we also assume, with Miroollo and Strogatz [44], that the neurons cooperate. For the numerical simulation, we select the condition

$$G \ll 1 \ll N \ll T_p \quad (23.47)$$

As a consequence of this choice, we obtain

$$\frac{1}{G} \approx \frac{T_p}{N} \ll T_p \quad (23.48)$$

thereby realizing the earlier mentioned timescale separation. It is evident that this condition of the noninteracting neuron fits Eq. (23.28) with $\alpha = 1$ and

$$\lambda(K=0) = G \quad (23.49)$$

In this case, the time truncation is not perceived because of the condition $1/G \ll T_p$.

In Figure 23.4, we show that the 2D condition is essentially equivalent to the ATA condition, provided that the cooperation strength is assumed to be an order of magnitude larger than that of the ATA condition. This is an important result, because in the case of a two-dimensional regular lattice, even though the neurons interact only with their nearest neighbors, the entire network generates the same sequence of bursts as in the ATA condition, provided that K is an order of magnitude larger. This is an indication of the fact that, when the critical values of K are used, two neurons become closely correlated regardless of the Euclidean length of their link, which is a clear manifestation of locality breakdown.

As far as the Mittag–Leffler time complexity is concerned, we adopt the same fitting procedure as that used in Ref. [47]. We evaluate the Laplace transform of the experimental $\Psi(t)$, and use as a fitting formula Eq. (23.28) with $\Gamma_t = 0$, to find the parameter α . Then we fit the short-time region with the stretched exponential

$$\Psi(t) = \exp(-(\lambda t)^\alpha) \quad (23.50)$$

to find λ . We determine that, in the 2D condition as in the ATA condition, switching on cooperation has the effect of generating the Mittag–Leffler time complexity. From Figure 23.5, we see that any nonvanishing value of K turns the Poisson condition $\alpha = 1$ into the Mittag–Leffler temporal complexity $\alpha < 1$. The only remarkable difference is that, in the case of large cooperation strength, the value of α tends to the limiting value of 0.2, whereas the ATA condition brings it to the limiting value of 0.6. Statistical analysis of data from real experiments may use this property to assess the topology of the neural network. It is expected, in fact, that all network topologies generate the Mittag–Leffler time complexity, but the actual value of α depends on the network topology. Thus, the joint use of theory and experiment may further our understanding of the neural network structure.

It is interesting to notice that Figure 23.6, in accordance with our expectation [see Eq. (23.39)], shows that the success rate undergoes a significant increase at the value of the cooperation parameter K at which a distinctly Mittag–Leffler survival probability emerges.

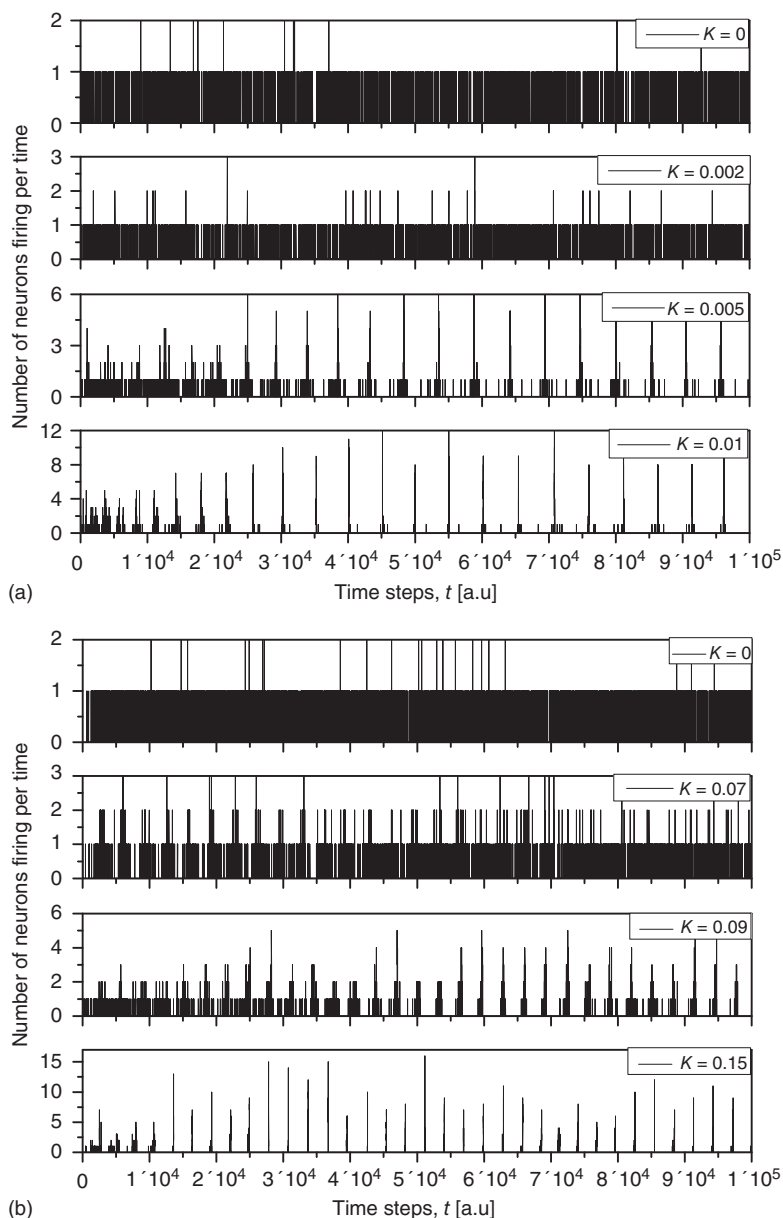


Figure 23.4 The number of neurons firing per unit of time in the ATA (a) and 2D (b) conditions for K ranging from no cooperation to a high level of cooperation. When increasing the value of K , the system immediately departs from a Poisson process at

$K = 0$ to display complex cooperative behavior, which then becomes strongly periodic for large K . The 2D condition shares the behavior of the ATA condition, only requiring more cooperation.

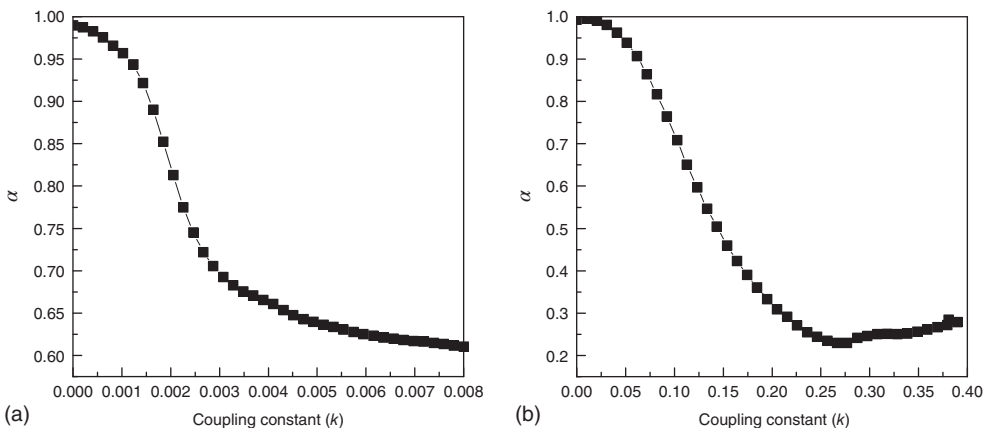


Figure 23.5 The value of the Mittag–Leffler parameter α for different cooperation levels in the ATA (a) and 2D (b) conditions. For any nonzero K , $\alpha < 1$, signifying Mittag–Leffler temporal complexity.

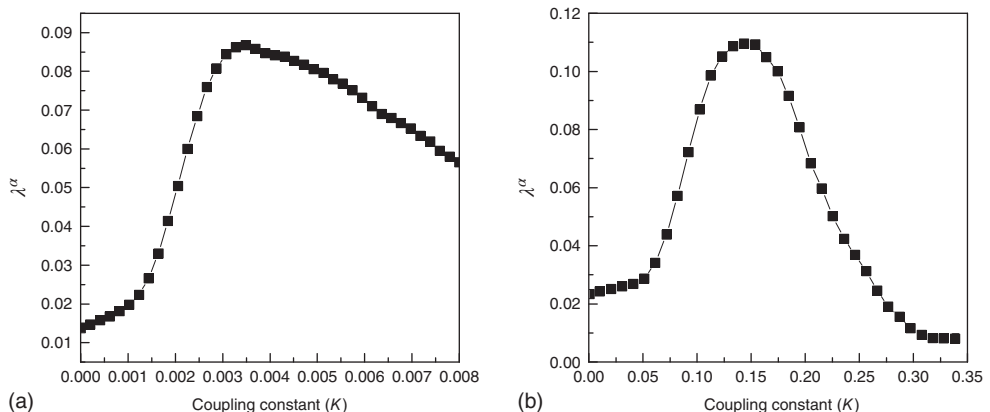


Figure 23.6 The value of the Mittag–Leffler parameter λ^α for different cooperation levels in the ATA (a) and 2D (b) conditions. In both cases, the success rate significantly

increases at the values of the cooperation strength, making $\Psi(t)$ depart from the condition of stretched exponential relaxation.

23.4 Avalanches and Entrainment

Neurophysiology is a field of research making significant contributions to the progress of the science of complexity. Sornette and Ouillon [42], who are proposing the new concept of dragon kings to go beyond the power law statistics shared by physical, natural, economic, and social sciences, consider the neural avalanches found by Plenz [21] to be a form of extreme events that are not confined to neurophysiology and may show up also at the geophysical and economic level. The

increasing interest in neural avalanches is connected to an effort to find a proper theoretical foundation, for which self-organized criticality [3] is a popular candidate, in spite of a lack of a self-contained theoretical derivation.

On the other hand, neurophysiology is challenging theoreticians with the well-known phenomenon of *neural entrainment*. At first sight, the phenomenon of neural entrainment, which is interpreted as the synchronization of the dynamics of a set of neurons with an external periodic signal, may be thought to find an exhaustive theoretical foundation in the field of chaos synchronization [48]. This latter phenomenon has attracted the attention of many scientists in the last 22 years since the pioneering paper by Pecora and Carroll [49]. However, this form of synchronization seems to be far beyond the popular chaos synchronization. According to the authors of Ref. [50], the auditory cortex neurons, under the influence of a periodic external signal, are entrained with the stimulus in such a way as to be in the excitatory phase when the stimulus arrives, in order to process it in the most efficient way [50]. The work of neurophysiologists [51] is, on one hand, a challenge for physicists because the experimental observation should force them to go beyond the conventional theoretical perspective of coupled oscillators, combining regular oscillations with irregular network activity while establishing a close connection with the ambitious issue of cognition [52]. Setting aside the latter, we can limit ourselves to noticing with Gross and Kowalski [6] that the entrainment between different channels of the same networks is due to excitatory synapses and consequently to neuron cooperation, rather than to the behavior of single neurons that never respond in the same way to the same stimulus.

Neural entrainment, on the contrary, is a global property of the whole network which is expected to generate the same response to the same stimulus. In this sense, it has a close similarity with the phenomenon of chaos synchronization, insofar as entrainment is a property of a single realization. The phenomenon of complexity management [29], on the other hand, requires averages over many responses to the same stimulus to make evident the correlation that an experimentalist may realize between response and stimulus, after designing the stimulus, so as to match the complexity of the system.

Our theoretical model generates both avalanches and entrainment, thereby making clear that the phenomenon of neural entrainment is quite different from that of chaos synchronization, in spite of the fact that it shares with the latter the attractive property of being evident at the level of single realizations. Figure 23.7 depicts an avalanche, with the typical power index of $\alpha = 1.5$, generated by the theoretical model of this chapter, in the case of a two-dimensional regular lattice, with $K = 0.125$, a strong cooperation value, corresponding to the realization of a sequence of well defined bursts, as illustrated in Figure 23.4.

As a phenomenon of entrainment we have in mind that of the pioneering work of Ref. [23]. These authors generated a condition of maximal cooperation by chemically killing the inhibitory links, and using as a stimulus a periodic electrical stimulation. The entrainment of two 2D neural network models is shown in Figure 23.8. Here we replace the periodic external stimulation with a neural network P identical to the perturbed neural network S . In addition, we assume

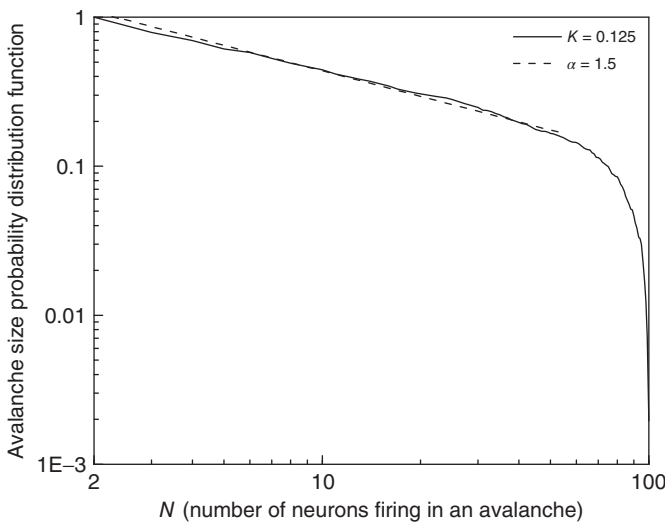


Figure 23.7 The avalanche size distribution in the 2D condition with cooperation $K = 0.125$. The slope of the distribution is given by the power index $\alpha = 1.5$.

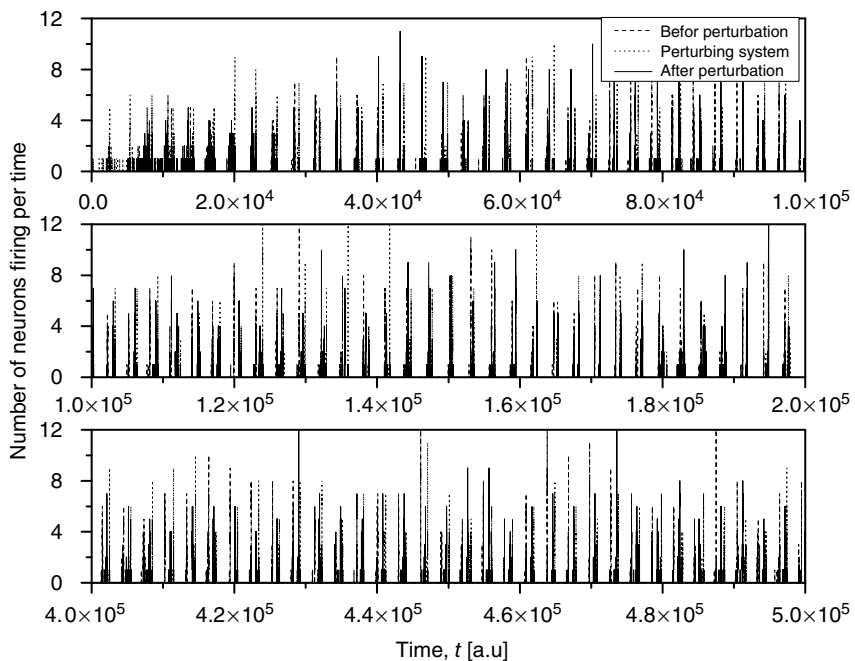


Figure 23.8 The entrainment of the 2D neural network S (dashed lines) to an identical neural network P (dotted lines) through the forced perturbation of 3% of the nodes of

S . The avalanches of the perturbed network S (solid lines) become synchronized to the perturbing network P .

that only 3% of the nodes of S are forced to fire at the same time as the neurons of the network P . This is a condition similar to that adopted elsewhere [30], with the 3% of nodes of S playing the same roles as the lookout birds [30]. These “look out” neurons are also similar to the committed minorities [5] used to realize the phenomenon of CI synchronization.

23.5

Concluding Remarks

There is a close connection between avalanches and neural entrainment. Criticality plays an important role to establish this connection, because, as is well known in the field of phase transition, at criticality, as an effect of long-range correlation, the limiting condition of local interaction is lost, and an efficient interaction between units that would not be correlated in the absence of cooperative interaction is established. This condition is confined to criticality, thereby implying that “intelligent” systems operate at criticality. Quite surprisingly, the model of neural dynamics illustrated in this chapter generates long-range interactions, so as to realize entrainment, for a wide range of values of K . This seems to be the EC advocated by Longo and coworkers [10, 11].

What is the relation between these properties and the emergence of consciousness which, according to Werner [13], must be founded on RGT? A theory as rigorous as RGT should be extended to the form of criticality advocated by Longo and coworkers [10, 11], and this may be a difficult issue making it more challenging, but not impossible, to realize the attractive goal of Werner [13]. Werner found it very promising to move along the lines outlined by Allegrini and coworkers [25] with their discovery that an intermittent behavior similar to that of Figure 23.2, with $\mu = 2$, may reflect cognition.

A promising but quite preliminary result is that of Ref. [24]. Making the assumption that cognition enters into play, with the capability of making choices generated by the intelligent observation of the decision made by the whole system, and moving along the lines that led us to Eq. (23.17), the authors of Ref. [24] found the following equation:

$$\frac{d}{dt}x = -\frac{\gamma}{x} + f(t) \quad (23.51)$$

which generates an intermittent process with $\mu = 2$, as illustrated in Ref. [24]. We think that this results suggests two possible roads, both worthy of investigation.

The first way to realize this ambitious purpose is based on a model similar to the DMM. The units cooperate through a structure similar to that of Eqs. (23.1 – 23.4). A given unit may make its decision on the basis of the history of the units linked to it rather than on their state at the time at which it makes its decision. This may be a dramatic change, with the effect of generating complexity for an extended range of the control parameter.

The second way is based on a model similar to the NFC model, namely the cooperative neuron model, where each unit, in the absence of cooperation, is

driven by Eq. (23.40). In this model, each unit has a time evolution that depends on the earlier history of the units linked to it, thereby fitting the key condition of earlier work [24]. To proceed along these lines we should settle a still open problem. The condition $\alpha = 1$, where the Mittag–Leffler function obtained from the inverse Laplace transform of Eq. (23.37) becomes an ordinary exponential function, is a singularity where the waiting-time distribution density $\psi(t)$, with index $\mu = 2$, may be abruptly replaced by a fast decaying function, an inverse power law with index $\mu > 2$, and, in principle, also by an exponential function. From an intuitive point of view, this weird condition may be realized by curves of the type of those of Figure 23.5, with the parameter $\alpha = 1$ ($\mu = 2$) remaining unchanged for an extended range of K values. In other words, $[(d/dK)\alpha(K)]_{K=0} = 0$. It is important to notice that the statistical analysis made by the authors of Ref. [53] to associate cognition with $\mu = 2$ is based on observing the rapid transition processes (RTPs) occurring in electroencephalography (EEG) monitoring different brain areas. These authors define the simultaneous occurrence of two or more RTPs as crucial events and determined that the waiting-time distribution density $\psi(\tau)$, where τ is the time interval between two consecutive crucial events, is characterized by $\mu \approx 2$. This suggests that the authors of Ref. [53] had in mind a cooperation model similar to the NFC model of this chapter, thereby making plausible our conjectures that a connection can be established between the DMM and NFC models of this chapter and the cognition model [24].

In spite of conceptual and technical difficulties that must be surpassed to achieve the important goal of Werner [13], we share his optimistic view [15]: “On account of this, self-similarity in neural organizations and dynamics poses one of the most intriguing and puzzling phenomenon, with potentially immense significance for efficient management of neural events on multiple spatial and temporal scales.”

References

1. Beggs, J.M. and Plenz, D. (2003) Neuronal avalanches in neocortical circuits. *J. Neurosci.*, **23** (35), 11–167.
2. Touboul, J. and Destexhe, A. (2010) Can power-law scaling and neuronal avalanches arise from stochastic dynamics? *PLoS One*, **5** (2), e8982.
3. de Arcangelis, L. and Herrmann, H. (2012) Activity-dependent neuronal model on complex networks. *Front. Physiol.*, **3**, 62.
4. Li, X. and Small, M. (2012) Neuronal avalanches of a self-organized neural network with active-neuron-dominant structure, *arXiv preprint arXiv:1204.6539*.
5. West, B., Turalska, M., and Grigolini, P. (2013) *Complex Networks: From Social Crises to Neuronal Avalanches, in this Volume*, John Wiley & Sons.
6. Gross, G. and Kowalski, J. (1999) Origins of activity patterns in self-organizing neuronal networks in vitro. *J. Intell. Mater. Syst. Struct.*, **10** (7), 558–564.
7. Chialvo, D. (2010) Emergent complex neural dynamics. *Nat. Phys.*, **6** (10), 744–750.
8. Plenz, D. (2012) Neuronal avalanches and coherence potentials. *Eur. Phys. J.-Spec. Top.*, **205** (1), 259–301.
9. Stanley, H. (1971) Introduction to phase transitions and critical phenomena, *Introduction to Phase Transitions and Critical Phenomena*, Clarendon Press.

10. Bailly, F. and Longo, G. (2011) *Mathematics and the Natural Sciences: The Physical Singularity of Life*, Imperial College Press, Singapore.
11. Longo, G. and Montévil, M. (2012) The inert vs. the living state of matter: extended criticality, time geometry, anti-entropy—an overview. *Front. Physiol.*, **3**, 39.
12. Montroll, E. (1981) On the dynamics of the ising model of cooperative phenomena. *Proc. Natl. Acad. Sci. U.S.A.*, **78** (1), 36–40.
13. Werner, G. (2013) Consciousness viewed in the framework of brain phase space dynamics, criticality, and the renormalization group. *Chaos, Solitons & Fractals*, **55**, 3–12.
14. Werner, G. (2007) Metastability, criticality and phase transitions in brain and its models. *Biosystems*, **90** (2), 496–508.
15. Werner, G. (2011) Letting the brain speak for itself. *Front. Physiol.*, **2**, 60.
16. Turalska, M., Geneston, E., West, B., Allegrini, P., and Grigolini, P. (2012) Cooperation-induced topological complexity: a promising road to fault tolerance and hebbian learning. *Front. Physiol.*, **3**, 52.
17. Fraiman, D., Balenzuela, P., Foss, J., and Chialvo, D. (2009) Ising-like dynamics in large-scale functional brain networks. *Phys. Rev. E*, **79** (6), 061–922.
18. Green, M. (1954) Markoff random processes and the statistical mechanics of time-dependent phenomena. II. Irreversible processes in fluids. *J. Chem. Phys.*, **22**, 398.
19. Kubo, R. (1957) Statistical-mechanical theory of irreversible processes. i. general theory and simple applications to magnetic and conduction problems. *J. Phys. Soc. Jpn.*, **12** (6), 570–586.
20. Turalska, M., Lukovic, M., West, B., and Grigolini, P. (2009) Complexity and synchronization. *Phys. Rev. E*, **80** (2), 021–110.
21. Klaus, A., Yu, S., and Plenz, D. (2011) Statistical analyses support power law distributions found in neuronal avalanches. *PloS One*, **6** (5), e19–779.
22. Gerstner, W. and Kistler, W. (2002) *Spiking Neuron Models: Single Neurons, Populations, Plasticity*, Cambridge university press.
23. Gross, G., Kowalski, J., and Rhoades, B. (1999) Spontaneous and evoked oscillations in cultured mammalian neuronal networks, in *Oscillations in Neural Systems*, Vol. 1, (eds D. Levine, V. Brown, and T. Shirey), Erlbaum Associates, New York, pp. 3–29.
24. Palatella, L. and Grigolini, P. (2012) Noise-induced intermittency of a reflexive model with symmetry-induced equilibrium. *Physica A*, **391** (23), 5900–5907.
25. Allegrini, P., Menicucci, D., Bedini, R., Gemignani, A., and Paradisi, P. (2010) Complex intermittency blurred by noise: theory and application to neural dynamics. *Phys. Rev. E*, **82** (1), 015–103.
26. Bianco, S., Geneston, E., Grigolini, P., and Ignaccolo, M. (2008) Renewal aging as emerging property of phase synchronization. *Physica A*, **387** (5), 1387–1392.
27. Bianco, S., Grigolini, P., and Paradisi, P. (2005) Fluorescence intermittency in blinking quantum dots: Renewal or slow modulation?, *J. Chem. Phys.*, **123** (17), 174704 (1–10).
28. Svenkeson, A., Bologna, M., and Grigolini, P. (2012) Linear response at criticality. *Phys. Rev. E*, **86** 041145(1–10).
29. Aquino, G., Bologna, M., Grigolini, P., and West, B. (2010) Beyond the death of linear response: 1/f optimal information transport. *Phys. Rev. Lett.*, **105** (4), 40–601.
30. Vanni, F., Luković, M., and Grigolini, P. (2011) Criticality and transmission of information in a swarm of cooperative units. *Phys. Rev. Lett.*, **107** (7), 78–103.
31. Allegrini, P., Bologna, M., Fronzoni, L., Grigolini, P., and Silvestri, L. (2009a) Experimental quenching of harmonic stimuli: universality of linear response theory. *Phys. Rev. Lett.*, **103** (3), 30–602.
32. Metzler, R. and Klafter, J. (2002) From stretched exponential to inverse power-law: fractional dynamics, Cole–Cole relaxation processes, and beyond. *J. Non-Cryst. Solids*, **305** (1), 81–87.

33. West, B., Bologna, M., and Grigolini, P. (2003) *Physics of Fractal Operators*, Springer.
34. Bianco, S., Ignaccolo, M., Rider, M., Ross, M., Winsor, P., and Grigolini, P. (2007) Brain, music, and non-poisson renewal processes. *Phys. Rev. E*, **75** (6), 061–911.
35. Failla, R., Grigolini, P., Ignaccolo, M., and Schwettmann, A. (2004) Random growth of interfaces as a subordinated process. *Phys. Rev. E*, **70** (1), 010–101.
36. Barabasi, A. (2005) The origin of bursts and heavy tails in human dynamics. *Nature*, **435** (7039), 207–211.
37. Sokolov, I. (2000) Lévy flights from a continuous-time process. *Phys. Rev. E*, **63** (1), 011–104.
38. Barkai, E. and Silbey, R. (2000) Distribution of variances of single molecules in a disordered lattice. *J. Phys. Chem. B*, **104** (2), 342–353.
39. Metzler, R. and Klafter, J. (2000) From a generalized Chapman-Kolmogorov equation to the fractional Klein-Kramers equation. *J. Phys. Chem. B*, **104** (16), 3851–3857.
40. Gorenflo, R., Mainardi, F., and Vivoli, A. (2007) Continuous-time random walk and parametric subordination in fractional diffusion. *Chaos, Solitons & Fractals*, **34** (1), 87–103.
41. Sokolov, I. and Klafter, J. (2005) From diffusion to anomalous diffusion: a century after einstein's brownian motion. *Chaos*, **15**, 026103–026109.
42. Sornette, D. and Ouillon, G. (2012) Dragon-kings: mechanisms, statistical methods and empirical evidence. *Eur. Phys. J.-Spec. Top.*, **205** (1), 1–26.
43. Werner, T., Gubiec, T., Kutner, R., and Sornette, D. (2012) Modeling of super-extreme events: an application to the hierarchical weierstrass-mandelbrot continuous-time random walk. *Eur. Phys. J.-Spec. Top.*, **205** (1), 27–52.
44. Mirolo, R. and Strogatz, S. (1990) Synchronization of pulse-coupled biological oscillators. *SIAM J. Appl. Math.*, **50** (6), 1645–1662.
45. Kim, B. (2004) Geographical coarse graining of complex networks. *Phys. Rev. Lett.*, **93** (16), 168–701.
46. Ham, M., Bettencourt, L., McDaniel, F., and Gross, G. (2008) Spontaneous coordinated activity in cultured networks: analysis of multiple ignition sites, primary circuits, and burst phase delay distributions. *J. Comput. Neurosci.*, **24** (3), 346–357.
47. Lovecchio, E., Allegrini, P., Geneston, E., West, B., and Grigolini, P. (2012) From self-organized to extended criticality. *Front. Physiol.*, **3**, 98.
48. Pikovsky, A., Rosenblum, M., and Kurths, J. (2003) *Synchronization: A Universal Concept in Nonlinear Sciences*, Vol. 12, Cambridge University Press.
49. Pecora, L. and Carroll, T. (1990) Synchronization in chaotic systems. *Phys. Rev. Lett.*, **64** (8), 821–824.
50. Schroeder, C. and Lakatos, P. (2009) Low-frequency neuronal oscillations as instruments of sensory selection. *Trends Neurosci.*, **32** (1), 9–18.
51. Wang, X. (2010) Neurophysiological and computational principles of cortical rhythms in cognition. *Physiol. Rev.*, **90** (3), 1195–1268.
52. Dehaene, S. and Changeux, J. (2011) Experimental and theoretical approaches to conscious processing. *Neuron*, **70** (2), 200–227.
53. Allegrini, P., Menicucci, D., Bedini, R., Fronzoni, L., Gemignani, A., Grigolini, P., West, B., and Paradisi, P. (2009b) Spontaneous brain activity as a source of ideal 1/f noise. *Phys. Rev. E*, **80** (6), 061–914.

24

Complex Networks: From Social Crises to Neuronal Avalanches

Bruce J. West, Małgorzata Turalska, and Paolo Grigolini

24.1 Introduction

Complex networks ranging from social gatherings to neuron clusters are described by highly heterogeneous, scale-free degree distributions [1, 2]. The seminal paper of Watts and Strogatz [3] established that real-world networks are distinct from the totally random theoretical networks of Erdős and Renyi [4]. The latter investigators established that networks with completely random connections have unimodal distributions of connections between elements. Real-world networks, on the other hand, are found not to be characterized by such weak clustering and, instead, show surprisingly large clustering coefficients. Several mechanisms have been proposed to explain the observed topology [1, 2, 5–8], the most popular one being that of preferential attachment, which is based on the assumption that scale-free networks grow in time and that the newly arriving elements tend to establish connections preferentially with the elements having the larger number of links [1, 5]. However, there exists a wide class of networks that do not originate by preferential attachment or growth, and the model presented here catalogs the properties of these latter networks.

Two central concepts arising in the application of dynamic networks to the understanding of the measurable properties of the brain have to do with topology and criticality. Topology is related to the inverse power-law distributions of such newly observed phenomena as neuronal avalanches [9], and criticality [2] has to do with the underlying dynamics that gives rise to the observed topology. Criticality was first systematically observed in physics for systems undergoing phase transitions as a control parameter is varied: for example, as temperature is lowered, water transitions from the liquid to the solid phase. Many physical systems consisting of a large number of structurally similar interacting units have properties determined by local interactions. At the critical value of the control parameter, the interactions suddenly change from local to long-range, and what had been the superposition of independent dynamic elements becomes dominated by long-range interactions and coordinated activity. The dynamical source of these properties is made explicit through the development of the decision-making model

(DMM), which is shown to be related to but distinctly different from the Ising model used by others in explaining criticality in the context of the brain.

Here, we present a way to generate topology characterized by the scale-free degree distribution $P(k) \propto k^{-\nu}$, where k is the number of links to an element, using the underlying network dynamics. We confirm that the scale-free topology emerges from the dynamical interactions between the elements of the network [2, 8]. Moreover, we show that, for a critical value of the control parameter $K = K_C$, the cooperative interaction between the dynamical elements of a regular two-dimensional lattice generates a phase transition in which the majority of the elements transition to a critical state. This critical state has a scale-free network of interdependent elements with $\nu \approx 1$.

The perspective of assessing a network's complexity solely by means of its topology has been widely adopted. Here, we adopt a different point of view and emphasize the emergence of temporal complexity through the intermittency of events in time, as well as through topological complexity entailed by the dynamics. An event is interpreted as a transition of a global variable from one critical state to another. In this way, we identify two distinct forms of complexity: one associated with the connectivity of the elements of the network, and the other associated with the variability of the time interval between events. Both power laws are a consequence of criticality.

This manifestation of dual complexity is demonstrated using a simple DMM [10–12] introduced in Section 24.2. We show by direct calculation that a DMM network undergoes a phase transition similar to that observed in the Ising model [2] resulting in an inverse power-law distribution in the connectivity of the network elements. In Section 24.3, we distinguish between a static network, where the constitutive elements form an unchanging structure, and a dynamic network generated by the self-organization of the elements located on the backbone structure of the former. We explore the propensity for cooperation of both the static and dynamic networks. These dynamic-based results are interpreted in a neuroscience context. In Section 24.4, temporal complexity is discussed, and calculations reveal a scale-free distribution density of the consensus times τ , $\psi(\tau) \propto \tau^{-\mu}$, which is separate and distinct from the scale-free degree distribution. The consensus time is the length of time the majority of the elements stay within one of the two available states. A handful of inflexible elements can have a dramatic influence on the overall behavior of the network, as we demonstrate in Section 24.5. Some conclusions are drawn in Section 24.6.

24.2

The Decision-Making Model (DMM)

The network dynamics of each element of a DMM network are determined by the two-state master equation [11, 12]

$$\frac{dp_1(t)}{dt} = -g_{12}(t)p_1(t) + g_{21}(t)p_2(t)$$

$$\frac{dp_2(t)}{dt} = -g_{21}(t)p_2(t) + g_{12}(t)p_1(t) \quad (24.1)$$

where p_j is the probability of being in the state $j = 1, 2$. The DMM uses a social paradigm of decision makers who choose between the state 1 (yes or +) and the state 2 (no or -) at each point in time t . The interaction among the elements in the network is realized by setting the coupling coefficients to the time-dependent forms:

$$g_{12}(t) \equiv \frac{g}{2} \exp \left[K \frac{M_2(t) - M_1(t)}{M} \right] \quad (24.2)$$

$$g_{21}(t) \equiv \frac{g}{2} \exp \left[-K \frac{M_2(t) - M_1(t)}{M} \right] \quad (24.3)$$

Here, M denotes the total number of nearest neighbors to each element, and $M_1(t)$ and $M_2(t)$ give the numbers of nearest neighbors in the decision states “yes” and “no,” respectively.

The single individuals are not static but change their opinions over time, thereby making $M_1(t)$ and $M_2(t)$ fluctuate in time, while, of course, the total number of nearest neighbors is conserved, that is, $M_1 + M_2 = M$. A single element in isolation has a vanishing control parameter $K = 0$ and consequently would fluctuate between “yes” and “no,” with Poisson statistics at the rate g .

When $K > 0$, an element in the state “yes” (“no”) makes a transition to the state “no” (“yes”) faster or slower according to whether $M_2 > M_1$ ($M_1 > M_2$) or $M_2 < M_1$ ($M_1 < M_2$), respectively. The quantity K_C is the critical value of the control parameter K , at which point a phase transition to a self-organized global majority state occurs. The efficiency of a network in facilitating consensus can be expressed as a quantity proportional to $1/K_C$. Here, that self-organized state is identified as the consensus. On the other hand, expressing network efficiency through consensus has the effect of establishing a close connection between network topology and the ubiquitous natural phenomenon of synchronization. In this way, a number of investigators have concluded that topology plays an important role in biology, ecology, climatology, and sociology [13–16].

We define the global variable in order to characterize the network fluctuations, as

$$\xi(t) \equiv \frac{N_1(t) - N_2(t)}{N} \quad (24.4)$$

where N is the total number of elements, and $N_1(t)$ and $N_2(t)$ are the number of elements in the state “yes” and “no” at time t , respectively. Typical DMM calculations of the global variable for the control parameter greater than the critical value in the all-to-all coupling configuration are shown on Figure 24.1 for three sizes of the network. The variability in the time series resembles thermal fluctuations in physical processes, but there is no such mechanism in the DMM. The erratic fluctuations are the result of the finite number of elements in the network.

The top panel in Figure 24.1 has the results for the fewest number of elements, in which case the dynamics seem to yield noise. In the middle panel, the number

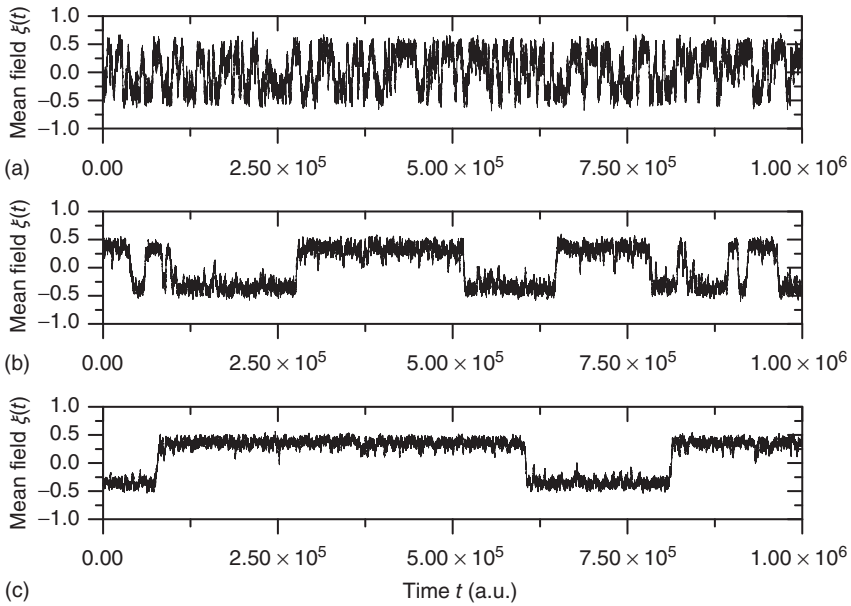


Figure 24.1 The fluctuation of the mean-field global variable as a function of time. For the network configuration: (a) $N = 500$, (b) $N = 1500$, and (c) $N = 2500$. In all cases, $K = 1.05$ and $g_0 = 0.01$. Adopted from Ref. [11].

of elements is tripled from that in the top panel and the two states of the DMM are now evident, but the fluctuations persist. In the bottom panel, the number of elements is increased by a factor of five from the top panel and the critical states are even sharper. It is clear that the fluctuations vanish as the number of elements increase to infinity and they do so as $N^{-1/2}$. In a similar way, the size of the fluctuations decreases with increasing control parameter values.

We evaluate the time duration τ of the consensus state, where either $\xi(t) > 0$ or $\xi(t) < 0$, and calculate the time average of the modulus $|\xi(t)|$. We denote this average with the symbol ξ_{eq} in the sequel.

Note that in the special case, when the number of nearest neighbors M is the same for all the nodes and the natural transition rate is very small $g_0 \ll 1$, the DMM generates a phase transition that is analogous to the two-dimensional Ising model discussed in the seminal paper of Onsager [17]. This is an expected result insofar as the Ising model rests on the Hamiltonian

$$H = -J \sum_{i \neq j=1}^N \sigma_i \sigma_j \quad (24.5)$$

where σ_i and σ_j denote the Pauli operators with eigenvalues ± 1 . Equilibrium is defined in terms of Boltzmann distribution described by the density matrix

$$\rho = \frac{\exp(-\beta H)}{Z} \quad (24.6)$$

with the inverse of the temperature given by $\beta = 1/k_B T$, with k_B being Boltzmann's constant and T the absolute temperature. Thus, the off-diagonal elements of the transfer matrix [18] become equivalent to the transition rates of Eqs. (24.2) and (24.3), under the condition that the control parameter is associated with the physical temperature, $K = M/T$. As examples of conditions yielding this equivalence, we consider two cases. The first case is for all-to-all coupling, where $M = N$ and there is no spatial structure for the network. The second case is a simple two-dimensional lattice where each node is coupled to its four nearest neighbors, thereby yielding $M = 4$.

The thermodynamic condition $M = N = \infty$ was discussed extensively by authors of Ref. [10, 11], who showed that under those conditions the ratios $M_{\pm 1}/M$ are equivalent to the probabilities $p_{\pm 1}$ for a node i to be in one of two allowed states. The dynamic evolution of a single unit state is then described by a two-state master equation

$$\frac{dp_{+1}}{dt} = -g_{12}p_{+1} + g_{21}p_{-1} \quad (24.7)$$

$$\frac{dp_{-1}}{dt} = -g_{12}p_{-1} + g_{21}p_{+1} \quad (24.8)$$

Solving this master equation using the difference in probabilities as a new variable $\Pi(t) = p_{+1}(t) - p_{-1}(t)$, which corresponds to the earlier defined global order parameter $\xi(t)$, we obtain the mean-field equation

$$\frac{d\Pi}{dt} = 2g_0[\sinh(K\Pi) - \Pi \cosh(K\Pi)]. \quad (24.9)$$

This equation yields two solutions, corresponding to global majority states, for the values of coupling constant $K > K_C$, where the critical value of the control parameter $K_C = 1$.

The solution in the second case, where $M = 4, N = \infty$, can be found in [19] and yields the critical value of the coupling constant $K_C = 2 \ln(1 + \sqrt{2}) \approx 1.7627$, which value corresponds to the critical temperature in the Ising model [17].

In Figure 24.2, the DMM is seen to undergo phase transitions at the two critical values mentioned. We see that, for a very small value of the coupling strength $g = 0.01$, the numerical evaluation of $\xi_{eq}(K)$ on a 100×100 lattice is very close to the theoretical prediction of Onsager [17]. The patterns generated by the Ising model at criticality corresponds to the emergence of correlation links yielding a scale-free network statistically indistinguishable from that observed experimentally within the brain using functional magnetic resonance imaging.

This equivalence between the DMM and the Ising model is a formal one, because the DMM does not have a physical origin (no Hamiltonian) and it does not require the action of a thermal bath at temperature T to generate fluctuations as does the Boltzmann picture. This explains why the equivalence with the Ising model requires that g_0 vanish, so as to freeze the dynamics of the single units, in the absence of cooperation.

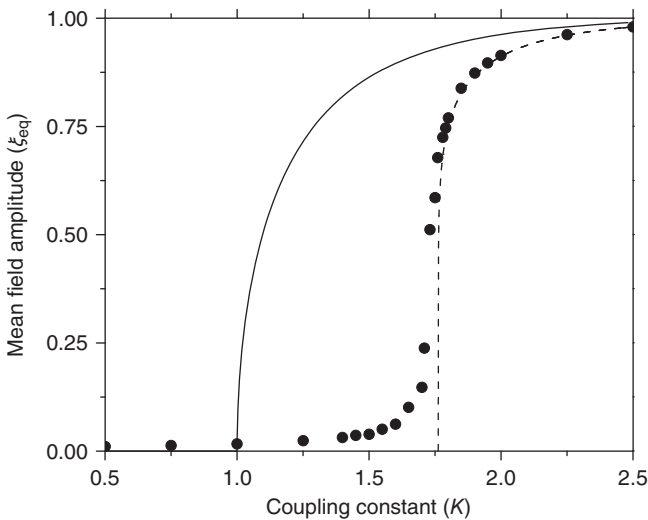


Figure 24.2 The phase diagram for the global variable ξ_{eq} . The solid and dashed lines are the theoretical predictions for the fully connected and two-dimensional regular lattice network, respectively. In both cases,

$N = \infty$ and the latter case is the Onsager prediction [17]. The circles are the DMM calculation for $K = 1.70$. (Adopted from Ref. [12].)

24.3

Topological Complexity

To realize temporal as well as topological complexity, we rely on numerical results and focus our attention on the condition $K = 1.70$, which, although slightly smaller than the Onsager theoretical prediction, is compatible with the emergence of cooperative behavior due to the phase transition. To derive the dynamically induced network topology, we apply the so-called correlation network approach, where a topology is generated by linking only those elements with cross-correlation levels above a given threshold [2]. Thus, we evaluate the two-point cross-correlation coefficient between all pairs of elements after the transients have faded in the DMM calculation. If the cross-correlation coefficient between two network elements is larger than the arbitrarily chosen threshold value $\Theta = 0.61$, we insert a link between them; if not, we leave them uncoupled. This prescription is found to generate a scale-free network with the inverse power index $\nu \approx 1$, as shown in Figure 24.3. We also evaluate the distribution density $p(l)$ of the Euclidian distance l between two linked elements and find that the average distance is of the order of 50, which is on the order of the size of the two-dimensional grid 100×100 . This average distance implies the emergence of long-range links that go far beyond the nearest neighbor coupling and is essential to realizing the rapid transfer of information over a complex network [21–23].

We construct from the DMM dynamically induced network a *network backbone*, called a dynamically generated complex topology (DGCT) and then study its

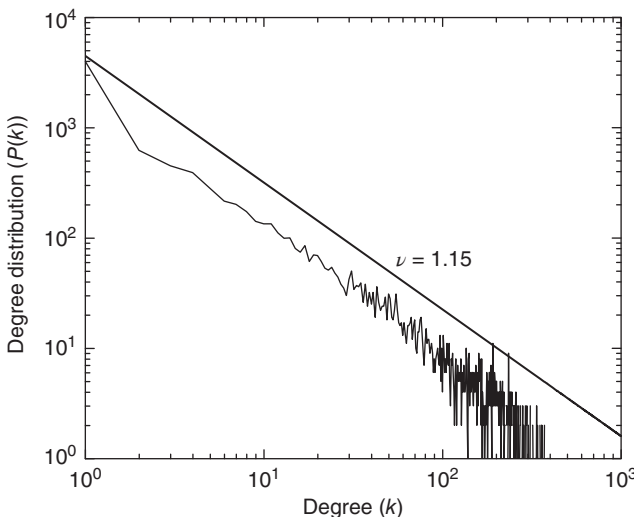


Figure 24.3 The degree distribution for the dynamically generated complex topology created by examining the dynamics of elements placed on a two-dimensional regular

lattice with the parameter values $K = 1.70$ and $g_0 = 0.01$ in the DMM. (Adapted from Ref. [20].)

efficiency by implementing the DMM dynamics on it. It is convenient to compare the cooperative behavior of the DGCT network with another seemingly equivalent scale-free degree network with the same $\nu \approx 1$. This latter scale-free network uses a probabilistic algorithm [24] and we refer to it as an *ad hoc* network, and implement the DMM on it as well as on the DGCT network. The phase-transition diagrams of the DGCT and the *ad hoc* network are illustrated in Figure 24.4a and the inset of Figure 24.4b, respectively. Notice that the phase transition occurs on both networks at $K = 1$, that is, at the same critical value corresponding to the all-to-all coupling condition. However, in Figure 24.4a a new phenomenon is observed, that being the emergence of both a consensus and a non-consensus state. The new state emerges because the self-organization process generates two weakly coupled identical clusters, each cluster being equivalent to an *ad hoc* network with $\nu \approx 1$. These two networks are virtually independent of each other, thereby yielding the states $++$; $--$; $+-$; $-+$, with equal probability. The states $+-$ and $-+$ are the non-consensus states. To support this interpretation, we generate two identical *ad hoc* networks with $\nu = 1$ and couple them with a single link. The resulting phase diagram, shown in Figure 24.4b, is very similar to that depicted in Figure 24.4a, thereby establishing that DGCT networks may give rise to the coexistence of communities with conflicting opinions, reminiscent of recent results obtained by others [25]. This result could not be obtained in the weak coupling limit where DMM becomes equivalent to the Ising model.

The earlier illustrated approach is consistent with the procedure widely adopted in neuroscience to define functional connections between different brain regions

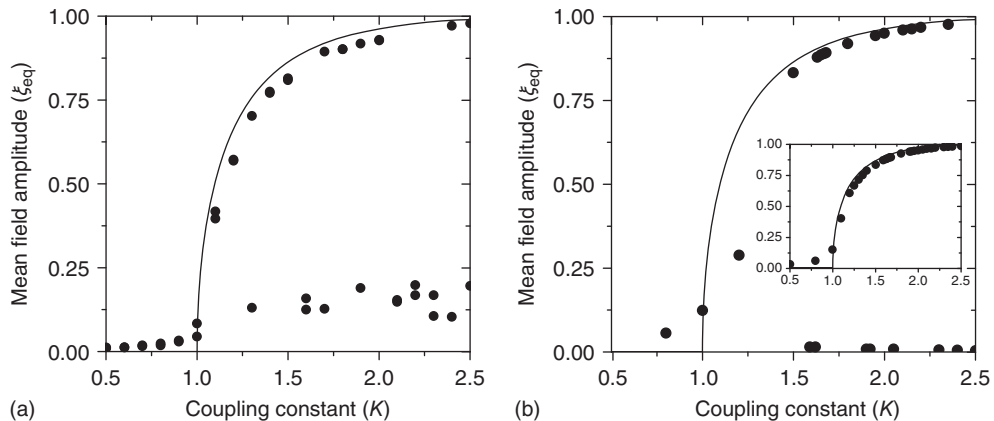


Figure 24.4 The phase diagram for global variable ξ_{eq} . (a) The solid line corresponds to the equilibrium states obtained in the case of fully connected $N = \infty$ network. Dots correspond to the equilibrium states obtained by evaluating the dynamics of the DMM on the DGCT network with $g_0 = 0.01$. (b) The solid line corresponds to the equilibrium states obtained in the fully connected case for the $N = \infty$ network. Dots

correspond to the equilibrium states obtained by evaluating the dynamics of the DMM on a system of two scale-free, *ad hoc* networks with power-law index $\nu = 1$. Both networks had $N = 1000$ elements and were coupled with only one link and $g_0 = 0.01$. The inset shows the phase diagram for an *ad hoc* network with $N = 2000$ elements and power-law index of the degree distribution $\nu = 1$. (Adapted from Ref. [20].)

[2, 26]. Numerous studies have shown the scale-free character of networks created by correlated brain activity as measured through EEG [27, 28], magnetoencephalography [26], or magnetic resonance imagining [29]. Fraiman *et al.* [2] used the Ising model to explain the origin of the scale-free neuronal network and found the remarkable result that the brain dynamics operate at the corresponding critical state. The present research was, in part, inspired by these results [2], and leads to the additional discovery that the emergence of consensus produces long-range connections as well as a scale-free topology.

Consider the earlier results in the light of the recent experimental findings on brain dynamics [30]. The analysis of Bonifazi *et al.* [30] established that, in a manner similar to other biological networks, neural networks evolve by gradual change, incrementally increasing their complexity, and rather than growing along the lines of preferential attachment, neurons tend to evolve in a parallel and collective manner. The function of the neuronal network is eventually determined by the coordinated activity of many elements, with each element contributing only to local short-range interactions. However, despite this restriction, correlation is observed between sites that are not adjacent to each other, which is a surprising property suggesting the existence of a previously incomprehensible long-distance communication [31, 32]. The DMM dynamical approach affords the explanation that the local but cooperative interactions embed the elements in a phase-transition condition that is compatible with long-range interdependence.

24.4

Temporal Complexity

Let us now turn our attention to temporal complexity. We show that the apparently intuitive notion that topological complexity with a scale-free distribution of links k , $P(k) \propto k^{-\nu}$ and time complexity with a scale-free distribution of consensus times τ , $\psi(\tau) \propto \tau^{-\mu}$ are closely related is wrong. Figure 24.5 illustrates the consensus survival probability $\Psi(t)$ corresponding to the critical value of the control parameter $K = 1.70$, generating the scale-free topology of Figure 24.3. Although emerging from a simple spatial network, that is, one with no structural complexity, the survival probability is scale-free with $\alpha = \mu - 1 \approx 0.55$ over more than four time decades.

The statistical analysis of the real brain activity led some investigators [33–36] to conclude that the brain dynamics are dominated by renewal quakes (neuronal avalanches) and that the probability density of the time distance between two consecutive quakes has the inverse power-law index $\mu \leq 2$. Theoretical arguments [37] establish that this condition is important for the cognitive brain function. On the basis of the plausible conjecture [31] that there is a close connection between the cooperative behavior of many elements and brain cognition, we believe that the emergence of the condition $\mu < 2$ from the interaction of the elements of the regular two-dimensional lattice is an important aspect of the dynamic approach to the scale-free condition.

On the other hand, the survival probability of the consensus state emerging from the *ad hoc* network, with $K = 1.10$, is limited to the time region $1/g$, and for

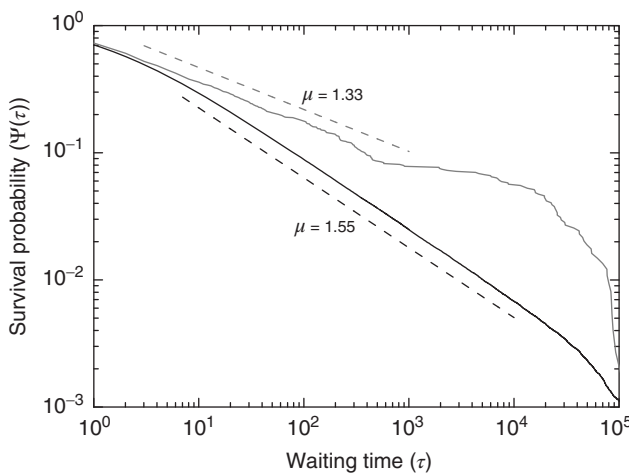


Figure 24.5 Consensus survival probability. Black and gray solid lines refer to the DMM implemented on a two-dimensional regular lattice with control parameter $K = 1.70$ and to dynamics of the *ad hoc* network

evaluated for $K = 1.10$, respectively. In both cases $g_0 = 0.01$. The dashed lines are visual guides corresponding to the scaling exponents $\mu = 1.55$ and $\mu = 1.33$, respectively.

$N \rightarrow \infty$ is expected [11] to be dominated by the exponential shoulder depicted in Figure 24.5. The exponential shoulder is a signature of the equilibrium regime of the network dynamics [11].

24.5

Inflexible Minorities

Understanding the influence that committed minorities can exert on both local and global properties of complex networks is an issue of overwhelming importance. What are the conditions under which the convictions of an inflexible minority dominate the future behavior of a complex network? Turalska *et al.* [38] demonstrate that the abrupt changes in the organization of social groups such as described by DMM, rather than being moments of disorder, are instances of increased spatial correlation between the elements of the network. This condition of extended cooperation, similar to the critical state of a physical phase transition, allows a small subgroup of the society to exert substantial influence over the entire social network. One limiting case might be viewed as Carlyle's great man theory of history in *On Heroes, Hero Worship, and the Heroes of History* [39], where a single individual can change world opinion for better or worse.

A member of the committed minority considered herein is a randomly selected element at a node on the lattice that keeps its decision of either "yes" or "no" independently of the opinion of its neighbors. Thus, this element communicates an unchanging message to the rest of the network through its interactions. To establish that the committed minority may operate efficiently in spite of their small number, in Figure 24.6 we compare the evolution of $\xi(t)$ in the absence of

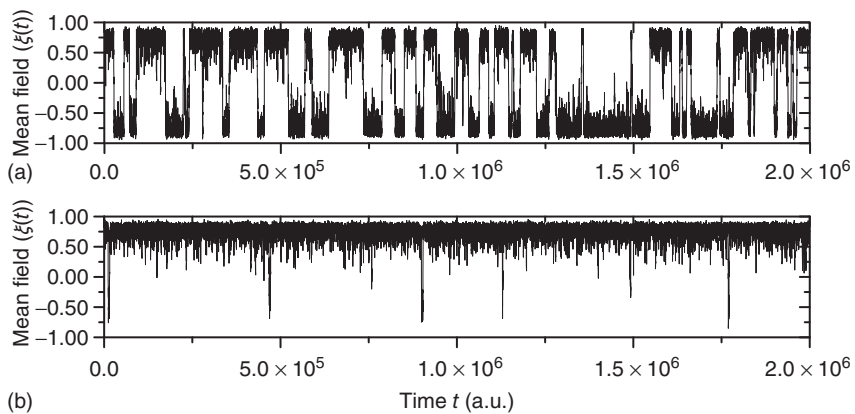


Figure 24.6 A small number of nodes maintaining constant opinion influence significantly the behavior of the system in the organized phase. (a) Fluctuations of the global order parameter $\xi(t)$ for $K = 1.66$ and

lattice of size $N = 20 \times 20$ nodes. (b) The behavior of $\xi(t)$ once 1% of the randomly selected elements are kept in state "yes" at all times. Transition rate is $g_0 = 0.10$ for both.

a committed minority to its evolution in the presence of a relatively small (1%) inflexible group. In the case considered here, values of the control parameter in excess of the critical value lead to the extended condition of global consensus. Turalska *et al.* [38] show that a rapidly decreasing correlation function reflects the rigidity of the network and prevents the global transmission of the perturbation. However, from time to time a crisis occurs where $\xi(t) = 0$. In crisis, the network may undergo an abrupt change of opinion, and the correlation length may be sufficiently large to make it possible for the inflexible minority to force the social network to adopt their view. As a consequence, during the time interval over which the minority acts, it imposes its opinion over the entire network.

Finally, to quantify the phenomenon of minority influence we study how introducing a committed minority affects the average lifetime of the consensus state, defined as

$$\langle \tau \rangle = \int_0^{\infty} \Psi(\tau) d\tau \quad (24.10)$$

It is important to note that, when no committed group is present, the distribution of time durations of global decision in “yes,” $\Psi(\tau_{yes})$, and in “no,” $\Psi(\tau_{no})$, coincide and are equal to the distribution evaluated for both time intervals, $\Psi(\tau) = \Psi(\tau_{yes}) = \Psi(\tau_{no})$. This symmetry is, however, broken once a minority is introduced, as shown in Figure 24.6 by an increase in temporal span of consensus states that correspond to the opinion of the minority.

In Figure 24.7 we compare $\langle \tau \rangle$ in the absence of the inflexible agents to the average lifetime in the presence of a committed minority of sizes 1% and 5%. First, in the native case the average consensus time increases exponentially with an increase in the control parameter K , showing a faster rise once $K > K_C$, with a discontinuous change at the critical interaction strength. This switch in the rate of increase confirms the validity of the approach used to determine K_C based on the temporal properties of $\xi(t)$. Consecutively, the introduction of a small minority leads to a linear increase in $\langle \tau \rangle$, and the fact that two exponential regimes are preserved confirms the crucial role that instances of crisis play in the global transmission of minority opinion.

It is also interesting to extend the committed minority results to the interaction between two complex networks. Suppose that the network P consists of a group of zealots and that of S the social group of interest. The dynamics of both S and P are determined by the DMM. At a given point in time, a small number of nodes in network S are replaced by elements whose dynamics are determined by P , but otherwise they are allowed to interact with the elements of network S . Figure 24.8 depicts three situations. In the upper panel, the dynamics of network S with 400 elements on a two-dimensional lattice is shown in the absence of consensus. The center panel indicates the dynamics of network P with 400 elements on a two-dimensional lattice when the control parameter is above the critical value. In the bottom panel, the dynamics of the two networks are superposed when 5% of randomly positioned S elements are replaced with P elements. The newly replaced nodes retain their P -dynamics but are coupled in to the S -dynamics.

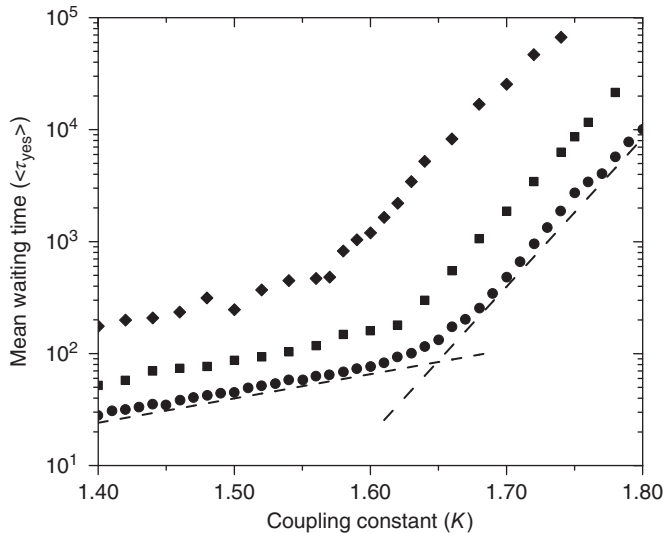


Figure 24.7 The mean waiting time $\langle \tau_{yes} \rangle$ obtained for a network with no acting minorities (dots) increases significantly once 1% (squares) or 5% (diamonds) committed minority is presented. Lattice size is $N = 20 \times 20$ nodes and $g_0 = 0.10$.

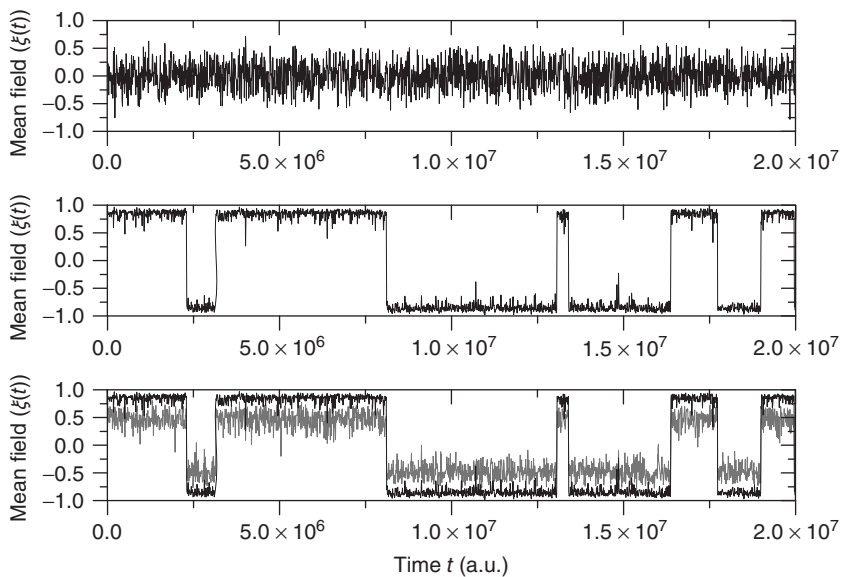


Figure 24.8 (a) The mean-field variable for network S , a 20×20 lattice with $K_S = 1.42$; (b) The mean-field variable for network P , a 20×20 lattice with $K_P = 1.76$; (c) The time series from the middle panel (black line) superposed on that of the S network when 5% of the elements are replaced by those of P (gray line).

It is evident that even this small number of elements from network P (20) is sufficient to completely dominate the dynamics of network S . It is also interesting to determine what happens if the zealots in network P are anarchists. We model an anarchist as advocating no particular opinion so that the control parameter of P is below the critical value and the zealot group appears random. Suppose further that network S was highly organized with a control parameter above the critical value, similar to the center panel of Figure 24.8. If the same replacement was made as was done in the above case, the well-defined switching between states would be lost and the social organization of network S would disintegrate. These interesting results are the topic of future investigations.

24.6 Conclusions

In summary, the self-organization of the DMM implemented on the two-dimensional network with $M = 4$ generates a scale-free topology with $\nu \approx 1$ as well as the long-range links essential for the collective mind of the network of self-organized elements of Couzin [31]. The exciting discovery of dynamic-hub neurons with $1.1 \leq \nu \leq 1.3$ [30] is a challenge for the dynamical derivation of the scale-free condition that is mainly confined to $\nu > 2$ [1, 5, 6], and it is remarkable that the approach used herein generates a power-law index in the range of the experimental results of Bonifazi *et al.* [30]. Wang *et al.* [40] use a weighted scale-free topology to promote or suppress synchronization. Here, these effects do not require a complex network structure. The DMM implemented on the DGCT networks shows the coexistence of two impenetrable [25] opinion clusters that develop independent decisions, with no influence of one cluster on the other. The regular topology generates time complexity, namely $\Psi(t)$ with $\mu - 1 < 1$, lasting for some decades, whereas the scale-free topology of the *ad hoc* network generates consensus with a smaller control parameter K , without yielding complexity in time. Aquino *et al.* [41] show that this kind of complex dynamical network shares the brain's sensitivity to $1/f$ noise. In short, the present research establishes that the scale-free distribution of links is a consequence of dynamic self-organization rather than being the cause of it.

Our approach does not allow us to confirm the observation made by Xie *et al.* [42] that the minimal size of the committed minority necessary to significantly affect the opinion of the entire network is 10%. We are convinced that difference in the size of the inflexible minority is a consequence of the interactions used in the two models. If we assume that a substantial effect of a committed minority is defined by an order of magnitude increase in the average consensus time, Figures 24.7 and 24.8 indicate that for DMM this requirement is realized by a committed minority of less than 5%. These considerations apparently generalize to the dynamic situation where the changes in the perturbing elements can dominate the dynamics of the host network.

References

1. Albert, R. and Barabási, A. (2002) Statistical mechanics of complex networks. *Rev. Mod. Phys.*, **74** (1), 47–97.
2. Fraiman, D., Balenzuela, P., Foss, J., and Chialvo, D. (2009) Ising-like dynamics in large-scale functional brain networks. *Phys. Rev. E*, **79** (6), 061922.
3. Watts, D. and Strogatz, S. (1998) Collective dynamics of “small-world” networks. *Nature*, **393**, 440–442.
4. Erdős, P. and Rényi, A. (1960) On the evolution of random graphs. *Magyar Tud. Akad. Mat. Kutató Int. Közl.*, **5**, 17–61.
5. Dorogovtsev, S. and Mendes, J. (2002) Evolution of networks. *Adv. Phys.*, **51** (4), 1079–1187.
6. Ferrer, R. and Sole, R. (2003) Optimization in complex networks, in *Statistical Mechanics of Complex Networks* (eds R. Pastor-Satorras, M. Rubí, and A. Diaz-Guilera), Springer, Berlin, pp. 114–126.
7. Baiesi, M. and Manna, S. (2003) Scale-free networks from a hamiltonian dynamics. *Phys. Rev. E*, **68** (4), 047103.
8. Perotti, J., Billoni, O., Tamarit, F., Chialvo, D., and Cannas, S. (2009) Emergent self-organized complex network topology out of stability constraints. *Phys. Rev. Lett.*, **103** (10), 108701.
9. Beggs, J.M. and Plenz, D. (2003) Neuronal avalanches in neocortical circuits. *J. Neurosci.*, **23** (35), 11167–11177.
10. Bianco, S., Geneston, E., Grigolini, P., and Ignaccolo, M. (2008) Renewal aging as emerging property of phase synchronization. *Physica A*, **387** (5), 1387–1392.
11. Turalska, M., Lukovic, M., West, B., and Grigolini, P. (2009) Complexity and synchronization. *Phys. Rev. E*, **80** (2), 021110.
12. Turalska, M., West, B., and Grigolini, P. (2011) Temporal complexity of the order parameter at the phase transition. *Phys. Rev. E*, **83** (6), 061142.
13. Arenas, A., Diaz-Guilera, A., Kurths, J., Moreno, Y., and Zhou, C. (2008) Synchronization in complex networks. *Phys. Rep.*, **469** (3), 93–153.
14. Castellano, C., Fortunato, S., and Loreto, V. (2009) Statistical physics of social dynamics. *Rev. Mod. Phys.*, **81** (2), 591–646.
15. Pikovsky, A., Rosenblum, M., and Kurths, J. (2003) *Synchronization: A Universal Concept in Nonlinear Sciences*, Vol. 12, Cambridge University Press.
16. West, B., Geneston, E., and Grigolini, P. (2008) Maximizing information exchange between complex networks. *Phys. Rep.*, **468** (1), 1–99.
17. Onsager, L. (1944) Crystal statistics. I. A two-dimensional model with an order-disorder transition. *Phys. Rev.*, **65** (3-4), 117–149.
18. Plischke, M. and Bergersen, B. (eds) (2006) *Equilibrium Statistical Physics*, World Scientific Publishing Company Incorporated.
19. McCoy, B. and Wu, T. (eds) (1973) *The Two-Dimensional Ising Model*, Harvard University Press.
20. Turalska, M., Geneston, E., West, B., Allegrini, P., and Grigolini, P. (2012) Cooperation-induced topological complexity: a promising road to fault tolerance and hebbian learning. *Front. Physiol.*, **3**, 52.
21. Kleinberg, J. (2000) Navigation in a small world. *Nature*, **406** (6798), 845.
22. Boguna, M., Krioukov, D., and Claffy, K. (2008) Navigability of complex networks. *Nat. Phys.*, **5** (1), 74–80.
23. Boguna, M. and Krioukov, D. (2009) Navigating ultrasmall worlds in ultra-short time. *Phys. Rev. Lett.*, **102** (5), 058701.
24. Kalisky, T., Cohen, R., Ben-Avraham, D., Havlin, S., Ben-Naim, E., and Frauenfelder, H. (2004) in *Tomography and stability of complex networks*, in *Complex Networks*, Lecture Notes in Physics, (ed. Z. Toroczkai), Springer, Berline, pp. 3–34.
25. Shao, J., Havlin, S., and Stanley, H. (2009) Dynamic opinion model and invasion percolation. *Phys. Rev. Lett.*, **103** (1), 018701.

26. Stam, C. (2004) Functional connectivity patterns of human magnetoencephalographic recordings: a 'small-world' network? *Neurosci. Lett.*, **355** (1-2), 25–28.
27. Micheloyannis, S., Pachou, E., Stam, C., Vourkas, M., Erimaki, S., and Tsirka, V. (2006) Using graph theoretical analysis of multi channel EEG to evaluate the neural efficiency hypothesis. *Neurosci. Lett.*, **402** (3), 273–277.
28. Stam, C. and de Bruin, E. (2004) Scale-free dynamics of global functional connectivity in the human brain. *Human Brain Mapp.*, **22** (2), 97–109.
29. Eguiluz, V., Chialvo, D., Cecchi, G., Baliki, M., and Apkarian, A. (2005) Scale-free brain functional networks. *Phys. Rev. Lett.*, **94** (1), 018102.
30. Bonifazi, P., Goldin, M., Picardo, M., Jorquera, I., Cattani, A., Bianconi, G., Represa, A., Ben-Ari, Y., and Cossart, R. (2009) Gabaergic hub neurons orchestrate synchrony in developing hippocampal networks. *Science*, **326** (5958), 1419–1424.
31. Couzin, I. (2007) Collective minds. *Nature*, **445** (7129), 715.
32. Couzin, I. (2009) Collective cognition in animal groups. *Trends Cogn. Sci.*, **13** (1), 36–43.
33. Gong, P., Nikolaev, A., and van Leeuwen, C. (2007) Intermittent dynamics underlying the intrinsic fluctuations of the collective synchronization patterns in electrocortical activity. *Phys. Rev. E*, **76** (1), 011904.
34. Bianco, S., Ignaccolo, M., Rider, M., Ross, M., Winsor, P., and Grigolini, P. (2007) Brain, music, and non-poisson renewal processes. *Phys. Rev. E*, **75** (6), 061911.
35. Buiatti, M., Papo, D., Baudonnier, P., and van Vreeswijk, C. (2007) Feedback modulates the temporal scale-free dynamics of brain electrical activity in a hypothesis testing task. *Neuroscience*, **146** (3), 1400–1412.
36. Allegrini, P., Menicucci, D., Bedini, R., Fronzoni, L., Gemignani, A., Grigolini, P., West, B., and Paradisi, P. (2009b) Spontaneous brain activity as a source of ideal 1/f noise. *Phys. Rev. E*, **80** (6), 061914.
37. Grigolini, P., Aquino, G., Bologna, M., Luković, M., and West, B. (2009) A theory of 1/f noise in human cognition. *Physica A*, **388** (19), 4192–4204.
38. Turalska, M., West, B. J., and Grigolini, P. (2013) Role of committed minorities in times of crisis. *Scientific Reports* **3**, 1371.
39. Carlyle, T. (1993) *On Heroes, Hero-Worship, and the Heroic in History*, Vol. 1, University of California Press.
40. Wang, W., Huang, L., Lai, Y., and Chen, G. (2009) Onset of synchronization in weighted scale-free networks. *Chaos*, **19** (1), 013134.
41. Aquino, G., Bologna, M., Grigolini, P., and West, B. (2010) Beyond the death of linear response: 1/f optimal information transport. *Phys. Rev. Lett.*, **105** (4), 040601.
42. Xie, J., Sreenivasan, S., Korniss, G., Zhang, W., Lim, C., and Szymanski, B. (2011) Social consensus through the influence of committed minorities. *Phys. Rev. E*, **84** (1), 011130.

25

The Dynamics of Neuromodulation

Gerhard Werner[†] and Bernhard J. Mitterauer

25.1

Introduction

We address three aspects of neuroscience, each for long being largely overshadowed by the neuron doctrine's hegemony [1]: neuroglia (including here also the systems of neuronal and glia gap junctions), extracellular fluid in neural tissue ("brain cell microenvironment" [2]), and neuromodulatory processes. Our leading notion is that the functional state of neurons, individually and in assemblies, is determined by a set of variables (ion conductances and membrane currents, thresholds for neural discharges, synaptic potentials, ion channel kinetics, etc.), whose values at any one time are to varying degrees affected by interactions and interdependencies of these three components, locally as well as globally, and at largely different time scales. In Section 25.2, we review the essential aspects of each of these components separately. This is to provide the basis for our principal objective to analyze in the Section 25.3 the global dynamics of the complex system these components jointly compose, covering a wide range of temporal scales that is characteristic of multifractals. Accordingly, self-similarity and the absence of any specific time scale ensure instant and automatic adaptation to neural impulse traffic over a wide range of frequencies.

25.2

Background

25.2.1

Gap Junctions and Neuroglia

In the normal brain neurons, astrocytes and oligodendrocytes are the most abundant and active cells. They express pannexins and connexins, with protein subunits of two families forming membrane channels. Most available evidence indicates that in mammals endogenously expressed pannexins form only hemichannels, whereas

connexins form both gap junction channels and hemichannels. Whereas gap junction channels connect the cytoplasm of contracting cells and coordinate electric and metabolic activity, hemichannels communicate the intra- and extracellular compartments and serve as a diffusional pathway for ions and small molecules. Importantly, continuous glial activation triggered by low levels of anomalous proteins expressed in several neurodegenerative diseases resembles those of acute inflammatory responses triggered by ischemia or infectious diseases [3].

Diffusive coupling by gap junctions between various interneuron types and neurogliaform cells in neocortex is now firmly established [4], as is their virtually boundless distribution [5]. Simulation studies have determined their role for supporting synchronous oscillations [6, 7], and identified complementary interrelations with chemical synapses in interneuronal networks [8]. Electrical coupling between axons is also amply documented [9], providing the opportunity for fast and efficient transfer of action potentials for generating highly coherent output pathways of neuronal networks.

It is not for the lack of compassionate reminders that glia did for a long time not get its proper due in the study of neural systems. Basing his argument on C.J. Herrick's electron micrographs, showing glia to attach itself to and surround nerve soma, axon, and dendrites, Galambos [10] persistently sought to persuade the neuroscience community to think of glia as imposing organization and structure on neurons for processing organized, coherent messages. Forty-five years later, evidence had accumulated to support Galambos' [11] claim. The observations cited in the following are merely a distillation of the multiplicity of the reported data on glia–neuronal interactions, intended to convey the richness and diversity of relevant observations.

Neurochemists generated an avalanche of data, promoting astrocytes [12], one of the members of the macroglia family, to full partnership with pre- and postsynaptic neurons in the “Tripartite Synapse” [13]. This has become a fertile concept for characterizing the complex and reciprocal patterns of interactions between astrocytes and neurons (reviewed by Araque and Navarette [14] and Halassa and Haydon [15]). The dynamics of these interactions is sustained by the astrocytes expressing receptors for virtually all important neurotransmitters [16], providing multiple opportunities for engaging neuron–astrocyte complexes at many target points [17–19]. A prevalent feature of astrocyte's role is their participation in the dynamics of calcium in extracellular space on two different space and time scales. For local, short-term interaction, astrocytes (although not electrically excitable) respond to glutamate liberated at presynaptic junctions with calcium spikes [20] which, in turn, release additional glutamate and ATP to neighboring neurons [21] for integrating coincident activity from different dendrites in the same tissue volume [22, 23]. Furthermore, activity-related changes of calcium levels within astrocytes contribute to mobilizing various transmitters and transmission-related substances [24]. Globally and on longer time scales, intercellular propagation of calcium waves [25–27] can support long-range signaling [28, 29]. Recent evidence from the family of connexins suggest that the astrocyte system constitutes a network

of communicating cells with definite spatial organization [30] where intercellular communication is controlled by endogenous signals [31].

The dynamics of neuron–glia interaction is complicated by two circumstances: first, due to activity-dependent morphological changes of astrogial processes ending at synaptic regions [32–34]; and, the second, due to a complex anatomical organization of spatial nonoverlapping domains with limited interdigitation of processes from adjacent cells [35–37]. Each domain encompasses some 2 million synapses in human brain [38] as an area of the neuropil that is controlled by a single astrocyte. Moreover, parts of this territory can be controlled autonomously by specialized astrocyte microdomains of filopodia with distinct motility [39]. Groups of neurons are also enwrapped by a layer of lattice-like material: this perineuronal net forms stable complexes surrounding synapses [40, 41], seemingly affecting short-term synaptic plasticity [42].

On a modular basis, computational simulations of different manifestations of astrocyte–neuron interactions contribute to gaining some insight into their functions. Astrocytes enwrapping synapses were shown to tune synaptic transmission to optimal efficiency [43]. Patterns of propagated calcium activation in astrocyte networks were modeled by Postnov *et al.* [44]. De Pita *et al.* [45] simulated local and global influences of astrocytes on short-term plasticity. Volman *et al.* [46] developed a biophysical model for the coupling between synaptic transmission and local calcium concentration on an enveloping astrocyte domain, and Goldberg *et al.*'s [47] simulation showed that nonlinear gap junctions can support long-distance propagation of calcium waves in astrocyte networks. Simulated astrocyte networks display attractor dynamics and bifurcations in phase space [48]. On the basis of theoretical arguments, Mitterauer [49] attributed a structural organization in the form of logical functions to astrocyte domain organization, suggesting its role in the economy of normal and pathological brain functions [50, 51]. From a global perspective, Allegrini *et al.* [52] examined the relation between neurons and astrocytes as a system of two interacting networks. This coarse-grained approach enabled identifying an augmenting effect of an astrocyte field on the computational complexity of a (simulated) neural network. A mean-field model of a neural-glia mass established quantitatively a strong and activity-dependent influence of astrocyte activity on synaptic transmission, and on the synchronization ratio between neurons, confirming the experimentally based conjectures of Sotero and Martinez-Cancino [53].

25.2.2

Brain Cell Microenvironment (Extracellular Fluid)

Extracellular fluid's coming of age is closely associated with the work of Kuffler and Nicholls [54], which identified the diffusion of ions and various neuroactive substances in intercellular clefts of neural tissue. This theme was again taken up by Vizi and Labos [55], documenting nonsynaptic interaction in nervous tissue, subsequently discussed in detail by Agnati *et al.* [56] and Zoli and Agnati [57], suggesting to view the intercellular communication among cells in the nervous

system in two complementary reference frames, one as “wiring” transmission and the other as “volume” transmission: the former being transmission of excitation between synaptically connected neurons, and the latter attributing diffusive distribution of various ions, neuropeptides, and neurotransmitters to extracellular fluid surrounding neurons. A wealth of experimental data, notably with the effects of ion accumulation in the extracellular fluid following tetanic nerve activity, corroborated this conjecture [58, 59]. In a computational model of a reaction–diffusion system, Werner [60] demonstrated that tetanic stimulation of a group of neurons causes extracellular accumulation of calcium ions, which induces spreading activity patterns in surrounding unstimulated neurons. More recently, Froehlich [61] showed that diffusive modulation of extracellular potassium concentration induces state transitions in neurons with distinct changes in oscillatory patterns. Changes of diffusive coupling in neural networks can change normal activity patterns and precipitate pathological ones [62, 63]. The relevance of nonsynaptic diffusion neurotransmission was further extended and refined by Bach-Y-Rita [64]. However, diffusion of neuroactive substances is slowed down by geometric tortuosity and viscosity of macromolecules in the extracellular space [65, 66]. By changing their geometric shape, dendritic spines can dynamically regulate diffusion in their vicinity [67].

Concerning glutamate, the important excitatory transmitter, disrupted regulation of extracellular glutamate in the central nervous system contributes to and can exacerbate the acute pathophysiology of traumatic brain injury [68]. Glutamate is normally released into the extracellular space by both neuronal and nonneuronal sources [69]. Glutamate uptake is driven by electrochemical gradients across neurons and glia with most (about 90%) glutamate uptake being performed by two glial transporters in the striatum, GLAST and GLT-1 [70].

25.2.3

Neuromodulatory Processes

The notion of neuromodulation originated with a diversity of observations that could not be accounted for within the established principles of the synaptic transmission with transmitter substances exclusively acting locally at synaptic sites [71, 72]. For the present purpose, we suggest reserving the term “neuromodulation” to designate the composite system of all processes affecting synaptic transmission as distinct from individual neuromodulatory processes in the narrower sense, as listed in the following. The foundational insights into the operational principles of neuromodulation originated with the investigation of the polyvalence of neural network functions in crustaceans. A succession of comprehensive reviews by Getting [73], Harris-Warrick and Marder [74], and Marder and Calabrese [75] summarize the repertoire of neuronal functions attributable to the modulating action of extrasynaptic processes on synaptic transmission. They include effects on synaptic efficacy and presynaptic transmitter release, intrinsic neuronal properties, changes of network connectivity, coupling of neural oscillators and filtering sensory input,

and spike-time-dependent plasticity [76]. All known neurotransmitter substances are involved in these effects, as are a multitude of peptides [77, 78].

Reports of neuromodulatory effects in higher functions of vertebrates followed the crustacean work in rapid sequence: Hasselmo and associates produced evidence for forebrain cholinergic neuromodulation of cognition (for a review, see [79]). Ascending brain stem neuromodulatory systems (NMSs) of vertebrate brains came to be implicated in learning mechanisms [80], in adaptive behavior [81], and in emotional control processes (for a recent example, see [82]). Central pattern generators are subject to neuron modulation in vertebrates as they are in invertebrates [83]. In totality, the accumulated observational evidence mandates expanding the classical view of a relatively static neuronal “wiring diagram” to a dynamic system subject to ongoing tuning and reconfiguring by a biochemical network of modulators, effective over a wide range of temporal and spatial scales [84]. Combining experimental observations with computational simulations reveals the combinatorial richness of the modulatory network for generating functionally appropriate and adaptive behavior [85–87].

The multitude of phenomena described as neuromodulation fall into two fundamentally different categories [88]. Intrinsic neuromodulation is the condition of the modulator being released by some of the same neurons that are also part of the circuit they modulate [89]. Hansson and Ronnback [90] review several instances of intrinsic modulation of synaptic transmission by astrocytes, related to release and uptake of glutamine at synaptic sites. Events at the “tripartite synapse” fall also in this category. Extrinsic modulation, on the other hand, consists of the activity of functionally distinct systems processes outside of and parallel to the actual synaptic activity, relying on the storage and transport of neuroactive substances in the extracellular fluid compartment. Most of the effects of neuroglia must be attributed to this category. Beyond regulating merely one synaptic region, extrinsic modulation can globally organize ensembles of circuits, and usually works at a time course up to several seconds rather than the milliseconds of synaptic actions of intrinsic modulation. In general, functional neuron ensembles subserving specific functions are multiply modulated, with the modulators themselves being subject to modulation by neurotransmitters stabilized by feedback regulation. The range and variety of this complex dynamic behavior can in principle be appreciated in computational models where changing the intrinsic properties of synapses and neurons and the communication pattern among them can replicate some of the observed phenomena, including state-dependent effects and bistability of neural networks, their moment-to-moment reconfigurations, conditional bursting, oscillations and synchronization [91], and the tuning of sensory pathways [92].

25.3

Discussion and Conclusions

In the following discussion, we will refer to the totality of the interacting complex of glia, extracellular fluid, and the processes of neuromodulation as the NMS. The

observations sketched in the Section 25.2 suggest viewing NMS as composed of numerous semiautonomous modules in nonlinear interactions. If it was not already intuitively obvious from the mere inspection of the wealth of diverse observations, a definite characterization of (NMS) as a nonlinear complex dynamic system (in the technical sense, see for instance [93]) follows from the revealing observations, reported by Marder [94] and based on numerous earlier studies, that NMS can be implicated in generating many different patterns of neural activity for identical tasks conditions. In other words, the NMS can deliver multiple and different solutions to a given demand or task. This phenomenon qualifies as Multiple Realization which is considered a universal attribute of nonlinear complex dynamical systems [95, 96].

For formulating ideas about NMS, it must of course not be overlooked that neurons themselves (individually and as assemblies) are integral participants, active by contributing to the flux of neuroactive substances in extracellular space, and passive by being affected by them. From moment-to-moment, NMS contributes to determining the neuronal parameters which by themselves constitute a smooth manifold over which they can vary for constraining compensatory combinations [97]. Since our aim is to characterize the function of NMS in its totality at a global level, we take a coarse-grained, nonreductive perspective. This sets our approach apart from studies of stochastic synaptic processes at the molecular level [98] and the multiscale analysis of molecular processes at cellular levels (for a recent overview: see Holcman [99]).

Depending on circumstances and objectives, several methods are typically applied to characterize complex biological reaction networks. For instance, Ederer *et al.* [100] recommend dividing the network into hierarchically structured modules, each amenable to simulation by ordinary differential equations. Piecewise-linear models are common practice for qualitative simulation of genetic regulatory networks [101]. Lima *et al.* rely on symbolic dynamics application to bifurcation analysis, and Galatolo *et al.* [102] advocate computing the long-time statistical limiting behavior and invariant measures. Cooperative complexification and adaptation to dynamic environments can originate from self-organization [103]. Phenomenological models of statistical habituation can be successfully based on linear response theory [104]. Recommending an engineering approach to metabolism, transcription, and translation signaling, Doyle and Csete [105] envision an organization framework of “highly optimized tolerance” (HOT) for ensuring structural stability and robustness of complex biological systems whose component processes involve a wide range of temporal scales.

Here, we adopt an alternative approach that aims at characterizing the global dynamics of NMS in its totality as it emerges from the interaction of its semiautonomous modules. We make the biologically plausible assumption that each process in the chain of neuromodulatory events can be considered a chemical rate process with exponential decay. Relaxation rates vary over at least a 1000-fold range: from milliseconds at the liberation of transmitter substances at intrinsic modulation, to many seconds of chemically mediated astrocyte network reconfigurations and propagating calcium waves, with the numerous extrinsic modulatory

processes exhibiting intermediate rates. This situation invites applying the observation of Hausdorff and Peng [106] that systems presenting time series with widely differing scales of component regulatory mechanisms summate to a system's power law ($1/f$) scaling, suggestive of its fractal character. Although there is no definitive mathematical proof presently available that time-scale-free functions emerge from superposition of independent relaxation processes, there exist a range of physical mechanisms that do in fact show such micro- to macroscopic conversion, generally in the context of fractal time series [107]. Moreover, numerical analyses of Montroll and Shlesinger [108] established that macroscopic scale-free functions emerge, provided the independent microscopic relaxation processes are of sufficiently large variance, as they are in NMS. This principle was subsequently applied by Anderson [109] to ascertain the power law dependency as an emergent property of systems that contain several exponentially decaying traces and was further extended by Fusi *et al.* [110] and Drew and Abbott [111] to include cascading exponential processes, the latter for sensory adaptation. However, NMS contains too many unknown rate constants to attempt numerical simulation and determination of a power law exponent. Thus, we need to confine the discussion to the exposition of plausible principles and analogies.

Placing the function of NMS into the domain of fractal time series allows gaining significant insights into its dynamic properties. In the first place, it identifies its scale-invariance as the property of relating the elements of its behavior in time across multiple time scales. This is a characteristic empirical feature of a large number of complex physiological phenomena [112]. It implies the global system's capacity for linking actions across many different time scales of the constituent processes: there is no privileged time scale, and the system's temporal performance is self-similar at any scale. This property endows the system with the ability to respond adaptively to perturbations (external events) over a wide range of their temporal patterns, and enables adaptation to impinging neural impulse trains that vary unpredictably over a wide range of time scales [113, 114].

In the application cited in the foregoing, the systems were sufficiently small so that power laws with only one exponent were considered adequate. Hence, they fall into the category of monofractals. Granting, however, the plausibility of the suggested approach, we consider it necessary to introduce a refinement: characteristic time scales of the NMS component processes known to extend over a 1000-fold range (as stated earlier) render fitting a power law function with only one exponent unlikely. Accordingly, several power law functions with different exponents, each covering a section of the entire spectrum of scales, are required. This places NMS into the category of multifractals [115, 116], commonly thought to be indispensable for very large systems (e.g., geophysics [117]) but also successfully applied in numerous biological systems [112, 93]. This underscores the wide range of temporal scales to which systems with fractal characteristic can successfully adapt.

Patterns of natural stimuli and of neural impulse sequences intrinsic to the nervous system can vary unpredictably over a wide range of time scales, precluding prediction and anticipation of future events. The section "Linking actions across

many scales” in [113] reviews numerous examples of neuronal structures that enable meeting this requirement, due to the fact that scale-invariant neural impulse trains adjust the dynamics of the recipient neuronal structures. This adaptation originates automatically from the basic properties of the neuronal processes being fractal and self-similar. By virtue of covering a wide spectrum of power law exponents, multifractals ensure sensitivity for unpredictable signals over a wider range of frequencies across multiple time scales [118, 119] and provide preparatory tuning to impending stimuli [120, 121]. Consequently, NMS provides considerable adaptive advantage for faithful processing of neural signals in unpredictable and uncertain environments.

25.4

A Final Thought

Given that the function of NMS is to satisfy the requirements stipulated in the foregoing, it is, from an engineering point of view, surely extremely clumsily designed, with many redundancies and duplications of functions. Why is this so? It gives the impression that NMS in its present state evolved in stages, one stage superimposed on the other as if to attain a progressively higher degree of robustness and stability for ensuring secure contact with an ever-changing and unpredictable environment: perhaps many stages of consecutive “tinkering”; yet, seemingly preserving modular semiautonomy.

25.5

Summary

Based on an overview of neuroglia, extracellular fluid, and neuromodulation, which are commonly considered as separate topics, we propose characterizing their joint function in the framework of complex nonlinear dynamic system theory. We view the continuous temporal flux of this global system’s activity as determining the characteristic parameters of neuronal function which, itself, participates in the system’s dynamics. Our analysis of this temporal dynamics leads to the conclusion that it is multifractal, implying a high degree of sensitivity and adaptability to the temporal flux of constantly and unpredictably changing neural impulse traffic.

References

1. Bullock, T.H., Bennett, M.V.L., Johnston, D., Josephson, R., Marder, E., and Fields, R.D. (2005) The neuron doctrine, redux. *Science*, **310**, 791–793.
2. Nicholson, C. (1980) The dynamics of brain-cell microenvironment. *Neurosci. Res. Program*, **18** (2), 175–222.
3. Orellana, J.A., Sáez, P.J., Shoji, K.F., Schalper, K.A., Palacios-Prado, N. et al. (2009) Modulation of brain hemichannels and gap junction channels by pro-inflammatory agents and their possible role in neurodegeneration. *Antioxid. Redox Signal*, **11**, 369–399.

4. Simon, A., Olah, S., Molnar, G., Szabadics, J., and Tamas, G. (2005) Gap junctional coupling between neurogliaform cells and various interneuron types in the neocortex. *J. Neurosci.*, **25** (27), 6278–6285.
5. Fukuda, T. (2007) Structural organization of the gap junction in the cerebral cortex. *Neuroscientist*, **13**, 199–207.
6. Traub, R.D., Schmitz, D., Jefferys, G.R., and Draguhn, A. (1999) High-frequency population oscillations are predicted to occur in hippocampal pyramidal neuronal networks interconnected by axoaxonal gap junctions. *Neuroscience*, **92**, 407–426.
7. Lewis, T.J. and Rinzel, J. (2000) Self-organized synchronous oscillations in a network of excitable cells coupled by gap junctions. *Comput. Neural Syst.*, **11**, 299–320.
8. Kopell, N. and Ermentrout, B. (2004) Chemical and electrical synapses perform complementary roles in the synchronization of interneuronal networks. *Proc. Natl. Acad. Sci. U.S.A.*, **101**, 15482–15487.
9. Debanne, D. and Rama, S. (2011) Astrocytes shape axonal signaling. *Sci. Signal.*, **4**, 162.
10. Galambos, R. (1960) A glia-neural theory of brain function. *Physiology*, **47**, 129–136.
11. Galambos, R. (2007) Reflections on the conceptual origins of neuron-glia interactions. *Neuron Glia Biol.*, **3**, 89–91.
12. Verkhratsky, S. and Butt, A. (2007) *Glia Neurobiology*, John Wiley & Sons, Inc., Hoboken, NJ.
13. Araque, A., Parpura, V., Sanzgiri, R.P., and Haydon, P.G. (1999) Tripartite synapses: glia, the unacknowledged partner. *Trends Neurosci.*, **22**, 208–215.
14. Araque, A. and Navarrete, M. (2010) Glial cells in neuronal network function. *Philos. Trans. R. Soc. B*, **365**, 2375–2381.
15. Halassa, M.M. and Haydon, P.G. (2010) Integrated brain circuits: astrocytic networks modulate neuronal activity and behavior. *Annu. Rev. Physiol.*, **72**, 335–355.
16. Kettenman, K. and Steinauer, C. (2005) in *Neuroglia* (eds K. Kettenmann and B.R. Ransom), Oxford University Press, Oxford, pp. 131–145.
17. Auld, D.S. and Robitaille, R. (2003) Glial cells and neurotransmission: an inclusive view of synaptic function. *Neuron*, **40**, 389–400.
18. Fields, R.D. and Stevens-Graham, B. (2002) New insights into neuron-glia communication. *Sci. Compass*, **298**, 551–562.
19. Perea, G., Navarrete, M., and Araque, A. (2009) Tripartite synapses: astrocytes process and control synaptic information. *Trends Neurosci.*, **32**, 421–431.
20. Ransom and Ye (2005) Gap junctions and hemichannels, in *Neuroglia* (eds K. Kettenmann and B.R. Ransom), Oxford University Press, Oxford, pp. 177–189.
21. Smith, M. and Pereda, A.E. (2003) Chemical synaptic activity modulates nearby electrical synapses. *Proc. Natl. Acad. Sci. U.S.A.*, **100** (8), 4849–4854.
22. Parpura, V. and Haydon, P.G. (2000) Physiological astrocytic calcium levels stimulate glutamate release to modulate adjacent neurons. *Proc. Natl. Acad. Sci. U.S.A.*, **97** (15), 8629–8634.
23. Bezzini, P., Domercq, M., Vesce, S., and Volterra, A. (2001) Neuron-astrocyte crosstalk during synaptic transmission. *Prog. Brain Res.*, **132**, 255–265.
24. Perea, G. and Araque, A. (2010) Glia modulates synaptic transmission. *Brain Res. Rev.*, **63**, 93–102.
25. Cornell-Bell, A.H., Finkbeiner, S.M., Cooper, M.S., and Smith, S.J. (1990) Glutamate induces calcium waves in cultured astrocytes: long-range glial signaling. *Science*, **247**, 470–473.
26. Charles, A. (1998) Intercellular calcium waves in glia. *Glia*, **24**, 39–49.
27. Harris, J. and Timofeeva, Y. (2010) Intercellular calcium waves in the fire-diffuse-fire framework: Green's function for gap junctional coupling. *Phys. Rev. E*, **82**, 051910.
28. Giaume, C. and Venance, L. (1998) Intercellular calcium signaling and gap junctional communication in astrocytes. *Glia*, **24**, 50–64.

29. Kuga, N., Sasaki, T., Takahara, Y., Matsuki, N., and Ikegaya, Y. (2011) Large-scale calcium waves traveling through astrocytic networks in vivo. *J. Neurosci.*, **31**, 2607–2614.
30. Pereira, A. Jr., and Furlan, F.A. (2010) Astrocytes and human cognition: modeling information integration and modulation of neuronal activity. *Progr. Neurobiol.*, **92**, 405–420.
31. Giaurne, C. and Liu, X. (2011) From a glial syncytium to a more restricted and specific glial networking. *J. Physiol. Paris* (epub) (2012) **106** (1-2), 34–39.
32. Hirrlinger, J., Hulsmann, S., and Kirchhoff, F. (2004) Astroglial processes show spontaneous motility at active synaptic terminals in situ. *Eur. J. Neurosci.*, **20**, 2235–2239.
33. Theodosius, D.T., Poulain, D.A., and Oliet, S.H.R. (2008) Activity-dependent structural and functional plasticity of astrocyte-neuron interactions. *Physiol. Rev.*, **88**, 983–1008.
34. Fellin, T. (2009) Communication between neurons and astrocytes: relevance to the modulation of synaptic and network activity. *J. Neurochem.*, **108**, 533–544.
35. Bushong, E.A., Martone, M.E., Jones, Y.Z., and Ellisman, M.H. (2002) Protoplasmic astrocytes in CA1 stratum radiatum occupy separate anatomical domains. *J. Neurosci.*, **22**, 183–192.
36. Ogata, K. and Kosaka, T. (2002) Structural and quantitative analysis of astrocytes in the mouse hippocampus. *Neuroscience*, **113**, 221–233.
37. Halassa, M.M., Fellin, T., Takano, H., Dong, J.-H., and Haydon, P.G. (2007) Synaptic islands defined by the territory of a single astrocyte. *J. Neurosci.*, **27**, 6473–6477.
38. Oberheim, N.A., Tian, G.-F., Han, X., Peng, W., Takano, T., Ransom, B., and Nedergaard, M. (2008) Loss of astrocytic domain organization in the epileptic brain. *J. Neurosci.*, **28**, 3264–3276.
39. Volterra, A. and Meldolesi, J. (2005) Astrocytes, from brain glue to communication elements: the revolution continues. *Natl. Rev. Neurosci.*, **6**, 626–640.
40. Kwok, J.C.F., Dick, G., Wang, D., and Fawcett, J.W. (2011) Extracellular matrix and perineuronal nets in CNS repair. *Dev. Neurobiol.*, **71**, 1073–1089.
41. Faissner, A., Pyka, M., Geissler, M., Sobik, T., Frischknecht, R., Gundelfinger, E.D., and Seidenbecher, C. (2010) Contributions of astrocytes to synapse formation and maturation – potential functions of the perisynaptic extracellular matrix. *Brain Res. Rev.*, **63**, 26–38.
42. Frischknecht, R., Heine, M., Perrais, D., Seidenbecher, C.I., Choquet, D., and Gundelfinger, E.D. (2009) Brain extracellular matrix affects AMPA receptor lateral mobility and short-term synaptic plasticity. *Nat. Neurosci.*, **12**, 897–904.
43. Nadkarni, S., Jung, P., and Levine, H. (2008) Astrocytes optimize the synaptic transmission of information. *PLoS Comput. Biol.*, **4** (5), e1000088.
44. Postnov, D.E., Koreshkov, R.N., Brazhe, N.A., Brazhe, A.R., and Sosnovtseva, O.V. (2009) Dynamical patterns of calcium signaling in a functional model of neuron-astrocyte networks. *J. Biol. Phys.*, **35**, 425–445.
45. De Pitta, M., Volman, V., Berry, H., and Ben-Jacob, E. (2011) A tale of two stories: astrocyte regulation of synaptic depression and facilitation. *PLoS Comput. Biol.*, **7** (12), e1002293.
46. Volman, V., Ben-Jacob, E., and Levine, H. (2007) The astrocyte as a gatekeeper of synaptic information transfer. *Neural Comput.*, **19**, 303–326.
47. Goldberg, M., Pitta, M.D., Volman, V., Berry, H., and Ben-Jacob, E. (2010) Nonlinear gap junctions enable long-distance propagation of pulsating calcium waves in astrocyte networks. *PLoS Comput. Biol.*, **6** (8), e1000909.
48. Matrosov, V.V. and Kazantsev, V.B. (2011) Bifurcation mechanisms of regular and chaotic network signaling in brain astrocytes. *Chaos*, **21**, 023103.
49. Mitterauer, B.J. (2012) Qualitative information processing in tripartite synapses: a hypothetical model. *Cognit. Comput.*, **4**, 181–194. doi: 10.1007/s12559-011-9115-2

50. Mitterauer, B.J. (2010) Significance of the astrocyte domain organization for qualitative information structuring in the brain. *Adv. Biosci. Biotech.*, **1**, 391–397.
51. Mitterauer, B.J. and Kofler-Westergren, B. (2011) Possible effects of synaptic imbalances on oligodendrocyte-axonic interactions in schizophrenia: a hypothetical model. *Front. Psychiatry*, **2**, 15. doi: 10.3389/fpsyg.2011.00015
52. Allegrini, P., Fronzoni, L., and Pirino, D. (2009) The influence of the astrocyte field on neuronal dynamics and synchronization. *J. Biol. Phys.*, **35**, 413–423.
53. Sotero, R. and Martinez-Cancino, R. (2010) Dynamical mean field model of a neural-glia mass. *Neural Comput.*, **22**, 969–997.
54. Kuffler, S.W. and Nicholls, J.G. (1966) The physiology of neuroglia cells. *Physiol. Biol. Chem. Exp. Pharmacol.*, **57**, 1–90.
55. Vizi, E.S. and Labos, E. (1991) Non-synaptic interactions at presynaptic level. *Progr. Neurobiol.*, **37**, 145–163.
56. Agnati, L.F., Zoli, M., Stromberg, I., and Fuxe, K. (1995) Intercellular communication in the brain: wiring versus volume transmission. *Neuroscience*, **69**, 711–726.
57. Zoli, M. and Agnati, L.F. (1996) Wiring and volume transmission in the central nervous system: the concept of closed and open synapses. *Progr. Neurobiol.*, **49**, 363–380.
58. Frankenhaeuser, B. and Hodgkin, A.L. (1956) The aftereffects of impulses in the giant nerve fibers of Loligo. *J. Physiol.*, **131**, 341–376.
59. Egelman, D.M. and Montague, P.R. (1998) Computational properties of peri-dendritic calcium fluctuations. *J. Neurosci.*, **18**, 8580–8589.
60. Werner, G. (2005) Neural Computation in Excitable Media, <http://cogprints.org/8022/7/ExcitableMediaSeminar.pdf> (accessed 20 November 2013).
61. Froehlich (2007).
62. Durand, E.M., Park, E.H., and Jensen, A.L. (2010) Potassium diffusive coupling in neural networks. *Philos. Trans. R. Soc. B*, **365**, 2347–2362.
63. Ullah, G., Cressman, J.R., Barreto, E., and Schiff, S.J. (2009) The influence of sodium and potassium dynamics on excitability, seizures, and the stability of persistent states: II. Network and glial dynamics. *Comput. Neurosci.*, **26**, 171–183.
64. Bach-Y-Rita, P. (1995) *Nonsynaptic Diffusion Neurotransmission and Late Brain Reorganization*, Demos Medical Publishing, New York.
65. Rusakov, D.A. and Kullmann, D.M. (1998) Geometric and viscous components of the tortuosity of the extracellular space in the brain. *Proc. Natl. Acad. Sci. U.S.A.*, **95**, 8975–8980.
66. Hrabe, J., Hrabetova, S., and Segeth, K. (2004) A model of effective diffusion and tortuosity in the extracellular space of the brain. *Biophys. J.*, **87**, 1606–1617.
67. Biess, A., Korkotian, E., and Holcman, D. (2007) Diffusion in a dendritic spine: the role of geometry. *Phys. Rev. E*, **76**, 021922.
68. Hinzman, J.M., Thomas, T.C., Quintero, J.E., Gerhardt, G.A., and Lifshitz, J. (2012) Disruptions in the regulation of extracellular glutamate by neurons and glia in the rat striatum two days after diffuse brain injury. *J. Neurotrauma*, **29**, 1197–1208.
69. Jensen, J.B., Pickering, D.S., and Schousboe, A. (2000) Depolarization-induced release of [³H]D-aspartate from GABAergic neurons caused by reversal of glutamate transporters. *Int. J. Dev. Neurosci.*, **18**, 309–315.
70. Danbolt, N.C. (2001) Glutamate uptake. *Prog. Neurobiol.*, **65**, 1–105.
71. Kaczmarek, L.K. and Levitan, J.B. (1987) *Neuromodulation*, Oxford University Press, New York.
72. Katz, P.S. (1999) *Beyond Neurotransmission: Neuromodulation and its Importance for Information Processing*, Oxford University Press, Oxford.
73. Getting, P.A. (1989) Emerging principles governing the operation of neural networks. *Annu. Rev. Neurosci.*, **12**, 185–204.

74. Harris-Warrick, R.M. and Marder, E. (1991) Modulation of neural networks for behavior. *Annu. Rev. Neurosci.*, **14**, 39–57.
75. Marder, E. and Calabrese, R.L. (1996) Principles of rhythmic motor pattern generation. *Physiol. Rev.*, **76**, 687–717.
76. Pawlak, V., Wickens, J.R., Kirkwood, A., and Kerr, J.N.D. (2010) Timing is not everything: neuromodulation opens the STDP gate. *Front. Synaptic Neurosci.*, **2**, 1–14.
77. Nusbaum, M.P. (2002) Regulating peptidergic modulation of rhythmically active neural circuits. *Brain Behav. Evol.*, **60**, 378–387.
78. Nassel, D.R. (2009) Neuropeptide signaling near and far: how localized and timed is the action of neuropeptides in brain circuits? *Invert Neurosci.*, **9**, 57–75.
79. Hasselmo, M.E. and Sarter, M. (2011) Modes and models of forebrain cholinergic neuromodulation of cognition. *Neuropharmacology*, **56**, 52–73.
80. Doya, K. (2002) Metalearning and neuromodulation. *Neural Networks*, **15**, 495–506.
81. Krichmar, J.L. (2008) The neuromodulatory system: a framework for survival and adaptive behavior in a challenging world. *Adapt. Behav.*, **16**, 385–399.
82. Cools, R., Roberts, A.C., and Robbins, T.W. (2007) Serotonergic regulation of emotional and behavioural control processes. *Trends Cogn. Sci.*, **12**, 31–40.
83. Dickinson, P.S. (2006) Neuromodulation of central pattern generators in invertebrates and vertebrates. *Curr. Opin. Neurobiol.*, **16**, 604–614.
84. Brezina, V. (2010) Beyond the wiring diagram: signaling through complex neuromodulator networks. *Philos. Trans. R. Soc. B*, **365**, 2363–2374.
85. Brezina, V., Orehkova, I.V., and Weiss, K.R. (2000) Optimization of rhythmic behaviors by modulation of the neuromuscular transform. *J. Neurophysiol.*, **83**, 260–279.
86. Stern, E., Fort, T.J., Miller, M.W., Peskin, C.S., and Brezina, V. (2007) Decoding modulation of the neuromuscular transform. *Neurocomputing*, **70**, 1753–1758.
87. Proekt, A., Brezina, V., and Weiss, K.R. (2004) Dynamical basis of intentions and expectations in a simple neuronal network. *Proc. Natl. Acad. Sci. U.S.A.*, **101**, 9447–9452.
88. Marder, E. and Thirumalai, V. (2002) Cellular, synaptic and network effects of neuromodulation. *Neural Networks*, **15**, 479–493.
89. Katz, P.S. and Frost, W.N. (1996) Intrinsic neuromodulation: altering neuronal circuits from within. *Trends Neurosci.*, **19**, 54–61.
90. Hansson, E. and Ronnback, L. (1994) Astroglial modulation of synaptic transmission. *Perspect. Dev. Neurobiol.*, **2**, 217–223.
91. Fellous, J.M. and Linster, C. (1998) Computational models of neuromodulation. *Neural Comput.*, **70**, 771–805.
92. Mukherjee, P. and Kaplan, E. (1995) Dynamics of neurons in the cat lateral geniculate nucleus: in vivo electrophysiology and computational modeling. *J. Neurophysiol.*, **74** (3), 1222–1243.
93. West, B.J. and Grigolini, P. (2011) *Complex Webs: Anticipating the Improbable*, Cambridge University Press, Cambridge, MA.
94. Marder, E. (2011) Variability, compensation, and modulation in neurons and circuits. *Proc. Natl. Acad. Sci. U.S.A.*, **108**, 15541–15548.
95. Batterman, R.W. (2002) *The Devil in the Details*, Oxford University Press, Oxford.
96. Batterman, R.W. (2010) On the explanatory role of mathematics in the empirical sciences. *Br. J. Philos. Sci.*, **61**, 1–25.
97. Olypher, A.V. and Calabrese, R.L. (2007) Using constraints on neuronal activity to reveal compensatory changes in neuronal parameters. *J. Neurophys.*, **98**, 3749–3758.
98. Ribrault *et al.* (2011) From the stochasticity of molecular processes to the variability of synaptic transmission. *Nat. Rev. Neurosci.*, **12** (7), pp. 375–387.
99. Holcman, D. (2012) The complexity of synaptic transmission revealed by a multiscale analysis approach from the molecular to the cellular level.

- arXiv.org/abs/1202.2034. (accessed 08 February 2014).
100. Ederer, M., Sauter, T., Bullinger, E., Gilles, E.-D., and Allgower, F. (2003) An approach for dividing models of biological reaction networks into functional units. *Simulation*, **79**, 703–716.
 101. De Jong, H.D., Gouze, J.-L., Hernandez, C., Page, M., Sari, T., and Geiselmann, J. (2004) Qualitative simulation of genetic regulatory networks using piecewise-linear models. *Bull. Math. Biol.*, **66**, 301–340.
 102. Galatolo, S., Hoyrup, M., and Rojas, C. (2012) Statistical properties of dynamical systems – simulation and abstract computation. *Chaos, Solitons Fractals*, **45**, 1–14.
 103. Ben-Jacob, E. (2010) Bacterial self-organization: co-enhancement of complexification and adaptability in dynamic environment. *Philos. Trans. R. Soc. London A*, **361**, 1283–1312.
 104. West, B.J. and Grigolini, P. (2010) Habituation and 1/f-noise. *Physica A*, **389**, 5706–5718.
 105. Doyle, J. and Csete, M. (2005) Motifs, control, and stability. *PLoS Biol.*, **3**, e392.
 106. Hausdorff, J.M. and Peng, C.-K. (1996) Multiscaled randomness: a possible source of 1/f noise in biology. *Phys. Rev. E*, **54**, 2154–2157.
 107. Marom, S. (2010) Neural timescales or lack thereof. *Prog. Neurobiol.*, **90**, 16–28.
 108. Montroll, E. and Shlesinger, M. (1982) On 1/f noise and other distributions with long tails. *Proc. Natl. Acad. Sci. U.S.A.*, **79** (10), 3380–3383.
 109. Anderson, R.B. (2001) The power law as an emergent property. *Memory Cognit.*, **29**, 1061–1068.
 110. Fusi, S., Drew, P.J., and Abbott, L.F. (2005) Cascade models of synaptically stored memories. *Neuron*, **45**, 599–611.
 111. Drew, P.J. and Abbott, L.F. (2006) Models and properties of power-law adaptation in neural systems. *J. Neurophysiol.*, **96**, 826–833.
 112. West, B.J. (2010) Fractal physiology and the fractional calculus: a perspective. *Front. Physiol.*, **1**, 1–17.
 113. Werner, G. (2010) Fractals in the nervous system: conceptual implications for theoretical neuroscience. *Front. Physiol.*, **1**, 1–28.
 114. Werner, G. (2011) Letting the brain speak for itself. *Front. Physiol.*, **2**, 1–9.
 115. Stanley, H.E. and Meakin, P. (1988) Multifractal phenomena in physics and chemistry. *Nature*, **335**, 405–409.
 116. Mandelbrot, B. (1999) *Multifractals and 1/f Noise*, Springer, New York.
 117. Mandelbrot (1989) Fractals in physics: essays in honor of Benoit B. Mandelbrot: proceedings of the international conference honouring Benoit B. Mandelbrot on his 65th birthday, Vence, France, 1-4 October, 1989, (eds. A. Aharony and J. Feder), Amsterdam, North-Holland.
 118. Halsey, T.C., Jensen, M.H., Kadanoff, L.P., Procaccia, I., and Shraiman, B.I. (1986) Fractal measures and their singularities: the characterization of strange sets. *Phys. Rev. A*, **33**, 1141–1151.
 119. Stephen, D.G. and Dixon, J.A. (2011) Strong anticipation: multifractal cascade dynamics modulate scaling in synchronization behaviors. *Chaos, Solitons Fractals*, **44**, 160–168.
 120. Stephen, D.G., Stepp, N., Dixon, J.A., and Turvey, M.T. (2008) Strong anticipation: sensitivity to long-range correlations in synchronization behavior. *Physica A*, **387**, 5271–5278.
 121. Stepp, N. and Turvey, M.T. (2010) On strong anticipation. *Cognit. Syst. Res.*, **11**, 148–164.

Color Plates

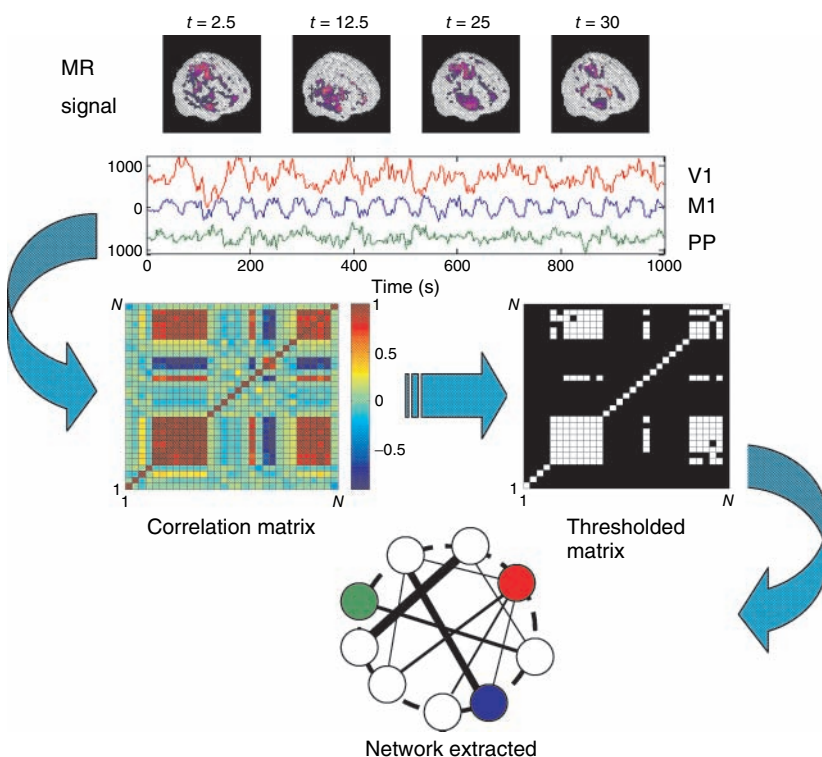


Figure 3.1 Methodology used to extract functional networks from the brain fMRI BOLD signals. The correlation matrix is calculated from all pairs of BOLD time series. The strongest correlations are selected to define the networks nodes. The top four images represent examples of snapshots

of activity at one moment and the three traces correspond to time series of activity at selected voxels from visual (V1), motor (M1), and posterioparietal (PP) cortices. (Figure redrawn from [41].) (This figure also appears on page 48.)

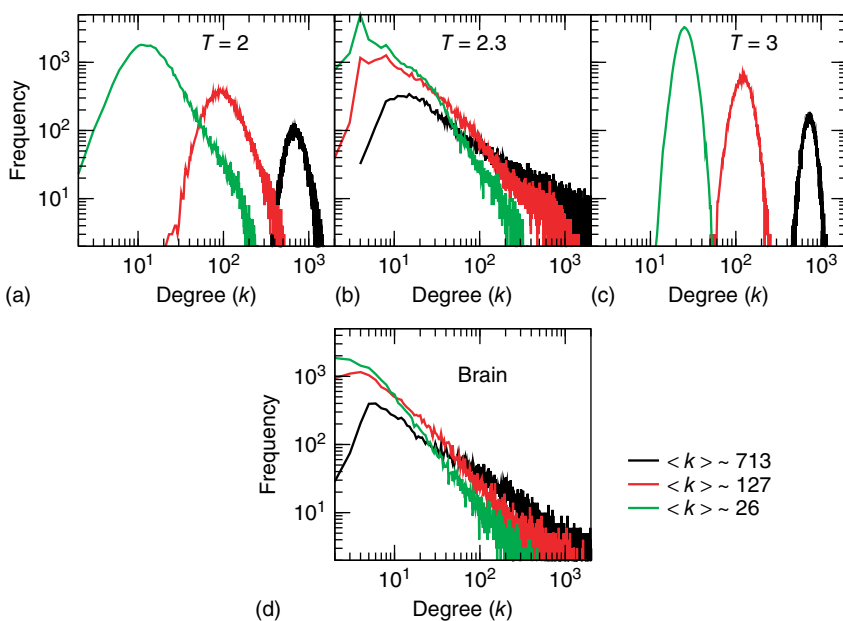


Figure 3.2 At criticality, brain and Ising networks are indistinguishable from each other. The graphs show a comparison of the link density distributions computed from correlation networks extracted from brain data (d) and from numerical simulations of the Ising model (a–c) at three temperatures: critical ($T = 2.3$), subcritical ($T = 2$), and

supercritical ($T = 3$). (a–c) The degree distribution for the Ising networks at $T = 2$, $T = 2.3$, and $T = 3$ for three representative values of $\langle k \rangle \approx 26, 127$, and 713 . (d) Degree distribution for correlated brain network for the same three values of $\langle k \rangle$. (Figure redrawn from Fraiman *et al.* [42].) (This figure also appears on page 50.)

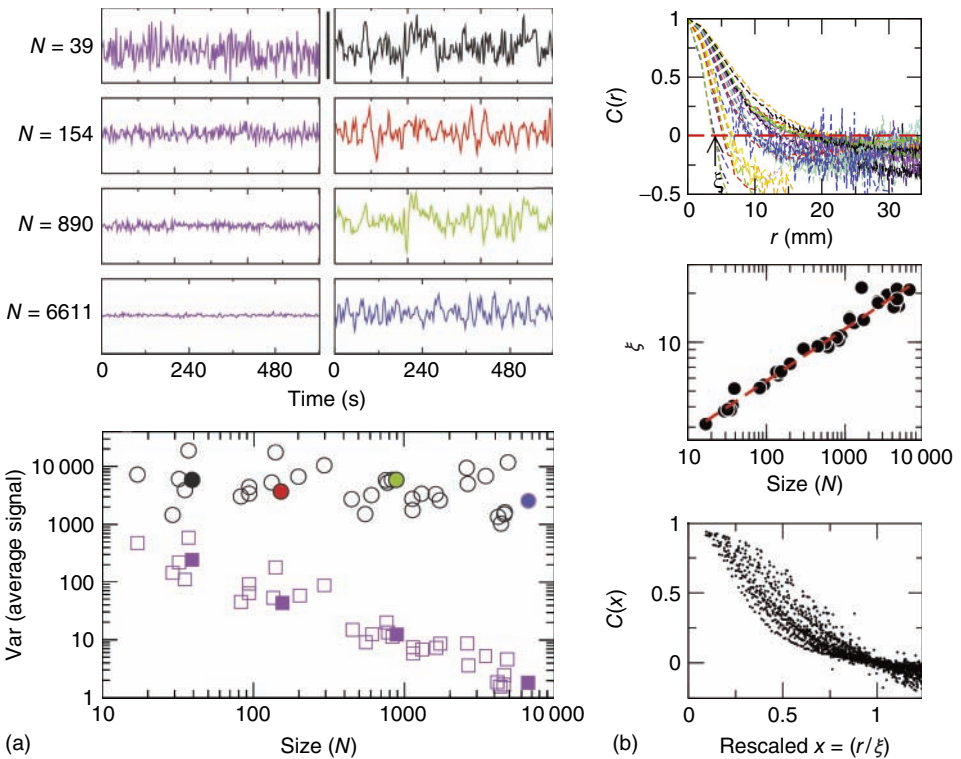


Figure 3.4 Spontaneous fluctuations of fMRI data show anomalous behavior of the variance (a) and divergence of the correlation length (b). Top figures in panel a show four examples of average BOLD time series (i.e., $\bar{B}(t)$ in Eq. (4.2)) computed from clusters of different sizes N . Note that while the amplitude of the raw BOLD signals (right panels) remains approximately constant, in the case of the shuffled data sets (left panels) the amplitude decreases drastically for increasing cluster sizes. The bottom graph in panel a shows the calculations for the 35 clusters (circles) plotted as a function of the cluster size, demonstrating that variance is independent of the RSN's cluster size. The square symbols show similar computations for a surrogate time series constructed by randomly reordering the original BOLD time series, which exhibit the expected $1/N$ scaling (dashed line). Filled symbols in the bottom panel are used to denote the values for

the time series used as examples in the top panel. In panel b, there are three graphs: the top one shows the correlation function $C(r)$ as a function of distance for clusters of different sizes. Contrary to naive expectations, large clusters are as correlated as relatively smaller ones: the correlation length increases with cluster size, a well-known signature of criticality. Each line in the top panel shows the mean cross-correlation $C(r)$ of BOLD activity fluctuations as a function of distance r averaged over all time series of each of the 35 clusters. The correlation length ξ , denoted by the zero crossing of $C(r)$ is not a constant. As shown in the middle graph scale, ξ grows linearly with the average cluster diameter d for all the 35 clusters (filled circles), $\xi \sim N^{1/3}$. The bottom graph shows the collapse of $C(r)$ by rescaling the distance with ξ . (Figure redrawn from Fraiman and Chialvo [56].) (This figure also appears on page 53.)

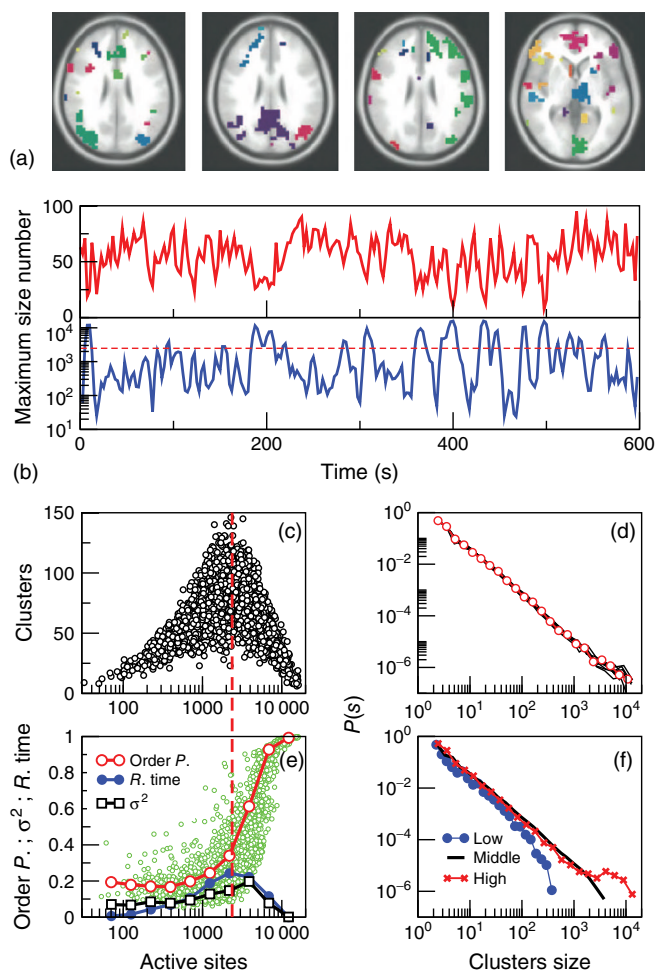


Figure 3.7 The level of brain activity continuously fluctuates above and below a phase transition. (a) Examples of coactivated clusters of neighbor voxels (clusters are 3D structures; thus, seemingly disconnected clusters may have the same color in a 2D slice). (b) Example of the temporal evolution of the number of clusters and its maximum size (in units of voxels) in one individual. (c) Instantaneous relation between the number of clusters versus the number of active sites (i.e., voxels above the threshold) showing a positive/negative correlation depending on whether activity is below/above a critical value (~ 2500 voxels, indicated by the dashed line here and in panel b). (d) The cluster size distribution follows a power law spanning four orders of magnitude. Individual statistics for each of the 10 subjects are plotted with lines and the average with symbols. (e) The order

parameter, defined here as the (normalized) size of the largest cluster, is plotted as a function of the number of active sites (isolated data points denoted by dots, averages plotted with circles joined by lines). The calculation of the residence time density distribution ("R. time," filled circles) indicates that the brain spends relatively more time near the transition point. Note that the peak of the R. time in this panel coincides with the peak of the number of clusters in panel c, as well as the variance of the order parameter (squares). (f) The computation of the cluster size distribution calculated for three ranges of activity (low: 0–800; middle: 800–5000; and high >5000) reveals the same scale invariance plotted in panel d for relatively small clusters, but shows changes in the cutoff for large clusters. (Figure redrawn from [58].) (This figure also appears on page 58.)

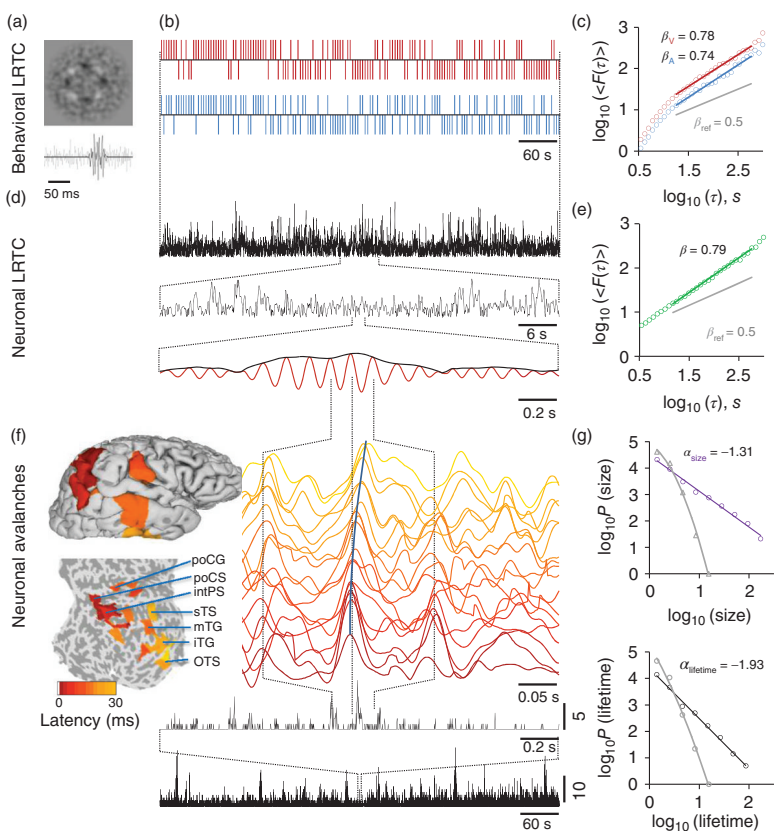


Figure 5.1 The individual scaling laws of individual behavioral LRTC, neuronal LRTC, and neuronal avalanches can be quantified with threshold-stimulus detection tasks (TSDT) and source-reconstructed M/EEG recordings. (a) Examples of noise-embedded visual and auditory stimuli whose signal-to-noise ratios are tuned before the experiment to yield a ~50% hit rate and then maintained constant. (b) Behavioral performance time series of detected (upward ticks) and undetected (downward ticks) display-rich dynamics in a bimodal audiovisual TSDT (visual, red; auditory, blue; time series are for the first 10 min of a 30 min session of a representative subject). (c) Visual and auditory detection time series exhibit long-range temporal correlations (LRTC) that can be characterized for each individual subject by DFA exponents, β_V and β_A . (d) Amplitude fluctuations of neuronal oscillations in local cortical patches (here, 10 Hz in inferior parietal

gyrus) are fractally self-similar and (e) show robust LRTC. (f) Avalanche dynamics are salient in source-reconstructed broadband data. The time series of cortical patches in the example avalanche are color coded by the peak latency. These colors correspond to those displayed on pial and flattened cortical surfaces and show the progression of this activity cascade from posterior parietal-to-temporal and post-central loci. The avalanche time series (bottom, black lines) show the number of cortical patches where a peak was found with zeros, indicating interavalanche periods. (g) The sizes and lifetimes of cortical avalanches are approximately power-law distributed with exponents, α , close to those of a critical branching process (-1.5 and -2 , respectively). All data in this figure are from the same 30 min session of a subject that is representative in having β closest to population mean. (Adapted from [18].) (This figure also appears on page 107.)

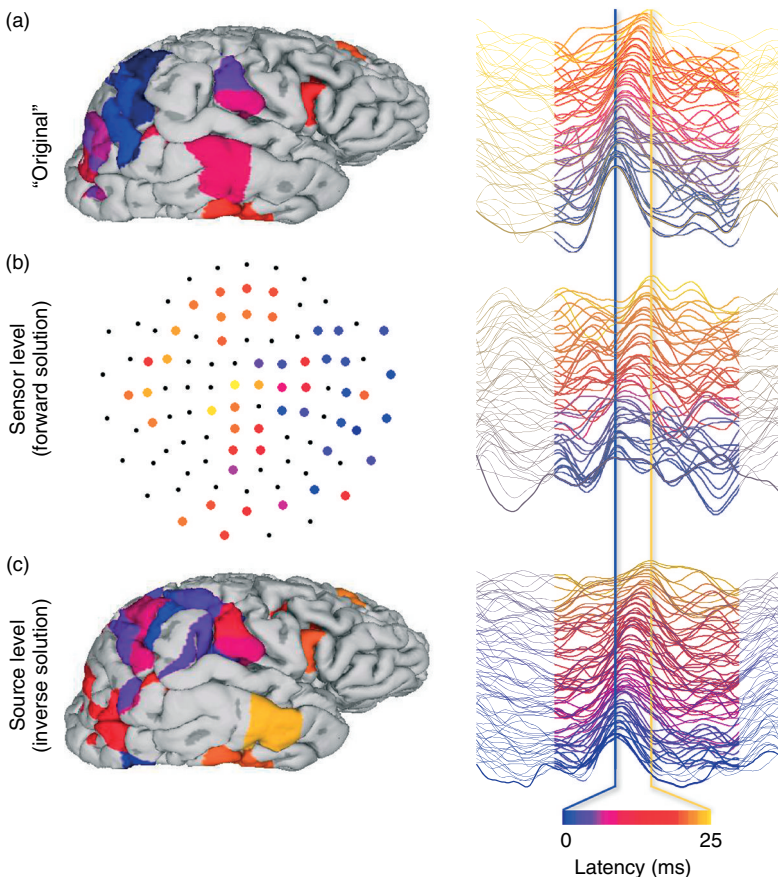


Figure 5.2 Source modeling of spontaneous M/EEG data can be used to reconstructs cortical current time series for analyses of LRTC and neuronal avalanches: a schematic illustration of the sensor- and source-level of a cortical activity cascade. (a) A neuronal avalanche was identified from source-reconstructed, real-valued, and broad-band (1–25 Hz) M/EEG data of a representative subject. In this illustration, we use these source time series as “original” waveforms of cortical currents. The left panel shows cortical patches where the peak amplitude exceeded a threshold of three standard deviations. The right panel shows the time

series of these patches. The patches and time series are color coded by the latency of the peak from the first peak in this cascade. (b) All patch time series in (a), including those not participating in the avalanche, were forward transformed to perform virtual M/EEG data acquisition and visualize the sensor level data in MEG planar gradiometers. (c) Cortically constrained minimum-norm-estimate source modeling of the sensor data (b) reconstructs the relatively well spatiotemporal characteristics of the original cascade. (This figure also appears on page 110.)

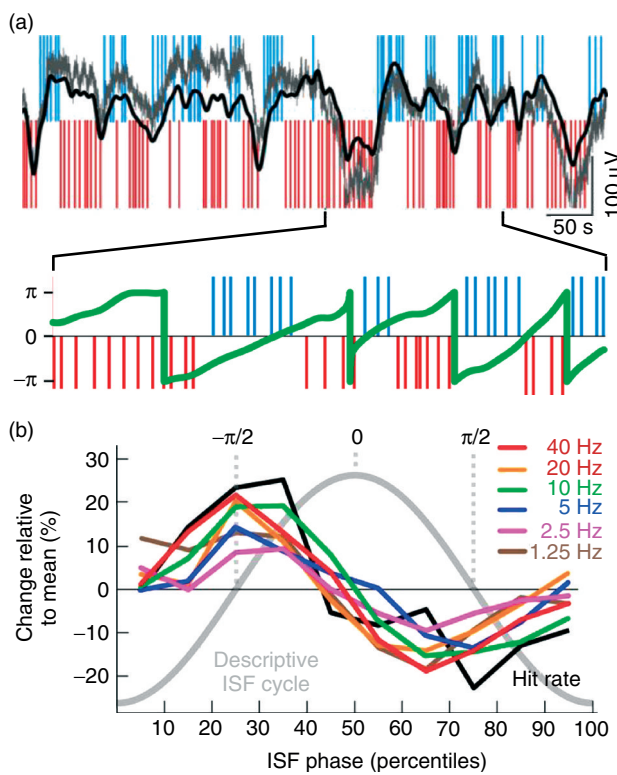


Figure 5.3 EEG ISFs are salient in an awake human EEG and correlated with behavioral ISFs. (a) Large-amplitude ISFs are readily observable in raw full-band EEG data (gray line: unfiltered, black line: band-pass filtering from 0.01 to 0.1 Hz) and reveal a correlation of the ISF phase (green line)

with psychophysical performance (blue and red ticks as in Figure 5.2). (b) Amplitudes of 1–40 Hz oscillations are correlated with the ISF phase similarly to behavior. (Adapted from [14].) (This figure also appears on page 112.)

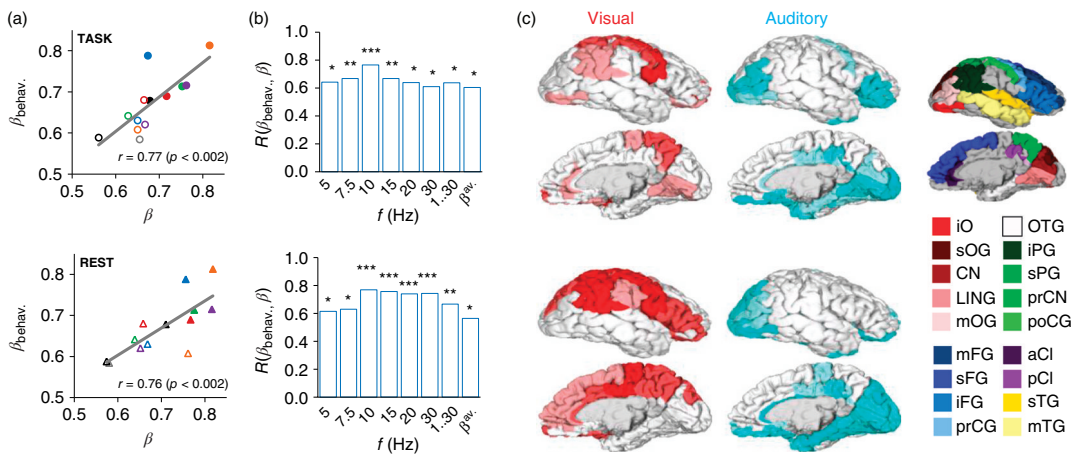


Figure 5.4 Scale-free neuronal dynamics are correlated with interindividual variability in behavioral scaling laws. (a) Mean local LRTC in the 10 Hz band (β) both during the TSDT task performance and in a separate resting-state session are correlated with the mean behavioral scaling exponents ($\beta_{\text{behav.}}$). (b) This correlation was significant in frequency bands from 5 to 30 Hz, in broadband data, and for the avalanche DFA (* $p < 0.05$, ** $p < 0.01$; *** $p < 0.005$). (c) Neuroanatomical source regions for the correlation between neuronal and behavioral LRTC scaling exponents. Pearson correlation coefficients were computed between $\beta_{\text{behav.}}$ and β in the beta and gamma (15, 20, and 30 Hz) bands for each cortical patch and significant ($p < 0.05$, FDR (false discovery rate) corrected) correlations were displayed on cortical surfaces. For each cortical patch of the Destrieux parcellation, the color intensity indicates the fraction of significant correlations across the three bands (pale 1/3, medium 2/3, full 3/3). Red: Correlation of visual behavioral scaling exponents, β_V , with the β of neuronal LRTC during visual task performance (upper panel) and in separate resting-state data (lower panel). Blue: Correlation of auditory behavioral scaling exponents, β_A , with the β of neuronal LRTC during auditory task performance and in separate resting-state data. Abbreviations: a, anterior; i, inferior; m, middle; p, posterior; pr, pre-s, superior; C, central; Cl, cingulate; CN, cuneus; F, frontal; G, gyrus; LIN, lingual; O, occipital; P, parietal; T, temporal. Red colors, occipital; green, parietal; blue, frontal; yellow, temporal; purple, cingulate. IPG shows the angular part. (Adapted from [18].) (This figure also appears on page 116.)

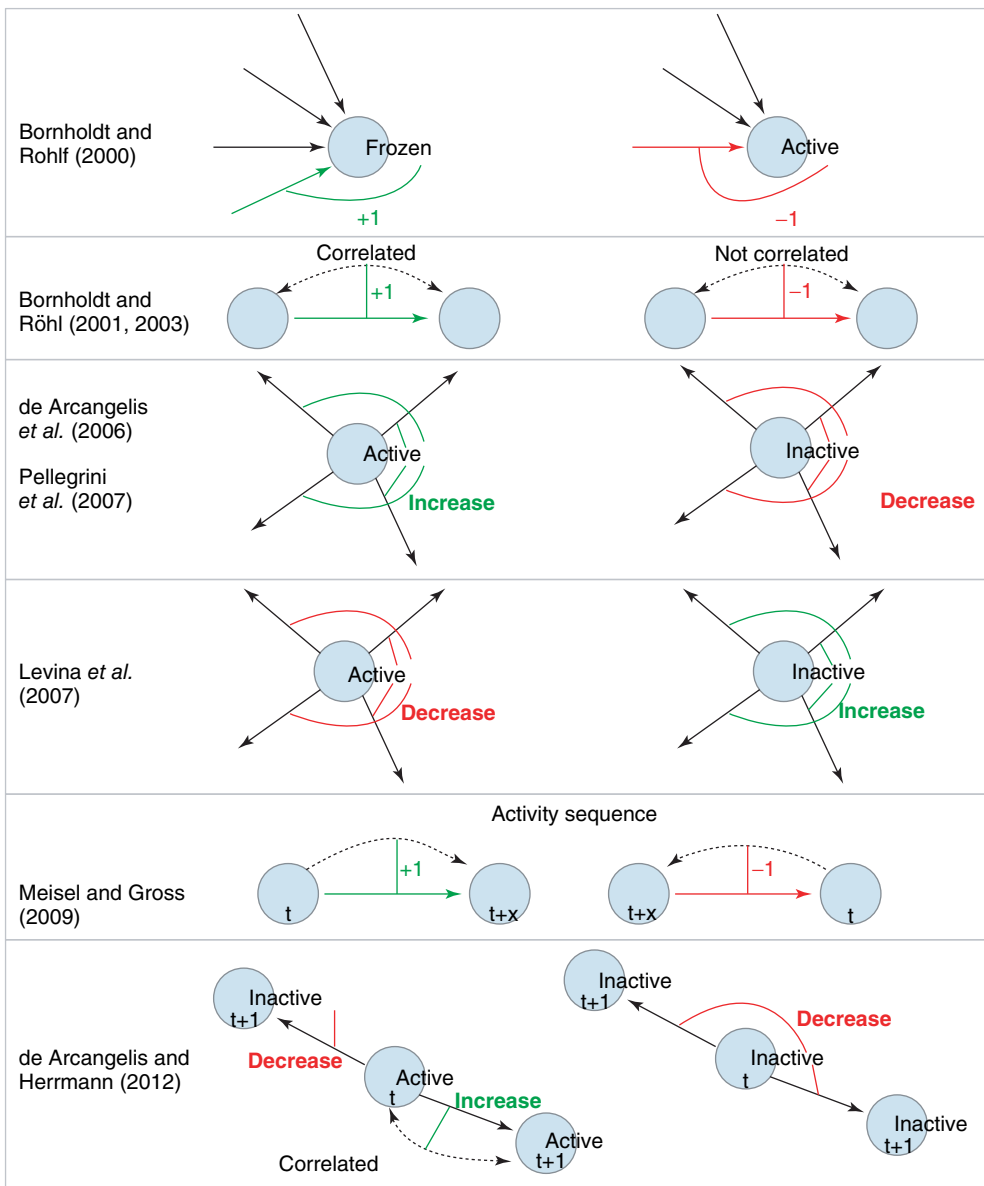


Figure 10.1 Schematic illustration of some of the different approaches to self-organization in neural network models. Rows 1 – 2: Links are either added (denoted by +1; green link) or removed (denoted by -1; red link) as a function of node activity or correlation between nodes. Rows 3 – 4: Here, activity or inactivity of a node affects all outgoings links (thin lines). All weights of the outgoing links from a node are decreased (red) or increased

(green) as a function of node activity. Row 5: Links are created and facilitated when nodes become active in the correct temporal sequence. Links directed against the sequence of activation are deleted. Row 6: Positive correlation in the activity between two nodes selectively increases the corresponding link, whereas there is non-selective weight decrease for links between uncorrelated or inactive nodes. (This figure also appears on page 232.)

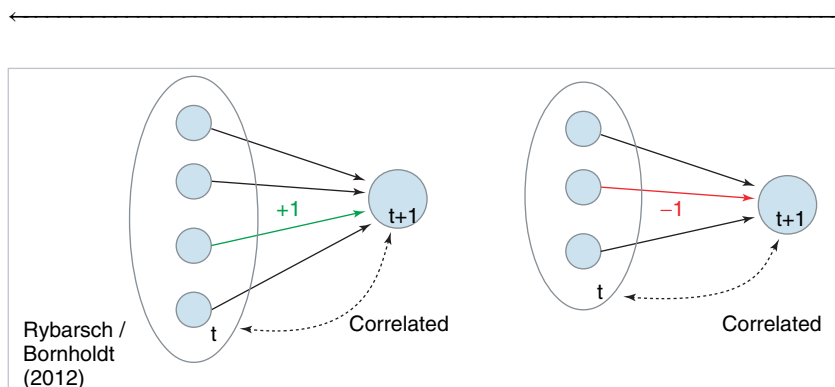


Figure 10.12 Schematic illustration of the rewiring mechanism based on average input correlation. In this example, the target node initially has three in-links. Left: If the addition of a fourth input increases the

average input correlation C_i^{avg} , a link will be inserted. Right: If removal of an existing in-link increases C_i^{avg} , the link will be deleted. (This figure also appears on page 246.)

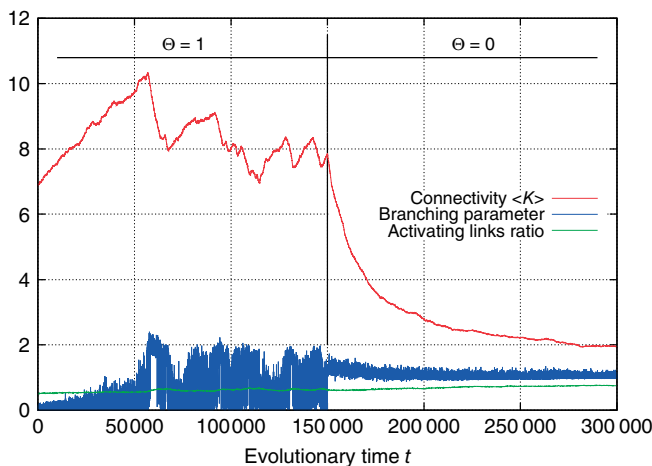


Figure 10.16 Rewiring response to a sudden decrease of activation thresholds. All Θ_i were set from 1 to 0 in the same time step. (This figure also appears on page 251.)

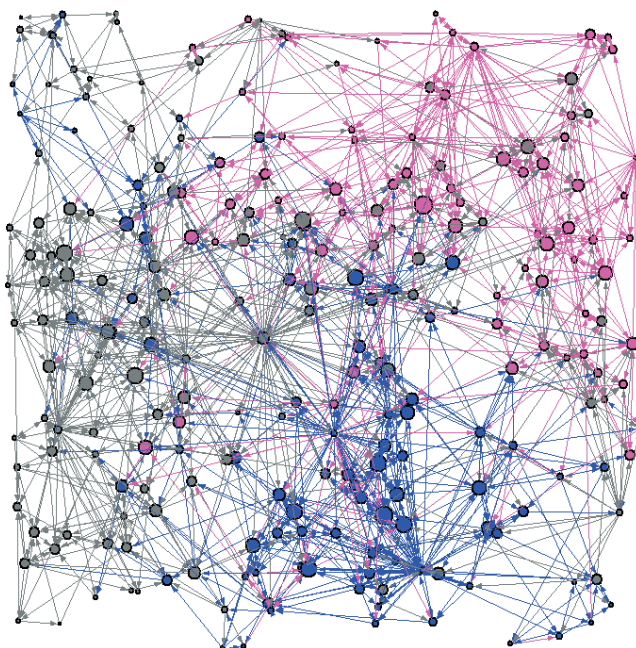
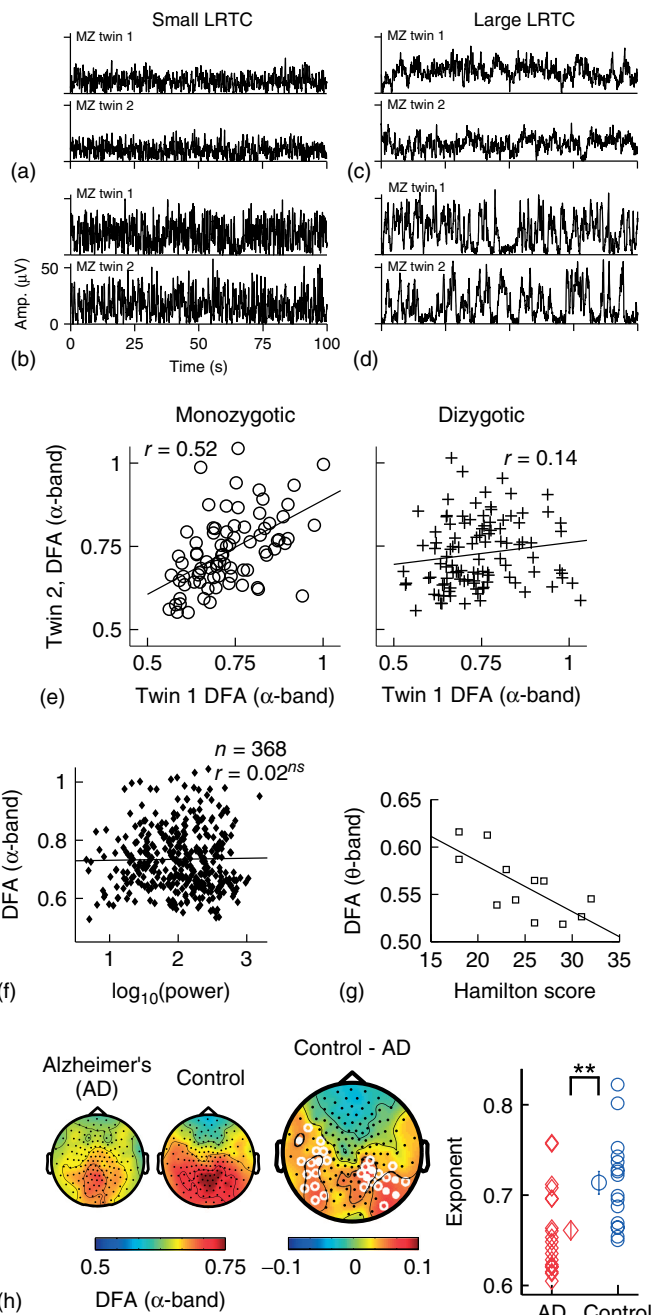


Figure 12.2 Two neuronal avalanches in the scale-free network. Two-hundred and fifty neurons are connected by directed bonds (direction indicated by the arrow at one edge), representing the synapses. The size of each neuron is proportional to the number

of in-connections, namely the number of dendrites. The two different avalanches are characterized by pink and blue colors. Connections and neurons not involved in the avalanche propagation are shown in gray. (This figure also appears on page 278.)

Figure 13.5 Results of applying DFA to neuronal oscillations. (a–d) Individual differences in long-range temporal correlations in α oscillations are, to a large extent, accounted for by genetic variation, which can be seen qualitatively by looking at four sets of monozygotic twins. (Figure modified from [32].) (e) The effect of genetic variation on LRTC can be quantified by the difference in correlations of DFA exponents between monozygotic and dizygotic twins. (Figure modified from [32].) (f) The DFA exponent is independent of oscillation power. Data were recorded using EEG on 368 subjects during a 3 min eyes-closed rest session. (Figure modified from [32].) (g) DFA exponents of θ oscillations in the left sensorimotor region correlate with the severity

of depression based on the Hamilton score. Data recorded from 12 depressed patients with MEG, during an eyes-closed rest session of 16 minutes. (Figure modified from [55].) (h) DFA of α oscillations shows a significant decrease in the parietal area in patients with Alzheimer's disease than in controls. MEG was recorded during 4 min of eyes-closed rest and the DFA exponent estimated in the time range of 1–25 s. (Right) Individual-subject DFA exponents averaged across significant channels are shown for the patients diagnosed with early-stage Alzheimer's disease ($n = 19$) and the age-matched control subjects ($n = 16$). (Figure modified from [56].) (This figure also appears on page 308.)



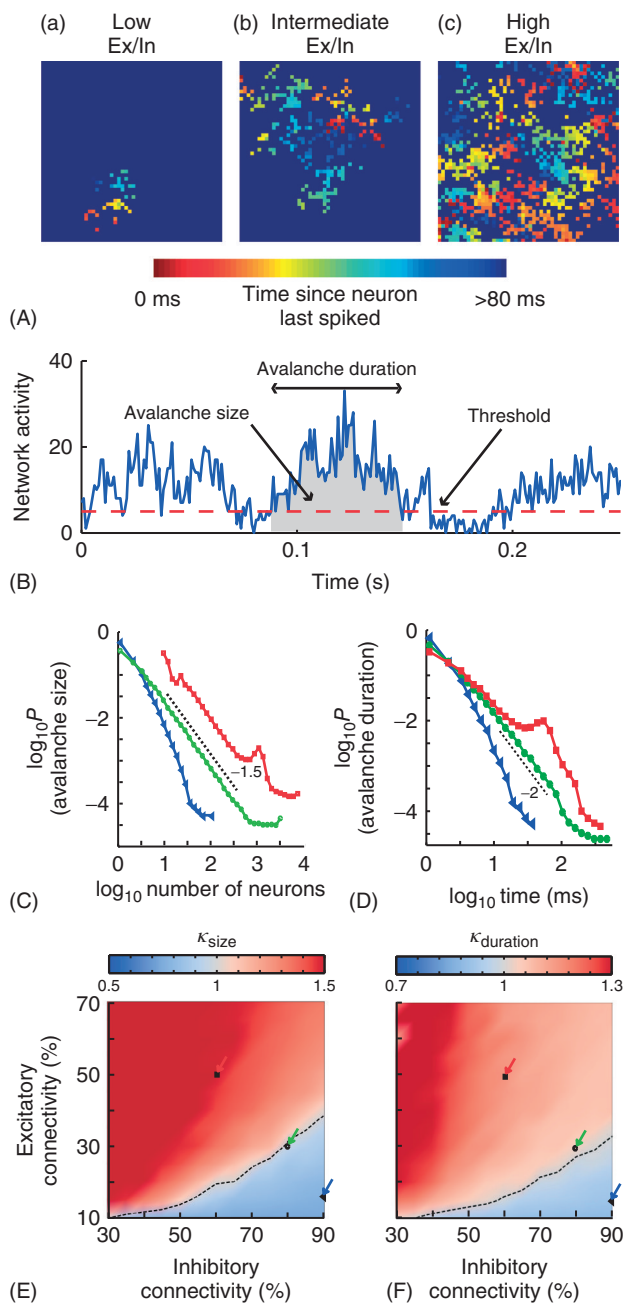


Figure 13.7 On short timescales (120 ms), activity spreads in the form of neuronal avalanches. (A) Example snapshot of network activity for three networks with different excitatory (Ex)/inhibitory (In) connectivity balance (E/I balance). Colors indicate the time since each neuron last spiked. (a) Networks with low E/I balance show wavelike propagation over short distances. (b) Networks with intermediate E/I balance often display patterns that are able to span the network and repeat. (c) Networks with high E/I balance have high network activity, but have little spatial coherence in their activity patterns. (B) An avalanche starts and ends when integrated network activity crosses a threshold value. (C) The avalanche-size distribution shows power-law scaling in the transition region (green circles) with a slope of -1.5 (dashed line). The subcritical region has

an exponential distribution (blue triangles). The supercritical region (red squares) has a clear characteristic scale. (D) The avalanche-size distribution shows power-law scaling in the transition region (green circles) with a slope of -2 (dashed line). The subcritical region has an exponential distribution (blue triangles). The supercritical region (red squares) has a clear characteristic scale. (E) The connectivity-parameter space shows a transition (dashed black line) from subcritical (*blue*) to supercritical (*red*) avalanches. Arrows indicate the connectivity parameters of networks in (C). (F) The connectivity-parameter space shows a transition (dashed black line) from subcritical (*blue*) to supercritical (*red*) avalanches. Arrows indicate the connectivity parameters of networks in (D). (Modified from [61].) (This figure also appears on page 312.)



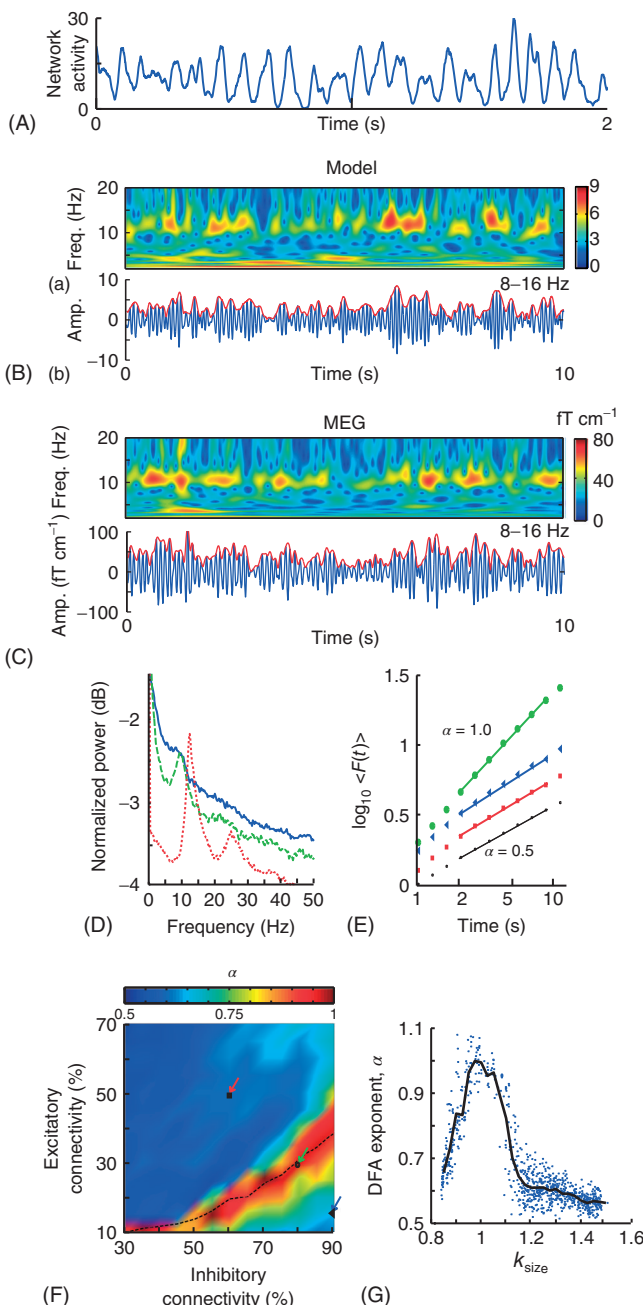


Figure 13.8 On long timescales (>2 s), the model produces oscillations qualitatively and quantitatively similar to human α -band oscillations. A: The spatially integrated network activity in a sliding window of 10 ms displays oscillatory variation. B: (a) Time-frequency plot of the integrated network activity from a network with 50% excitatory and 90% inhibitory connectivity. (b) Integrated network activity filtered at 8–16 Hz (blue), and the amplitude envelope (red). C: The same plots as in (A), but for a representative subject and MEG planar gradiometer above the parietal region. D: Power spectrum of the integrated network activity shows a clear peak frequency at ~ 10 Hz for three networks with Excitatory:Inhibitory connectivity of 50%:60% (red),

30%:80% (green), and 15%:90% (blue), respectively. E: DFA in double-logarithmic coordinates shows power-law scaling in the critical regime with $\alpha = 0.9$ (green circles). The subcritical ($\alpha = 0.6$, blue triangles) and supercritical ($\alpha = 0.6$, red squares) regimes display similar correlations to a random signal (black dots). F: The connectivity-parameter space shows a clear peak region with stronger long-range temporal correlations. Overlaying the transition line from Figure 13.7E indicates that peak DFA occurs at $\kappa \sim 1$. G: DFA exponents peak when the networks produce neuronal avalanches with critical exponents ($\kappa \sim 1$). (Modified from [61].) (This figure also appears on page 314.)

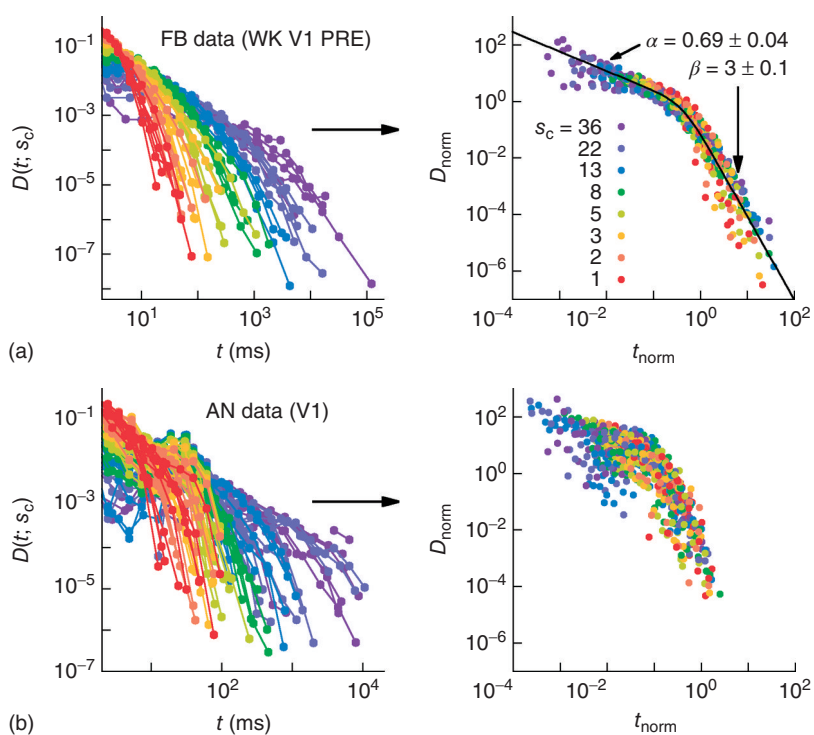
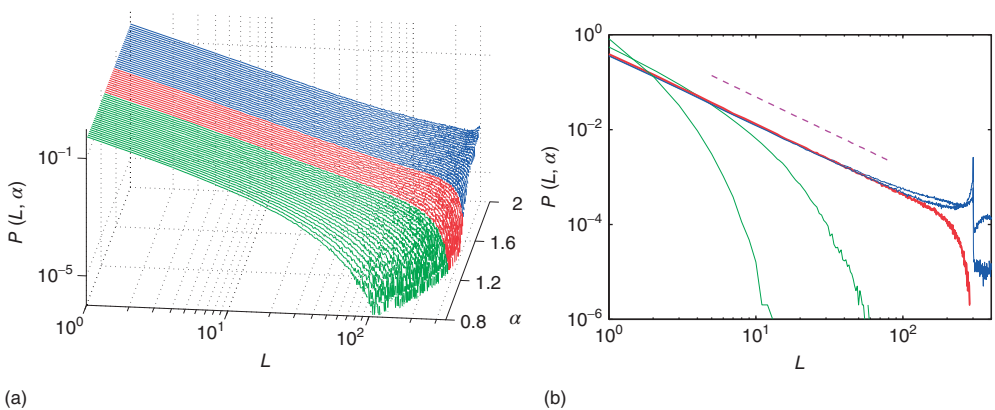


Figure 16.7 Families of distributions of inter-avalanche intervals $D(t; s_c)$ for (a) freely behaving animals and (b) anesthetized animals. Left column: regular distributions.

Right column: rescaled distributions (see text for details). Different colors denote different values of s_c . (Adapted from Ref. [50].) (This figure also appears on page 360.)

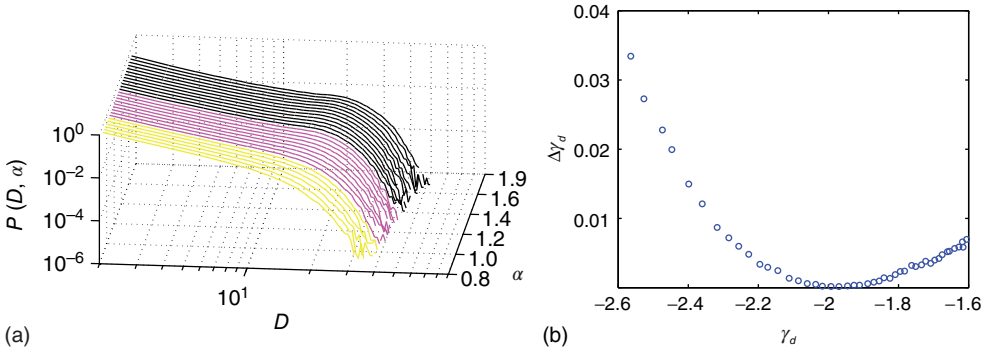


(a)

(b)

Figure 20.2 Distribution of avalanche sizes for different values of the connection parameter α . (a) At $\alpha < 1.3$, the distribution is subcritical (green). It becomes critical in an interval around $\alpha = 1.4$ (red). For $\alpha > 1.6$, the distribution is supercritical (blue). (Figure first published in Ref. [23].) (b) Characteristic

examples of all three kinds of distributions with the same color code. Results are obtained for $N = 300$, $\nu = 10$, $u = 0.2$, $I^{\text{ext}} = 0.025$. (Figure adapted from Ref. [39].) <http://www.nature.com/reprints/permission-requests.html>. (This figure also appears on page 422.)



(a)

(b)

Figure 20.4 (a) Avalanche duration distribution for different values of the connectivity parameter α . (b) Power law exponent γ_d fitted for small avalanche durations as a function of the goodness of the power law fit to the avalanche size distribution. $N = 100$,

$\nu = 10$, $u = 0.2$. In (a), green gray traces correspond to subcritical distributions of avalanche sizes, red gray traces critical and blue ones supercritical. For details see Figure 20.2. (This figure also appears on page 423.)

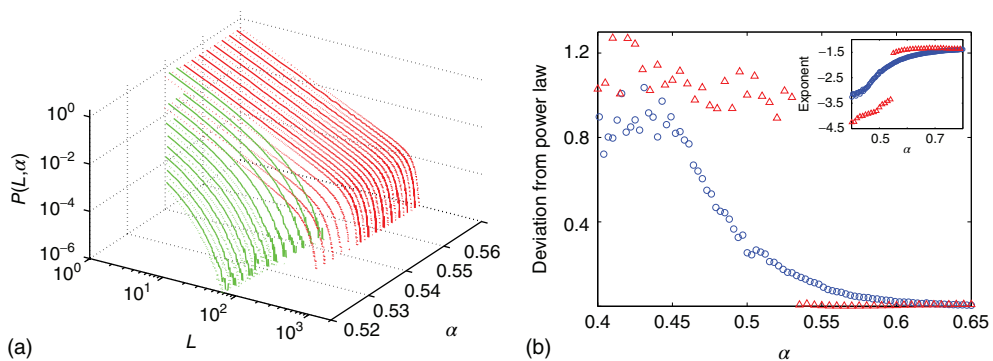


Figure 20.8 (a) Distribution of avalanche sizes for different values of α . Below $\alpha < 0.543$, a subcritical distribution exists (green). Critical behavior can be observed above $\alpha = 0.53$ (blue/red). The picture indicates a hysteresis with respect to α , which is illustrated by the section through the 3-D plot and shown in the inset. For large networks, all distributions of the upper branch are critical, while the lower branch remains

subcritical. See also Figure 20.9. (b) Deviation of avalanche size distribution from a power law for different α . Triangles represent facilitatory synapses, while circles represent depressing synapses. The inset shows the exponent of the nearest power law distribution. For both, $N = 300$, $\nu = 10$, $u_0 = 0.1$, $I_0 = 7.5$ [39]. (Copyright 2009 by The American Physical Society). (This figure also appears on page 428.)

Index

a

Abelian distribution 419
 absorbing state 349
 activated random walk model 263
 active inference neurobiological implementation 199–202, 204–205
 – action 204
 – perception and predictive coding 202–204
 activity dependent model, for neuronal avalanches 273–274
 – learning 280–283
 – model 274–275
 – plastic adaptation 276–277
 – spontaneous activity 277
 – power spectra 278–280
 – temporal organization 283–288
 adaptive rates 263–265, 267
 adjacency matrix and network representation 368
 all-to-all (ATA) condition 486, 488, 497–501
 Andronov–Hopf bifurcation 474
 anomalous scaling 51–52
 anti-Hebbian weights 475–476
 Apollonian networks 230
 approximate Bayesian inference 198
 attractor riddling 193
 attractor ruins 193
 autoactivation 193
 avalanche. *See* neuronal avalanche

b

balanced synchronization 208
 basic reproductive number 396
 beamformers 139
 bifurcation theory 473
 bimanual coordination 75–76
 biological coordination 72–74
 – critical fluctuations 81–82

– critical slowing down 80
 – fluctuations enhancement 81
 biologically realistic networks 449
 – NMDA and inhibition 450, 452
 – small-world connectivity 449
 birdsong, attractors, and critical slowing 211, 221, 223
 – perception 219–221
 – perceptual categorization 214–216
 – perceptual instability and switching 216–219
 – stimulus generation and generative model 213–214
 – synthetic avian brain 212–213
 Birkeland currents 131
 bistable states in clustered network 412–413
 block spin transformation 69–70
 blood-oxygenated-level-dependent (BOLD) signal 48–57, 87, 89, 108, 111, 114, 178
 Bogdanov–Takens (BT) bifurcation 473–475
 Boltzmann distribution 512
 Boolean networks 430
 Boolean state model 243
 – model definitions 244
 – observations 245–249
 – rewiring algorithm 244–245
 Bowen shadow lemma 138
 brain cell microenvironment (extracellular fluid) 527–528
 brain noise variance and correlation scaling 50–55
 branching parameter 17, 178
 branching process
 – Experimental link to avalanches 17–20, 31, 34, 177–188
 – Model 365–367, 373–387, 403–405, 429–431
 BTW sandpile model 12, 262–263

C

- cellular automata (CA) 5, 7, 30, 154
 - random cellular automata on lattice 158–159
 - statistical characterization of critical dynamics 163–164
- chaos theory 6
- chaotic itinerancy 193–194
- chimera 91–92
- codimension, of bifurcation 394–395, 473
- coherence potentials 7, 30–33
- combined mean-field equations simulation 470–471
- complex networks 509. See also critical dynamics in complex network
 - decision-making model (DMM) 510–514
 - inflexible minorities 518
 - temporal complexity 517–518
 - topological complexity 514–516
- complexity management 502
- conditional density 197–198
- conditional Lyapunov exponents (CLEs) 205
 - critical slowing 207–210
 - generalized synchrony 205–206
- connectivity versus functional collectivity 60–62
- continuous performance tasks (CPTs) 106
- control parameter 70, 393
- cooperation-induced (CI) synchronization 485–486, 493
- coordination dynamics (CD) 67–68
 - beyond analogy 74–75
 - bimanual coordination 75–76
 - biological coordination 72–74
 - critical fluctuations 81–82
 - critical slowing down 80–81
 - fluctuations enhancement 81
 - criticality, timescales, and related factors 82–84
 - mesoscopic protectorates 92–93
 - neural field modeling of multiple states and phase transitions in brain 88–89
 - nonequilibrium phase transitions in human brain 87–88
 - study of matter 68–72
 - symmetry and phase transitions 76–80
 - symmetry breaking and metastability 84–86
 - transitions, transients, chimera, and spatiotemporal metastability 89–90
 - coordinative structure 73
 - bimanual coordination 75–76
 - correlation length 52–55
 - cortex
 - coherence potential 30–32
 - critical dynamics 5–7
 - cortex design principles supporting critical neuronal cascades 8–11
 - study through local perturbations 7
 - neuronal avalanches 11, 23
 - as cascades of cascades 20–23
 - cortical oscillations 23–28
 - dynamics 23–29
 - functional architecture, and coherence potentials 33–36
 - linking of avalanche size to critical branching 17–20
 - neuronal activity unbiased concatenation into spatiotemporal patterns 11–15
 - power law 15–17
 - specific to cortex superficial layers 17
 - cortical networks peak variability and optimal performance 335–336
 - cortex dynamics high entropy functional implications 343–344
 - fluctuations are highest near criticality 336
 - high variability and non-random 342–343
 - phase synchrony variability 339–342
 - spatial activity patterns variability 338–339
 - cortical networks with lognormal synaptic connectivity 403–404
 - bistable states in clustered network 412–413
 - critical dynamics in neuronal wiring development 404–405
 - local clustering structure 410–412
 - SSWD networks
 - possible implications for neuronal avalanches 413–414
 - recurrent networks generating optimal intrinsic noise 409–410
 - stochastic resonance by highly inhomogeneous synaptic weights on spike neurons 405–408
 - critical brain dynamics 43, 45
 - complex spontaneous brain activity 46–47
 - consequences 60
 - connectivity versus functional collectivity 60–62
 - network approach 62
 - river beds, floods, and fuzzy paths 63
 - problem definition 43–45
 - spatiotemporal brain dynamics 55–56
 - fMRI 56–57
 - phase transition 58–59
 - variability and criticality 59
 - statistical signatures 47–48

- – brain noise variance and correlation scaling 50–55
 - – search for power laws in density functions 48–50
 - cortex design principles supporting critical neuronal cascades 8–11
 - critical dynamics in complex networks
 - branching processes in complex networks 373–378
 - critical regime 383–387
 - subcritical regime 378–381
 - supercritical regime 381–382
 - critical branching process 365–367
 - network description and properties 367–368
 - degree correlations 370–372
 - degree distribution 369–370
 - largest eigenvalue and corresponding eigenvector 372–373
 - network representation by adjacency matrix 368
 - node degrees 368–369
 - critical exponents, universality class, and thermodynamic temperature 319–320
 - finite-size scaling (FSS) 324–325, 327–329
 - neuronal avalanche thermodynamic properties study at different scales 325–330
 - thermodynamic quantities at critical point and neuronal interpretations 320–324
 - critical networks and response to stimuli 347, 351
 - separation of time scales 351
 - connection with neuronal avalanches 350
 - phase transition in simple model 347–349
 - prediction of theory 352
 - dynamic range enhancement 354–355
 - nonlinear collective response and maximal dynamic range at criticality 355
 - self-regulated amplification via excitable waves 352–354
 - critical oscillations model (CROS) 310
 - producing neuronal avalanches with balanced Ex/In connectivity 311–313
 - producing oscillations with LRTC 313–315
 - critical slowing 80–81, 191, 399
 - active inference neurobiological implementation 199–202, 204–205
 - perception and predictive coding 202–204
 - birdsong, attractors, and critical slowing 211, 221, 223
 - perception 219–221
 - – perceptual categorization 214–216
 - – perceptual instability and switching 216–219
 - stimulus generation and generative model 213–214
 - synthetic avian brain 212–213
 - free energy principle 196–197, 199
 - action and perception 197–198
 - maximum entropy principle and Laplace assumption 198–199
 - itinerant dynamics 193
 - – chaotic itinerary 193–194
 - – heteroclinic cycling 194
 - multistability and switching 194–195
 - stability and critical slowing 195–196
 - neurodynamics 191–192
 - – overview 192–193
 - self-organized instability 205, 210–211
 - conditional Lyapunov exponents (CLEs) and generalized synchrony 205–206
 - critical slowing and conditional Lyapunov exponents 207–210
- d**
- Dale's principle 426
 - decision-making model (DMM) 487–489, 504, 505, 509–519, 521
 - intermittency 489–492
 - response to perturbation 492–493
 - detrended fluctuation analysis (DFA) 295, 302–307
 - amplitude envelope extraction 305
 - applied to neuronal oscillations 304
 - as biomarker of neurophysiological disorder 309–310
 - filter design 305
 - filter temporal integration effect determination 305
 - signals preprocessing 304
 - directed percolation 468
 - disordered state 322
 - downstates 273–274
 - drift-diffuse equation 440
 - dynamical correlation 244
 - dynamically generated complex topology (DGCT) 514–516, 521
- e**
- edge degree correlations 371
 - effective circuits 61
 - effective feed-forward system 479
 - E-I neural network 475
 - balanced amplification 477–479

- E–I neural network (*contd.*)
 - combined mean-field equations simulation 477
 - Markov processes analysis and simulation 479–481
 - modifiable synapses 475, 477
- electroencephalography (EEG) 109–111, 178, 187, 288, 304, 307
- electron–cyclotron resonances 143
- epidemic threshold 395
- Erdős–Rényi random graphs and networks 348, 350, 378, 380, 382
- ergodicity 194, 196
- Eurich model of criticality 417–418
 - model description 418–419
 - simulations and analysis 419–420
- event-related oscillations (EROs) 141
- excitatory postsynaptic potential (EPSP) 403, 405–409, 414
- extended criticality (EC) 487, 494

- f**
- first-order phase transition 83
- fluctuation–dissipation theorem 80
- Fokker–Planck equation 82, 407, 439, 441, 455
 - numerical evolution 441–442
- fractional Brownian motion (fBm) 298
- fractional Gaussian noise (fGn) 298
- free energy principle 196–197, 199
 - action and perception 197–198
 - maximum entropy principle and Laplace assumption 199
- Freeman K-models 154–155
- functional magnetic resonance imaging (fMRI) 48, 49, 51, 53, 56–57, 61, 87, 89, 114, 187, 274, 370, 486
- fuzzy paths, river beds, and floods 63

- g**
- Galton–Watson branching processes 17, 429–430
- gap junctions and neuroglia 525
- Gibbs–Boltzmann distribution 321
- Gibbs energy 198, 208
- Gillespie algorithm 481
- Gutenberg–Richter law 24

- h**
- Hall effect 143
- Hebbian learning effects 170–173, 236, 497
- Hebbian weights 475–476
- heteroclinic channels 86
- heteroclinic cycling 194
- highly optimized tolerance (HOT) 530
- Hilbert transform 305, 341
- HKB model 77–79, 81–82, 85, 87
- Hodgkin–Huxley (HH) model 256, 257
- homeokinetics 69
- homeostatic plasticity and criticality 429
 - branching processes 429–430
 - self-organization by long-term plasticity 430–431
 - spike-time-dependent plasticity and network structure 431–433
- homeostatic system 477
- hysteresis cycle 470

- i**
- identical synchronization 205
- ignition 192, 216
- independent component analysis (ICA) 178
- Ising model 60
- itinerant dynamics 193
 - chaotic itinerancy 193–194
 - heteroclinic cycling 194
 - multistability and switching 195
 - stability and critical slowing 195–196

- j**
- Jacobian Matrix 480

- k**
- Kaplan–Yorke conjecture 206
- kinetic dynamo problem 131
- Kolmogorov entropy 140

- l**
- Langevin equation 82, 490, 493
- Laplace code 200
- leaky integrate-and-fire (LIF) networks 439
 - heterogeneous synapses 454
 - – results for realistic synaptic distributions in absence of recurrence and STSD 456–458
 - – synaptic depression 458–459
 - – synaptic weight distribution influence 454–455
 - – voltage distributions 455–456
 - analytical solution 440–441
 - fixed-point analysis 442–444
 - Fokker–Plack equation numerical evolution 441–442
 - biologically realistic networks 449–452
 - robustness of results 452
 - up- and down-states 444–448
- LHG model 420
 - mean-field approximation 423–424

- model description 420–423
- network structure, leakage, and inhibition 424–427
- synaptic facilitation 427–429
- linear response theory (LRT) 486
- local field potential (LFP) 11–14, 17, 31, 326–328, 338, 341, 358, 414, 438
- locally tree-like networks 374
- long-range temporal correlations (LRTCs) 106–109, 115–117, 294, 305, 307, 309–310
- scaling laws interindividual variability
 - mechanistic insights 118–119
- physiological substrates 111
- – infra-slow potential fluctuations 111–113
 - slow BOLD signal fluctuations in resting-state networks 114
 - slow fluctuations in oscillation amplitudes and scalp potentials 113
- Lorenz attractor 211–213
- Lotka–Volterra equations 478, 479, 481
- Lyapunov exponents 195–196
 - conditional (CLEs) 205
 - critical slowing 207–210
 - generalized synchrony 205–206

- m**
- magnetic dynamos 143
- magnetic field induction and turbulence 130–139
- magnetocardiogram (MCG) 178
- magnetoencephalography (MEG) 49, 89, 109–111, 177–179, 183, 186–188
- magnetohydrodynamic approach 127–128
- autonomous, intermittent, hierarchical motions, from brain proteins fluctuations to emergent magnetic fields 129–130
- localization of regions of neocortical pyramidal cell networks 139–142
- magnetic field induction and turbulence 130–139
- majority rule 159–160
- Markov process 469
 - analysis and simulation 479–481
 - combined Markov processes simulation 471–472
- Mauthner cells 142
- maximum entropy principle and Laplace assumption 198–199
- mean-field approximation 423–424, 443–444
- memory-less process 299
- Milnor attractors 193–194, 207, 208

- Mittag–Leffler function model cooperation 494–496
- cooperation effort in fire-and-integrate neural model 496–501
- Morlet wavelet transformations 134–135
- multilevel criticality 315–316
- multiple realization 530
- multistability and switching 194–195

- n**
- negative local field potential (nLFP) 12–20, 22, 23, 27, 31, 33, 326
- negative log evidence 197
- nervous system criticality
 - critical-state dynamics empirical evidence in neuronal systems 108–109
 - human task performance 106–108
 - magnetoencephalography and electroencephalography (MEG/EEG) 109–111
- neuronal avalanches, LRTC, and oscillations 117–118
 - scaling laws interindividual variability
 - mechanistic insights 118–119
- neuronal scaling laws and interindividual variability 115–117
- slow neuronal fluctuations 111
- – infra-slow potential fluctuations 111–113
 - slow BOLD signal fluctuations in resting-state networks 114
 - slow fluctuations in oscillation amplitudes and scalp potentials 113
- neural dynamics 485–487, 493–494
 - avalanches and entrainment 486–504
 - decision-making model (DMM) 487–489
 - – intermittency 489–492
 - – response to perturbation 492
 - Mittag–Leffler function model cooperation 494–496
 - – cooperation effort in fire-and-integrate neural model 496–501
- neural field modeling of multiple states and phase transitions in brain 88–89
- neural firing cooperation (NFC) 487, 496, 504–505
- neuromodulation dynamics 525
 - discussion 529–532
 - gap junctions and neuroglia 525–527
 - processes 528–529
- neuronal avalanches
 - Critical exponents 319–320
 - Definition 7, 11–23
 - Detrended fluctuation analysis 312–314

- neuronal avalanches (*contd.*)
 - Earthquakes 23
 - Finite-size scaling 12, 18, 182, 234–241, 324–325, 431
 - Functional architecture 33–36, 403, 454–455
 - In humans 16, 58, 106, 109, 115–117, 177–188
 - – Scaling laws 118–119
 - Learning 280–283
 - Model SOC 229–252, 273–279, 393–399, 417, 430–433, 437–439, 465–468
 - Omori-Utsu law 21, 24
 - Optimization 28–30, 314, 335–344, 352–357
 - Oscillations 23–28, 117–118, 310–315
 - Plasticity 233–252, 273–278, 431–433
 - Power law
 - sizes 12, 15–17, 20, 21, 24–26, 58–59, 107, 251, 279, 312, 326, 340, 360, 386, 406, 413, 419–423, 426–429, 448–451, 454, 472, 479, 503
 - in spatial correlations 330
 - – lifetimes 25, 207, 448, 491
 - – temporal recurrences 21, 24, 284–287, 314, 360, 386
 - STDP 9–10, 431–433, 470
 - Synfire chains 9–11, 405
 - Temporal organization 20–23, 283–288, 359–360
 - Under sampling effects 358–359
 - Up and Down states 444–449, 472
 - neuronal synchronization 8, 9
 - neuroperturbation 154, 156–157, 173
 - mathematical formulation
 - double-layered lattice 161–162
 - random cellular automata on lattice 158–159
 - – statistical characterization of critical dynamics of cellular automata 163–164
 - – two-dimensional lattice with rewiring 160–161
 - – two double-layered lattices coupling 162
 - – update rules 159–160
 - motivation to neurodynamics 157–158
 - node degrees 368–369
 - correlations 370–371
 - nontrivial scaling properties 357
- o**
 - Omori law 21–22, 24
 - Omori sequences 22
 - ordered state 322
- order parameters 70
- Oseledets Theorem 206, 209
- p**
 - Perron–Frobenius Theorem 372
 - phase synchrony variability 339–342
 - phase transition in simple model 347–349
 - plastic adaptation 276–277
 - power law 15–17, 136, 277, 297, 413, 423, 425–426, 437
 - cascade-size distributions 181–182
 - in density functions 48–50
 - power spectra 278–280
 - power spectral density (PSD) 260, 262
 - productivity law 24
- r**
 - random graph theory (RGT) 154, 157
 - random-walk fluctuations 299
 - rank vector entropy 128
 - rapid transition processes (RTPs) 505
 - recognition density. *See* conditional density
 - renormalization group 69, 486
 - resting-state networks (RSNs) 49, 61
- s**
 - saddle homoclinic–orbit bifurcation 474
 - scale-free networks 370
 - scale-free systems 293, 295
 - second-order phase transition 83
 - self-affinity 294–298
 - self-organized criticality (SOC) 5, 25–28, 153, 158, 195–196, 227–228, 288, 289, 293, 397, 417, 420. *See also* leaky integrate-and-fire (LIF) networks
 - nonconservative neurons; single neuron response fluctuations; self-organized near-criticality (SONC)
 - avalanche dynamics in neuronal systems
 - – existing models 229–231
 - – experimental results 228
 - mechanisms in adaptive networks
 - – basic considerations 393–395
 - – implications for information processing 399–400
 - – self-organization mechanism 397–399
 - – toy model 395–397, 399–400
 - simple models for adaptive neural networks
 - – activity-dependent criticality 239–241
 - – Boolean state model 243–249
 - – correlation as criterion for rewiring 234–237
 - – model definitions 239

- – node activity and connectivity regulation 231, 233–234
 - – response to external perturbations 249–251
 - – thermal noise 241–243
 - – transition from spins to Boolean node states 238
 - self-organized instability 205, 210–211
 - conditional Lyapunov exponents (CLEs) and generalized synchrony 205–206
 - critical slowing and conditional Lyapunov exponents 207–210
 - self-organized near-criticality (SONC) 465–466
 - E-I neural network 475
 - – balanced amplification 477–479
 - – combined mean-field equations simulation 477
 - – Markov processes analysis and simulation 479–481
 - – modifiable synapses 475, 477
 - excitatory and inhibitory neural network dynamics 472–473
 - – Wilson–Cowan mean-field equations 473–475
 - neural network dynamics 466–468
 - – stochastic effects near critical point 468
 - neural network exhibiting self-organized criticality 468–470
 - combined Markov processes simulation 471–472
 - – combined mean-field equations simulation 470–471
 - separation of time scales 25, 350
 - Shannon entropy 140, 336, 339, 340, 343
 - short-term synaptic depression (STSD). *See* leaky integrate-and-fire (LIF) networks
 - nonconservative neurons
 - signal profile 298
 - signal-to-noise ratio (SNR) 304, 307
 - single neuron response fluctuations 255
 - adaptive rates and contact processes 263–265
 - experimental observations on excitability dynamics 257–261
 - neuronal excitability 255–257
 - SOC interpretation 261–263
 - skew product structure 205, 206
 - slow neuronal fluctuations 111
 - infra-slow potential fluctuations 111–113
 - slow BOLD signal fluctuations in resting-state networks 114
 - slow fluctuations in oscillation amplitudes and scalp potentials 113
 - social coordination spontaneous patterns 90
 - sparse-strong and weak-dense (SSWD) networks 405–407
 - possible implications for neuronal avalanches 413–414
 - recurrent networks generating optimal intrinsic noise 409–410
 - spatial activity patterns variability 338–339
 - spike-time-dependent plasticity (STDP) 9
 - and network structure 431–433
 - spiking model 310
 - spins to Boolean node states transition 238
 - ds transformation 132, 135, 137
 - stochastic effects near critical point 468
 - stochastic forces 80
 - stochastic resonance by highly inhomogeneous synaptic weights on spike neurons 405–408
 - strudels 134, 136
 - subcritical regime 10, 44, 79, 119, 237, 247–251, 313, 337–340, 349–351, 366, 378, 419–429, 443–448, 492
 - supercritical regime 10, 19, 45, 50, 238, 247–251, 313, 337–351, 365–366, 381–387, 419–429, 489–492
 - susceptible-infected-susceptible (SIS) model 395
 - switching time 82
 - synaptic plasticity 274
 - synaptic pruning 276
 - synfire chains 9, 405
 - synthetic aperturemagnetometer (SAM) 139–140
- t**
- thermodynamic model of criticality 153–154
 - broadband chaotic oscillations
 - – Hebbian learning effects 170–173
 - – intermittent synchronization of oscillations in three coupled double arrays 170
 - – two double arrays dynamics 167–170
 - coupled hierarchical lattices critical regimes
 - – 2D lattices dynamic behavior with rewiring 164
 - – narrow band oscillations in coupled excitatory–inhibitory lattices 165–167
 - hierarchical brain models principles
 - – Freeman K-models 154–155

- thermodynamic model of criticality (*contd.*)
 - neurodynamics basic building blocks 155–157
 - neuropercolation approach motivation to neurodynamics 157–158
 - neuropercolation mathematical formulation
 - double-layered lattice 161–162
 - random cellular automata on lattice 158–159
 - statistical characterization of critical dynamics of cellular automata 158–164
 - two-dimensional lattice with rewiring 160–161
 - two double-layered lattices coupling 162
 - update rules 159–160
- threshold stimulus-detection tasks (TSDTs) 106–108
- timescale of interest 498
- toy model 395–397, 399–400
- transcranial magnetic stimulation (TMS) therapies 144
- transcritical bifurcation 397
- transitions to criticality in neural systems with dynamic synapses, 417
- criticality by homeostatic plasticity 429
 - branching processes 429–430
 - self-organization by long-term plasticity 430–431
- spike-time-dependent plasticity and network structure 431–433
- Eurich model of criticality 417–418
- model description 418–419
- simulations and analysis 419–420
- LHG model 420
- mean-field approximation 423–424
- model description 420
- network structure, leakage, and inhibition 424–427
- synaptic facilitation 427–429
- turbulent eddies 136

- u**
- universality class 468. See also critical exponents, universality class, and thermodynamic temperature
- unweighted adjacency matrix 368
- up- and down-states 444–446

- v**
- van Kampen system-size expansion 468, 480
- variational free energy 197
- Vogels formulation 470

- w**
- wavelet transforms 305
- white noise 295
- Wilson–Cowan mean-field equations 473–475, 477–479